Chen Zhang
Jeffrey L. Myers
Editors

Atlas of Lung Pathology

Springer

Atlas of Anatomic Pathology

Series Editor:

Liang Cheng
Indianapolis, Indiana, USA

This Atlas series is intended as a "first knowledge base" in the quest for diagnosis of usual and unusual diseases. Each atlas will offer the reader a quick reference guide for diagnosis and classification of a wide spectrum of benign, congenital, inflammatory, nonneoplastic, and neoplastic lesions in various organ systems. Normal and variations of "normal" histology will also be illustrated. Each atlas will focus on visual diagnostic criteria and differential diagnosis. It will be organized to provide quick access to images of lesions in specific organs or sites. Each atlas will adapt the well-known and widely accepted terminology, nomenclature, classification schemes, and staging algorithms. Each volume in this series will be authored by nationally and internationally recognized pathologists. Each volume will follow the same organizational structure. The first Section will include normal histology and normal variations. The second Section will cover congenital defects and malformations. The third Section will cover benign and inflammatory lesions. The fourth Section will cover benign tumors and benign mimickers of cancer. The last Section will cover malignant neoplasms. Special emphasis will be placed on normal histology, gross anatomy, and gross lesion appearances since these are generally lacking or inadequately illustrated in current textbooks. The detailed figure legends will concisely summarize the critical information and visual diagnostic criteria that the pathologist must recognize, understand, and accurately interpret to arrive at a correct diagnosis. This book series is intended chiefly for use by pathologists in training and practicing surgical pathologists in their daily practice. The atlas series will also be a useful resource for medical students, cytotechnologists, pathologist assistants, and other medical professionals with special interest in anatomic pathology. Trainees, students, and readers at all levels of expertise will learn, understand, and gain insights into the complexities of disease processes through this comprehensive resource. Macroscopic and histological images are aesthetically pleasing in many ways. This new series will serve as a virtual pathology museum for the edification of our readers.

More information about this series at http://www.springer.com/series/10144

Chen Zhang • Jeffrey L. Myers
Editors

Atlas of Lung Pathology

Springer

Editors
Chen Zhang
Department of Pathology and Laboratory Medicine
Indiana University School of Medicine
Indianapolis, IN
USA

Jeffrey L. Myers
Department of Pathology
University of Michigan
Ann Arbor, MI
USA

Atlas of Anatomic Pathology
ISBN 978-1-4939-8687-3 ISBN 978-1-4939-8689-7 (eBook)
https://doi.org/10.1007/978-1-4939-8689-7

Library of Congress Control Number: 2018951998

© Springer Science+Business Media, LLC, part of Springer Nature 2018
This work is subject to copyright. All rights are reserved by the Publisher, whether the whole or part of the material is concerned, specifically the rights of translation, reprinting, reuse of illustrations, recitation, broadcasting, reproduction on microfilms or in any other physical way, and transmission or information storage and retrieval, electronic adaptation, computer software, or by similar or dissimilar methodology now known or hereafter developed.
The use of general descriptive names, registered names, trademarks, service marks, etc. in this publication does not imply, even in the absence of a specific statement, that such names are exempt from the relevant protective laws and regulations and therefore free for general use.
The publisher, the authors, and the editors are safe to assume that the advice and information in this book are believed to be true and accurate at the date of publication. Neither the publisher nor the authors or the editors give a warranty, express or implied, with respect to the material contained herein or for any errors or omissions that may have been made. The publisher remains neutral with regard to jurisdictional claims in published maps and institutional affiliations.

This Springer imprint is published by the registered company Springer Science+Business Media, LLC part of Springer Nature.
The registered company address is: 233 Spring Street, New York, NY 10013, U.S.A.

To my mentor, colleague, and lifelong friend, Anna-Luise A. Katzenstein, who taught me most of what I know but only a fraction of what she knows!

To countless pathology colleagues like Tom Colby, Henry Tazelaar, Marie-Christine Aubry, and Kris Unni. To generations of fellows and residents who taught me far more than I taught them, and to an amazing community of non-pathology colleagues who so generously served as teachers and tutors to fill in the gaps.

And most importantly to my wife, who never seems to tire of offering loving support.

Jeffrey L. Myers

To my family for their constant support and encouragement.

Chen Zhang

Series Preface

One Picture Is Worth Ten Thousand Words

— Frederick Barnard, 1927

Remarkable progress has been made in anatomic and surgical pathology during the last 10 years. The ability of surgical pathologists to reach a definite diagnosis is now enhanced by immunohistochemical and molecular techniques. Many new clinically important histopathologic entities and variants have been described using these techniques. Established diagnostic entities are more fully defined for virtually every organ system. The emergence of personalized medicine has also created a paradigm shift in surgical pathology. Both promptness and precision are required of modern pathologists. Newer diagnostic tests in anatomic pathology, however, cannot benefit the patient unless the pathologist recognizes the lesion and requests the necessary special studies. An up-to-date Atlas encompassing the full spectrum of benign and malignant lesions, their variants, and evidence-based diagnostic criteria for each organ system is needed. This Atlas is not intended as a comprehensive source of detailed clinical information concerning the entities shown. Clinical and therapeutic guidelines are served admirably by a large number of excellent textbooks. This Atlas, however, is intended as a "first knowledge base" in the quest for definitive and efficient diagnosis of both usual and unusual diseases.

The *Atlas of Anatomic Pathology* is presented to the reader as a quick reference guide for diagnosis and classification of benign, congenital, inflammatory, nonneoplastic, and neoplastic lesions organized by organ systems. Normal and variations of "normal" histology are illustrated for each organ. The Atlas focuses on visual diagnostic criteria and differential diagnosis. The organization is intended to provide quick access to images and confirmatory tests for each specific organ or site. The Atlas adopts the well-known and widely accepted terminology, nomenclature, classification schemes, and staging algorithms.

This book series is intended chiefly for use by pathologists in training and practicing surgical pathologists in their daily practice. It is also a useful resource for medical students, cytotechnologists, pathologist assistants, and other medical professionals with special interest in anatomic pathology. We hope that our trainees, students, and readers at all levels of expertise will learn, understand, and gain insight into the pathophysiology of disease processes through this comprehensive resource. Macroscopic and histological images are aesthetically pleasing in many ways. We hope that the new series will serve as a virtual pathology museum for the edification of our readers.

Indianapolis, IN, USA — Liang Cheng

Preface

The surgical pathology of lung and pleural diseases has evolved substantially since the earliest days in which Averill Liebow, Charles Carrington, and others gave birth to the seminal observations that framed pulmonary pathology as a subspecialty discipline. The principal objective of this Atlas is to provide pathologists in training as well as experienced practitioners an easy-to-use practical diagnostic guide for lesions involving the lung and pleura. This Atlas may also serve as a good resource for clinicians interested in the histopathologic features that define the entities that afflict their patients. It covers a breadth of common problems likely to cross your microscope but without a level of detail likely to satisfy a desire for deep knowledge of their biology. The 14 chapters begin with a brief overview of normal histology before moving on to incidental findings followed by nonneoplastic and finally neoplastic diseases. Each chapter begins with a heading outline to summarize the contents. Individual diseases include a brief introduction followed by gross photographs for selected entities and multiple photomicrographs at different magnifications with detailed legends describing the findings. The introductory narratives are intentionally concise, including only essential clinical and radiological information and key pathologic features. Detailed descriptions of pathologic findings are found in the figure legends.

The emphasis in this book is on the histologic diagnosis of diseases using routinely stained slides as the foundation with a focus on high-quality hematoxylin-eosin-stained sections. Gross illustrations are included for those entities in which gross examination may play an important role in diagnosis. Illustrations of immunohistochemical stains are limited to those that are diagnostically relevant and/or necessary for certain tumor categories.

We hope that pathologists and practitioners at every level of experience will find this Atlas useful in evaluating the sorts of lung and pleural diseases likely to be encountered in any busy pathology practice.

Indianapolis, IN, USA — Chen Zhang
Ann Arbor, MI, USA — Jeffrey L. Myers

Acknowledgments

We would like to acknowledge Dr. Lindsay A. Schmidt for her initial efforts getting this project started—were it not for Lindsay, this project would not have seen the light of day. We also would like to thank Dr. Oscar W. Cummings for allowing us to take photos of his teaching collections. And finally we are grateful to the referring pathologists and non-pathology providers who have entrusted their patients to us in consultation.

Contents

1 **Normal Structures and Common Artifacts** 1
Chen Zhang and Jeffrey L. Myers

2 **Incidental Findings and Lesions of Limited Clinical Significance** 7
Chen Zhang and Jeffrey L. Myers

3 **Pediatric Disorders** 13
Chen Zhang and Jeffrey L. Myers

4 **Infectious Diseases** 31
Chen Zhang and Jeffrey L. Myers

5 **Diseases of Cartilaginous and Noncartilaginous Airways** 65
Chen Zhang and Jeffrey L. Myers

6 **Diffuse Nongranulomatous Lung Disorders** 87
Chen Zhang and Jeffrey L. Myers

7 **Noninfectious Diffuse Granulomatous Lung Diseases** 137
Chen Zhang and Jeffrey L. Myers

8 **Transplant-Related Disorders** 147
Chen Zhang and Jeffrey L. Myers

9 **Pneumoconiosis** 155
Chen Zhang and Jeffrey L. Myers

10 **Pulmonary Vascular Diseases** 165
Chen Zhang and Jeffrey L. Myers

11 **Pulmonary Lymphoproliferative Diseases** 181
Chen Zhang and Jeffrey L. Myers

12 **Benign Lung Neoplasms** 203
Chen Zhang and Jeffrey L. Myers

13 **Lung Carcinoma** 219
Chen Zhang and Jeffrey L. Myers

14 **Malignant Nonepithelial Lung and Pleural Neoplasms** 255
Chen Zhang and Jeffrey L. Myers

Index 281

Contributors

Jeffrey L. Myers Department of Pathology, Michigan Medicine, Ann Arbor, MI, USA

Chen Zhang Department of Pathology and Laboratory Medicine, Indiana University School of Medicine, Indianapolis, IN, USA

List of Figures

Fig. 1.1 Normal lung. Gross photograph of a peripheral portion of normal lung. On the cut surface, the tan brown spongy lung parenchyma is composed of secondary lobules in which multiple acini are aggregated. Proximal acinar structures are clustered in the center, and distal alveolar spaces are concentrated at the periphery adjacent to the thin fibrous interlobular septa that separate the lobules. The airways and blood vessels are barely visible. The outer surface of the lung is lined by the visceral pleura (upper left)

Fig. 1.2 Normal bronchus. (**a**) Low-magnification photomicrograph of a main stem bronchus showing bronchial wall cartilage and submucosal seromucous glands. (**b**) High-magnification photomicrograph showing bronchial epithelium composed of ciliated, pseudostratified, columnar epithelium with scattered mucin-secreting cells (goblet cells). (**c**) High magnification of the submucosal glands consisting of mixed serous and mucous cells

Fig. 1.3 Normal terminal bronchiole. Intermediate magnification view of a normal bronchovascular bundle. The bronchiole (left) is a small, noncartilaginous airway lined by columnar respiratory epithelial cells with a muscular wall and without intervening submucosal glands. The bronchiole is accompanied by a small muscular pulmonary artery (right) of similar caliber. Associated connective tissue and lymphatic spaces (asterisk) compose the bronchovascular bundle

Fig. 1.4 Intermediate-magnification photomicrograph showing the respiratory bronchiole (RB) and the associated alveolar duct (AD). Note the transition from the respiratory epithelium lining the respiratory bronchiole to the flattened alveolar epithelium of the alveolar duct

Fig. 1.5 High-magnification photomicrograph of a respiratory bronchiole. The epithelium is still predominantly ciliated but more cuboidal in shape compared with the columnar pseudostratified epithelium in the larger airway in Fig. 1.2b. Mucous cells or goblet cells become rare in respiratory bronchioles with a relative increase in nonciliated, nonmucinous Clara cells. The bronchiole wall consists of fibrous tissue and an incomplete smooth muscle layer

Fig. 1.6 High-magnification photomicrograph of normal alveoli. The alveolar septa are very thin and consist of flattened alveolar epithelium (pneumocytes) and delicate capillaries

Fig. 1.7 Photomicrographs showing pleural and chest wall soft tissues in transbronchial biopsies. (**a**) Fragments of mesothelium-lined pleural tissue and mediastinum/chest wall adipose tissue are seen in a transbronchial biopsy. (**b**) Chest wall skeletal muscle and adipose tissue immediately adjacent to normal lung parenchyma in a transbronchial biopsy representing an unintended procedural artifact

Fig. 1.8 Low-magnification photomicrograph showing artifactually collapsed lung and intra-alveolar hemorrhage. Mechanically compressed lung may mimic interstitial lung disease as a result of nonspecific thickening of collapsed interstitial structures; finding normal lung adjacent to the collapsed focus is helpful in sorting out the problem. Lack of hyperplastic alveolar pneumocytes is another helpful feature

in distinguishing this artifact from interstitial lung disease. Procedure-related hemorrhage is distinguished from clinically significant intra-alveolar hemorrhage by the lack of fibrin, organizing spindle cells, hemosiderin, and associated secondary interstitial abnormalities

Fig. 1.9 "Pseudolipids," also termed "bubble artifact," is a processing artifact that may mimic exogenous lipid pneumonia. This artifact occurs commonly in mechanically compressed lung parenchyma, especially in areas of hemorrhage, edema, or inflammation. Lack of foreign body giant cells and other aspiration-related changes are the keys to recognizing "pseudolipids"

Fig. 2.1 High-magnification photomicrograph showing corpora amylacea within an alveolar space in normal lung. It is a round, eosinophilic structure consisting of concentric lamellae and spoke-like structures radiating from the center. It is partially rimmed by alveolar macrophages. Corpora amylacea have no known significance but are more prominent in older patients. Their origin is unknown. It is important not to confuse them with aspirated foreign materials

Fig. 2.2 Meningothelial-like nodule (MLN). (**a**) Intermediate-magnification view of characteristic stellate-shaped nodule in which the interstitium is expanded by whorls of bland epithelioid cells arranged in a nested growth pattern. The nodules vary in size, but they are usually small and easily missed; missing them has no diagnostic consequence, and they need not be routinely noted in autopsy or surgical reports. The background lung is unremarkable. (**b**) At high magnification, the nodule is composed of uniform epithelioid cells with bland, round to oval nuclei, abundant amphophilic cytoplasm, and indistinct cell borders. The cells usually stain for epithelial membrane antigen (EMA) and are negative for cytokeratins, TTF1, and neuroendocrine markers (not shown). The morphologic and immunohistochemical features closely resemble meningothelium. (**c**) Rarely, MLNs can be numerous and cause a form of diffuse lung disease referred to as "diffuse meningotheliomatosis," as illustrated in this surgical lung biopsy

Fig. 2.3 Carcinoid tumorlet. (**a**) Low-magnification photomicrograph shows a well-demarcated cellular nodule surrounded by normal lung. The lesion is by definition less than 5 mm in greatest dimension. (**b**) At high magnification, the nodule is composed of uniform, oval to elongated epithelioid cells with finely dispersed ("salt and pepper") nuclear chromatin. These lesions stain strongly positive for neuroendocrine markers such as synaptophysin and chromogranin (not shown) and are distinguished from typical carcinoid tumors mainly by their size (less than 5 mm) and location (peribronchiolar interstitium) of the lesion

Fig. 2.4 Intermediate-magnification photomicrograph illustrating neuroendocrine cell hyperplasia. Neuroendocrine cell hyperplasia commonly accompanies carcinoid tumorlets and is characterized by a proliferation of neuroendocrine cells distributed in a pagetoid fashion within the respiratory epithelium of a bronchiole (top half of photomicrograph). The lumina of affected bronchioles may be narrowed by a pattern of concentric fibrosis characteristic of constrictive (obliterative) bronchiolitis (lower left). Diffuse idiopathic neuroendocrine cell hyperplasia (DIPNECH) is a rare disease in which the combination of neuroendocrine cell hyperplasia and constrictive bronchiolitis is affiliated with progressive airflow limitation. Carcinoid tumorlets and neuroendocrine cell hyperplasia are common incidental findings in resection specimens harboring carcinoid tumors and should not be overdiagnosed as DIPNECH

Fig. 2.5 Nodular metaplastic ossification (osseous metaplasia). A single focus of branching woven bone is present within an area of fibrosis from a patient with usual interstitial pneumonia (UIP). This sort of osseous metaplasia is common in UIP but is not specific and can be seen in various histologic contexts, including relatively normal lung

Fig. 2.6 Dendriform ossification. In this photomicrograph multiple elongated, branching lamellar bone spicules are seen within the interstitium, which is in turn affected by a subtle pattern of mild, paucicellular fibroelastosis. The fibrosis sometimes associated with dendriform ossification often has this distinctive "aponeurosis-like" quality. Dendriform ossification may occur as an isolated finding, in which case it may not be affiliated with respiratory symptoms and is instead an incidental finding of little consequence. In other cases, however, this pattern of osseous metaplasia is more extensive and superimposed on a pattern of fibrosis that may resemble usual interstitial pneumonia and account for a syndrome of progressive lung disease

Fig. 2.7 Metastatic calcification is characterized by alveolar septal deposition of basophilic calcium particles. The alveolar structure is preserved with mild septal thickening. Metastatic calcification is a diffuse form of dystrophic calcification that is usually seen in patients with longstanding renal failure requiring hemodialysis

Fig. 2.8 Blue bodies are round, often fragmented, lamellated basophilic structures within alveolar macrophages. They are the breakdown products of cell metabolism and are of no clinical significance. Blue bodies contain calcium and are not polarizable. They should not be confused with aspirated particulates such as microcrystalline cellulose

Fig. 2.9 Megakaryocytes within the alveolar septa. High-magnification photomicrograph showing irregularly shaped and deeply basophilic megakaryocytes within the lumina of alveolar septal capillaries. They are common incidental findings in surgical lung biopsies and autopsies and are especially common in patients with sepsis, cardiovascular diseases, or metastatic malignancies

Fig. 2.10 Apical cap (fibroelastosis). (**a**) Low-magnification view of an upper lobe lung biopsy showing a subpleural zone of scarring. The underlying lung parenchyma is normal. (**b**) High-magnification view of the scarred area showing the distinctive elastotic collagen and mild chronic inflammation. The apical cap is a common incidental finding in the upper lobes but can also be seen in the superior segments of the lower lobes. In a few patients, apical caps present as mass-like lesions with radiologic features resembling malignancy. Because well-differentiated adenocarcinomas occasionally arise in this setting, small closed biopsies performed for a radiologic suspicion of malignancy that show only apical cap should be interpreted with caution

Fig. 2.11 Low-magnification photomicrograph showing round atelectasis. Round (also termed rounded) atelectasis occurs when fibrotic pleura retracts and invaginates into underlying lung parenchyma, causing a portion of the lung to collapse. The collapsed lung may mimic a mass radiologically and therefore be viewed as a potential "pseudoneoplasm"

Fig. 3.1 Intralobar pulmonary sequestration (bronchial atresia with systemic vascular connection) combined with features of congenital pulmonary airway malformation. (**a**) Gross photograph showing cut surface of a partially resected lung that is nearly completely replaced by a yellow-white solid cystic lesion. The lesion is well demarcated, and minimal remaining normal lung tissue is seen at the periphery of the specimen. A centrally located thick-walled feeding blood vessel (arrow) is identified. This example illustrates the overlap between intralobar sequestration and CPAMs. (**b**) Cross section of the identified feeding blood vessel confirms a systemic elastic artery

Fig. 3.2 Intralobar pulmonary sequestration combined with features of congenital pulmonary airway malformation. (**a**) Intermediate-magnification photomicrograph showing an area of the lesion illustrated in Fig. 3.1 characterized by back-to-back smaller bronchiolar type cysts. (**b**) High-magnification photomicrograph showing ciliated respiratory epithelial lining of maldeveloped parenchymal cysts

Fig. 3.3 Pulmonary sequestration. In this low-magnification photomicrograph showing a long-standing lesion, the cysts contain mucus admixed with inflammatory debris and macrophages. The lining epithelium is focally attenuated and flattened. The stroma is fibrotic, with abundant collagen deposition and focal osseous metaplasia (upper right)

Fig. 3.4 CPAM/congenital cystic adenomatoid malformation (CCAM), type 1. The cut surface of this surgical specimen shows multiple variably sized cysts separated by grossly normal lung parenchyma. The cyst walls are fibrotic with a smooth interior surface

Fig. 3.5 CPAM type 1. (**a**) Low-magnification view of section from the CPAM illustrated in Fig. 3.4 showing a large cyst lined by nonmucinous ciliated columnar epithelium. The cyst is located immediately next to normally developed lung parenchyma. (**b**) High-magnification view of cyst lining that is ciliated respiratory epithelium

Fig. 3.6 CPAM type 1 with mucinous epithelium, a potential precursor to mucinous adenocarcinomas with a lepidic architecture referred to historically as bronchioloalveolar carcinoma. (**a**) Low-magnification photomicrograph of the type 1 CPAM illustrated in Figs. 3.4 and 3.5 showing multiple variably sized cysts and bronchiole-like structures, some of which are lined by nonciliated mucinous columnar epithelium. (**b**) Higher-magnification photomicrograph demonstrates mixed respiratory and mucinous epithelium. The mucinous epithelium includes tall columnar cells with abundant apical mucin and bland basally located nuclei

Fig. 3.7 CPAM type 2 typically occurs in the first year of life and tends to be associated with other anomalies that account for poorer outcomes. (**a**) Low-magnification photomicrograph showing multiple small cysts (0.5–2 cm) scattered within relatively preserved distal lung parenchyma. (**b**) At higher magnification, the bronchiole-like cysts are lined by ciliated respiratory epithelium and surrounded by a thin, incomplete layer of smooth muscle resembling a bronchiole

Fig. 3.8 Congenital pulmonary overinflation (emphysema). (**a**) Low-magnification view of overinflated lung showing enlarged air spaces, thin alveolar septa, and preserved alveolar architecture. (**b**) High-magnification photomicrograph showing thin incomplete alveolar septa

Fig. 3.9 Pulmonary interstitial emphysema. Gross photograph showing the cut surface of a lung segment resected from a 7-week-old infant on mechanical ventilation for respiratory failure. The cut surface shows multiple air-filled cysts tracking along visceral pleura, interlobular septa, and bronchovascular bundles with compression of intervening parenchyma

Fig. 3.10 Pulmonary interstitial emphysema. (**a**) Low-magnification photomicrograph showing multiple linear air-filled spaces distributed within bronchovascular bundles and interlobular connective tissue. The lung parenchyma between the air spaces is compressed and shows procedure-related hemorrhage. (**b**) At higher magnification, an elongated air-filled interstitial space is located next to a bronchiole with procedure-related hemorrhage in the background. The air-filled space shows no lining epithelium and is instead partially lined by macrophages, including multinucleated giant cells. (**c**) High-magnification view of multinucleated giant cells lining an air-filled interstitial space

Fig. 3.11 Pulmonary lymphangiectasis secondary to congenital heart disease. The interlobular septum is widened by dilated lymphatic vessels. The dilated spaces follow lymphatic routes that may superficially resemble interstitial emphysema. Identifying the proteinaceous lymphatic fluid and flattened endothelial lining cells combined with the absence of multinucleated giant cells is helpful in making the distinction. The key to differentiating lymphangiectasis from diffuse lymphangiomatosis (see Fig. 3.15) is that the number of lymphatic spaces is not increased in the former

Fig. 3.12 Pulmonary lymphangiectasia. (**a**) In this example of long-standing pulmonary lymphangiectasia secondary to chronic heart failure, significant perilymphatic fibrosis is present. (**b**) An elastic stain shows lack of elastin within the vessel walls, a finding helpful in differentiating dilated lymphatics from blood vessels

Fig. 3.13 Diffuse pulmonary lymphangiomatosis. (**a**) Low-magnification photomicrograph shows marked expansion and distortion of interlobular septa by numerous irregular anastomosing lymphatic spaces. The number of lymphatic spaces is markedly increased compared to preservation of the normal number of lymphatic channels in lymphangiectasis (Figs. 3.11 and 3.12). (**b**) Intermediate-magnification photomicrograph showing complex anastomosing lymphatic channels lined by attenuated endothelial cells without cytologic atypia

Fig. 3.14 Pleuropulmonary blastoma, type I. Gross photograph shows cut surface of a portion of a large multiloculated cystic lesion within the pleura

Fig. 3.15 Pleuropulmonary blastoma, type I. (**a**) Low-magnification view demonstrates epithelial-lined cysts with a "cambium" layer of undifferentiated mesenchymal cells. (**b**) High-magnification view of cyst wall showing small and primitive mesenchymal cells. Note the ciliated respiratory epithelial lining of the cyst. (**c**) Another area of the same lesion in which the cyst wall shows only paucicellular fibrous stroma without neoplastic mesenchymal cells. This area by itself is indistinguishable from CPAM type 4, a term and concept that should be abandoned. This also serves as a reminder that adequate sampling and careful examination for areas of increased stromal cellularity are important when evaluating cystic lesions in infants and young children

Fig. 3.16 Pleuropulmonary blastoma. (**a**) Intermediate-magnification photomicrograph showing an area in which a portion of a cyst wall shows rhabdomyoblastic differentiation in neoplastic mesenchymal cells. (**b**) High-magnification view showing cytoplasmic striations typical of rhabdomyoblasts

Fig. 3.17 Pleuropulmonary blastoma, type III. (**a**) Low-magnification photomicrograph of type III pleuropulmonary blastoma showing a solid sheet of undifferentiated blastomatous tumor cells. (**b**) At high magnification, the tumor cells are relatively uniform, with high nuclear-to-cytoplasmic ratio, mild pleomorphism, and inconspicuous nucleoli

Fig. 3.18 Pleuropulmonary blastoma, type III. (**a**) Low-magnification view of a type III pleuropulmonary blastoma showing an area of stromal overgrowth with increased pleomorphism and focal rhabdomyosarcomatous differentiation. (**b**) High-magnification view of the rhabdomyosarcoma-like area showing tumor cells with enlarged, eccentric, pleomorphic nuclei and abundant eosinophilic cytoplasm

Fig. 3.19 Pleuropulmonary blastoma with chondrosarcomatous differentiation. (**a**) Low-magnification photomicrograph showing cartilage-like nodules within a cellular undifferentiated stroma. (**b**) High-magnification view of the cartilage-like nodule showing chondroid differentiation with enlarged atypical nuclei

Fig. 3.20 Fetal lung interstitial tumor (FLIT). (**a**) Low-magnification photomicrograph showing a well-circumscribed FLIT in which the neoplasm is separated from developmentally normal lung parenchyma (top left) by a fibrous capsule. (**b**) Intermediate-magnification view showing maldeveloped air spaces separated by septa that are markedly expanded by a uniform monolayer of cytologically bland mesenchymal cells. (**c**) High-magnification photomicrograph showing bland mesenchymal cells with round to oval-shaped nuclei, small capillary vessels, and an attenuated epithelial lining with cytologic features typical of type 2 pneumocytes

Fig. 3.21 Infantile hemangiomas have only rarely been reported as primary solitary lung masses. (**a**) Computed tomography (CT) scan of the chest of a 7-month-old girl shows an enhancing opacity occupying much of her left lower lobe. (**b**) Gross

photograph of the cut surface of her left lower lobectomy shows a circumscribed, soft, spongy pink mass that is sharply demarcated from normal-appearing lung parenchyma

Fig. 3.22 Infantile hemangioma. (**a**) Low-magnification photomicrograph of the tumor illustrated in Fig. 3.21 shows a highly vascularized neoplasm that is unencapsulated but sharply demarcated from adjacent lung tissue (bottom). (**b**) Higher-magnification photomicrograph shows distortion of alveolar walls by complex anastomosing capillaries lined by bland endothelial cells that were strongly positive for glucose transporter-1 (GLUT-1)

Fig. 3.23 Chronic pneumonitis of infancy. (**a**) Low-magnification photomicrograph of a surgical lung biopsy shows uniform thickening of alveolar septa with minimal architectural distortion. Alveolar spaces often contain proteinaceous exudates, macrophages, and cholesterol clefts resembling pulmonary alveolar proteinosis (PAP-like) in chronic pneumonitis of infancy. However, that feature was not seen in this example. (**b**) A high-magnification view shows expansion of alveolar septa by fibroblasts, myofibroblasts, and minimal collagen deposition with only rare inflammatory cells. Reactive pneumocyte hyperplasia is prominent

Fig. 3.24 Pulmonary interstitial glycogenosis. (**a**) Photomicrograph showing the uniform thickening of alveolar septa by bland-appearing mesenchymal cells. No significant inflammation or pneumocyte hyperplasia is present. (**b**) At high magnification, the thickened alveolar septa contain cells with bland round to oval nuclei and abundant clear to eosinophilic cytoplasm

Fig. 3.25 Pulmonary interstitial glycogenosis. (**a**) Photomicrograph of a periodic acid–Schiff (PAS) stained section shows abundant granular cytoplasmic staining of the mesenchymal cells within the alveolar septa. (**b**) The positive PAS staining within the cytoplasm is washed away following diastases digestion, which is indicative of glycogen deposition

Fig. 4.1 Acute bronchopneumonia. Low-magnification photomicrograph shows an exquisitely air-space-centered process in which acute inflammatory cells and fibrin fill the lumens of distal airways and air spaces. Alveolar septae are congested and focally disrupted, but the overall alveolar structure is preserved

Fig. 4.2 Acute bronchopneumonia. High-magnification photomicrograph shows that the air-space exudate is composed mainly of neutrophils with prominent karyopyknosis and karyorrhexis, histiocytes, and fibrin

Fig. 4.3 Acute bronchopneumonia. High-magnification photomicrographs showing bacterial colonies of the kind occasionally observed in acute bronchopneumonia on routine H&E (**a**) and GMS (**b**) stains

Fig. 4.4 Legionnaires' disease. (**a**) Low-magnification photomicrograph showing acute bronchopneumonia with prominent intra-alveolar fibrinous exudates in a patient with Legionnaires' disease. (**b**) Higher-magnification photomicrograph showing acute bronchopneumonia with prominent necrosis, an inflammatory infiltrate in which histiocytes predominate, and fibrin. (**c**) Intermediate-magnification view of autopsy findings in the same patient illustrating a combination of acute bronchopneumonia and diffuse alveolar damage with well-formed hyaline membranes, a finding characteristic of Legionnaires' disease in a subset of patients

Fig. 4.5 *Nocardia pneumonia*. (**a**) Low-magnification photomicrograph showing a patchy necrotizing acute bronchopneumonia forming circumscribed microabscesses with a vaguely granulomatous appearance. (**b**) Higher-magnification photomicrograph showing a vaguely granulomatous microabscess at higher magnification but without the giant cells, epithelioid macrophages, or associated non-necrotizing granulomas more typical of granulomatous infection. (**c**) High-magnification photomicrograph in which a tissue gram (Brown-Brenn) stain shows the filamentous bacteria typical of *Nocardia spp*.

Fig. 4.6 Actinomycosis. (**a**) Low-magnification photomicrograph showing patchy necrotizing acute bronchopneumonia with multifocal microabscesses. (**b**) Low-magnification photomicrograph from the same patient showing a macroscopic abscess with the suppurative inflammation characteristic of actinomycosis. (**c**) Intermediate-magnification photomicrograph showing a circumscribed abscess resembling the vaguely granulomatous microabscesses seen in nocardiosis. (**d**) Intermediate-magnification photomicrograph in which a GMS stain illustrates filamentous *Actinomyces spp*. forming a sulfur granule

Fig. 4.7 *Rhodococcus equi* pneumonia (malakoplakia). (**a**) Low-magnification photomicrograph showing massive proliferation of histiocytes/macrophages arranged in confluent sheets (right side) and focally filling the alveoli in a pattern mimicking desquamative interstitial pneumonia (left side). Most of the macrophages are round to oval in shape, while others may assume a more spindled appearance. (**b**) High-magnification view shows epithelioid histiocytes with abundant eosinophilic cytoplasm and the intracytoplasmic round basophilic targetoid inclusions (Michaelis-Gutmann bodies) (arrows) diagnostic of malakoplakia. Michaelis-Gutmann bodies are usually easily identified on H&E stain, but calcium stains such as the von Kossa stain may also be helpful in identifying them

Fig. 4.8 Tuberculosis. Photomicrograph showing characteristic necrotizing (caseating) granuloma with central bland necrosis surrounded by epithelioid histiocytes and multinucleated giant cells. While typical of tuberculosis, this same histology and distribution of disease also occurs in patients with nontuberculous mycobacterial infections

Fig. 4.9 Tuberculosis. Photomicrograph showing a necrotizing granuloma in which central necrosis comprises necrotizing neutrophils. The purulent necrotic center is surrounded by epithelioid histiocytes admixed with lymphocytes and plasma cells (**a**). Occasionally vascular inflammation is prominent, although a true necrotizing vasculitis is rare (**b**)

Fig. 4.10 Tuberculosis. High-magnification photomicrograph showing acid-fast organisms (arrows) in a section stained using a Ziehl-Neelsen technique. While there are subtle differences between *Mycobacterium tuberculosis* and nontuberculous mycobacterial organisms, they cannot be reliably separated based on morphology alone; speciation is accomplished more reliably with culture or molecular techniques. The organisms are usually scarce even when necrosis is extensive. Careful examination under high magnification is necessary

Fig. 4.11 Nontuberculous mycobacteria infection due to MAC. Low-magnification photomicrograph showing necrotizing granulomatous inflammation at autopsy in a patient with culture-proven MAC. The histology strongly suggests granulomatous infection but is not specific to MAC, a diagnosis that requires a combination of special stains, cultures, and molecular techniques

Fig. 4.12 Nontuberculous mycobacterial infection in a patient with bronchiectasis. Low-magnification photomicrograph showing an ectatic airway with severe chronic inflammation typical of bronchiectasis. In this case, the inflammation is complicated by loose non-necrotizing granulomas in the airway wall, a finding virtually diagnostic of atypical mycobacterial infection (usually MAC) in the context of bronchiectasis. This type of atypical mycobacterial infection in the setting of large airway disease is commonly seen in the middle lobe and/or lingula (middle lobe syndrome) but may affect any area of localized bronchiectasis

Fig. 4.13 MAC infection in a patient with a hypersensitivity pneumonia-like syndrome linked to hot-tub exposure (hot-tub lung). (**a**) Low-magnification photomicrograph showing a combination of chronic bronchiolitis and relatively well-formed non-necrotizing and focally necrotizing granulomas situated predominantly within the

lumens of distal airways. (**b**) Higher magnification view from the same biopsy specimen showing a small focus of central necrosis with neutrophils

Fig. 4.14 Cytomegalovirus (CMV) pneumonia. High-magnification photomicrograph shows the histologic hallmark of CMV pneumonia, the enlarged cells containing both intranuclear and intracytoplasmic inclusions. The intranuclear inclusion is dark purple and is surrounded by a clear halo (owl's eye). The cytopathic changes are usually seen in bronchiolar epithelium and endothelial cells but may occasionally affect other cells, including macrophages

Fig. 4.15 Herpes simplex virus (HSV) pneumonia. (**a**) Photomicrograph showing necrotizing bronchitis and bronchopneumonia with prominent karyorrhexis typical of HSV infection. The bronchiolocentric necrotizing process destroys the airway and surrounding parenchyma. (**b**) High-magnification photomicrograph showing characteristic Cowdry type A inclusions that are round, eosinophilic, and surrounded by a clear halo. Peripheral margination of chromatin is also seen. Other inclusions are characterized by dense, ground-glass change filling up the entire nucleus with a surrounding basophilic rim

Fig. 4.16 Herpes simplex virus (HSV) pneumonia. Photomicrograph showing positive immunohistochemical staining with HSV-I antibody. Immunostains can be helpful in cases with equivocal or atypical inclusions

Fig. 4.17 Adenovirus pneumonia. (**a**) Intermediate magnification photomicrograph showing diffuse alveolar damage with hyaline membranes and an associated air-space exudate that includes macrophages, neutrophils, and fibrin. (**b**) High-magnification view demonstrating adenovirus intranuclear inclusion with the typical dark and smudged appearance (arrow)

Fig. 4.18 Measles pneumonia. (**a**) Photomicrograph showing numerous large multinucleated giant cells in diffuse alveolar damage. (**b**) High-magnification view of the multinucleated giant cell with intranuclear eosinophilic inclusions and chromatin margination

Fig. 4.19 Respiratory syncytial virus (RSV) pneumonia is a significant cause of respiratory disease in children but rarely requires biopsy for diagnosis. (**a**) Photomicrograph of a surgical lung biopsy showing multinucleated giant cells in diffuse alveolar damage with prominent hyperplasia of type 2 pneumocytes. Diffuse alveolar damage (DAD) is a relatively uncommon finding in RSV pneumonia, seen only in those with severe disease. (**b**) High-magnification photomicrograph showing a multinucleated giant cell with round, eosinophilic intracytoplasmic inclusions

Fig. 4.20 Influenza virus H1N1 pneumonia. (**a**) Low magnification showing a combination of diffuse alveolar damage and a necrotizing inflammatory infiltrate typical of influenza pneumonia. Diagnostic cytopathic changes are absent in influenza pneumonia. (**b**) Low-magnification photomicrograph from the same patient showing a large area of hemorrhagic infarct, a characteristic feature of influenza virus type H1N1 infection

Fig. 4.21 Histoplasmosis. Gross photograph showing cut surface of a well-circumscribed lesion with prominent central necrosis showing concentric rings (resembling the rings of a tree) that are characteristic of histoplasmosis

Fig. 4.22 Histoplasmosis. (**a**) Low-magnification photomicrograph of the lesion shown in Fig. 4.21. The lesion shows a rounded border and prominent central necrosis with calcification, surrounded by a thin rim of epithelioid histiocytes and collagen fibrosis. The organisms are few in quantity and are invisible on H&E-stained slides. (**b**) High-magnification photomicrograph of GMS stain showing small, uniform, oval-shaped yeasts with narrow-based budding

Fig. 4.23 Histoplasmosis. (**a**) The necrotizing granulomatous inflammation in acute histoplasmosis as illustrated in this low-magnification photomicrograph can include irregular (geographic) zones of necrosis with nuclear debris resembling the granu-

lomatous inflammation more typical of granulomatosis with polyangiitis (Wegener's granulomatosis). (**b**) A GMS stain reveals small, frequently teardrop-shaped yeasts of *Histoplasma capsulatum*

Fig. 4.24 Disseminated histoplasmosis. (**a**) Photomicrograph showing disseminated histoplasmosis characterized by sheets of histiocytes filling air spaces without well-formed granulomas. (**b**) A higher-magnification photomicrograph shows "parasitized" organisms filling the cytoplasm of engorged histiocytes. Yeast within the cytoplasm of macrophages are visible as dot-like nuclei surrounded by a clear space. This is the only form of histoplasmosis in which you can see the organisms on routinely stained sections. (**c**) High-magnification view of a GMS stain reveals numerous small round and oval-shaped yeast clustered within the cytoplasm of histiocytes

Fig. 4.25 Blastomycosis. (**a**) Low-magnification photomicrograph showing a combination of necrotizing and non-necrotizing granulomatous inflammation in a patient with blastomycosis. (**b**) A higher-magnification view shows suppurative granulomatous inflammation that is characteristic of blastomycosis. The central necrosis shows abundant neutrophils with karyorrhexis surrounded by plump epithelioid histiocytes and giant cells. (**c**) Photomicrograph from the same biopsy showing a budding yeast form in a giant cell in the upper center portion of the image. (**d**) High-magnification view of the same budding yeast showing characteristic doubly refractile wall and central basophilic nucleoplasm. A second organism is present below and to the left in the same giant cell but lacks the central basophilic nucleoplasm

Fig. 4.26 Blastomycosis. (**a**) Low-magnification photomicrograph of a needle biopsy from a solitary lung nodule showing poorly formed non-necrotizing granulomas including multinucleated giant cells. (**b**) High-magnification view showing multiple large, rounded yeasts with thick, refractile cell walls (arrows). Some yeasts show broad-based budding. The organisms are larger than *Cryptococcus* neoformans with which they may be confused and lack the central endospores typical of *Coccidioides immitis*

Fig. 4.27 Blastomycosis in the acute respiratory distress syndrome (ARDS). Photomicrograph of autopsy lung showing numerous round yeasts with thick doubly refractile walls typical of *Blastomyces dermatitidis* with diffuse alveolar damage. This is an uncommon manifestation of blastomycosis that occurs most commonly in immunocompromised patients

Fig. 4.28 Cryptococcosis. (**a**) Low-magnification photomicrograph showing a nodule in which poorly formed non-necrotizing granulomas comprise loose clusters of multinucleated giant cells with variably conspicuous cytoplasmic vacuoles. (**b**) High-magnification view showing that many of the cytoplasmic vacuoles contain delicate, pale-staining, thin-walled yeast with associated halos representing mucinous capsules. (**c**) High-magnification photomicrograph of GMS stain showing the round and misshapen fractured yeast forms typical of *Cryptococcus neoformans*

Fig. 4.29 Cryptococcosis. (**a**) Photomicrograph showing necrotizing granuloma that contributed to the same nodule illustrated in Fig. 4.28. This combination of necrotizing granulomas and loose clusters of multinucleated giant cells is a common tissue manifestation of pulmonary cryptococcosis. (**b**) Higher-magnification view showing necrotic center of granuloma at the bottom surrounded by a mixed inflammatory infiltrate of mononuclear cells in which epithelioid histiocytes predominate. (**c**) High-magnification photomicrograph of GMS illustrating yeast typical of *Cryptococcus neoformans* randomly scattered with the necrotic center of the granuloma

Fig. 4.30 Cryptococcosis. (**a**) Organizing pneumonia is a common manifestation of cryptococcosis, as illustrated in this low-magnification photomicrograph. It is distinguished by associated granulomatous inflammation, including clusters of epithelioid and multinucleated macrophages. (**b**) High-magnification view showing the delicate, pale-staining, thin-walled yeast with associated halos that are the histologic hallmarks of *Cryptococcus neoformans*

Fig. 4.31 Cryptococcosis. (**a**) Low-magnification photomicrograph of a needle biopsy from a lung nodule in an immunocompromised patient. Areas of pale-colored necrosis and vaguely granulomatous inflammation are seen. (**b**) High-magnification photomicrograph showing the pale-colored necrosis in which there are numerous round yeasts with minimal inflammatory reaction and without well-formed granulomas. The yeasts vary markedly in size and shape and are surrounded by a prominent clear space corresponding to a mucinous capsule. (**c**) High-magnification view of the GMS stain highlights the characteristic features of *Cryptococcus*: variation in size and frequent fragmentation of the yeast. (**d**) High-magnification photomicrograph illustrating the brightly mucicarminophilic capsule seen in most (but not all) strains of *Cryptococcus neoformans*. Capsule-deficient strains may lack this characteristic

Fig. 4.32 Coccidioidomycosis. (**a**) Necrotizing granulomatous inflammation is the most common finding in *Coccidioides* infections. This low-magnification photomicrograph shows a large area of bland necrosis surrounded by epithelioid histiocytes and giant cells with non-necrotizing granulomas at the periphery. (**b**) High-magnification photomicrograph showing large empty spherules (arrows) with a thick, somewhat refractile wall at the edge of necrosis. Note that the spherules are much larger than adjacent histiocytes

Fig. 4.33 Coccidioidomycosis with eosinophilia. (**a**) Photomicrograph showing necrotizing granuloma with associated eosinophilia in a patient with coccidioidomycosis. Tissue eosinophilia is commonly associated with necrotizing granulomatous inflammation in coccidioidomycosis and may include areas resembling eosinophilic pneumonia, as illustrated in the same biopsy in (**b**)

Fig. 4.34 Cavitary coccidioidomycosis. (**a**) This low-magnification photomicrograph illustrates necrotizing granulomatous inflammation with cavitation in a patient with coccidioidomycosis. (**b**) Photograph of surgical specimen corresponding to photomicrograph in **a** showing a cavitary lesion with an irregular rim of firm inflammatory tissue

Fig. 4.35 Coccidioidomycosis. (**a**) High-magnification photomicrograph showing a multinucleated giant cell containing a *Coccidioides* spherule with multiple small slightly basophilic endospores. Note the eosinophils in the lower left corner. (**b**) Photomicrograph of a GMS-stained section showing multiple large empty spherules, spherules containing endospores, and free endospores. (**c**) High-magnification photomicrograph of a routinely stained section showing a combination of spherules, endospores, and hyphae (upper right) in a patient with cavitary disease. Hyphae are an uncommon finding in surgical specimens of coccidioidomycosis and represent the mycelial form of the organism

Fig. 4.36 *Aspergillus* mycetoma (aspergilloma). (**a**) Photograph of resected aspergilloma forming a fungus ball within a cavitary space. (**b**) Low-magnification view of fungus ball situated within a dilated airway. Note that there is no tissue response or invasion by the fungus ball

Fig. 4.37 *Aspergillus* hyphae. (**a**) Photomicrograph of routinely stained H&E section showing the organisms comprising an aspergilloma arranged as radially aligned elongated septate hyphae with acute-angle branching. (**b**) High-magnification photomicrograph showing the conidial heads that are occasionally seen and may be helpful in identifying the specific species of *Aspergillus*

Fig. 4.38 Allergic bronchopulmonary aspergillosis (ABPA). (**a**) Low-magnification photomicrograph showing dilated bronchus filled up with dense mucus plugs demonstrating a layered appearance typical of mucoid impaction of bronchi (MIB) in ABPA. (**b**) High-magnification view showing that the layers of the "allergic mucin" typical of MIB in ABPA constitute a combination of desiccated eosinophils and inspissated mucus in which there are variably conspicuous Charcot-Leyden crystals. (**c**) Low-magnification photomicrograph showing bronchocentric granulomatosis, a finding that in the context of MIB and eosinophilia is characteristic of ABPA. Bronchocentric necrotizing granulomatous inflammation without other features of ABPA occurs in other conditions, including granulomatosis with polyangiitis (Wegener's granulomatosis) and granulomatous infections

Fig. 4.39 Invasive aspergillosis. (**a**) Low-magnification photomicrograph showing necrotizing pneumonia characteristic of invasive aspergillosis. The air spaces are filled with a fibrinous exudate that includes neutrophils and karyorrhexis. (**b**) High-magnification photomicrograph of GMS-stained section showing fungal hyphae with the necrotizing exudate with branching septate hyphae characteristic of *Aspergillus spp.*

Fig. 4.40 Invasive aspergillosis. (**a**) Low-magnification photomicrograph of a needle biopsy from a lung mass in an immunocompromised patient showing areas of infarction and adjacent organizing pneumonia. (**b**) Higher-magnification view of the infarcted area showing a necrotic blood vessel with questionable fungal hyphae filling up the lumen. (**c**) A GMS stain reveals *Aspergillus* fungal hyphae within the vascular lumen and invading the vascular wall

Fig. 4.41 Necrotizing tracheobronchitis as a manifestation of invasive aspergillosis. (**a**) Low-magnification photomicrograph of bronchial wall showing extensive ulceration, necrosis, and invasion by *Aspergillus* fungal hyphae. (**b**) High-magnification photomicrograph of routinely stained section of the bronchial wall showing thin, septate *Aspergillus* hyphae. (**c**) High-magnification view showing extensive invasion of bronchial wall cartilage

Fig. 4.42 Invasive mucormycosis. (**a**) Low-magnification photomicrograph showing parenchymal necrosis with acute and chronic inflammation, including epithelioid and multinucleated histiocytes resulting in a vaguely granulomatous appearance. Fungal hyphae are present predominantly within the necrotic tissue. (**b**) High-magnification photomicrograph showing the wide, irregular, ribbon-shaped, nonseptate hyphae with 90-degree branching. (**c**) Invasive mucormycosis. GMS staining showing irregular, ribbon-shaped hyphae with 90-degree branching

Fig. 4.43 Invasive mucormycosis. High-magnification photomicrograph showing a blood vessel completely occluded by mucor hyphae

Fig. 4.44 Candidiasis. (**a**) Low-magnification photomicrograph showing blood vessel lumen rimmed by inflammatory cells with a partially necrotic thrombus containing numerous fungal pseudohyphae radially arranged to form a central nidus. (**b**) Low-magnification photomicrograph of a small artery filled with numerous fungal organisms. (**c**) High magnification of the intravascular organisms showing yeasts and pseudohyphae

Fig. 4.45 Candidiasis in chronic granulomatous disease. (**a**) Photomicrograph showing suppurative granuloma in a lung biopsy from a patient with chronic granulomatous disease. (**b**) High-magnification photomicrograph of GMS-stained section showing small, narrow-budding yeast in granuloma illustrated above. Cultures grew *Candida spp.*

Fig. 4.46 *Pneumocystis* pneumonia. (**a**) Low-magnification photomicrograph of *Pneumocystis* pneumonia showing classic histologic features. The air spaces are filled with frothy eosinophilic exudates. There is nonspecific chronic inflammation within the mildly thickened alveolar septa. (**b**) High-magnification photomicro-

graph shows the characteristic intra-alveolar frothy exudate. The trophozoites of the organisms, represented by the tiny dot-like structures within the clear space of the frothy materials, are difficult to see on H&E-stained slides but are an important clue to the diagnosis. (**c**) High-magnification view of GMS stain showing numerous round to helmet-shaped cysts within the intra-alveolar frothy exudates. The cysts demonstrate frequent fragmentation and have been described as crushed structures shaped like ping-pong balls. Trophozoites are not visible on GMS-stained slides

Fig. 4.47 Diffuse alveolar damage is a common manifestation of *Pneumocystis* pneumonia, making a GMS stain mandatory in any immunocompromised patient with this finding. (**a**) Low-magnification photomicrograph of a lung biopsy with *Pneumocystis* pneumonia showing early-stage diffuse alveolar damage with prominent hyaline membranes. (**b**) High-magnification photomicrograph showing the subtle frothy appearance focally present within the lush hyaline membranes. (**c**) High-magnification photomicrograph of GMS-stained section showing organisms typical of *Pneumocystis jirovecii* clustered within the hyaline membranes

Fig. 4.48 *Pneumocystis* pneumonia. The vasculitis illustrated in this photomicrograph is a rare, atypical finding in *Pneumocystis* pneumonia that may resemble autoimmune or lymphoproliferative diseases. However, the focal presence of the intra-alveolar frothy exudate typical of pneumocystis (arrow) combined with the patient's immunocompromised status are important clues to the diagnosis

Fig. 4.49 *Pneumocystis* pneumonia. (**a**) Photomicrograph showing granulomatous inflammation in a patient with *Pneumocystis* pneumonia. The poorly formed granulomas are located within the air space. (**b**) Higher-magnification photomicrograph showing the typical frothy exudates that are often only a focal finding when affiliated with granulomatous features. (**c**) High-magnification photomicrograph of GMS-stained section showing numerous round and somewhat fragmented cysts within the central fibrinonecrotic exudates

Fig. 4.50 *Pneumocystis* pneumonia with coexisting HSV infection. As illustrated in this high-magnification photomicrograph, more than one organism may be present in a lung biopsy from an immunocompromised patient. This biopsy shows frothy exudates characteristic of *Pneumocystis* pneumonia as well as viral cytopathic changes (arrows) and an associated necrotizing exudate typical of HSV infection

Fig. 4.51 Toxoplasmosis. (**a**) Low-magnification view of a lung biopsy from an immunocompromised patient showing patchy parenchymal necrosis with minimal inflammation. (**b**) High-magnification view at the edge of the necrosis showing an intracellular bradyzoite-containing cyst. (**c**) High-magnification view from elsewhere in the same biopsy showing multiple tachyzoites present within the extracellular exudates

Fig. 4.52 Amoebiasis. (**a**) Low-magnification photomicrograph showing a large, geographic area of necrosis with mild peripheral inflammatory infiltrates. (**b**) High-magnification view at the edge of necrosis showing multiple round to oval trophozoites with a thin cell membrane and single nucleus with prominent nuclear border and central karyosome

Fig. 4.53 Dirofilarial nodule (dog heartworm disease). Photograph of wedge biopsy from a patient with an asymptomatic solitary nodule showing a solitary well-demarcated centrally necrotic nodule mimicking an infectious granuloma

Fig. 4.54 Dirofilarial nodule. (**a**) Low-magnification photomicrograph showing well-circumscribed infarct-like necrosis surrounded by fibrosis and a chronic inflammatory infiltrate rich in eosinophils without well-developed granulomatous features. (**b**) Higher-magnification photomicrograph showing a thrombosed blood vessel containing multiple cross sections of dirofilarial organisms. (**c**) High-magnification view of the organism cut in cross section showing the thick cuticle surrounding complex internal structures

Fig. 4.55 Paragonimiasis (lung fluke). High-magnification view of the wall of a cystic lung lesion showing several oval-shaped eggs with a refractile wall. There are associated fibrosis, chronic inflammation with eosinophils, and multinucleated foreign body giant cells
Fig. 4.56 Strongyloidiasis. Papanicolaou stain of bronchoalveolar lavage fluid showing a curved larva of *Strongyloides stercoralis* in a background of mixed inflammation
Fig. 5.1 Asthma. At low magnification, multiple airways are filled with mucus plugs. No significant inflammation is present. The lung parenchyma is normal
Fig. 5.2 Asthma. At higher magnification, the bronchial epithelium is remarkable for prominent goblet cell hyperplasia and thickened basement membrane (*arrows*). The bronchial wall shows smooth muscle hyperplasia and mild chronic inflammation. The lumen of the airway is almost completely occluded with a mucus plug
Fig. 5.3 Asthma. Another high-magnification photomicrograph showing an inflamed airway in a patient with asthma showing prominent smooth muscle hyperplasia, acute and chronic inflammatory infiltrates, and mucus plugging
Fig. 5.4 Asthma. High-magnification view of mucus plug containing eosinophils and accompanied by epithelial necrosis
Fig. 5.5 Allergic bronchopulmonary aspergillosis associated with asthma. Gross photograph of a lobectomy specimen showing multiple dilated airways filled with green-gray, friable, desiccated mucus typical of mucoid impaction of bronchi
Fig. 5.6 Allergic bronchopulmonary aspergillosis associated with asthma. Low-magnification view of mucoid impaction of bronchi characterized by a dilated and inflamed cartilaginous airway impacted with allergic mucin. The allergic mucin contains layered cellular components in which eosinophils predominate within the lightly stained mucus
Fig. 5.7 Allergic mucin characteristic of mucoid impaction of bronchi (MIB) in allergic bronchopulmonary aspergillosis (ABPA). (**a**) Expectorated casts from a patient with MIB in ABPA. The gross appearance resembles plastic bronchitis (*see* Fig. 5.14); histologic features are helpful in distinguishing the two. (**b**) Low-magnification photomicrograph showing expectorated cast from a patient with ABPA. The alternating layers of inspissated mucus and degenerating eosinophils are characteristic of the allergic mucin that defines MIB in ABPA. (**c**) High-magnification photomicrograph of the allergic mucin illustrated in **b**, showing degenerating eosinophils and numerous Charcot-Leyden crystals, which are the breakdown products of eosinophilic granules
Fig. 5.8 Allergic mucin in allergic bronchopulmonary aspergillosis (ABPA) associated with asthma. (**a**) Another high-magnification view of allergic mucin with Charcot-Leyden crystals and degenerating eosinophils. (**b**) High-magnification view of Gomori methenamine silver (GMS) stained section showing fragmented, degenerating fungal hyphae in the allergic mucin from a patient with ABPA. The organisms are often rare in this condition and are largely limited to the allergic mucin without evidence of tissue invasion
Fig. 5.9 Localized bronchiectasis. Gross photograph of a surgical specimen showing localized bronchiectasis. Dilated bronchi and associated bronchopneumonia and scarring are seen in the lower lobe, extending almost to the pleural surface. The bronchi and lung parenchyma in the upper lobe are normal
Fig. 5.10 Localized bronchiectasis. A close-up photograph of another resection specimen showing dilated bronchi with a characteristic corrugated mucosal surface
Fig. 5.11 Diffuse bronchiectasis. (**a**) Gross photograph of explanted lungs from a patient with cystic fibrosis. The cut surface shows diffusely dilated bronchi, some of which are filled with purulent exudates. (**b**) A close-up view showing the dilated bronchi filled with purulent exudates. There is also prominent peribronchial fibrosis and scarring, with very limited intervening normal lung parenchyma

Fig. 5.12 Bronchiectasis. (**a**) Low-magnification photomicrograph showing a dilated bronchus with prominent acute and chronic inflammation with lymphoid aggregates and scarring of more distal peribronchial lung tissue. The integrity of the bronchial wall has been destroyed by inflammation and fibrosis, with an incomplete smooth muscle layer and attenuation of cartilage. (**b**) A higher-magnification photomicrograph shows focal necrosis of the lining respiratory epithelium with tufts of granulation tissue that are common and contribute to the risk of hemoptysis in these patients

Fig. 5.13 Bronchiectasis. A photomicrograph showing another example of bronchiectasis in which there is severe acute and chronic inflammation with extensive necrosis of respiratory epithelium, peribronchial fibrosis, and an incomplete smooth muscle layer. The lumen contains sloughed epithelial cells and neutrophils

Fig. 5.14 Plastic bronchitis. Gross photograph of an expectorated bronchial cast resembling a tree with branches. The size and shape of the casts may vary from small segmental casts to large casts filling the entire tracheobronchial tree of a lung

Fig. 5.15 Plastic bronchitis. Low-magnification photomicrograph of an expectorated cast showing a combination of fibrin and small lymphocytes

Fig. 5.16 Respiratory bronchiolitis. Low-magnification photomicrograph of respiratory bronchiolitis in a patient with RBILD. Lightly pigmented alveolar macrophages are clustered within the lumina of bronchioles and spill into adjacent air spaces

Fig. 5.17 Respiratory bronchiolitis. High-magnification photomicrograph from the same biopsy illustrated in Fig. 5.16 showing finely granular brown (smoker's) pigment in the cytoplasm of alveolar macrophages

Fig. 5.18 Respiratory bronchiolitis. High-magnification photomicrograph showing the finely granular brown pigment typical of respiratory bronchiolitis. Occasional eosinophils are often present but should not be numerous

Fig. 5.19 Respiratory bronchiolitis. Another example showing a confluent aggregate of pigmented macrophages filling the entire lumen of the respiratory bronchiole and extending into adjacent alveolar spaces

Fig. 5.20 Constrictive bronchiolitis. (**a**) Low-magnification photomicrograph of a lung wedge biopsy showing largely unremarkable alveolar lung parenchyma. A few bronchioles (*arrows*) have thickened walls, a feature that is inconspicuous and easily overlooked at this magnification. (**b**) Intermediate-magnification view showing a narrowed lumen caused by subepithelial fibrosis. (**c**) High-magnification photomicrograph illustrating prominent fibroblast proliferation in a collagenous and myxoid stroma situated between the respiratory epithelium and the smooth muscle layer (*arrows*)

Fig. 5.21 Constrictive bronchiolitis. High-magnification photomicrograph of an elastic tissue stain highlights the fibrosis that separates the respiratory epithelium from the subepithelial elastic layer

Fig. 5.22 Constrictive bronchiolitis. (**a**) High-magnification photomicrograph of bronchiole illustrated in Fig. 5.20a. The lumen of the bronchiole is completely obliterated by fibrosis with a scant infiltrate of inflammatory cells, including foamy histiocytes. The bronchiole is recognizable by its residual smooth muscle layer and the adjacent small muscular pulmonary artery. (**b**) An elastic stain highlights the residual elastic layer (*arrows*) of the obliterated bronchiole

Fig. 5.23 Constrictive bronchiolitis. High-magnification photomicrograph showing the accumulation of foamy macrophages in peribronchiolar alveolar spaces, a common nonspecific finding indicating small airway obstruction

Fig. 5.24 Diffuse neuroendocrine cell hyperplasia (multiple carcinoid tumorlets) with constrictive bronchiolitis. (**a**) Low-magnification photomicrograph showing a carcinoid tumorlet in a cartilaginous airway with an obliterated lumen from a patient who had never smoked. Mosaic attenuation on a high-resolution computed tomog-

raphy scan and airflow limitation on pulmonary function studies were found. (**b**) Low-magnification photomicrograph of the same lung biopsy showing an obliterated bronchiolar lumen associated with a carcinoid tumorlet

Fig. 5.25 Diffuse panbronchiolitis. Photomicrograph showing a characteristic combination of peribronchiolar inflammation rich in lymphocytes accompanied by a striking accumulation of foamy macrophages in the peribronchiolar interstitium

Fig. 5.26 Diffuse panbronchiolitis. High-magnification view of another bronchiole showing a chronic bronchiolitis in which lymphocytes predominate and large numbers of foamy macrophages expand the wall of the bronchiole and extend into adjacent alveolar septa

Fig. 5.27 Diffuse panbronchiolitis-like changes in a patient with sequestration. This low- magnification photomicrograph shows histologic findings typical of diffuse panbronchiolitis but in a patient with an intralobar sequestration, illustrating that histology by itself is insufficient to establish the diagnosis of diffuse panbronchiolitis

Fig. 5.28 Acute bronchiolitis caused by bacterial infection. (**a**) Low-magnification photomicrograph showing an acute inflammatory exudate distending bronchiole lumina with an acute and chronic inflammatory infiltrate expanding bronchiolar walls. The inflammation is exquisitely localized to the airways, leaving the surrounding lung parenchyma uninvolved. (**b**) High-magnification photomicrograph showing an acute suppurative inflammatory infiltrate distending the bronchiolar lumina. Chronic inflammation predominates in the bronchiole wall. A tissue Gram stain demonstrated bacterial cocci

Fig. 5.29 Chronic bronchiolitis, NOS in a patient with systemic lupus erythematosus. (**a**) Low-magnification photomicrograph showing an inflammatory reaction involving the bronchioles without extending into the adjacent lung parenchyma. (**b**) At high magnification, the inflammatory infiltrate is composed of lymphocytes and plasma cells

Fig. 5.30 Peribronchiolar metaplasia in chronic bronchiolitis, NOS. Photomicrograph showing chronic bronchiolitis accompanied by fibrosis that extends into peribronchiolar interstitium accompanied by hyperplasia of columnar respiratory epithelial cells. This is a relatively nonspecific manifestation of chronic small airway injury that can occur in a variety of contexts, including in patients with underlying hypersensitivity pneumonia and usual interstitial pneumonia. Occasionally peribronchiolar metaplasia occurs in isolation in patients with mild restrictive lung disease in whom there is no radiologic or histologic evidence of other forms of diffuse lung disease, a circumstance referred to as *peribronchiolar metaplasia-interstitial lung disease*

Fig. 5.31 Chronic bronchiolitis, NOS. Low-magnification photomicrograph showing the prominent smooth muscle hyperplasia sometimes associated with chronic small airway injury of any cause, including chronic bronchiolitis, NOS

Fig. 5.32 Centrilobular emphysema. Gross photograph showing the cut surface of lung with enlarged air spaces distributed in a centrilobular fashion, leaving relatively spared parenchyma between emphysematous spaces and interlobular septa. No significant fibrosis is seen

Fig. 5.33 Centrilobular emphysema. Low-magnification photomicrograph showing centrilobular emphysema characterized by enlarged air spaces and alveolar wall destruction

Fig. 5.34 Panacinar emphysema. Low-magnification photomicrograph showing panacinar emphysema characterized by diffusely enlarged air spaces. The alveolar walls are thin and fragmented

Fig. 5.35 Distal acinar (paraseptal) emphysema. Gross photograph showing the cut surface of the lung with striking distal acinar emphysema characterized by paraseptal and subpleural bullae and blebs

Fig. 5.36 Pleural blebs in distal acinar (paraseptal) emphysema. Low-magnification view of pleural blebs containing air collection within the visceral pleura resulting from rupture of subpleural alveoli and dissection of air into the pleural connective tissue. Fibrosis and chronic inflammation are commonly seen associated with pleural blebs. The immediately adjacent subpleural parenchyma also shows enlarged air spaces

Fig. 5.37 Placental transmogrification in severe emphysema. (**a**) A large emphysematous bulla contains fragmented alveolar walls in which the interstitium is expanded by a combination of inflammation, fibrosis, and stromal mucins, resulting in papillary structures superficially resembling placental villi. (**b**) High-magnification photomicrograph showing fibrovascular cores lined by hyperplastic alveolar pneumocytes resembling placental chorionic villi

Fig. 5.38 Aspiration pneumonia. Photomicrograph showing degenerated vegetable matter within the bronchiolar lumen associated with a suppurative and fibrinous exudate. No granuloma or giant-cell reaction is present in this example

Fig. 5.39 Aspiration pneumonia. (**a**) Low-magnification photomicrograph showing bronchiolocentric chronic and granulomatous inflammation. (**b**) High-magnification view of granuloma composed of multiple giant cells surrounding aspirated vegetable matter

Fig. 5.40 Aspiration pneumonia. High-magnification photomicrograph showing degenerated vegetable matter associated with suppurative granulomatous inflammation

Fig. 5.41 Aspiration pneumonia showing multiple forms of degenerated vegetable matter. (**a**) High-magnification view showing multifaceted large eosinophilic particles lacking internal structures that are situated within the peribronchiolar interstitium and surrounded by a thin rim of histiocytes. (**b**) Another high-power view showing round eosinophilic structures (*arrows*) within multinucleated giant cells. (**c**) High-magnification photomicrograph showing brown amorphous matter within a giant cell. (**d**) High-power view showing collapsed, curved, elongated eosinophilic structures superficially resembling hyalinized blood vessels with an associated giant-cell reaction in peribronchiolar interstitium

Fig. 5.42 Aspiration pneumonia. (**a**) Low-magnification photomicrograph showing changes of organizing pneumonia characterized by polypoid fibroblast plugs filling up air spaces. Organizing pneumonia is a common finding in aspiration and should prompt a search for other features that might establish aspiration as a likely etiology. (**b**) High-magnification view of the circled area in **a** showing pale-gray crystalline material (*arrows*) characteristic of microcrystalline cellulose, a common inert filler (excipient) in oral medications. (**c**) Microcrystalline cellulose is strongly birefringent when viewed with polarized light

Fig. 5.43 Aspiration pneumonia. (**a**) Low-magnification photomicrograph showing necrotizing granulomatous inflammation centered on an airway ("bronchocentric granulomatosis"). (**b**) Higher magnification of the necrotic center demonstrates pale-gray particulates of microcrystalline cellulose. (**c**) The microcrystalline cellulose shows strong birefringence when viewed with polarized light

Fig. 5.44 Aspiration pneumonia. High-magnification photomicrograph showing a combination of granulomatous inflammation and organizing pneumonia associated with deeply basophilic, coral-like material consistent with crospovidone, another common filler in oral medications

Fig. 6.1 Summary of entities included in this chapter, spanning a spectrum from acute to chronic diseases

Fig. 6.2 Proportion of patients with ARDS showing exudative, proliferative, and fibrotic phase DAD at autopsy. The exudative phase is the earliest change and dominates in the first week following injury. Proliferative phase changes become more conspicuous after the first week and are the dominant finding after the first 2 weeks. Collagen fibrosis is a late-stage event that does not occur in all patients

Fig. 6.3 DAD with a patchy distribution. (**a**) Low-magnification view of surgical lung biopsy from a patient with ARDS showing nearly normal lung in the upper right and DAD in the lower left portions of the field (H&E). (**b**) High-magnification photomicrograph of the nearly normal lung in the upper right portion of the field illustrated in **a** showing minimal alveolar septal thickening and congestion, which may reflect the earliest and least specific exudative phase of DAD (H&E). (**c**) High-magnification photomicrograph of DAD in the lower left portion of the field illustrated in **a** showing the early proliferative (organizing) phase with persistent hyaline membranes (H&E)

Fig. 6.4 DAD, early exudative phase. (**a**) Scanning magnification photomicrograph of the early exudative phase of DAD in a patient with ARDS (H&E). At low magnification the lung parenchyma looks nearly normal with only minimal alveolar septal thickening and overall preservation of lung architecture. (**b**) High-magnification photomicrograph of field illustrated in **a** showing alveolar septal congestion and thickening with very focal hemorrhage and fibrin in air spaces (asterisk) (H&E). In this early phase, it is very difficult and perhaps impossible to diagnose DAD on the basis of this combination of nonspecific findings alone. It is only the clinical context (i.e., ARDS) that allows more confident speculation that this is DAD in an early exudative phase. (**c**) High-magnification photomicrograph of field illustrated in **a** showing an area in which alveolar septal thickening and associated congested and air space hemorrhage are more advanced than that seen in **b** (H&E). In addition, this field shows early hyaline membrane formations (*arrow*), which allows a more confident diagnosis of DAD

Fig. 6.5 Diffuse alveolar damage, exudative phase. Intermediate-magnification photomicrograph from patient with ARDS who had acute bronchopneumonia complicated by early DAD (H&E). Alveolar septa are mildly congested with minimal inflammation, hemorrhage, and fibrin in air spaces and hyaline membranes (arrows)

Fig. 6.6 DAD, exudative phase. (**a**) Low-magnification photomicrograph showing acute DAD (H&E). Alveolar septa are mildly thickened by a combination of interstitial edema and a relatively scant infiltrate of predominantly mononuclear cells. Acellular, brightly eosinophilic hyaline membranes are the histologic hallmark of acute DAD. (**b**) High-magnification photomicrograph showing acute DAD (H&E). Acellular, eosinophilic hyaline membranes are arranged in linear arrays along mildly thickened alveolar septa

Fig. 6.7 Diffuse alveolar damage, exudative phase. Intermediate-magnification photomicrograph of surgical lung biopsy from a patient with ARDS demonstrating prominent hyaline membranes affecting mainly alveolar ducts (asterisks)

Fig. 6.8 DAD, proliferative phase. Low-magnification photomicrograph showing the early proliferative or organizing phase of DAD (H&E). Hyaline membranes remain a distinctive feature and are accompanied by expansion and distortion of the interstitium owing mainly to fibroblasts and myofibroblasts within a pale-staining basophilic matrix. In areas there is alveolar collapse (asterisks), which accounts for the increasingly distorted architecture

Fig. 6.9 DAD, proliferative phase. Intermediate-magnification photomicrograph showing expansion and distortion of alveolar septa by mesenchymal cells accompanied by persistent and increasingly fragmented hyaline membranes (H&E)

Fig. 6.10 DAD, late proliferative phase. (**a**) Low-magnification photomicrograph demonstrating the proliferative or organizing phase of DAD in a surgical lung biopsy from a patient with unexplained (idiopathic) ARDS (i.e., acute interstitial pneumonia) (H&E). There is uniform interstitial expansion and distortion resulting in markedly abnormal lung architecture with only a few widely scattered hyaline membranes (arrow). (**b**) High-magnification photomicrograph illustrating expanded, distorted, and collapsed alveolar septa in the late proliferative or orga-

nizing phase of DAD (H&E). (**c**) High-magnification photomicrograph from another patient with ARDS illustrating the proliferative phase of DAD in which collapsed alveolar septa are separated by ectatic alveolar ducts (H&E). Hyaline membrane remnants are present within the areas of collapsed and distorted interstitium

Fig. 6.11 DAD, late proliferative phase. Intermediate-magnification photomicrograph shows fibroblasts and myofibroblasts forming polypoid intraluminal structures (*arrows*) closely mimicking the appearance of organizing pneumonia (H&E). This demonstrates the considerable histologic overlaps between the proliferative or organizing phase of DAD and organizing pneumonia. In small biopsies organizing DAD may be indistinguishable from organizing pneumonia, but correlation with clinical and radiologic information will often resolve the diagnostic distinction

Fig. 6.12 DAD, proliferative phase. (**a**) Fibrin thrombi are a common although nonspecific finding in DAD, as illustrated in this photomicrograph of a surgical lung biopsy from a patient with ARDS (H&E). (**b**) High-magnification photomicrograph showing a distinctive pattern of squamous metaplasia involving bronchiolar epithelium in a patient with ARDS (H&E)

Fig. 6.13 Pneumocyte hyperplasia with reactive atypia in DAD. A high-magnification photomicrograph demonstrates hyperplastic pneumocytes in a patient with DAD (H&E). There is focal cytomegaly with nuclear enlargement and prominent nucleoli but without viral inclusions. This degree of reactive atypia is common in the organizing phase of DAD and should not be construed as either a malignancy or a marker for any specific etiology such as drug toxicity or viral infection

Fig. 6.14 Mallory hyaline in hyperplastic pneumocytes in DAD. This high-magnification photomicrograph illustrates densely eosinophilic cytoplasmic inclusions identical to the Mallory hyaline more commonly affiliated with hepatocytes in alcoholic hepatitis (H&E). This cytologic curiosity is not specific for DAD, occurring in other forms of diffuse lung disease including usual interstitial pneumonia

Fig. 6.15 DAD, proliferative phase. Low-magnification photomicrograph showing the proliferative phase of DAD in a patient with unexplained (idiopathic) ARDS (i.e., acute interstitial pneumonia, referred to historically as Hamman-Rich syndrome) (H&E). The lung architecture is distorted by proliferating fibroblasts and myofibroblasts and concomitant alveolar collapse. Rare hyaline membrane remnants mark some of the collapsed air spaces (*arrow*)

Fig. 6.16 End-stage fibrosis at autopsy in a patient with acute interstitial pneumonia. A gross photograph illustrates the cut surface of a lung from a young woman less than 35 years of age who died within 2 months of the acute onset of rapidly progressive respiratory failure. At autopsy her lung showed extensive fibrosis and honeycomb change. A surgical lung biopsy performed in the course of her hospitalization showed organizing DAD

Fig. 6.17 DAD due to cytomegalovirus (CMV) infections. (**a**) Intermediate-magnification photomicrograph showing both acute and organizing DAD in which there are both well-formed hyaline membranes and organizing fibroblast/myofibroblasts; in this field, they form polypoid structures closely mimicking the appearance of organizing pneumonia (H&E). Two hyperplastic pneumocytes show nuclear inclusions typical of CMV (*arrow*). (**b**) High-magnification photomicrograph showing the CMV-infected cells with typical intranuclear inclusions (H&E). The cell in the upper right portion of the field shows basophilic cytoplasmic inclusions (*arrow*), another feature helpful in recognizing CMV (H&E)

Fig. 6.18 DAD caused by infection with *Pneumocystis jiroveci* (*Pneumocystis* pneumonia). (**a**) Low-magnification photomicrograph of surgical lung biopsy from a patient with ARDS showing acute DAD with thick, lush hyaline membranes typical of those sometimes seen in patients with *Pneumocystis*-associated DAD (H&E). (**b**) High-

magnification photomicrograph showing a small focus of frothy exudate (*arrows*) within one of the thick hyaline membranes in the same patient with *Pneumocystis*-associated DAD (H&E). (**c**) High-magnification photomicrograph illustrating organisms typical of *Pneumocystis jiroveci* in the same surgical lung biopsy showing DAD characterized by thick hyaline membranes (Gomori methenamine silver stain)

Fig. 6.19 Gross photograph of surgical lung biopsy from patient with COP. Areas of pallor were firm on palpation and corresponded to the areas of organizing pneumonia (*arrows*)

Fig. 6.20 Organizing pneumonia in a patient with COP. (**a**) This scanning magnification photomicrograph shows the sharp contrast between the area of organizing pneumonia at lower right and relatively normal lung in the upper left (H&E). Organizing pneumonia fills air spaces and therefore appears solid at lowest magnification. (**b**) Intermediate-magnification photomicrograph of organizing pneumonia illustrated in lower right portion of **a** showing to better advantage the characteristic polypoid plugs of organizing fibroblasts and myofibroblasts, in this case with an associated infiltrate of lymphocytes and plasma cells within the central areas of the plugs themselves (H&E). The configuration of the organizing fibrosis reflects the anatomy of the respiratory bronchioles and alveolar ducts in which it resides

Fig. 6.21 Organizing pneumonia in a patient with COP. (**a**) Low-magnification photomicrograph showing organizing pneumonia in a well-inflated lung surgical lung biopsy (H&E). The patchy abnormality comprises very distinctive plugs of organizing fibroblasts and myofibroblasts situated mainly within the lumina of branching airways and alveolar ducts. (**b**) Intermediate-magnification photomicrograph from same surgical lung biopsy shows to better advantage the intraluminal plugs of organizing tissue affiliated with a scant infiltrate of mononuclear inflammatory cells (H&E). Alveolar septa show a similar infiltrate of mononuclear inflammatory cells, but the interstitial changes are limited to the areas with intraluminal fibrosis

Fig. 6.22 Organizing pneumonia in a patient with COP. Higher-magnification view of the surgical lung biopsy illustrated in Fig. 6.21 showing the characteristic branching pattern of organizing pneumonia in a well-inflated lung biopsy. Note that while organizing pneumonia is centered on the airways, there are concomitant interstitial abnormalities that are limited to the areas of intraluminal fibrosis

Fig. 6.23 Organizing pneumonia in a patient with COP. (**a**) Low-magnification photomicrograph showing the polypoid plugs of organizing fibroblasts and myofibroblasts outlined in sharp relief against a backdrop of collapsed intervening air spaces (H&E). The plugs of intraluminal fibroblastic tissue are centered on respiratory bronchioles and alveolar ducts, which accounts for this peculiar and distinctive low-magnification appearance. (**b**) Higher-magnification photomicrograph from low-magnification field illustrated in **a** showing bland fibroblasts and myofibroblasts arranged in a vaguely linear fashion within an edematous and focally collagenized matrix to form a cast of the affected distal airway surrounded by compressed alveolar spaces (H&E)

Fig. 6.24 Foamy alveolar macrophages in organizing pneumonia. Intermediate-magnification photomicrograph shows prominent foamy macrophages in the region of organizing pneumonia (H&E). This is a common although nonspecific finding in organizing pneumonia that represents microscopic obstructive pneumonia resulting from small airway dysfunction

Fig. 6.25 Organizing pneumonia in a patient with aspiration of gastric particulates. (**a**) Low-magnification photomicrograph showing organizing pneumonia that might easily be construed as COP (H&E). In multiple areas throughout the biopsy, however, the organizing pneumonia is accompanied by foreign particulates with an associated

giant cell reaction (*arrow*), as illustrated at higher magnification in **b**, **c**. (**b**) Intermediate-magnification photomicrograph from surgical lung biopsy showing extensive organizing pneumonia and associated multinucleated giant cells containing basophilic, coral-like cytoplasmic inclusions (*arrows*) typical of crospovidone, a chemically inactive filler (excipient) used in oral medications (H&E). (**c**) High-magnification photomicrograph showing crospovidone (*arrow*) affiliated with a foreign body giant cell reaction in the midst of what is otherwise typical organizing pneumonia (H&E)

Fig. 6.26 Secondary organizing pneumonia in cryptococcosis. (**a**) Low-magnification photomicrograph showing organizing pneumonia (*arrows*) with prominent foamy macrophages and a dense inflammatory infiltrate (H&E). (**b**) Intermediate-magnification photomicrograph showing organizing pneumonia with foamy alveolar macrophages and an inflammatory background that includes loose clusters of epithelioid macrophages and giant cells (*arrow*), resulting in a vaguely granulomatous appearance (H&E). (**c**) High-magnification photomicrograph showing poorly formed granulomatous inflammation illustrated in **b** (H&E). (**d**) High-magnification photomicrograph of the granulomatous inflammation illustrated in **c** showing multiple fungal yeast forms (*arrows*) with clear halos, thin delicate pale-staining walls, and narrow-neck budding typical of *Cryptococcus neoformans* (H&E)

Fig. 6.27 BOOP-like variant of granulomatosis with polyangiitis (Wegener). (**a**) Low-magnification photomicrograph showing features typical of organizing pneumonia (H&E). (**b**) Intermediate-magnification photomicrograph from the same biopsy showing a necrotizing vasculitis characterized by a focal, transmural infiltrate of predominantly neutrophils with associated karyorrhexis (H&E). (**c**) Intermediate-magnification photomicrograph showing a palisaded granuloma typical of granulomatosis with polyangiitis (Wegener) in the same lung biopsy in which organizing pneumonia was the dominant feature (H&E). This combination of findings has been described in patients with the BOOP-like variant of Wegener granulomatosis

Fig. 6.28 Eosinophilic pneumonia in a patient with CEP. (**a**) Low-magnification photomicrograph of CEP showing patchy air space-filling process (H&E). (**b**) Intermediate-magnification photomicrograph showing a combination of inflammatory cells and fibrin in air spaces accompanied by expansion of the interstitium by a similar inflammatory infiltrate (H&E)

Fig. 6.29 Eosinophilic pneumonia in a patient with CEP. (**a**) High-magnification photomicrograph from patient with CEP whose biopsy is also illustrated in Fig. 6.28 showing air space and interstitial chronic inflammatory infiltrate in which eosinophils predominate (H&E). (**b**) High-magnification photomicrograph of a different field in the same biopsy showing both eosinophils and alveolar macrophages (H&E). Macrophages are often a prominent component of the air space exudate in eosinophilic pneumonia and sometimes overshadow the eosinophils

Fig. 6.30 Eosinophilic pneumonia in a patient with CEP. This high-magnification photomicrograph of a surgical lung biopsy from a patient with CEP shows focal necrosis in an air space exudate made up mainly of macrophages with eosinophils clustered at the periphery and within an expanded interstitial structure (H&E)

Fig. 6.31 Eosinophilic pneumonia in a patient with CEP. (**a**, **b**) Two high-magnification photomicrographs show a prominent fibrinous air space exudate that was a focal finding in a patient with biopsy findings that were otherwise typical of CEP (H&E). Fibrin predominates in the air spaces, but clusters of eosinophils are present within the air spaces as well as the interstitium and are key to distinguishing eosinophilic pneumonia from acute fibrinous and organizing pneumonia (AFOP)

Fig. 6.32 Eosinophilic pneumonia in a patient with chronic eosinophilic pneumonia. (**a**) Low-magnification photomicrograph showing a very patchy air space-filling pro-

cess in which fibrin is a prominent feature (H&E). Note multiple corpora amylacea (*arrows*) embedded in the fibrinous inflammatory infiltrate, an incidental finding of no special significance. (**b**) High-magnification photomicrograph of eosinophilic pneumonia showing a combination of fibrin, eosinophils, and macrophages in eosinophilic pneumonia (H&E). Note portion of corpora amylacea at lower right, an incidental finding

Fig. 6.33 Organizing eosinophilic pneumonia in a patient with chronic eosinophilic pneumonia. (**a**) Low-magnification photomicrograph showing a combination of air space fibrin, interstitial and air space inflammation, and organizing intraluminal fibrosis resembling organizing pneumonia (H&E). (**b**) High-magnification photomicrograph showing air space fibrin associated with a mixed inflammatory infiltrate that includes clusters of eosinophils, organizing fibroblasts, and myofibroblasts, resulting in a pattern of intraluminal fibrosis resembling organizing pneumonia (H&E)

Fig. 6.34 AEP. (**a**) Low-magnification photomicrograph of a surgical lung biopsy from a patient with AEP showing a combination of interstitial thickening and a variably cellular fibrinous air space exudate with associated hyaline membranes (H&E). (**b**) High-magnification photomicrograph from same biopsy showing well-formed hyaline membrane (asterisk) and a cellular air space exudate that includes eosinophils and neutrophils (H&E). Some of the eosinophils are degranulated and recognizable only on the basis of a characteristic bilobed nucleus

Fig. 6.35 Acute fibrinous and organizing pneumonia (AFOP). (**a**) Low-magnification photomicrograph of AFOP in a patient with unexplained bilateral opacities on CT scan (H&E). There is a patchy air space-filling process in which fibrin predominates and is accompanied by a very mild air space and interstitial infiltrate of mononuclear cells. In this field there is minimal organization of the fibrinous air space exudate. (**b**) Higher-magnification photomicrograph showing a fibrinous air space exudate with minimal association inflammation (H&E). Special stains and cultures were negative, and there was minimal eosinophilia to suggest eosinophilic pneumonia as an alternative to AFOP. (**c**) High-magnification photomicrograph from same surgical lung biopsy showing an area in which the fibrinous air space exudate illustrated in **a**, **b** is affiliated with ingrowth of organizing fibroblasts (H&E). This feature, common in AFOP, results in considerable histologic overlaps with organizing pneumonia. Indeed, some patients with lesions resembling AFOP almost certainly have a variant of organizing pneumonia (COP)

Fig. 6.36 AFOP. (**a**) Intermediate-magnification photomicrograph of core needle biopsy from patient with unexplained localized opacities on a chest CT scan (H&E). All special stains and cultures were negative for organisms, and there were no other histologic features (such as eosinophilia) to suggest a specific etiology. (**b**) Higher-magnification photomicrograph of area in lower right of field illustrated in **a** showing an organizing fibrinous air space exudate. This associated acute inflammation in this focus should at least raise the possibility of an infectious etiology (H&E)

Fig. 6.37 PAP. Scanning magnification photomicrograph of surgical lung biopsy from a patient with primary acquired (autoimmune) PAP (H&E). Most of the air spaces in this sample are filled with eosinophilic debris that at first blush resembles pulmonary edema. Alveolar septa are nearly normal, showing only a mild, patchy infiltrate of chronic inflammatory cells without significant fibrosis

Fig. 6.38 PAP. (**a**) Low-magnification photomicrograph showing characteristic patchy distribution of a granular air space exudate in a patient with primary acquired (autoimmune) PAP (H&E). In many areas the air space exudate retracts from alveolar septa in a manner that is sometimes helpful in separating PAP from pulmonary edema. (**b**) High-magnification photomicrograph showing to better advantage the granular texture of the alveolar exudate with occasional coarse eosinophilic aggregates (*arrows*), rare mononuclear inflammatory cells, and degenerating erythro-

cytes (H&E). The granular nature of the exudate and associated cellular detritus is key to separating PAP from pulmonary edema

Fig. 6.39 PAP. (**a**) Low-magnification photomicrograph from another patient with primary acquired (autoimmune) PAP showing pulmonary edema-like eosinophilic air space exudate (H&E). Focal cholesterol-like clefts and granular debris with cell ghosts (asterisk) are important clues to the diagnosis of PAP. (**b**) High-magnification view of the same lung biopsy showing granular eosinophilic background, cholesterol-like clefts, macrophages, and cell ghost characteristic of PAP (H&E). Staining for periodic acid-Schiff stain, while characteristic, is relatively nonspecific. Diagnosis hinges instead on recognizing the distinctive histologic and cytologic characteristics that separate alveolar exudates of PAP from edema fluid

Fig. 6.40 PAP. (**a**) Intermediate magnification of ThinPrep preparation demonstrating bronchoalveolar lavage fluid from patient with PAP. Irregularly shaped fragments of a paucicellular granular exudate with coalescent globules and cell ghosts are characteristic of PAP. (**b**) High-magnification photomicrograph of one of the fragments illustrated in **a** showing PAP characterized by granular, paucicellular debris containing cell ghosts. (**c**) Low-magnification photomicrograph of cell block from a different patient using PAP (H&E). A paucicellular granular exudate shows larger aggregates or clumps of eosinophilic debris, a common finding in PAP. (**d**) High-magnification photomicrograph of cell block from same patient with PAP illustrated in **c**. A granular exudate is associated with rare macrophages, cell ghosts, and characteristic large eosinophilic aggregates (H&E)

Fig. 6.41 PAP. (**a**) Low-magnification photomicrograph of transbronchial lung biopsy from a patient with primary acquired (autoimmune) PAP (H&E). The upper third of the photomicrograph shows alveolated lung parenchyma with a distinctive, paucicellular, granular air space exudate. Alveolated lung parenchyma at the bottom is unremarkable, attesting to the often patchy distribution of PAP. (**b**) High-magnification photomicrograph of the same transbronchial biopsy showing granular, eosinophilic, air space exudate typical of PAP (H&E)

Fig. 6.42 RB. Intermediate-magnification photomicrograph showing a respiratory bronchiole and its adjacent alveoli filled with lightly pigmented macrophages typical of those seen in cigarette smokers. The air spaces away from the respiratory bronchiole are less involved

Fig. 6.43 RB. High-magnification photomicrograph showing smokers' macrophages within the air spaces that contained finely granular light brown pigment in the cytoplasm. The pigment is faintly positive on a Prussian-blue iron stain but lacks the coarse, refractile granules and bright blue staining characteristics of bleeding-related hemosiderin

Fig. 6.44 Smoking-related interstitial fibrosis (SRIF). (**a**) Low-magnification photomicrograph showing patchy areas of lung parenchyma with thickened septa. The fibrosis involves the subpleural and centrilobular parenchyma with abrupt demarcation from uninvolved lung parenchyma. (**b**) At intermediate magnification, the involved areas show interstitial thickening by hyalinized collagen fibrosis with minimal inflammation. The alveolar spaces are enlarged and distorted. (**c**) High-magnification view of the thickened alveolar septa with hyalinized collagen bundles. No significant inflammation is present

Fig. 6.45 SRIF with respiratory bronchiolitis. (**a**) At low magnification, alveolar septa are thickened, and some alveolar spaces are filled with pigmented macrophages. (**b**) High-magnification view showing alveolar septa thickened with hyalinized collagen bundles. Note the pigmented smokers' macrophages within the alveolar spaces

Fig. 6.46 Chest CT scan image of a patient with desquamative interstitial pneumonia (DIP). Patchy ground-glass opacities and emphysematous changes are commonly

described. No significant fibrosis is noted, as evidenced by traction bronchiectasis and/or honeycomb change

Fig. 6.47 DIP. (**a**) At low magnification, air spaces are diffusely filled by numerous pigmented macrophages. (**b**) Intermediate-magnification view showing intra-alveolar accumulation of pigmented macrophages with preserved alveolar structure and mildly thickened alveolar septa. (**c**) High-magnification photomicrograph demonstrating macrophages with light brown cytoplasmic pigment within the air spaces. The alveolar septa are expanded by chronic inflammation without the paucicellular hyalinized collagen typical of SRIF, and they are lined by reactive pneumocytes

Fig. 6.48 Changes resembling DIP in smoking-related interstitial fibrosis (SRIF). (**a**) At low magnification, there is diffuse air space filling of pigmented macrophages. The alveolar architecture is preserved, but the alveolar septa are markedly thickened. (**b**) High-magnification view showing the typical pigmented macrophages filling up the air spaces and alveolar septa thickened with hyalinized collagen fibrosis

Fig. 6.49 DIP with emphysema. In addition to the typical pigmented macrophages filling up air spaces, there are also air space enlargement and concomitant interstitial pneumonia that include mild fibrosis

Fig. 6.50 Chest CT scan images of a patient with Langerhans cell histiocytosis (LCH). (**a**) A horizontal cross section of the chest showing numerous cysts and nodular densities. (**b**) A coronal cross section showing that the cystic and nodular lesions are predominantly within the upper lobes of the lung

Fig. 6.51 LCH. Gross image of a lung wedge biopsy from a patient with early-stage LCH showing multiple tan-white centrilobular nodules on the cut surface

Fig. 6.52 LCH. Gross image of an explanted lung from a patient with late-stage LCH. Numerous cysts and tan-white nodules (*arrows*) are seen on the cut surface

Fig. 6.53 LCH. Low-magnification photomicrograph showing multiple cellular, stellate nodules within the lung. Note the background lung parenchyma with emphysematous change and respiratory bronchiolitis

Fig. 6.54 LCH. Low-magnification view of a centrally cystic nodule from a patient with LCH. The central cyst represents the ectatic lumen of the affected airway, which is surrounded by a polymorphic infiltrate in which there are numerous Langerhans cells resulting in a vaguely granulomatous appearance

Fig. 6.55 LCH. (**a**) High-magnification view of Langerhans cells within the nodule illustrated in Fig. 6.54, mononuclear cells with folded or kidney bean-shaped nuclei, and abundant eosinophilic cytoplasm. (**b**) Immunohistochemical stain for CD1a shows positive membranous staining in Langerhans cells. (**c**) Immunohistochemical stain for S-100 shows positive nuclear and cytoplasmic staining in Langerhans cells. (**d**) Electron microscopy image of a Langerhans cell with intracytoplasmic rod-shaped Birbeck granules (*arrows*)

Fig. 6.56 LCH. (**a**) In this example, the lesion is almost completely replaced by fibrosis, forming a stellate-shaped scar with scar emphysema. At the periphery of the lesion, there are smaller clusters of cellular infiltrates (*arrows*). (**b**) High-magnification view of the cellular focus demonstrating typical Langerhans cells with folded or kidney bean-shaped nuclei and admixed eosinophils and lymphocytes

Fig. 6.57 LCH. (**a**) A stellate-shaped scar with the characteristic pattern of associated scar emphysema. Nonspecific chronic inflammatory cells and pigmented macrophages are present. This finding suggests LCH and should trigger careful examination for cellular lesion diagnostic of LCH. (**b**) Another low-magnification field from the same specimen shows two cellular nodules. (**c**) High-magnification view of one of the nodules illustrated in part **b** demonstrating numerous Langerhans cells admixed with scattered eosinophils and pigmented macrophages

Fig. 6.58 UIP. High-resolution CT scan of the chest of a patient with UIP. (**a**) A horizontal cross-sectional image showing the typical findings of UIP: bilateral reticular marking with traction bronchiectasis and honeycomb change, more severe in the periphery. (**b**) A coronal cross-sectional image demonstrating the basilar predominant distribution of the lesions

Fig. 6.59 UIP. Gross photograph of an autopsy showing the right lung from a patient with end-stage UIP. The entire lung is smaller than normal, with diffuse scarring and subpleural honeycomb change that is more severe in the base

Fig. 6.60 UIP. In this explanted right lung, dense scarring and honeycomb changes are mainly seen in the shrunken lower lobe and the periphery of upper lobe

Fig. 6.61 UIP. Whole-mount sections of a lung wedge biopsy showing dense scarring and cystic changes are distributed in a patchwork pattern with peripheral accentuation (geographic or spatial heterogeneity). Areas of fibrosis completely efface the alveolar lung architecture and are juxtaposed with less affected or nearly normal lung parenchyma

Fig. 6.62 UIP. Low-magnification photomicrograph of a surgical lung biopsy showing the typical patchwork and random distribution of collagen fibrosis that effaces the alveolar structure (architectural distortion). Less affected and nearly normal lung parenchyma is present between the areas of more severe fibrosis. Honeycomb change, architectural distortion in the form of cystic spaces containing mucus, is present at the upper left and lower right

Fig. 6.63 UIP. Intermediate-magnification view of an area with significant architectural distortion caused by a dense collage scar (middle) and honeycomb change (right). A small amount of nearly normal lung parenchyma is seen in the lower left. Fibroblast foci (*arrows*) are visible at this magnification

Fig. 6.64 UIP. Temporal heterogeneity, an important feature that is necessary for the diagnosis of UIP, is demonstrated in this intermediate-magnification photomicrograph. The fibrosis is composed of a mixture of newer active fibrosis in the form of a fibroblast focus (*arrow*) and older collagenous scar (right upper)

Fig. 6.65 UIP. High-magnification view of a fibroblast focus that is composed of plump spindle-shaped fibroblasts and myofibroblasts arranged in parallel within a lightly stained myxoid stroma. The luminal surface is covered with a layer of flattened pneumocytes and is sitting immediately on a bed of dense collagen fibrosis

Fig. 6.66 UIP. High-magnification view of an area with honeycomb change. Multiple enlarged air spaces lined by ciliated respiratory epithelium are seen within a background of dense collagen fibrosis and chronic inflammation. There are mucin and mucin-containing macrophages within the enlarged air spaces

Fig. 6.67 UIP. Honeycomb areas are commonly associated with acute and chronic inflammation. Dense inflammatory infiltrates are present in the enlarged air spaces as well as the interstitium and an adjacent bronchiolar lumen (lower right)

Fig. 6.68 UIP. Bundles of hyperplastic smooth muscles are admixed with collagen scars in an area of honeycomb change. The term muscular cirrhosis was used historically to convey prominent smooth muscle hyperplasia often affiliated with cobble stoning of the pleural surface

Fig. 6.69 UIP. High-magnification photomicrograph showing alveolar pneumocyte hyperplasia and amorphous eosinophilic material (Mallory hyaline) within the cytoplasm of a hyperplastic pneumocyte. Mallory hyaline is a common finding in UIP, but it is not specific and has no known clinical significance

Fig. 6.70 Vascular changes in UIP. Hypertensive changes of small muscular pulmonary arteries characterized by intimal and medial hypertrophy are commonly seen associated with honeycomb changes. If the vascular hypertensive changes are prominent away from the honeycombing area, underlying collagen vascular disease such as scleroderma should be considered

Fig. 6.71 UIP with diffuse alveolar damage (DAD) (acute exacerbation of idiopathic pulmonary fibrosis). (**a**) Low-magnification view showing patchy fibrosis and honeycomb change in the upper left. The nonfibrotic lung parenchyma on the right shows frequent hyaline membranes (*arrows*). (**b**) High-magnification view of the hyaline membranes, an eosinophilic membranous material lining alveolar septa. Pneumocyte hyperplasia with prominent reactive atypia is also present. (**c**) Fibrin thrombi within small arteries and arterioles are a common but nonspecific finding in DAD. (**d**) Bronchiolar squamous metaplasia is another common but nonspecific finding in DAD. Also present are changes of late organizing DAD, polypoid intraluminal proliferation of fibroblasts, and myofibroblasts mimicking organizing pneumonia

Fig. 6.72 UIP with DIP-like changes. (**a**) Low-magnification photomicrograph showing the patchwork fibrosis typical of UIP. Note the dense scarring on the lower left and relatively nonfibrotic lung parenchyma on the right. (**b**) High-magnification view of the relatively nonfibrotic lung parenchyma demonstrating the accumulation of pigmented macrophages (smoker's macrophages) within the alveolar spaces, closely mimicking the appearance of DIP

Fig. 6.73 UIP with coexisting emphysema. Low-magnification photomicrograph showing the patchwork fibrosis (lower left and lower right) and honeycomb change (upper middle and lower right) typical of UIP. The nonfibrotic lung parenchyma demonstrates emphysematous changes, including enlarged air spaces, and thinned, fragmented alveolar septa

Fig. 6.74 UIP with coexisting eosinophilic pneumonia. (**a**) Low-magnification photomicrograph showing end-stage fibrosis and honeycomb change (upper right), typical of UIP. The residual air spaces are filled up with cellular infiltrates. (**b**) Higher-magnification view of the cellular air space infiltrates composed entirely of eosinophils

Fig. 6.75 UIP with coexisting carcinoma. (**a**) End-stage fibrotic lung with honeycomb change (left) and squamous cell carcinoma (right). (**b**) Honeycomb change and fibroblast foci typical of UIP (right upper) with coexisting adenocarcinoma in the lower left

Fig. 6.76 NSIP. (**a**) Low-magnification photomicrograph showing uniform alveolar septal thickening by a cellular infiltrate. (**b**) At high magnification, the alveolar septa are thickened by a dense lymphoplasmacytic infiltrate. There is mild pneumocyte hyperplasia. No significant collagen deposition is present

Fig. 6.77 Cellular NSIP. (**a**) At low magnification there is diffuse, uniform thickening of the alveolar septa. (**b**) In this example, the high-magnification view shows that the thickened alveolar septa contain lymphoplasmacytic infiltrates and minimal collagen deposition. Alveolar pneumocyte hyperplasia is also more prominent than the example in Fig. 6.76

Fig. 6.78 Fibrotic NSIP. Gross photograph of an explant lung with fibrotic NSIP. On a cut surface, the lung parenchyma is diffusely fibrotic, with no significant cystic or subpleural honeycomb change

Fig. 6.79 Fibrotic NSIP. Chest CT scan of a patient with fibrotic NISP showing diffuse bilateral ground-glass opacities and interstitial reticular markings. No honeycomb change is present

Fig. 6.80 Fibrotic NSIP. (**a**) At low magnification there is diffuse uniform thickening of alveolar septa by collagen fibrosis. The fibrosis does not cause significant architectural distortion in the form of honeycomb change or scars. (**b**) At high magnification the alveolar septa are thickened by collagen deposition and scant chronic inflammatory cells. There is also alveolar pneumocyte hyperplasia and focal intra-alveolar accumulation of macrophages. Fibroblast foci can be seen in NSIP (not shown in this image) but are generally scarce and are not a typical feature

Fig. 6.81 NSIP-like area in UIP. (**a**) This area of uniform alveolar septal thickening by collagen fibrosis and mild chronic inflammation was taken from the upper lobe of an explanted lung with UIP. The features are consistent with fibrotic NSIP if the same changes were seen in the entire lung. However, a section taken from the lower lobe lung. (**b**) Demonstrated dense interstitial scars and honeycomb change typical of UIP. NSIP-like areas are actually common in otherwise typical UIP, which is why a pathologic diagnosis of NSIP requires correlation with the clinical and radiologic contexts to understand the significance of this finding

Fig. 6.82 CTD-associated fibrotic NSIP. The underlying CTDs are rheumatoid arthritis (**a**), scleroderma (**b**), and dermatomyositis (**c**). Both cellular and fibrotic variants of NSIP have been described in CTD-associated interstitial lung diseases. The histologic features are indistinguishable from those of idiopathic NSIP

Fig. 6.83 Rheumatoid nodule. (**a**) Low-magnification photomicrograph showing a portion of lung parenchyma replaced by an irregularly shaped granuloma with a large geographic area of central necrosis. (**b**) At high magnification, the granuloma is characterized by central coagulative necrosis surrounded by peripheral palisading histiocytes admixed with acute and chronic inflammatory cells. No multinucleated giant cells are seen

Fig. 6.84 Acute lupus pneumonitis. (**a**) Intermediate-magnification photomicrograph showing extensive intra-alveolar hemorrhage, reactive pneumocytes, and patchy acute inflammatory infiltrates centered on alveolar septa. (**b**) At high magnification, acute inflammatory cells with karyorrhexis are seen within alveolar septa, indicating necrotizing capillaritis

Fig. 6.85 Thromboembolic pulmonary hypertension in systemic lupus erythematosus. High-magnification view of an artery with eccentric intimal fibrosis and a recanalized lumen, indicating an organized thrombus

Fig. 6.86 LAM. Gross photograph of surgical lung biopsy from a 35-year-old woman with recurrent pneumothorax. The cut surface of the lung shows multiple variably sized thin-walled cysts. The intervening lung parenchyma is unremarkable, without significant fibrosis

Fig. 6.87 LAM. A high-resolution chest CT scan from the same patient whose surgical lung biopsy is illustrated in Fig. 6.86 shows a large right-sided pneumothorax with right upper lobe collapse. Numerous thin-walled cysts and some parenchymal nodules are seen in the non-collapsed lung

Fig. 6.88 LAM. Gross photograph of an explant lung from a patient with end-stage LAM. The lung is extensively involved with cystic lesions, with very few residual lung parenchyma

Fig. 6.89 LAM. Whole-mount section of a surgical lung biopsy showing multiple cystic lesions, some of which are surrounded by a variably thick and focally nodular wall. The two most nodular and cellular lesions are present in the lower piece of tissue

Fig. 6.90 LAM. Intermediate-magnification view of the lower piece of tissue illustrated in Fig. 6.89 showing nodular and cystic lesions. The thickened cyst walls comprise a proliferation of smooth muscle-like spindle cells. Some of the air spaces contain hemosiderin-laden macrophages, indicating old hemorrhage

Fig. 6.91 LAM. High-magnification photomicrograph showing spindle and epithelioid LAM cells with bland, elongated nuclei and clear to eosinophilic cytoplasm. The cytoplasm is subtly vacuolated and slightly basophilic, resulting in tinctorial properties that differ from normal smooth muscle cells

Fig. 6.92 LAM. The lesional cells are usually positive for smooth muscle actin (**a**), HMB-45 (**b**), estrogen receptor (**c**), and progesterone receptor (**d**). Staining for HMB-45 can be very patchy and therefore requires careful review of immunostained sections

Fig. 6.93 LAM. (**a**) In this example, a thin-walled cyst is seen within the lung parenchyma, and the wall is focally thickened by bundles of smooth muscle-like LAM cells (*arrows*). (**b**) High-magnification view of the thickened area of the cyst wall showing bland-appearing spindle and epithelioid cells with overlying hyperplastic pneumocytes

Fig. 6.94 Angiomyolipoma in the lung of a patient with tuberous sclerosis complex (TSC). (**a**) Low-magnification photomicrograph showing a well-demarcated lipomatous lesion next to a bronchus. (**b**) Higher-magnification photomicrograph from the center of the lesion shows features of angiomyolipoma: mature adipocytes, smooth muscle proliferation, and thick-walled blood vessels. Angiomyolipoma is more commonly seen in the kidneys of patients with TSC and has been reported in both sporadic and TSC-associated LAM

Fig. 7.1 Hypersensitivity pneumonia. A low-magnification whole-mount section showing a cellular interstitial pneumonia that is accentuated around the small airways. The more distal alveoli are less involved. The overall alveolar architecture is preserved with no significant fibrosis

Fig. 7.2 Hypersensitivity pneumonia. Low-magnification photomicrograph showing a variably dense, lymphocyte-rich, cellular inflammatory infiltrate that expands the interstitium and is accentuated around distal bronchioles (*asterisks*)

Fig. 7.3 Hypersensitivity pneumonia. Intermediate-magnification photomicrograph showing a small poorly formed granuloma composed of a loose cluster of multinucleated giant cells (arrow) situated within the peribronchiolar interstitium. Note the background cellular interstitial pneumonia with peribronchiolar accentuation. It is this combination of features that is most helpful in establishing a histologic diagnosis of hypersensitivity pneumonia

Fig. 7.4 Granulomatous inflammation in hypersensitivity pneumonia. (**a**) Photomicrograph showing a characteristic pattern of loosely formed granulomas (*arrows*) consisting of epithelioid histiocytes and giant cells centered on the peribronchiolar interstitium. (**b**) High-magnification view of a loosely formed granuloma consisting of a giant cell and a few histiocytes and surrounded by mononuclear inflammatory cells in which lymphocytes predominate. (**c**) Another example of a loosely formed granuloma consisting of epithelioid histiocytes within the peribronchiolar interstitium accompanied by a dense infiltrate of chronic inflammatory cells. (**d**) An isolated giant cell is seen within the interstitium in a background of chronic inflammatory cells

Fig. 7.5 Granulomatous inflammation in hypersensitivity pneumonia. The giant cells in hypersensitivity pneumonia often contain a variety of nonspecific endogenous cytoplasmic inclusions, including cholesterol-like clefts (**a**), calcified Schaumann bodies (**b**), and other nonspecific pale-staining birefringent crystalline salts (not illustrated). These inclusions are not linked to any specific antigenic exposures

Fig. 7.6 Chronic bronchiolitis in hypersensitivity pneumonia. (**a**) High-magnification photomicrograph showing chronic bronchiolitis characterized by a chronic inflammatory infiltrate that expands the peribronchiolar interstitium. The hyperplastic columnar respiratory epithelium extends along peribronchiolar alveolar septa thickened by inflammation and fibrosis, a combination of findings referred to as peribronchiolar metaplasia (*see* Fig. 7.7). (**b**) Another high-magnification view showing chronic bronchiolitis with focal intraluminal fibroblast proliferation (bronchiolitis obliterans also referred to simply as organizing pneumonia). (**c**) Photomicrograph showing focal organizing pneumonia made up of a polypoid plug of organizing fibroblasts situated within the lumen of a respiratory bronchiole in a patient with hypersensitivity pneumonia. (**d**) Accumulation of foamy alveolar macrophages in peribronchiolar air spaces is a form of microscopic obstructive

pneumonia and is another sign of small airway dysfunction that is common in lung biopsies from patients with hypersensitivity pneumonia

Fig. 7.7 Fibrotic hypersensitivity pneumonia. Photomicrograph showing prominent peribronchiolar metaplasia in a surgical lung biopsy from a patient with hypersensitivity pneumonia. Peribronchiolar metaplasia is not specific but is a very characteristic and universal finding in fibrotic hypersensitivity pneumonia. It is not sufficient to establish the diagnosis on its own but should spark a careful search for the other findings helpful in establishing a histologic diagnosis of hypersensitivity pneumonia

Fig. 7.8 Fibrotic hypersensitivity pneumonia. (**a**) Photomicrograph showing long-standing hypersensitivity pneumonia characterized by a considerable degree of fibrosis that includes architectural distortion in the form of scarring and early honeycomb change resembling usual interstitial pneumonia. However, the patchy peribronchiolar infiltrate of lymphocytes combined with the cluster of multinucleated giant cells (*arrows*) are clues to the diagnosis of hypersensitivity pneumonia. (**b**) High-magnification view of the small clusters of multinucleated giant cells, one of which contains calcified cytoplasmic inclusions

Fig. 7.9 Fibrotic hypersensitivity pneumonia. (**a**) Low-magnification photomicrograph of surgical lung biopsy showing patchwork fibrosis and microscopic honeycomb changes resembling UIP. (**b**) Photomicrograph from same biopsy showing prominent peribronchiolar metaplasia. (**c**) Low-magnification photomicrograph of a biopsy obtained from a different lobe from the same patient showing features typical of hypersensitivity pneumonia, including a bronchiolocentric lymphocytic infiltrate and a poorly formed granuloma in the peribronchiolar interstitium. (**d**) High-magnification photomicrograph showing a loose cluster of multinucleated giant cells in the peribronchiolar interstitium

Fig. 7.10 Sarcoidosis. Gross photograph demonstrating the cut surface of a surgical lung biopsy involved by sarcoidosis. The abnormalities have an exquisitely lymphangitic distribution and include pale nodular and linear fibrous bands that expand interlobular septa, bronchovascular bundles, and visceral pleura

Fig. 7.11 Sarcoidosis. Low-magnification photomicrograph showing the lymphangitic distribution of non-necrotizing granulomas. The granulomas are confined to the interstitium and distributed within interlobular septa, bronchovascular bundles, and visceral pleura. As a consequence, vessel walls are frequently affected but without true necrotizing vasculitis

Fig. 7.12 Sarcoidosis. Low-magnification photomicrograph showing another example of sarcoidosis with classic lymphangitic distribution. Well-formed non-necrotizing granulomas are located along the visceral pleura, interlobular septa, and bronchovascular bundles

Fig. 7.13 Sarcoidosis. As illustrated in this low-magnification photomicrograph, sometimes the granulomas are confluent and form larger nodules that replace portions of lung parenchyma. The granulomas maintain their interstitial location and lymphangitic distribution

Fig. 7.14 Nodular sarcoidosis. (**a**) Low-magnification photomicrograph showing coalescence of well-formed granulomas in a collagenous stroma resulting in macroscopic nodules. (**b**) Cut surface of surgical lung specimen showing macroscopic nodules situated along visceral pleura and bronchovascular bundles in a patient with nodular sarcoidosis

Fig. 7.15 Sarcoidosis. Photomicrograph showing multiple well-formed non-necrotizing granulomas next to a bronchiole, expanding the bronchovascular bundle. Dense collagen fibrosis characterized by concentric lamellar bands is characteristic of, but not specific for, sarcoidosis

Fig. 7.16 Sarcoidosis. Photomicrograph showing non-necrotizing granulomas within a bronchovascular bundle (bronchiole in right upper corner), in this example involving

the wall of a small muscular pulmonary artery. Non-necrotizing granulomatous vasculitis is a common finding in surgical lung biopsies from patients with sarcoidosis and is occasionally present in smaller transbronchial biopsies

Fig. 7.17 Sarcoidosis. High-magnification photomicrograph showing a well-formed non-necrotizing granuloma consisting of tightly clustered multinucleated giant cells and epithelioid histiocytes, surrounded by a rim of fibroblasts and concentric bands of collagen fibrosis

Fig. 7.18 Sarcoidosis. A number of cytoplasmic inclusions are commonly seen within the histiocytes and especially the giant cells of sarcoidosis, including asteroid bodies (**a**), Schaumann bodies (**b**), and calcium oxalate crystals (**c**), as illustrated in these high-magnification photomicrographs. The calcium oxalate crystals are relatively translucent in routinely stained sections but are brightly birefringent when viewed with polarized light. These inclusions are not specific for sarcoidosis and can be seen in any chronic granulomatous lesions, including infections and hypersensitivity pneumonia

Fig. 7.19 Sarcoidosis. Photomicrograph showing a small focus of central necrosis in a granuloma in a patient with sarcoidosis. Although the predominant pattern of granulomatous inflammation in sarcoidosis is non-necrotizing, small foci of necrosis like this one in occasional granulomas are not uncommon in well-sampled cases

Fig. 7.20 Sarcoidosis. Low-magnification photomicrograph showing an example of late-stage disease characterized by a large area of dense hyalinized fibrosis. Tightly formed (sarcoidal) non-necrotizing granulomas are still appreciated at the edge of the fibrosis. This combination of features overlaps with the histology of hyalinizing infectious granulomas and is a finding that sometimes complicates diagnostic interpretation

Fig. 7.21 Sarcoidosis in transbronchial and endobronchial biopsies. (**a**) Photomicrograph of transbronchial biopsy showing a classic combination of well-formed non-necrotizing granulomas with associated collagen fibrosis confined to the interstitium and involving a bronchovascular bundle. (**b**) High-magnification photomicrograph of endobronchial biopsy showing poorly formed granuloma containing a loose cluster of isolated multinucleated giant cells in a bronchial wall from a patient with sarcoidosis. In the appropriate clinical and radiologic setting, even poorly formed granulomas are supportive of sarcoidosis

Fig. 8.1 Minimal acute cellular rejection (A1). (**a**) Low-magnification photomicrograph of a transbronchial biopsy showing a single small focus of perivascular inflammation in the background of unremarkable alveolar lung parenchyma. (**b**) At high magnification, there is a circumferential infiltrate of predominantly mononuclear inflammatory cells with occasional eosinophils within the loose perivascular interstitium, without extension into the adjacent alveolar septa. No significant expansion of the perivascular interstitium is present

Fig. 8.2 Mild acute cellular rejection (A2). (**a**) Two small blood vessels show significant circumferential expansion of the perivascular interstitium by mononuclear inflammatory infiltrates, which are easily identifiable under low magnification. (**b**) and (**c**) At high magnification, the infiltrates consist largely of mononuclear cells with occasional activated lymphocytes and plasmacytoid lymphocytes. Accumulated alveolar macrophages are seen within the adjacent alveolar spaces. No inflammatory infiltrate is present within the adjacent alveolar septa

Fig. 8.3 Moderate acute cellular rejection (A3). (**a**) Low-magnification photomicrograph illustrates easily recognizable perivascular mononuclear inflammatory infiltrates that percolate into the adjacent alveolar septa. (**b**) High-magnification view showing expansion of perivascular interstitium by mononuclear cells with extension of the inflammatory infiltrate into adjacent perivascular alveolar septa. There is associated alveolar pneumocyte hyperplasia along thickened alveolar septa and alveolar macrophages clustered within alveolar spaces

Fig. 8.4 Severe acute cellular rejection (A4). (**a**) Low-magnification photomicrograph showing perivascular spaces expanded by a mononuclear inflammatory infiltrate that percolates into alveolar septa. (**b**) High-magnification photomicrograph showing that the infiltrates are composed of lymphocytes, plasma cells, and occasional eosinophils and neutrophils. The characteristic feature of severe acute cellular rejection is pronounced acute lung injury, with alveolar collapse, reactive pneumocyte hyperplasia, and interstitial organization. Hyaline membranes are not evident in this example

Fig. 8.5 Endothelialitis in acute rejection. High-magnification photomicrograph showing endothelialitis, which is present in most moderate and all severe acute cellular rejections. Subendothelial infiltrates of small round and plasmacytoid lymphocytes are characteristic and are often accompanied by eosinophils. The endothelial cells are swollen and often detached from the vascular wall

Fig. 8.6 Low-grade lymphocytic bronchiolitis (B1R). High-magnification photomicrograph demonstrating a bronchiole with a mild peribronchiolar and submucosal mononuclear cell infiltrate that spares the respiratory epithelium

Fig. 8.7 High-grade lymphocytic bronchiolitis (B2R). High-magnification photomicrograph showing a bronchiole with a dense mononuclear cell infiltrate that expands the submucosa and involves the respiratory epithelium. Occasional neutrophils and eosinophils are also present

Fig. 8.8 Chronic rejection (obliterative bronchiolitis, C1). (**a**) Intermediate-magnification photomicrograph showing a bronchiole with patchy areas of scarring in the submucosa, associated with a peribronchiolar mononuclear infiltrate. The overlying epithelium appears injured, and the lumen of the airway is mildly narrowed. (**b**) An elastic stain shows that the scarring is located immediately beneath the epithelium and above the elastic layer. The scarring is most prominent in the lower right of the airway (*arrow*)

Fig. 8.9 Chronic rejection (obliterative bronchiolitis, C1). Photomicrograph showing an eccentric plaque of organizing fibroblasts and myofibroblasts within a myxoid stroma situated between the respiratory epithelium and the smooth muscle wall of the airway. The respiratory epithelium is focally attenuated, and the airway lumen is significantly narrowed

Fig. 8.10 Chronic rejection (obliterative bronchiolitis, C1). High-magnification photomicrograph showing an obliterated airway in which the entire airway lumen is occluded by scar tissue and mononuclear cells. There are rare fragments of residual respiratory epithelium (*arrows*) within the scarred lumen. The circumference of the small airway is defined by a relatively preserved layer of smooth muscle

Fig. 8.11 Chronic vascular rejection/accelerated graft vascular sclerosis. High-magnification photomicrograph showing alloreactive injury resulting in fibrointimal thickening of a muscular pulmonary artery, which is similar to coronary artery disease in transplanted hearts. The changes are seen in large- and intermediate-sized arteries and are generally not seen in transbronchial biopsies

Fig. 9.1 Simple silicosis. (**a**) Cut surface of autopsy lung showing classic simple silicosis with multiple pigmented lung nodules measuring less than 1 cm in their greatest dimension. (**b**) Low-magnification photomicrograph of a section from the same autopsy lung showing multiple silicotic nodules consisting of concentric, hyalinized collagen bundles, and a peripheral rim of inflammatory cells in which dust-laden macrophages predominate

Fig. 9.2 Silicotic nodule. Higher-magnification view of nodule illustrated in Fig. 9.1b showing the coarse collagen bundles typical of silicotic nodules with the usual degree of associated dust-laden macrophages

Fig. 9.3 Silicotic nodule. High-magnification photomicrograph taken using polarized light showing small, dimly birefringent crystalline particulates characteristic of free

crystalline silica. Finding crystalline particles does not by itself establish the diagnosis of silicosis, which is predicated on the finding of particulates in the appropriate histologic context

Fig. 9.4 Complicated silicosis (progressive massive fibrosis). (**a**) This low-magnification photomicrograph shows a conglomeration of silicotic nodules to form a larger complex lesion measuring more than 1 cm in greatest dimension. (**b**) Low-magnification photomicrograph showing another example of progressive massive fibrosis that involved nearly all of the right upper and middle lobes in an explanted lung from a patient with complicated silicosis

Fig. 9.5 Mixed dust fibrosis. (**a**) Low-magnification photomicrograph showing irregularly shaped dust macule without well-formed nodules. (**b**) Higher-magnification view showing epithelioid and spindled dust-laden macrophages making up the dust macule

Fig. 9.6 Mixed dust fibrosis. High-magnification view of another dust macule surrounding a bronchiole in a patient with mixed dust fibrosis. The stellate macule consists of macrophages, fibroblasts, and various pigmented particulates without silicotic nodules

Fig. 9.7 Mixed dust fibrosis with nonasbestos ferruginous bodies. A high-magnification photomicrograph shows pigmented particulates and ferruginous bodies containing central black cores (*arrows*) that differ from the translucent cores typical of asbestos

Fig. 9.8 Asbestosis. Low-magnification photomicrograph showing diffuse fibrosis with patchy scarring and honeycomb changes indistinguishable from usual interstitial pneumonia

Fig. 9.9 Asbestosis. At high magnification, the interstitial fibrosis includes fibroblast foci (*arrow*) typical of those commonly seen in usual interstitial pneumonia of unknown cause (i.e., idiopathic pulmonary fibrosis)

Fig. 9.10 Asbestosis. High-magnification photomicrograph showing a club-shaped asbestos body with a clear central core, a finding helpful in establishing the histologic diagnosis of asbestosis

Fig. 9.11 Asbestosis. High-magnification photomicrograph showing another example of an asbestos body with a beaded appearance. Note the clear, refractile central core that distinguishes asbestos bodies from other forms of nonasbestos ferruginous bodies

Fig. 9.12 Coal workers' pneumoconiosis (CWP). Cut surface of autopsy lung from a patient with CWP. There are numerous black pigmented macules and nodules with early complicated lesions measuring just over 1 cm in greatest dimension

Fig. 9.13 Simple CWP. Specially prepared Gough section of thinly sliced lung showing darkly pigmented dust macules characteristic of simple CWP

Fig. 9.14 Simple CWP. (**a**) Low-magnification photomicrograph showing a dust macule marked by deposits of black coal dust. (**b**) Higher-magnification view showing black coal dust in a dust macule characteristic of simple CWP

Fig. 9.15 Complicated CWP. Low-magnification photomicrograph of autopsy lung showing large area of progressive massive fibrosis in a patient with advanced CWP

Fig. 9.16 Berylliosis. (**a**) low-magnification view showing interstitial fibrosis associated with multiple non-necrotizing granulomas. In this example, many of the granulomas show prominent cytoplasmic inclusions consisting of concentric calcifications (Schaumann bodies). Schaumann bodies are characteristic of the granulomas seen in berylliosis but are nonspecific and commonly seen in other granulomatous conditions such as sarcoidosis

Fig. 9.17 *Berylliosis*. A high-magnification view of a non-necrotizing granuloma consisting of histiocytes, multinucleated giant cells, and a rim of lymphocytes

Fig. 9.18 Hard metal pneumoconiosis (giant cell interstitial pneumonia). A low-magnification view showing patchy interstitial thickening and cellular infiltrates distributed

in a bronchiolocentric fashion. At this low magnification, you can see numerous multinucleated giant cells, many of them with hyperchromatic nuclei
Fig. 9.19 Hard metal pneumoconiosis (giant cell interstitial pneumonia). A higher-magnification view showing expansion of peribronchiolar interstitium by inflammation with prominent multinucleated giant cells composed of both epithelium and alveolar macrophages. The multinucleated epithelial giant cells are TTF-1 positive (not shown) and represent pneumocytes
Fig. 9.20 Hard metal pneumoconiosis (giant cell interstitial pneumonia). High-magnification view showing intra-alveolar and surface epithelial giant cells
Fig. 9.21 *Aluminum pneumoconiosis.* Low-magnification photomicrograph showing multiple dust macules in which peribronchiolar interstitium is expanded by prominent collections of dust-laden macrophages
Fig. 9.22 *Aluminum pneumoconiosis.* High-magnification view of a dust macule showing macrophages containing finely granular, grayish-brown particles characteristic of aluminum
Fig. 10.1 Pulmonary arterial hypertension. (**a**) Photomicrograph of routinely stained section showing severe intimal hyperplasia and fibrosis with medial hypertrophy in a muscular pulmonary artery, leading to marked luminal narrowing. (**b**) An elastic tissue stain highlights the double elastic layers of the artery, with both intimal and medial thickening
Fig. 10.2 Pulmonary arterial hypertension. (**a**) In this example, a photomicrograph of a routinely stained section demonstrates more prominent intimal fibrosis leading to near complete obliteration of the lumen. (**b**) An elastic tissue stain highlights the thickened intima
Fig. 10.3 Pulmonary arterial hypertension. (**a**) Photomicrograph showing a plexiform lesion, which in this example is a diverticular outpouching of the artery into perivascular connective tissue characterized by a proliferation of small vascular spaces and hyperplastic endothelial cells resulting in a glomeruloid appearance, often with associated fibrin thrombi resembling organized and recanalized thrombi. (**b**) Photomicrograph showing a plexiform lesion forming a glomeruloid proliferation of small vascular spaces with plump endothelial cells involving the wall of a small muscular artery. (**c**) Photomicrograph of an elastic tissue stained section from the same biopsy showing that the plexiform lesion penetrates from the intima through the vessel wall
Fig. 10.4 Severe pulmonary arterial hypertension with necrotizing arteritis. Photomicrograph showing a small muscular pulmonary artery in which the arterial wall shows marked fibrinoid necrosis with an acute inflammatory infiltrate. This is an uncommon finding that only occurs in severe pulmonary hypertension
Fig. 10.5 Hypertensive changes in chronic fibrotic disease. High-magnification photomicrograph of a routinely stained section showing severe intimal and medial thickening in a small muscular pulmonary artery in a patient with usual interstitial pneumonia. Note the dense collagen fibrosis and honeycomb change (*arrow*) in the background
Fig. 10.6 *Fat emboli.* Photomicrograph showing an oil red O stain in which multiple fat droplets are situated within the lumina of small pulmonary arterioles. This 70-year-old man underwent a hip arthroplasty for a femoral head fracture. Fat droplets within the bone marrow space circulated to the pulmonary artery through the heart, embolizing to small arterioles resulting in acute pulmonary hypertension. Fat emboli are a rare cause of acute pulmonary hypertension and not usually accompanied by the morphologic features characteristic of chronic pulmonary hypertension
Fig. 10.7 Intravenous (IV) drug abusers' lung. IV injection of pulverized oral medications can result in embolization of inert fillers (excipients), commonly used as binding

agents, in small pulmonary vessels, eliciting a foreign body giant cell reaction. In some patients, this may cause a syndrome of chronic pulmonary hypertension. In this example, a low-magnification photomicrograph shows patchy nodular lesions that seem to follow a lymphangitic distribution. Foreign body granulomatous reactions are visible at low magnification

Fig. 10.8 IV drug abusers' lung. A higher-magnification photomicrograph shows foreign body granulomas affiliated with plate-like, pale-gray particulates of microcrystalline cellulose expanding the vessel wall

Fig. 10.9 IV drug abusers' lung. (**a**) High-magnification view showing mainly large, elongated, pale-gray microcrystalline cellulose, which is a common filler in drugs intended for oral use. (**b**) The same microscopic field viewed at the same magnification using polarized light. The microcrystalline cellulose particles show strong birefringence under polarized light

Fig. 10.10 IV drug abusers' lung. (**a**) A high-magnification view showing giant cells containing deeply basophilic crospovidone, another filler common in oral medications and dietary supplements. Microcrystalline cellulose particles and associated giant cells are also present. (**b**) Crospovidone is not birefringent when viewed with polarized light

Fig. 10.11 Pulmonary veno-occlusive disease (PVOD). Low-magnification photomicrograph shows congested lung parenchyma and several pulmonary veins that are narrowed or occluded by fibrosis (*arrows*). These vessels do not have accompanying airways and are situated within interlobular septa, a finding helpful in identifying them as veins

Fig. 10.12 PVOD. A high-magnification photomicrograph showing a vein completely occluded by fibrosis

Fig. 10.13 PVOD. A high-magnification photomicrograph showing a small vein nearly occluded by fibrous thickening of its wall

Fig. 10.14 PVOD. An elastic tissue stain reveals the single elastic layer of this nearly occluded vein

Fig. 10.15 PVOD. A high-magnification photomicrograph shows chronic congestive changes, including thickened alveolar septa with capillary hemangiomatosis-like changes (upper right) and a narrowed vein in the center. The wall of the narrowed vein demonstrates deeply basophilic elastic lamina resulting from encrustation by hemosiderin and calcium deposits, a finding referred to historically as endogenous pneumoconiosis. These are signs of severe chronic venous congestion, which can be caused by PVOD, left-sided heart disease, and extrapulmonary venous outflow obstruction

Fig. 10.16 PVOD. High-magnification photomicrograph of a Prussian blue iron-stained section showing iron deposition in the elastic lamina of a vein with fibrosis and a narrowed lumen

Fig. 10.17 Capillary hemangiomatosis. Intermediate-magnification photomicrograph showing expansion of alveolar septa by redundant blood-filled capillary loops. The changes can also be seen in PVOD and chronic venous hypertension caused by left-sided heart disease and venous outflow obstruction. The absence of fibrous obliterations of veins is the key to ruling out PVOD

Fig. 10.18 Capillary hemangiomatosis-like change in venous outflow obstruction. High-magnification photomicrograph showing visceral pleura expanded by proliferating blood-filled capillary loops resembling capillary hemangiomatosis (capillary hemangiomatosis-like change) in a patient with fibrosing mediastinitis causing venous outflow obstruction

Fig. 10.19 Chronic congestive changes. Alveolar space containing numerous hemosiderin-laden macrophages and thickened alveolar septa with redundant capillaries that are features of chronic venous congestion; this can be seen in any condition caus-

ing venous hypertension, including PVOD, pulmonary capillary hemangiomatosis, left-sided heart disease, and venous outflow obstruction. In some patients, the thickened alveolar septa may mimic nonspecific interstitial pneumonia and can be affiliated with radiologic abnormalities resembling other forms of diffuse lung disease

Fig. 10.20 Chronic thrombotic pulmonary hypertension. (**a**) Photomicrograph showing enlarged small muscular pulmonary arteries with multiple lumens (vascular webs) representing recanalized thrombi. The presence of these vascular webs combined with acute and organizing thrombi is an important clue to the diagnosis of chronic thrombotic pulmonary hypertension. An organizing thrombus occludes one of the lumens in the vessel on the right. (**b**) Photomicrograph from the same patient showing another recanalized thrombus involving a small muscular artery with an organizing thrombus and endothelial hyperplasia resembling a plexiform lesion (*arrow*)

Fig. 10.21 Granulomatosis with polyangiitis (GPA; formerly Wegener granulomatosis), classic type. (**a**) Low-magnification photomicrograph showing the typical necrotizing granulomatous inflammation with irregular, geographic, basophilic dirty necrosis and background dense inflammatory infiltrates and fibrosis. (**b**) Higher-magnification view showing collagen necrosis as well as granular, basophilic nuclear debris. The necrotic area is surrounded by epithelioid histiocytes and rare multinucleated giant cells

Fig. 10.22 Classic GPA. High-magnification photomicrograph showing a granulomatous microabscess characterized by a small focus of necrotic neutrophils surrounded by epithelioid histiocytes, multinucleated giant cells, and a mixed inflammatory infiltrate. Granulomatous microabscesses with these features are an extremely helpful finding in establishing a histologic diagnosis of GPA

Fig. 10.23 Classic GPA. High-magnification photomicrograph showing another smaller and more subtle granulomatous microabscess with multinucleated giant cells demonstrating the hyperchromatic nuclei characteristic of GPA

Fig. 10.24 Classic GPA. Large and/or small airways are commonly involved in GPA and when a dominant feature has been referred to by some as a bronchocentric variant. (**a**) High-magnification photomicrograph showing granulomatous inflammation with giant cells involving and partially destroying a cartilaginous airway. (**b**) Photomicrograph showing a small bronchiole circumferentially involved by a mixed inflammatory infiltrate that includes multinucleated giant cells resulting in a vaguely granulomatous appearance

Fig. 10.25 Vasculitis in classic GPA. (**a**) Low-magnification photomicrograph showing necrotizing granulomatous inflammation involving several blood vessels. (**b**) High-magnification view of a small muscular artery involved by necrotizing granulomatous inflammation with fibrinoid necrosis, necrotic neutrophils, and a multinucleated giant cell

Fig. 10.26 Vasculitis in classic GPA. High-magnification photomicrograph showing another small muscular pulmonary artery involved by necrotizing inflammation with prominent karyorrhexis and granulomatous microabscesses

Fig. 10.27 Vasculitis in classic GPA. In this example, the blood vessel is involved by necrotizing inflammation with abundant neutrophils and eosinophils but without well-developed granulomatous features

Fig. 10.28 BOOP-like GPA. (**a**) Low-magnification photomicrograph showing extensive organizing pneumonia, a lesion referred to historically as bronchiolitis obliterans organizing pneumonia (BOOP). (**b**) Higher-magnification photomicrograph showing a granulomatous microabscess typical of GPA in which there is central necrosis with prominent karyorrhexis of neutrophils surrounded by a mixed inflammatory infiltrate that includes palisaded and multinucleated macrophages. (**c**)

Photomicrograph showing a pulmonary vein in the same biopsy in which there is necrotizing vasculitis characterized by a transmural infiltrate of inflammatory cells with fibrinoid necrosis and karyorrhexis

Fig. 10.29 Hemorrhage and necrotizing capillaritis in GPA. (**a**) Low-magnification photomicrograph showing prominent intra-alveolar hemorrhage and thickened alveolar septa with hemosiderin and inflammatory cells. (**b**) High-magnification view showing capillaritis characterized by expansion of alveolar septa predominantly by neutrophils, with karyorrhexis and occasional eosinophils. This variant may lack the necrotizing granulomas, granulomatous microabscesses, and giant cells typical of classic GPA. In the absence of classic features, the diagnosis of GPA cannot be made on the basis of histology alone because hemorrhage with capillaritis may occur in patients with other vasculitic syndromes, including microscopic polyangiitis and systemic lupus erythematosus

Fig. 10.30 Eosinophilic variant of GPA. (**a**) Low-magnification photomicrograph shows necrotizing granulomatous inflammation with dirty basophilic necrosis typical of GPA. (**b**) At higher magnification, there is prominent eosinophilia, a relatively common finding that does not by itself suggest eosinophilic granulomatosis with polyangiitis (formerly Churg-Strauss syndrome) as an alternative. Because eosinophils are nearly universal in GPA, prominent eosinophilia simply reflects an extreme in the histologic spectrum of classic GPA, although others separate these as eosinophilic variants

Fig. 10.31 Eosinophilic granulomatosis with polyangiitis (EGPA; formerly Churg-Strauss syndrome). (**a**) Low-magnification photomicrograph showing necrotizing granulomatous inflammation with prominent eosinophilic infiltrates. (**b**) High-magnification view of a granuloma composed of a necrotic center, palisading epithelioid histiocytes, and multinucleated giant cells. The surrounding inflammatory cells are rich in eosinophils

Fig. 10.32 EGPA. Photomicrograph showing eosinophilic pneumonia characterized by intra-alveolar accumulation of eosinophils and macrophages in a patient with EGPA

Fig. 10.33 Vasculitis in EGPA. (**a**) High-magnification photomicrograph showing necrotizing vasculitis in which the vascular wall is infiltrated by an eosinophil-rich mixed inflammatory infiltrate with associated vessel wall necrosis and fibrin thrombus. (**b**) Photomicrograph showing another example of vasculitis in EGPA in which the blood vessel is partially destroyed by necrosis with an eosinophil-rich inflammatory infiltrate. Note the background eosinophilic pneumonia characterized by intra-alveolar accumulation of eosinophils and macrophages

Fig. 11.1 *Nodular lymphoid hyperplasia.* (**a**) Low-magnification photomicrograph showing a combination of fibrotic scarring and a patchy infiltrate of mononuclear cells with lymphoid aggregates, one of which demonstrates a secondary germinal center. (**b**) Higher-magnification photomicrograph of the same lesion illustrated in **a** showing lymphoid aggregates with germinal centers in a background of dense collagen fibrosis and chronic inflammatory infiltrates. It lacks the tumefactive sheets of monocytoid B cell and plasma cells more characteristic of MALT lymphoma; however, distinguishing the two can be difficult and sometimes requires molecular testing for clonal light-chain expression or heavy-chain gene rearrangements

Fig. 11.2 *Follicular bronchiolitis.* (**a**) Low-magnification photomicrograph showing nodular lymphoid aggregates with germinal centers surrounding small bronchioles. The bronchiole lumens are narrowed. (**b**) Higher-magnification view showing the nodular lymphoid hyperplasia with germinal centers immediately beneath the respiratory epithelium. Follicular bronchiolitis is sometimes seen as a secondary feature in other conditions, including bronchiectasis; the term follicular bronchiolitis is generally reserved for those cases in which it represents the primary pathologic finding

Fig. 11.3 Lymphoid interstitial pneumonia (LIP). Chest CT scan of a patient with Castleman disease and a surgical lung biopsy showing LIP. The CT scan shows a number of abnormalities, including numerous bilateral cysts that are a common finding in patients with LIP. This change is not specific for LIP and is also seen in patients with clonal B-cell lymphoproliferative disorders such as MALT lymphoma complicated by amyloid

Fig. 11.4 Lymphoid interstitial pneumonia. (**a**) Low-magnification photomicrograph showing diffuse alveolar thickening by a dense inflammatory infiltrate without fibrosis. The predominantly lymphocytic infiltrate is accentuated around distal bronchioles, where it includes occasional lymphoid aggregates with germinal centers. (**b**) Higher-magnification view of lesion illustrated in **a** showing dense lymphoplasmacytic infiltrate with loose clusters of epithelioid and multinucleated histiocytes comprising poorly formed granulomas. This combination of findings resembles hypersensitivity pneumonia (*see* Chap. 7), although the clinical context combined with the presence of germinal centers and a conspicuous population of plasma cells is often helpful in making the distinction

Fig. 11.5 Lymphoid interstitial pneumonia. High-magnification photomicrograph demonstrates alveolar septa expanded by predominantly plasma cells in this example

Fig. 11.6 Extranodal marginal zone lymphoma of MALT lymphoma. (**a**) Low-magnification photomicrograph showing dense lymphocytic infiltrates expanding the interstitium forming a tumefactive mass that extends along bronchovascular bundles and interlobular septa. The cellular infiltrate includes lymphoid aggregates with germinal centers and ill-defined islands of pallor that correspond to sheets of monocytoid B lymphocytes. (**b**) Higher-magnification view illustrating extension along lymphatic pathways at the periphery of the tumefactive mass

Fig. 11.7 Extranodal marginal zone lymphoma of MALT lymphoma. (**a**) Photomicrograph highlighting area in which tumefactive lymphocytic infiltrate overruns the normal lung architecture and includes ill-defined zones of pallor corresponding to monocytoid B cells. There are numerous lymphoepithelial lesions in which bronchiolar epithelium is partially or completely obscured by intraepithelial lymphocytes. (**b**) High-magnification photomicrograph showing lymphoepithelial lesion in which lymphocytes percolate into bronchiolar epithelium, partially or completely obscuring the airway lumen

Fig. 11.8 Lymphoepithelial lesion in extranodal marginal zone lymphoma of MALT lymphoma. (**a**) High-magnification view showing the neoplastic lymphocytes and plasma cells, some of which are within the bronchiolar epithelium. (**b**) Immunohistochemical staining with a pancytokeratin cocktail highlights the bronchiolar epithelium infiltrated by lymphoid cells

Fig. 11.9 Extranodal marginal zone lymphoma of MALT lymphoma. High-magnification view of the dense cellular infiltrate showing predominantly small lymphocytes, some with a narrow rim of cytoplasm resulting in a monocytoid appearance with associated plasma cells. Some of the plasma cells show brightly eosinophilic intranuclear immunoglobulin pseudoinclusions called Dutcher bodies (*arrow*), a helpful finding that is seen more commonly in lymphomas with plasmacytic differentiation than in benign lymphoplasmacytic infiltrates

Fig. 11.10 Extranodal marginal zone lymphoma of MALT lymphoma. (**a**) Photomicrograph showing prominent Russell bodies, immunoglobulin-filled cytoplasmic inclusions, in a MALT lymphoma. The inclusions in this example compress and distort pyknotic nuclei. Unlike intranuclear Dutcher bodies, Russell bodies are not specific and frequently occur in benign lymphoplasmacytic infiltrates as well as immunoglobulin-synthesizing neoplasms. (**b**) and (**c**), Immunohistochemical

stains show monotypical expression of lambda (**b**) compared to kappa (**c**) in the cytoplasmic Russell bodies illustrated in **a**

Fig. 11.11 Extranodal marginal zone lymphoma of MALT lymphoma. (**a**) The lymphoid cells are predominantly B cells as highlighted by CD20 immunostaining. (**b**) There are also variably abundant admixed T cells as highlighted by CD3 immunostaining. There remains a substantial subset of cells that stained with neither CD20 nor CD3, primarily plasma cells

Fig. 11.12 Extranodal marginal zone lymphoma of MALT lymphoma. In situ hybridization studies using probes that recognize immunoglobulin light-chain RNA show monotypic expression of kappa (**a**) compared to lambda (**b**) in this example. Monotypic light-chain expression is not always demonstrable using immunohistochemistry and/or RNA in situ hybridization in otherwise typical examples of MALT lymphoma. Therefore failure to demonstrate light-chain restriction does not preclude the diagnosis in histologically classic cases

Fig. 11.13 Extranodal marginal zone lymphoma of MALT lymphoma. Photomicrograph showing non-necrotizing granulomas in MALT lymphoma, an uncommon finding that may confound the diagnosis in rare cases

Fig. 11.14 Extranodal marginal zone lymphoma of MALT lymphoma. (**a**) Occasionally, as illustrated in this photomicrograph, amyloid deposits consisting of excessive immunoglobulin light chains are seen on H&E staining. Note also the plasma cell-rich lymphoid infiltrates in the background. Indeed, most cases of nodular amyloidosis are probably MALT lymphomas that have been overrun by amyloid deposits. (**b**) The amyloid deposits stain red on Congo red staining when viewed with normal illumination. (**c**) When viewed using polarized light, the Congo red-stained amyloid deposits show apple-green birefringence

Fig. 11.15 Extranodal marginal zone lymphoma of MALT lymphoma. (**a**) Low-magnification photomicrograph of MALT lymphoma with associated giant lamellar bodies. Giant lamellar bodies are uncommon and not specific for MALT lymphoma, but when it comes to lymphoproliferative lesions, they occur almost exclusively in MALT lymphomas compared to benign, nonneoplastic lymphoplasmacytic proliferations. (**b**) Higher-magnification photomicrograph showing giant lamellar bodies in an air space entrapped within a MALT lymphoma. Giant lamellar bodies are extracellular inclusions consisting of concentric rings of surfactant degradation and cell breakdown products

Fig. 11.16 Crystal-storing histiocytosis associated with extranodal marginal zone lymphoma of MALT lymphoma. (**a**) On rare occasions, tumor-related light chains may illicit a histiocytic response, arrayed as sheets of large polygonal cells as illustrated in this low-magnification photomicrograph of a lesion that presented as an asymptomatic solitary nodule. There are rare reports of crystal-storing histiocytosis unrelated to a clonal lymphoproliferative disorder, but most occur in the context of MALT lymphoma. (**b**) and (**c**) Higher-magnification photomicrographs show eosinophilic, linearly striated immunoglobulin inclusions characteristic of crystal-storing histiocytosis. The inclusions lack the globular configuration of Russell bodies (*see* Fig. 11.10) and are present in nonneoplastic histiocytes rather than plasma cells

Fig. 11.17 Crystal-storing histiocytosis associated with extranodal marginal zone lymphoma of MALT lymphoma. (**a**) Another example of crystal-storing histiocytosis showing characteristic cytoplasmic inclusions in this high-magnification photomicrograph. (**b**) A CD68 immunostain confirms that the accumulated cells are histiocytes rather than plasma cells. (**c**) The cytoplasmic contents of the histiocytes show pale staining for kappa light chains with a monotypic pattern of dark cytoplasmic staining in a minor subpopulation of neoplastic plasma cells. (**d**) The cytoplasmic con-

tents of histiocytes and neoplastic plasma cells are negative for lambda light-chain expression

Fig. 11.18 Lymphomatoid granulomatosis. Low-magnification photomicrograph showing a central area of necrosis surrounded by a lymphocyte-rich cellular rim without the epithelioid, palisaded, and multinucleated histiocytes characteristic of granulomatous inflammation

Fig. 11.19 Lymphomatoid granulomatosis. High-magnification photomicrograph demonstrates a polymorphic infiltrate comprising mainly small lymphocytes with widely scattered large atypical cells, including occasional variants with multilobated nuclei resembling Reed-Sternberg cells (*arrows*)

Fig. 11.20 Lymphomatoid granulomatosis. (**a**) Low-magnification photomicrograph showing large area of necrosis surrounded by a polymorphic infiltrate without frankly granulomatous features. (**b**) Higher-magnification view showing that the polymorphic infiltrate is composed of small lymphocytes, histiocytes, and scattered large atypical cells

Fig. 11.21 Lymphomatoid granulomatosis. (**a**) High-magnification photomicrograph showing a portion of the polymorphic infiltrate illustrated in Fig. 11.20b. Large atypical cells with prominent eosinophilic nucleoli, vesicular chromatin, and irregularly shaped nuclei are scattered against a backdrop of small lymphocytes. (**b–d**), Immunostains shown in photomicrographs taken at the same magnification as **a** show that the predominant population of small cells is positive for CD3 (**b**), while the large atypical cells are positive for CD20 (**c**) and for EBV (**d**) in RNA in situ hybridization studies using probes that recognize EBV RNA (EBER). Almost all the large atypical cells are CD20- and EBV-positive

Fig. 11.22 Lymphomatoid granulomatosis. High-magnification photomicrograph of a blood vessel cut in cross section showing a dense mononuclear cell infiltrate that infiltrates and expands the vessel wall without vessel wall necrosis. The infiltrate consists of a combination of large and small lymphocytes. Vessel wall involvement is not unique to lymphomatoid granulomatosis and occurs in other benign and malignant lymphoproliferative disorders. But this pattern of vessel infiltration in the context of centrally necrotic nodules composed of predominantly small lymphocytes with variable numbers of large atypical cells is characteristic and should prompt appropriate phenotyping studies

Fig. 11.23 Acute histoplasmosis mimicking lymphomatoid granulomatosis. (**a**) Low-magnification photomicrograph showing a lymphocyte-rich nodule in a patient with a 4-day history of chest pain and sweats affiliated with multiple bilateral small (< 1 cm) nodules on chest imaging studies. (**b**) Intermediate-magnification view shows a polymorphic infiltrate in which small lymphocytes predominate without granulomatous features. (**c**) High-magnification view shows vessel infiltration and scattered large cells that were positive for CD3 and CD30 on paraffin section immunostains (not shown) and negative for EBV on in situ hybridization studies (not shown). The atypical CD3-positive cells had an aberrant phenotype (partial loss of CD2, CD5, and CD7), and molecular studies showed clonal rearrangements of the T-cell receptor gamma gene locus. (**d**) Despite phenotypical evidence of a "lymphomatoid granulomatosis-like" peripheral T-cell lymphoma, a Gomori methenamine silver (GMS) stain showed numerous fungal yeast forms typical of *Histoplasma capsulatum* supporting the diagnosis of acute histoplasmosis

Fig. 11.24 Follicular lymphoma. (**a**) Low-magnification view showing a nodular lymphoid infiltrate with a predilection for visceral pleura, interlobular septa, and bronchovascular bundles. In addition to having a "lymphangitic" distribution typical of lymphomas and leukemic infiltrates in general, in some areas the confluent lymphoid nodules have a tumefactive growth pattern. (**b**) Higher-magnification photo-

micrograph showing ill-defined uniform follicles without well-demarcated germinal centers in which small and large lymphocytes were positive for CD20, CD10, BCL2, and BCL6 (not shown). This patient proved to have bone marrow and nodal disease

Fig. 11.25 Mantle cell lymphoma. (**a**) Low-magnification view showing multiple uniform lymphoid nodules randomly distributed in mildly fibrotic lung without the tumefactive growth and lymphangitic spread characteristic of other low-grade B-cell lymphomas involving the lung. (**b**) Intermediate-magnification view showing the uniform lymphoid follicles for which diagnostic concerns might reasonably include benign conditions and other low-grade B-cell lymphoproliferative disorders, especially follicular lymphoma

Fig. 11.26 Mantle cell lymphoma. (**a**) High-magnification view of one of the neoplastic nodules illustrated in Fig. 11.25 consisting of homogeneous tumor cells with coarse, evenly dispersed chromatin and inconspicuous nucleoli. (**b**) and (**c**), Paraffin section immunostains showed the neoplastic cells were positive not only for CD20 and BCL2 (not shown) but also for CD5 (**b**) and cyclin D1 (**c**). This patient proved to have bone marrow involvement

Fig. 11.27 Intravascular large B-cell lymphoma. (**a**) Low-magnification view showing preserved alveolar architecture with thickened alveolar septa in which alveolar septal capillaries are distended by a cellular infiltrate resembling an interstitial pneumonia. (**b**) High-magnification view showing large atypical neoplastic lymphocytes filling alveolar septal capillaries. (**c**) The neoplastic cells within the capillaries are positive for CD20 in paraffin section immunostains

Fig. 11.28 Posttransplant lymphoproliferative disorder (PTLD), polymorphic type. (**a**) Low-magnification photomicrograph showing an area of necrosis bounded by a dense polymorphic lymphocytic infiltrate closely resembling lymphomatoid granulomatosis. (**b**) High-magnification photomicrograph showing a heterogeneous population of small to large lymphoid cells. (**c**) The large cells are positive for CD20 in paraffin section immunostain. (**d**) Some large cells are positive for EBV in in situ hybridization studies. The polymorphic type of PTLD may be indistinguishable from lymphomatoid granulomatosis based on morphology and immunostains alone; a history of organ transplant is key to the diagnosis in these patients

Fig. 11.29 Anaplastic large cell lymphoma. Low-magnification photomicrograph showing that the lung architecture is focally effaced by a well-demarcated nodular lesion

Fig. 11.30 Anaplastic large cell lymphoma (ALCL). (**a**) High-magnification view of the nodule illustrated in Fig. 11.29 showing that the lesion consists mainly of large cells with a rim of cytoplasm and large irregular nuclei. Prominent nucleoli are also seen. (**b**) High-magnification photomicrograph showing strong positivity for CD30 in the large atypical CD3-positive cells of ALCL. The cells may or may not be anaplastic lymphoma kinase (ALK)-positive

Fig. 11.31 Extranodal natural killer/T-cell lymphoma, nasal type. (**a**) Low-magnification photomicrograph showing an ill-defined localized area of increased cellularity. (**b**) High-magnification photomicrograph showing intravascular tumor cells that are markedly atypical with hyperchromatic chromatin, small nucleoli, and pale staining finely vacuolated cytoplasm. (**c**) and (**d**), The tumor cells are positive for CD2 on paraffin section immunostains (**c**) and for EBV on EBER in situ hybridization studies (**d**)

Fig. 11.32 Classic Hodgkin lymphoma. (**a**) Whole mount slide of a lung wedge biopsy showing multiple subpleural and intraparenchymal nodular lesions consisting of a polymorphic infiltrate with associated sclerosis. (**b**) Low-magnification view showing that the areas of abnormality are well-demarcated from the uninvolved lung parenchyma and are composed of cellular infiltrates separated by broad collagen bands

Fig. 11.33 Classic Hodgkin lymphoma. (**a**) High-magnification view of the cellular infiltrates demonstrates mixed small lymphocytes, plasma cells, histiocytes, abundant eosinophils, and multiple large atypical cells with prominent nucleoli. A binucleated Reed-Sternberg cell is seen (arrow). Note the dense collagen bands in the background. (**b**) The majority of the large atypical cells are positive for CD30 with a characteristic membranous and paranuclear dot-like distribution. (**c**) Some of the large atypical cells are also positive for CD15 with the same membrane and paranuclear dot-like staining pattern

Fig. 11.34 Classic Hodgkin lymphoma. (**a**) Low-magnification photomicrograph showing a necrotizing nodule closely mimicking the appearance of a necrotizing granuloma. (**b**) At higher magnification the polymorphic infiltrate included prominent "smudge cells" aligned at the periphery of the necrosis. (**c**) The atypical cells illustrated in **b** were strongly positive for CD30 and focally positive for CD15. (**d**) Elsewhere, the biopsy showed classic mononuclear and binucleated Hodgkin cells

Fig. 12.1 Exophytic squamous cell papilloma. (**a**) Low-magnification photomicrograph shows an exophytic lesion featuring arborizing loose fibrovascular cores covered by stratified squamous epithelium. (**b**) Intermediate-magnification photomicrograph showing that the overlying squamous epithelium has an orderly epithelial maturation with surface keratinization

Fig. 12.2 Inverted growth pattern in recurrent respiratory papillomatosis. Low-magnification photomicrograph showing the inverted growth pattern typical of lower respiratory tract involvement in patients with recurrent respiratory papillomatosis

Fig. 12.3 Inverted growth pattern in recurrent respiratory papillomatosis. Photomicrograph of another lesion from same patient illustrated in Fig. 12.2 with parenchymal involvement featuring solid intra-alveolar nests of cytologically bland nonkeratinizing squamous cells

Fig. 12.4 Mixed squamous and glandular papilloma. (**a**) Low-magnification photomicrograph shows broad epithelial-lined fronds with connective tissue cores lined by both nonciliated columnar and squamous epithelia. (**b**) Higher-magnification view showing both squamous and glandular epithelia

Fig. 12.5 Ciliated muconodular papillary tumor. (**a**) Low-magnification photomicrograph showing a peripheral papillary tumor unassociated with a bronchus and affiliated with acellular mucinous lakes in adjacent parenchyma. (**b**) High-magnification photomicrograph showing the combination of ciliated columnar cells, goblet mucinous cells, and basal cells that constitute this tumor. The findings overlap with those seen in mixed squamous and glandular papillomas, differing mainly in their peripheral location, associated mucinosis, and characteristic ciliated respiratory epithelium

Fig. 12.6 *Pleomorphic adenoma.* (**a**) Low-magnification photomicrograph showing solid exophytic endobronchial mass covered by a surface layer of nonneoplastic respiratory epithelium. Pleomorphic adenomas of the lung show the same range of histologic heterogeneity typical of those seen more commonly in major salivary glands. (**b**) High-magnification photomicrograph showing the combination of epithelial cells, myoepithelial cells, and stroma that define pleomorphic adenomas at any site

Fig. 12.7 Carcinoma arising in pleomorphic adenoma (carcinoma ex pleomorphic adenoma). (**a**) Low-magnification photomicrograph showing an exophytic endobronchial mass characterized by a combination of epithelium and stroma typical of pleomorphic adenoma. (**b**) Photomicrograph showing that a portion of the tumor comprises epithelial cells, myoepithelial cells, and both hyalinized and chondroid stromata characteristic of pleomorphic adenoma. (**c**) High-magnification photomicrograph showing that elsewhere this heterogeneous tumor demonstrates a population of highly atypical infiltrating carcinoma cells with associated coagulative tumor necrosis

Fig. 12.8 Mucous gland adenoma. (**a**) Low-magnification photomicrograph showing an exophytic endobronchial mass covered by a smooth surface of benign respiratory epithelium without the arborizing papillary architecture of a papilloma. (**b**) Higher-magnification view showing cytologically bland columnar mucinous cells lining glandular and cystic spaces. The cystic spaces show mucinous lakes surrounded by attenuated mucinous epithelial cells

Fig. 12.9 Alveolar adenoma. (**a**) Low-magnification photomicrograph showing a solitary, well-circumscribed non-fluorodeoxyglucose (FDG) avid 1-cm lung tumor made up of a collection of cystic spaces separated by stroma of variable thickness. Some of the cystic spaces contain eosinophilic granular proteinaceous material. (**b**) High-magnification photomicrograph showing the septa separating the cystic spaces. The septa constitute bland mesenchymal spindle cells and occasional mononuclear inflammatory cells lined by surface cuboidal type 2 pneumocytes

Fig. 12.10 Alveolar adenoma. (**a**) Low-magnification photomicrograph illustrating another example of alveolar adenoma with a sharply circumscribed interface with nonneoplastic lung tissue and cystic spaces partially filled with amorphous proteinaceous debris, macrophages, and procedure-related blood. (**b**) Higher-magnification photomicrograph shows that the cystic spaces are lined by cytologically bland, flattened to cuboidal cells resembling reactive type 2 pneumocytes. The intervening stroma contains cytologically bland oval to spindle cells as well as rare inflammatory cells

Fig. 12.11 Papillary adenoma. (**a**) Low-magnification photomicrograph shows a solid well-circumscribed peripheral lung tumor that consists of papillary structures containing fibrovascular cores lined by a single layer of epithelium. (**b**) High-magnification photomicrograph showing cuboidal epithelium lining the surface of the fibrovascular cores. The lining epithelial cells resemble reactive type 2 pneumocytes. Nuclear atypia, mitoses, and necrosis are absent

Fig. 12.12 Gross photograph of sclerosing pneumocytoma. Sclerosing pneumocytomas are traditionally solitary and peripherally located in the lung. The tumor is well circumscribed, with a solid and frequently hemorrhagic microcystic cut surface. Solid areas without hemorrhage vary from gray-white to tan in color

Fig. 12.13 Sclerosing pneumocytoma. Low-magnification photomicrograph shows a well-circumscribed tumor with a variegated pattern, ranging from cystic and hemorrhagic to solid

Fig. 12.14 Sclerosing pneumocytoma. Photomicrograph showing an area with prominent hemorrhagic "hemangioma-like" pattern. The tumor forms ectatic spaces filled with blood and separated by sclerotic stroma

Fig. 12.15 Sclerosing pneumocytoma. Photomicrograph showing an area with solid growth pattern. Tumor cells form solid sheets with scant sclerotic stroma. The tumor cells are round and uniform, with a moderate amount of eosinophilic cytoplasm and small inconspicuous nucleoli. Cytologic atypia and mitoses are absent

Fig. 12.16 *Sclerosing pneumocytoma.* Photomicrograph showing a sclerotic area. Dense collagen fibrosis and interstitial round tumor cells are seen

Fig. 12.17 Sclerosing pneumocytoma. (**a**) Photomicrograph showing an area with prominent papillary growth pattern. Type 2 pneumocytes with "reactive" atypia line the surface of sclerotic papillae that show, to varying degrees, associated interstitial round cells. (**b**) High-magnification view showing that papillary structures are covered with surface cuboidal to "hob-nailing" cells with mild cytologic atypia typical of type 2 pneumocytes. Underlying the surface cells are sclerotic connective tissue cores showing both inflammatory and interstitial round tumor cells

Fig. 12.18 Sclerosing pneumocytoma. High-magnification photomicrograph showing an area with abundant foamy macrophages. This is a common but nonspecific finding in sclerosing pneumocytoma

Fig. 12.19 Sclerosing pneumocytoma. Photomicrograph showing a pan-cytokeratin immunohistochemical stain in a papillary area. The surface cells are strongly positive for cytokeratin, whereas the interstitial round cells show only focal weak staining and are frequently negative altogether
Fig. 12.20 Sclerosing pneumocytoma. (**a**) Photomicrograph showing a TTF-1 immunohistochemical stain in sclerosing pneumocytoma. Both surface cells and interstitial round cells are positive for TTF-1, with relatively stronger staining in the surface cells. (**b**) Photomicrograph showing napsin A immunohistochemical stain in which the surface cells are strongly positive and the interstitial round cells are negative
Fig. 12.21 Pulmonary hamartoma. (**a**) Gross photograph shows a well-circumscribed tumor adjacent to a major bronchus. The cut surface is gray-white to yellow-tan in color, with grossly discernable cartilaginous components. (**b**) Gross photograph of another large (7.7 cm) hamartoma showing irregular-shaped spicules of glistening hyaline cartilage separated by yellow soft tissue composed mainly of benign fat
Fig. 12.22 Pulmonary hamartoma. Low-magnification photomicrograph shows a tumor composed predominantly of hyaline cartilage and mature adipose tissue, with a minor component of myxoid loose connective tissue. The clefted spaces lined by respiratory epithelium represent entrapment of normal nonneoplastic structures by the expanding tumor
Fig. 12.23 Pulmonary hamartoma. Photomicrograph showing another example of a hamartoma made up of a combination of hyaline cartilage, the pale staining fibromyxoid tissue characteristic of hamartoma, and entrapped, nonneoplastic respiratory epithelial cells
Fig. 12.24 Pulmonary hamartoma. Photomicrograph of an immunohistochemical stain for glial fibrillary acidic protein (GFAP) showing positive staining in hyaline cartilage and peri-cartilaginous fibromyxoid spindle cells. This pattern of GFAP staining is characteristic of hamartomas
Fig. 12.25 Chondroma. Gross photograph showing a well-circumscribed, lobulated cartilaginous nodule. The cut surface is white and glistening
Fig. 12.26 Chondroma. Intermediate magnification photomicrograph shows a well-demarcated tumor composed entirely of hyaline and myxohyaline cartilage. Cytologic atypia is absent. The surrounding lung parenchyma is compressed to form a pseudocapsule
Fig. 12.27 PEComa (clear cell "sugar" tumor). (**a**) Photomicrograph showing tumor cells with clear to pale finely vacuolated cytoplasm forming solid nests separated by thin-walled sinusoidal vessels. (**b**) High-magnification photomicrograph shows rounded tumor cells with abundant clear or pale eosinophilic cytoplasm, mild variation of nuclear size, and occasional small nucleoli. Necrosis and mitoses are absent. Tumor cells were positive for HMB45 and S100 and negative for cytokeratins (not shown)
Fig. 12.28 PEComa (clear cell "sugar" tumor). (**a**) Low-magnification photomicrograph showing unencapsulated interface with nonneoplastic lung parenchyma and associated entrapment of nonneoplastic respiratory epithelium. (**b**) High-magnification photomicrograph showing cytologically bland cells with pale-staining eosinophilic to clear cytoplasm and mild anisonucleosis. The cells are arranged in a compact nested growth pattern. No mitotic figures or necrosis is seen. (**c**) Photomicrograph showing patchy staining for HMB45 in PEComa (clear cell "sugar" tumor)
Fig. 12.29 Granular cell tumor. (**a**) Photomicrograph showing neoplastic granular cells infiltrating bronchial mucosa and submucosa without destruction of submucosal glands. Although lacking in this example, the overlying bronchial epithelium often shows a combination of squamous metaplasia and pseudo-epitheliomatous hyperplasia. (**b**) High-magnification photomicrograph showing large spindled and epi-

thelioid cells with small, hyperchromatic, eccentrically located nuclei and abundant granular eosinophilic cytoplasm. (**c**) High-magnification photomicrograph showing strong cytoplasmic staining for S100 protein

Fig. 12.30 Pneumocytic adenomyoepithelioma. (**a**) Low-magnification photomicrograph showing a circumscribed mixed epithelial and spindle cell tumor resembling pleomorphic adenoma. (**b**) Higher-magnification view shows a combination of epithelial cells, some of which form glandular spaces containing colloid-like secretions and blunt spindled cells

Fig. 12.31 Pneumocytic adenomyoepithelioma. High-magnification photomicrographs of the tumor illustrated in Fig. 12.30 showing a population of cytokeratin (**a**) and TTF-1 (**b**)-positive epithelial cells affiliated with a population of smooth muscle actin (**c**) and S100 (**d**)-positive myoepithelial cells

Fig. 13.1 Atypical adenomatous hyperplasia. (**a**) Low-magnification photomicrograph shows a small (2-mm) localized lesion. Compared to normal lung parenchyma, the lesion shows slightly thickened alveolar septa and atypical pneumocyte hyperplasia along the septa. The alveolar lung architecture is preserved, and there is no invasive component. (**b**) Higher magnification of area illustrated in **a** showing interface between atypical adenomatous hyperplasia (above) and normal lung (below). The former is characterized by thickening of alveolar septa and a proliferation of mildly atypical pneumocytes. (**c**) High-magnification view highlighting the atypical cells characterized by enlarged nuclei but with a very orderly single-cell layer without nuclear crowding or tufting. These atypical cells are positive for TTF-1 (not shown)

Fig. 13.2 Adenocarcinoma in situ. Gross photograph shows a 2-cm, poorly defined tan nodular lesion beneath the pleura. These lesions are commonly described as ground-glass opacities on chest CT scan

Fig. 13.3 Nonmucinous adenocarcinoma in situ. (**a**) Low-magnification photomicrograph shows a nonmucinous epithelial tumor growing along the preserved but thickened alveolar septa; no invasive foci are seen. (**b**) High-magnification view shows crowded tumor cells with hyperchromatic and occasional small nucleoli. Tumor cells grow along alveolar septa in a lepidic growth pattern without invasion

Fig. 13.4 Nonmucinous adenocarcinoma in situ. (**a**) Low-magnification view of another small (1.1 cm) adenocarcinoma in situ in which thickened but intact interstitial structures are lined by a population of atypical nonmucinous columnar cells. (**b**) Intermediate-magnification photomicrograph showing the interface between adenocarcinoma in situ and normal lung (right). (**c**) High-magnification view showing more rounded, cuboidal, and hobnail cells with a higher degree of cytologic atypia as evidenced by nuclear enlargement, anisonucleosis, and relatively scant cytoplasm

Fig. 13.5 Minimally invasive adenocarcinoma. (**a**) Low-magnification photomicrograph shows a small localized lesion (<3 cm) with a predominantly lepidic growth pattern and a small (<5 mm) focus of invasion (*arrow*). (**b**) Higher-magnification view of the noninvasive component in which tumor cells grow along intact alveolar septa in a lepidic pattern. (**c**) Photomicrograph showing the invasive component. The scarred area shows a small focus (<5 mm) of invasive adenocarcinoma, acinar type. The invasive component consists of small angulated glands inciting a myofibroblastic ("desmoplastic") stromal response. The tumor should be classified as a lepidic-predominant adenocarcinoma when the invasive component measures more than 5 mm

Fig. 13.6 Minimally invasive adenocarcinoma. (**a**) Low-magnification view of another example of a minimally invasive adenocarcinoma in which most of this small (just over 1 cm) peripheral, subpleural tumor has a lepidic growth pattern except for a small area of invasion in an area of scarring (*arrow*). (**b**) Photomicrograph show-

ing the invasive component that measures only 4 mm and demonstrates features similar to those illustrated and described in Fig. 13.5c

Fig. 13.7 Acinar adenocarcinoma. Photomicrograph showing a tumor composed of irregularly shaped glands with central luminal spaces invading a myofibroblastic stroma. Nuclei are enlarged and hyperchromatic, with anisonucleosis and occasionally prominent nucleoli

Fig. 13.8 Papillary adenocarcinoma. (**a**) Photomicrograph shows a tumor in which malignant columnar cells are growing on the surface of fibrovascular cores. (**b**) Higher-magnification view reveals cuboidal to columnar tumor cells growing on the surface of a true fibrovascular core

Fig. 13.9 Micropapillary adenocarcinoma. (**a**) Low-magnification photomicrograph shows tumor cells growing in numerous papillary tufts detached from or connected to alveolar walls. (**b**) High-magnification view shows tumor cells forming tufts and florets without a fibrovascular core. (**c**) Another high-magnification view shows detached small tumor aggregates with psammoma bodies floating in the alveolar air space. Tumor cells in this field show a higher degree of cytologic atypia

Fig. 13.10 Solid adenocarcinoma. (**a**) Photomicrograph showing tumor cells arranged as solid nests with abundant pale-staining eosinophilic to clear cytoplasm resembling squamous cell carcinoma. (**b**) Higher-magnification photomicrograph of an immunohistochemical-stained section shows strong positivity for TTF-1 in tumor cells. (**c**) Photomicrograph showing a mucicarmine stain that highlights intracellular mucin in occasional tumor cells

Fig. 13.11 Invasive mucinous adenocarcinoma. Low-magnification photomicrograph showing columnar neoplastic cells with abundant apical cytoplasmic mucin and basally oriented nuclei. This area shows both lepidic and papillary growth patterns, with variably conspicuous extracellular mucin

Fig. 13.12 Invasive mucinous adenocarcinoma. Photomicrograph showing a mucinous adenocarcinoma in which columnar mucinous cells are arranged in an acinar growth pattern characterized by closely packed, back-to-back glands separated by thin fibrotic septa. Foci of micropapillary growth are also present

Fig. 13.13 Invasive mucinous adenocarcinoma. (**a**) Low-magnification photomicrograph of another example of invasive mucinous adenocarcinoma with a predominantly lepidic growth pattern. (**b**) High-magnification photomicrograph showing the remarkably bland cytologic features in neoplastic cells distributed along alveolar septa with small basally oriented nuclei and abundant apical mucin

Fig. 13.14 Colloid adenocarcinoma. (**a**) Low-magnification photomicrograph showing a tumor characterized by pools of paucicellular pale-staining mucin, distending air spaces, and dissecting interstitial connective tissue. Tumor cells are rare and may be remarkably bland. (**b**) High-magnification view showing rare well-differentiated mucinous glandular epithelium growing along the fibrous septa and floating in pools of extracellular mucin

Fig. 13.15 Colloid adenocarcinoma. (**a**) Low-magnification photomicrograph showing another example of colloid adenocarcinoma in which large pools of paucicellular extracellular mucin distend air spaces. (**b**) High-magnification photomicrograph showing isolated clusters of neoplastic epithelium resembling intestinal epithelium with goblet cells

Fig. 13.16 Fetal adenocarcinoma. (**a**) Low-magnification photomicrograph showing an adenocarcinoma with a well-developed glandular growth pattern resembling fetal lungs with well-differentiated endometrioid adenocarcinomas. (**b**) High-magnification view showing columnar tumor cells with cytoplasmic glycogen vacuoles and nuclear stratification, furthering the resemblance to endometrioid adenocarcinoma

Fig. 13.17 Enteric adenocarcinoma. (**a**) Low-magnification photomicrograph shows an adenocarcinoma with well-formed glands and abundant inflammatory infiltrates next to a cartilaginous airway (*). (**b**) High-magnification view showing the tall, columnar stratified tumor cells forming glands with luminal necrosis. The morphologic features and immunoprofile are indistinguishable from those of colorectal adenocarcinoma. A clinical history and radiologic information are required to differentiate these two entities. (**c**) and (**d**), Immunohistochemical-stained sections showing strong, diffuse staining for CDX-2 (**c**) and negative staining for TTF-1 (**d**) in enteric adenocarcinoma

Fig. 13.18 Squamous cell carcinoma in situ. (**a**) Low-magnification photomicrograph showing squamous cell carcinoma in situ arising in a large respiratory airway with concomitant squamous metaplasia. (**b**) High-magnification photomicrograph showing dysplastic squamous cells with enlarged hyperchromatic nuclei, prominent nucleoli, mitotic figures above the basal cell layer, and anisonucleosis in the context of a disordered architecture extending from the base to the surface of the epithelium

Fig. 13.19 Squamous cell carcinoma. (**a**) Gross photograph showing a centrally located obstructing mass extensively involving a large bronchus and surrounding lung parenchyma, with post-obstructive bronchiectasis in which dilated airways are filled with mucus. (Courtesy of J. Carvalho, Minneapolis, MN). (**b**) Closer view of the endobronchial mass. (Courtesy of J. Carvalho, Minneapolis, MN)

Fig. 13.20 Keratinizing squamous cell carcinoma. (**a**) Photomicrograph showing infiltrating nests with central keratinization in a desmoplastic stroma. (**b**) High-magnification photomicrograph showing another squamous cell carcinoma in which there are prominent intercellular bridges

Fig. 13.21 Nonkeratinizing squamous cell carcinoma. (**a**) High-magnification photomicrograph showing poorly differentiated squamous cell carcinoma constituting infiltrating tumor cells with abundant cytoplasm but without easily identifiable intercellular bridging or keratinization. It is the sort of carcinoma that might be difficult to recognize as squamous based on routine histology alone. (**b–d**) Photomicrographs showing strong diffuse staining for high molecular weight cytokeratins (CK5/6) (**b**) and p63 (**c**) with negative staining for TTF-1 (**d**)

Fig. 13.22 Basaloid squamous cell carcinoma. (**a**) Low-magnification photomicrograph of basaloid squamous cell carcinoma shows solid, anastomosing nests with peripheral palisading and central comedo-type necrosis. (**b**) High-magnification view showing tumor cells that lack keratinization and intercellular bridges but demonstrate peripheral palisading and comedo-type necrosis. The tumor cells are relatively small and monomorphic, with hyperchromatic finely granular chromatin resembling small cell carcinoma. (**c**) As illustrated in this photomicrograph, the tumor may show focal and generally weak staining for synaptophysin, which may further confound the differential diagnosis with small cell carcinoma. However, positive staining for p63 (**d**) and CK5/6 (**e**) with negative staining for TTF-1 (**f**) can be extremely helpful, especially on small biopsies

Fig. 13.23 Adenosquamous carcinoma. (**a**) Photomicrograph of core needle biopsy from a lung tumor showing both adenocarcinoma (upper left) and squamous cell carcinoma (lower right). (**b**) and (**c**), An immunohistochemical stain for TTF-1 highlights the adenocarcinoma component on the left (**b**), while p63 strongly and diffusely stains the squamous cell component on the right (**c**)

Fig. 13.24 Carcinoid tumor. (**a**) Gross photograph of a centrally located well-circumscribed tan-brown mass, partially obstructing the bronchus with post-obstructive mucus plugging on the left. (Courtesy of J. Carvalho, Minneapolis, MN). (**b**) Photograph showing cut surface of another centrally situated endobronchial carcinoid tumor.

About three fourths of carcinoid tumors present as endobronchial masses. (**c**) Gross photograph of a peripheral carcinoid tumor with a deep mahogany color

Fig. 13.25 Typical carcinoid tumor. (**a**) Photomicrograph showing tumor composed of bland cuboidal cells with a moderate amount of pale eosinophilic cytoplasm and finely granular chromatin. The cells are arranged in an organoid nesting pattern with delicate vascular stroma. No mitosis or necrosis is seen. (**b**) Photomicrograph showing trabecular pattern in a typical carcinoid tumor. Prominent edematous and pale-staining stroma are present between the trabecular bands of tumor cells. (**c**) Photomicrograph showing pseudoglandular and papillary patterns in a typical carcinoid tumor. Tumor cells demonstrate finely granular nuclear chromatin and inconspicuous nuclei, distinguishing them from adenocarcinoma. (**d**) Photomicrograph of a typical carcinoid tumor with rosette formation

Fig. 13.26 Typical carcinoid tumor with prominent spindle cells. Photomicrograph showing a tumor composed of spindle cells with focally pronounced nuclear pleomorphism, which should not be taken as criteria for atypical carcinoid tumors. The tumor maintains a distinctly nested growth pattern without necrosis or mitotic figures

Fig. 13.27 Typical carcinoid tumor with oncocytic features. (**a**) Photomicrograph showing tumor cells with abundant eosinophilic granular cytoplasm and occasional prominent nucleoli on H&E stain. Immunohistochemical stains show strong cytoplasmic positivity for synaptophysin (**b**) and chromogranin (**c**)

Fig. 13.28 Typical carcinoid tumor with ossification. (**a**) Gross photograph shows cut surface of heavily calcified endobronchial mass that required a saw to cut. (**b**) Photomicrograph shows osseous metaplasia of the stroma complete with bone marrow (lower right)

Fig. 13.29 Atypical carcinoid tumor. Gross photograph of a peripheral, well-circumscribed atypical carcinoid tumor measuring just over 3 cm in greatest dimension. There is no grossly detectable necrosis to distinguish this example from a low-grade typical carcinoid tumor. Microscopic necrosis and mitotic rate (≥2/2 mm^2) are the features that separate atypical from typical carcinoid tumor

Fig. 13.30 Atypical carcinoid tumor. Photomicrograph shows a carcinoid tumor with small foci of comedo-type necrosis in tumor nests

Fig. 13.31 Atypical carcinoid tumor. High-magnification photomicrograph shows a single mitotic figure in the center. Tumor cells show carcinoid morphology with a moderate amount of eosinophilic cytoplasm and finely granular nuclear chromatin

Fig. 13.32 Small cell carcinoma. Gross photograph of autopsy specimen showing small cell carcinoma distributed as a large centrally located mass involving the major bronchi, with bulky lymph node metastases

Fig. 13.33 Small cell carcinoma. High-magnification photomicrograph illustrating the distinctive cytologic features of small cell carcinoma in a smear prepared from a fine needle aspirate. Tumor cells show very scant cytoplasm, hyperchromatic nuclei, finely dispersed "salt and pepper" chromatin, absent nucleoli, nuclear molding, and prominent apoptosis. Cytology specimens can be extremely helpful in patients whose bronchial biopsies show extensive crush artifact

Fig. 13.34 Small cell carcinoma. (**a**) Low-magnification photomicrograph shows densely packed small- to intermediate-sized tumor cells. Crushing artifact is seen at the upper-left edge. (**b**) High-magnification view showing tumor cells with scant cytoplasm, dense chromatin, and occasional small nucleoli. Mitoses and apoptosis are frequently seen

Fig. 13.35 Small cell carcinoma. (**a**–**d**), Photomicrographs of immunostained slides showing characteristic cytoplasmic perinuclear dot-like staining for cytokeratin (AE1/AE3) (**a**), diffuse membranous and cytoplasmic staining for CD56 (**b**), cytoplasmic staining for synaptophysin (**c**), and nuclear staining for TTF-1 (**d**). Not all small cell carcinomas show all of these features, including rare examples with a "null"

phenotype. Absence of staining for CD20 and p63/p40 can be extremely helpful, especially in those with an otherwise "null" phenotype, in separating small cell carcinoma from lymphomas and basaloid squamous cell carcinomas on small biopsies

Fig. 13.36 Combined small cell carcinoma and adenocarcinoma. Photomicrograph showing malignant glands with cribriform architecture (*left*) immediately next to small cell carcinoma (*right*)

Fig. 13.37 Combined small cell carcinoma and squamous cell carcinoma. Photomicrograph showing a nest of squamous cell carcinomas consisting of polygonal cells with prominent intercellular bridging and occasional single dyskeratotic cells situated in the midst of an otherwise classic small cell carcinoma

Fig. 13.38 Large cell neuroendocrine carcinoma. (**a**) Low-magnification photomicrograph shows a nested growth pattern with peripheral palisading and multifocal "comedo" necrosis situated centrally within the cell nests. The necrotic foci are much more extensive than that usually seen in atypical carcinoid tumors. (**b**) Higher-magnification view showing a tumor nest with peripheral palisading and foci of necrosis. The tumor cells show vesicular chromatin and abundant eosinophilic cytoplasm. Numerous mitoses are seen

Fig. 13.39 Immunostaining of large cell neuroendocrine carcinoma. (**a**–**c**), A series of photomicrographs of immunostained sections from the tumor illustrated in Fig. 13.38 showing patchy cytoplasmic staining for synaptophysin (**a**) and chromogranin (**b**) and nuclear staining for TTF-1 in isolated tumor cells (**c**). TTF-1 immunoreactivity is not a consistent feature of large cell neuroendocrine carcinoma

Fig. 13.40 Large cell neuroendocrine carcinoma. (**a**) Low-magnification photomicrograph showing another example of large cell neuroendocrine carcinoma with a nested growth pattern mimicking carcinoid tumor but with multifocal coagulative tumor necrosis (asterisk). (**b**) Higher-magnification photomicrograph showing coarse chromatin and easily identifiable nucleoli in tumor cells with abundant eosinophilic cytoplasm. Numerous mitotic figures are present. (**c**) Photomicrograph of an immunostained section shows diffuse immunoreactivity for synaptophysin. Tumor cells were also positive for CD56 but were negative for chromogranin (not shown)

Fig. 13.41 Large cell carcinoma. (**a**) Photomicrograph showing sheets of large polygonal cells with prominent nucleoli and abundant finely vacuolated clear to eosinophilic cytoplasm on H&E stain. By definition, the tumor lacks staining for markers of squamous differentiation such as p40 (**b**) and markers affiliated with adenocarcinoma such as TTF-1 (**c**)

Fig. 13.42 Large cell carcinoma. (**a**) Photomicrograph showing high-grade carcinoma in which large polygonal cells are discohesive and arranged in sheets without evidence of glandular or squamous differentiation. (**b**) High-magnification view shows vesicular chromatin with giant solitary nucleoli and an eccentric rim of densely eosinophilic cytoplasm. Based on these findings alone, the differential diagnosis is likely to include not only large cell carcinoma but also other pleomorphic high-grade tumors such as anaplastic large cell lymphoma and melanoma. (**c**) High-magnification photomicrograph showing strong cytoplasmic staining using a pancytokeratin cocktail (AE1/AE3 and CAM5.2). Tumor cells were negative for all other markers tested including TTF-1, napsin A, CK5/CK6, and p63 (not shown)

Fig. 13.43 Sarcomatoid carcinoma. Photograph illustrating cut surface of a large centrally necrotic sarcomatoid carcinoma. (Courtesy of Dr. J. Carvalho, Minneapolis, MN)

Fig. 13.44 Pleomorphic carcinoma. (**a**) High-magnification photomicrograph demonstrates an undifferentiated carcinoma with large bizarre nuclei, multinucleated giant cells, and spindle cells. (**b**) High-magnification photomicrograph showing that

tumor cells are positive for pancytokeratins (AE1/AE3) but were negative for TTF-1 and p63 (not shown)

Fig. 13.45 Pleomorphic and giant cell carcinoma. (**a**) Photomicrograph showing a high-grade non-small cell carcinoma with prominent multinucleated giant cells. (**b**) and (**c**), Photomicrographs of a "pure" giant cell carcinoma, an extremely rare variant of sarcomatoid carcinoma that is associated with an extremely aggressive course

Fig. 13.46 Spindle-cell carcinoma. (**a**) High-magnification photomicrograph showing a tumor consisting entirely of spindle cells. The tumor cells are relatively uniform, growing in fascicles and whorls with surprisingly mild cytologic atypia. (**b**) High-magnification view of immunostained section showing that the spindle cells are positive for pancytokeratins (AE1/AE3)

Fig. 13.47 Spindle-cell carcinoma with adenocarcinoma. (**a**) Low-magnification photomicrograph showing a tumor consisting of both spindle cells (at least 10% of the tumor) and adenocarcinoma with an acinar and cribriform growth pattern. (**b**) Higher-magnification photomicrograph showing an intimate admixture of neoplastic glands and spindle cells. (**c**) Photomicrograph of immunostained sections showing that both spindle-cell and glandular components are positive for pancytokeratins (AE1/AE3)

Fig. 13.48 Spindle-cell carcinoma with squamous cell carcinoma. (**a**) Low-magnification view of large, necrotizing, polypoid endobronchial tumor consisting of a combination of spindle cells (at least 10% of the tumor) and squamous cell carcinoma with clear cell change. (**b**) High-magnification photomicrograph showing squamous cell carcinoma in which polygonal cells have abundant clear cytoplasm and are arranged in a well-developed epidermoid growth pattern without keratinization. (**c**) High-magnification view of immunostained section shows staining for high molecular weight cytokeratins (CK5/6) limited to the squamous component. A stain for p63 showed the same distribution (not shown)

Fig. 13.49 Carcinosarcoma. (**a**) Photomicrograph of a tumor with admixed squamous cell carcinoma and both sarcomatoid (spindle-cell) and sarcomatous (osteosarcoma) components. (**b**) High-magnification view of differentiated sarcomatous component closely resembling osteosarcoma with spicules of neoplastic osteoid affiliated with undifferentiated neoplastic and osteoclast-like giant cells. (**c**) High-magnification view of the carcinomatous component in which there is abrupt squamous differentiation in the form of keratinizing squamous pearls. (**d**) Photomicrograph of immunostained sections showing that much of the tumor, including relatively undifferentiated spindle cells, was positive for p63

Fig. 13.50 Pulmonary blastoma. Gross photograph showing cut surface of a large, well-circumscribed pulmonary blastoma with patchy necrosis

Fig. 13.51 Pulmonary blastoma. (**a**) Photomicrograph showing a biphasic tumor consisting of an adenocarcinoma resembling endometrioid carcinoma and a primitive ("blastematous") stromal component. (**b**) Higher-magnification photomicrograph showing pseudostratified nonmucinous columnar cells with a well-developed acinar and cribriform growth pattern. Associated morules may also be present, furthering the resemblance to endometrioid carcinomas. When present in pure form without the primitive stromal component, the "monophasic" epithelial component is termed fetal adenocarcinoma. (**c**) Photomicrograph of an immunostained section showing strong staining of the adenocarcinomatous component for TTF-1 with negative staining in the stromal component. The stromal cells are usually negative for TTF-1 and are also frequently negative for cytokeratins

Fig. 13.52 Adenoid cystic carcinoma. Gross photograph of sleeve resection for adenoid cystic carcinoma. The tumor extensively infiltrates the submucosal tissues, extending beyond the airway cartilage to form a well-defined unencapsulated peribronchial mass

Fig. 13.53 Adenoid cystic carcinoma. (**a**) Low-magnification photomicrograph shows a tumor with a predominantly tubular growth pattern diffusely involving the bronchial wall and infiltrating into peribronchial soft tissue. (**b**) A higher-magnification view shows characteristic small myoepithelial cells with hyperchromatic angulated nuclei and occasional central clusters of cytologically distinct ductal epithelial cells. This tumor shows the characteristic pattern of associated extracellular pseudoglandular spaces containing granular and pale-staining basophilic myxoid secretions

Fig. 13.54 Adenoid cystic carcinoma. High-magnification photomicrograph of another example showing classic cribriform architecture in which small tumor cells with scant cytoplasm and angulated hyperchromatic nuclei constitute the majority of the neoplasm with only scattered ductal epithelial cells with eosinophilic cytoplasm. No mitosis or necrosis is seen. The cribriform structure is created by pale-staining extracellular myxoid secretions accumulated within pseudoglandular spaces ("pseudocysts"). The stroma is fibrotic, with focal areas of eosinophilic basement membrane-like materials (upper left)

Fig. 13.55 Adenoid cystic carcinoma. Photomicrograph of an immunostained section shows that tumor cells may be focally positive for TTF-1

Fig. 13.56 Mucoepidermoid carcinoma. Gross photograph showing the cut surface of a well-demarcated polypoid endobronchial mass. Note that the tumor is focally cystic and affiliated with "golden [obstructive] pneumonia" at lower left. (Courtesy of J. Carvalho, Minneapolis, MN)

Fig. 13.57 Mucoepidermoid carcinoma. (**a**) Low-magnification photomicrograph shows an endobronchial tumor with mixed solid and cystic growth patterns. The cystic areas are affiliated with variably abundant extracellular mucin. (**b**) High-magnification view shows solid nests composed of a mixture of cuboidal "intermediate" cells and mucinous goblet cells

Fig. 13.58 Mucoepidermoid carcinoma. Photomicrograph of another mucoepidermoid carcinoma showing dramatic admixture of mucinous goblet cells and squamoid "intermediate" cells

Fig. 14.1 Inflammatory myofibroblastic tumor. Gross image shows a large, firm, circumscribed tumor. The cut surface is fleshy white and tan with focal cystic degeneration and has gritty calcifications

Fig. 14.2 Inflammatory myofibroblastic tumor (IMT). Low-magnification photomicrograph showing an endobronchial IMT that involves the mucosa and submucosa of a bronchus

Fig. 14.3 Inflammatory myofibroblastic tumor. (**a**) Low-magnification photomicrograph shows a cellular tumor composed of spindle cells, arranged in an orderly fascicular pattern admixed with inflammatory cells. (**b**) High-magnification photomicrograph shows spindled tumor cells with pale eosinophilic cytoplasm and indistinct borders arranged in ill-defined short fascicles. Nuclear atypia is minimal, and mitotic figures are rare. The lesional cells are associated with a chronic inflammatory infiltrate in which plasma cells predominate. Entrapped alveolar space lined by reactive pneumocytes is present, resulting in a pseudo-biphasic appearance

Fig. 14.4 Inflammatory myofibroblastic tumor. High-magnification photomicrograph from another inflammatory myofibroblastic tumor shows focal cytologic atypia, including occasionally prominent nucleoli

Fig. 14.5 Inflammatory myofibroblastic tumor. (**a**) Low-magnification photomicrograph showing a well-circumscribed spindle-cell neoplasm demonstrating an unencapsulated interface with nonneoplastic lung tissue. (**b**) High-magnification view shows neoplastic myofibroblasts partially obscured by a variably dense infiltrate of plasma cells

Fig. 14.6 Inflammatory myofibroblastic tumor. (**a**) Low-magnification photomicrograph showing an inflammatory myofibroblastic tumor with sclerosis. (**b**) Higher-magnification photomicrograph showing prominent stromal sclerosis with associated calcifications. (**c**) and (**d**), High-magnification photomicrographs showing coarse collagen bundles in the sclerotic zone (**c**) immediately adjacent to a histologically typical inflammatory myofibroblastic tumor (**d**)

Fig. 14.7 Inflammatory myofibroblastic tumor. Photomicrograph showing prominent foamy histiocytes, a relatively common finding in inflammatory myofibroblastic tumors of the lung

Fig. 14.8 Inflammatory myofibroblastic tumor. The tumor cells variably react to smooth muscle actin (**a**) and ALK1 (**b**) in paraffin section immunostains. Staining for ALK1 is usually cytoplasmic and is seen in about half of inflammatory myofibroblastic tumors. Staining for ALK1 correlates with clonal rearrangements of the *ALK* gene and is more common in pediatric patients

Fig. 14.9 Solitary fibrous tumor. Cut surface of resected solitary fibrous tumor arising from visceral pleura. Despite its large size, the tumor was histologically benign and completely resected, a combination of findings that favors a benign course

Fig. 14.10 Solitary fibrous tumor. (**a**) Low-magnification photomicrograph showing solitary fibrous tumor with visceral pleural attachment. (**b**) Higher-magnification photomicrograph showing characteristic bland spindle cells arranged haphazardly in a collagenous stroma characterized by thick, keloidal collagen bundles. (**c**) High-magnification view showing plump spindle cells haphazardly distributed within thick collagen bundles

Fig. 14.11 Solitary fibrous tumor. (**a**) Low-magnification view of a more cellular example of a solitary fibrous tumor, a lesion synonymous with tumors referred to historically as hemangiopericytomas. (**b**) High-magnification photomicrograph showing a compact arrangement of neoplastic cells with minimal collagenous stroma and easily identifiable mitotic figures. (**c**) Elsewhere, as illustrated in this photomicrograph, this tumor showed histologic features typical of a solitary fibrous tumor; it lacked coagulative tumor necrosis and other features often affiliated with a recurrence risk

Fig. 14.12 Malignant solitary fibrous tumor. Cut surface of a large visceral pleural-based mass shows patchy necrosis and a fleshy surface different from the more typical firm, rubbery consistency of a conventional solitary fibrous tumor (*see* Fig. 14.9)

Fig. 14.13 Malignant solitary fibrous tumor. (**a**) Low-magnification photomicrograph showing tumor necrosis in a highly cellular neoplasm without the collagenous stroma and other architectural features more characteristic of a solitary fibrous tumor. (**b**) Low-magnification view of another field in the same tumor showing a highly cellular neoplasm resembling other high-grade sarcomas such as monophasic synovial sarcoma and malignant peripheral nerve sheath tumor. (**c**) High-magnification photomicrograph illustrating hyperchromatic nuclei and easily identifiable mitotic figures. (**d**) Very small foci representing a minor component of this well-sampled tumor showed histologic findings more closely resembling a classic solitary fibrous tumor

Fig. 14.14 Solitary fibrous tumor. (**a**) Photomicrograph showing bland spindle cells arranged in the patternless pattern of Stout typical of the solitary fibrous tumor. (**b**) Photomicrograph showing strong, diffuse, nuclear staining for STAT6, a very specific and helpful finding in establishing the diagnosis of the solitary fibrous tumor in diagnostically challenging cases

Fig. 14.15 Solitary fibrous tumor, fat-forming (lipomatous) variant. (**a**) Low-magnification photomicrograph of a needle biopsy from an intrathoracic mass discovered in a 36-year-old man. The tumor consists of bland adipose tissue and a spindle-cell neoplasm. (**b**) High-magnification photomicrograph showing the intersection

between the more cellular spindle-cell component that dissects into adipose tissue. (**c**) Another high-magnification photomicrograph showing spindle cells sprinkled between the fat cells. (**d**) Photomicrograph of the same area showing strong diffuse staining for STAT6 in spindle cells

Fig. 14.16 Epithelioid hemangioendothelioma. Gross photograph shows multiple circumscribed nodules with a gray-white chondroid cut surface

Fig. 14.17 Epithelioid hemangioendothelioma with a hypocellular hyalinized center and a polypoid intra-alveolar growth pattern at the periphery. (**b**) and (**c**), Higher-magnification views showing intra-alveolar extension of hypocellular polyps (**b**) with centrally hyalinized stroma and plump epithelioid histiocyte-like cells at the periphery (**c**). (**d**) High magnification of the intra-alveolar tumor nodule shows short cords of tumor cells with round-to-oval nuclei and intracytoplasmic vacuoles/lumina

Fig. 14.18 Epithelioid hemangioendothelioma. (**a**) Photomicrograph showing polypoid intraluminal growth pattern typical of epithelioid hemangioendothelioma in the lung. (**b**) Higher-magnification view showing bland cytology in a low-grade variant in which neoplastic cells show a characteristic combination of cytoplasmic intranuclear pseudoinclusions, coarse cytoplasmic vacuoles, and a pale-staining chondroid matrix. (**c**) and (**d**) Immunostains show strong nuclear staining for ERG (**c**) and negative staining for cytokeratins (**d**). Tumor cells are positive for various endothelial-associated antigens, including not only ERG but also CD31, CD34, and factor VIII. Tumor cells may be focally positive for cytokeratins, depending on the antibody used, which can be a diagnostic trap

Fig. 14.19 Epithelioid hemangioendothelioma. (**a**) Gross photograph showing cut surface of epithelioid hemangioendothelioma that presented as a solitary lung nodule with gross features resembling a necrotizing granuloma. (**b**) Low-magnification photomicrograph showing a centrally necrotic nodule. (**c**) Higher-magnification view showing a population of epithelioid cells at the periphery, furthering resemblance to a granuloma. (**d**) High-magnification photomicrograph showing epithelioid cells with abundant cytoplasm, cytoplasmic intranuclear pseudoinclusions, coarse cytoplasmic vacuoles, and polypoid growth characteristic of epithelioid hemangioendotheliomas

Fig. 14.20 Epithelioid hemangioendothelioma involving the pleura. (**a**) Gross photograph shows that the tumor diffusely thickens the pleura, mimicking malignant mesothelioma. (**b**) Low-magnification photomicrograph shows that the pleura is thickened by a paucicellular tumor with myxohyaline stroma associated with intraluminal polypoid growth at the interface with lung parenchyma in a pattern more typical of epithelioid hemangioendothelioma

Fig. 14.21 Epithelioid hemangioendothelioma arising in mediastinum. (**a**) Photograph showing cut surface of a large 11-cm mediastinal mass with areas of hemorrhagic necrosis. (**b**) Photomicrograph showing epithelioid neoplastic cells with numerous intranuclear pseudoinclusions and coarse cytoplasmic vacuoles

Fig. 14.22 Synovial sarcoma. A chest CT image showing two peripheral pleural-based masses that infiltrate chest wall soft tissue

Fig. 14.23 Monophasic synovial sarcoma. (**a**) Low-magnification photomicrograph showing cellular intrapulmonary neoplasm. (**b**) At high magnification, the tumor consists of sheets and fascicles of uniform spindle cells with scant cytoplasm and indistinct cell borders

Fig. 14.24 *Biphasic synovial sarcoma.* (**a**) Low-magnification photomicrograph showing mixed spindle-cell and epithelioid cell components. The epithelioid cells form solid nests, cords, and acini. (**b**) Photomicrograph showing patchy immunoreactivity for cytokeratins in the clearly identifiable epithelial component

Fig. 14.25 Angiomatoid fibrous histiocytoma. (**a**) Low-magnification photomicrograph showing a polypoid endobronchial tumor with a peripheral fibrous pseudocapsule, ectatic blood-filled spaces, and calcifications. (**b**) and (**c**) Photomicrographs at higher magnification demonstrating the vascular pattern typical of angiomatoid fibrous histiocytoma, including areas in which sinusoidal blood vessels have a hemangiopericytoma-like pattern. (**d**) High-magnification photomicrograph showing bland plump spindle cells arranged in ill-defined, short fascicles resulting in a vaguely storiform architecture. Associated histiocytes and scattered hemosiderin deposits are characteristic

Fig. 14.26 Primary pulmonary myxoid sarcoma. (**a**) Scanning magnification photomicrograph showing a variably cellular well-circumscribed bronchus-associated neoplasm with a lobulated appearance and a fibrous pseudocapsule accompanied by a peripheral lymphocytic infiltrate. (**b**) Higher-magnification view showing that in much of the tumor neoplastic cells are arranged in a reticular growth pattern with a pale-staining myxoid matrix. (**c**) Neoplastic cells in the reticular areas have eccentric nuclei and a relatively nondescript appearance. (**d**) Solid areas are common but rarely the dominant finding and comprise variably atypical spindle cells

Fig. 14.27 Diffuse malignant mesothelioma. (**a**) CT scan showing right-sided diffuse pleural thickening and nodularity extending along the interlobular septum and involving the mediastinal pleura, a useful finding in separating benign from malignant diffuse pleural lesions. (**b**) Cut surface of an extrapleural pneumonectomy specimen showing a diffuse mesothelioma that encases the lung as a rind. The tumor also grows along the interlobar septa and compresses the lung parenchyma

Fig. 14.28 Epithelioid malignant mesothelioma. (**a**) Low-magnification view showing a classic tubular (sometimes called tubulopapillary) mesothelioma forming a parietal pleural nodule. (**b**) High-magnification view showing remarkably bland cuboidal cells arranged in a well-developed tubular growth pattern

Fig. 14.29 Epithelioid malignant mesothelioma. Photomicrograph showing another example of a classic tubular epithelioid mesothelioma

Fig. 14.30 Epithelioid malignant mesothelioma. (**a**) Photomicrograph showing an epithelioid mesothelioma with a class tubular growth pattern invading into chest wall fat, an extremely helpful finding in distinguishing malignant from benign atypical mesothelial proliferations. (**b**) High-magnification view showing bland, low columnar cells invading chest wall fat with an associated stromal reaction

Fig. 14.31 Epithelioid malignant mesothelioma, immunophenotype. (**a**–**c**) Photomicrographs demonstrating immunostains performed on sections of the tumor illustrated in Fig. 14.30. Tumor cells were strongly positive for high molecular weight cytokeratins (CK5/6) (**a**) and calretinin (**b**), the latter with strong cytoplasmic and nuclear staining. There was patchy, weak, nuclear staining for WT-1 (**c**). Cytoplasmic staining for WT-1 is of no diagnostic value in distinguishing metastatic adenocarcinoma from mesothelioma

Fig. 14.32 Epithelioid malignant mesothelioma, histologic variants. (**a**) *Papillary* growth pattern in mesothelioma in which tumor cells lining fibrovascular cores are cuboidal and relatively bland, with occasional small nucleoli and a moderate amount of cytoplasm. (**b**) Combined papillary and *micropapillary* growth pattern, the latter characterized by detached papillary fragments of tumor cells without associated connective tissue cores. (**c**) *Solid* growth pattern in mesothelioma invading the lung as solid sheets of relatively noncohesive epithelioid tumor cells with uniform nuclei, small nucleoli, and abundant eosinophilic cytoplasm. (**d**) *Microcystic* (*adenomatoid*) growth pattern in which attenuated tumor cells line cystic spaces of variable sizes and shapes resembling adenomatoid tumors. (**e**) *Pleomorphic* cytology in mesothelioma composed of a population of highly anaplastic cells, including multinucleated giant cells. (**f**) Deciduoid features in a mesothelioma composed

of large polygonal cells with abundant eosinophilic cytoplasm and distinct cell borders resembling decidual cells of the pregnant endometrium

Fig. 14.33 Sarcomatoid mesothelioma. (**a**) Low-magnification photomicrograph showing a mesothelioma consisting of a pure population of keratin-positive (immunostain not shown) neoplastic spindle cells. (**b**) Higher-magnification view shows plump spindle cells with mild nuclear atypia and a vaguely fascicular growth pattern

Fig. 14.34 Sarcomatoid mesothelioma. (**a**) Low-magnification photomicrograph showing highly atypical spindle cells arranged in sheets without distinct architectural features in sarcomatoid mesothelioma. (**b**) High-magnification photomicrograph shows marked atypia characterized by pleomorphic nuclei with vesicular chromatin and prominent nucleoli

Fig. 14.35 Mesothelioma with heterologous differentiation. (**a**) Low-magnification photomicrograph showing a biopsy from a diffuse pleural lesion with only a very minor epithelial component (top left) and a predominantly sarcomatoid component in which there are heterologous elements, including neoplastic bone and cartilage. (**b**) Higher-magnification view showing osseous differentiation resembling osteosarcoma. (**c**) Low-magnification view of the same field depicted in part (**a**) showing strong staining for pancytokeratins in the surface epithelial component (top left) as well as much of the sarcomatoid component. Cytoplasmic and nuclear staining for calretinin showed a similar distribution (not shown)

Fig. 14.36 Desmoplastic mesothelioma. (**a**) Low-magnification photomicrograph shows diffuse pleural thickening characterized by random variation in cellularity in a densely collagenous stroma. At the interface with the chest wall the soft-tissue tumor extends into adipose tissue. (**b**) High-magnification photomicrograph shows that the more cellular areas include a population of mildly atypical spindle-cell proliferation with a vaguely storiform architecture in hyalinized fibrous stroma. This storiform growth pattern in areas of increased cellularity is nearly universal in desmoplastic mesothelioma and is a helpful diagnostic feature

Fig. 14.37 Desmoplastic mesothelioma. Photomicrograph showing abrupt transition from atypical spindle cells in a densely hyalinized stroma (top right) to bland acellular necrosis (lower left). Bland necrosis is another feature helpful in distinguishing desmoplastic mesothelioma from benign fibrous lesions of the pleura

Fig. 14.38 Desmoplastic mesothelioma. (**a**) High-magnification photomicrograph showing tumor invading the chest wall adipose tissue, perhaps the single most helpful histologic feature in distinguishing desmoplastic mesothelioma from nonneoplastic diffuse fibrotic lesions of the pleura. (**b**) Positive staining for cytokeratins does not by itself distinguish benign from malignant mesothelial proliferations but can be helpful in identifying the invasion of adipose tissue with greater confidence

Fig. 14.39 Biphasic malignant mesothelioma. The tumor consists of a tubular epithelioid component and a sarcomatoid spindle-cell component

List of Tables

Table 3.1 Types of congenital pulmonary airway malformations (CPAMs)
Table 4.1 List of pulmonary infections encountered in lung biopsies, surgical resections, and autopsies
Table 5.1 Major airway diseases
Table 6.1 The common manifestations of lung involvements associated with major connective tissue diseases
Table 8.1 Classification and grading of pulmonary allograft rejection (based on ISHLT 2007 formulation)
Table 9.1 Major types of pneumoconiosis and their typical pathologic features
Table 10.1 Adult pulmonary hypertension classification
Table 11.1 Summary of primary pulmonary lymphoproliferative diseases
Table 12.1 Major benign lung neoplasms
Table 13.1 Histologic subtypes and variants of adenocarcinoma
Table 13.2 Grading lung adenocarcinomas predominantly using histology
Table 13.3 Growth patterns seen in carcinoid tumors
Table 13.4 Comparison between typical and atypical carcinoids
Table 14.1 Common histologic types of diffuse malignant mesothelioma
Table 14.2 Immunohistochemical markers useful in the differential diagnosis of epithelioid mesothelioma and metastatic adenocarcinoma

Normal Structures and Common Artifacts

1

Chen Zhang and Jeffrey L. Myers

A general knowledge of normal lung structure (Figs. 1.1, 1.2, 1.3, 1.4 and 1.5) and common artifacts (Figs. 1.6, 1.7, 1.8 and 1.9) is critical for interpreting lung biopsies. Histologically, there are two major types of epithelium within the lungs: respiratory (bronchial/bronchiolar) and alveolar epithelium. The respiratory epithelium lines the proximal and distal airways that start with the trachea, followed by bronchi and variable generations of terminal and respiratory bronchioles. The major histologic difference between a bronchus and a bronchiole is the presence of airway cartilage and submucosal seromucous glands in the former.

Alveolar epithelium lines portions of the respiratory bronchiole, alveolar ducts, and alveoli. Flat type I pneumocytes with highly attenuated cytoplasm and small flattened nuclei account for 95% of alveolar epithelial cells in normal lung; the remaining 5% consist of cuboidal type II pneumocytes with rounded nuclei. Type II pneumocytes become more conspicuous and profuse in injured lung and are therefore a nonspecific finding in a broad range of conditions.

The pulmonary acinus consists of a respiratory bronchiole and the distal alveolar ducts and alveoli that it serves. The pulmonary acinus is the fundamental physiologic unit of the lung but cannot be appreciated as a discrete anatomic structure in routine histologic preparations. Anatomically, each lobe of the lung is further subdivided into segments and secondary lobules that are separated by thin fibrous interlobular septa. The proximal portions of multiple pulmonary acini are clustered within the central zones of the secondary lobules, which are defined by interlobular septa (e.g., proximal acinar or centrilobular emphysema). Distal portions of the acinus are clustered next to the septa themselves (e.g., distal acinar or paraseptal emphysema). An airway (bronchus or bronchiole) courses with a small muscular pulmonary artery, and together they are referred to as a bronchovascular bundle. The veins are located within the interlobular septa and visceral pleura. The lymphatics are located within the bronchovascular bundles, interlobular septa, and pleura. Diseases such as sarcoidosis that follow lymphatic routes are often referred to as having a "lymphangitic distribution."

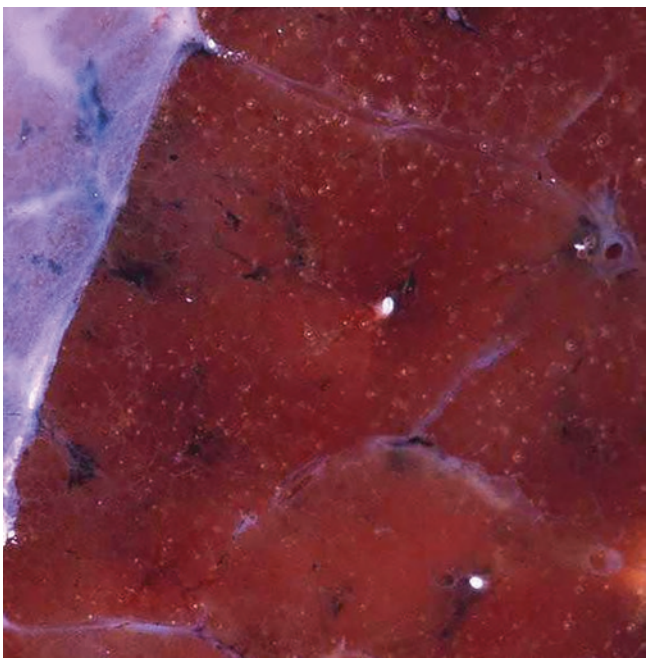

Fig. 1.1 Normal lung. Gross photograph of a peripheral portion of normal lung. On the cut surface, the tan brown spongy lung parenchyma is composed of secondary lobules in which multiple acini are aggregated. Proximal acinar structures are clustered in the center, and distal alveolar spaces are concentrated at the periphery adjacent to the thin fibrous interlobular septa that separate the lobules. The airways and blood vessels are barely visible. The outer surface of the lung is lined by the visceral pleura (upper left)

C. Zhang (✉)
Department of Pathology and Laboratory Medicine, Indiana University School of Medicine, Indianapolis, IN, USA
e-mail: chenzhan@iupui.edu

J. L. Myers
Department of Pathology, Michigan Medicine, Ann Arbor, MI, USA
e-mail: myerjeff@med.umich.edu

© Springer Science+Business Media, LLC, part of Springer Nature 2018

C. Zhang, J. L. Myers (eds.), *Atlas of Lung Pathology*, Atlas of Anatomic Pathology,
https://doi.org/10.1007/978-1-4939-8689-7_1

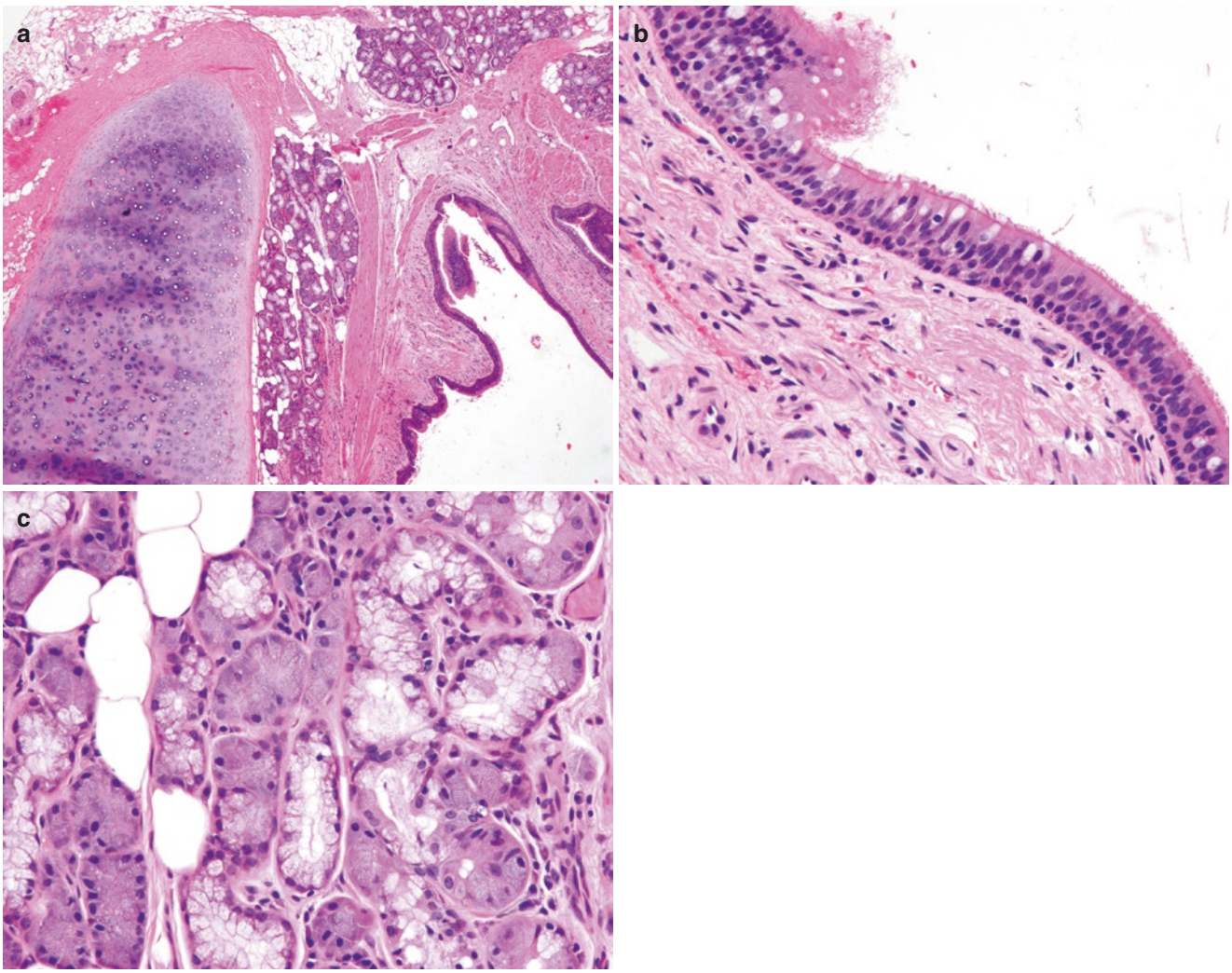

Fig. 1.2 Normal bronchus. (**a**) Low-magnification photomicrograph of a main stem bronchus showing bronchial wall cartilage and submucosal seromucous glands. (**b**) High-magnification photomicrograph showing bronchial epithelium composed of ciliated, pseudostratified, columnar epithelium with scattered mucin-secreting cells (goblet cells). (**c**) High magnification of the submucosal glands consisting of mixed serous and mucous cells

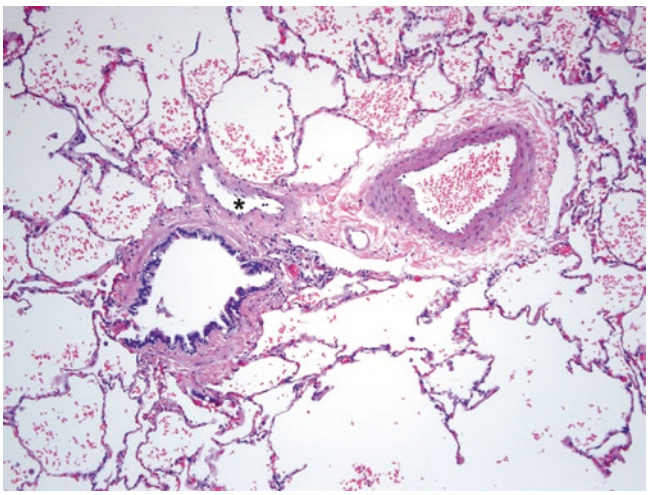

Fig. 1.3 Normal terminal bronchiole. Intermediate magnification view of a normal bronchovascular bundle. The bronchiole (left) is a small, noncartilaginous airway lined by columnar respiratory epithelial cells with a muscular wall and without intervening submucosal glands. The bronchiole is accompanied by a small muscular pulmonary artery (right) of similar caliber. Associated connective tissue and lymphatic spaces (asterisk) compose the bronchovascular bundle

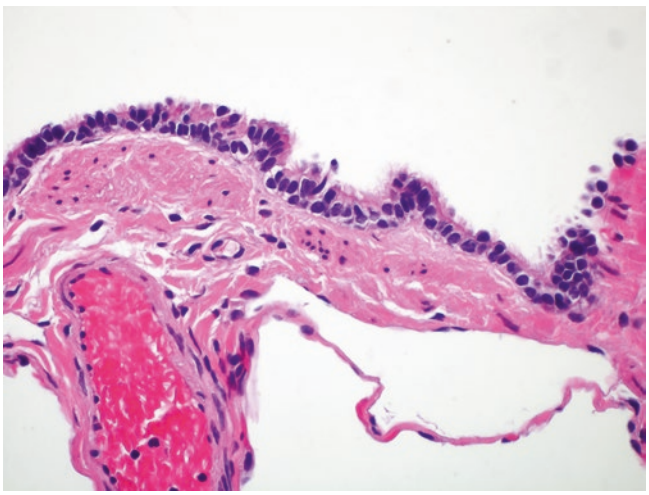

Fig. 1.5 High-magnification photomicrograph of a respiratory bronchiole. The epithelium is still predominantly ciliated but more cuboidal in shape compared with the columnar pseudostratified epithelium in the larger airway in Fig. 1.2b. Mucous cells or goblet cells become rare in respiratory bronchioles with a relative increase in nonciliated, nonmucinous Clara cells. The bronchiole wall consists of fibrous tissue and an incomplete smooth muscle layer

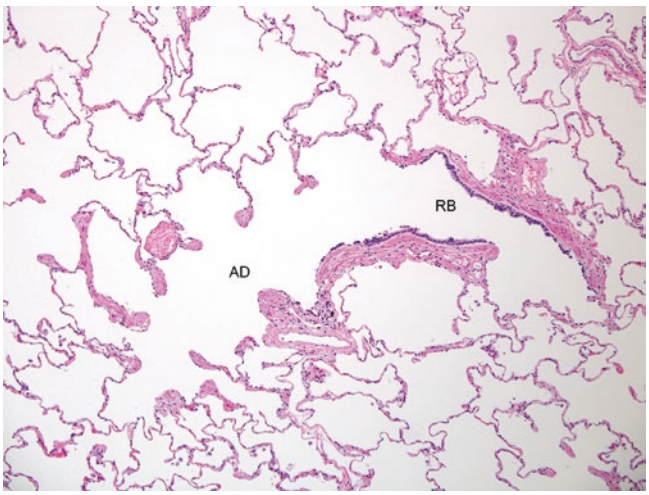

Fig. 1.4 Intermediate-magnification photomicrograph showing the respiratory bronchiole (RB) and the associated alveolar duct (AD). Note the transition from the respiratory epithelium lining the respiratory bronchiole to the flattened alveolar epithelium of the alveolar duct

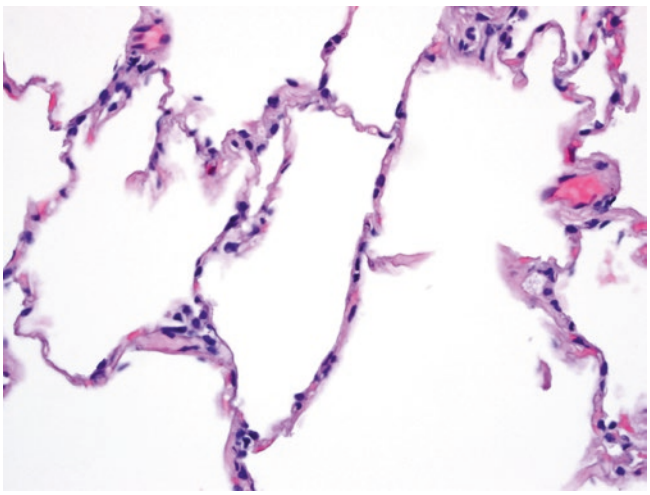

Fig. 1.6 High-magnification photomicrograph of normal alveoli. The alveolar septa are very thin and consist of flattened alveolar epithelium (pneumocytes) and delicate capillaries

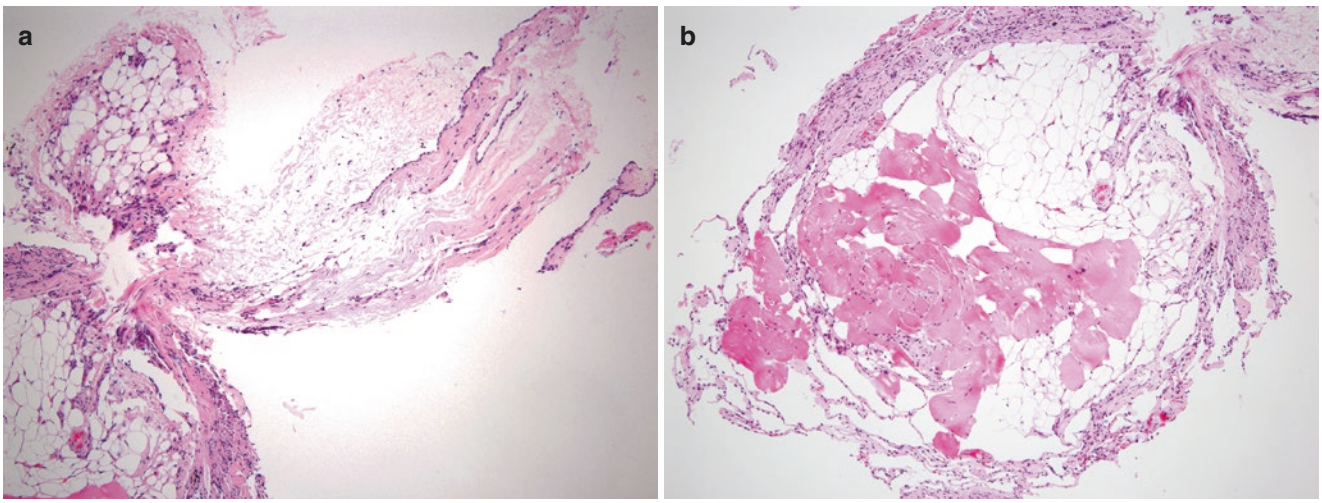

Fig. 1.7 Photomicrographs showing pleural and chest wall soft tissues in transbronchial biopsies. (**a**) Fragments of mesothelium-lined pleural tissue and mediastinum/chest wall adipose tissue are seen in a transbronchial biopsy. (**b**) Chest wall skeletal muscle and adipose tissue immediately adjacent to normal lung parenchyma in a transbronchial biopsy representing an unintended procedural artifact

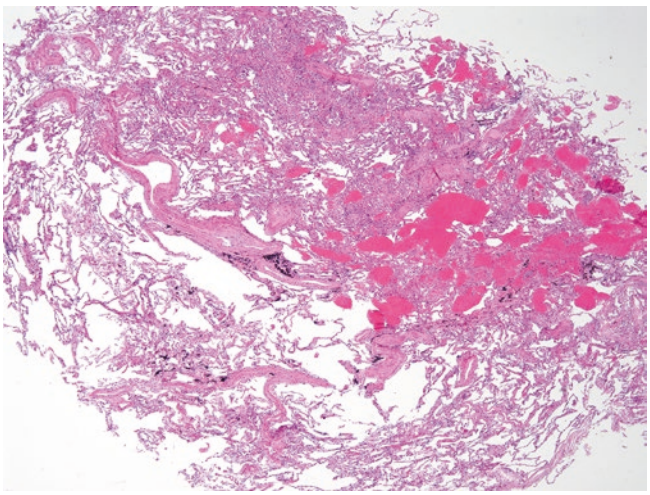

Fig. 1.8 Low-magnification photomicrograph showing artifactually collapsed lung and intra-alveolar hemorrhage. Mechanically compressed lung may mimic interstitial lung disease as a result of nonspecific thickening of collapsed interstitial structures; finding normal lung adjacent to the collapsed focus is helpful in sorting out the problem. Lack of hyperplastic alveolar pneumocytes is another helpful feature in distinguishing this artifact from interstitial lung disease. Procedure-related hemorrhage is distinguished from clinically significant intra-alveolar hemorrhage by the lack of fibrin, organizing spindle cells, hemosiderin, and associated secondary interstitial abnormalities

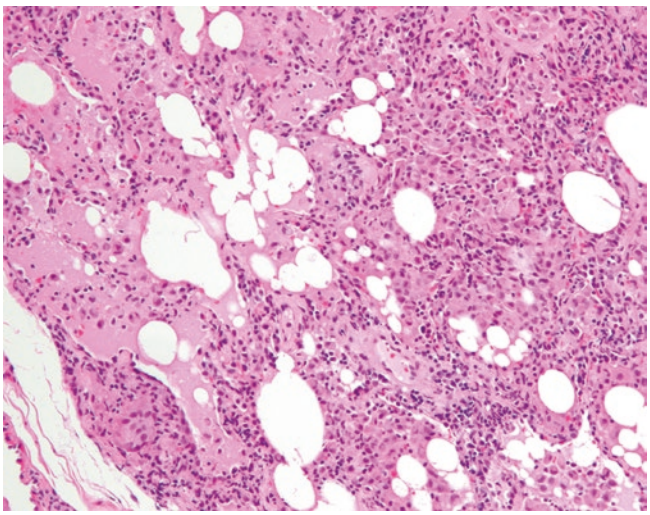

Fig. 1.9 "Pseudolipids," also termed "bubble artifact," is a processing artifact that may mimic exogenous lipid pneumonia. This artifact occurs commonly in mechanically compressed lung parenchyma, especially in areas of hemorrhage, edema, or inflammation. Lack of foreign body giant cells and other aspiration-related changes are the keys to recognizing "pseudolipids"

Suggested Reading

Albertine KH. Anatomy of the lungs. In: Mason RJ, Broaddus VC, Martin TR, King TE, Schraufnagel D, Murray J, et al., editors. Murray and Nadel's textbook of respiratory medicine, vol. 1. 5th ed. Philadelphia: Saunders/Elsevier; 2010. p. 3–25.

Colby TV, Yousem SA. Pulmonary histology for the surgical pathologist. Am J Surg Pathol. 1998;12:223–39.

Katzenstein A-LA. Handling and interpretation of lung biopsies. In: Katzenstein and Askin's surgical pathology of non-neoplastic lung disease. 4th ed. Philadelphia: Elsevier; 2006. p. 1–6.

Incidental Findings and Lesions of Limited Clinical Significance

2

Chen Zhang and Jeffrey L. Myers

Incidental findings of little, unknown, or limited diagnostic significance (Figs. 2.1, 2.2, 2.3, 2.4, 2.5, 2.6, 2.7, 2.8, 2.9, 2.10 and 2.11) are common and may confound histologic interpretation of both large and small lung specimens. Some lesions that are usually of little diagnostic significance occasionally account for small nodules or opacities on radiologic images. Although little significance is attributable to these lesions in most patients, it is important to be aware of them in order to avoid assigning them undue diagnostic value.

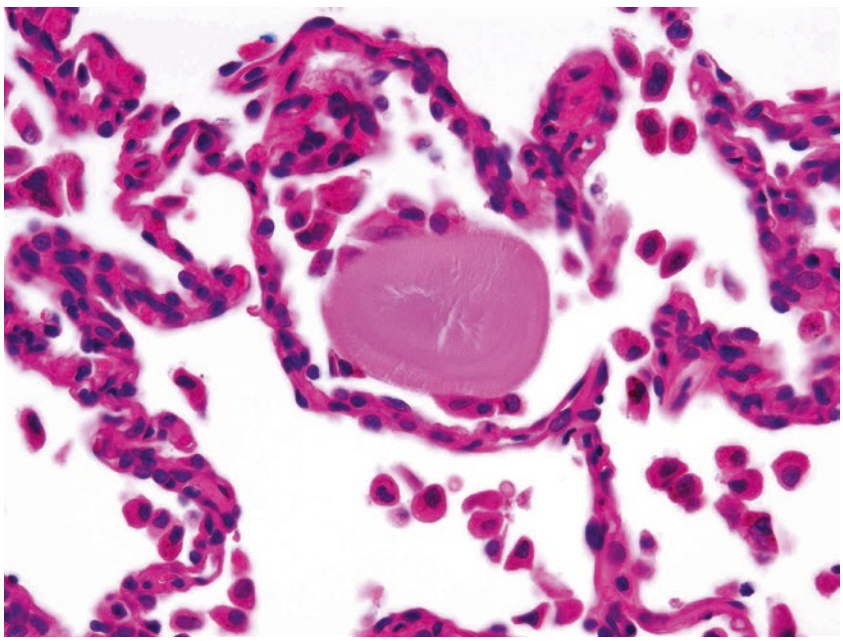

Fig. 2.1 High-magnification photomicrograph showing corpora amylacea within an alveolar space in normal lung. It is a round, eosinophilic structure consisting of concentric lamellae and spoke-like structures radiating from the center. It is partially rimmed by alveolar macrophages. Corpora amylacea have no known significance but are more prominent in older patients. Their origin is unknown. It is important not to confuse them with aspirated foreign materials

C. Zhang (✉)
Department of Pathology and Laboratory Medicine, Indiana University School of Medicine, Indianapolis, IN, USA
e-mail: chenzhan@iupui.edu

J. L. Myers
Department of Pathology, Michigan Medicine, Ann Arbor, MI, USA
e-mail: myerjeff@med.umich.edu

© Springer Science+Business Media, LLC, part of Springer Nature 2018

C. Zhang, J. L. Myers (eds.), *Atlas of Lung Pathology*, Atlas of Anatomic Pathology,
https://doi.org/10.1007/978-1-4939-8689-7_2

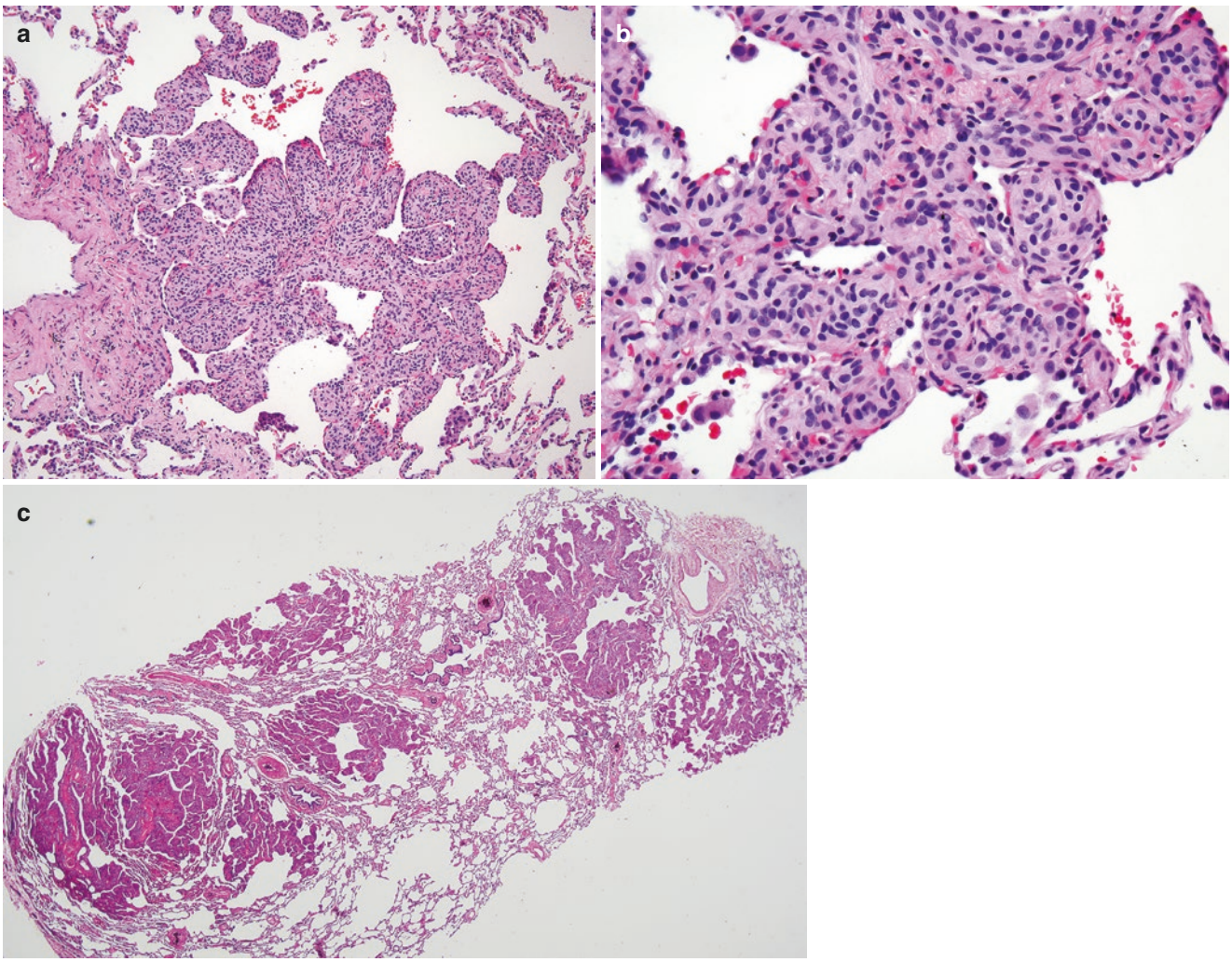

Fig. 2.2 Meningothelial-like nodule (MLN). (**a**) Intermediate-magnification view of characteristic stellate-shaped nodule in which the interstitium is expanded by whorls of bland epithelioid cells arranged in a nested growth pattern. The nodules vary in size, but they are usually small and easily missed; missing them has no diagnostic consequence, and they need not be routinely noted in autopsy or surgical reports. The background lung is unremarkable. (**b**) At high magnification, the nodule is composed of uniform epithelioid cells with bland, round to oval nuclei, abundant amphophilic cytoplasm, and indistinct cell borders. The cells usually stain for epithelial membrane antigen (EMA) and are negative for cytokeratins, TTF1, and neuroendocrine markers (not shown). The morphologic and immunohistochemical features closely resemble meningothelium. (**c**) Rarely, MLNs can be numerous and cause a form of diffuse lung disease referred to as "diffuse meningotheliomatosis," as illustrated in this surgical lung biopsy

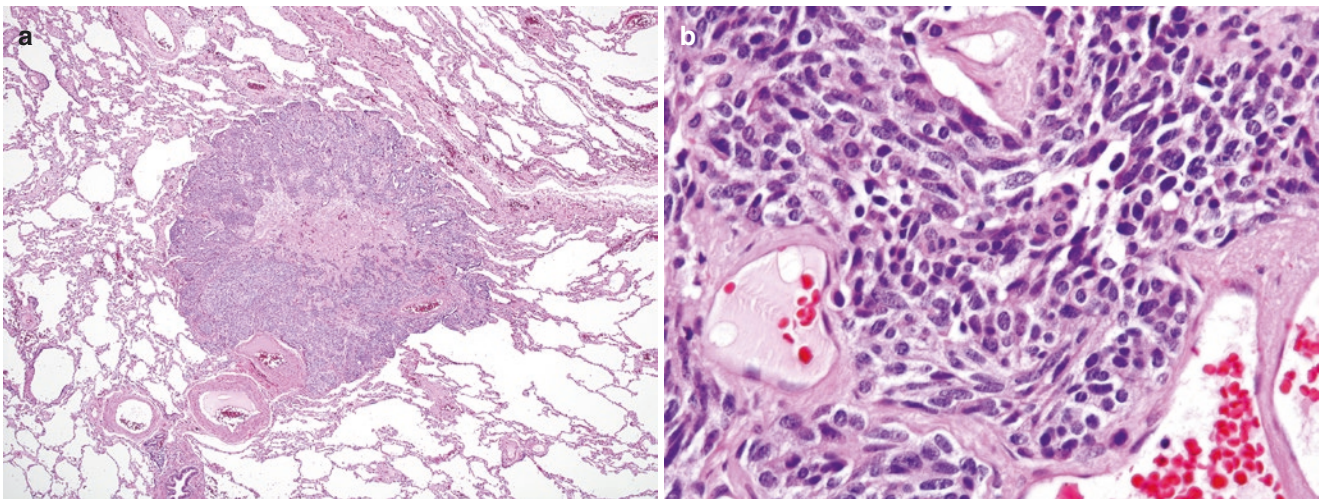

Fig. 2.3 Carcinoid tumorlet. (**a**) Low-magnification photomicrograph shows a well-demarcated cellular nodule surrounded by normal lung. The lesion is by definition less than 5 mm in greatest dimension. (**b**) At high magnification, the nodule is composed of uniform, oval to elongated epithelioid cells with finely dispersed ("salt and pepper") nuclear chromatin. These lesions stain strongly positive for neuroendocrine markers such as synaptophysin and chromogranin (not shown) and are distinguished from typical carcinoid tumors mainly by their size (less than 5 mm) and location (peribronchiolar interstitium) of the lesion

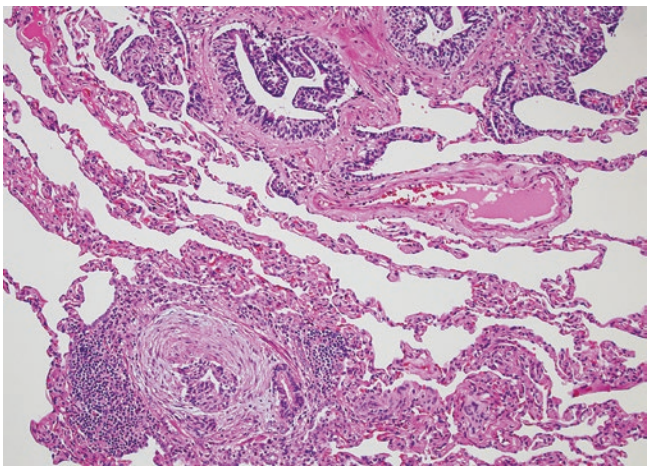

Fig. 2.4 Intermediate-magnification photomicrograph illustrating neuroendocrine cell hyperplasia. Neuroendocrine cell hyperplasia commonly accompanies carcinoid tumorlets and is characterized by a proliferation of neuroendocrine cells distributed in a pagetoid fashion within the respiratory epithelium of a bronchiole (top half of photomicrograph). The lumina of affected bronchioles may be narrowed by a pattern of concentric fibrosis characteristic of constrictive (obliterative) bronchiolitis (lower left). Diffuse idiopathic neuroendocrine cell hyperplasia (DIPNECH) is a rare disease in which the combination of neuroendocrine cell hyperplasia and constrictive bronchiolitis is affiliated with progressive airflow limitation. Carcinoid tumorlets and neuroendocrine cell hyperplasia are common incidental findings in resection specimens harboring carcinoid tumors and should not be overdiagnosed as DIPNECH

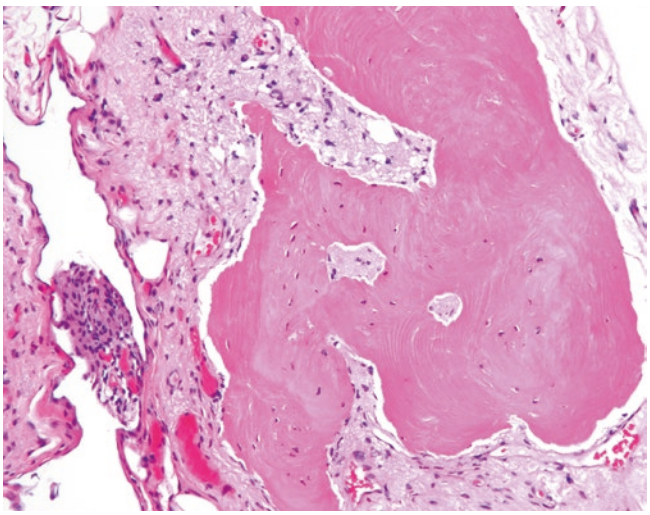

Fig. 2.5 Nodular metaplastic ossification (osseous metaplasia). A single focus of branching woven bone is present within an area of fibrosis from a patient with usual interstitial pneumonia (UIP). This sort of osseous metaplasia is common in UIP but is not specific and can be seen in various histologic contexts, including relatively normal lung

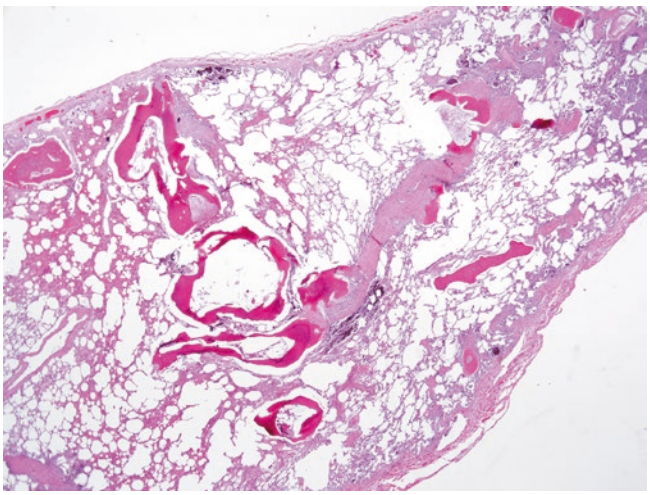

Fig. 2.6 Dendriform ossification. In this photomicrograph multiple elongated, branching lamellar bone spicules are seen within the interstitium, which is in turn affected by a subtle pattern of mild, paucicellular fibroelastosis. The fibrosis sometimes associated with dendriform ossification often has this distinctive "aponeurosis-like" quality. Dendriform ossification may occur as an isolated finding, in which case it may not be affiliated with respiratory symptoms and is instead an incidental finding of little consequence. In other cases, however, this pattern of osseous metaplasia is more extensive and superimposed on a pattern of fibrosis that may resemble usual interstitial pneumonia and account for a syndrome of progressive lung disease

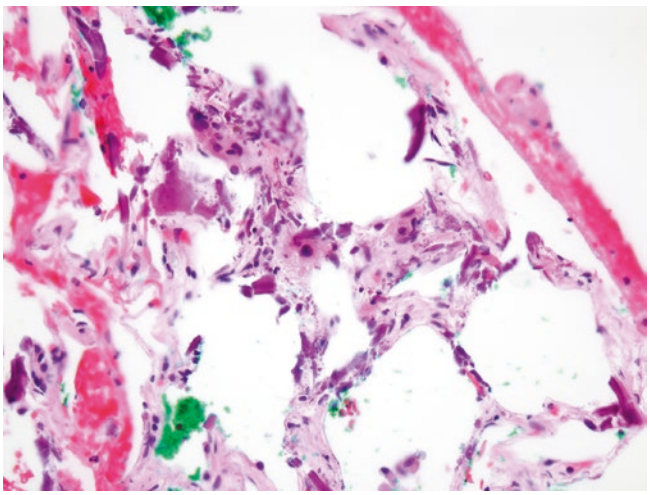

Fig. 2.7 Metastatic calcification is characterized by alveolar septal deposition of basophilic calcium particles. The alveolar structure is preserved with mild septal thickening. Metastatic calcification is a diffuse form of dystrophic calcification that is usually seen in patients with longstanding renal failure requiring hemodialysis

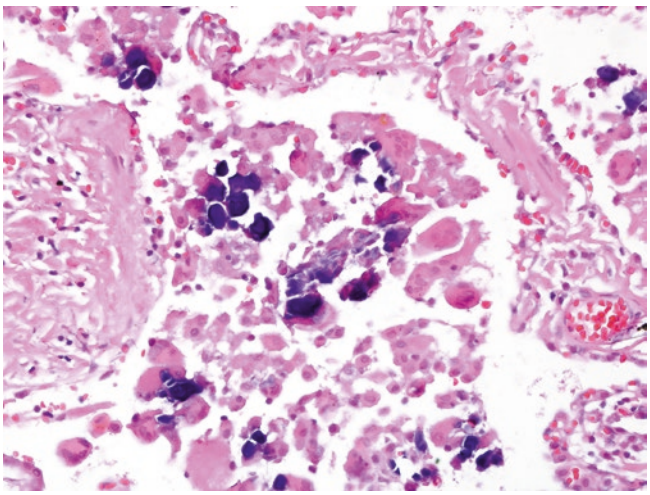

Fig. 2.8 Blue bodies are round, often fragmented, lamellated basophilic structures within alveolar macrophages. They are the breakdown products of cell metabolism and are of no clinical significance. Blue bodies contain calcium and are not polarizable. They should not be confused with aspirated particulates such as microcrystalline cellulose

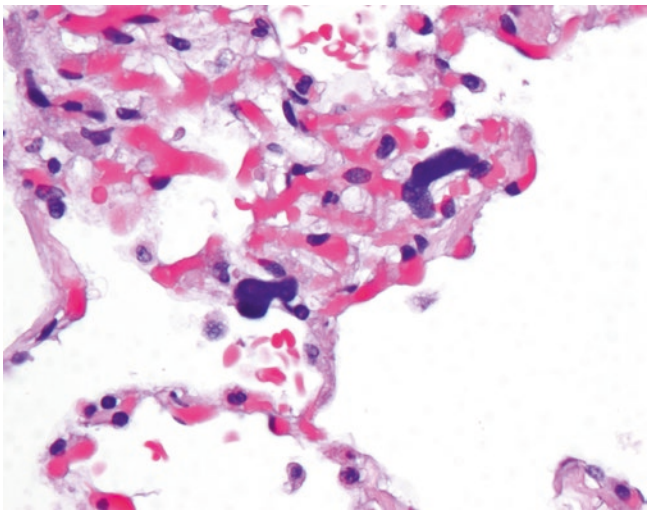

Fig. 2.9 Megakaryocytes within the alveolar septa. High-magnification photomicrograph showing irregularly shaped and deeply basophilic megakaryocytes within the lumina of alveolar septal capillaries. They are common incidental findings in surgical lung biopsies and autopsies and are especially common in patients with sepsis, cardiovascular diseases, or metastatic malignancies

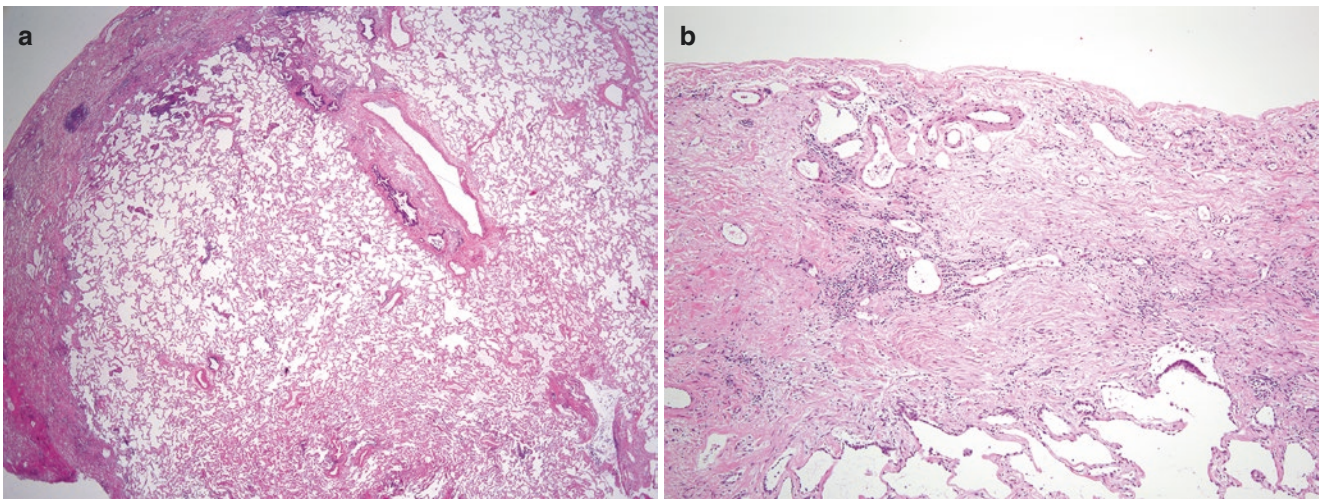

Fig. 2.10 Apical cap (fibroelastosis). (**a**) Low-magnification view of an upper lobe lung biopsy showing a subpleural zone of scarring. The underlying lung parenchyma is normal. (**b**) High-magnification view of the scarred area showing the distinctive elastotic collagen and mild chronic inflammation. The apical cap is a common incidental finding in the upper lobes but can also be seen in the superior segments of the lower lobes. In a few patients, apical caps present as mass-like lesions with radiologic features resembling malignancy. Because well-differentiated adenocarcinomas occasionally arise in this setting, small closed biopsies performed for a radiologic suspicion of malignancy that show only apical cap should be interpreted with caution

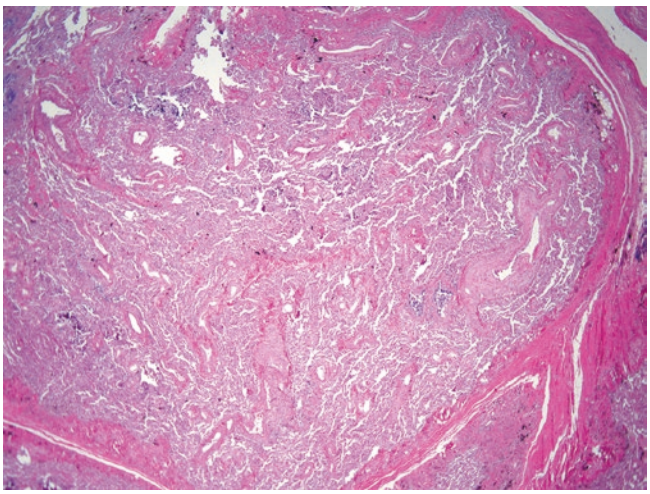

Fig. 2.11 Low-magnification photomicrograph showing round atelectasis. Round (also termed rounded) atelectasis occurs when fibrotic pleura retracts and invaginates into underlying lung parenchyma, causing a portion of the lung to collapse. The collapsed lung may mimic a mass radiologically and therefore be viewed as a potential "pseudoneoplasm"

Suggested Reading

Dobashi M, Yuda F, Narabayashi M, Imai Y, Isoda N, Obata K, et al. Histopathological study of corpora amylacea pulmonum. Histol Histopathol. 1989;4:153–65.

Ionescu DN, Sasatomi E, Aldeeb D, Omalu BI, Finkelstein SD, Swalsky PA, Yousem SA. Pulmonary meningothelial-like nodules: a genotypic comparison with meningiomas. Am J Surg Pathol. 2004;28:207–14.

Katzenstein A-LA. Handling and interpretation of lung biopsies. In: Katzenstein and Askin's surgical pathology of non-neoplastic lung disease. 4th ed. Philadelphia: Elsevier; 2006. p. 7–13.

Koss MN, Johnson FB, Hochholzer L. Pulmonary blue bodies. Hum Pathol. 1981;12:258–66.

Leslie KO, Wick MR. Miscellaneous distinctive histopathologic findings. In: Practical pulmonary pathology: a diagnostic approach. Philadelphia: Elsevier/Churchill Livingstone; 2005. p. 776–91.

Sharma GK, Talbot IC. Pulmonary megakaryocytes: "missing link" between cardiovascular and respiratory disease? J Clin Pathol. 1986;39:969–76.

Pediatric Disorders

3

Chen Zhang and Jeffrey L. Myers

Diseases commonly encountered in pediatric lung biopsies and resections are significantly different from those encountered in adult surgical lung specimens. Certain tumor types, including solitary fibrous tumor, carcinoid tumors, and low-grade mucoepidermoid carcinomas, occur in pediatric patients and are discussed and illustrated in other chapters. Developmental disorders, conditions resulting from prematurity, and certain rare tumor types largely limited to children constitute a large proportion of pediatric disorders and are the focus of this chapter. The diagnostic approach to many of these pediatric lung diseases is different. Clinical and radiologic information is often extremely important for accurate and meaningful interpretation. This chapter illustrates the disorders most commonly encountered in pediatric surgical pathology.

Pulmonary Sequestration

Pulmonary sequestration (Figs. 3.1, 3.2 and 3.3) is defined as a portion of lung receiving blood supply from the systemic circulation and not communicating with the main tracheobronchial tree, a condition for which the term bronchial atresia with systemic vascular connection may be more appropriate. It may occur within an otherwise normal lung lobe (intralobar sequestration) or outside the lung with its own pleural covering (extralobar sequestration). Gross examination of the resected specimen for the atretic bronchus and the systemic feeding artery, followed by microscopic confirmation, is important for the diagnosis. Radiologic and/or intraoperative confirmation of systemic blood supply is necessary if the feeding artery cannot be identified at gross examination. The gross and microscopic features are identical to those seen in bronchial atresia without a systemic vascular connection and are frequently combined with features of congenital pulmonary airway malformation (CPAM). CPAM shares bronchial atresia as a common underlying feature (*see* section "Congenital Pulmonary Airway Malformation"). Microscopic changes in the sequestered lung tissue typically include cystic change with mucostasis (cystic bronchiectasis) in cartilaginous airways nearest the site of bronchial atresia and cystic bronchiolar structures in more distal lung parenchyma resembling type 2 CPAM.

C. Zhang (✉)
Department of Pathology and Laboratory Medicine, Indiana University School of Medicine, Indianapolis, IN, USA
e-mail: chenzhan@iupui.edu

J. L. Myers
Department of Pathology, Michigan Medicine, Ann Arbor, MI, USA
e-mail: myerjeff@med.umich.edu

© Springer Science+Business Media, LLC, part of Springer Nature 2018
C. Zhang, J. L. Myers (eds.), *Atlas of Lung Pathology*, Atlas of Anatomic Pathology,
https://doi.org/10.1007/978-1-4939-8689-7_3

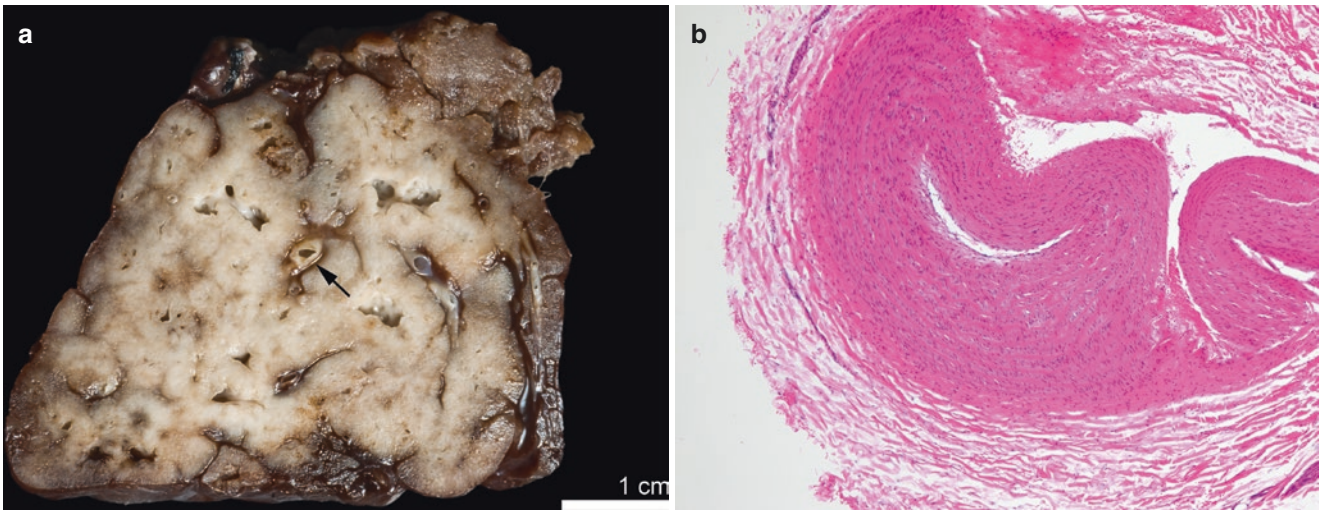

Fig. 3.1 Intralobar pulmonary sequestration (bronchial atresia with systemic vascular connection) combined with features of congenital pulmonary airway malformation. (**a**) Gross photograph showing cut surface of a partially resected lung that is nearly completely replaced by a yellow-white solid cystic lesion. The lesion is well demarcated, and minimal remaining normal lung tissue is seen at the periphery of the specimen. A centrally located thick-walled feeding blood vessel (arrow) is identified. This example illustrates the overlap between intralobar sequestration and CPAMs. (**b**) Cross section of the identified feeding blood vessel confirms a systemic elastic artery

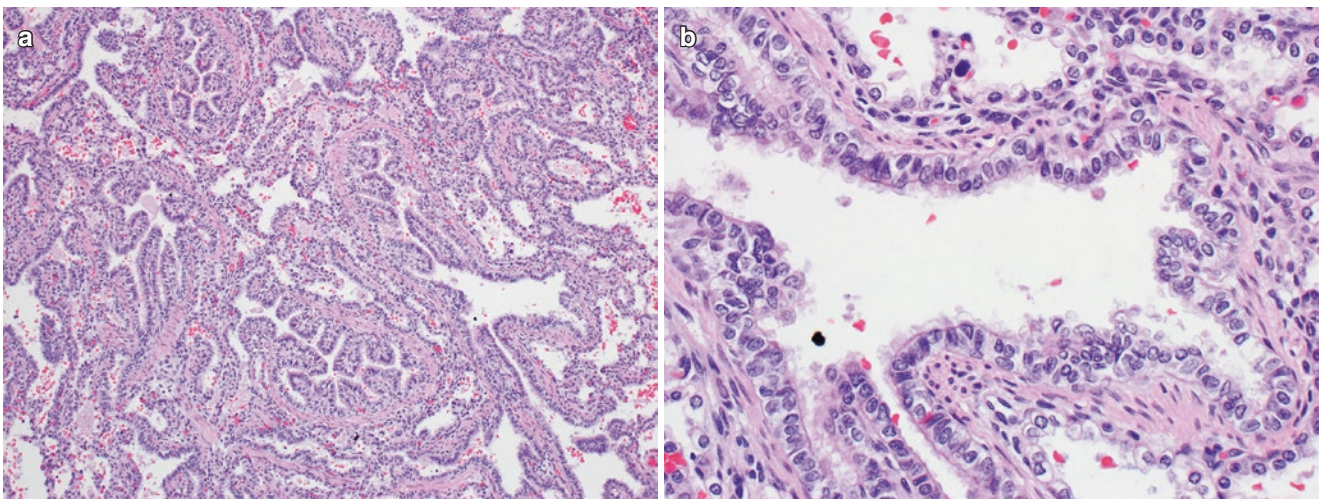

Fig. 3.2 Intralobar pulmonary sequestration combined with features of congenital pulmonary airway malformation. (**a**) Intermediate-magnification photomicrograph showing an area of the lesion illustrated in Fig. 3.1 characterized by back-to-back smaller bronchiolar type cysts. (**b**) High-magnification photomicrograph showing ciliated respiratory epithelial lining of maldeveloped parenchymal cysts

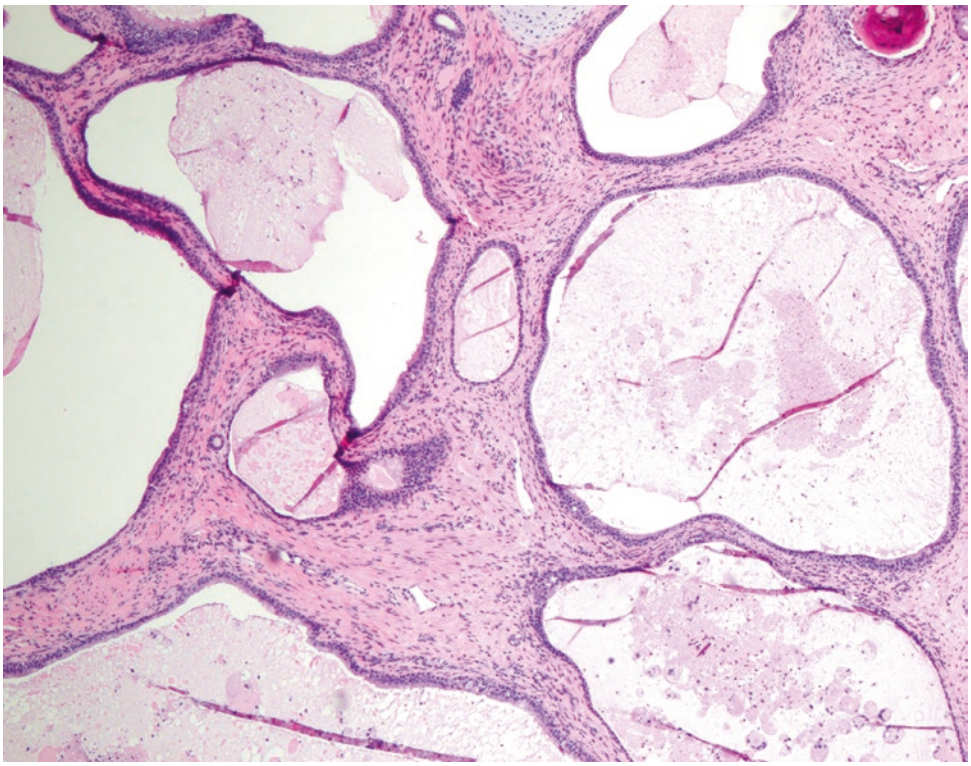

Fig. 3.3 Pulmonary sequestration. In this low-magnification photomicrograph showing a long-standing lesion, the cysts contain mucus admixed with inflammatory debris and macrophages. The lining epithelium is focally attenuated and flattened. The stroma is fibrotic, with abundant collagen deposition and focal osseous metaplasia (upper right)

Congenital Pulmonary Airway Malformation

Congenital pulmonary airway malformation (CPAM), referred to historically as congenital cystic adenomatoid malformation (CCAM), is a developmental anomaly of small airways and lung parenchyma characterized by variably sized cyst formation (Figs. 3.4, 3.5, 3.6 and 3.7). CPAM overlaps with other congenital airway malformations that have in common bronchial atresia as a foundation for the developmental abnormality. CPAM has traditionally been divided into five subtypes. Types 0–4 are based on their gross and microscopic features. Application of this nomenclature remains controversial, given that some of the entities are probably not the consequence of airway malformations (Table 3.1). Types 0 and 3 are incompatible with life. Type 4 is indistinguishable from type 1 pleuropulmonary blastoma; the latter term is preferred to convey the malignant potential of this often banal-appearing cystic lesion. The types of CPAM most commonly encountered in surgical lung specimens are types 1 and 2, which have similar histologic features. Separating types 1 and 2 CPAM has minimal clinical significance. Bronchial atresia is the underlying malformation in type 2 CPAM, a pathogenesis shared with isolated bronchial atresia and both intralobar and extralobar sequestrations.

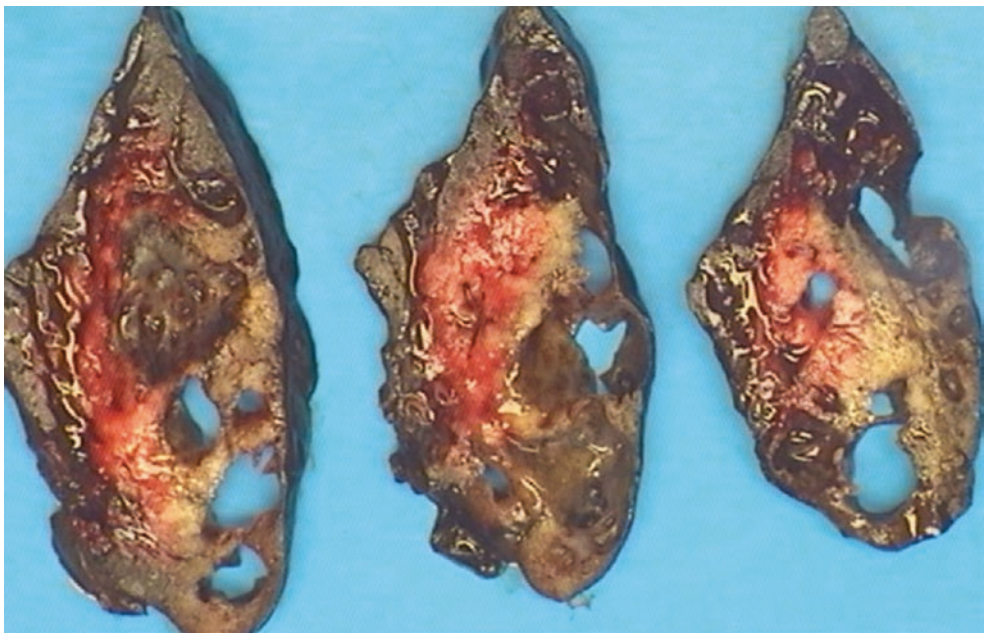

Fig. 3.4 CPAM/congenital cystic adenomatoid malformation (CCAM), type 1. The cut surface of this surgical specimen shows multiple variably sized cysts separated by grossly normal lung parenchyma. The cyst walls are fibrotic with a smooth interior surface

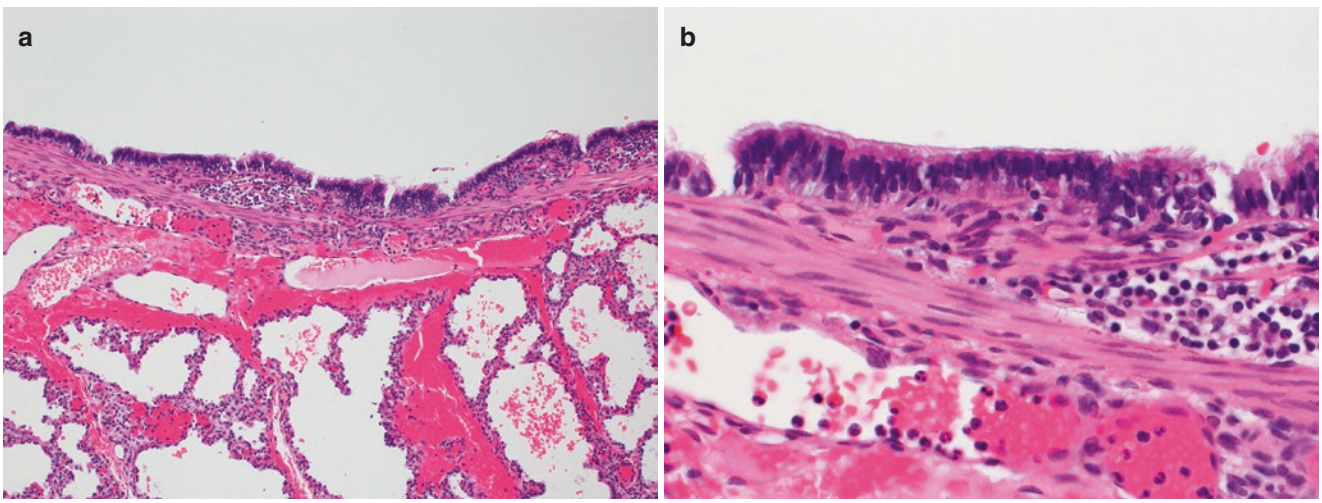

Fig. 3.5 CPAM type 1. (**a**) Low-magnification view of section from the CPAM illustrated in Fig. 3.4 showing a large cyst lined by nonmucinous ciliated columnar epithelium. The cyst is located immediately next to normally developed lung parenchyma. (**b**) High-magnification view of cyst lining that is ciliated respiratory epithelium

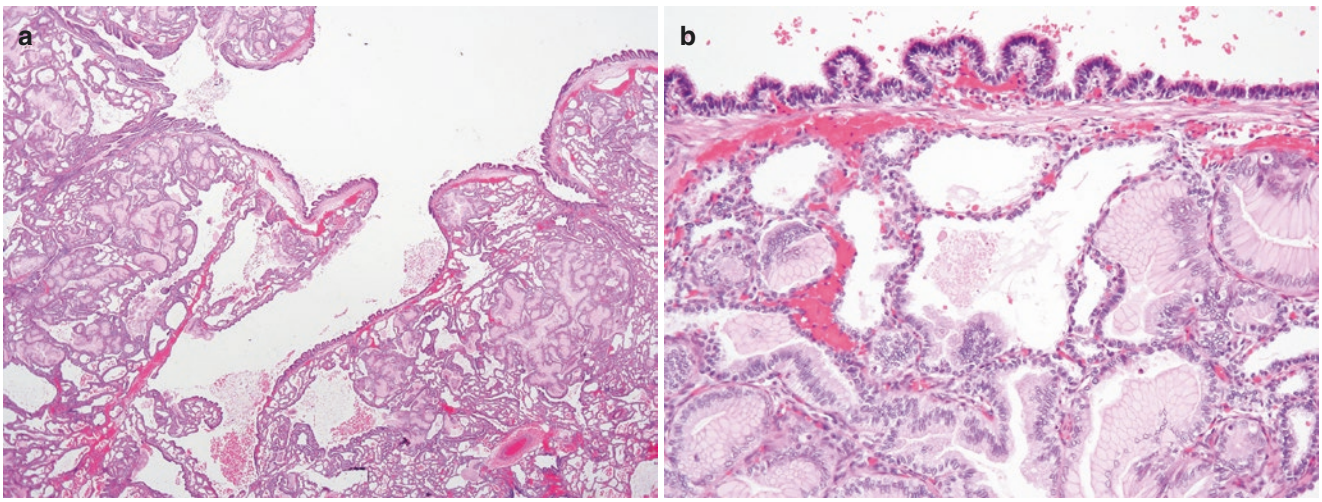

Fig. 3.6 CPAM type 1 with mucinous epithelium, a potential precursor to mucinous adenocarcinomas with a lepidic architecture referred to historically as bronchioloalveolar carcinoma. (**a**) Low-magnification photomicrograph of the type 1 CPAM illustrated in Figs. 3.4 and 3.5 showing multiple variably sized cysts and bronchiole-like structures, some of which are lined by nonciliated mucinous columnar epithelium. (**b**) Higher-magnification photomicrograph demonstrates mixed respiratory and mucinous epithelium. The mucinous epithelium includes tall columnar cells with abundant apical mucin and bland basally located nuclei

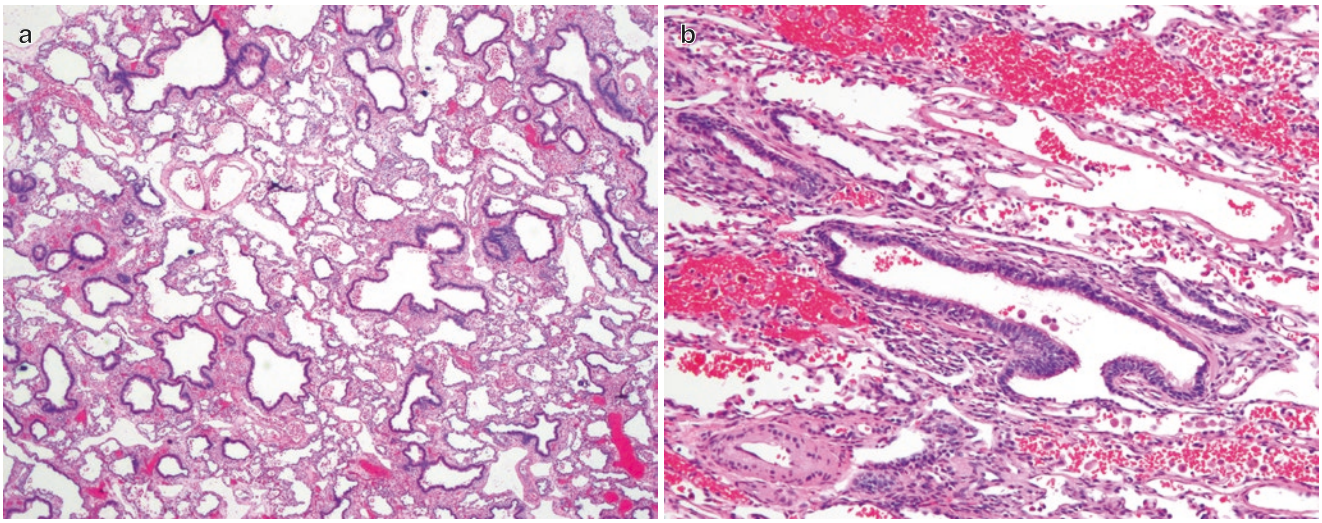

Fig. 3.7 CPAM type 2 typically occurs in the first year of life and tends to be associated with other anomalies that account for poorer outcomes. (**a**) Low-magnification photomicrograph showing multiple small cysts (0.5–2 cm) scattered within relatively preserved distal lung parenchyma. (**b**) At higher magnification, the bronchiole-like cysts are lined by ciliated respiratory epithelium and surrounded by a thin, incomplete layer of smooth muscle resembling a bronchiole

Table 3.1 Types of congenital pulmonary airway malformations (CPAMs)

Type	Gross features	Synonyms/preferred terminology	Microscopic features
0	Solid	Acinar dysplasia	Disordered pseudoglandular structures in simplified lobules that lack alveolar spaces
1	Large cysts 3–10 cm	CPAMs, type 1	Cysts with ciliated respiratory epithelial lining and occasional columnar mucinous cells
2	Smaller cysts 0.2–2 cm	Bronchial atresia	Bronchiolar structures lined by ciliated respiratory epithelium without columnar mucinous cells; occasional skeletal muscle differentiations (i.e., rhabdomyomatous cells)
3	Solid and cysts <0.2 cm	Pulmonary hyperplasia	Canalicular structures lined by flattened, nonciliated epithelium resembling fetal lung
4	Large peripheral/ subpleural cyst	Type 1 pleuropulmonary blastoma	Large thin wall cysts with flattened epithelial linings resembling bullous emphysema with/without primitive mesenchymal cells within the cyst walls

Congenital Pulmonary Overinflation

Congenital pulmonary overinflation (emphysema) is characterized by enlarged alveolar spaces without destruction of alveolar architecture (Fig. 3.8). It may involve a portion of a lobe or an entire lobe, leading to hyperlucency on radiographs. The etiology is usually attributable to partial or complete bronchial obstruction. On rare occasions, overinflation is caused by increased numbers of alveoli relative to corresponding airways and arteries, so-called polyalveolar lobe.

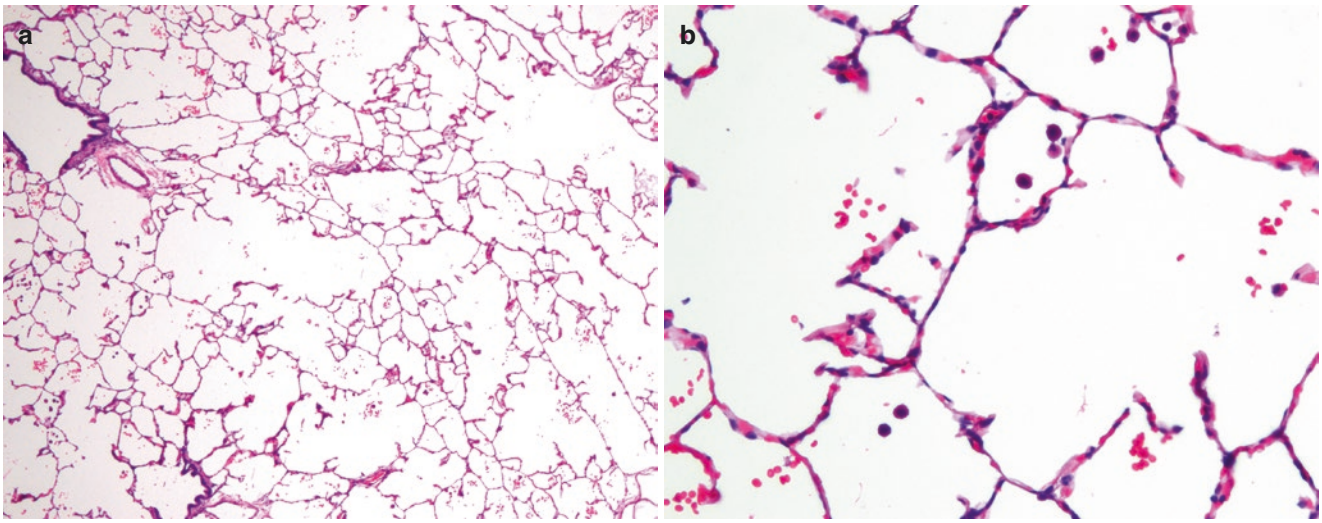

Fig. 3.8 Congenital pulmonary overinflation (emphysema). (**a**) Low-magnification view of overinflated lung showing enlarged air spaces, thin alveolar septa, and preserved alveolar architecture. (**b**) High-magnification photomicrograph showing thin incomplete alveolar septa

Pulmonary Interstitial Emphysema

Pulmonary interstitial emphysema (Figs. 3.9 and 3.10) is characterized by dissection of air into the peribronchial, interlobular, and subpleural loose connective tissue (lymphangitic distribution). Severe cases may present with pneumomediastinum. Most of the cases are related to mechanical ventilation in infants with respiratory failure. Identifying air spaces following a lymphangitic distribution with a foreign body giant cell reaction around the air-filled spaces is the key to diagnosis.

Fig. 3.9 Pulmonary interstitial emphysema. Gross photograph showing the cut surface of a lung segment resected from a 7-week-old infant on mechanical ventilation for respiratory failure. The cut surface shows multiple air-filled cysts tracking along visceral pleura, interlobular septa, and bronchovascular bundles with compression of intervening parenchyma

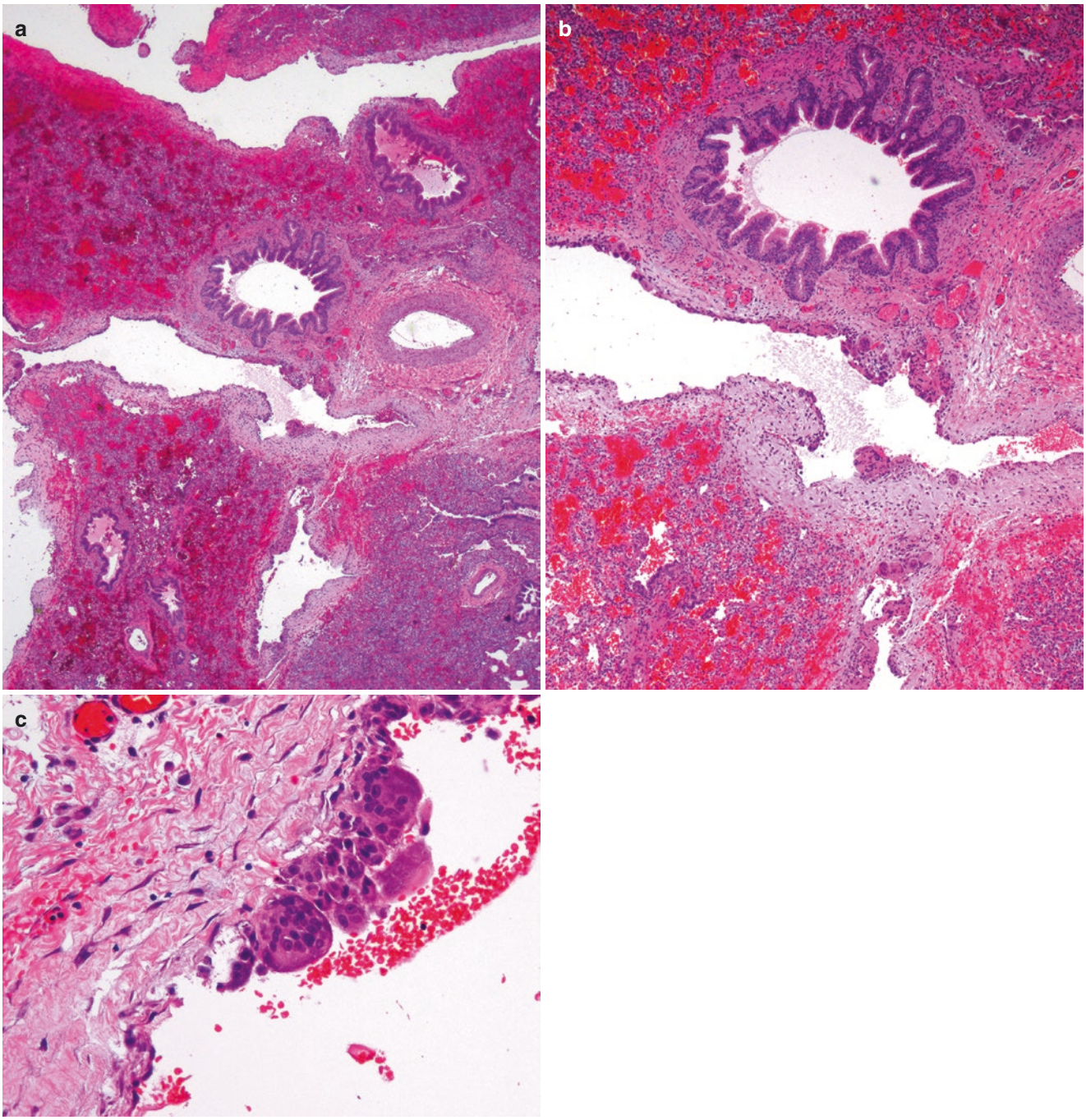

Fig. 3.10 Pulmonary interstitial emphysema. (**a**) Low-magnification photomicrograph showing multiple linear air-filled spaces distributed within bronchovascular bundles and interlobular connective tissue. The lung parenchyma between the air spaces is compressed and shows procedure-related hemorrhage. (**b**) At higher magnification, an elongated air-filled interstitial space is located next to a bronchiole with procedure-related hemorrhage in the background. The air-filled space shows no lining epithelium and is instead partially lined by macrophages, including multinucleated giant cells. (**c**) High-magnification view of multinucleated giant cells lining an air-filled interstitial space

Congenital Pulmonary Lymphangiectasia

Congenital pulmonary lymphangiectasia is a rare disease of newborns and is incompatible with life. Secondary pulmonary lymphangiectasia caused by chronic heart failure or venous obstruction is commonly encountered in lung biopsies. Both congenital and secondary pulmonary lymphangiectasia are characterized by dilated lymphatic channels located within the bronchovascular bundle, interlobular septa, and subpleural connective tissue (Figs. 3.11, 3.12 and 3.13). The number of lymphatic channels is normal. In contrast, diffuse pulmonary lymphangiomatosis (Fig. 3.13) is characterized by an increased number of anastomosing lymphatic spaces that are usually not significantly dilated.

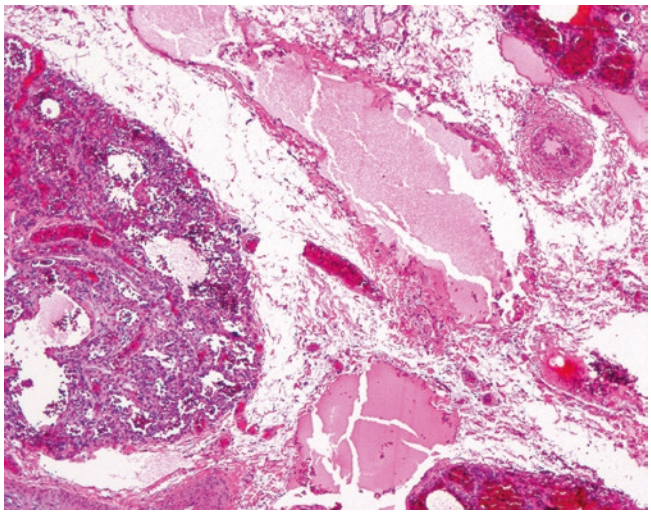

Fig. 3.11 Pulmonary lymphangiectasia secondary to congenital heart disease. The interlobular septum is widened by dilated lymphatic vessels. The dilated spaces follow lymphatic routes that may superficially resemble interstitial emphysema. Identifying the proteinaceous lymphatic fluid and flattened endothelial lining cells combined with the absence of multinucleated giant cells is helpful in making the distinction. The key to differentiating lymphangiectasia from diffuse lymphangiomatosis (see Fig. 3.15) is that the number of lymphatic spaces is not increased in the former

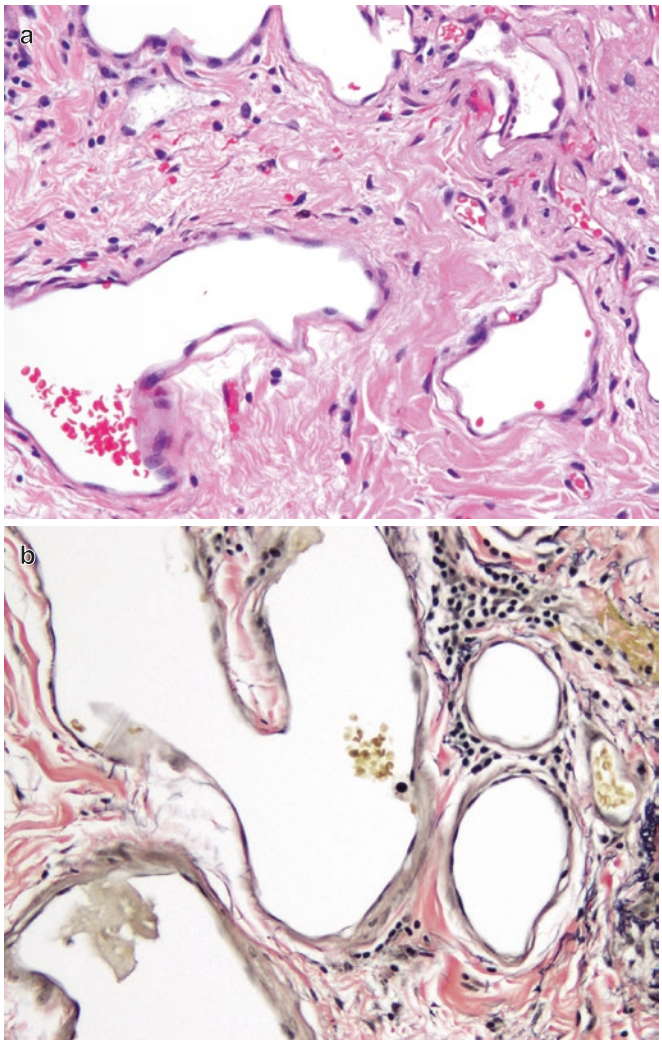

Fig. 3.12 Pulmonary lymphangiectasia. (**a**) In this example of long-standing pulmonary lymphangiectasia secondary to chronic heart failure, significant perilymphatic fibrosis is present. (**b**) An elastic stain shows lack of elastin within the vessel walls, a finding helpful in differentiating dilated lymphatics from blood vessels

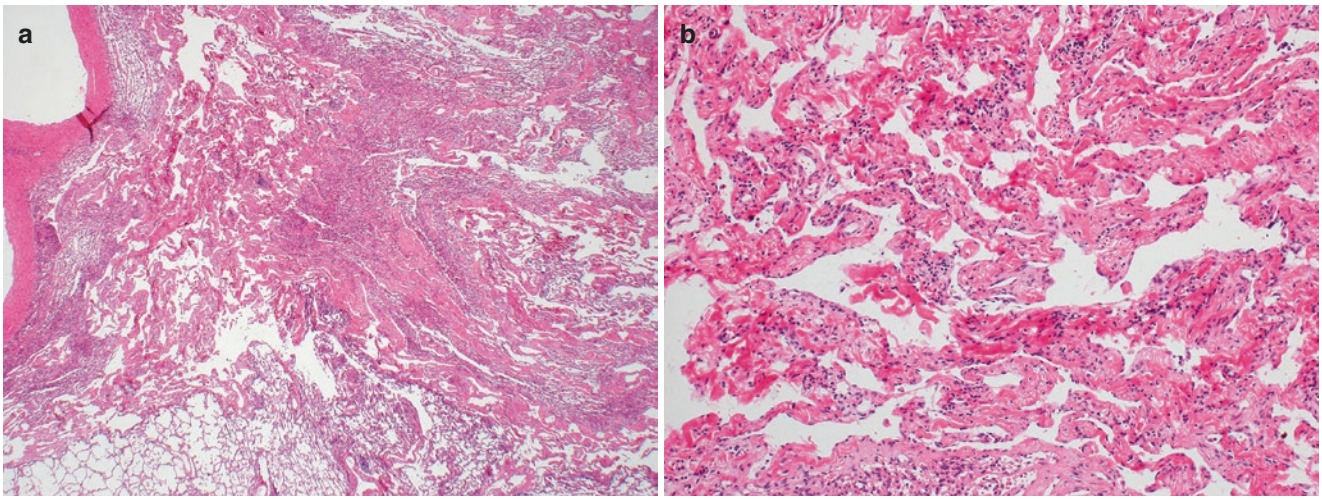

Fig. 3.13 Diffuse pulmonary lymphangiomatosis. (**a**) Low-magnification photomicrograph shows marked expansion and distortion of interlobular septa by numerous irregular anastomosing lymphatic spaces. The number of lymphatic spaces is markedly increased compared to preservation of the normal number of lymphatic channels in lymphangiectasia (Figs. 3.11 and 3.12). (**b**) Intermediate-magnification photomicrograph showing complex anastomosing lymphatic channels lined by attenuated endothelial cells without cytologic atypia

Pleuropulmonary Blastoma

Pleuropulmonary blastoma (Figs. 3.14, 3.15, 3.16, 3.17, 3.18 and 3.19) is a malignant mesenchymal tumor of infancy or early childhood. It is subgrouped into type I (cystic), type II (solid and cystic), and type III (solid), although these represent a biologic continuum in which type III has the worst prognosis. Type I pleuropulmonary blastoma is indistinguishable from CPAM type 4 in that both of these entities have bland respiratory epithelium-lined cystic structures located peripherally in the lungs. Pleuropulmonary blastoma differs in that the intervening stroma demonstrates variably conspicuous undifferentiated mesenchymal cells distributed in a pattern reminiscent of the cambium layer characteristic of botryoid variants of embryonal rhabdomyosarcoma. Recognition of type I pleuropulmonary blastomas in which neoplastic mesenchymal cells are sparse or absent altogether as a consequence of presumed regression has caused many to argue that the term CPAM type 4 should be abandoned in favor of type I pleuropulmonary blastoma. Types II and III pleuropulmonary blastoma have solid areas comprising sheets of primitive undifferentiated mesenchymal cells with or without stromal overgrowth by heterologous elements such as fibrosarcoma, rhabdomyosarcoma, or chondrosarcoma. Pleuropulmonary blastoma lacks malignant epithelial foci, which is one of its several important differences from adult pulmonary blastoma.

Fig. 3.14 Pleuropulmonary blastoma, type I. Gross photograph shows cut surface of a portion of a large multiloculated cystic lesion within the pleura

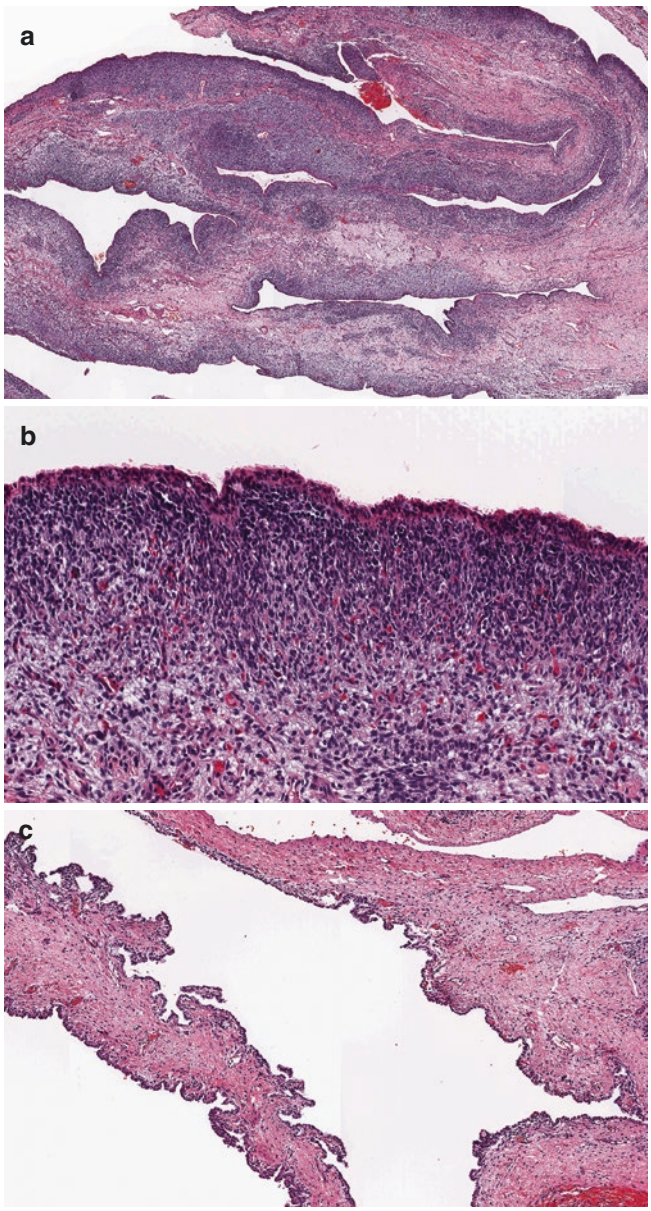

Fig. 3.15 Pleuropulmonary blastoma, type I. (**a**) Low-magnification view demonstrates epithelial-lined cysts with a "cambium" layer of undifferentiated mesenchymal cells. (**b**) High-magnification view of cyst wall showing small and primitive mesenchymal cells. Note the ciliated respiratory epithelial lining of the cyst. (**c**) Another area of the same lesion in which the cyst wall shows only paucicellular fibrous stroma without neoplastic mesenchymal cells. This area by itself is indistinguishable from CPAM type 4, a term and concept that should be abandoned. This also serves as a reminder that adequate sampling and careful examination for areas of increased stromal cellularity are important when evaluating cystic lesions in infants and young children

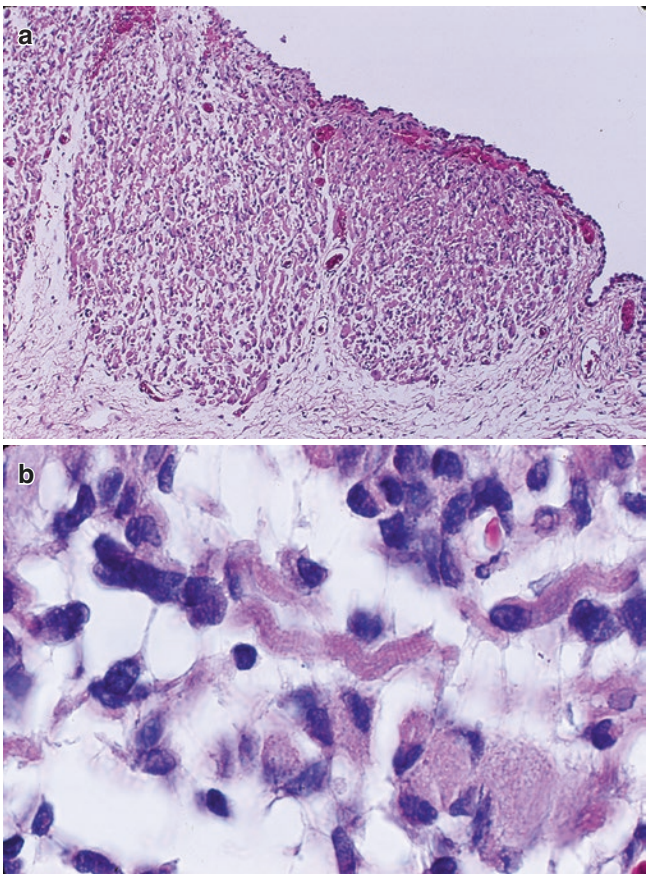

Fig. 3.16 Pleuropulmonary blastoma. (**a**) Intermediate-magnification photomicrograph showing an area in which a portion of a cyst wall shows rhabdomyoblastic differentiation in neoplastic mesenchymal cells. (**b**) High-magnification view showing cytoplasmic striations typical of rhabdomyoblasts

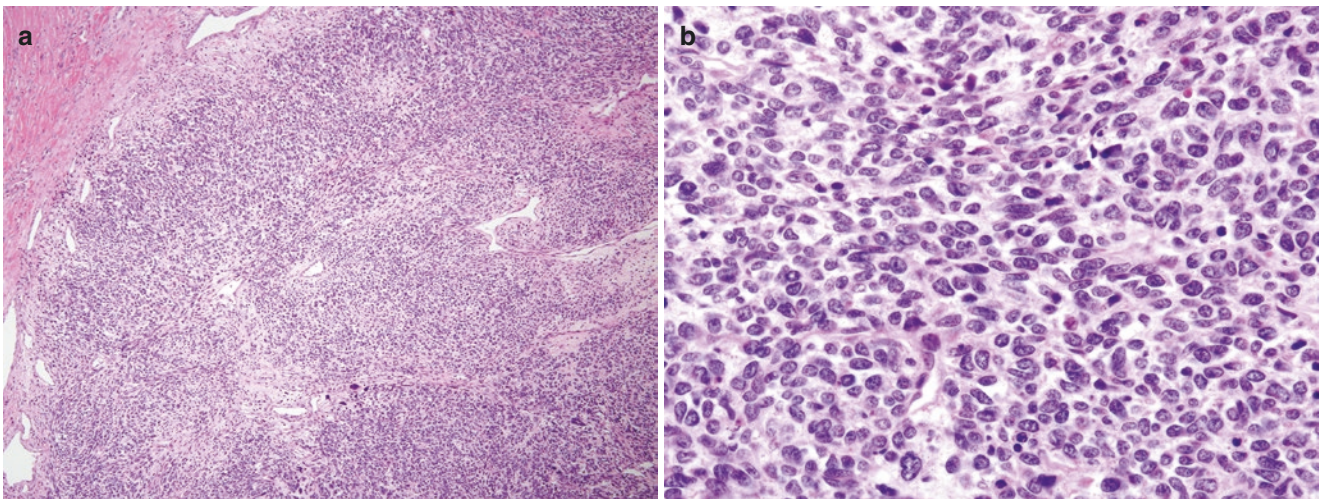

Fig. 3.17 Pleuropulmonary blastoma, type III. (**a**) Low-magnification photomicrograph of type III pleuropulmonary blastoma showing a solid sheet of undifferentiated blastomatous tumor cells. (**b**) At high magnification, the tumor cells are relatively uniform, with high nuclear-to-cytoplasmic ratio, mild pleomorphism, and inconspicuous nucleoli

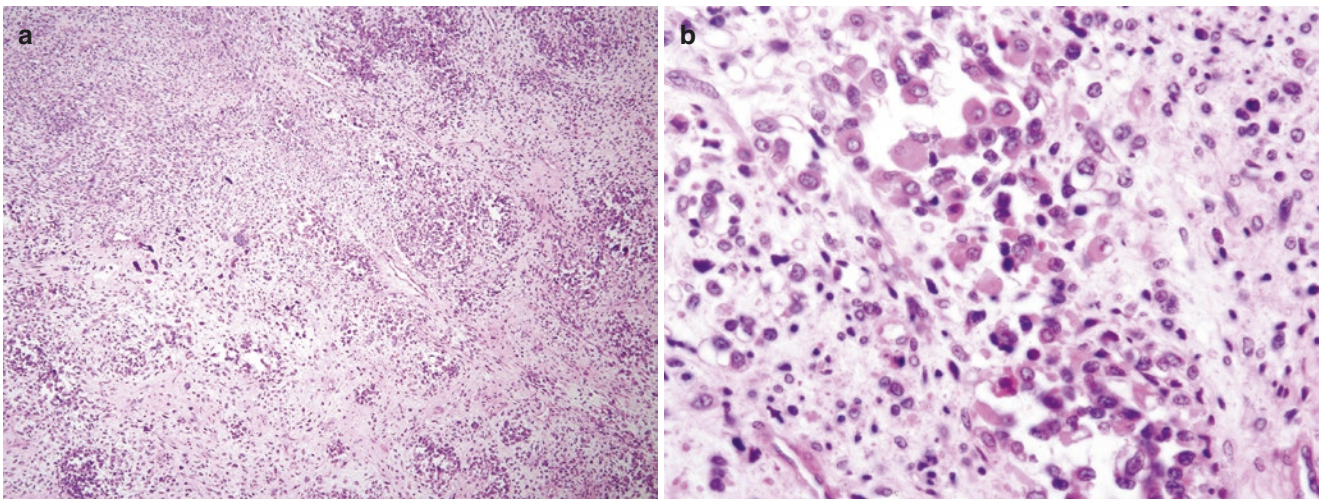

Fig. 3.18 Pleuropulmonary blastoma, type III. (**a**) Low-magnification view of a type III pleuropulmonary blastoma showing an area of stromal overgrowth with increased pleomorphism and focal rhabdomyosarcomatous differentiation. (**b**) High-magnification view of the rhabdomyosarcoma-like area showing tumor cells with enlarged, eccentric, pleomorphic nuclei and abundant eosinophilic cytoplasm

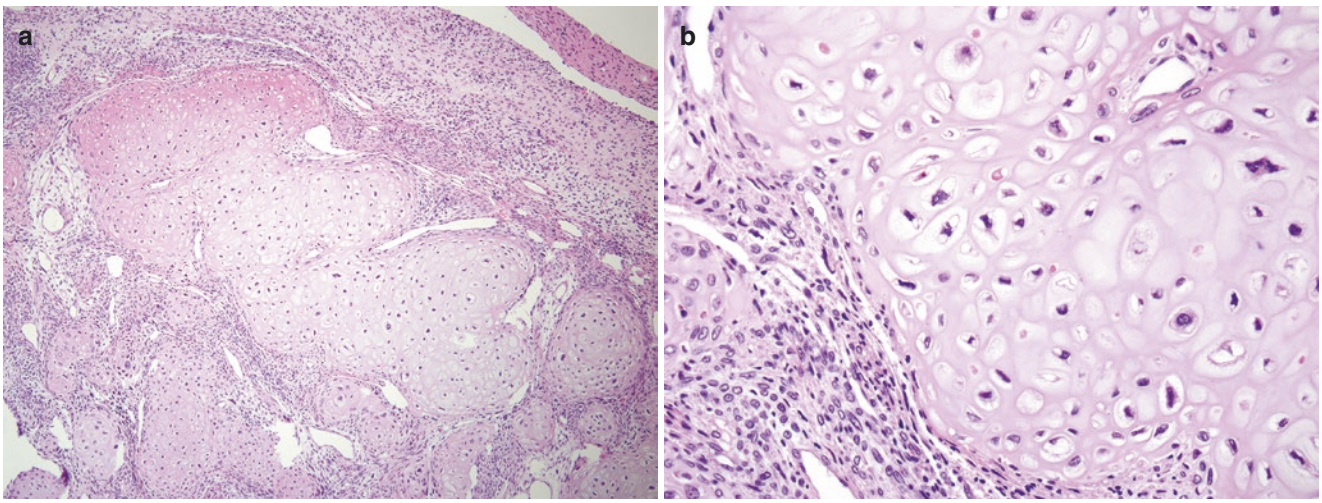

Fig. 3.19 Pleuropulmonary blastoma with chondrosarcomatous differentiation. (**a**) Low-magnification photomicrograph showing cartilage-like nodules within a cellular undifferentiated stroma. (**b**) High-magnification view of the cartilage-like nodule showing chondroid differentiation with enlarged atypical nuclei

Fetal Lung Interstitial Tumor

Fetal lung interstitial tumor (FLIT) (Fig. 3.20) is a rare solid or mixed solid and cystic congenital lung tumor usually discovered in the prenatal or early postnatal period. It presents as a circumscribed tumor that appears to be cured with complete surgical excision, which usually requires lobectomy. FLIT differs from pleuropulmonary blastoma in that the interstitial mesenchymal cells are distributed as a more uniform monolayer without the subepithelial condensation (cambium layer) typical of pleuropulmonary blastoma. The interstitial mesenchymal cells also tend to be more cytologically bland with less hyperchromatic round to oval-shaped nuclei separated by a pale slightly vacuolated stroma. Mitotic figures are absent or rare. Mesenchymal cells express vimentin and may stain focally for desmin and smooth muscle actin but are negative for myogenin. A novel anaplastic lymphoma kinase (*ALK*) gene rearrangement has been identified in the single example studied. Cartilaginous islands resembling airway-associated cartilaginous plates may be present, but heterologous differentiation of the sort seen in pleuropulmonary blastoma does not occur. Occasional examples show focal overgrowth by bland spindled cells resembling those seen in congenital peribronchial myofibroblastic tumor. The expanded septa are lined by an attenuated layer of keratin-positive epithelial cells that express thyroid transcription factor-1 (TTF-1).

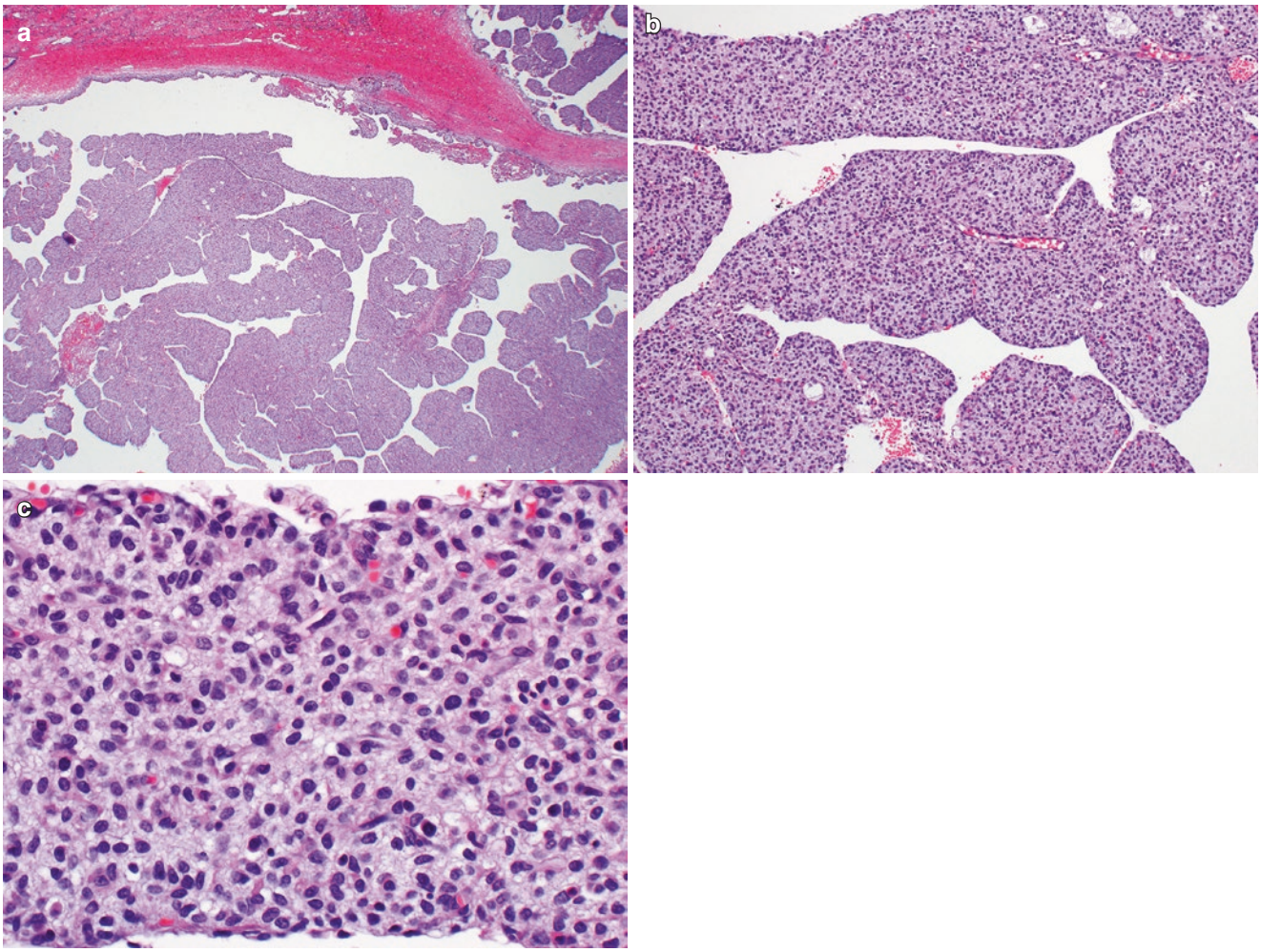

Fig. 3.20 Fetal lung interstitial tumor (FLIT). (**a**) Low-magnification photomicrograph showing a well-circumscribed FLIT in which the neoplasm is separated from developmentally normal lung parenchyma (top left) by a fibrous capsule. (**b**) Intermediate-magnification view showing maldeveloped air spaces separated by septa that are markedly expanded by a uniform monolayer of cytologically bland mesenchymal cells. (**c**) High-magnification photomicrograph showing bland mesenchymal cells with round to oval-shaped nuclei, small capillary vessels, and an attenuated epithelial lining with cytologic features typical of type 2 pneumocytes

Infantile Hemangioma

Solitary capillary hemangiomas (Figs. 3.21 and 3.22) of the lung are uncommon and include rare reports of glucose transporter-1 (GLUT-1)-positive infantile hemangiomas, lesions seen more frequently in the skin and soft tissues. The gross appearance may mimic other solid lung lesions of childhood, including congenital pulmonary overinflation (emphysema). They are histologically distinct and unlikely to be a source of great diagnostic difficulty. Immunostains for GLUT-1 are helpful in separating infantile hemangiomas from other vasoformative neoplasms and vascular malformations.

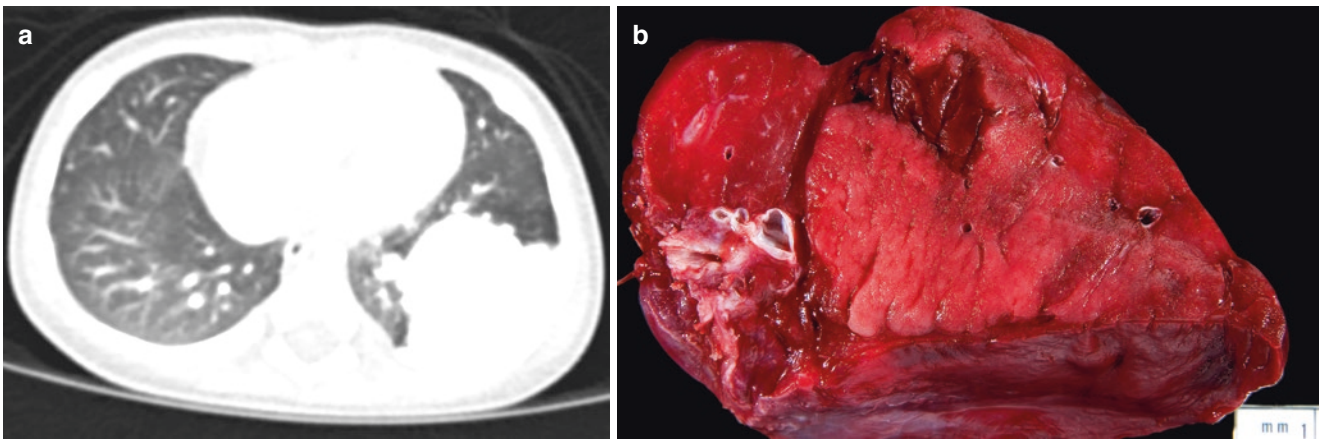

Fig. 3.21 Infantile hemangiomas have only rarely been reported as primary solitary lung masses. (**a**) Computed tomography (CT) scan of the chest of a 7-month-old girl shows an enhancing opacity occupying much of her left lower lobe. (**b**) Gross photograph of the cut surface of her left lower lobectomy shows a circumscribed, soft, spongy pink mass that is sharply demarcated from normal-appearing lung parenchyma

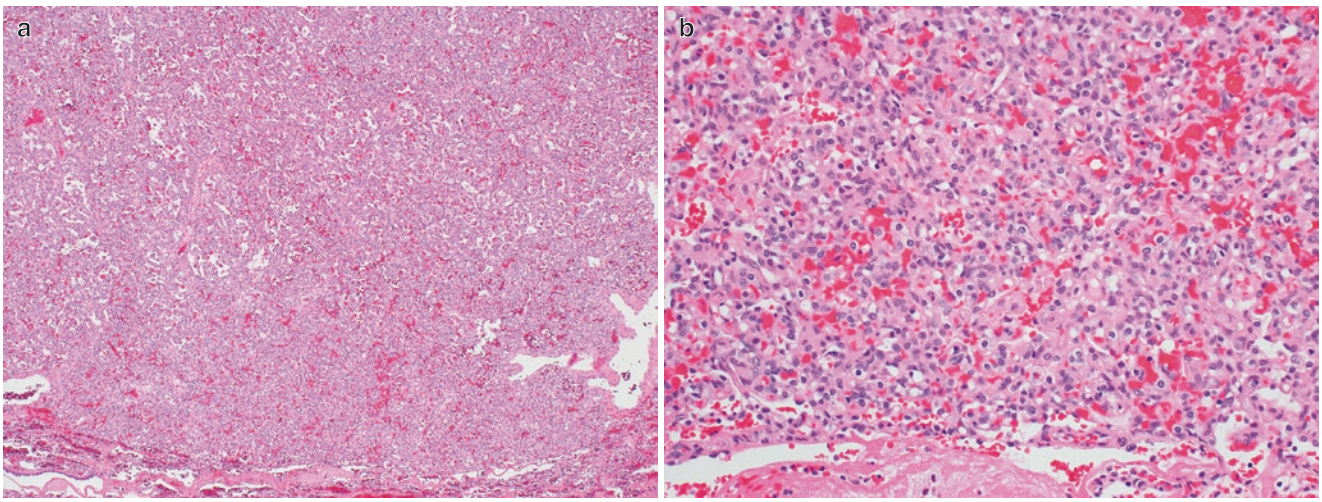

Fig. 3.22 Infantile hemangioma. (**a**) Low-magnification photomicrograph of the tumor illustrated in Fig. 3.21 shows a highly vascularized neoplasm that is unencapsulated but sharply demarcated from adjacent lung tissue (bottom). (**b**) Higher-magnification photomicrograph shows distortion of alveolar walls by complex anastomosing capillaries lined by bland endothelial cells that were strongly positive for glucose transporter-1 (GLUT-1)

Major Types of Diffuse Interstitial Lung Diseases in Children

Major types of diffuse interstitial lung diseases in children include bronchopulmonary dysplasia (chronic neonatal lung disease) that occurs following ventilator therapy in premature infants, chronic pneumonitis of infancy, and pulmonary interstitial glycogenosis. Chronic pneumonitis of infancy (Fig. 3.23) occurs weeks to months following full-term birth. Most cases are associated with mutations of genes encoding surfactant proteins. The prognosis is poor. Pulmonary interstitial glycogenosis (Figs. 3.24 and 3.25) affects both premature and full-term infants shortly after birth. Most patients respond to corticosteroids, and the prognosis is good.

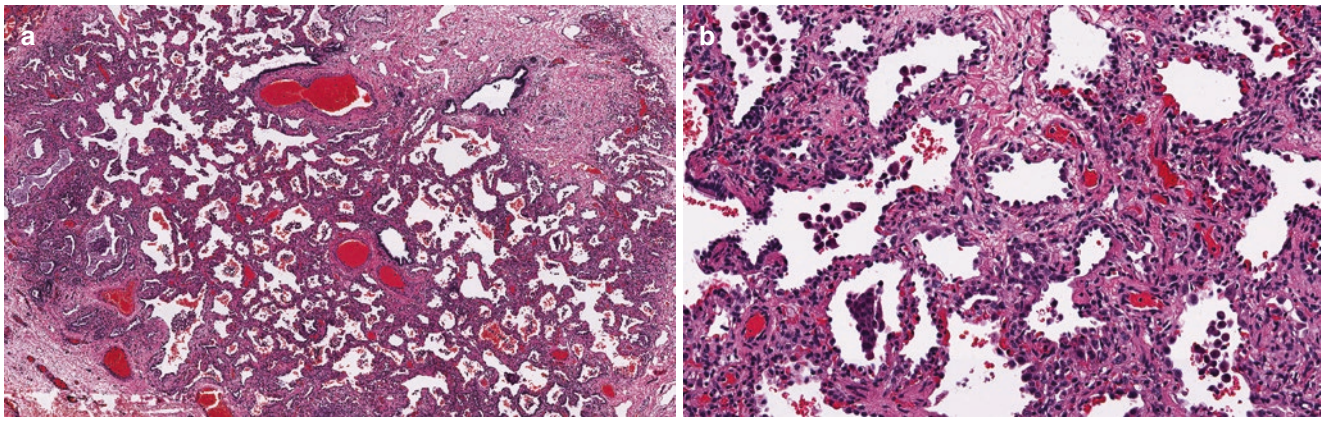

Fig. 3.23 Chronic pneumonitis of infancy. (**a**) Low-magnification photomicrograph of a surgical lung biopsy shows uniform thickening of alveolar septa with minimal architectural distortion. Alveolar spaces often contain proteinaceous exudates, macrophages, and cholesterol clefts resembling pulmonary alveolar proteinosis (PAP-like) in chronic pneumonitis of infancy. However, that feature was not seen in this example. (**b**) A high-magnification view shows expansion of alveolar septa by fibroblasts, myofibroblasts, and minimal collagen deposition with only rare inflammatory cells. Reactive pneumocyte hyperplasia is prominent

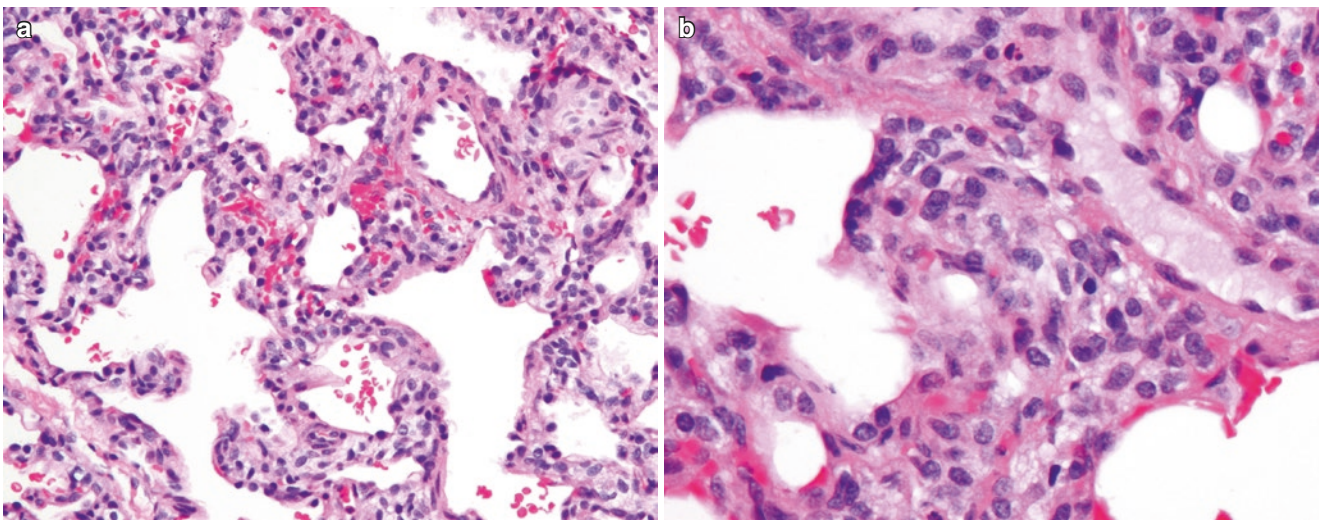

Fig. 3.24 Pulmonary interstitial glycogenosis. (**a**) Photomicrograph showing the uniform thickening of alveolar septa by bland-appearing mesenchymal cells. No significant inflammation or pneumocyte hyperplasia is present. (**b**) At high magnification, the thickened alveolar septa contain cells with bland round to oval nuclei and abundant clear to eosinophilic cytoplasm

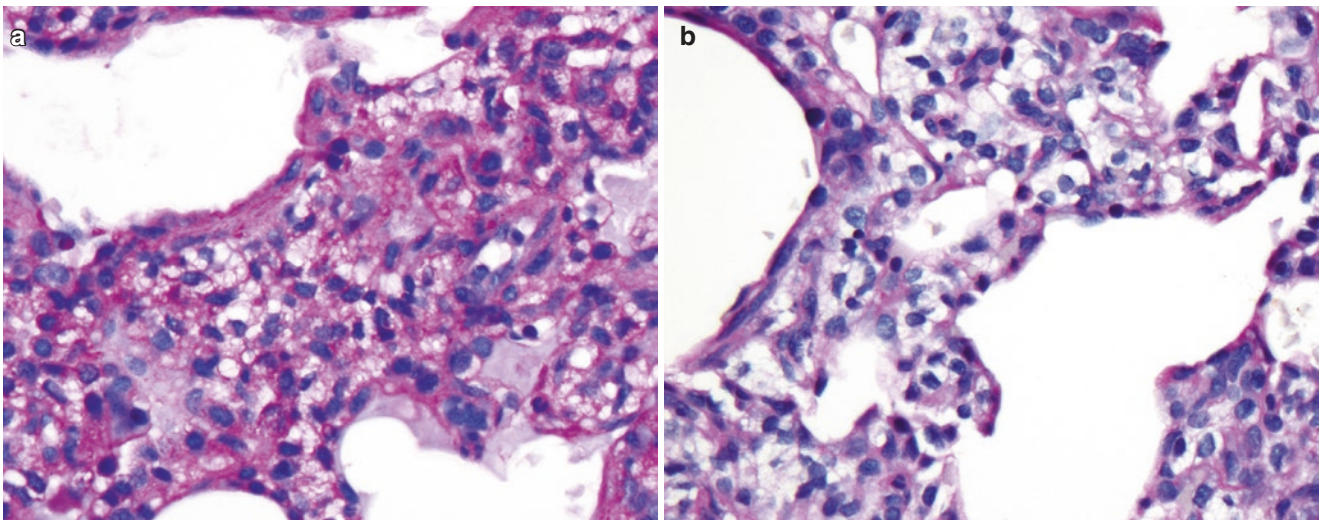

Fig. 3.25 Pulmonary interstitial glycogenosis. (**a**) Photomicrograph of a periodic acid–Schiff (PAS) stained section shows abundant granular cytoplasmic staining of the mesenchymal cells within the alveolar septa. (**b**) The positive PAS staining within the cytoplasm is washed away following diastases digestion, which is indicative of glycogen deposition

Suggested Readings

Canakis AM, Cutz E, Manson D, O'Brodovich H. Pulmonary interstitial glycogenosis: a new variant of neonatal interstitial lung disease. Am J Respir Crit Care Med. 2002;165:1557–65.

Dishop MK, McKay EM, Kreiger PA, Priest JR, Williams GM, Langston C, et al. Fetal lung interstitial tumor (FLIT): a proposed newly recognized lung tumor of infancy to be differentiated from cystic pleuropulmonary blastoma and other developmental pulmonary lesions. Am J Surg Pathol. 2010;34:1762–72.

Hill DA, Jarzembowski A, Priest JR, Williams G, Schoettler P, Dehner LP. Type I pleuropulmonary blastoma: pathology and biology study of 51 cases from the international pleuropulmonary blastoma registry. Am J Surg Pathol. 2008;32:282–95.

Katzenstein AL, Gordon LP, Oliphant M, Swender PT. Chronic pneumonitis of infancy. A unique form of interstitial lung disease occurring in early childhood. Am J Surg Pathol. 1995;19:439–47.

Kreiger PA, Ruchelli ED, Mahboubi S, Hedrick H, Scott Adzick N, Russo PA. Fetal pulmonary malformations: defining histopathology. Am J Surg Pathol. 2006;30:643–9.

Kunisaki S, Fauza M, Nemes LP, Barnewolt CE, Estroff JA, Kozakewich HP, Jennings RW. Bronchial atresia: the hidden pathology within a spectrum of prenatally diagnosed lung masses. J Pediatr Surg. 2006;41:61–5.

Langston C. New concepts in the pathology of congenital lung malformations. Semin Pediatr Surg. 2003;12:17–37.

Louie HW, Martin SM, Mulder DG. Pulmonary sequestration: 17-year experience at UCLA. Am Surg. 1993;59:801–5.

MacSweene F, Papagiannopoulos K, Goldstraw P, Sheppard MN, Corrin B, Nicholson AG. An assessment of the expanded classification of congenital cystic adenomatoid malformations and their relationship to malignant transformation. Am J Surg Pathol. 2003;27:1139–46.

Mani H, Suarez E, Stocker JT. The morphologic spectrum of infantile lobar emphysema: a study of 33 cases. Paediatr Respir Rev. 2004;5(Suppl A):S313–20.

Nicolette LA, Kosloske M, Bartow SA, Murphy S. Intralobar pulmonary sequestration: a clinical and pathological spectrum. J Pediatr Surg. 1993;28:802–5.

Ramani P, Shah A. Lymphangiomatosis. Histologic and immunohistochemical analysis of four cases. Am J Surg Pathol. 1993;17:329–35.

Rice A, Tran-Dang MA, Bush A, Nicholson AG. Diffuse lung disease in infancy and childhood: expanding the child classification. Histopathology. 2013;63:743–55.

Stocker JT. Cystic lung disease in infants and children. Fetal Pediatr Pathol. 2009;28:155–84.

Tazelaar HD, Kerr D, Yousem SA, Saldana MJ, Langston C, Colby TV. Diffuse pulmonary lymphangiomatosis. Hum Pathol. 1993;24:1313–22.

Infectious Diseases

4

Chen Zhang and Jeffrey L. Myers

Pulmonary infections are caused by a wide range of pathogenic microorganisms, including bacteria, viruses, fungi, and parasites. The most common lung infections in immunocompetent hosts are caused by pyogenic bacteria (e.g., *Streptococcus pneumoniae*), common respiratory viruses, and mycoplasma. These infections are usually diagnosed by clinical and microbiologic studies, including cultures and serology tests. Lung biopsy is rarely used in these diagnoses. Patients with life-threatening pneumonia, especially those who are immunocompromised, are more likely to undergo lung biopsy to rule out unusual infections not easily diagnosed using conventional microbiologic methods and for which treatment strategies may be different. Pathogens more likely to be diagnosed using lung biopsy for which there are characteristic pathologic changes are highlighted in this chapter and listed in Table 4.1.

C. Zhang (✉)
Department of Pathology and Laboratory Medicine, Indiana University School of Medicine, Indianapolis, IN, USA
e-mail: chenzhan@iupui.edu

J. L. Myers
Department of Pathology, Michigan Medicine, Ann Arbor, MI, USA
e-mail: myerjeff@med.umich.edu

© Springer Science+Business Media, LLC, part of Springer Nature 2018
C. Zhang, J. L. Myers (eds.), *Atlas of Lung Pathology*, Atlas of Anatomic Pathology,
https://doi.org/10.1007/978-1-4939-8689-7_4

Table 4.1 List of pulmonary infections encountered in lung biopsies, surgical resections, and autopsies

Bacteria (non-mycobacteria)
Community-acquired pneumonia: *Streptococcus pneumoniae*, *Mycoplasma pneumoniae*, *Chlamydia pneumoniae*, *Haemophilus influenzae*
Health care-associated pneumonia with or without resistance risk factors: Drug-resistant *Streptococcus pneumoniae*, *Legionella spp.*, *Haemophilus influenzae*, *Mycoplasma pneumoniae*, *Chlamydia pneumoniae*, enteric gram-negative bacilli
Nocardiosis
Actinomycosis
Rhodococcus equi pneumonia (malakoplakia)
Mycobacteria
Mycobacterium tuberculosis (tuberculosis)
Atypical/nontuberculous mycobacterial infections
Viruses
Cytomegalovirus pneumonia
Herpes simplex virus pneumonia
Adenovirus pneumonia
Measles pneumonia
Respiratory syncytial virus pneumonia
Influenza virus pneumonia
Fungi
Aspergillosis
Mucormycosis
Candidiasis
Cryptococcosis
Histoplasmosis
Blastomycosis
Coccidioidomycosis
Pneumocystis jirovecii
Parasites
Toxoplasmosis
Amoebiasis
Dirofilarial nodule (dog heartworm disease)
Paragonimiasis
Strongyloidiasis

Bacterial Pneumonia

Acute bronchopneumonia (Figs. 4.1, 4.2 and 4.3) is caused by various gram-positive or gram-negative bacteria that are sometimes visible on a Gomori methenamine silver (GMS) stain. Bacterial identification using tissue gram stains has low sensitivity and specificity and is neither necessary nor possible in most cases.

Legionnaires' disease (Fig. 4.4) is an acute bronchopneumonia often characterized by prominent necrosis, karyorrhexis, and histiocyte-rich fibrinous exudates. Special stains are of limited value in identifying the gram-negative bacillus responsible for Legionnaires' disease and have been largely supplanted by a combination of cultures and serology.

Nocardiosis (Fig. 4.5) occurs almost exclusively in immunocompromised patients and is caused by a gram-positive filamentous organism (*Nocardia spp.*) common in soil and as normal oral microflora. *Nocardia* pneumonia may follow a fulminant course, and about half of patients develop disseminated infections, which frequently involve the central nervous system. Actinomycosis (Fig. 4.6) is also caused by gram-positive, anaerobic, filamentous bacteria (*Actinomyces spp.*) common in the oral cavity and oropharynx. Actinomycosis often occurs in patients with poor oral and dental hygiene. Lung involvement frequently includes fistulous involvement of pleural and chest wall soft tissues. Microscopically, the histologic findings are similar to those described in nocardiosis, but the organisms have a propensity to form larger macroscopic colonies in vivo that are identifiable in routinely stained sections as sulfur granules; these are indistinguishable from those seen more commonly in tonsils.

Rhodococcus equi pneumonia (malakoplakia) (Fig. 4.7) is caused by a gram-positive bacillus commonly found in soil. Pulmonary infection occurs primarily in immunocompromised patients, most commonly in AIDS patients but also in other immunocompromised populations and occasionally in immunocompetent adults. The histologic findings unique to malakoplakia are the key to establishing the diagnosis in biopsy specimens.

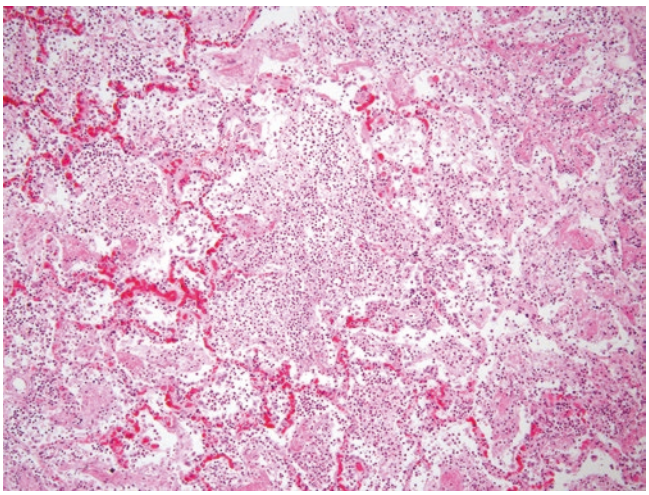

Fig. 4.1 Acute bronchopneumonia. Low-magnification photomicrograph shows an exquisitely air-space-centered process in which acute inflammatory cells and fibrin fill the lumens of distal airways and air spaces. Alveolar septa are congested and focally disrupted, but the overall alveolar structure is preserved

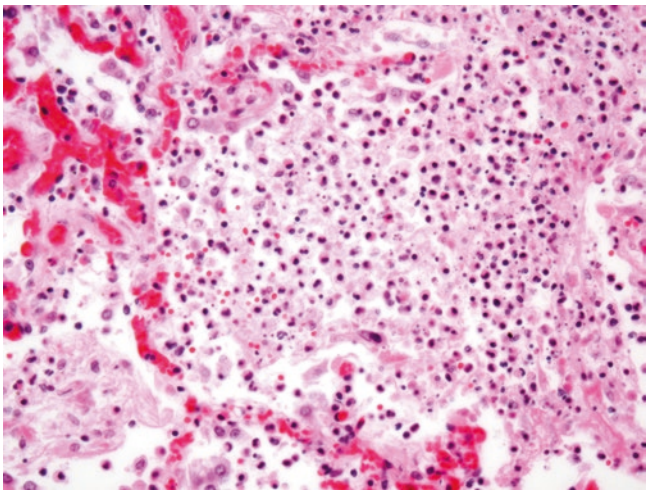

Fig. 4.2 Acute bronchopneumonia. High-magnification photomicrograph shows that the air-space exudate is composed mainly of neutrophils with prominent karyopyknosis and karyorrhexis, histiocytes, and fibrin

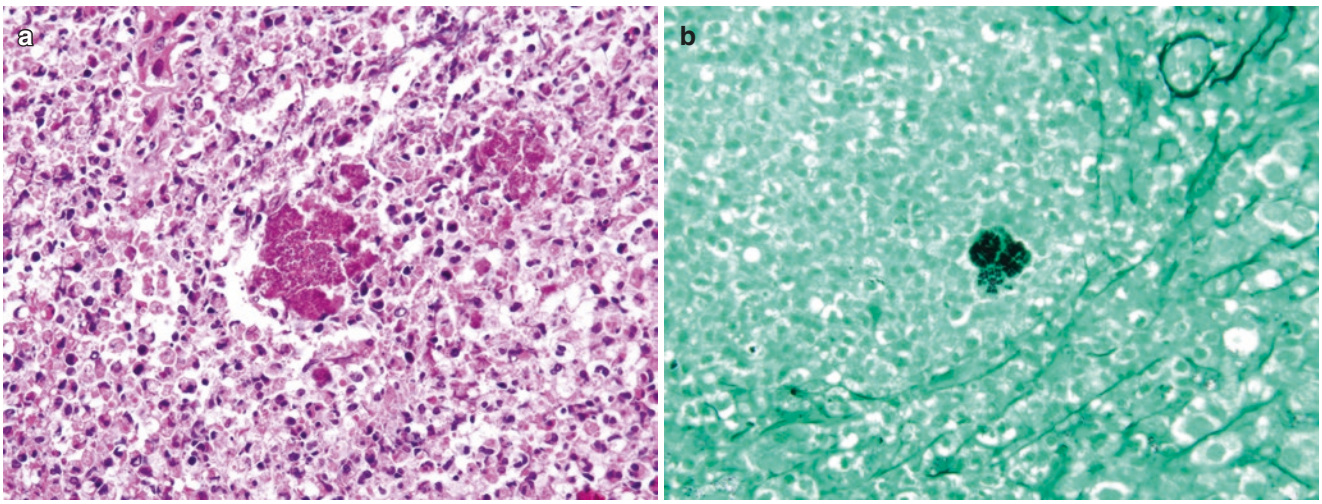

Fig. 4.3 Acute bronchopneumonia. High-magnification photomicrographs showing bacterial colonies of the kind occasionally observed in acute bronchopneumonia on routine H&E (**a**) and GMS (**b**) stains

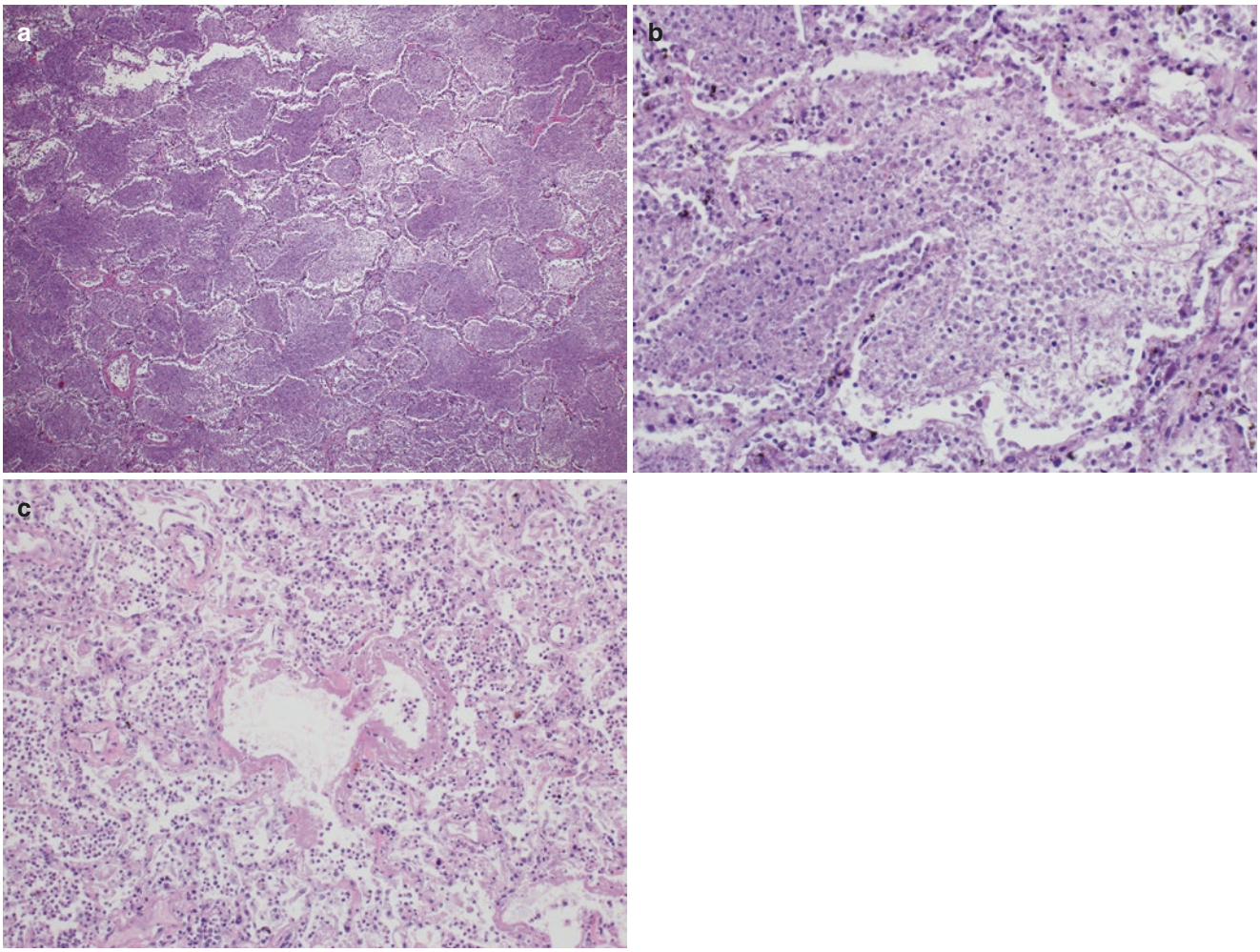

Fig. 4.4 Legionnaires' disease. (**a**) Low-magnification photomicrograph showing acute bronchopneumonia with prominent intra-alveolar fibrinous exudates in a patient with Legionnaires' disease. (**b**) Higher-magnification photomicrograph showing acute bronchopneumonia with prominent necrosis, an inflammatory infiltrate in which histiocytes predominate, and fibrin. (**c**) Intermediate-magnification view of autopsy findings in the same patient illustrating a combination of acute bronchopneumonia and diffuse alveolar damage with well-formed hyaline membranes, a finding characteristic of Legionnaires' disease in a subset of patients

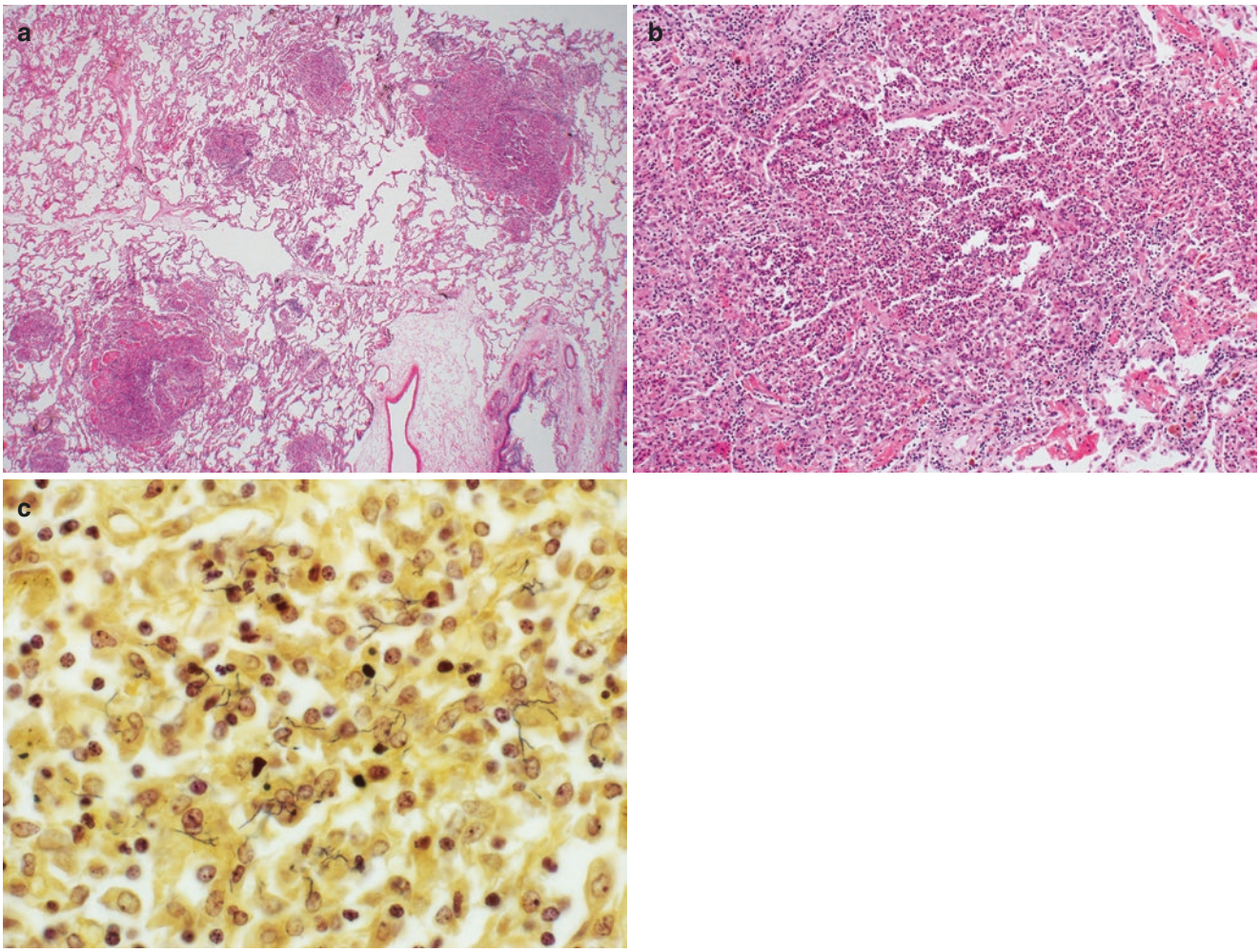

Fig. 4.5 *Nocardia* pneumonia. (**a**) Low-magnification photomicrograph showing a patchy necrotizing acute bronchopneumonia forming circumscribed microabscesses with a vaguely granulomatous appearance. (**b**) Higher-magnification photomicrograph showing a vaguely granulomatous microabscess at higher magnification but without the giant cells, epithelioid macrophages, or associated non-necrotizing granulomas more typical of granulomatous infection. (**c**) High-magnification photomicrograph in which a tissue gram (Brown-Brenn) stain shows the filamentous bacteria typical of *Nocardia spp*.

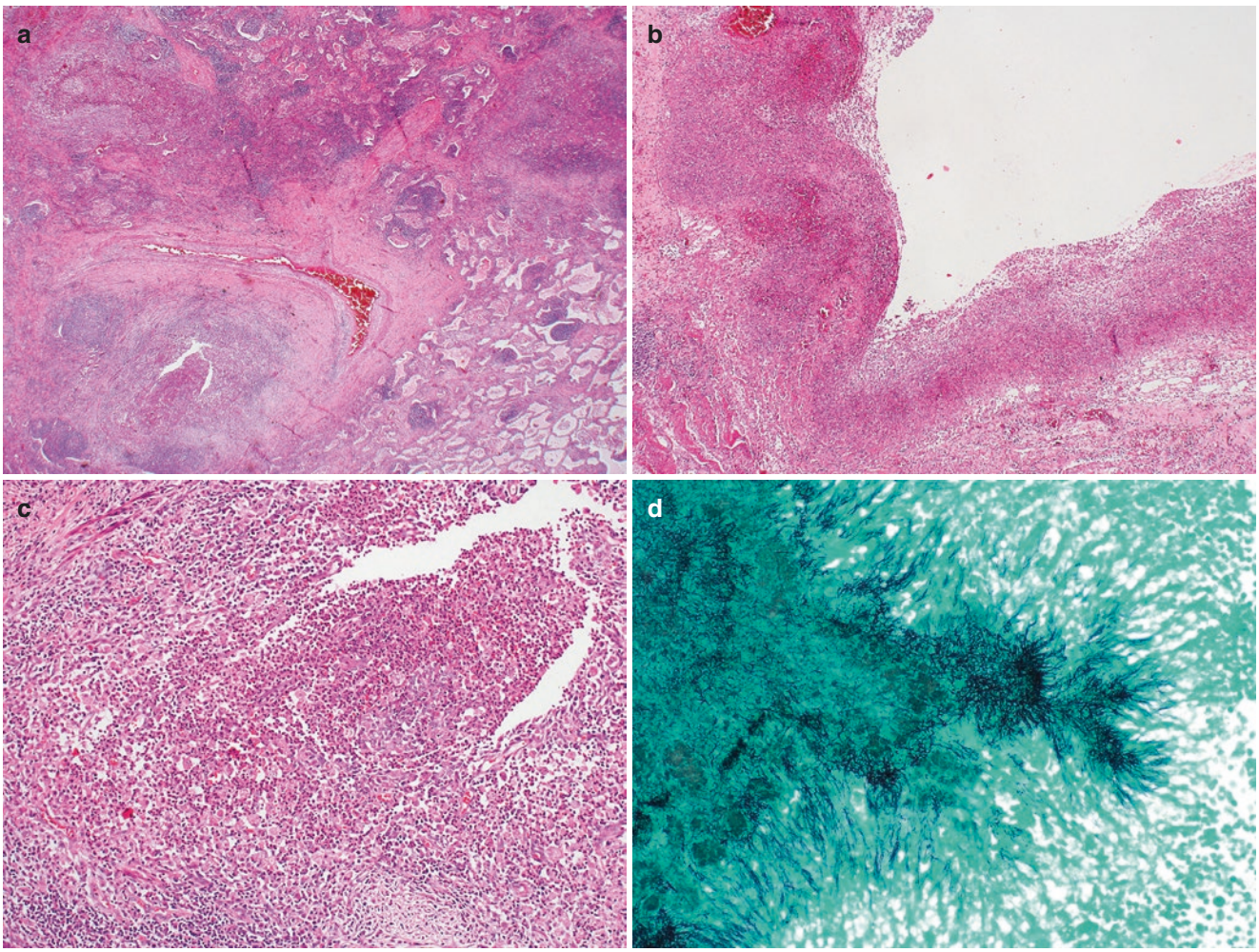

Fig. 4.6 Actinomycosis. (**a**) Low-magnification photomicrograph showing patchy necrotizing acute bronchopneumonia with multifocal microabscesses. (**b**) Low-magnification photomicrograph from the same patient showing a macroscopic abscess with the suppurative inflammation characteristic of actinomycosis. (**c**) Intermediate-magnification photomicrograph showing a circumscribed abscess resembling the vaguely granulomatous microabscesses seen in nocardiosis. (**d**) Intermediate-magnification photomicrograph in which a GMS stain illustrates filamentous *Actinomyces spp.* forming a sulfur granule

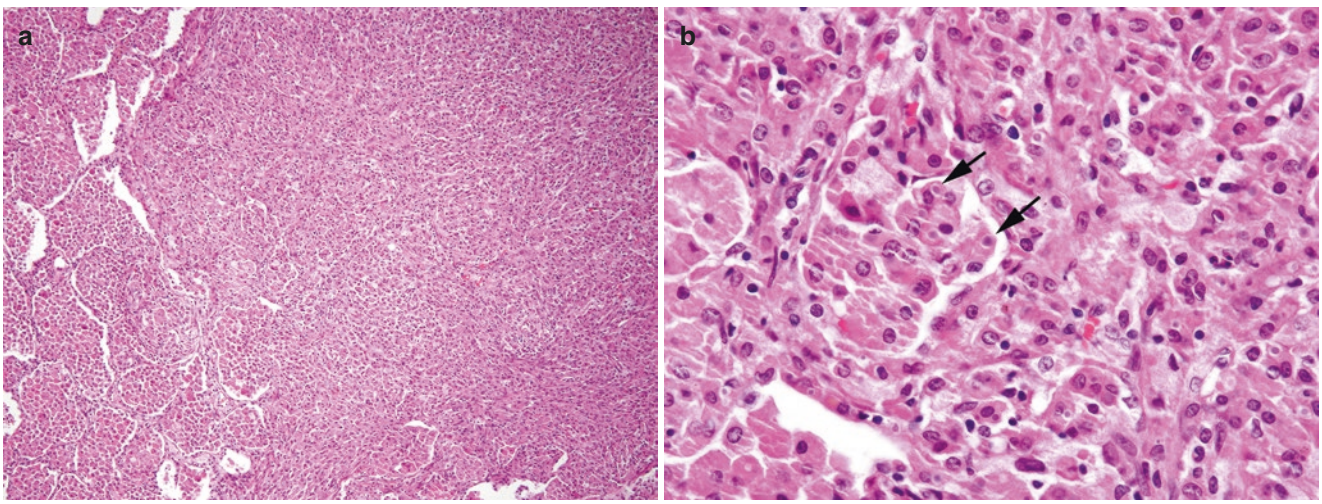

Fig. 4.7 *Rhodococcus equi* pneumonia (malakoplakia). (**a**) Low-magnification photomicrograph showing massive proliferation of histiocytes/macrophages arranged in confluent sheets (right side) and focally filling the alveoli in a pattern mimicking desquamative interstitial pneumonia (left side). Most of the macrophages are round to oval in shape, while others may assume a more spindled appearance. (**b**) High-magnification view shows epithelioid histiocytes with abundant eosinophilic cytoplasm and the intracytoplasmic round basophilic targetoid inclusions (Michaelis-Gutmann bodies) (arrows) diagnostic of malakoplakia. Michaelis-Gutmann bodies are usually easily identified on H&E stain, but calcium stains such as the von Kossa stain may also be helpful in identifying them

Mycobacterial Disease (Figs. 4.8, 4.9, 4.10, 4.11, 4.12 and 4.13)

The prevalence of *Mycobacterium tuberculosis* infection (tuberculosis) is low in the United States. Incident cases have fallen dramatically, and most newly diagnosed cases represent reactivation disease in immigrants who acquired the infection elsewhere. Most cases are diagnosed clinically by means of skin tests, cultures, and other laboratory tests. Occasionally, tuberculosis manifesting as a solitary lung nodule or miliary lesions may be biopsied or resected owing to a preoperative concern for malignancy.

Atypical/nontuberculous mycobacterial infections of the lung (Figs. 4.11, 4.12 and 4.13) commonly resemble tuberculosis in terms of clinical presentations and patterns of disease in both immunocompetent and immunocompromised hosts. Definitive diagnosis relies on culture and molecular techniques. *Mycobacterium avium complex (*MAC*)* is the most commonly encountered nontuberculous mycobacterium. In addition to causing patterns of disease resembling those seen in tuberculosis, MAC also causes a hypersensitivity pneumonia-like syndrome resulting from sensitization to contaminated hot tubs ("hot-tub lung").

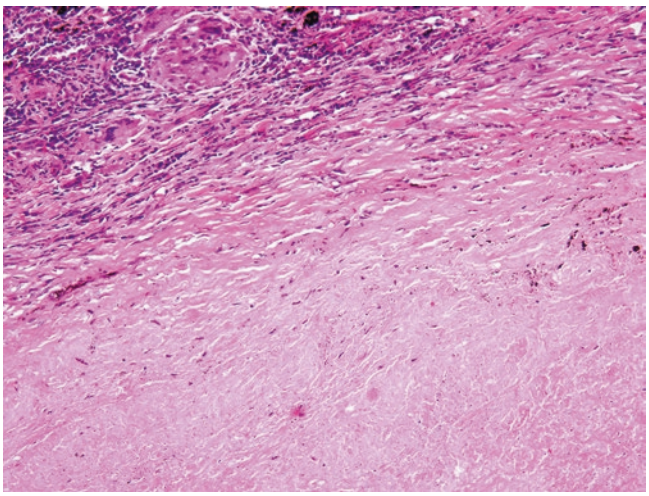

Fig. 4.8 Tuberculosis. Photomicrograph showing characteristic necrotizing (caseating) granuloma with central bland necrosis surrounded by epithelioid histiocytes and multinucleated giant cells. While typical of tuberculosis, this same histology and distribution of disease also occurs in patients with nontuberculous mycobacterial infections

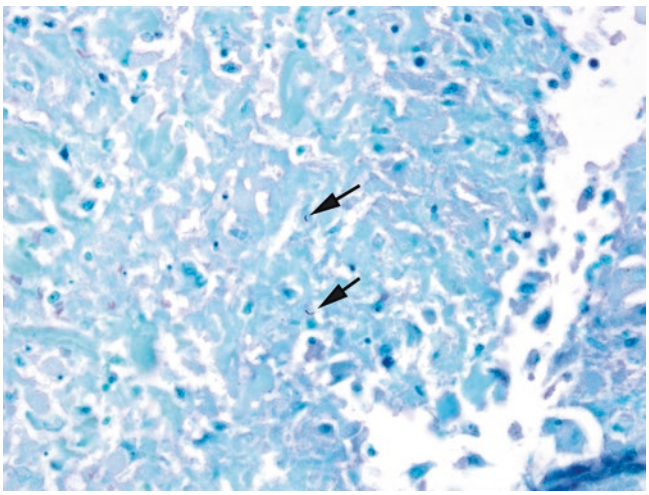

Fig. 4.10 Tuberculosis. High-magnification photomicrograph showing acid-fast organisms (arrows) in a section stained using a Ziehl-Neelsen technique. While there are subtle differences between *Mycobacterium tuberculosis* and nontuberculous mycobacterial organisms, they cannot be reliably separated based on morphology alone; speciation is accomplished more reliably with culture or molecular techniques. The organisms are usually scarce even when necrosis is extensive. Careful examination under high magnification is necessary

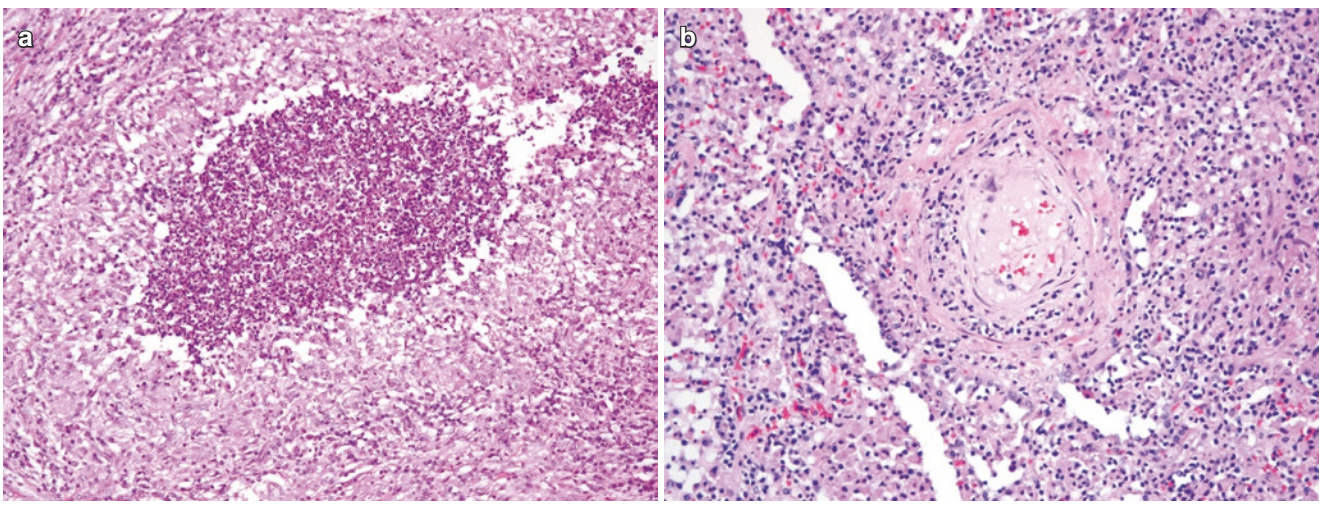

Fig. 4.9 Tuberculosis. Photomicrograph showing a necrotizing granuloma in which central necrosis comprises necrotizing neutrophils. The purulent necrotic center is surrounded by epithelioid histiocytes admixed with lymphocytes and plasma cells (**a**). Occasionally vascular inflammation is prominent, although a true necrotizing vasculitis is rare (**b**)

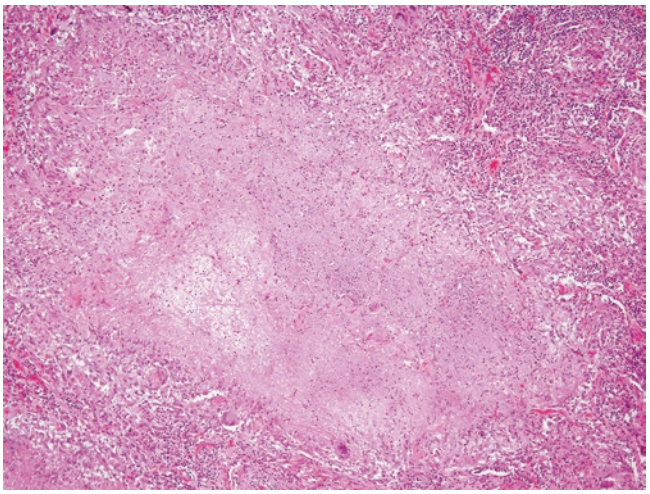

Fig. 4.11 Nontuberculous mycobacteria infection due to MAC. Low-magnification photomicrograph showing necrotizing granulomatous inflammation at autopsy in a patient with culture-proven MAC. The histology strongly suggests granulomatous infection but is not specific to MAC, a diagnosis that requires a combination of special stains, cultures, and molecular techniques

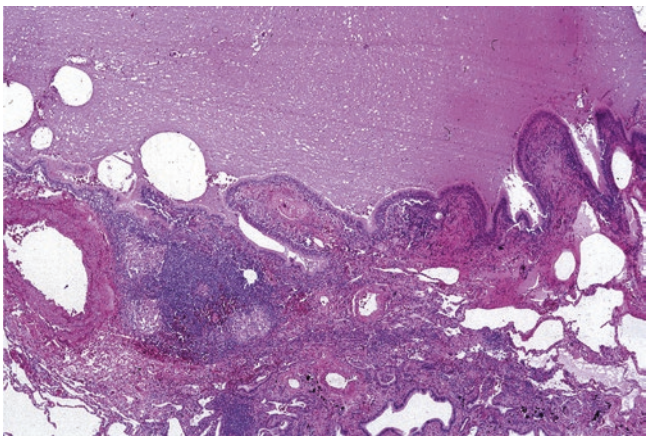

Fig. 4.12 Nontuberculous mycobacterial infection in a patient with bronchiectasis. Low-magnification photomicrograph showing an ectatic airway with severe chronic inflammation typical of bronchiectasis. In this case, the inflammation is complicated by loose non-necrotizing granulomas in the airway wall, a finding virtually diagnostic of atypical mycobacterial infection (usually MAC) in the context of bronchiectasis. This type of atypical mycobacterial infection in the setting of large airway disease is commonly seen in the middle lobe and/or lingula (middle lobe syndrome) but may affect any area of localized bronchiectasis

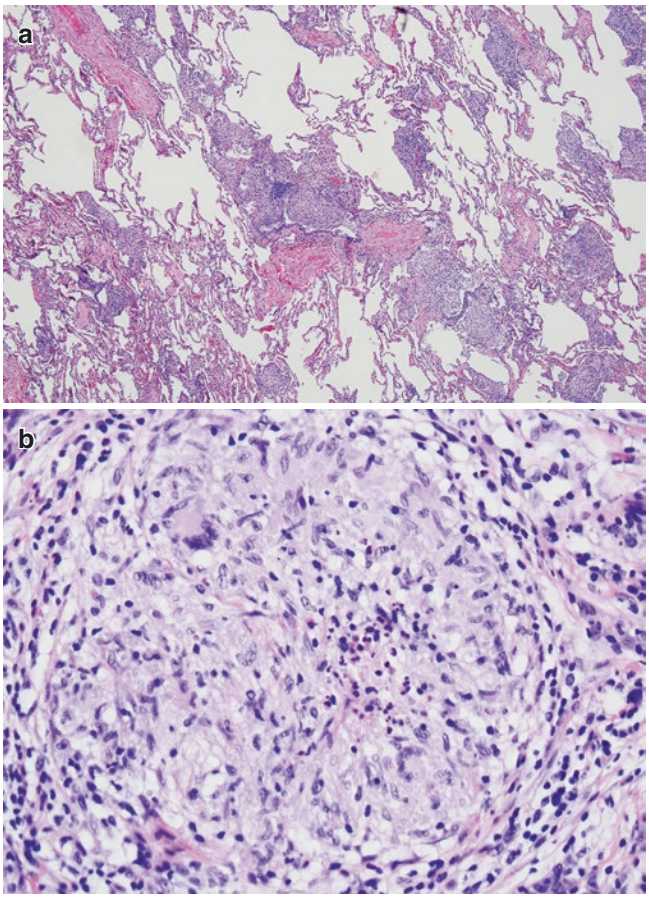

Fig. 4.13 MAC infection in a patient with a hypersensitivity pneumonia-like syndrome linked to hot-tub exposure (hot-tub lung). (**a**) Low-magnification photomicrograph showing a combination of chronic bronchiolitis and relatively well-formed non-necrotizing and focally necrotizing granulomas situated predominantly within the lumens of distal airways. (**b**) Higher magnification view from the same biopsy specimen showing a small focus of central necrosis with neutrophils

Viral Pneumonia

Viral pneumonia is common, especially in immunocompromised patients. Some viral infections cause unique cytopathic changes that can be identified on routinely stained sections (Figs. 4.14, 4.15, 4.16, 4.17, 4.18, 4.19 and 4.20). Immunohistochemical staining with specific antibodies is helpful in identifying some of the viruses with overlapping histologic features with greater confidence.

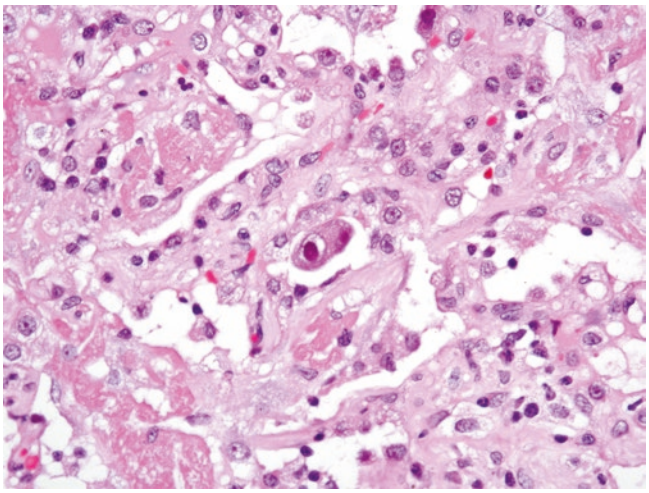

Fig. 4.14 Cytomegalovirus (CMV) pneumonia. High-magnification photomicrograph shows the histologic hallmark of CMV pneumonia, the enlarged cells containing both intranuclear and intracytoplasmic inclusions. The intranuclear inclusion is dark purple and is surrounded by a clear halo (owl's eye). The cytopathic changes are usually seen in bronchiolar epithelium and endothelial cells but may occasionally affect other cells, including macrophages

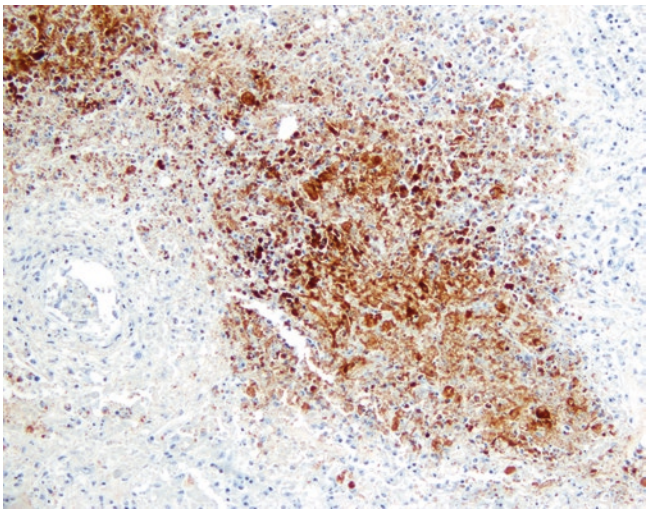

Fig. 4.16 Herpes simplex virus (HSV) pneumonia. Photomicrograph showing positive immunohistochemical staining with HSV-I antibody. Immunostains can be helpful in cases with equivocal or atypical inclusions

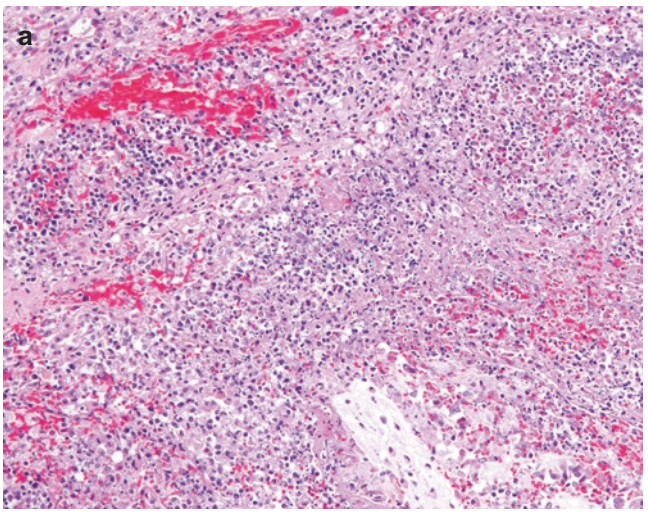

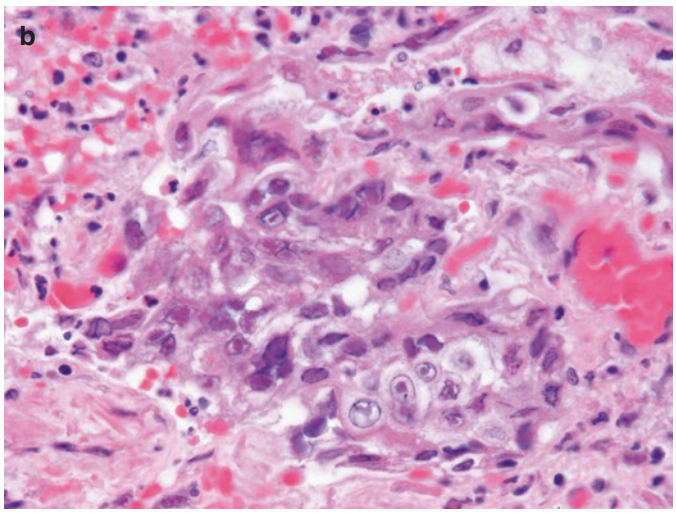

Fig. 4.15 Herpes simplex virus (HSV) pneumonia. (**a**) Photomicrograph showing necrotizing bronchitis and bronchopneumonia with prominent karyorrhexis typical of HSV infection. The bronchiolocentric necrotizing process destroys the airway and surrounding parenchyma. (**b**) High-magnification photomicrograph showing characteristic Cowdry type A inclusions that are round, eosinophilic, and surrounded by a clear halo. Peripheral margination of chromatin is also seen. Other inclusions are characterized by dense, ground-glass change filling up the entire nucleus with a surrounding basophilic rim

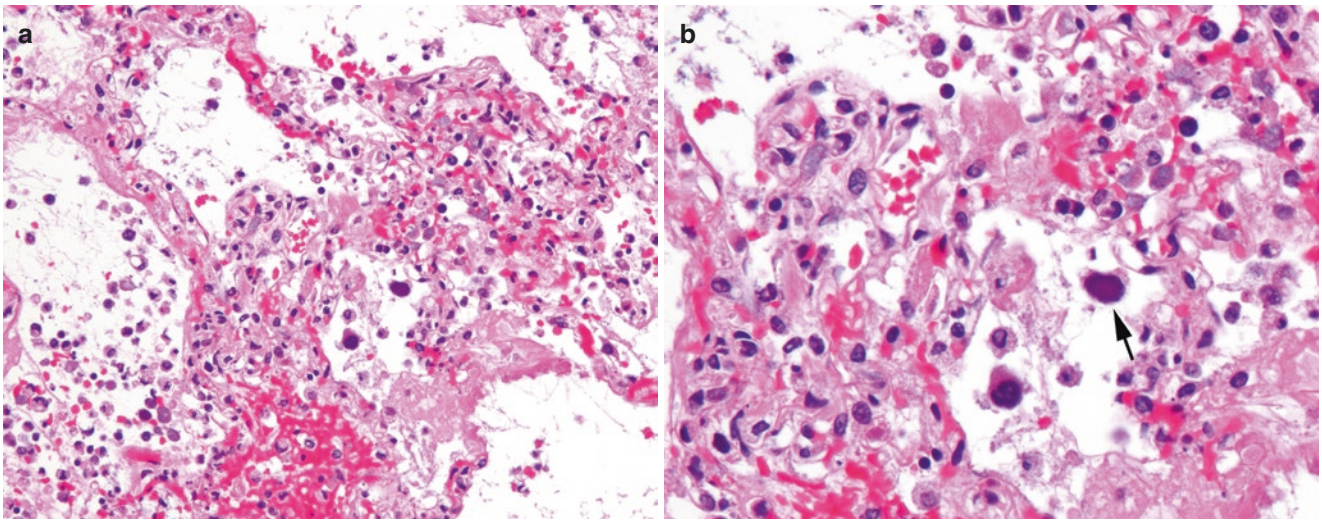

Fig. 4.17 Adenovirus pneumonia. (**a**) Intermediate magnification photomicrograph showing diffuse alveolar damage with hyaline membranes and an associated air-space exudate that includes macrophages, neutrophils, and fibrin. (**b**) High-magnification view demonstrating adenovirus intranuclear inclusion with the typical dark and smudged appearance (arrow)

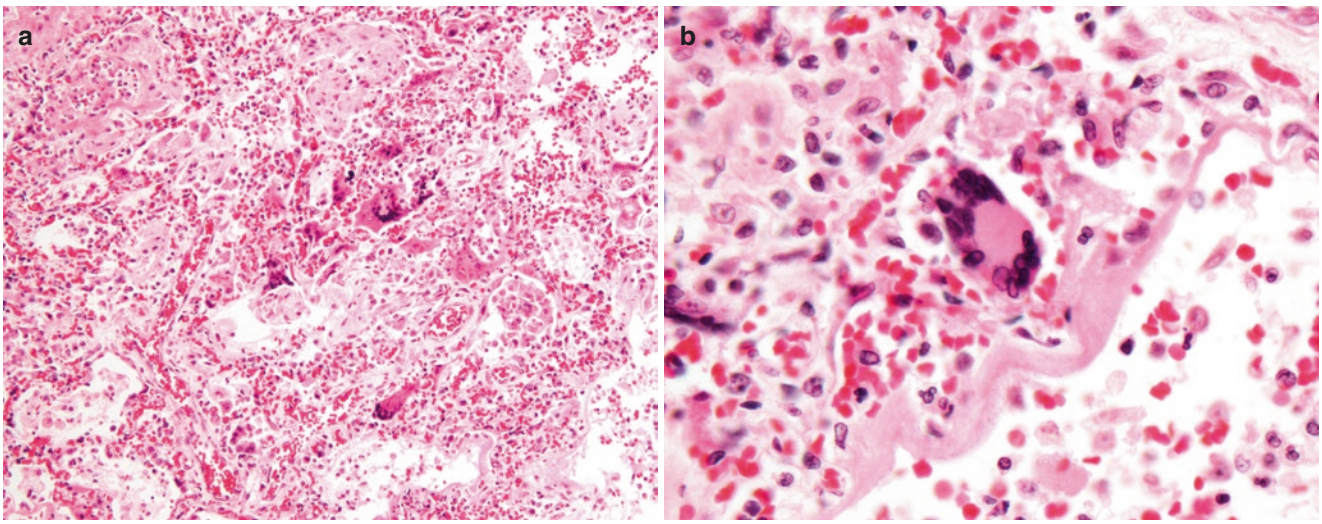

Fig. 4.18 Measles pneumonia. (**a**) Photomicrograph showing numerous large multinucleated giant cells in diffuse alveolar damage. (**b**) High-magnification view of the multinucleated giant cell with intranuclear eosinophilic inclusions and chromatin margination

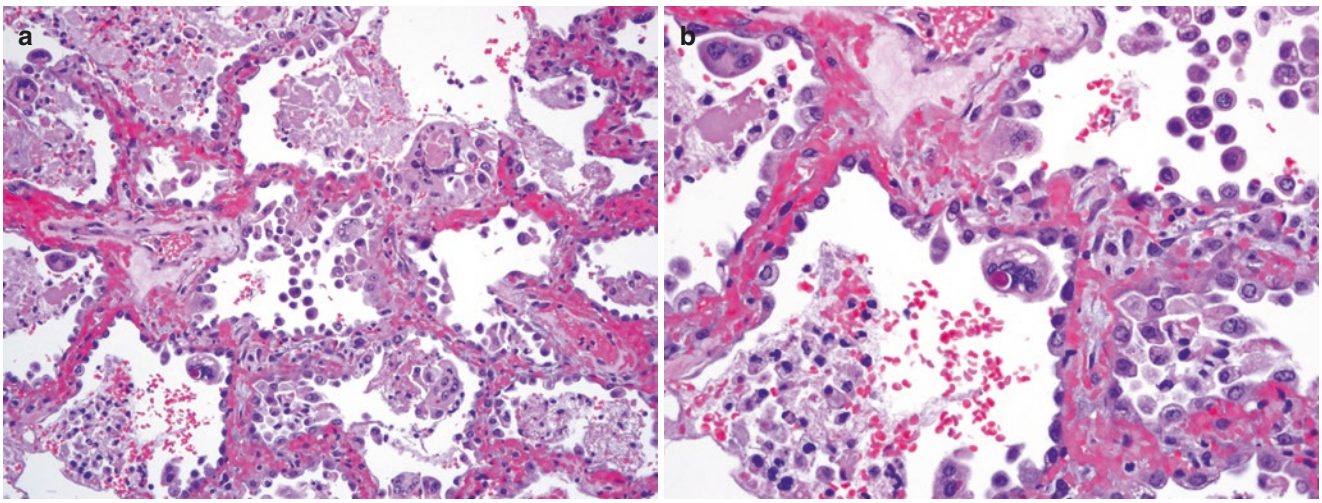

Fig. 4.19 Respiratory syncytial virus (RSV) pneumonia is a significant cause of respiratory disease in children but rarely requires biopsy for diagnosis. (**a**) Photomicrograph of a surgical lung biopsy showing multinucleated giant cells in diffuse alveolar damage with prominent hyperplasia of type 2 pneumocytes. Diffuse alveolar damage (DAD) is a relatively uncommon finding in RSV pneumonia, seen only in those with severe disease. (**b**) High-magnification photomicrograph showing a multinucleated giant cell with round, eosinophilic intracytoplasmic inclusions

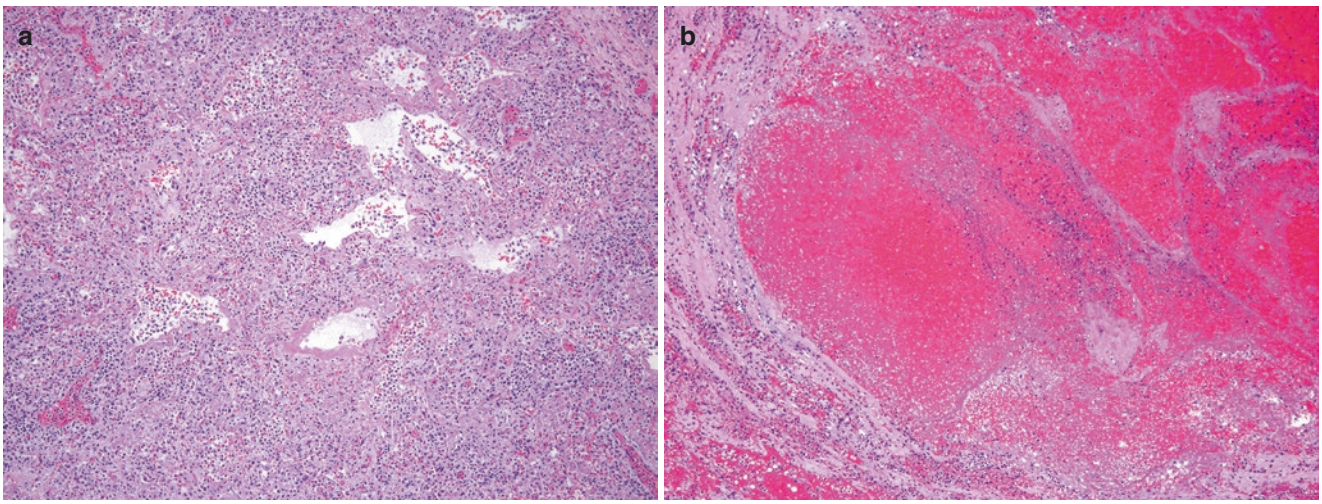

Fig. 4.20 Influenza virus H1N1 pneumonia. (**a**) Low magnification showing a combination of diffuse alveolar damage and a necrotizing inflammatory infiltrate typical of influenza pneumonia. Diagnostic cytopathic changes are absent in influenza pneumonia. (**b**) Low-magnification photomicrograph from the same patient showing a large area of hemorrhagic infarct, a characteristic feature of influenza virus type H1N1 infection

Fungal Pneumonia

The types of fungal infections encountered in lung biopsies or surgical lung specimens are heavily dependent on whether the patient is immunocompetent or immunocompromised. Fungal infections more commonly seen in immunologically intact hosts may also occur in immunocompromised patients in whom the histologic findings may be more variable. Histoplasmosis, blastomycosis, cryptococcosis, and coccidioidomycosis are the fungal infections likely to be encountered in lung biopsies from immunocompetent hosts living in North America. Other fungal diseases are seen almost exclusively in immunocompromised patients.

Histoplasmosis

Histoplasmosis (Figs. 4.21, 4.22, 4.23, 4.24) is endemic in the Mississippi and Ohio River valleys of the United States. The disease is usually asymptomatic and self-limited but may cause a persistent lung nodule that leads to a needle biopsy or excision of the lesion. Necrotizing granulomatous inflammation is the usual finding, except for disseminated histoplasmosis, which is an uncommon form of the disease seen more often in immunocompromised patients.

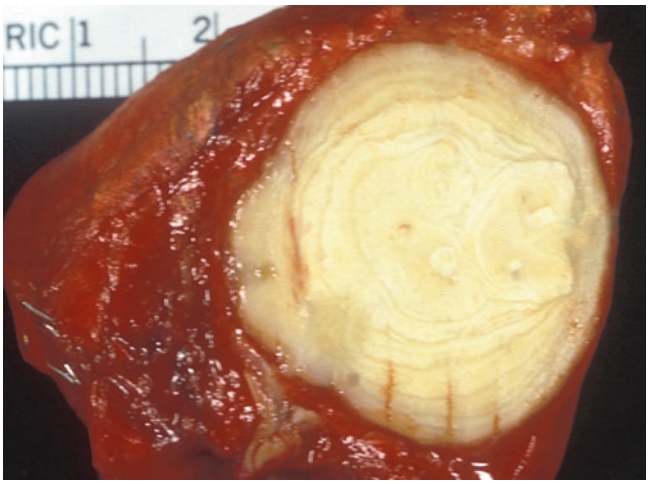

Fig. 4.21 Histoplasmosis. Gross photograph showing cut surface of a well-circumscribed lesion with prominent central necrosis showing concentric rings (resembling the rings of a tree) that are characteristic of histoplasmosis

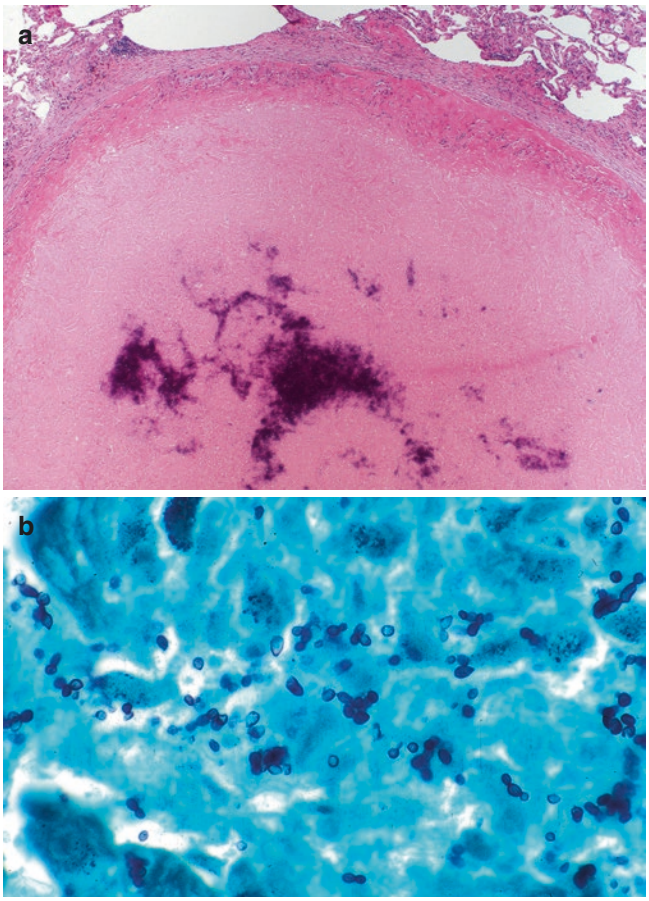

Fig. 4.22 Histoplasmosis. (**a**) Low-magnification photomicrograph of the lesion shown in Fig. 4.21. The lesion shows a rounded border and prominent central necrosis with calcification, surrounded by a thin rim of epithelioid histiocytes and collagen fibrosis. The organisms are few in quantity and are invisible on H&E-stained slides. (**b**) High-magnification photomicrograph of GMS stain showing small, uniform, oval-shaped yeasts with narrow-based budding

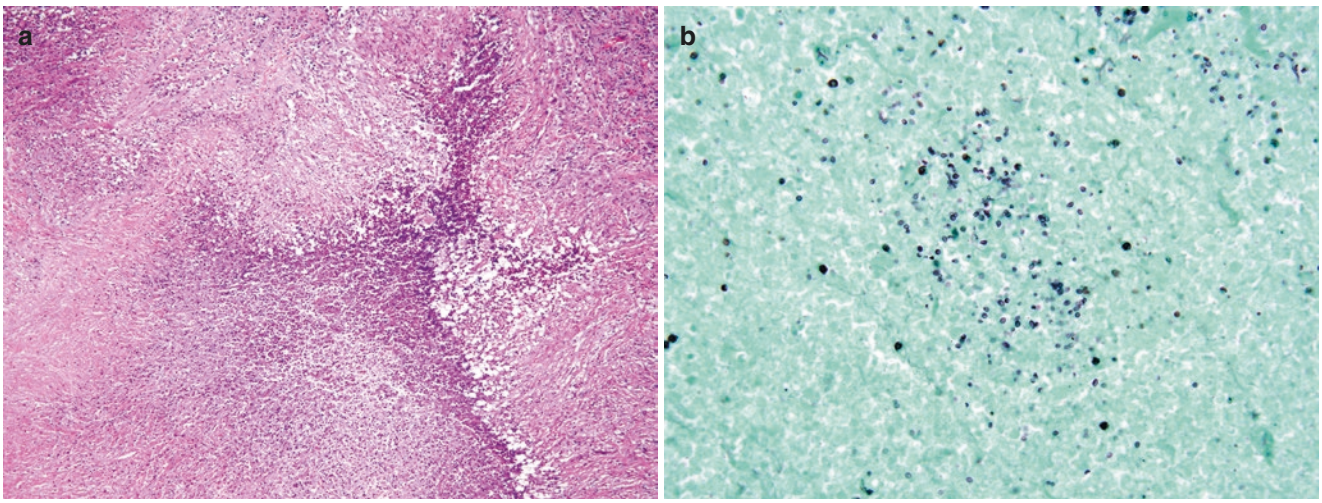

Fig. 4.23 Histoplasmosis. (**a**) The necrotizing granulomatous inflammation in acute histoplasmosis as illustrated in this low-magnification photomicrograph can include irregular (geographic) zones of necrosis with nuclear debris resembling the granulomatous inflammation more typical of granulomatosis with polyangiitis (Wegener's granulomatosis). (**b**) A GMS stain reveals small, frequently teardrop-shaped yeasts of *Histoplasma capsulatum*

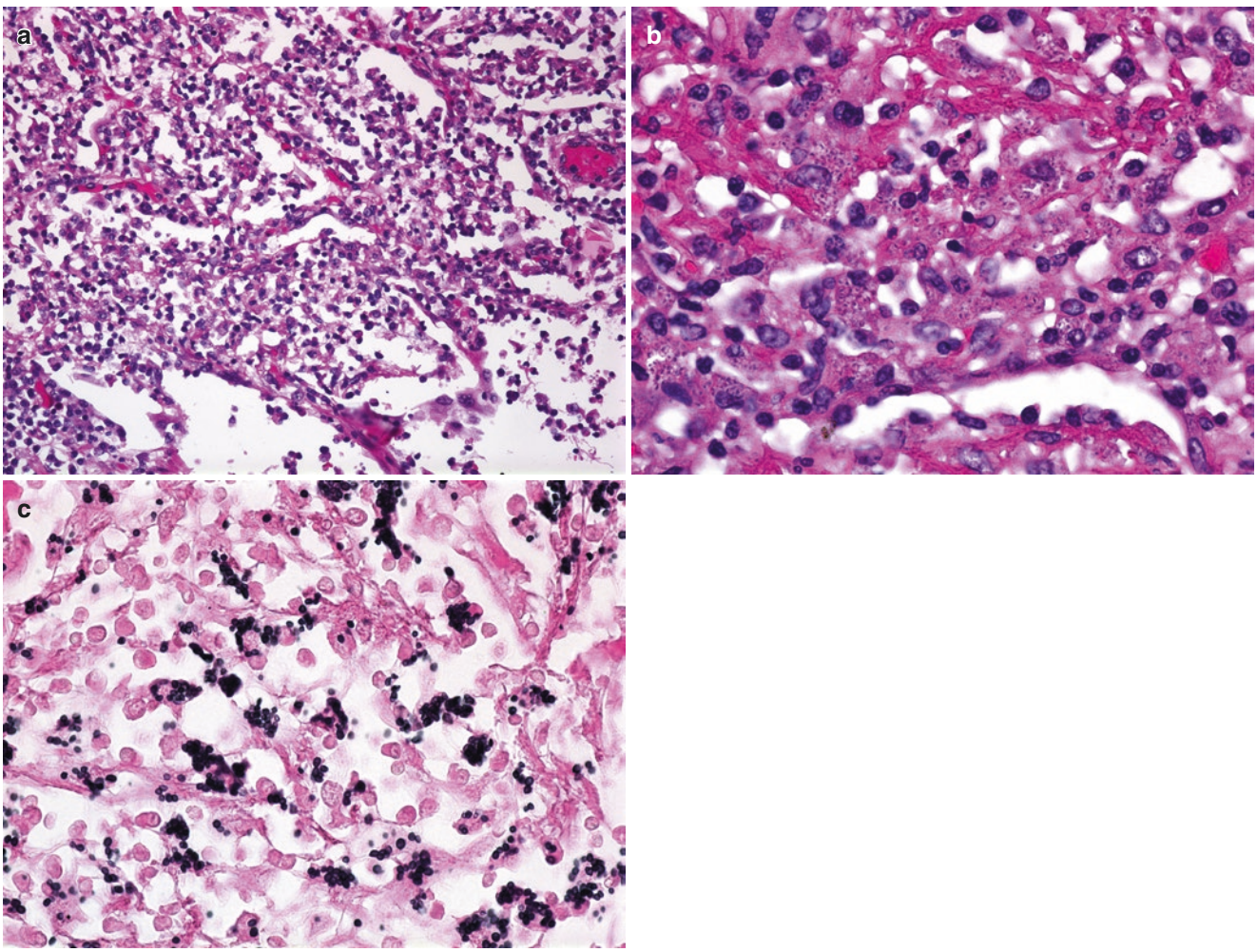

Fig. 4.24 Disseminated histoplasmosis. (**a**) Photomicrograph showing disseminated histoplasmosis characterized by sheets of histiocytes filling air spaces without well-formed granulomas. (**b**) A higher-magnification photomicrograph shows "parasitized" organisms filling the cytoplasm of engorged histiocytes. Yeasts within the cytoplasm of macrophages are visible as dot-like nuclei surrounded by a clear space. This is the only form of histoplasmosis in which you can see the organisms on routinely stained sections. (**c**) High-magnification view of a GMS stain reveals numerous small round and oval-shaped yeasts clustered within the cytoplasm of histiocytes

Blastomycosis

Blastomycosis (Figs. 4.25, 4.26 and 4.27), also termed North American blastomycosis, is caused by *Blastomyces dermatitidis* and is endemic in the south and central United States. Blastomycosis occurs in both immunocompetent and immunocompromised patients. Like other endemic fungal diseases included in this section, blastomycosis has several different clinical phenotypes that extend to involvement of extrapulmonary sites, primarily the skin. Asymptomatic disease is less common compared to histoplasmosis. Yeast forms are morphologically characteristic and are visible on H&E-stained sections.

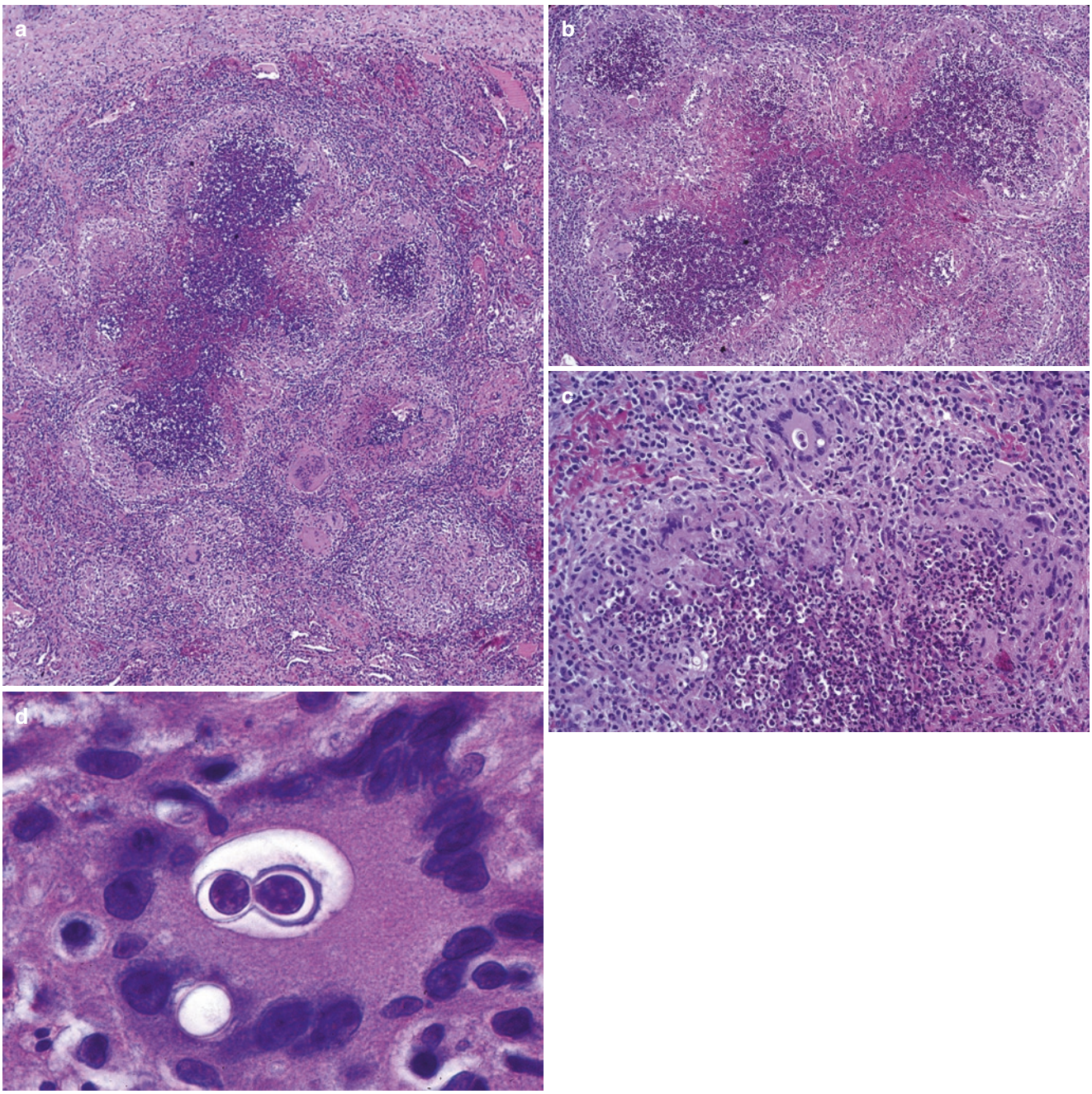

Fig. 4.25 Blastomycosis. (**a**) Low-magnification photomicrograph showing a combination of necrotizing and non-necrotizing granulomatous inflammation in a patient with blastomycosis. (**b**) A higher-magnification view shows suppurative granulomatous inflammation that is characteristic of blastomycosis. The central necrosis shows abundant neutrophils with karyorrhexis surrounded by plump epithelioid histiocytes and giant cells. (**c**) Photomicrograph from the same biopsy showing a budding yeast form in a giant cell in the upper center portion of the image. (**d**) High-magnification view of the same budding yeast showing characteristic doubly refractile wall and central basophilic nucleoplasm. A second organism is present below and to the left in the same giant cell but lacks the central basophilic nucleoplasm

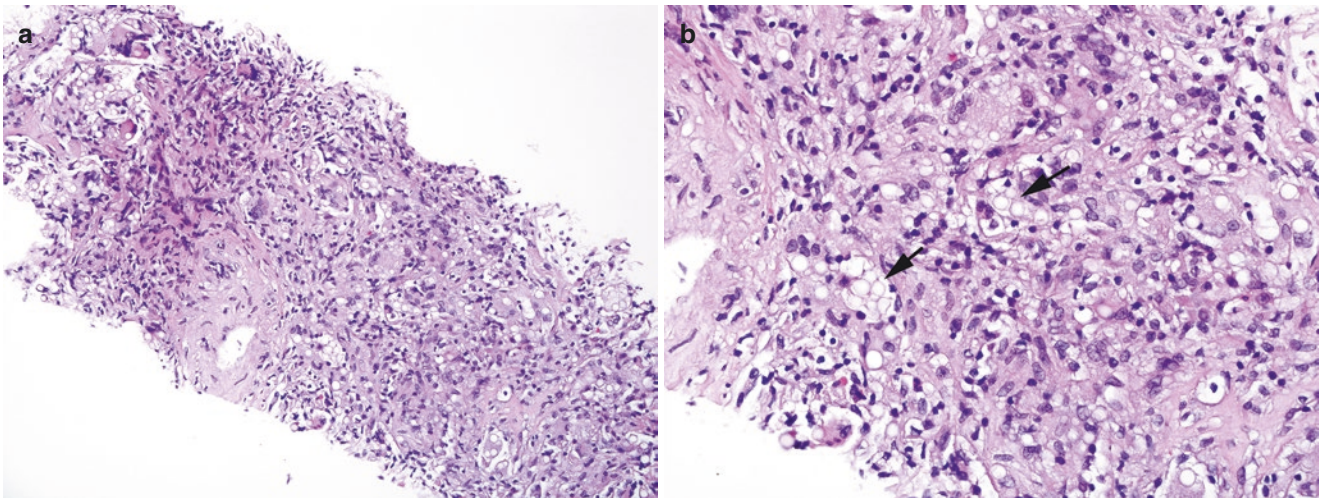

Fig. 4.26 Blastomycosis. (**a**) Low-magnification photomicrograph of a needle biopsy from a solitary lung nodule showing poorly formed non-necrotizing granulomas including multinucleated giant cells. (**b**) High-magnification view showing multiple large, rounded yeasts with thick, refractile cell walls (arrows). Some yeasts show broad-based budding. The organisms are larger than *Cryptococcus neoformans* with which they may be confused and lack the central endospores typical of *Coccidioides immitis*

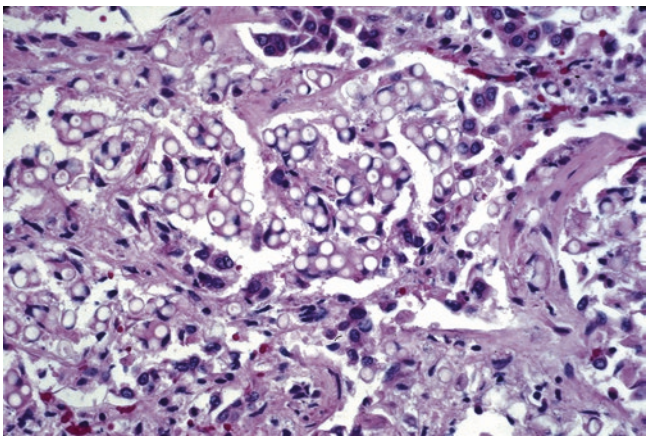

Fig. 4.27 Blastomycosis in the acute respiratory distress syndrome (ARDS). Photomicrograph of autopsy lung showing numerous round yeasts with thick doubly refractile walls typical of *Blastomyces dermatitidis* with diffuse alveolar damage. This is an uncommon manifestation of blastomycosis that occurs most commonly in immunocompromised patients

Cryptococcosis

Cryptococcosis (Figs. 4.28, 4.29, 4.30 and 4.31) may affect immunocompetent hosts, but symptomatic disease occurs more commonly in patients who are immunocompromised or have other underlying comorbidities. *Cryptococcus neoformans* has a worldwide distribution with no geographically defined variation in incidence. Patients with cryptococcal infections may be asymptomatic or may have a range of respiratory syndromes, including a subset with isolated lung nodules and ipsilateral nodal disease mimicking tuberculosis or histoplasmosis. In its classic form, *Cryptococcus neoformans* is distinguished by a mucicarminophilic capsule, but capsule-deficient strains lack this feature.

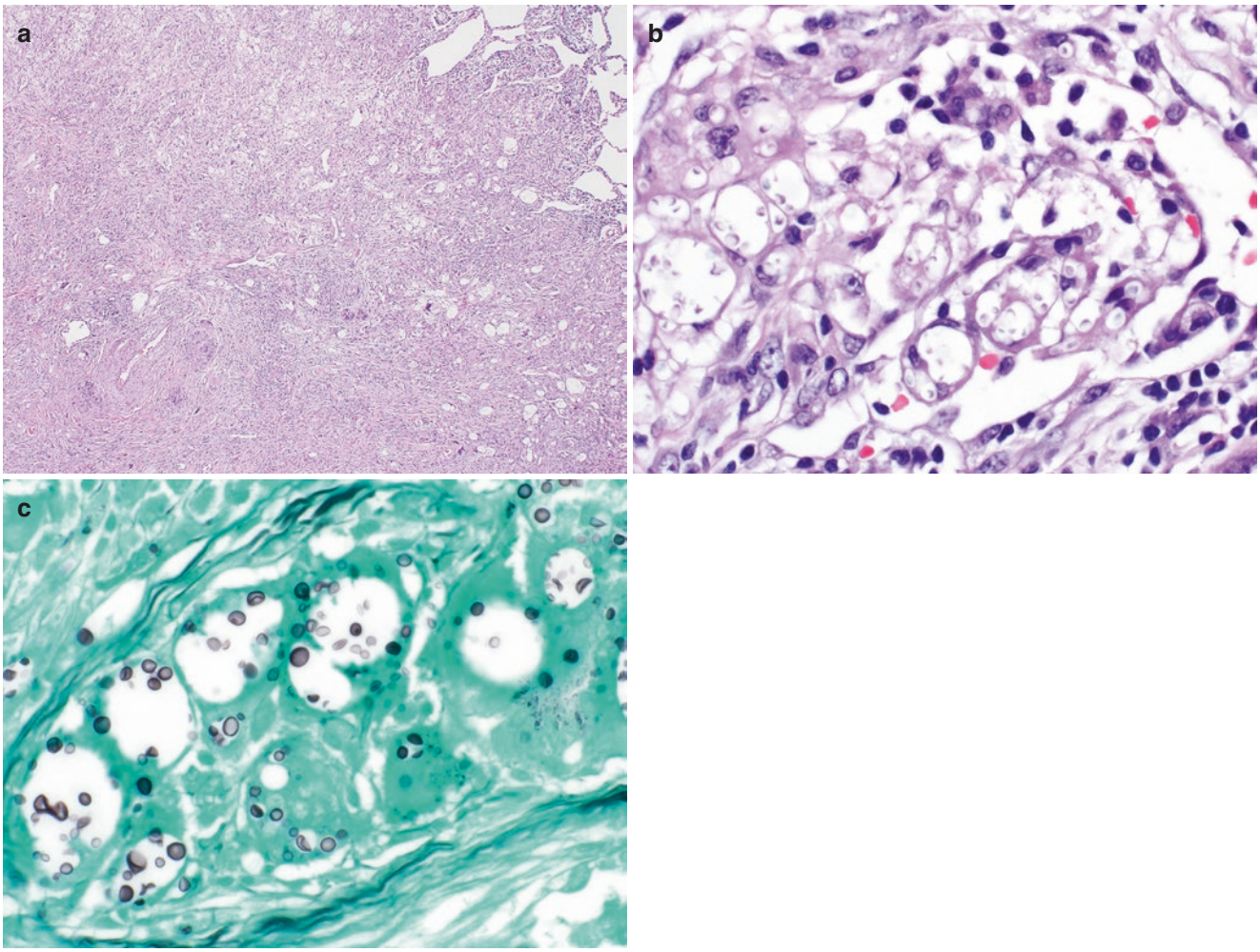

Fig. 4.28 Cryptococcosis. (**a**) Low-magnification photomicrograph showing a nodule in which poorly formed non-necrotizing granulomas comprise loose clusters of multinucleated giant cells with variably conspicuous cytoplasmic vacuoles. (**b**) High-magnification view showing that many of the cytoplasmic vacuoles contain delicate, pale-staining, thin-walled yeast with associated halos representing mucinous capsules. (**c**) High-magnification photomicrograph of GMS stain showing the round and misshapen fractured yeast forms typical of *Cryptococcus neoformans*

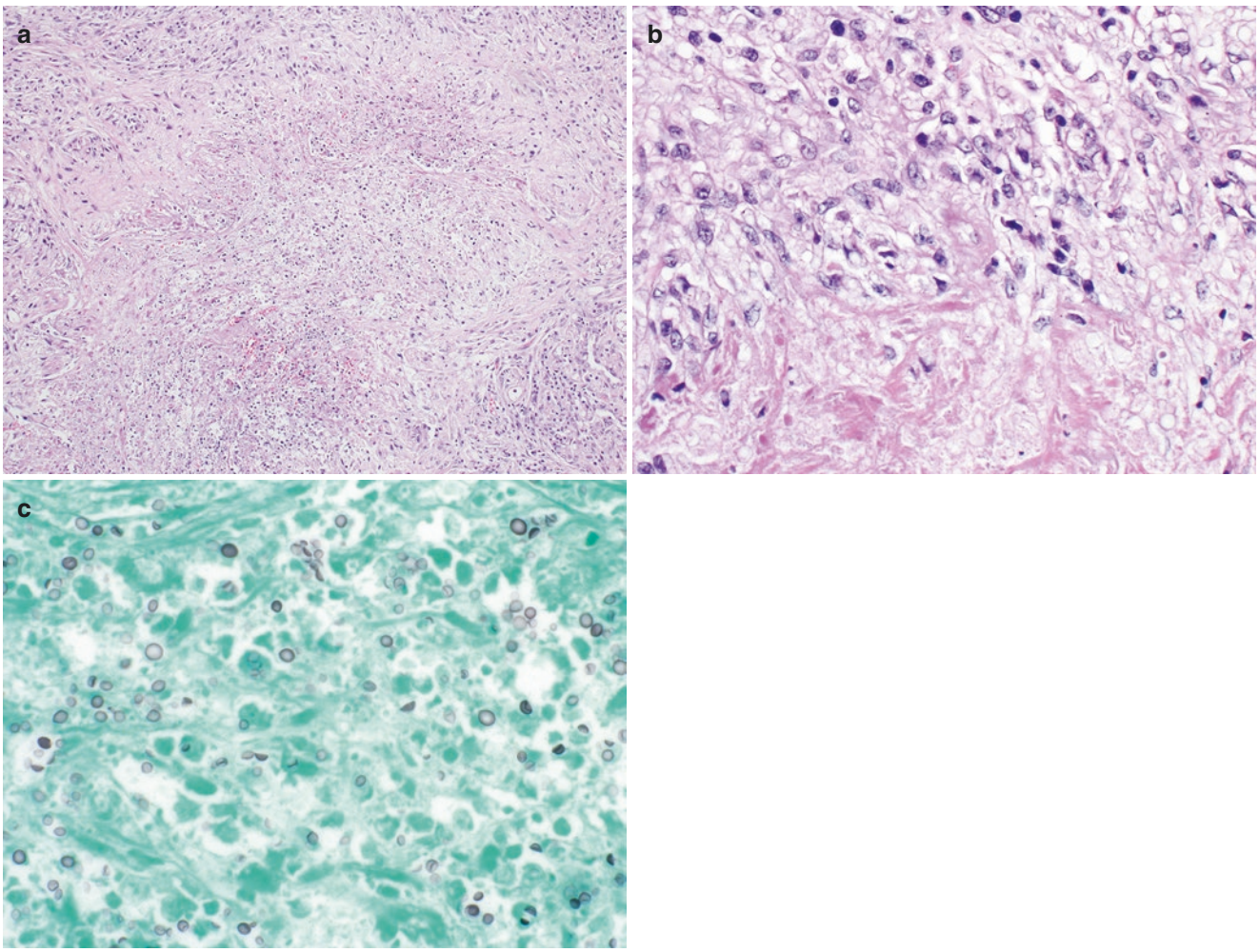

Fig. 4.29 Cryptococcosis. (**a**) Photomicrograph showing necrotizing granuloma that contributed to the same nodule illustrated in Fig. 4.28. This combination of necrotizing granulomas and loose clusters of multinucleated giant cells is a common tissue manifestation of pulmonary cryptococcosis. (**b**) Higher-magnification view showing necrotic center of granuloma at the bottom surrounded by a mixed inflammatory infiltrate of mononuclear cells in which epithelioid histiocytes predominate. (**c**) High-magnification photomicrograph of GMS illustrating yeast typical of *Cryptococcus neoformans* randomly scattered with the necrotic center of the granuloma

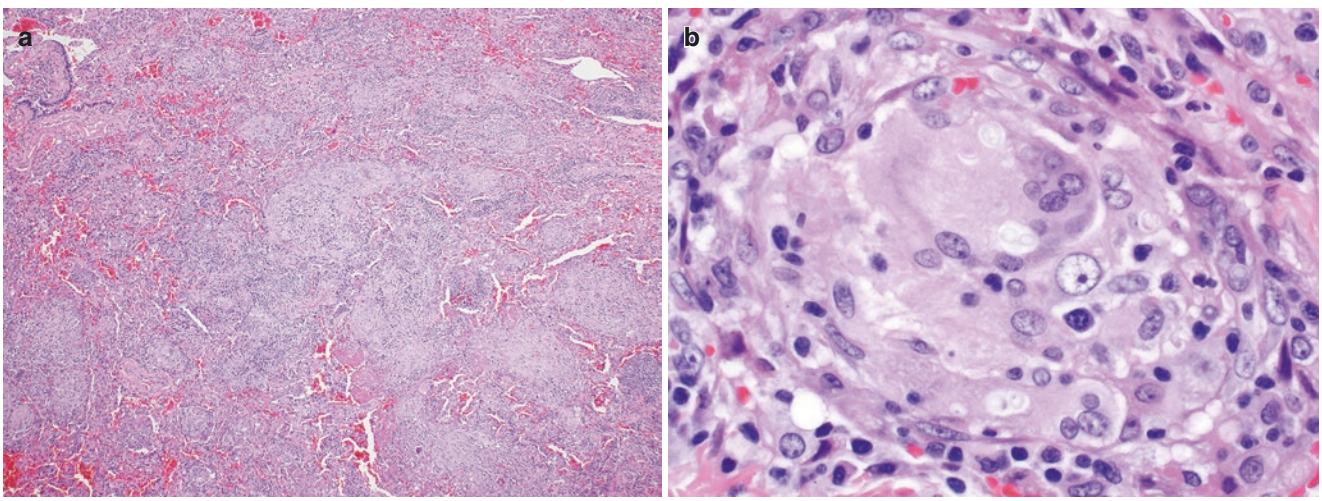

Fig. 4.30 Cryptococcosis. (**a**) Organizing pneumonia is a common manifestation of cryptococcosis, as illustrated in this low-magnification photomicrograph. It is distinguished by associated granulomatous inflammation, including clusters of epithelioid and multinucleated macrophages. (**b**) High-magnification view showing the delicate, pale-staining, thin-walled yeast with associated halos that are the histologic hallmarks of *Cryptococcus neoformans*

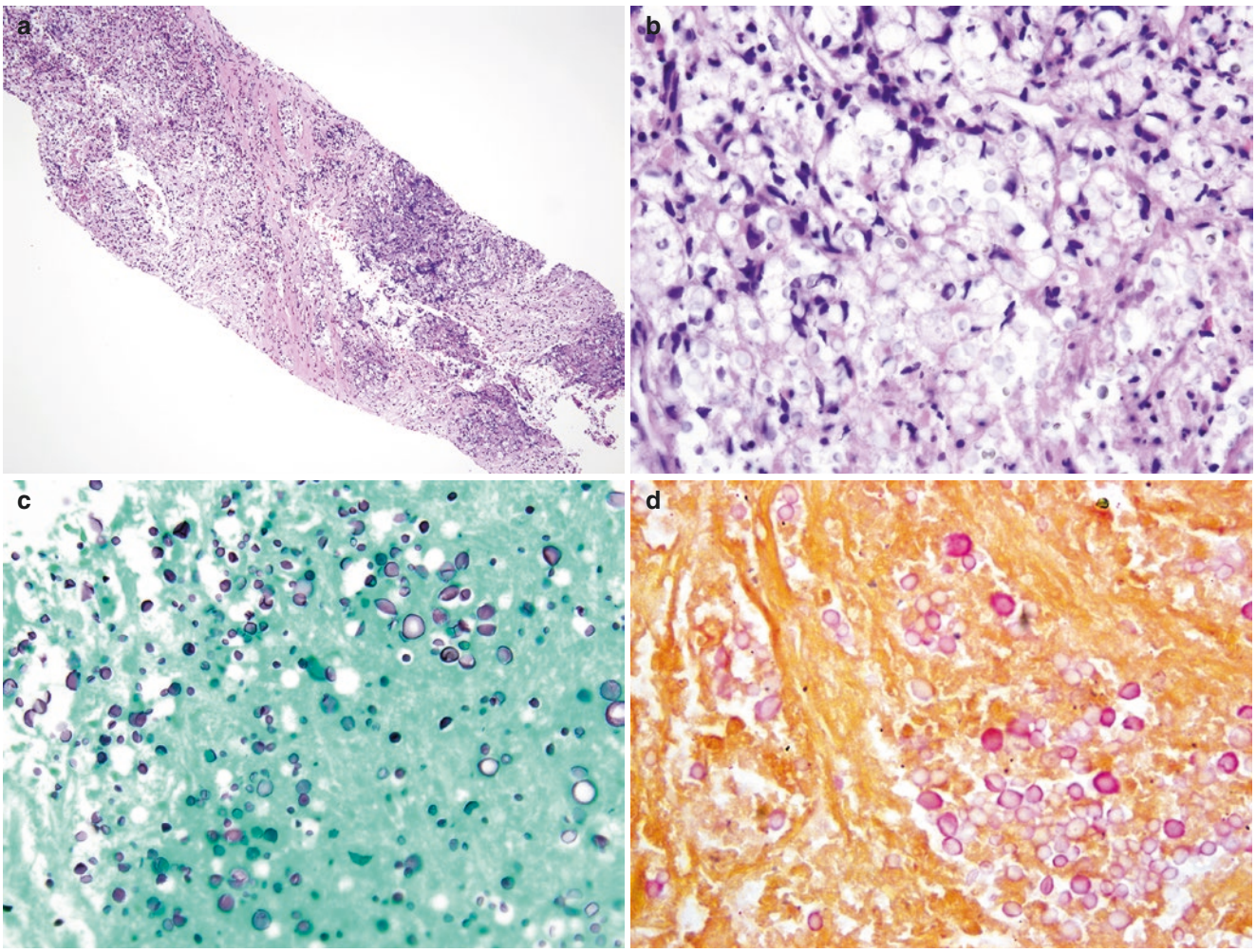

Fig. 4.31 Cryptococcosis. (**a**) Low-magnification photomicrograph of a needle biopsy from a lung nodule in an immunocompromised patient. Areas of pale-colored necrosis and vaguely granulomatous inflammation are seen. (**b**) High-magnification photomicrograph showing the pale-colored necrosis in which there are numerous round yeasts with minimal inflammatory reaction and without well-formed granulomas. The yeasts vary markedly in size and shape and are surrounded by a prominent clear space corresponding to a mucinous capsule. (**c**) High-magnification view of the GMS stain highlights the characteristic features of *Cryptococcus*: variation in size and frequent fragmentation of the yeast. (**d**) High-magnification photomicrograph illustrating the brightly mucicarminophilic capsule seen in most (but not all) strains of *Cryptococcus neoformans*. Capsule-deficient strains may lack this characteristic

Coccidioidomycosis

Coccidioidomycosis (Figs. 4.32, 4.33, 4.34 and 4.35) is endemic in the southwestern United States and is caused by the dimorphic fungi *Coccidioides immitis* and *Coccidioides posadasii*. It causes disease in both immunocompetent and immunocompromised patients and may be biopsied or excised because of its tendency to form a localized lung nodule. The organism divides by a process of endosporulation, a feature helpful in identifying *Coccidioides* in routinely and specially stained sections. The mycelial form is much less commonly found in surgical lung specimens.

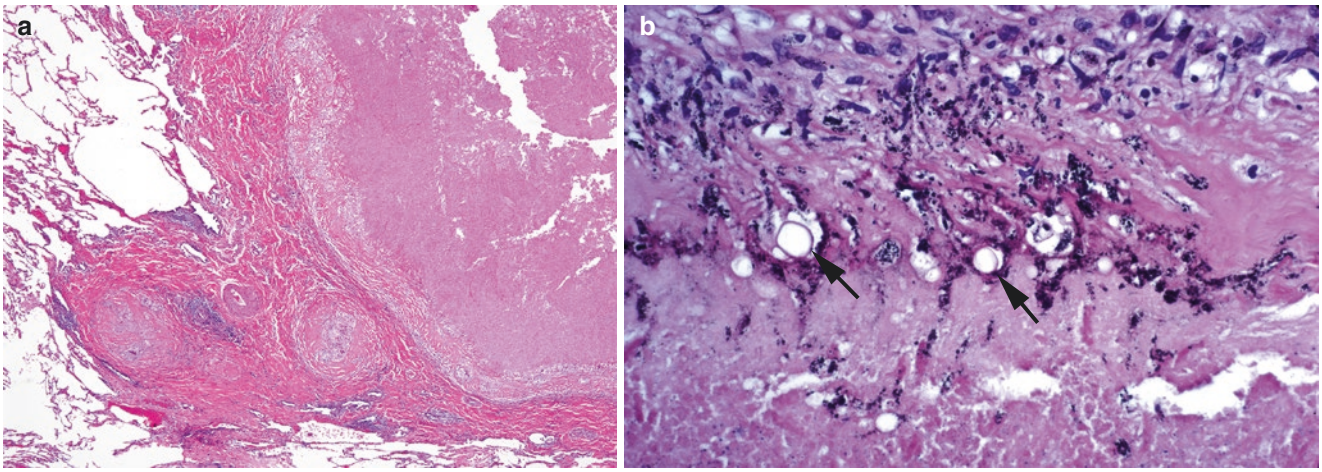

Fig. 4.32 Coccidioidomycosis. (**a**) Necrotizing granulomatous inflammation is the most common finding in *Coccidioides* infections. This low-magnification photomicrograph shows a large area of bland necrosis surrounded by epithelioid histiocytes and giant cells with non-necrotizing granulomas at the periphery. (**b**) High-magnification photomicrograph showing large empty spherules (arrows) with a thick, somewhat refractile wall at the edge of necrosis. Note that the spherules are much larger than adjacent histiocytes

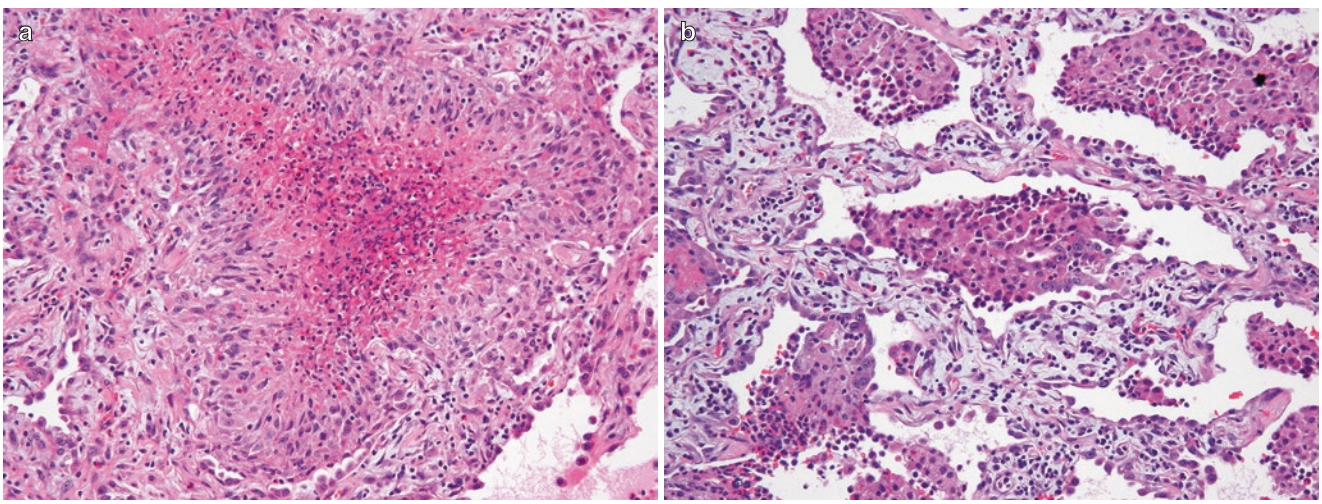

Fig. 4.33 Coccidioidomycosis with eosinophilia. (**a**) Photomicrograph showing necrotizing granuloma with associated eosinophilia in a patient with coccidioidomycosis. Tissue eosinophilia is commonly associated with necrotizing granulomatous inflammation in coccidioidomycosis and may include areas resembling eosinophilic pneumonia, as illustrated in the same biopsy in (**b**)

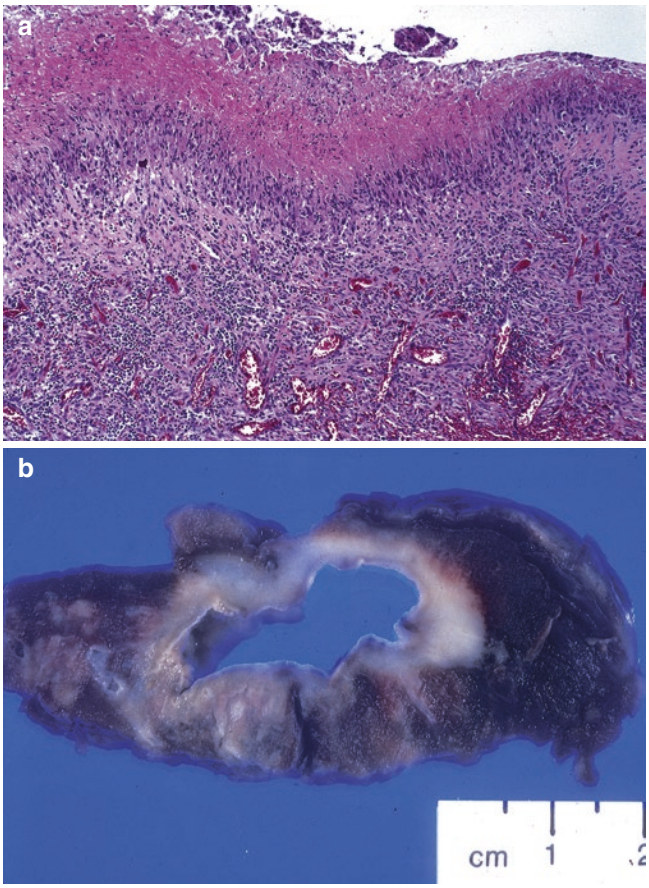

Fig. 4.34 Cavitary coccidioidomycosis. (**a**) This low-magnification photomicrograph illustrates necrotizing granulomatous inflammation with cavitation in a patient with coccidioidomycosis. (**b**) Photograph of surgical specimen corresponding to photomicrograph in **a** showing a cavitary lesion with an irregular rim of firm inflammatory tissue

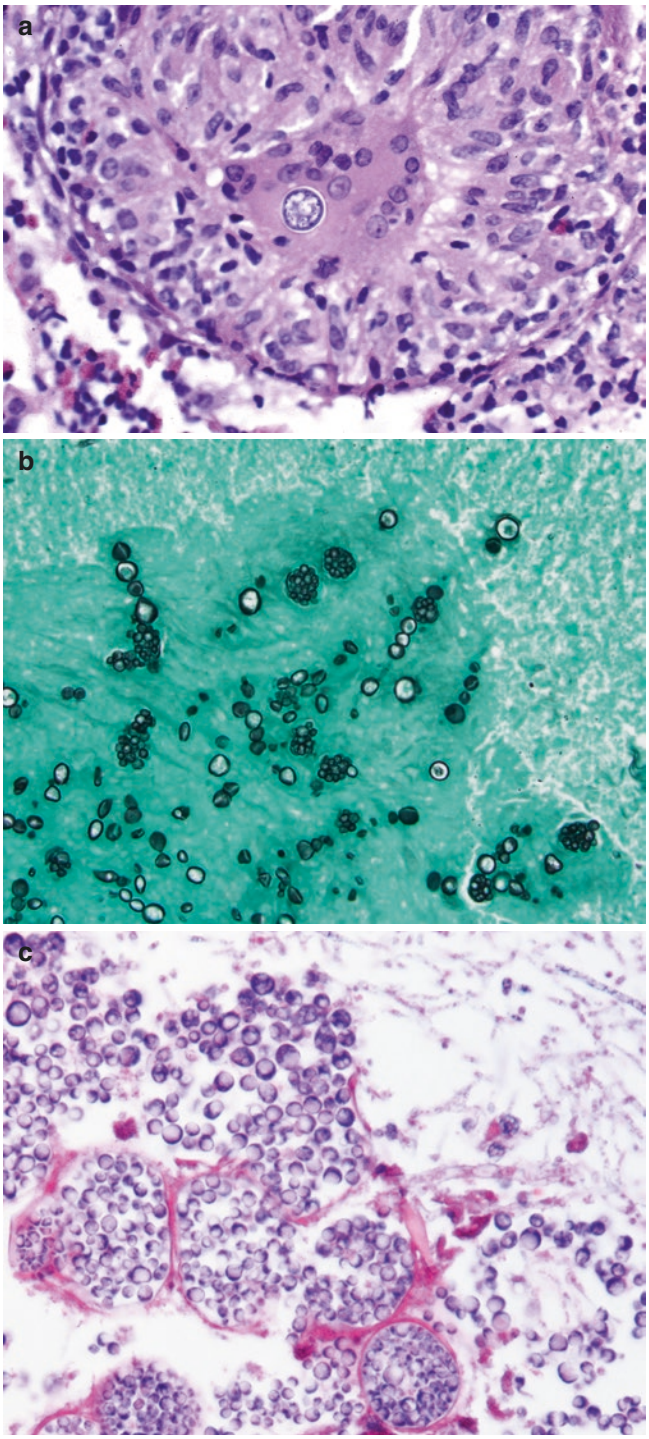

Fig. 4.35 Coccidioidomycosis. (**a**) High-magnification photomicrograph showing a multinucleated giant cell containing a *Coccidioides* spherule with multiple small slightly basophilic endospores. Note the eosinophils in the lower left corner. (**b**) Photomicrograph of a GMS-stained section showing multiple large empty spherules, spherules containing endospores, and free endospores. (**c**) High-magnification photomicrograph of a routinely stained section showing a combination of spherules, endospores, and hyphae (upper right) in a patient with cavitary disease. Hyphae are an uncommon finding in surgical specimens of coccidioidomycosis and represent the mycelial form of the organism

Aspergillus Infections

Aspergillus infections (Figs. 4.36, 4.37, 4.38, 4.39, 4.40 and 4.41) in the lungs can be noninvasive or invasive. The commonly recognized forms include noninvasive mycetoma or *Aspergillus* fungus ball, allergic bronchopulmonary aspergillosis (ABPA), invasive *Aspergillus* pneumonia, and necrotizing tracheobronchitis. Aspergillomas form in immunocompetent patients with underlying cavitary or cystic lung disease. ABPA affects patients with asthma or cystic fibrosis, and invasive forms of the disease occur in immunocompromised patients. Chronic cavitary aspergillosis is a progressive form of disease that has features intermediate between noninvasive and invasive forms of aspergillosis. It is characterized by radiologic progression and tends to occur in patients with underlying comorbidities, particularly chronic lung disease.

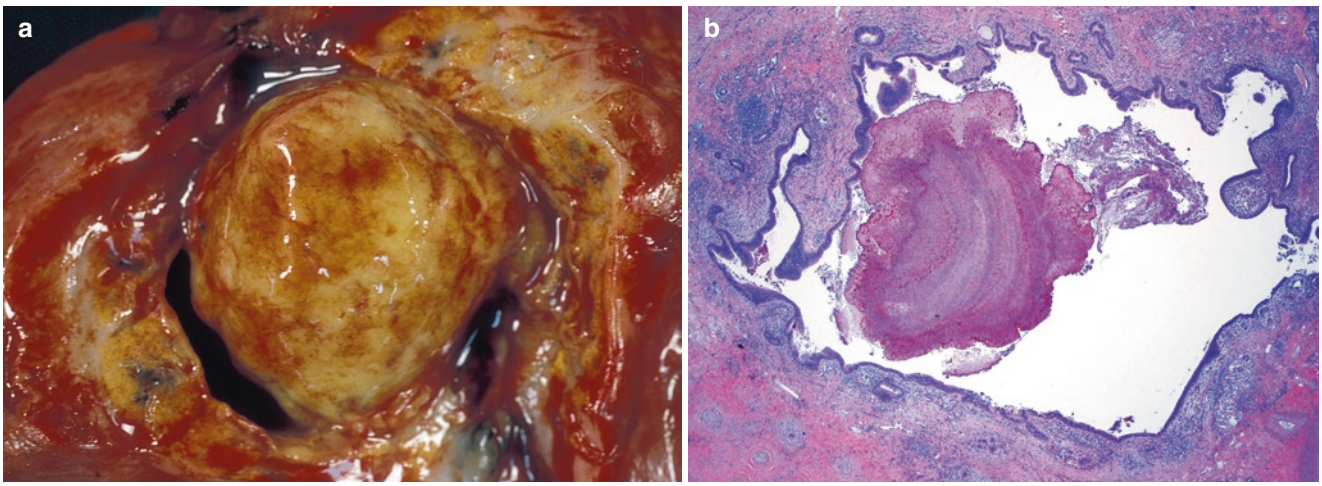

Fig. 4.36 *Aspergillus* mycetoma (aspergilloma). (**a**) Photograph of resected aspergilloma forming a fungus ball within a cavitary space. (**b**) Low-magnification view of fungus ball situated within a dilated airway. Note that there is no tissue response or invasion by the fungus ball

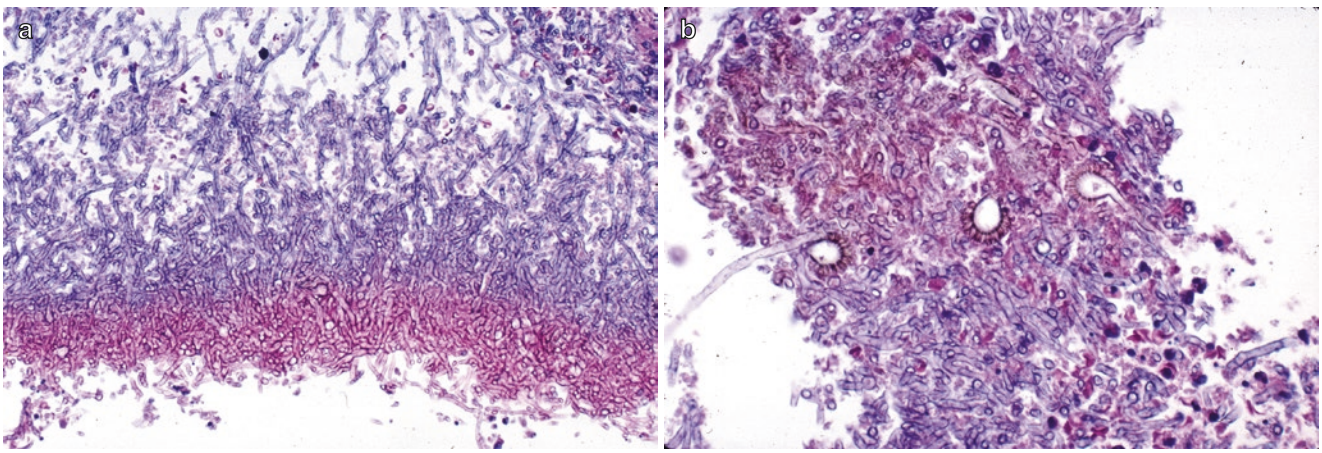

Fig. 4.37 *Aspergillus* hyphae. (**a**) Photomicrograph of routinely stained H&E section showing the organisms comprising an aspergilloma arranged as radially aligned elongated septate hyphae with acute-angle branching. (**b**) High-magnification photomicrograph showing the conidial heads that are occasionally seen and may be helpful in identifying the specific species of *Aspergillus*

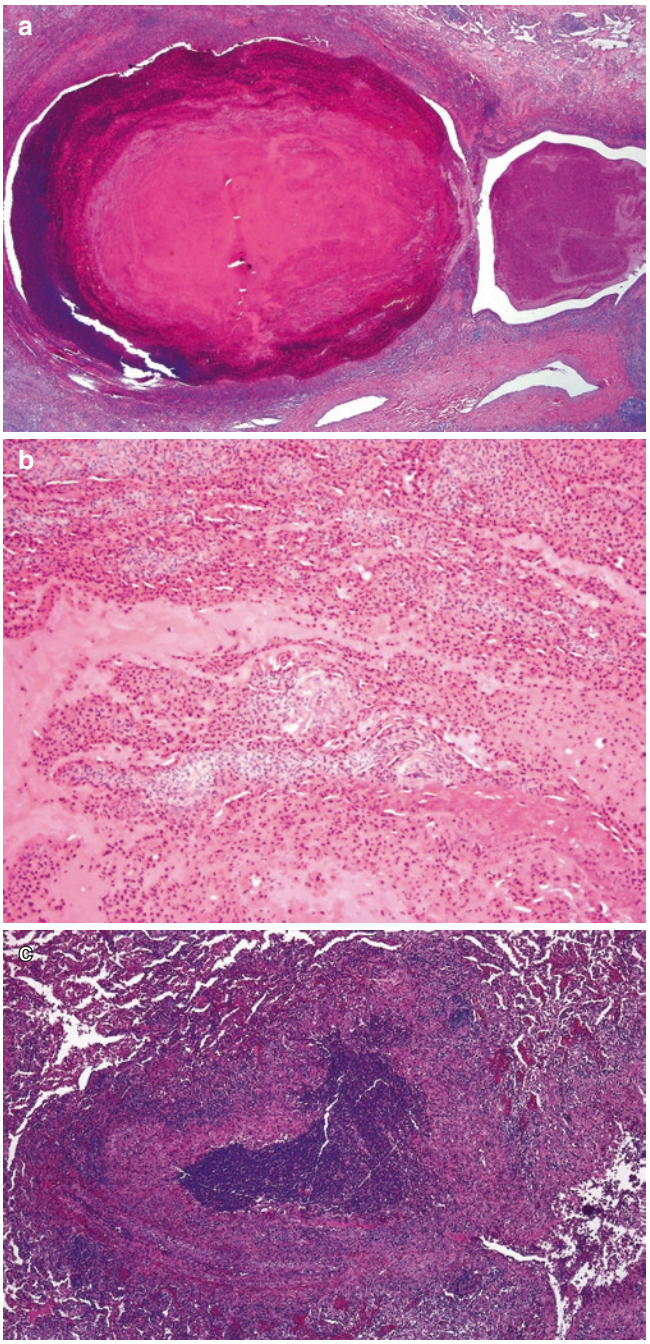

Fig. 4.38 Allergic bronchopulmonary aspergillosis (ABPA). (**a**) Low-magnification photomicrograph showing dilated bronchus filled up with dense mucus plugs demonstrating a layered appearance typical of mucoid impaction of bronchi (MIB) in ABPA. (**b**) High-magnification view showing that the layers of the "allergic mucin" typical of MIB in ABPA constitute a combination of desiccated eosinophils and inspissated mucus in which there are variably conspicuous Charcot-Leyden crystals. (**c**) Low-magnification photomicrograph showing bronchocentric granulomatosis, a finding that in the context of MIB and eosinophilia is characteristic of ABPA. Bronchocentric necrotizing granulomatous inflammation without other features of ABPA occurs in other conditions, including granulomatosis with polyangiitis (Wegener's granulomatosis) and granulomatous infections

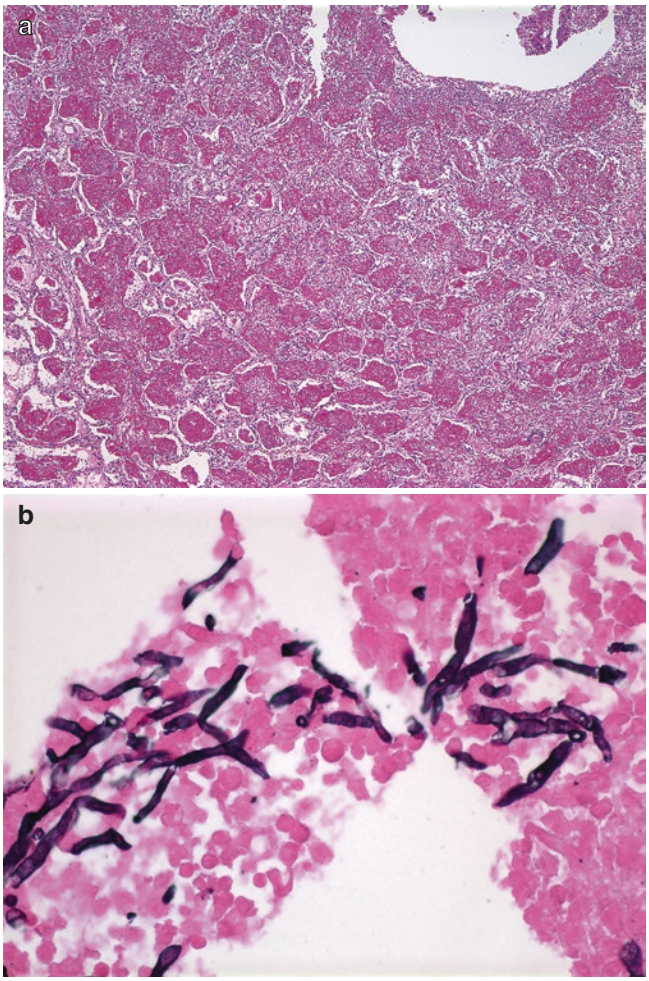

Fig. 4.39 Invasive aspergillosis. (**a**) Low-magnification photomicrograph showing necrotizing pneumonia characteristic of invasive aspergillosis. The air spaces are filled with a fibrinous exudate that includes neutrophils and karyorrhexis. (**b**) High-magnification photomicrograph of GMS-stained section showing fungal hyphae with the necrotizing exudate with branching septate hyphae characteristic of *Aspergillus spp.*

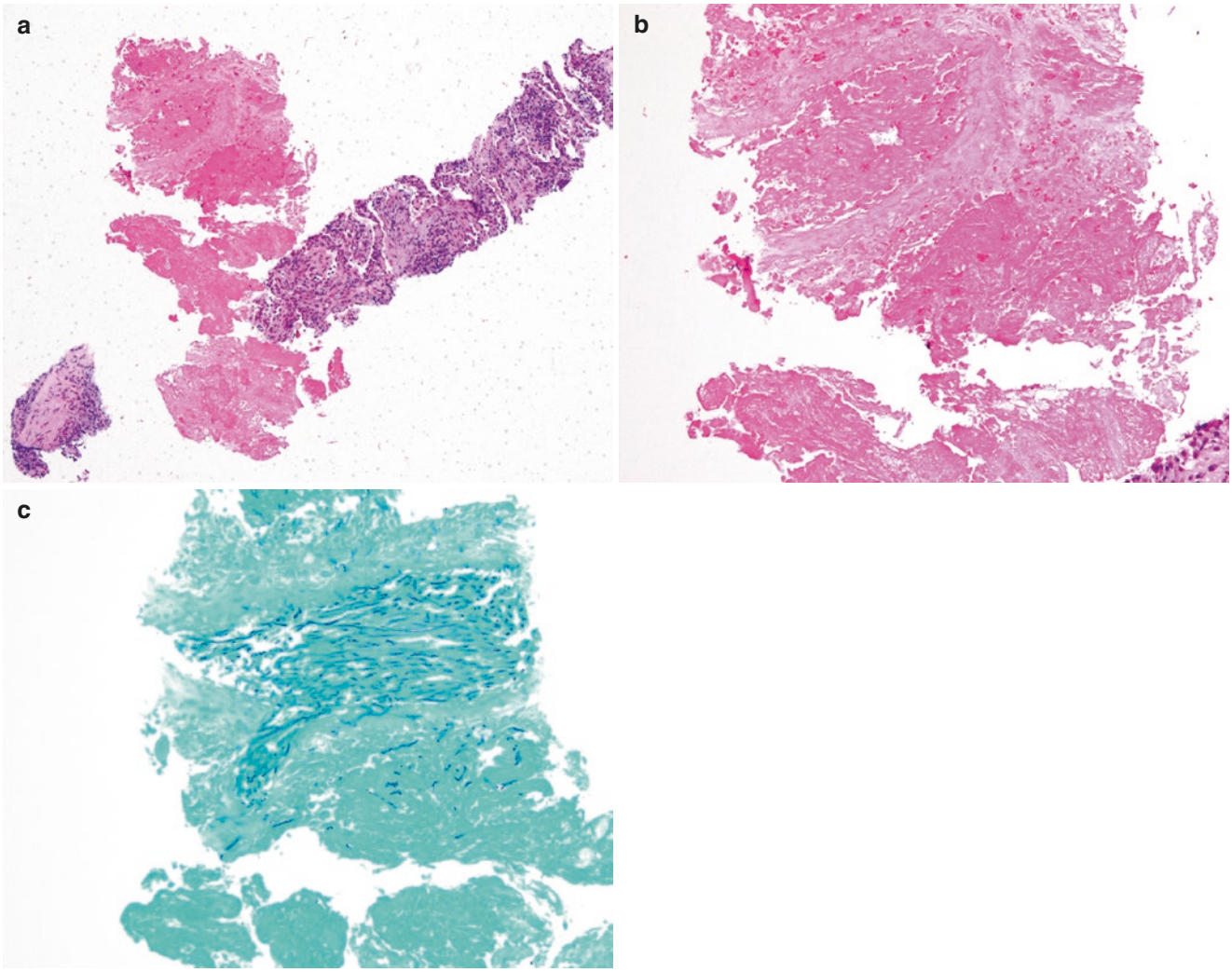

Fig. 4.40 Invasive aspergillosis. (**a**) Low-magnification photomicrograph of a needle biopsy from a lung mass in an immunocompromised patient showing areas of infarction and adjacent organizing pneumonia. (**b**) Higher-magnification view of the infarcted area showing a necrotic blood vessel with questionable fungal hyphae filling up the lumen. (**c**) A GMS stain reveals *Aspergillus* fungal hyphae within the vascular lumen and invading the vascular wall

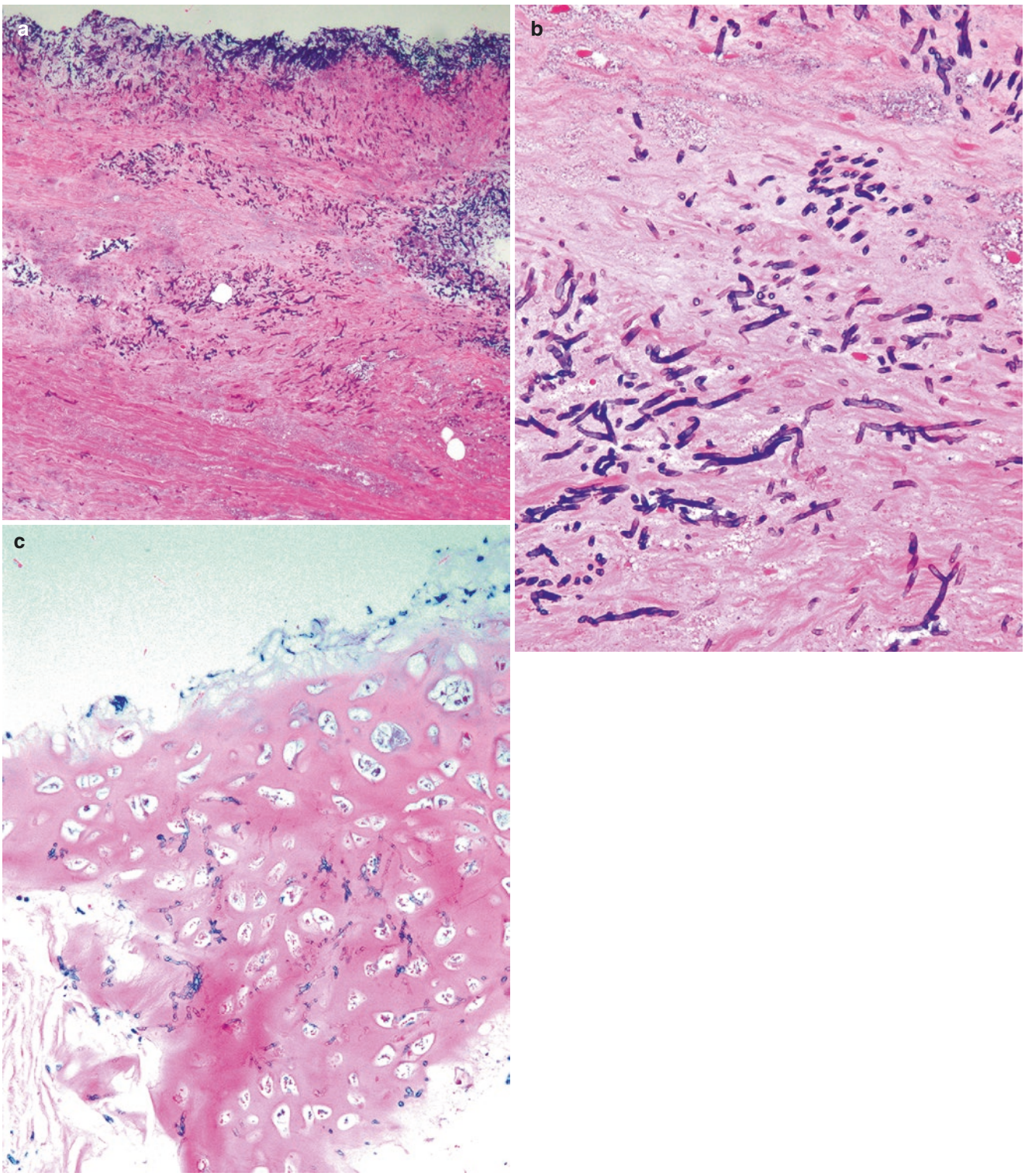

Fig. 4.41 Necrotizing tracheobronchitis as a manifestation of invasive aspergillosis. (**a**) Low-magnification photomicrograph of bronchial wall showing extensive ulceration, necrosis, and invasion by *Aspergillus* fungal hyphae. (**b**) High-magnification photomicrograph of routinely stained section of the bronchial wall showing thin, septate *Aspergillus* hyphae. (**c**) High-magnification view showing extensive invasion of bronchial wall cartilage

Invasive Mucormycosis

Invasive mucormycosis (Figs. 4.42 and 4.43) is caused by a group of fungi referred to as mucormycetes, also referred to as *Mucoromycotina* or *Zygomycota* (zygomycetes). Mucormycosis occurs almost exclusively in immunocompromised patients and frequently involves the lungs. Given the high mortality rate, frozen sections are sometimes requested in order to make a rapid diagnosis and promptly start antifungal therapy.

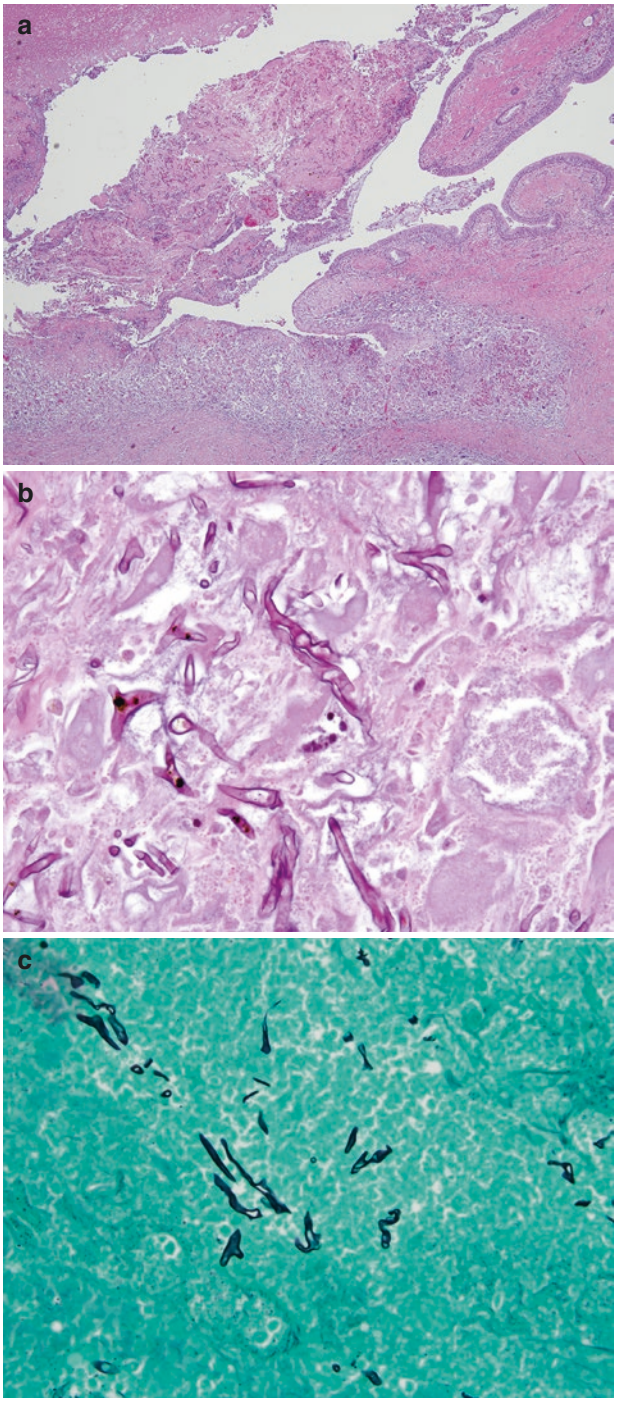

Fig. 4.42 Invasive mucormycosis. (**a**) Low-magnification photomicrograph showing parenchymal necrosis with acute and chronic inflammation, including epithelioid and multinucleated histiocytes resulting in a vaguely granulomatous appearance. Fungal hyphae are present predominantly within the necrotic tissue. (**b**) High-magnification photomicrograph showing the wide, irregular, ribbon-shaped, nonseptate hyphae with 90-degree branching. (**c**) GMS staining showing irregular, ribbon-shaped hyphae with 90-degree branching

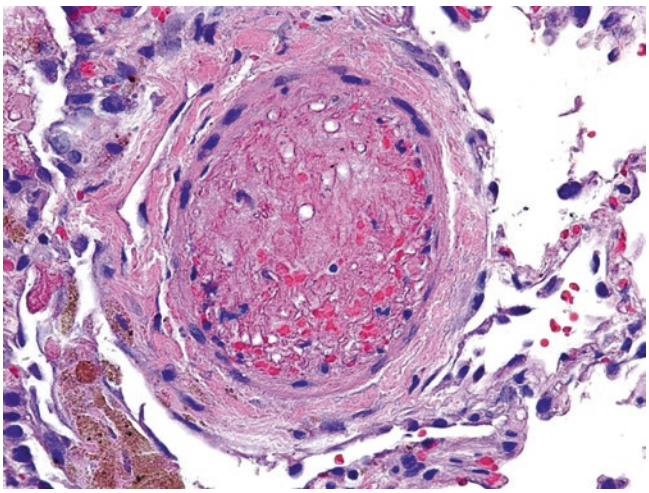

Fig. 4.43 Invasive mucormycosis. High-magnification photomicrograph showing a blood vessel completely occluded by mucor hyphae

Candidiasis

Candidiasis (Figs. 4.44 and 4.45) is rare and occurs primarily in immunocompromised hosts, usually presenting as angioinvasive disease with necrotizing acute bronchopneumonia and abscess formation. Occasionally, candidiasis is more exquisitely localized to blood vessels (intravascular candidiasis). Rarely, the disease is associated with granulomatous inflammation, mainly in patients with underlying chronic granulomatous disease.

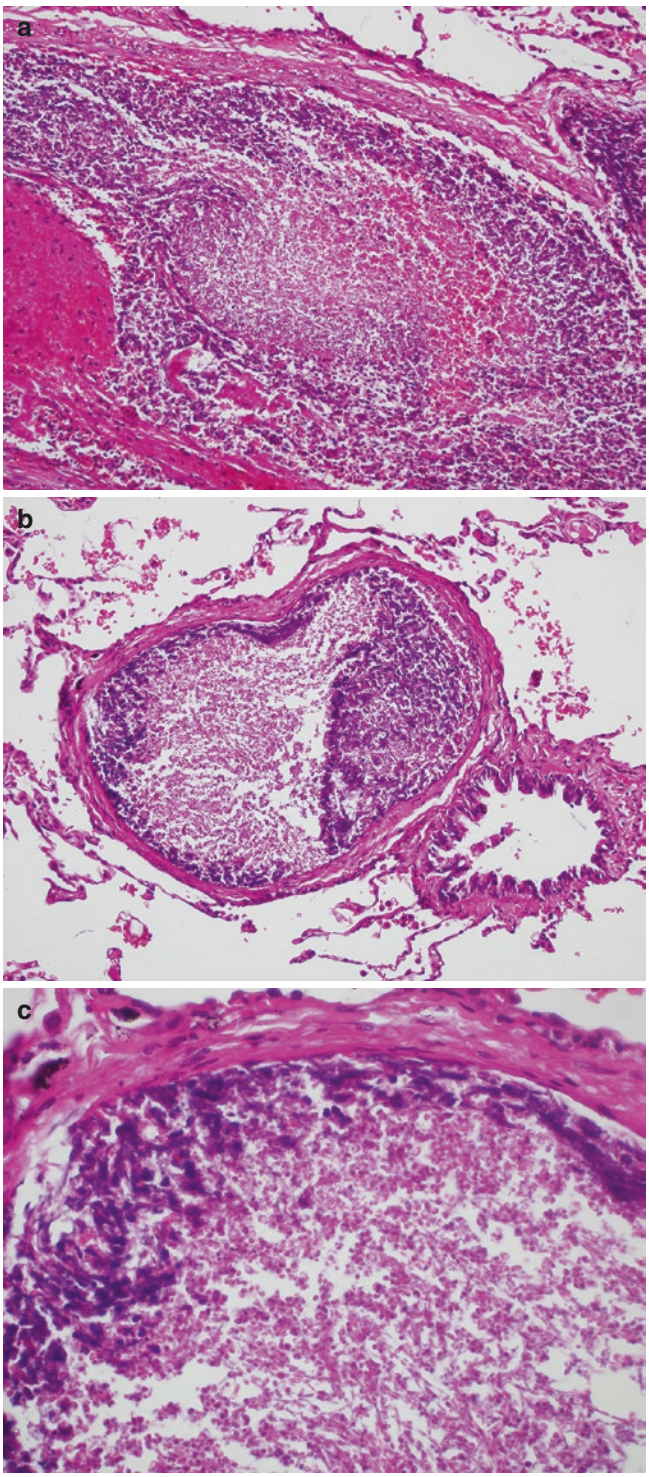

Fig. 4.44 Candidiasis. (**a**) Low-magnification photomicrograph showing blood vessel lumen rimmed by inflammatory cells with a partially necrotic thrombus containing numerous fungal pseudohyphae radially arranged to form a central nidus. (**b**) Low-magnification photomicrograph of a small artery filled with numerous fungal organisms. (**c**) High magnification of the intravascular organisms showing yeasts and pseudohyphae

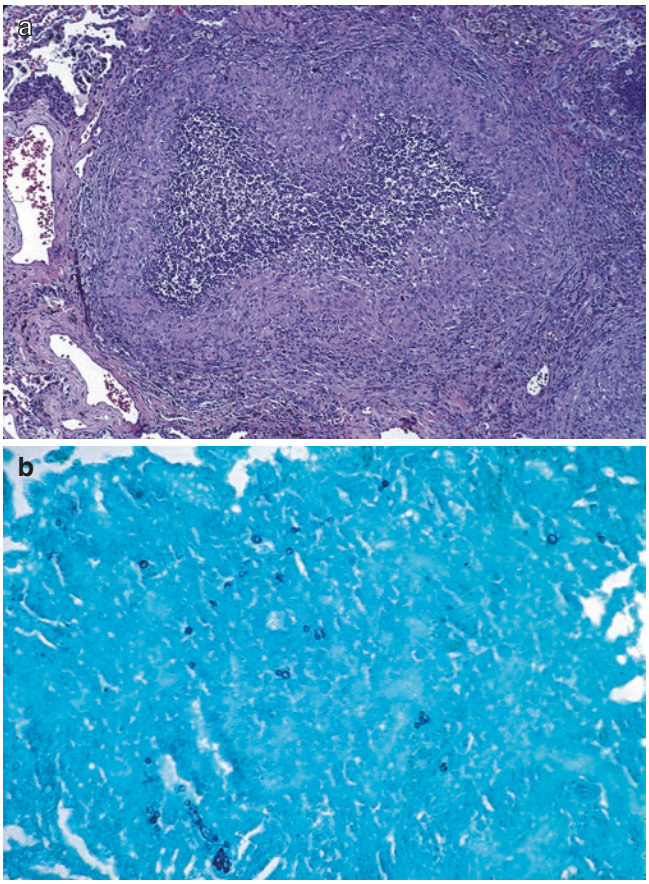

Fig. 4.45 Candidiasis in chronic granulomatous disease. (**a**) Photomicrograph showing suppurative granuloma in a lung biopsy from a patient with chronic granulomatous disease. (**b**) High-magnification photomicrograph of GMS-stained section showing small, narrow-budding yeast in granuloma illustrated above. Cultures grew *Candida spp.*

Pneumocystis Pneumonia

Pneumocystis pneumonia (Figs. 4.46, 4.47, 4.48, 4.49 and 4.50) occurs exclusively in immunocompromised patients. The organism *Pneumocystis jirovecii* was historically considered a protozoon but was reclassified as a fungus on the basis of molecular evidence demonstrating its close relationship to fungi. *Pneumocystis* pneumonia is affiliated with highly variable histologic features and therefore should always be in the differential diagnosis of infections in immunocompromised patients. In its most classic form, the organisms cluster within a fibrinous air-space exudate, producing a characteristic frothy or bubbly appearance on routinely stained sections. Other relatively common variants include granulomatous inflammation and diffuse alveolar damage.

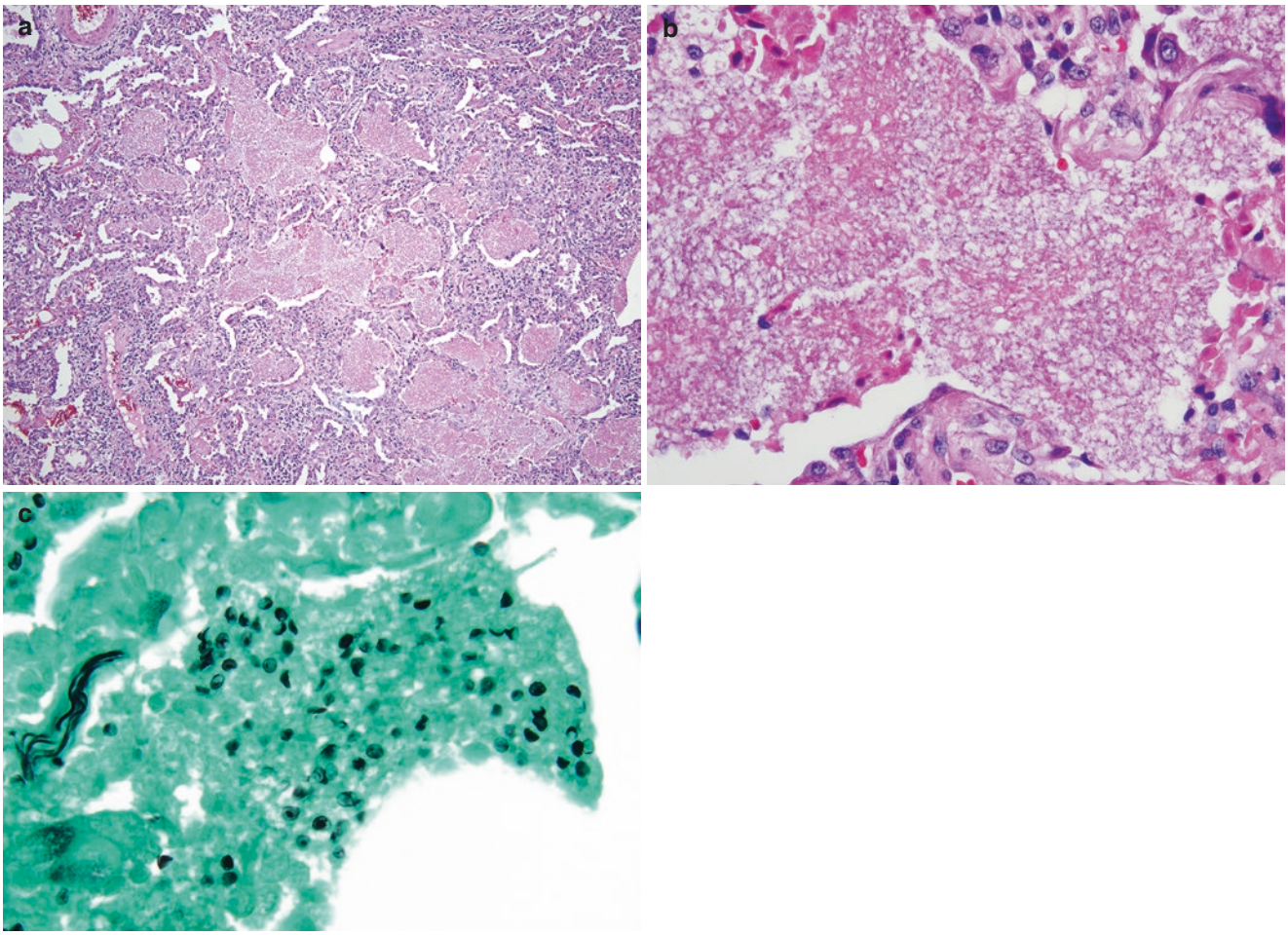

Fig. 4.46 *Pneumocystis* pneumonia. (**a**) Low-magnification photomicrograph of *Pneumocystis* pneumonia showing classic histologic features. The air spaces are filled with frothy eosinophilic exudates. There is nonspecific chronic inflammation within the mildly thickened alveolar septa. (**b**) High-magnification photomicrograph shows the characteristic intra-alveolar frothy exudate. The trophozoites of the organisms, represented by the tiny dot-like structures within the clear space of the frothy materials, are difficult to see on H&E-stained slides but are an important clue to the diagnosis. (**c**) High-magnification view of GMS stain showing numerous round to helmet-shaped cysts within the intra-alveolar frothy exudates. The cysts demonstrate frequent fragmentation and have been described as crushed structures shaped like ping-pong balls. Trophozoites are not visible on GMS-stained slides

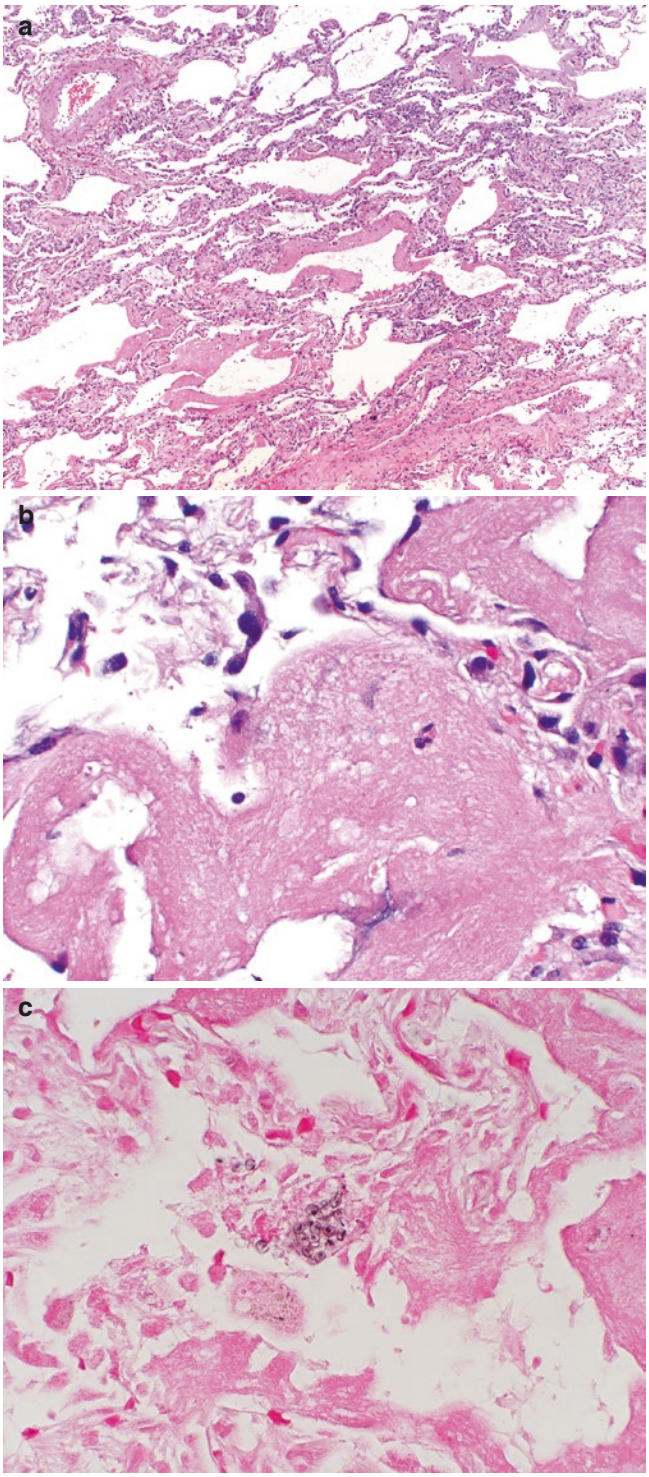

Fig. 4.47 Diffuse alveolar damage is a common manifestation of *Pneumocystis* pneumonia, making a GMS stain mandatory in any immunocompromised patient with this finding. (**a**) Low-magnification photomicrograph of a lung biopsy with *Pneumocystis* pneumonia showing early-stage diffuse alveolar damage with prominent hyaline membranes. (**b**) High-magnification photomicrograph showing the subtle frothy appearance focally present within the lush hyaline membranes. (**c**) High-magnification photomicrograph of GMS-stained section showing organisms typical of *Pneumocystis jirovecii* clustered within the hyaline membranes

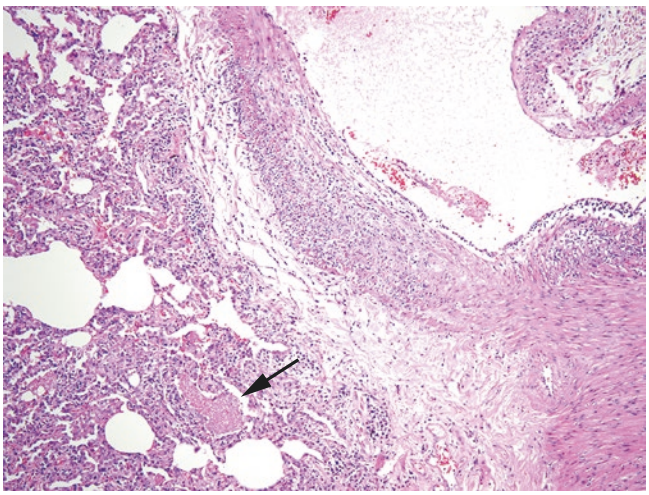

Fig. 4.48 *Pneumocystis* pneumonia. The vasculitis illustrated in this photomicrograph is a rare, atypical finding in *Pneumocystis* pneumonia that may resemble autoimmune or lymphoproliferative diseases. However, the focal presence of the intra-alveolar frothy exudate typical of pneumocystis (arrow) combined with the patient's immunocompromised status are important clues to the diagnosis

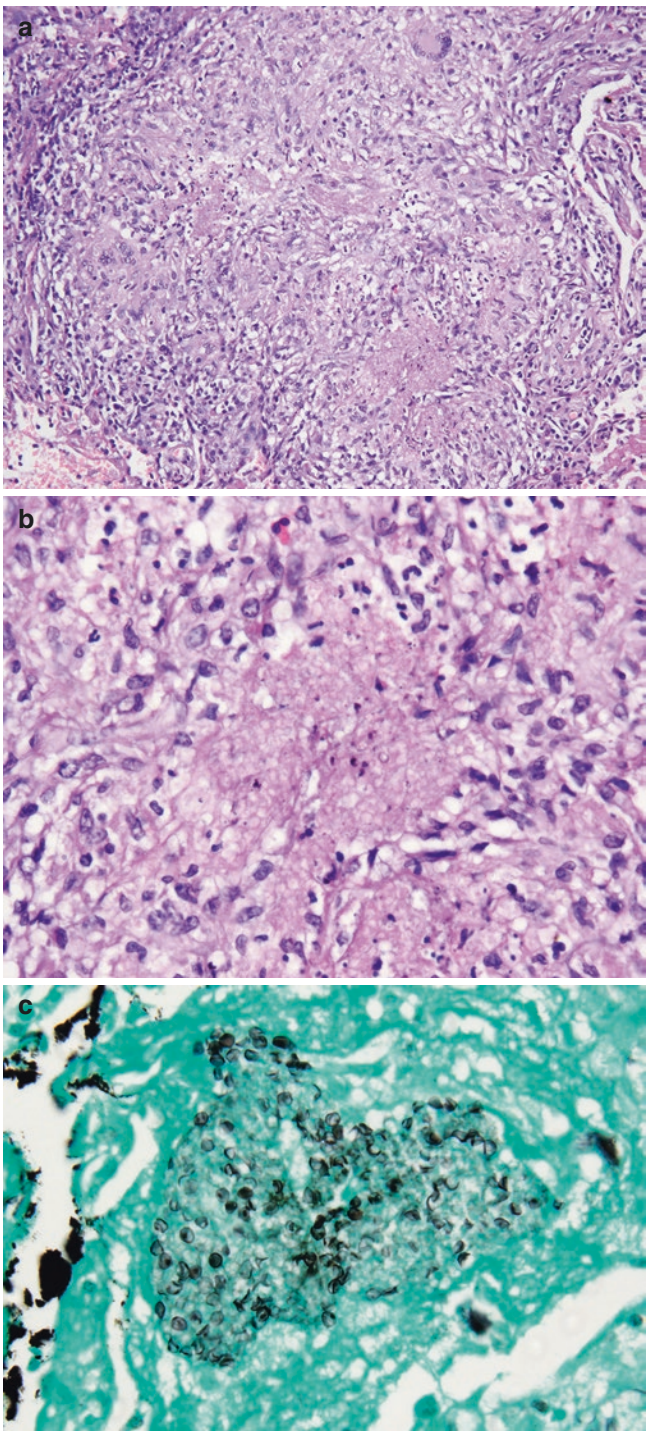

Fig. 4.49 *Pneumocystis* pneumonia. (**a**) Photomicrograph showing granulomatous inflammation in a patient with *Pneumocystis* pneumonia. The poorly formed granulomas are located within the air space. (**b**) Higher-magnification photomicrograph showing the typical frothy exudates that are often only a focal finding when affiliated with granulomatous features. (**c**) High-magnification photomicrograph of GMS-stained section showing numerous round and somewhat fragmented cysts within the central fibrinonecrotic exudates

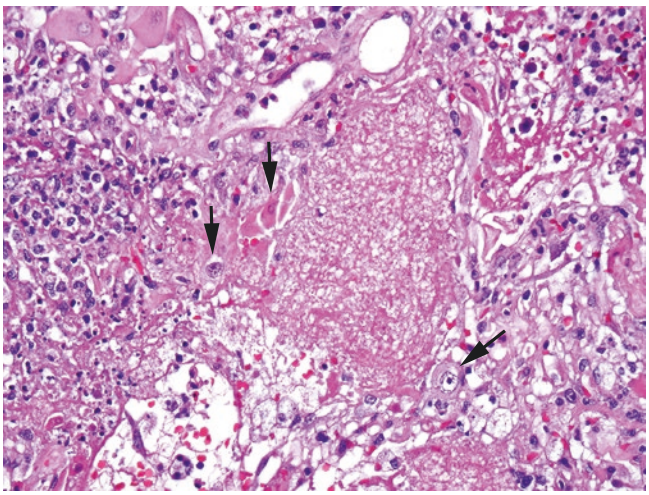

Fig. 4.50 *Pneumocystis* pneumonia with coexisting HSV infection. As illustrated in this high-magnification photomicrograph, more than one organism may be present in a lung biopsy from an immunocompromised patient. This biopsy shows frothy exudates characteristic of *Pneumocystis* pneumonia as well as viral cytopathic changes (arrows) and an associated necrotizing exudate typical of HSV infection

Protozoal and Parasitic Infestations

Protozoal and parasitic infestations (Figs. 4.51, 4.52, 4.53, 4.54, 4.55 and 4.56) in the lungs are rare. Except for dirofilarial nodules, these typically occur in immunocompromised patients.

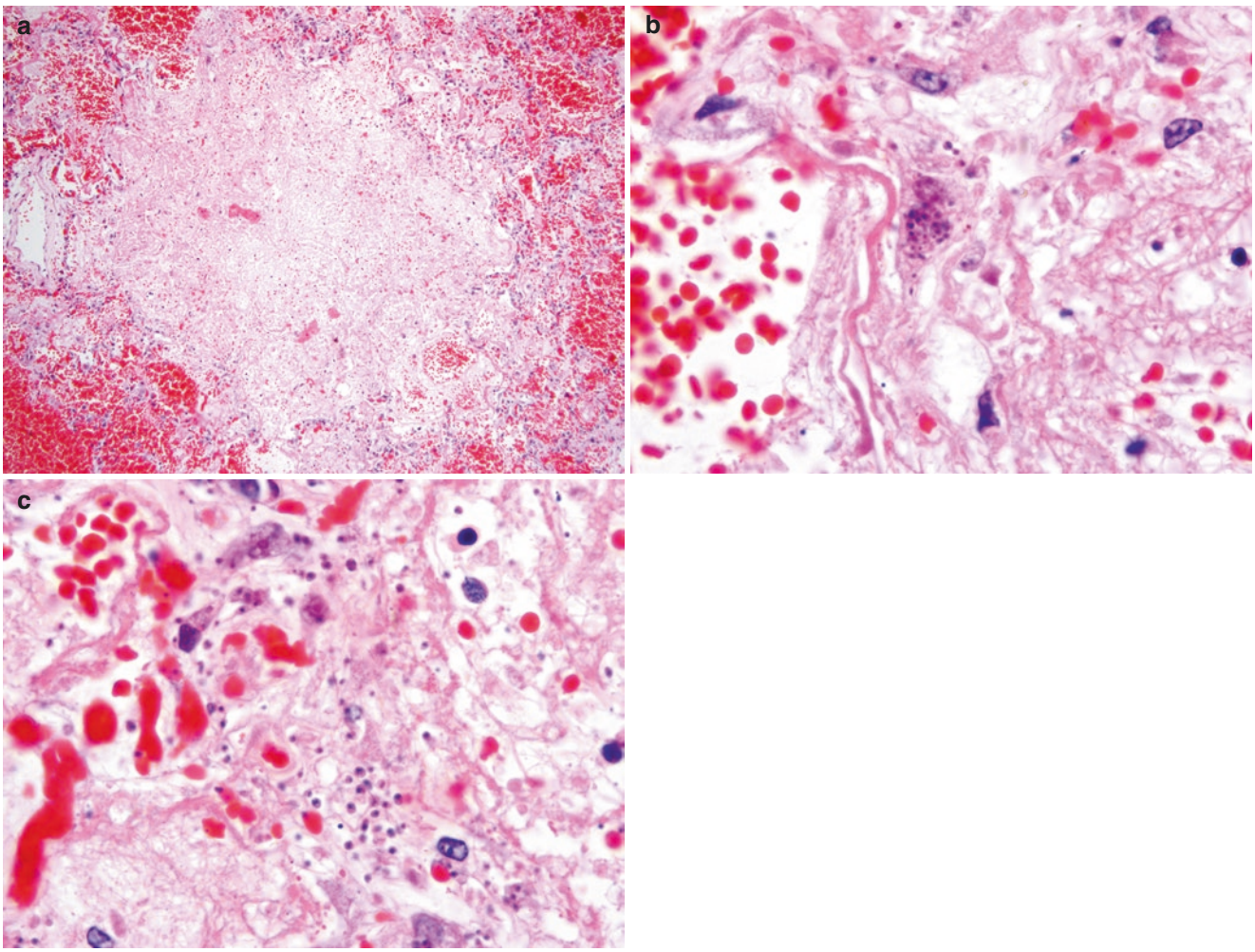

Fig. 4.51 Toxoplasmosis. (**a**) Low-magnification view of a lung biopsy from an immunocompromised patient showing patchy parenchymal necrosis with minimal inflammation. (**b**) High-magnification view at the edge of the necrosis showing an intracellular bradyzoite-containing cyst. (**c**) High-magnification view from elsewhere in the same biopsy showing multiple tachyzoites present within the extracellular exudates

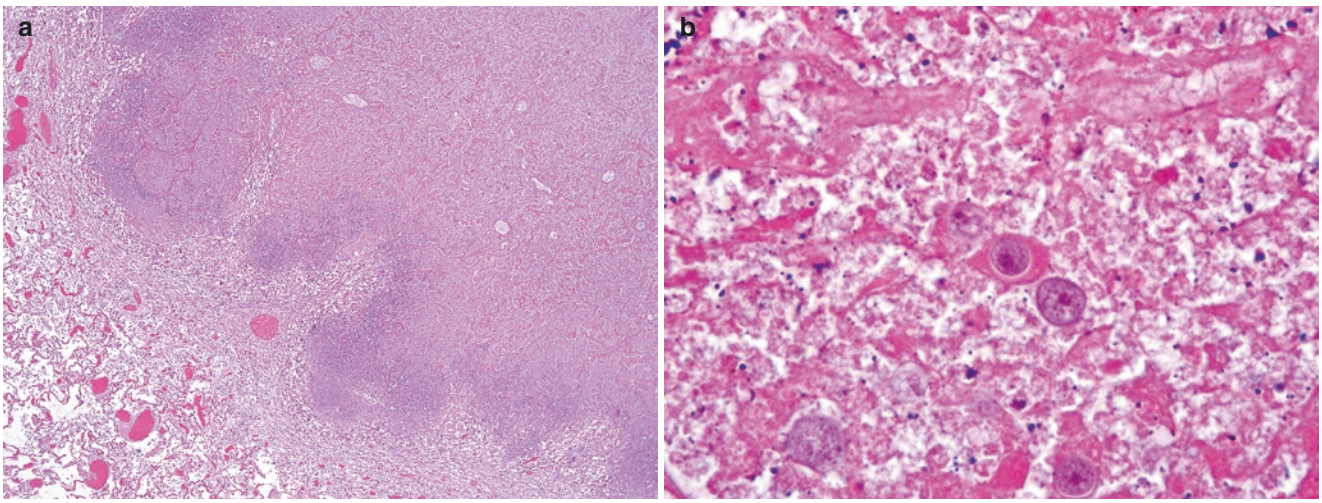

Fig. 4.52 Amoebiasis. (**a**) Low-magnification photomicrograph showing a large, geographic area of necrosis with mild peripheral inflammatory infiltrates. (**b**) High-magnification view at the edge of necrosis showing multiple round to oval trophozoites with a thin cell membrane and single nucleus with prominent nuclear border and central karyosome

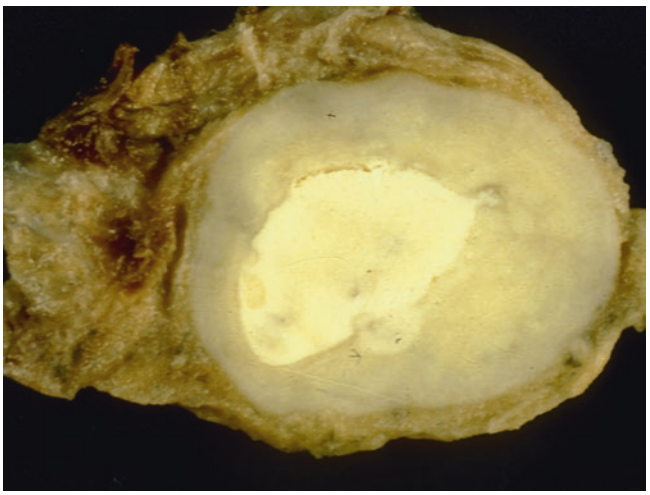

Fig. 4.53 Dirofilarial nodule (dog heartworm disease). Photograph of wedge biopsy from a patient with an asymptomatic solitary nodule showing a solitary well-demarcated centrally necrotic nodule mimicking an infectious granuloma

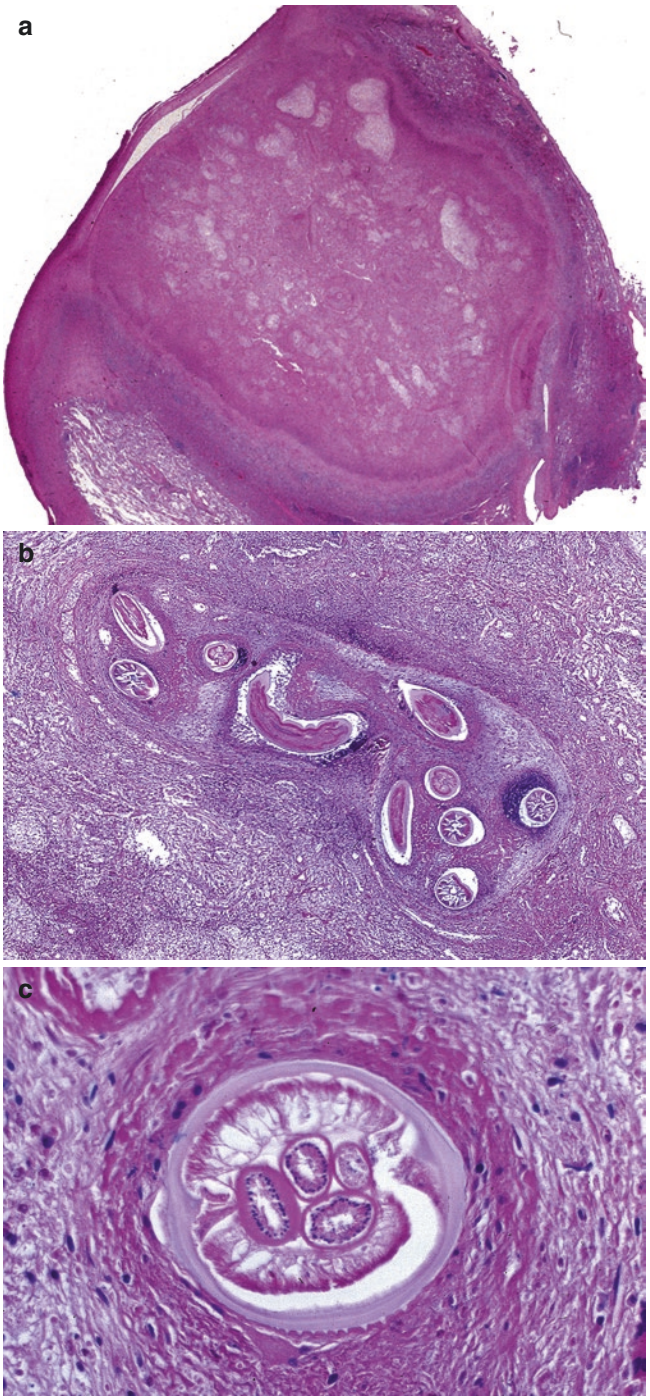

Fig. 4.54 Dirofilarial nodule. (**a**) Low-magnification photomicrograph showing well-circumscribed infarct-like necrosis surrounded by fibrosis and a chronic inflammatory infiltrate rich in eosinophils without well-developed granulomatous features. (**b**) Higher-magnification photomicrograph showing a thrombosed blood vessel containing multiple cross sections of dirofilarial organisms. (**c**) High-magnification view of the organism cut in cross section showing the thick cuticle surrounding complex internal structures

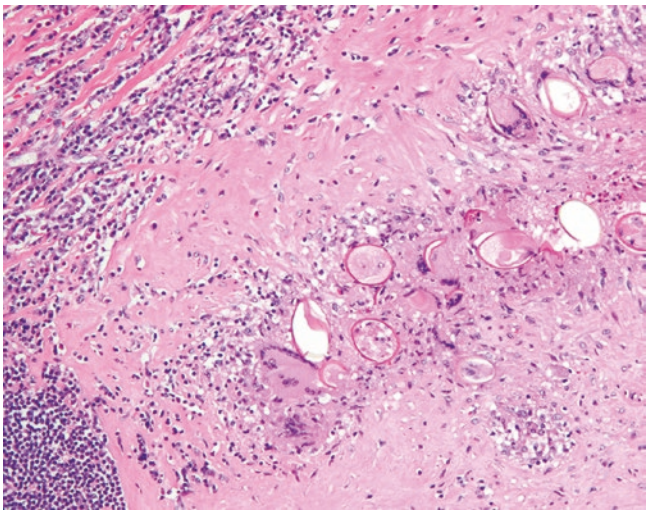

Fig. 4.55 Paragonimiasis (lung fluke). High-magnification view of the wall of a cystic lung lesion showing several oval-shaped eggs with a refractile wall. There are associated fibrosis, chronic inflammation with eosinophils, and multinucleated foreign body giant cells

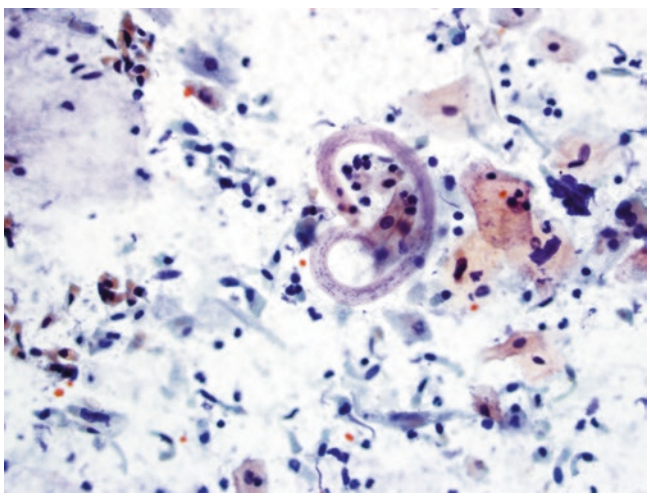

Fig. 4.56 Strongyloidiasis. Papanicolaou stain of bronchoalveolar lavage fluid showing a curved larva of *Strongyloides stercoralis* in a background of mixed inflammation

Suggested Reading

El-Zammar OA, Katzenstein AL. Pathological diagnosis of granulomatous lung disease: a review. Histopathology. 2007;50:289–310.

Gill JR, Sheng ZM, Ely SF, Guinee DG, Beasley MB, Suh J, et al. Pulmonary pathologic findings of fatal 2009 pandemic influenza A/H1N1 viral infections. Arch Pathol Lab Med. 2010;134:235–43.

Hartel PH, Shilo K, Klassen-Fischer M, Neafie RC, Ozbudak IH, Galvin JR, et al. Granulomatous reaction to *Pneumocystis jirovecii*: clinicopathologic review of 20 cases. Am J Surg Pathol. 2010;34:730–4.

Katzenstein A. Unusual pneumonias and granulomatous infections. In: Katzenstein and Askin's surgical pathology of non-neoplastic lung disease. 4th ed. Philadelphia: Elsevier; 2006. p. 261–350.

Kwon KY, Colby TV. *Rhodococcus equi* pneumonia and pulmonary malakoplakia in acquired immunodeficiency syndrome. Pathologic features. Arch Pathol Lab Med. 1994;118:744–8.

Oddo D, Gonzalez S. Actinomycosis and nocardiosis. A morphologic study of 17 cases. Pathol Res Pract. 1986;181:320–6.

Sangoi AR, Rogers WM, Longacre TA, Montoya JG, Baron EJ, Banaei N. Challenges and pitfalls of morphologic identification of fungal infections in histologic and cytologic specimens: a ten-year retrospective review at a single institution. Am J Clin Pathol. 2009;131:364–75.

Travis WD, Pittaluga S, Lipschik GY, Ognibene FP, Suffredini AF, Masur H, et al. Atypical pathologic manifestations of *Pneumocystis carinii* pneumonia in the acquired immune deficiency syndrome. Review of 123 lung biopsies from 76 patients with emphasis on cysts, vascular invasion, vasculitis, and granulomas. Am J Surg Pathol. 1990;14:615–25.

Winn WC Jr, Myerowitz RL. The pathology of the legionella pneumonias. A review of 74 cases and the literature. Hum Pathol. 1981;12:401–22.

Diseases of Cartilaginous and Noncartilaginous Airways

5

Chen Zhang and Jeffrey L. Myers

Diseases of cartilaginous (large) and noncartilaginous (small) airways include various nonspecific inflammatory and destructive lesions. The diagnoses of these diseases are usually made clinically and rarely require biopsy. However, histologic abnormalities involving the airways are commonly encountered in lung biopsies, lobectomy specimens, lung explants, and autopsies, either as primary diagnoses or as secondary findings in other conditions. Table 5.1 lists the major disease categories discussed in this chapter.

Table 5.1 Major airway diseases

Large airway diseases
Asthma
Allergic bronchopulmonary aspergillosis
Bronchiectasis
Cystic fibrosis
Plastic bronchitis
Small airway diseases
Follicular bronchiolitis (discussed in Chap. 11)
Respiratory bronchiolitis
Constrictive bronchiolitis
Diffuse panbronchiolitis
Bronchiolitis not otherwise specified
Emphysema
Aspiration pneumonia

C. Zhang (✉)
Department of Pathology and Laboratory Medicine, Indiana University School of Medicine, Indianapolis, IN, USA
e-mail: chenzhan@iupui.edu

J. L. Myers
Department of Pathology, Michigan Medicine, Ann Arbor, MI, USA
e-mail: myerjeff@med.umich.edu

© Springer Science+Business Media, LLC, part of Springer Nature 2018
C. Zhang, J. L. Myers (eds.), *Atlas of Lung Pathology*, Atlas of Anatomic Pathology,
https://doi.org/10.1007/978-1-4939-8689-7_5

Asthma

Asthma is a chronic relapsing inflammatory disorder characterized by hyperreactive airways and is usually diagnosed clinically. Changes of asthma (Figs. 5.1, 5.2, 5.3, 5.4, 5.5, 5.6, 5.7 and 5.8) are usually incidental findings in transbronchial biopsies or surgical specimens removed for tumors or other lesions. Characteristic changes include goblet cell hyperplasia, thickened basement membrane, smooth muscle hyperplasia, and eosinophilic infiltrates. Although none of these changes is specific for asthma, recognizing the features of asthma may help in making correct diagnoses of other diseases commonly associated with asthma, such as eosinophilic pneumonia, eosinophilic granulomatosis with polyangiitis (Churg-Strauss disease), and allergic bronchopulmonary aspergillosis (ABPA). ABPA is distinguished by various combinations of eosinophilia that often take the form of eosinophilic pneumonia, mucoid impaction of bronchi characterized by histologically distinctive ("allergic") mucin, and bronchocentric granulomatosis.

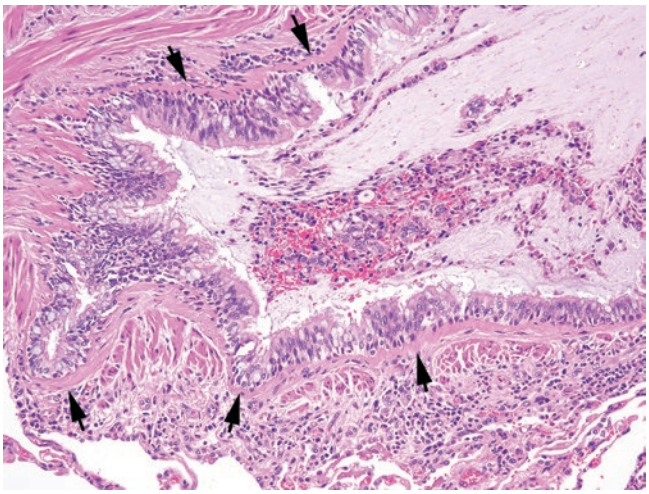

Fig. 5.2 Asthma. At higher magnification, the bronchial epithelium is remarkable for prominent goblet cell hyperplasia and thickened basement membrane (*arrows*). The bronchial wall shows smooth muscle hyperplasia and mild chronic inflammation. The lumen of the airway is almost completely occluded with a mucus plug

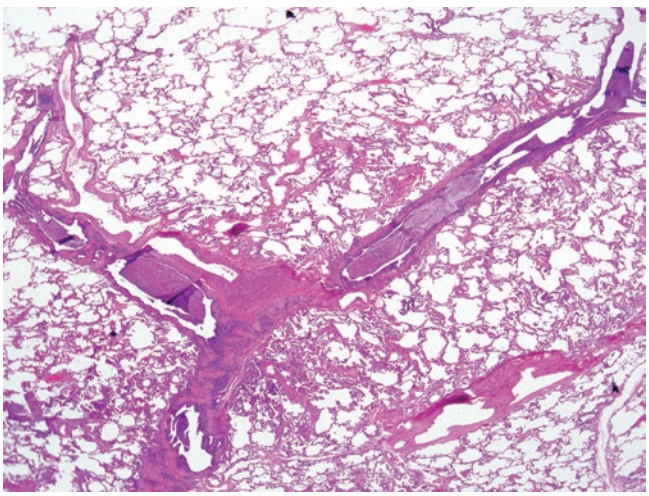

Fig. 5.1 Asthma. At low magnification, multiple airways are filled with mucus plugs. No significant inflammation is present. The lung parenchyma is normal

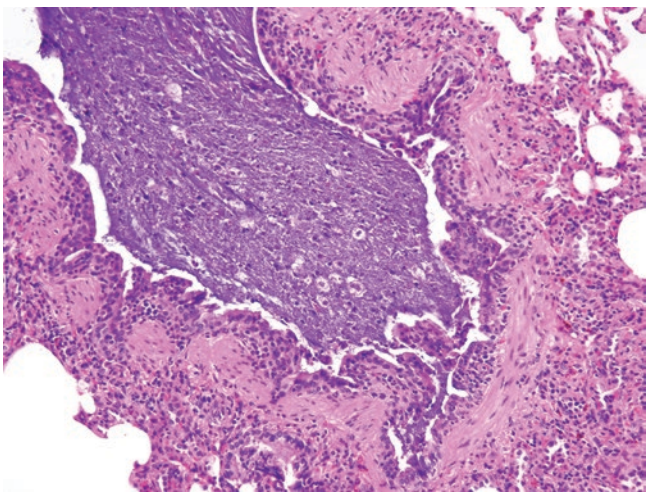

Fig. 5.3 Asthma. Another high-magnification photomicrograph showing an inflamed airway in a patient with asthma showing prominent smooth muscle hyperplasia, acute and chronic inflammatory infiltrates, and mucus plugging

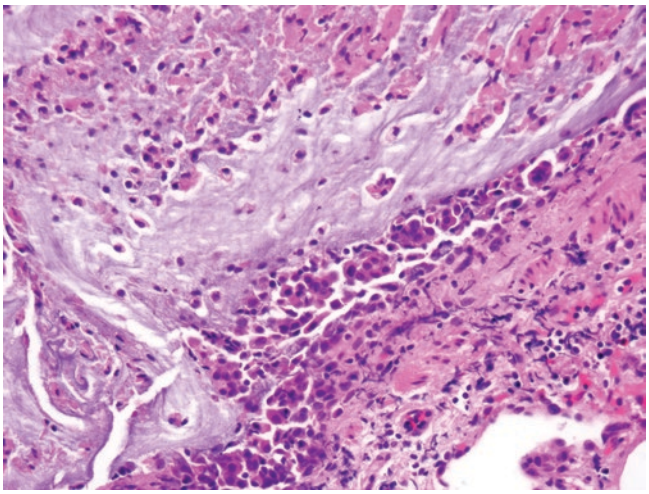

Fig. 5.4 Asthma. High-magnification view of mucus plug containing eosinophils and accompanied by epithelial necrosis

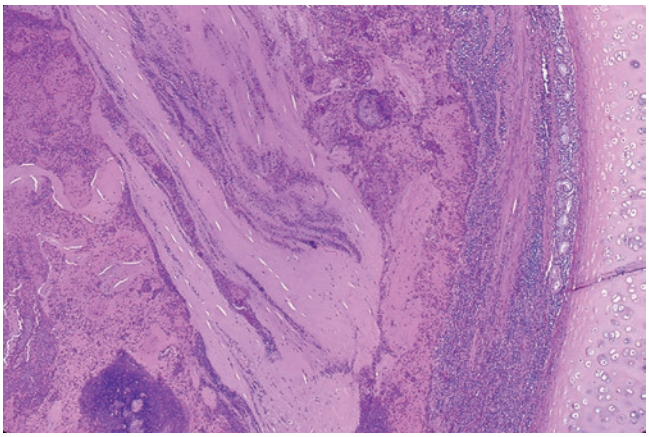

Fig. 5.6 Allergic bronchopulmonary aspergillosis associated with asthma. Low-magnification view of mucoid impaction of bronchi characterized by a dilated and inflamed cartilaginous airway impacted with allergic mucin. The allergic mucin contains layered cellular components in which eosinophils predominate within the lightly stained mucus

Fig. 5.5 Allergic bronchopulmonary aspergillosis associated with asthma. Gross photograph of a lobectomy specimen showing multiple dilated airways filled with green-gray, friable, desiccated mucus typical of mucoid impaction of bronchi

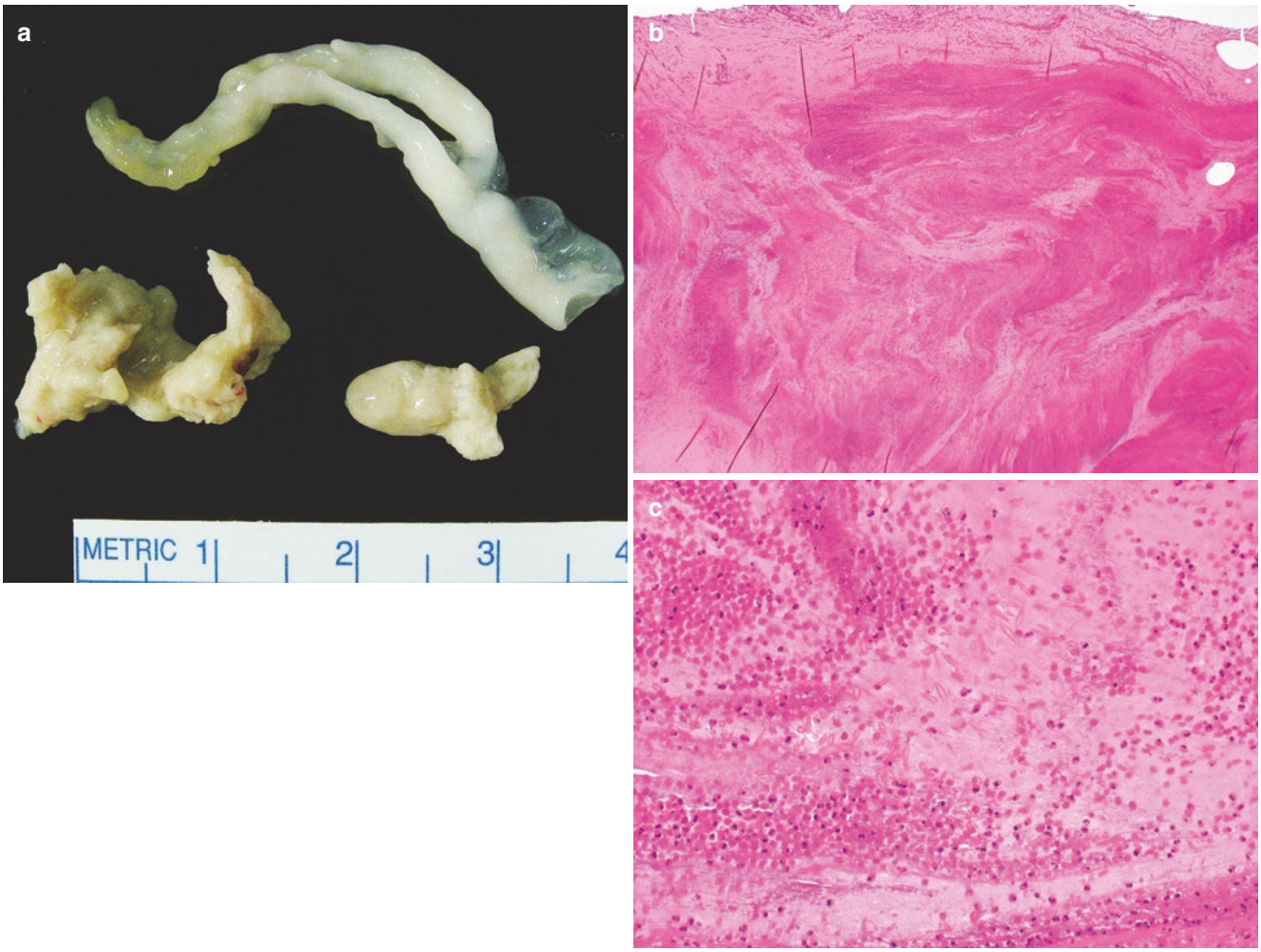

Fig. 5.7 Allergic mucin characteristic of mucoid impaction of bronchi (MIB) in allergic bronchopulmonary aspergillosis (ABPA). (**a**) Expectorated casts from a patient with MIB in ABPA. The gross appearance resembles plastic bronchitis (*see* Fig. 5.14); histologic features are helpful in distinguishing the two. (**b**) Low-magnification photomicrograph showing expectorated cast from a patient with ABPA. The alternating layers of inspissated mucus and degenerating eosinophils are characteristic of the allergic mucin that defines MIB in ABPA. (**c**) High-magnification photomicrograph of the allergic mucin illustrated in **b**, showing degenerating eosinophils and numerous Charcot-Leyden crystals, which are the breakdown products of eosinophilic granules

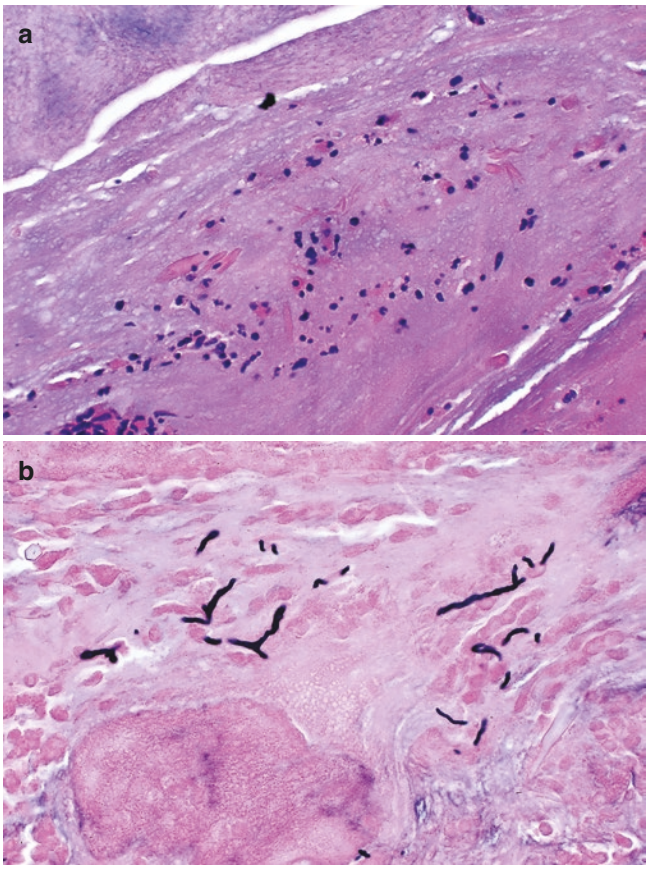

Fig. 5.8 Allergic mucin in allergic bronchopulmonary aspergillosis (ABPA) associated with asthma. (**a**) Another high-magnification view of allergic mucin with Charcot-Leyden crystals and degenerating eosinophils. (**b**) High-magnification view of Gomori methenamine silver (GMS) stained section showing fragmented, degenerating fungal hyphae in the allergic mucin from a patient with ABPA. The organisms are often rare in this condition and are largely limited to the allergic mucin without evidence of tissue invasion

Bronchiectasis

Bronchiectasis (Figs. 5.9, 5.10, 5.11, 5.12 and 5.13) is permanent dilation of bronchi and bronchioles, usually associated with necrotizing infections. Localized bronchiectasis is usually post-inflammatory following poorly treated or persistent pneumonia. The right middle lobe and lingula are especially susceptible to localized bronchiectasis (middle lobe syndrome). Obstruction caused by tumors or aspirated foreign bodies may lead to localized post-obstructive bronchiectasis. Diffuse bilateral bronchiectasis is most commonly associated with cystic fibrosis.

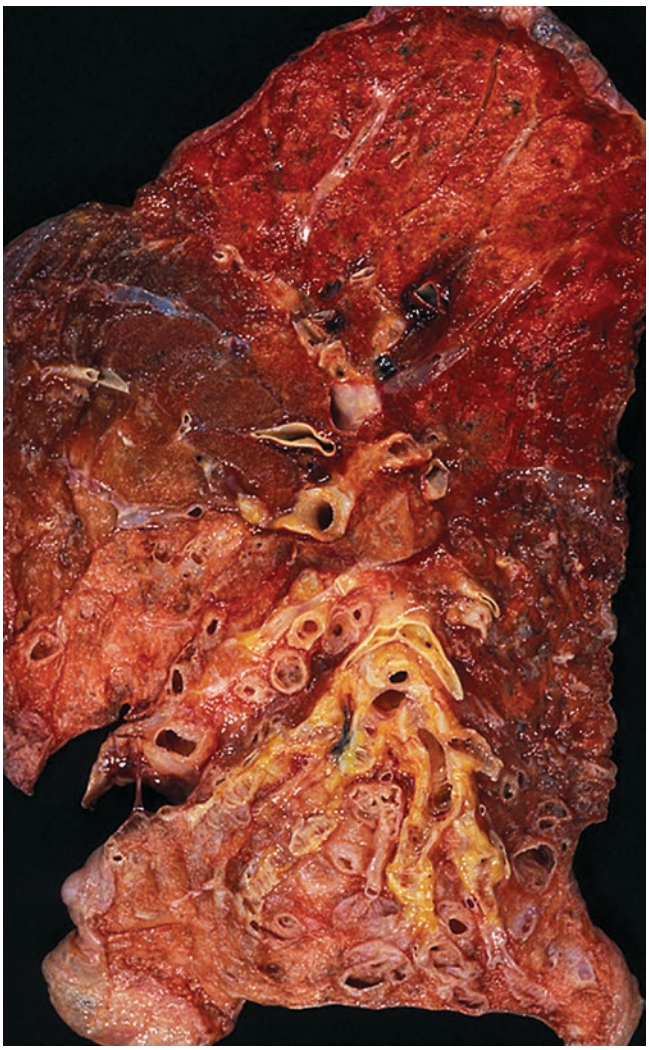

Fig. 5.9 Localized bronchiectasis. Gross photograph of a surgical specimen showing localized bronchiectasis. Dilated bronchi and associated bronchopneumonia and scarring are seen in the lower lobe, extending almost to the pleural surface. The bronchi and lung parenchyma in the upper lobe are normal

Fig. 5.10 Localized bronchiectasis. A close-up photograph of another resection specimen showing dilated bronchi with a characteristic corrugated mucosal surface

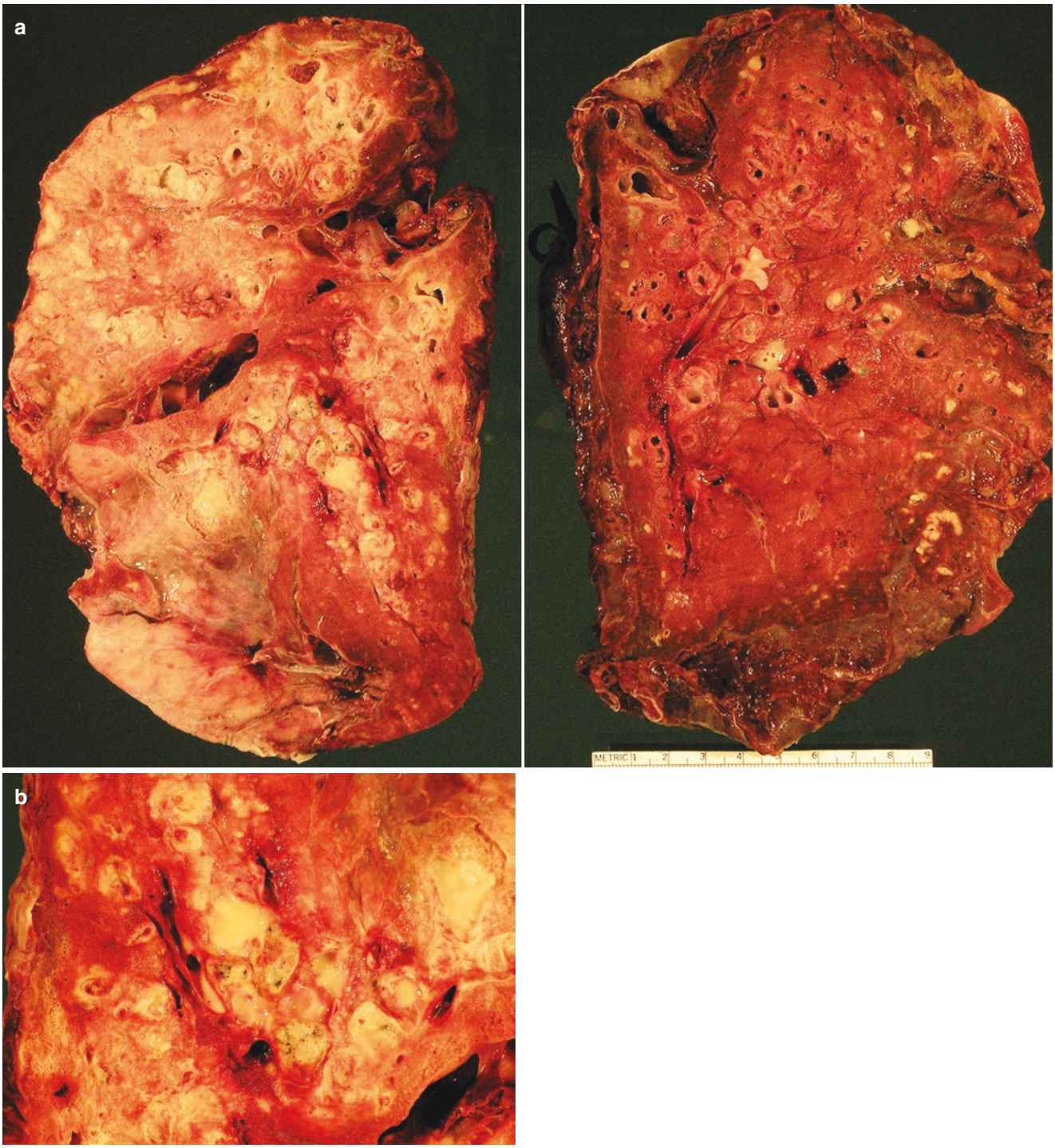

Fig. 5.11 Diffuse bronchiectasis. (**a**) Gross photograph of explanted lungs from a patient with cystic fibrosis. The cut surface shows diffusely dilated bronchi, some of which are filled with purulent exudates. (**b**) A close-up view showing the dilated bronchi filled with purulent exudates. There is also prominent peribronchial fibrosis and scarring, with very limited intervening normal lung parenchyma

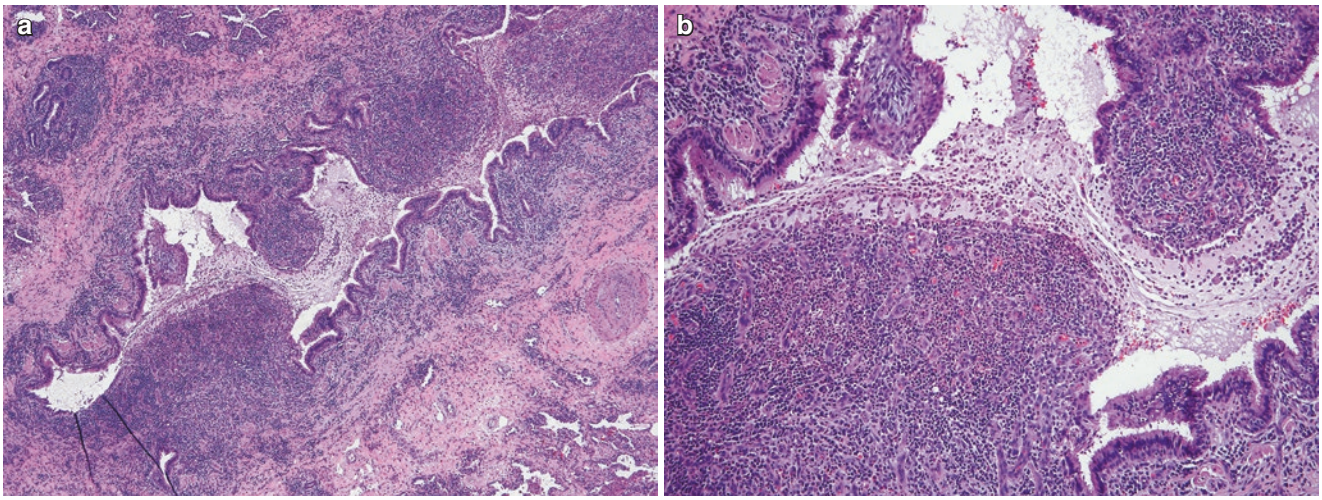

Fig. 5.12 Bronchiectasis. (**a**) Low-magnification photomicrograph showing a dilated bronchus with prominent acute and chronic inflammation with lymphoid aggregates and scarring of more distal peribronchial lung tissue. The integrity of the bronchial wall has been destroyed by inflammation and fibrosis, with an incomplete smooth muscle layer and attenuation of cartilage. (**b**) A higher-magnification photomicrograph shows focal necrosis of the lining respiratory epithelium with tufts of granulation tissue that are common and contribute to the risk of hemoptysis in these patients

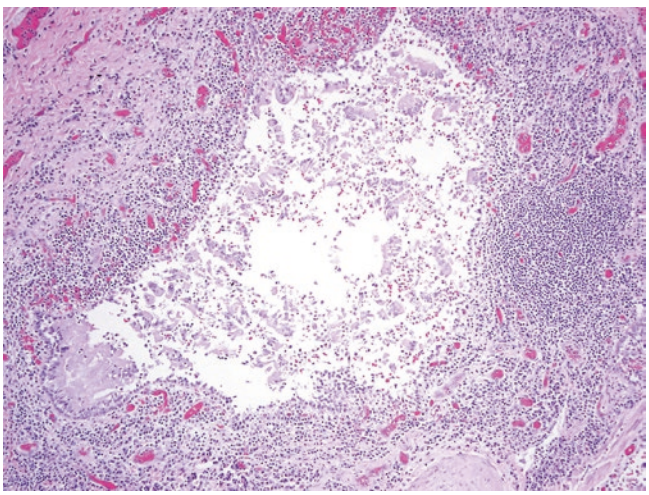

Fig. 5.13 Bronchiectasis. A photomicrograph showing another example of bronchiectasis in which there is severe acute and chronic inflammation with extensive necrosis of respiratory epithelium, peribronchial fibrosis, and an incomplete smooth muscle layer. The lumen contains sloughed epithelial cells and neutrophils

Plastic Bronchitis

Plastic bronchitis (Figs. 5.14 and 5.15) is a rare condition in which casts form in the tracheobronchial tree, causing potentially life-threatening airway obstruction and asphyxiation. It has been reported mainly in children with congenital heart diseases, especially in those patients who underwent corrective surgical procedures. Other associated conditions include infections, cystic fibrosis, and sickle cell disease. In rarely reported sporadic adult patients, the etiology is unknown. The expectorated bronchial casts grossly resemble the mucus plugs of mucoid impaction in patients with allergic bronchopulmonary aspergillosis (ABPA); however, the casts in plastic bronchitis are mainly made up of fibrin with variable numbers of mononuclear inflammatory cells rather than the allergic mucin typical of ABPA.

Fig. 5.14 Plastic bronchitis. Gross photograph of an expectorated bronchial cast resembling a tree with branches. The size and shape of the casts may vary from small segmental casts to large casts filling the entire tracheobronchial tree of a lung

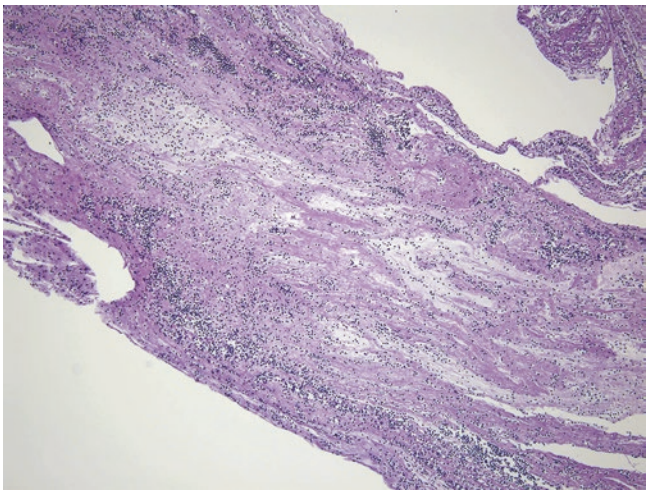

Fig. 5.15 Plastic bronchitis. Low-magnification photomicrograph of an expectorated cast showing a combination of fibrin and small lymphocytes

Respiratory Bronchiolitis

Respiratory bronchiolitis (RB) (Figs. 5.16, 5.17, 5.18 and 5.19) is a lesion that is present in almost all current (and many former) smokers in whom it usually represents an incidental finding of limited clinical and physiologic significance beyond corroborating a smoking history. It may remain for a prolonged period (years) after a patient stops smoking. The characteristic feature is clusters of lightly pigmented macrophages situated within the lumens of distal airways and peribronchiolar air spaces. The pigment is finely granular and usually stains positive with a Prussian blue iron stain, but it lacks the coarse refractile granules more characteristic of bleeding-associated hemosiderin. On rare occasions, this lesion may cause a syndrome of mild restrictive lung disease referred to as respiratory bronchiolitis/interstitial lung disease (RBILD) (*see* Chap. 6).

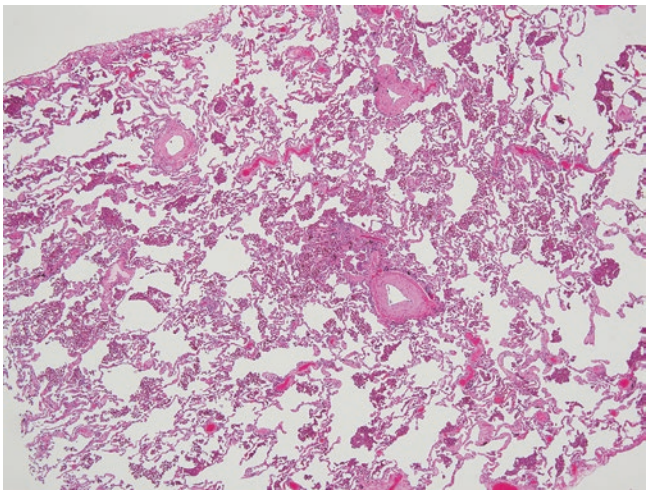

Fig. 5.16 Respiratory bronchiolitis. Low-magnification photomicrograph of respiratory bronchiolitis in a patient with RBILD. Lightly pigmented alveolar macrophages are clustered within the lumina of bronchioles and spill into adjacent air spaces

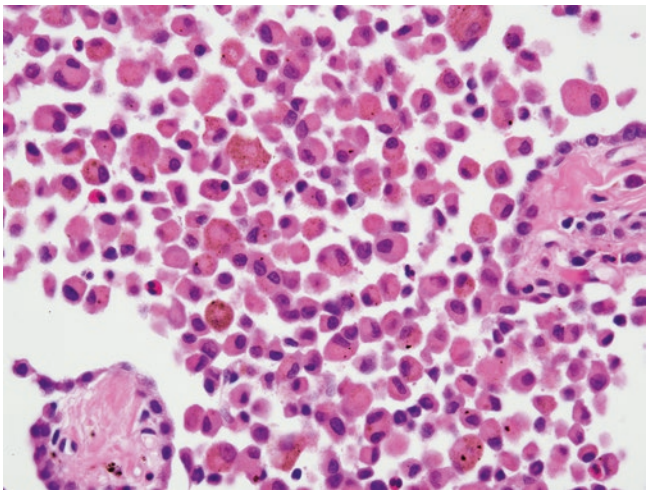

Fig. 5.18 Respiratory bronchiolitis. High-magnification photomicrograph showing the finely granular brown pigment typical of respiratory bronchiolitis. Occasional eosinophils are often present but should not be numerous

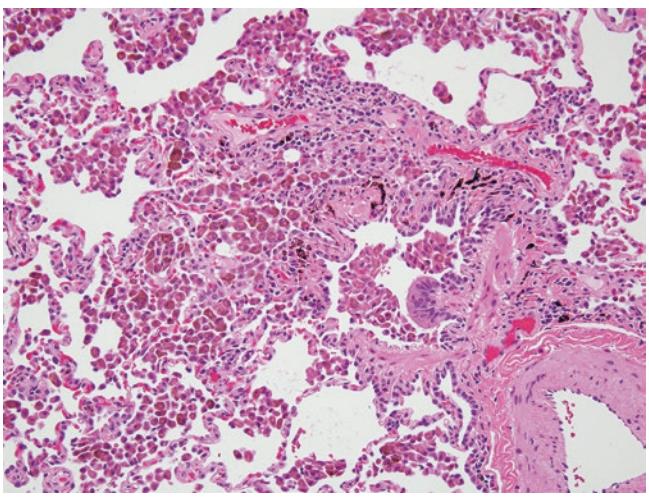

Fig. 5.17 Respiratory bronchiolitis. High-magnification photomicrograph from the same biopsy illustrated in Fig. 5.16 showing finely granular brown (smoker's) pigment in the cytoplasm of alveolar macrophages

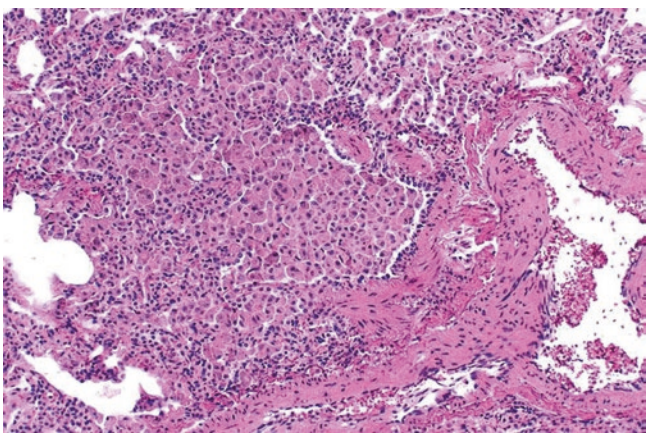

Fig. 5.19 Respiratory bronchiolitis. Another example showing a confluent aggregate of pigmented macrophages filling the entire lumen of the respiratory bronchiole and extending into adjacent alveolar spaces

Constrictive (Obliterative) Bronchiolitis

Constrictive (obliterative) bronchiolitis (Figs. 5.20, 5.21, 5.22, 5.23 and 5.24) is a rare small airway disease that is most commonly encountered in lung or stem-cell transplant recipients in whom it is a manifestation of chronic rejection or graft-versus-host disease, respectively. Other less common causes include infections, drug toxicities, connective tissue diseases (rheumatoid arthritis), and diffuse idiopathic pulmonary neuroendocrine cell hyperplasia (DIPNECH). In rare patients it may be a form of idiopathic small airway disease. Patients usually are first seen with severe cough and dyspnea. Pulmonary function tests show obstructive changes. Over-inflation and air-trapping are the usual findings radiologically. The disease is progressive in most patients.

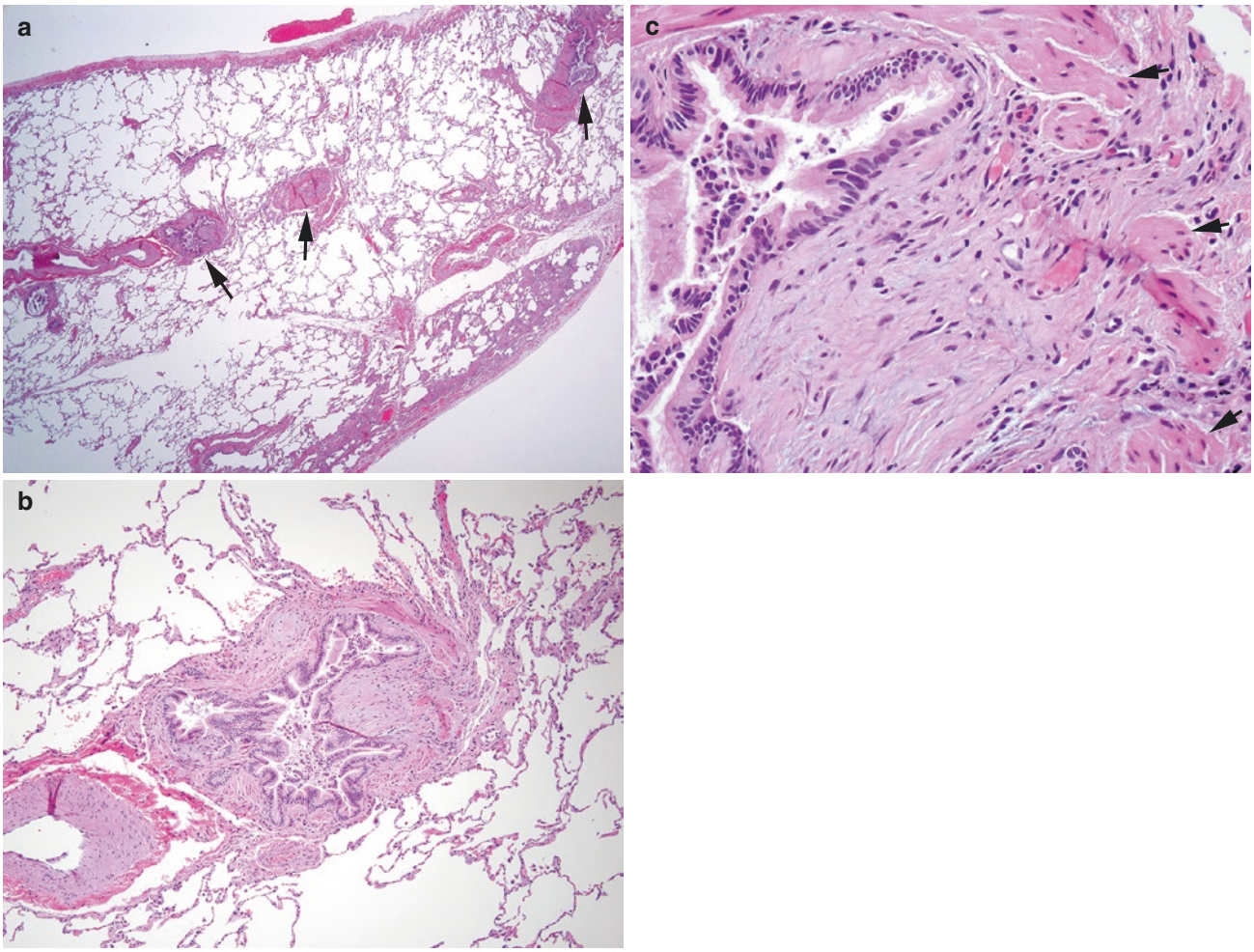

Fig. 5.20 Constrictive bronchiolitis. (**a**) Low-magnification photomicrograph of a lung wedge biopsy showing largely unremarkable alveolar lung parenchyma. A few bronchioles (*arrows*) have thickened walls, a feature that is inconspicuous and easily overlooked at this magnification. (**b**) Intermediate-magnification view showing a narrowed lumen caused by subepithelial fibrosis. (**c**) High-magnification photomicrograph illustrating prominent fibroblast proliferation in a collagenous and myxoid stroma situated between the respiratory epithelium and the smooth muscle layer (*arrows*)

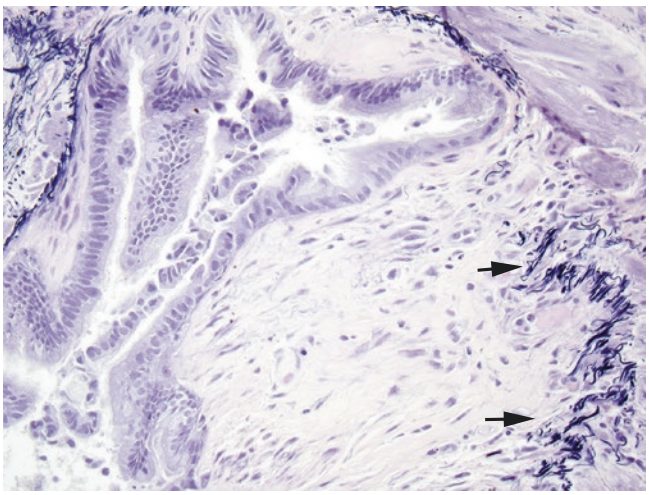

Fig. 5.21 Constrictive bronchiolitis. High-magnification photomicrograph of an elastic tissue stain highlights the fibrosis that separates the respiratory epithelium from the subepithelial elastic layer (*arrows*)

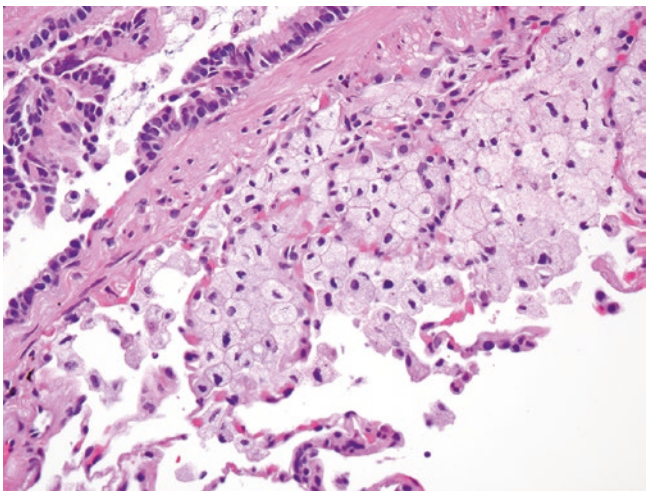

Fig. 5.23 Constrictive bronchiolitis. High-magnification photomicrograph showing the accumulation of foamy macrophages in peribronchiolar alveolar spaces, a common nonspecific finding indicating small airway obstruction

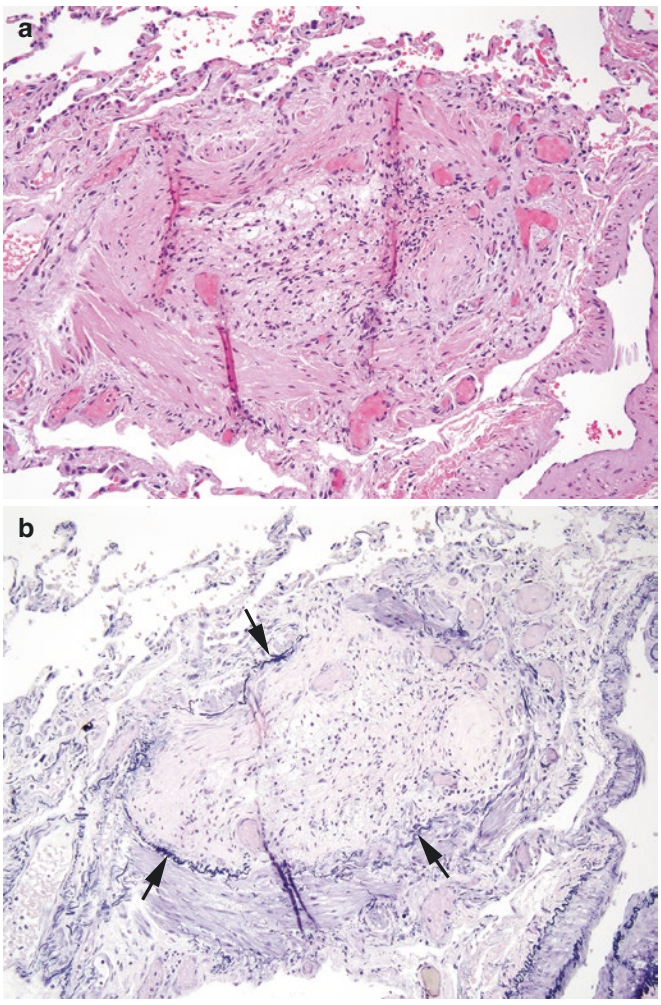

Fig. 5.22 Constrictive bronchiolitis. (**a**) High-magnification photomicrograph of bronchiole illustrated in Fig. 5.20a. The lumen of the bronchiole is completely obliterated by fibrosis with a scant infiltrate of inflammatory cells, including foamy histiocytes. The bronchiole is recognizable by its residual smooth muscle layer and the adjacent small muscular pulmonary artery. (**b**) An elastic stain highlights the residual elastic layer (*arrows*) of the obliterated bronchiole

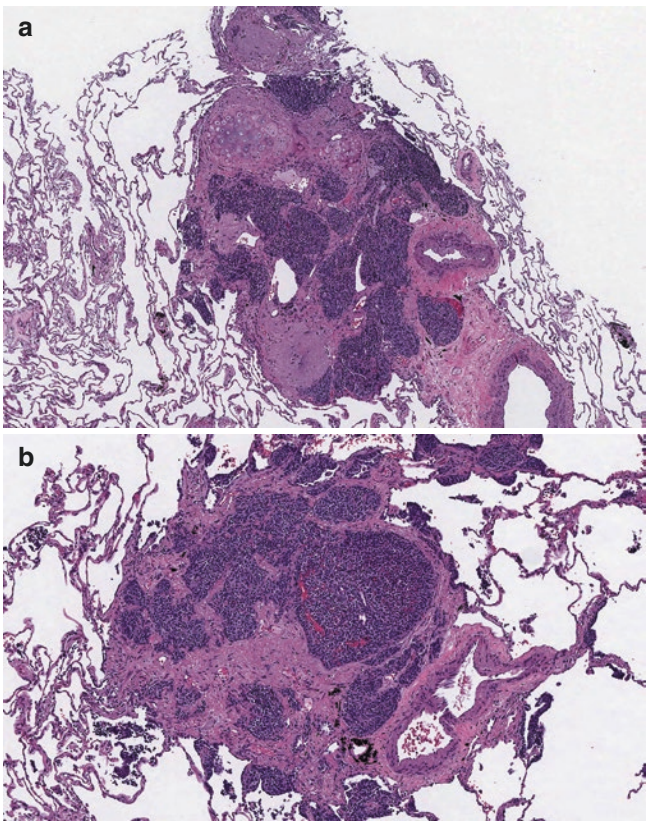

Fig. 5.24 Diffuse neuroendocrine cell hyperplasia (multiple carcinoid tumorlets) with constrictive bronchiolitis. (**a**) Low-magnification photomicrograph showing a carcinoid tumorlet in a cartilaginous airway with an obliterated lumen from a patient who had never smoked. Mosaic attenuation on a high-resolution computed tomography scan and airflow limitation on pulmonary function studies were found. (**b**) Low-magnification photomicrograph of the same lung biopsy showing an obliterated bronchiolar lumen associated with a carcinoid tumorlet

Diffuse Panbronchiolitis

Diffuse panbronchiolitis (Figs. 5.25, 5.26 and 5.27) is a rare form of chronic bronchiolitis involving mainly the respiratory bronchioles with a striking infiltrate of foamy macrophages. Diffuse panbronchiolitis occurs primarily in Japan, although rare examples have been reported in Western countries. Extended therapy with macrolide antibiotics has significantly improved the prognosis of this potentially fatal condition. The diagnosis should be made only in the appropriate clinical setting, given that similar histologic findings have been reported in other conditions.

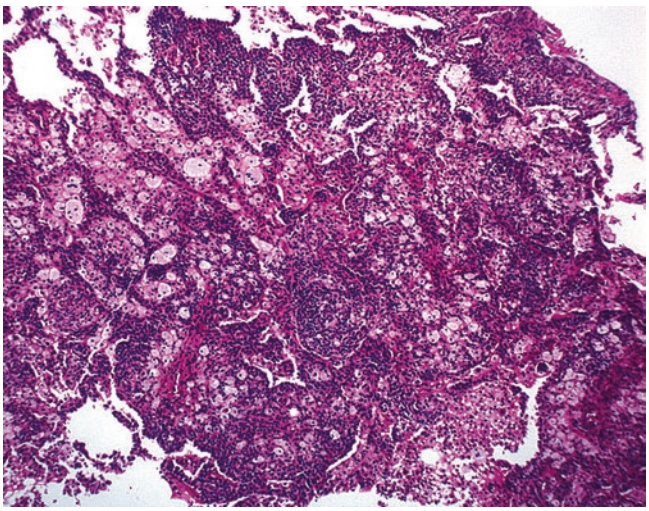

Fig. 5.25 Diffuse panbronchiolitis. Photomicrograph showing a characteristic combination of peribronchiolar inflammation rich in lymphocytes accompanied by a striking accumulation of foamy macrophages in the peribronchiolar interstitium

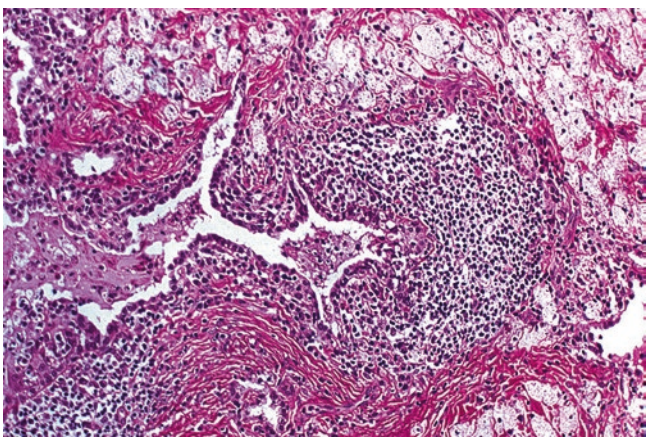

Fig. 5.26 Diffuse panbronchiolitis. High-magnification view of another bronchiole showing a chronic bronchiolitis in which lymphocytes predominate and large numbers of foamy macrophages expand the wall of the bronchiole and extend into adjacent alveolar septa

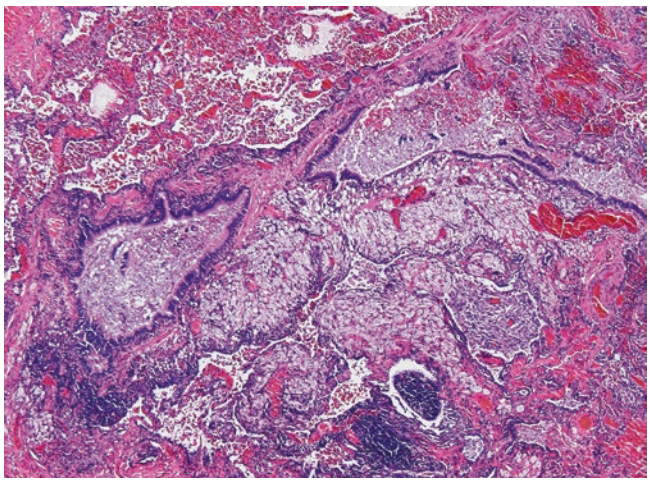

Fig. 5.27 Diffuse panbronchiolitis-like changes in a patient with sequestration. This low- magnification photomicrograph shows histologic findings typical of diffuse panbronchiolitis but in a patient with an intralobar sequestration, illustrating that histology by itself is insufficient to establish the diagnosis of diffuse panbronchiolitis

Bronchiolitis, NOS

Bronchiolitis, not otherwise specified (NOS) (Figs. 5.28, 5.29, 5.30 and 5.31), is sometimes encountered in patients without evidence of infection, bronchiectasis, underlying systemic disease, or other potential causes for primary airway disease. Patients with unexplained bronchiolitis may or may not have evidence of physiologically significant airflow limitation. Various combinations of acute and chronic inflammation are exquisitely localized to small airways with minimal extension into adjacent lung parenchyma. Inflammation of bronchiole walls may be accompanied by luminal inflammatory exudates, bronchiolectasis, and/or mucostasis. Acute bronchiolitis is commonly caused by bacterial infections, including classic *Mycoplasma* pneumonia. Chronic bronchiolitis may be accompanied by a distinctive combination of peribronchiolar fibrosis and extension of hyperplastic columnar respiratory epithelium onto fibrotic alveolar septa, a combination of findings referred to as *peribronchiolar metaplasia*. Peribronchiolar metaplasia may also occur in patients with other forms of diffuse parenchymal lung disease, including usual interstitial pneumonia and hypersensitivity pneumonia.

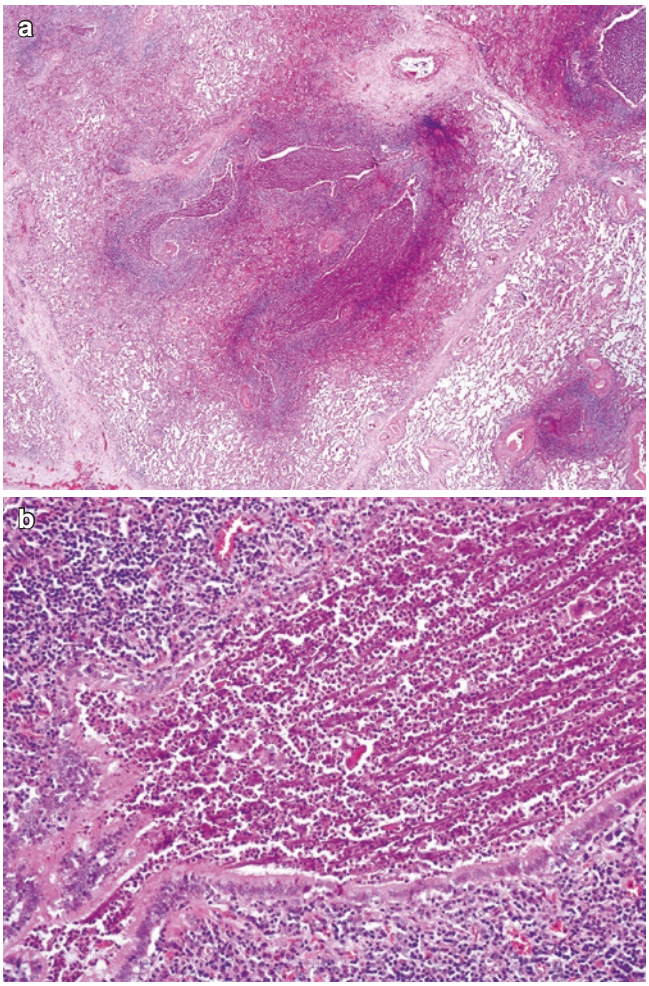

Fig. 5.28 Acute bronchiolitis caused by bacterial infection. (**a**) Low-magnification photomicrograph showing an acute inflammatory exudate distending bronchiole lumina with an acute and chronic inflammatory infiltrate expanding bronchiolar walls. The inflammation is exquisitely localized to the airways, leaving the surrounding lung parenchyma uninvolved. (**b**) High-magnification photomicrograph showing an acute suppurative inflammatory infiltrate distending the bronchiolar lumina. Chronic inflammation predominates in the bronchiole wall. A tissue Gram stain demonstrated bacterial cocci

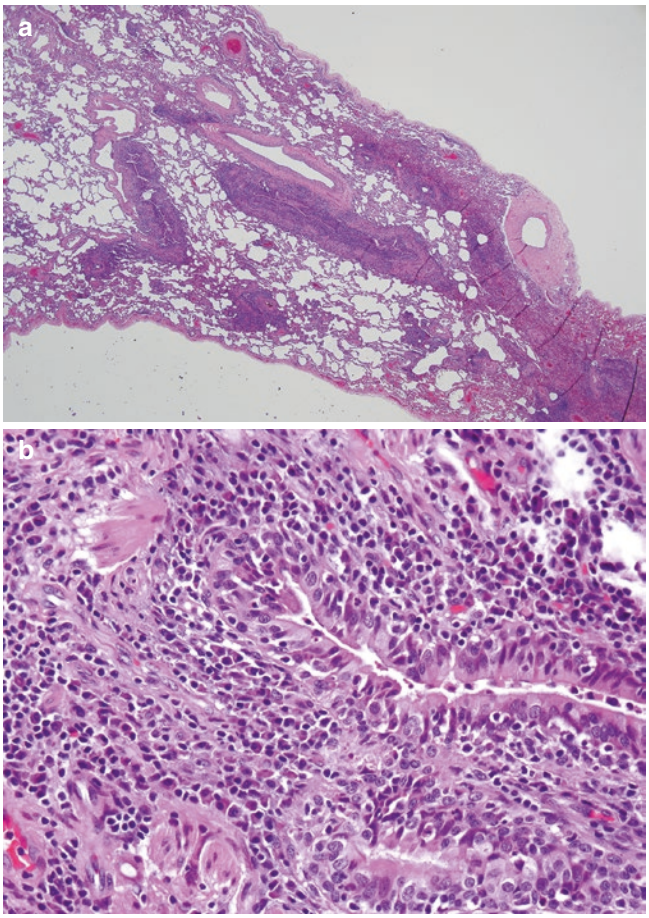

Fig. 5.29 Chronic bronchiolitis, NOS in a patient with systemic lupus erythematosus. (**a**) Low-magnification photomicrograph showing an inflammatory reaction involving the bronchioles without extending into the adjacent lung parenchyma. (**b**) At high magnification, the inflammatory infiltrate is composed of lymphocytes and plasma cells

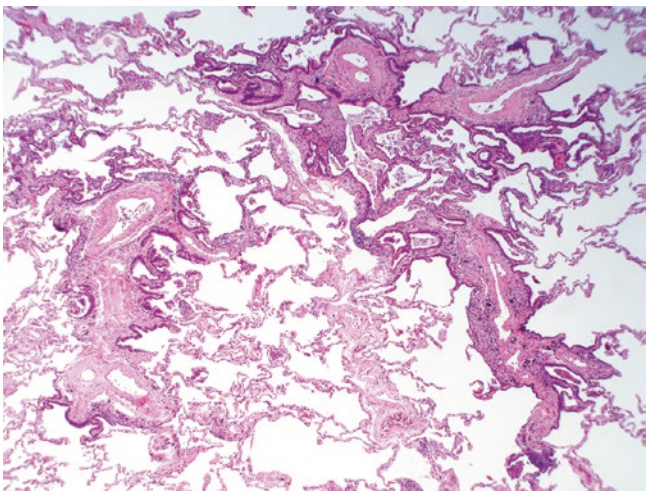

Fig. 5.30 Peribronchiolar metaplasia in chronic bronchiolitis, NOS. Photomicrograph showing chronic bronchiolitis accompanied by fibrosis that extends into peribronchiolar interstitium accompanied by hyperplasia of columnar respiratory epithelial cells. This is a relatively nonspecific manifestation of chronic small airway injury that can occur in a variety of contexts, including in patients with underlying hypersensitivity pneumonia and usual interstitial pneumonia. Occasionally peribronchiolar metaplasia occurs in isolation in patients with mild restrictive lung disease in whom there is no radiologic or histologic evidence of other forms of diffuse lung disease, a circumstance referred to as *peribronchiolar metaplasia-interstitial lung disease*

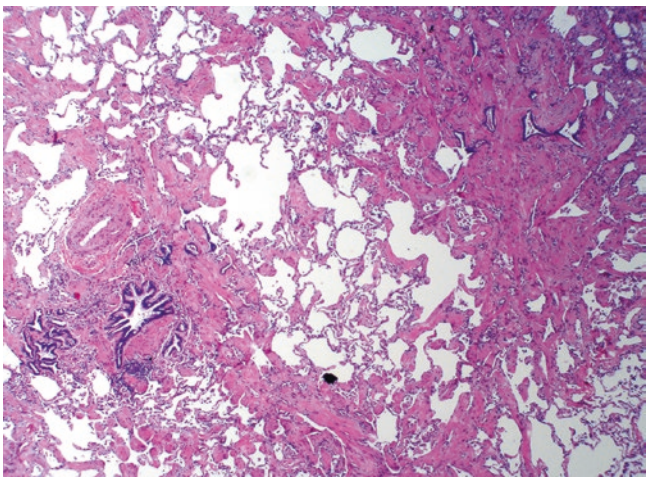

Fig. 5.31 Chronic bronchiolitis, NOS. Low-magnification photomicrograph showing the prominent smooth muscle hyperplasia sometimes associated with chronic small airway injury of any cause, including chronic bronchiolitis, NOS

Emphysema

Emphysema (Figs. 5.32, 5.33, 5.34, 5.35, 5.36 and 5.37) is defined as permanent enlargement of air spaces distal to terminal bronchioles accompanied by destruction of the walls without significant fibrosis. Emphysema is classified into three subtypes: centriacinar (centrilobular), distal acinar (paraseptal), and panacinar subtypes. Centrilobular emphysema shows a predilection for the upper lobes, is usually smoking-related, and is the most common subtype. Panacinar emphysema is associated with alpha-1 antitrypsin deficiency and tends to involve both upper and lower lung zones. Distal acinar emphysema, also commonly referred to as paraseptal emphysema, mainly involves paraseptal and subpleural parenchyma and may cause bullae and/or pleural blebs affiliated with spontaneous pneumothorax. Diagnosis of emphysema is usually based on clinical and radiologic features. Surgical specimens in which emphysema is encountered include lung resected for tumors, pleural bleb resections, and explanted lungs.

Placental transmogrification is an unusual pattern of parenchymal fragmentation seen in severe bullous emphysema, including rare examples of localized giant bullous emphysema presenting as enlarging unilocular cysts.

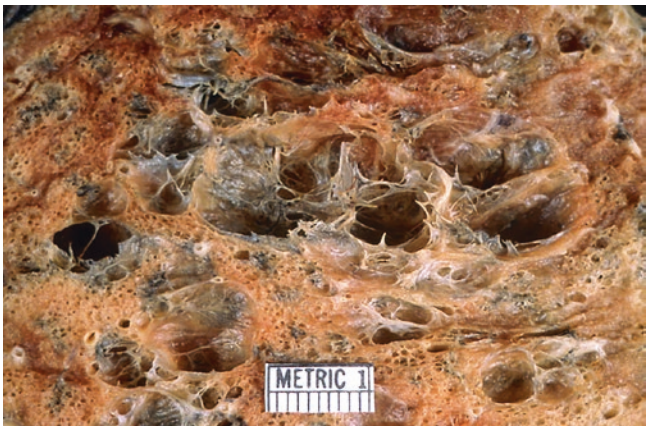

Fig. 5.32 Centrilobular emphysema. Gross photograph showing the cut surface of lung with enlarged air spaces distributed in a centrilobular fashion, leaving relatively spared parenchyma between emphysematous spaces and interlobular septa. No significant fibrosis is seen

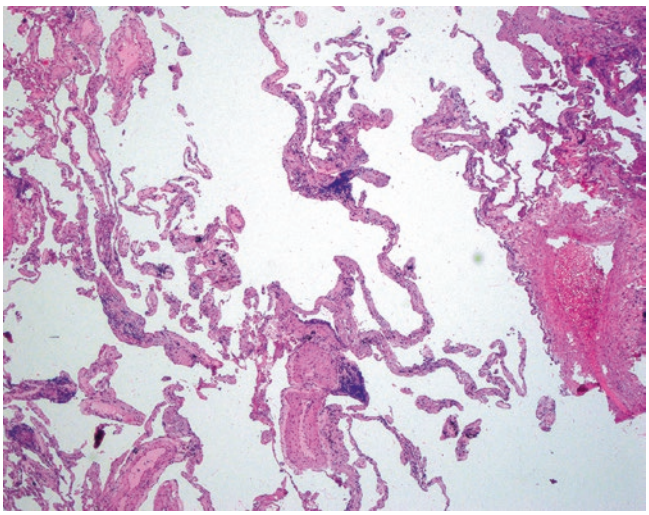

Fig. 5.33 Centrilobular emphysema. Low-magnification photomicrograph showing centrilobular emphysema characterized by enlarged air spaces and alveolar wall destruction

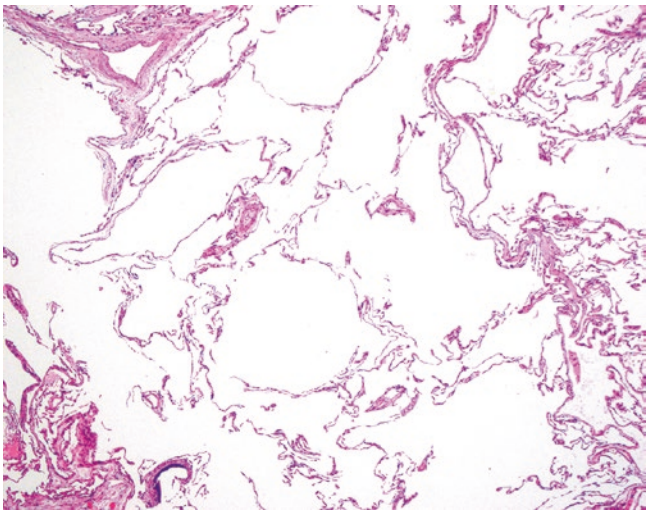

Fig. 5.34 Panacinar emphysema. Low-magnification photomicrograph showing panacinar emphysema characterized by diffusely enlarged air spaces. The alveolar walls are thin and fragmented

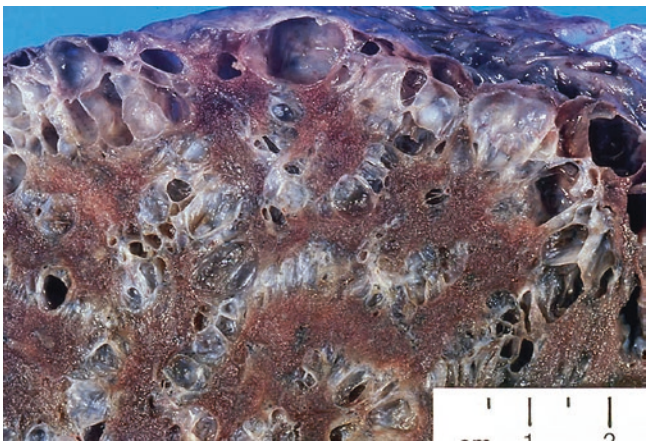

Fig. 5.35 Distal acinar (paraseptal) emphysema. Gross photograph showing the cut surface of the lung with striking distal acinar emphysema characterized by paraseptal and subpleural bullae and blebs

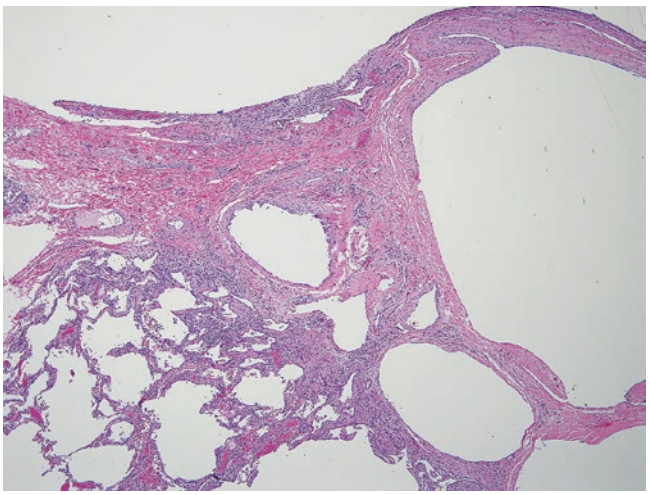

Fig. 5.36 Pleural blebs in distal acinar (paraseptal) emphysema. Low-magnification view of pleural blebs containing air collection within the visceral pleura resulting from rupture of subpleural alveoli and dissection of air into the pleural connective tissue. Fibrosis and chronic inflammation are commonly seen associated with pleural blebs. The immediately adjacent subpleural parenchyma also shows enlarged air spaces

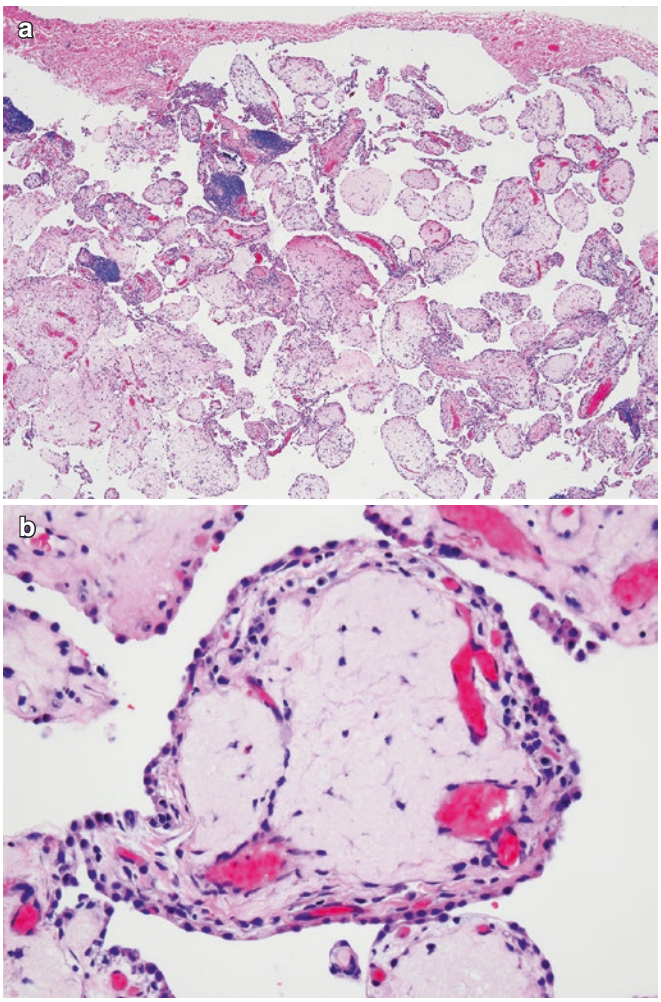

Fig. 5.37 Placental transmogrification in severe emphysema. (**a**) A large emphysematous bulla contains fragmented alveolar walls in which the interstitium is expanded by a combination of inflammation, fibrosis, and stromal mucins, resulting in papillary structures superficially resembling placental villi. (**b**) High-magnification photomicrograph showing fibrovascular cores lined by hyperplastic alveolar pneumocytes resembling placental chorionic villi

Aspiration Pneumonia

Aspiration pneumonia (Figs. 5.38, 5.39, 5.40, 5.41, 5.42, 5.43 and 5.44) caused by foreign material aspiration may present acutely as necrotizing bacterial bronchopneumonia or chronically with mild symptoms and pulmonary nodules or infiltrates. The latter presentation in patients without obvious risk factors for aspiration may raise the clinical suspicion of tumors and atypical infections. Granulomas and organizing pneumonia are commonly seen in aspiration pneumonia. The key to the diagnosis is the presence of foreign material. The aspirated foreign material varies in appearance and in amount. The most commonly encountered aspirated material is degenerated vegetable matter, followed by inert fillers (excipients) common in oral medications, including microcrystalline cellulose and crospovidone, and rarely degenerated skeletal muscle.

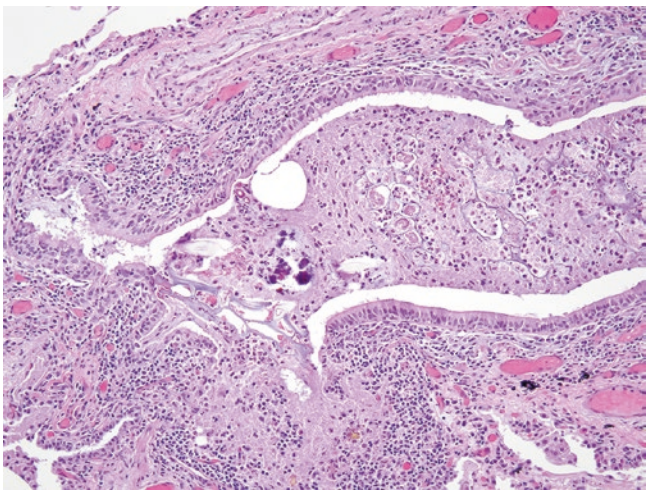

Fig. 5.38 Aspiration pneumonia. Photomicrograph showing degenerated vegetable matter within the bronchiolar lumen associated with a suppurative and fibrinous exudate. No granuloma or giant-cell reaction is present in this example

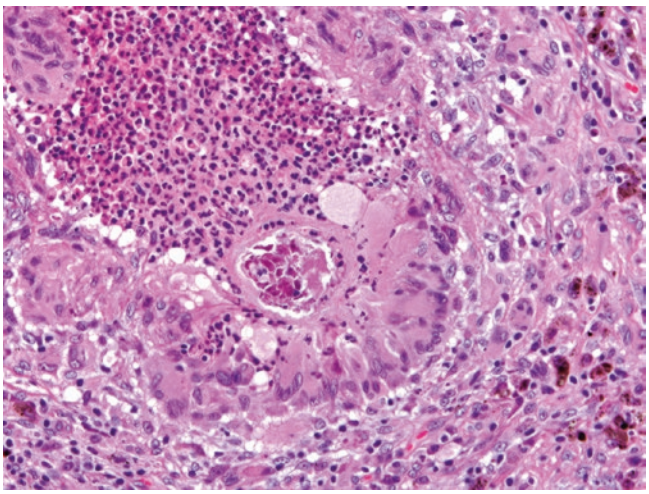

Fig. 5.40 Aspiration pneumonia. High-magnification photomicrograph showing degenerated vegetable matter associated with suppurative granulomatous inflammation

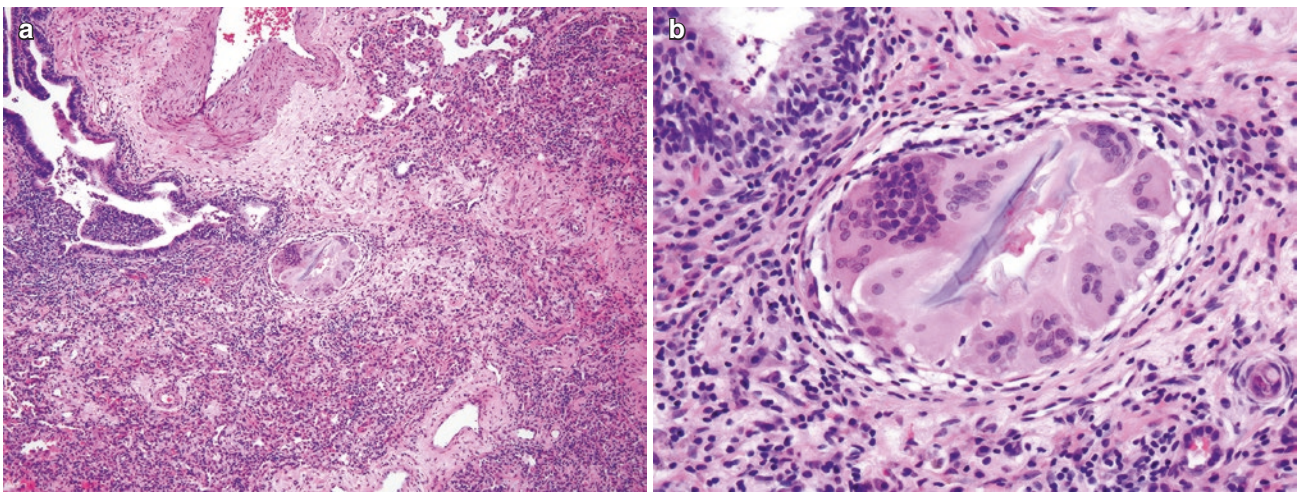

Fig. 5.39 Aspiration pneumonia. (**a**) Low-magnification photomicrograph showing bronchiolocentric chronic and granulomatous inflammation. (**b**) High-magnification view of granuloma composed of multiple giant cells surrounding aspirated vegetable matter

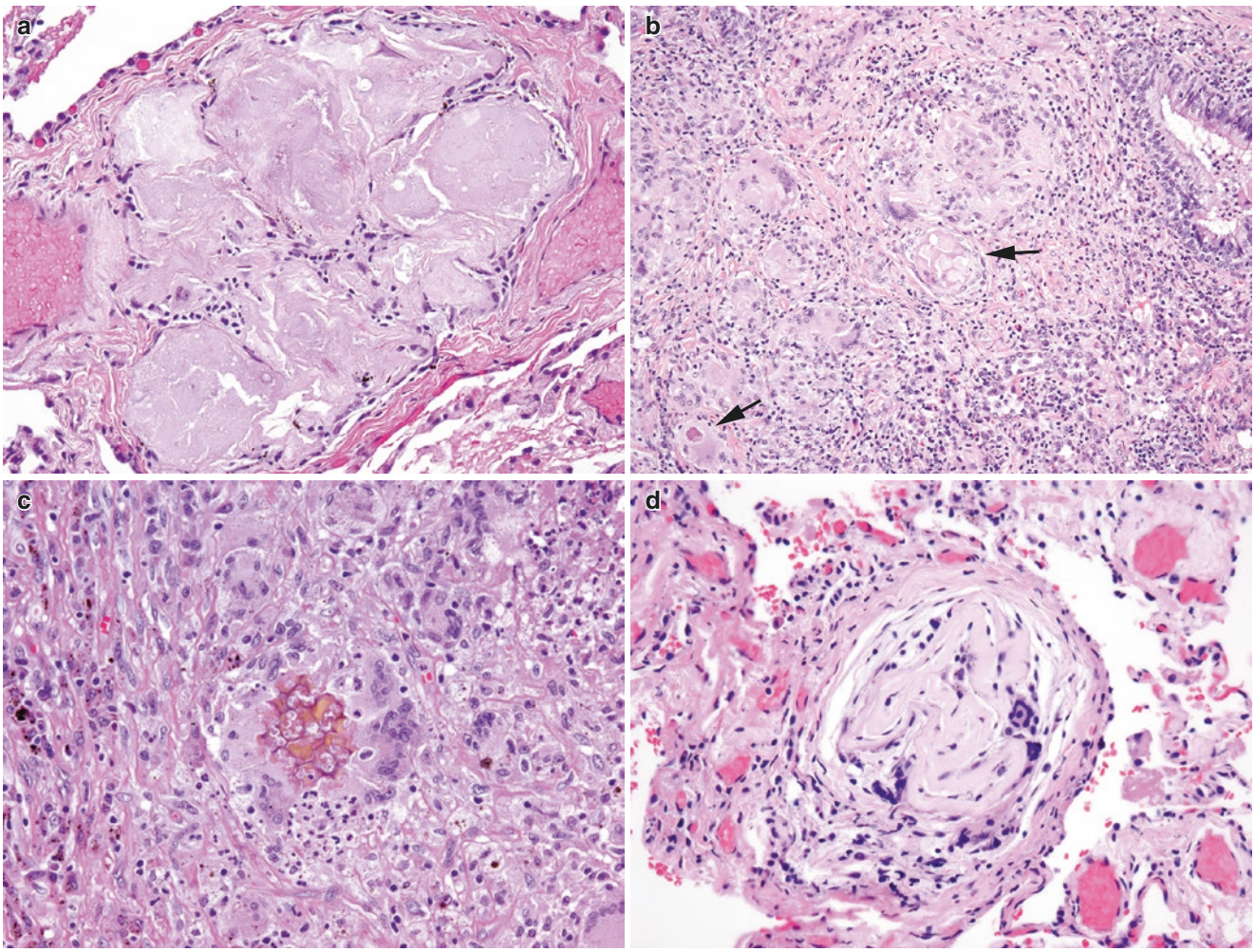

Fig. 5.41 Aspiration pneumonia showing multiple forms of degenerated vegetable matter. (**a**) High-magnification view showing multifaceted large eosinophilic particles lacking internal structures that are situated within the peribronchiolar interstitium and surrounded by a thin rim of histiocytes. (**b**) Another high-power view showing round eosinophilic structures (*arrows*) within multinucleated giant cells. (**c**) High-magnification photomicrograph showing brown amorphous matter within a giant cell. (**d**) High-power view showing collapsed, curved, elongated eosinophilic structures superficially resembling hyalinized blood vessels with an associated giant-cell reaction in peribronchiolar interstitium

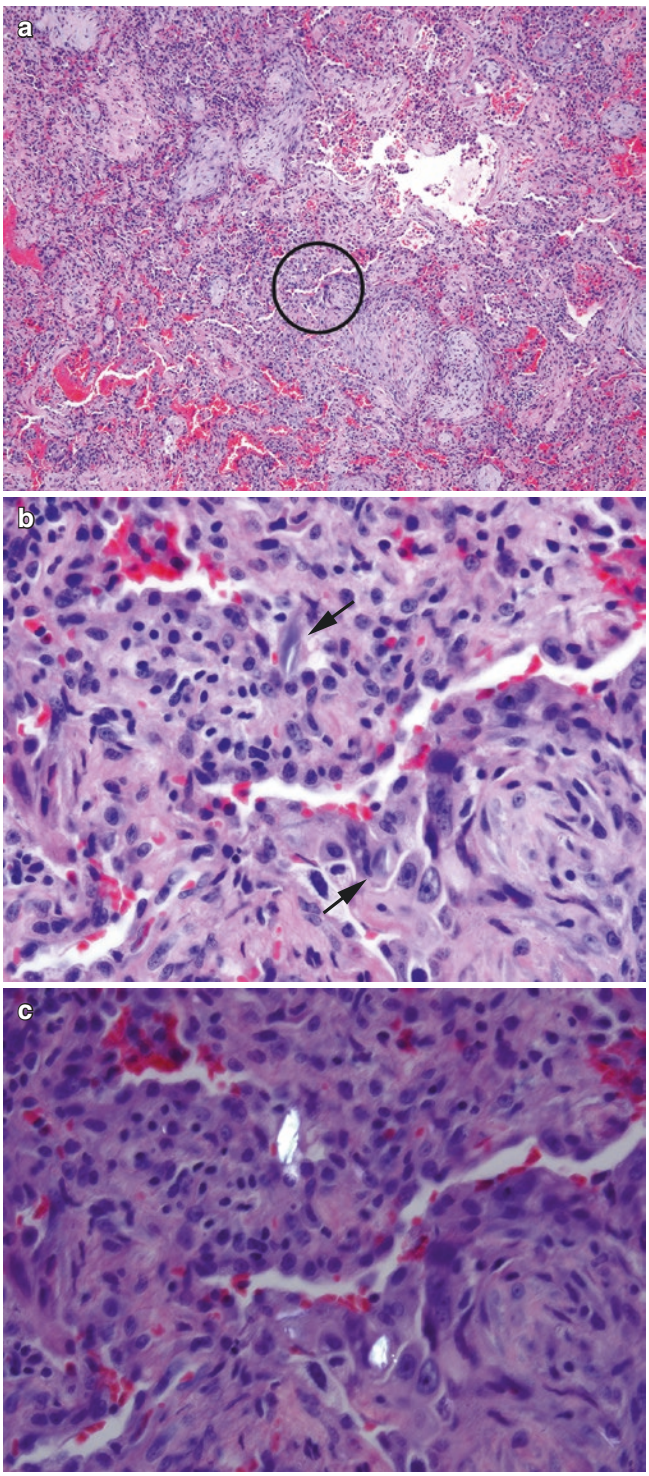

Fig. 5.42 Aspiration pneumonia. (**a**) Low-magnification photomicrograph showing changes of organizing pneumonia characterized by polypoid fibroblast plugs filling up air spaces. Organizing pneumonia is a common finding in aspiration and should prompt a search for other features that might establish aspiration as a likely etiology. (**b**) High-magnification view of the circled area in **a** showing pale-gray crystalline material (*arrows*) characteristic of microcrystalline cellulose, a common inert filler (excipient) in oral medications. (**c**) Microcrystalline cellulose is strongly birefringent when viewed with polarized light

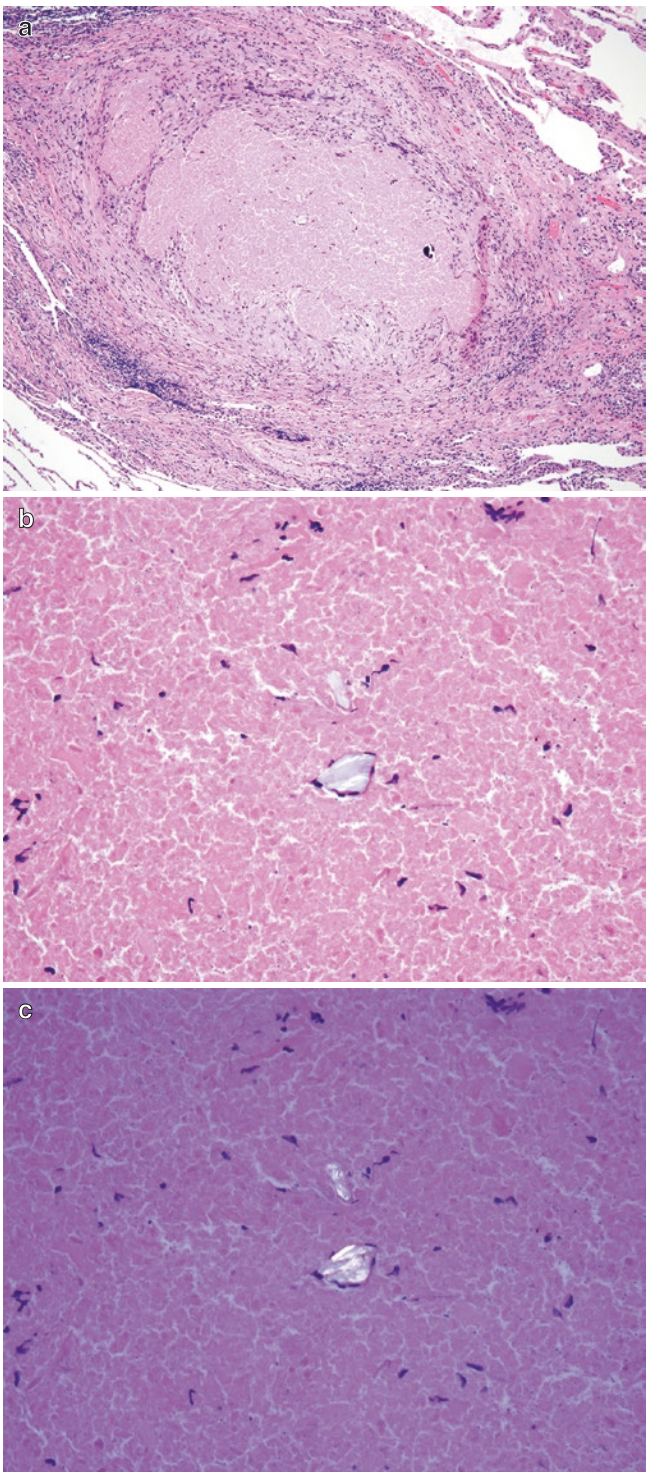

Fig. 5.43 Aspiration pneumonia. (**a**) Low-magnification photomicrograph showing necrotizing granulomatous inflammation centered on an airway ("bronchocentric granulomatosis"). (**b**) Higher magnification of the necrotic center demonstrates pale-gray particulates of microcrystalline cellulose. (**c**) The microcrystalline cellulose shows strong birefringence when viewed with polarized light

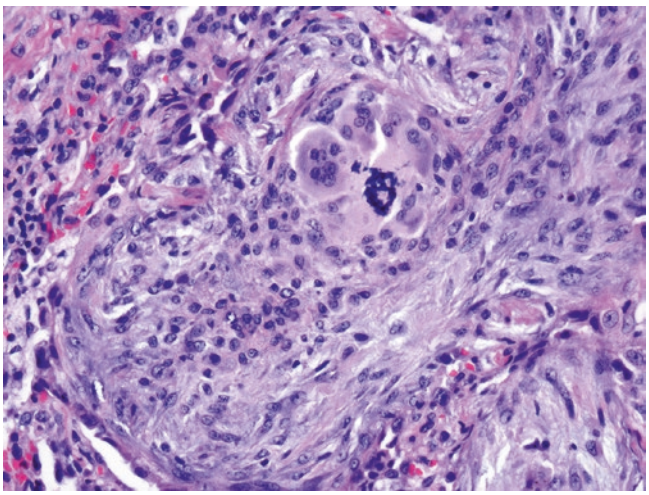

Fig. 5.44 Aspiration pneumonia. High-magnification photomicrograph showing a combination of granulomatous inflammation and organizing pneumonia associated with deeply basophilic, coral-like material consistent with crospovidone, another common filler in oral medications

Suggested Readings

Barnes TW, Vassallo R, Tazelaar HD, Hartman TE, Ryu JH. Diffuse bronchiolar disease due to chronic occult aspiration. Mayo Clin Proc. 2006;81:172–6.

Bosken CH, Myers JL, Greenberger PA, Katzenstein AL. Pathologic features of allergic bronchopulmonary aspergillosis. Am J Surg Pathol. 1998;12:216–22.

Fraig M, Shreesha U, Savici D, Katzenstein AL. Respiratory bronchiolitis: a clinicopathologic study in current smokers, ex-smokers, and never-smokers. Am J Surg Pathol. 2002;26:647–53.

Iwata M, Colby TV, Kitaichi M. Diffuse panbronchiolitis: diagnosis and distinction from various pulmonary diseases with centrilobular interstitial foam cell accumulations. Hum Pathol. 1994;25:357–63.

Kraft M, Mortenson RL, Colby TV, Newman L, Waldron JA, King TE Jr. Cryptogenic constrictive bronchiolitis. A clinicopathologic study. Am Rev Respir Dis. 1993;148(4, Pt 1):1093–101.

Kudoh S, Keicho N. Diffuse panbronchiolitis. Clin Chest Med. 2012;33:297–305.

Kwon KY, Myers JL, Swensen SJ, Colby TV. Middle lobe syndrome: a clinicopathological study of 21 patients. Hum Pathol. 1995;26:302–7.

Markopoulo KD, Cool CD, Elliot TL, Lync DA, Newell JD, Hale VA, et al. Obliterative bronchiolitis: varying presentations and clinicopathological correlation. Eur Respir J. 2002;19:20–30.

Mukhopadhyay S, Katzenstein AL. Pulmonary disease due to aspiration of food and other particulate matter: a clinicopathologic study of 59 cases diagnosed on biopsy or resection specimens. Am J Surg Pathol. 2007;31:752–9.

Yousem SA, Faber C. Histopathology of aspiration pneumonia not associated with food or other particulate matter: a clinicopathologic study of 10 cases diagnosed on biopsy. Am J Surg Pathol. 2011;35:426–31.

Diffuse Nongranulomatous Lung Disorders

6

Chen Zhang and Jeffrey L. Myers

Diffuse, nonneoplastic lung diseases are a large and heterogeneous group of disorders with overlapping clinical features, usually including breathlessness and cough; diffuse radiologic abnormalities are also common. Affected patients frequently have evidence of physiologic dysfunction and defective oxygenation. High-resolution computed tomography (HRCT) scans play an increasingly important role in diagnosis of the conditions included in this category, but lung biopsy is still an essential step in the diagnostic algorithm for many of these conditions.

This chapter focuses on those diffuse lung diseases for which granulomatous inflammation is usually absent and includes both acute and chronic disorders (Fig. 6.1). Those diseases for which a subacute or chronic course is typical are separated into disorders in which air space filling is a dominant feature, as are lesions resulting from cigarette smoking, chronic idiopathic interstitial pneumonias, lung lesions in patients with systemic connective tissue diseases, and lymphangiomyomatosis.

6.1 Diffuse alveolar damage/acute interstitial pneumonia	6.2 Non-infectious air space diseases	6.3 Smoking-related interstitial lung disorders	6.4 Idiopathic chronic interstitial pneumonias	6.5 Connective tissue diseases	6.6 Lymphangioleio-myomatosis
	Organizing pneumonia Eosinophilic pneumonia Acute fibrinous & organizing pneumonia Pulmonary alveolar proteinosis	Respiratory bronchiolitis Smoking-related interstitial fibrosis Desquamative interstitial pneumonia Langerhans cell histiocytosis	Usual interstitial pneumonia Nonspecific interstitial pneumonia	Rheumatoid arthritis Systemic lupus erythematosus Scleroderma	

Fig. 6.1 Summary of entities included in this chapter, spanning a spectrum from acute to chronic diseases

C. Zhang (✉)
Department of Pathology and Laboratory Medicine, Indiana University School of Medicine, Indianapolis, IN, USA
e-mail: chenzhan@iupui.edu

J. L. Myers
Department of Pathology, Michigan Medicine, Ann Arbor, MI, USA
e-mail: myerjeff@med.umich.edu

© Springer Science+Business Media, LLC, part of Springer Nature 2018
C. Zhang, J. L. Myers (eds.), *Atlas of Lung Pathology*, Atlas of Anatomic Pathology,
https://doi.org/10.1007/978-1-4939-8689-7_6

Diffuse Alveolar Damage (DAD)

DAD (Figs. 6.2, 6.3, 6.4, 6.5, 6.6, 6.7, 6.8, 6.9, 6.10, 6.11, 6.12, 6.13, 6.14, 6.15, 6.16, 6.17 and 6.18) is a nonspecific manifestation of catastrophic acute lung injury usually seen in the context of the acute respiratory distress syndrome (ARDS). Ninety percent of patients discovered to have DAD in a surgical lung biopsy have ARDS. ARDS is defined as a syndrome of acute onset (≤1 week) characterized by diffuse radiologic abnormalities resembling pulmonary edema not explained by cardiac failure alone and hypoxemia. Mortality rates are high, ranging from 40% to over 50% depending on disease severity, the presence or absence of pre-existing lung disease, and comorbidities. DAD is seen in about half of patients with ARDS and is most common in those with severe and prolonged respiratory failure. Risk factors for developing ARDS and therefore DAD include sepsis, trauma, multiple transfusions, aspiration of gastric contents, pulmonary contusion, pneumonia, and smoke inhalation. DAD occasionally occurs in patients with no identifiable risk factors or cause for ARDS, a syndrome referred to as acute interstitial pneumonia (Hamman-Rich syndrome).

The etiology or cause for DAD is often not identifiable on the basis of histology alone, but infection should always be an important consideration and often requires special stains as well as other microbiologic assays. A specific infection accounted for about one third of diagnoses in several reports of patients with ARDS who underwent surgical lung biopsy. Viruses, especially cytomegalovirus (CMV), accounted for the majority of infectious causes; less common pathogens include bacteria, *Pneumocystis jiroveci* and other fungi, and *Mycobacterium* species. Clues to an infectious etiology include a concomitant bronchopneumonia, viral cytopathic changes, frothy exudate characteristic of *Pneumocystis* pneumonia, and granulomatous inflammation. Special stains, including a silver stain for pneumocystis and other fungi, are key to identifying many of the pathogens likely to cause DAD.

Underlying collagen fibrosis, especially when coupled with honeycomb change in a patient older than 60 years of age, is another important clue that may signify pre-existing fibrotic lung disease such as usual interstitial pneumonia (UIP). In this context, and assuming no other cause for DAD, this combination of findings is characteristic of a syndrome of rapid worsening referred to as acute exacerbation (*see* section "Usual Interstitial Pneumonia (UIP)"). Acute exacerbation is occasionally the presenting manifestation of UIP in patients with previously undiagnosed disease.

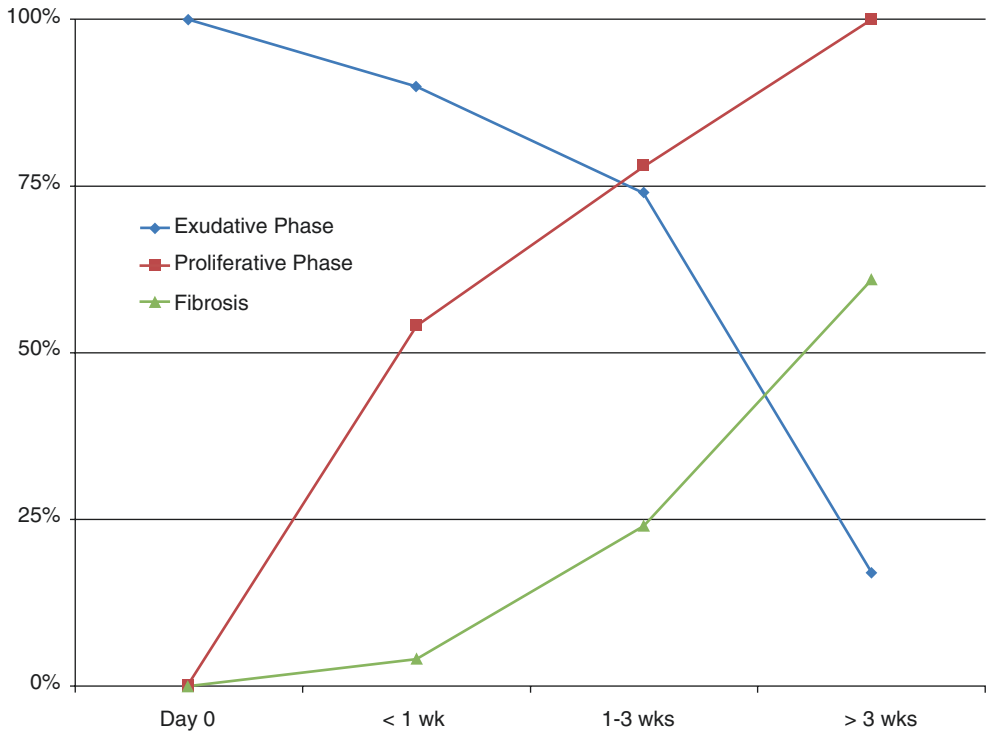

Fig. 6.2 Proportion of patients with ARDS showing exudative, proliferative, and fibrotic phase DAD at autopsy. The exudative phase is the earliest change and dominates in the first week following injury. Proliferative phase changes become more conspicuous after the first week and are the dominant finding after the first 2 weeks. Collagen fibrosis is a late-stage event that does not occur in all patients

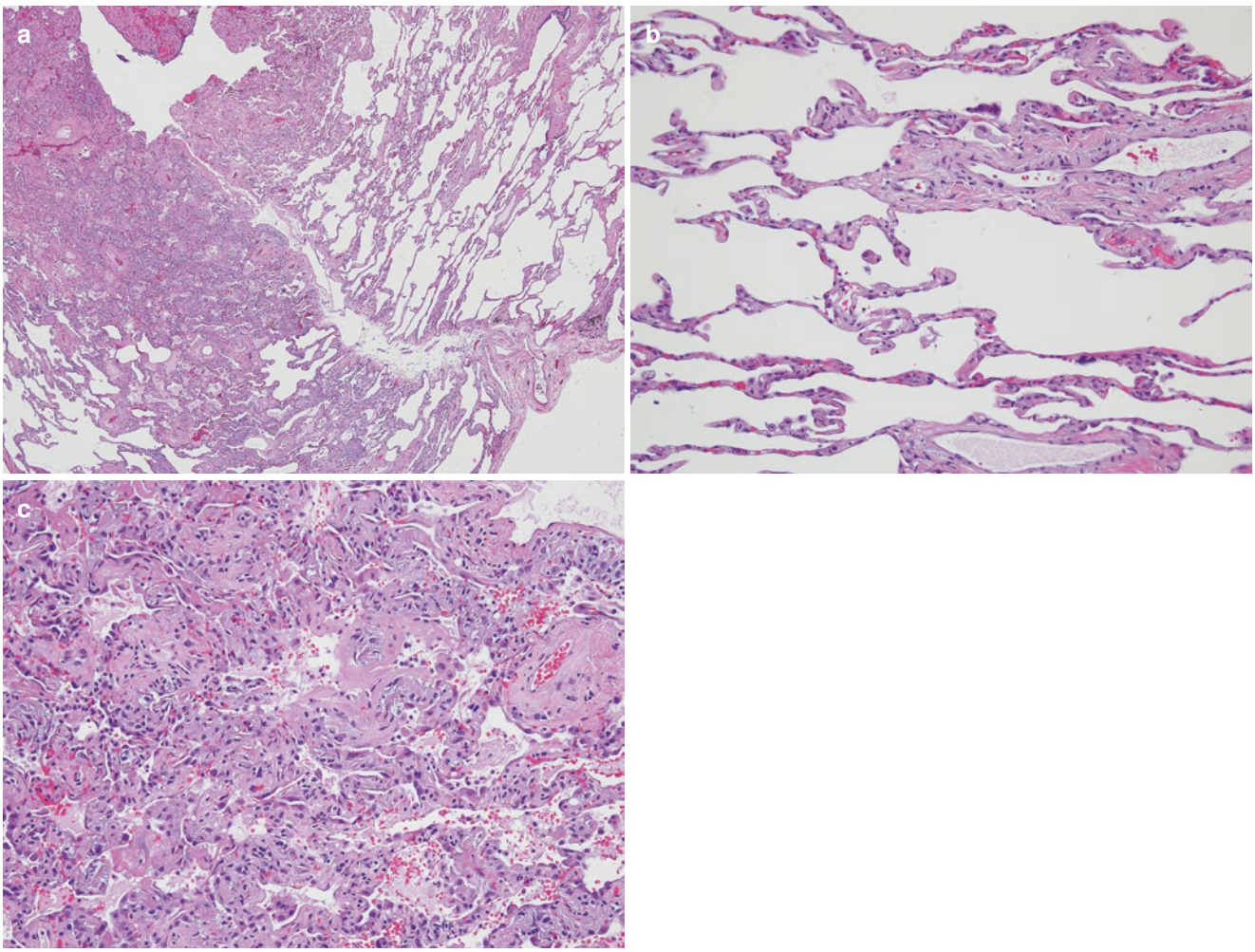

Fig. 6.3 DAD with a patchy distribution. (**a**) Low-magnification view of surgical lung biopsy from a patient with ARDS showing nearly normal lung in the upper right and DAD in the lower left portions of the field (H&E). (**b**) High-magnification photomicrograph of the nearly normal lung in the upper right portion of the field illustrated in **a** showing minimal alveolar septal thickening and congestion, which may reflect the earliest and least specific exudative phase of DAD (H&E). (**c**) High-magnification photomicrograph of DAD in the lower left portion of the field illustrated in **a** showing the early proliferative (organizing) phase with persistent hyaline membranes (H&E)

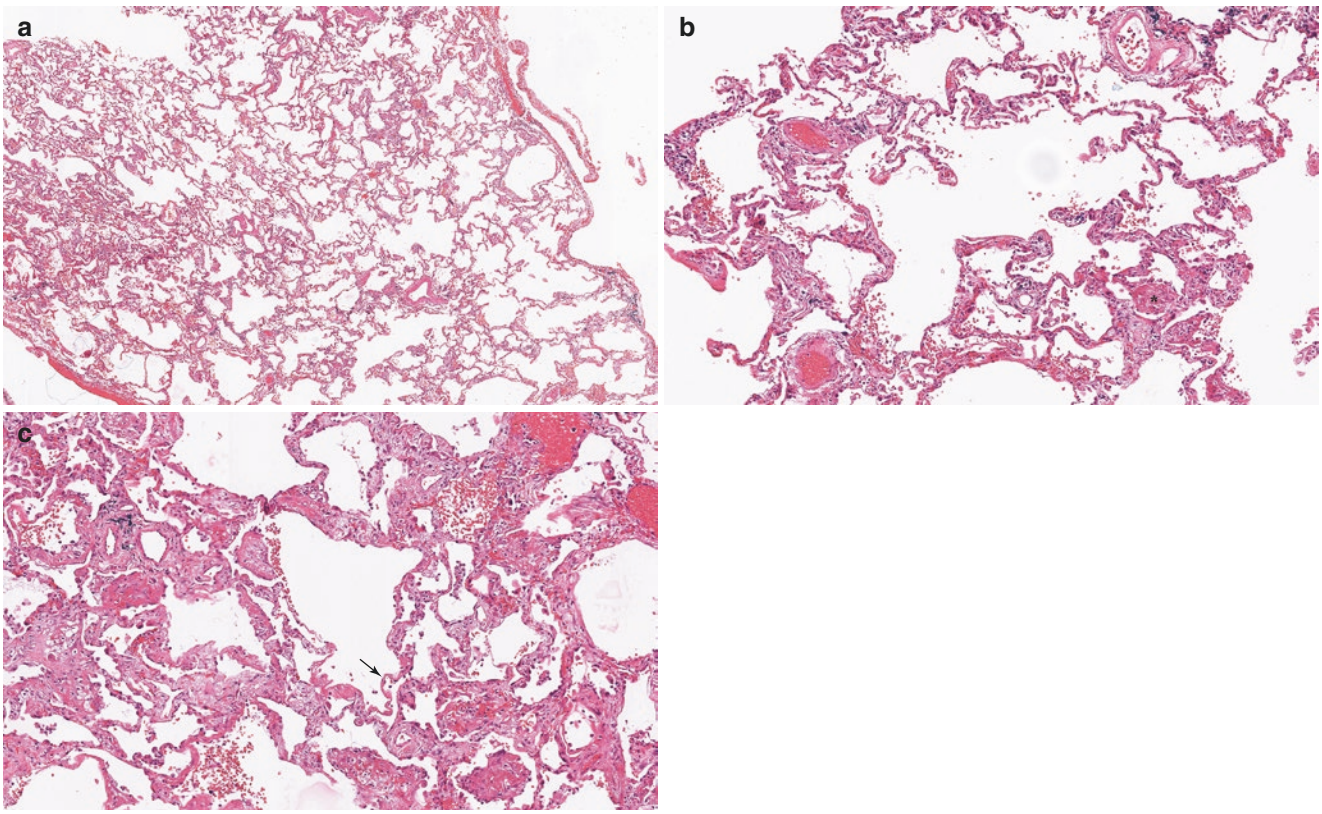

Fig. 6.4 DAD, early exudative phase. (**a**) Scanning magnification photomicrograph of the early exudative phase of DAD in a patient with ARDS (H&E). At low magnification the lung parenchyma looks nearly normal with only minimal alveolar septal thickening and overall preservation of lung architecture. (**b**) High-magnification photomicrograph of field illustrated in **a** showing alveolar septal congestion and thickening with very focal hemorrhage and fibrin in air spaces (asterisk) (H&E). In this early phase, it is very difficult and perhaps impossible to diagnose DAD on the basis of this combination of nonspecific findings alone. It is only the clinical context (i.e., ARDS) that allows more confident speculation that this is DAD in an early exudative phase. (**c**) High-magnification photomicrograph of field illustrated in **a** showing an area in which alveolar septal thickening and associated congestion and air space hemorrhage are more advanced than that seen in **b** (H&E). In addition, this field shows early hyaline membrane formations (*arrow*), which allows a more confident diagnosis of DAD

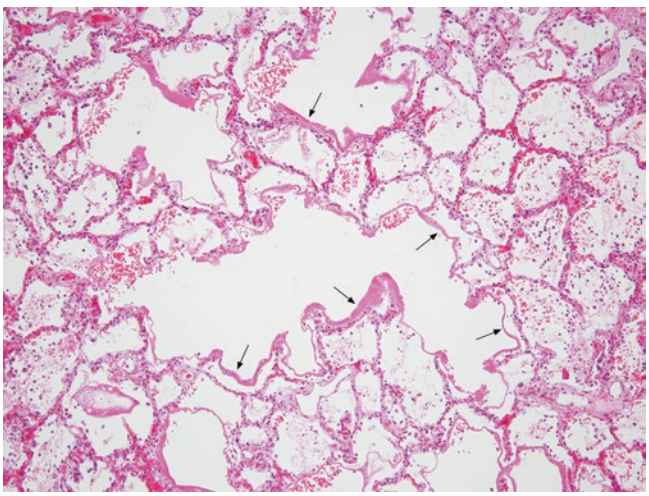

Fig. 6.5 Diffuse alveolar damage, exudative phase. Intermediate-magnification photomicrograph from patient with ARDS who had acute bronchopneumonia complicated by early DAD (H&E). Alveolar septa are mildly congested with minimal inflammation, hemorrhage, and fibrin in air spaces and hyaline membranes (arrows)

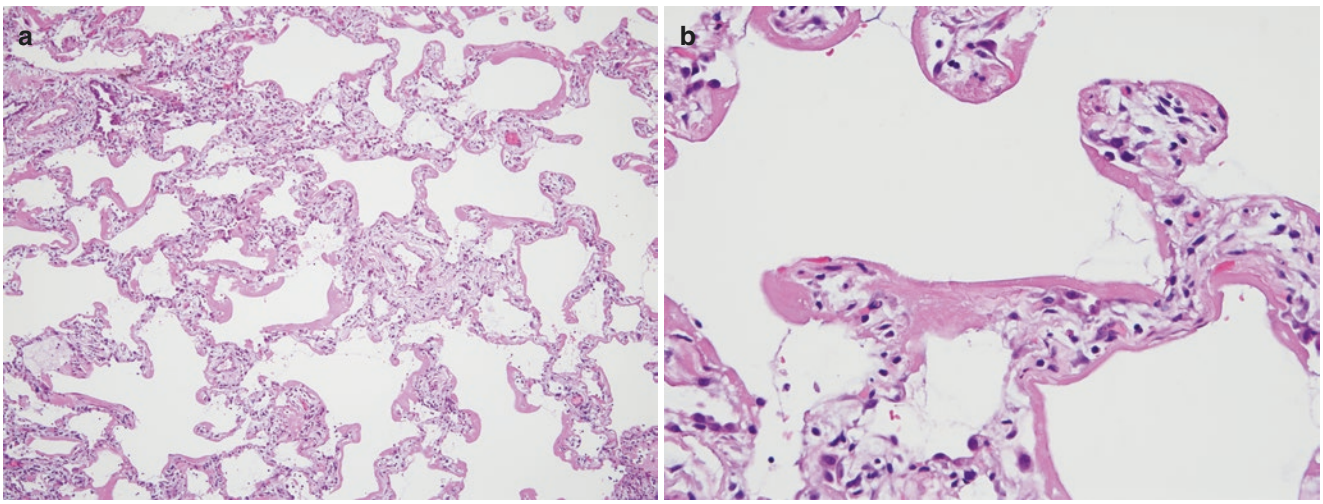

Fig. 6.6 DAD, exudative phase. (**a**) Low-magnification photomicrograph showing acute DAD (H&E). Alveolar septa are mildly thickened by a combination of interstitial edema and a relatively scant infiltrate of predominantly mononuclear cells. Acellular, brightly eosinophilic hyaline membranes are the histologic hallmark of acute DAD. (**b**) High-magnification photomicrograph showing acute DAD (H&E). Acellular, eosinophilic hyaline membranes are arranged in linear arrays along mildly thickened alveolar septa

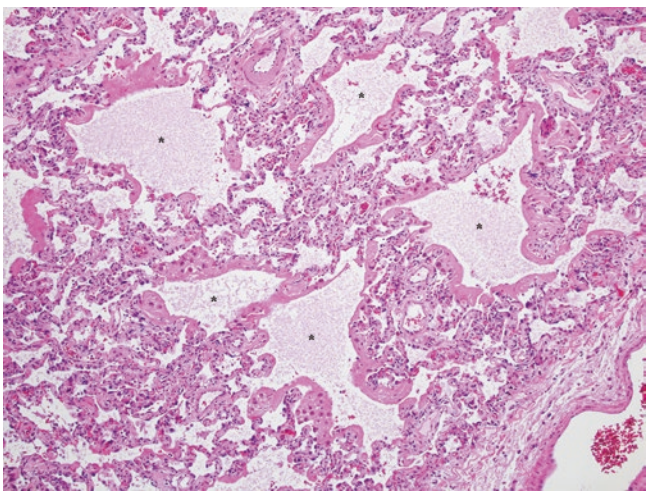

Fig. 6.7 Diffuse alveolar damage, exudative phase. Intermediate-magnification photomicrograph of surgical lung biopsy from a patient with ARDS demonstrating prominent hyaline membranes affecting mainly alveolar ducts (asterisks)

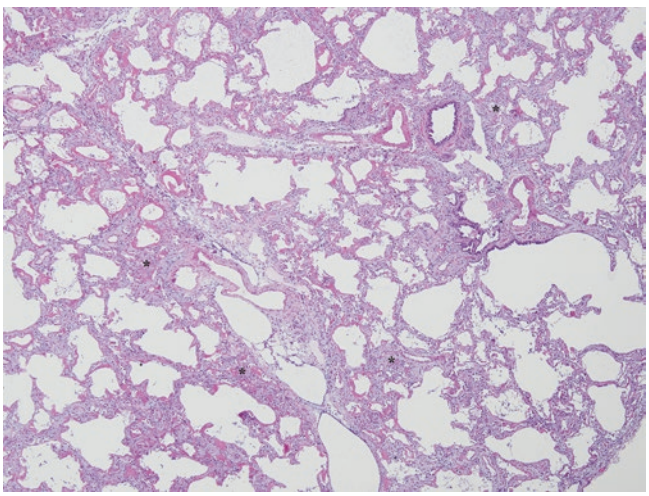

Fig. 6.8 DAD, proliferative phase. Low-magnification photomicrograph showing the early proliferative or organizing phase of DAD (H&E). Hyaline membranes remain a distinctive feature and are accompanied by expansion and distortion of the interstitium owing mainly to fibroblasts and myofibroblasts within a pale-staining basophilic matrix. In areas there is alveolar collapse (asterisks), which accounts for the increasingly distorted architecture

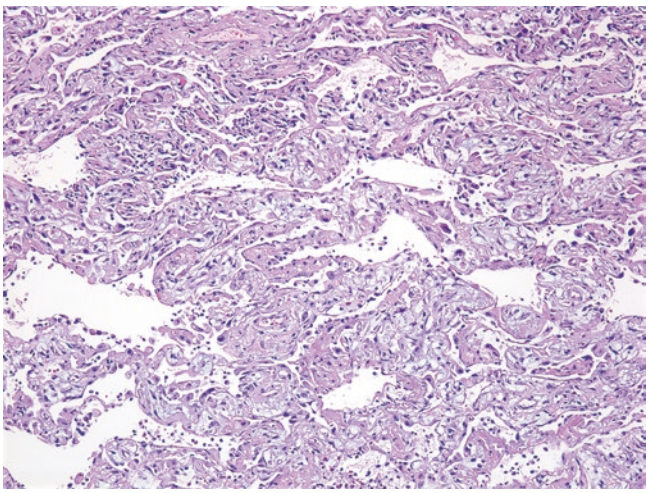

Fig. 6.9 DAD, proliferative phase. Intermediate-magnification photomicrograph showing expansion and distortion of alveolar septa by mesenchymal cells accompanied by persistent and increasingly fragmented hyaline membranes (H&E)

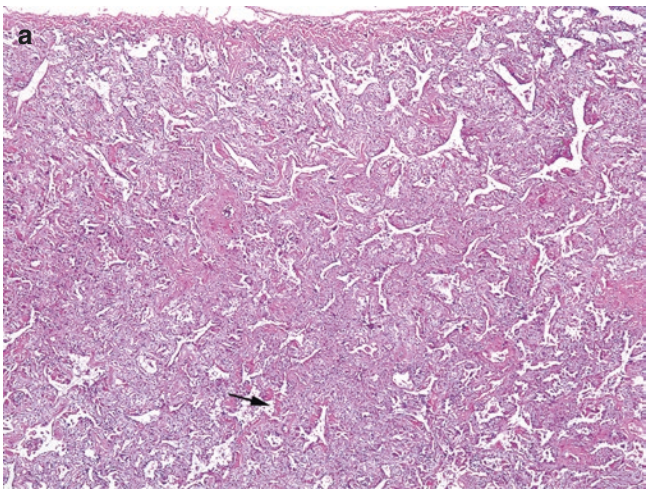

Fig. 6.10 DAD, late proliferative phase. (**a**) Low-magnification photomicrograph demonstrating the proliferative or organizing phase of DAD in a surgical lung biopsy from a patient with unexplained (idiopathic) ARDS (i.e., acute interstitial pneumonia) (H&E). There is uniform interstitial expansion and distortion resulting in markedly abnormal lung architecture with only a few widely scattered hyaline membranes (arrow). (**b**) High-magnification photomicrograph illustrating expanded, distorted, and collapsed alveolar septa in the late proliferative or organizing phase of DAD (H&E). (**c**) High-magnification photomicrograph from another patient with ARDS illustrating the proliferative phase of DAD in which collapsed alveolar septa are separated by ectatic alveolar ducts (H&E). Hyaline membrane remnants are present within the areas of collapsed and distorted interstitium

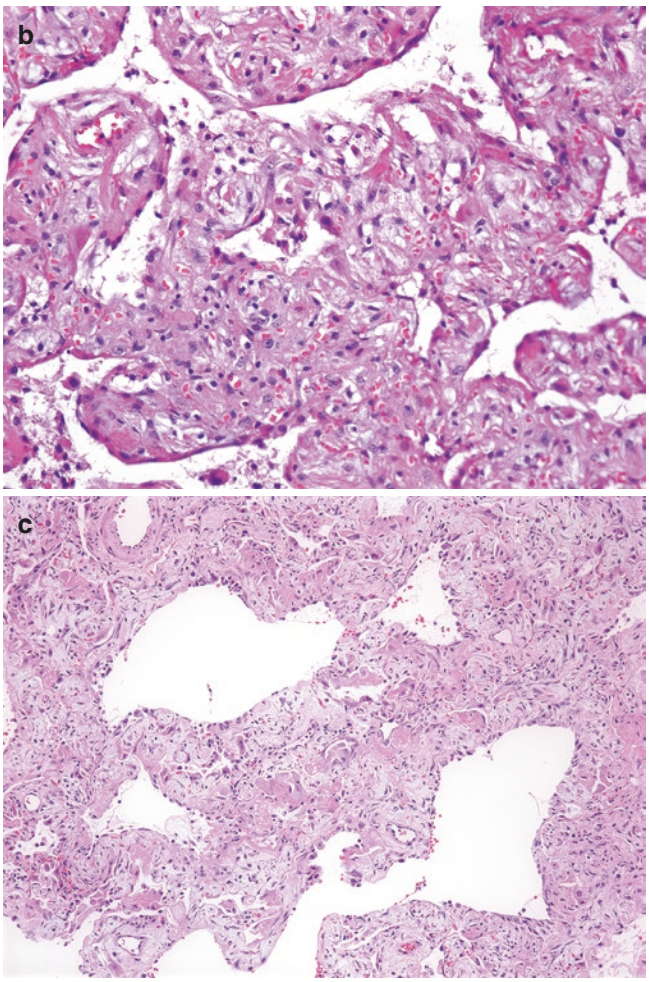

Fig. 6.10 (continued)

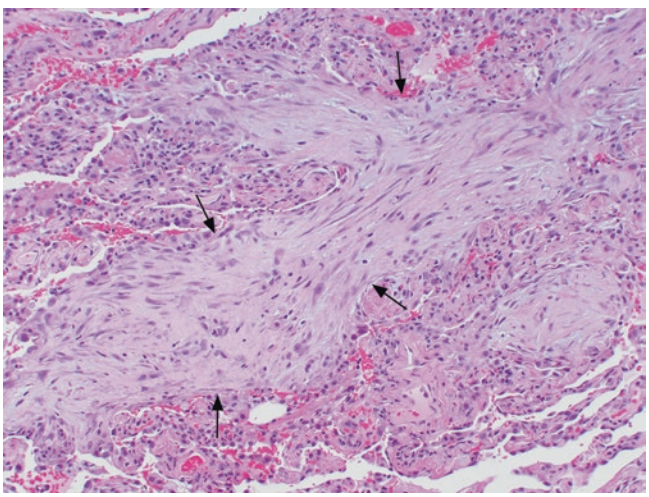

Fig. 6.11 DAD, late proliferative phase. Intermediate-magnification photomicrograph shows fibroblasts and myofibroblasts forming polypoid intraluminal structures (arrows) closely mimicking the appearance of organizing pneumonia (H&E). This demonstrates the considerable histologic overlaps between the proliferative or organizing phase of DAD and organizing pneumonia. In small biopsies organizing DAD may be indistinguishable from organizing pneumonia, but correlation with clinical and radiologic information will often resolve the diagnostic distinction

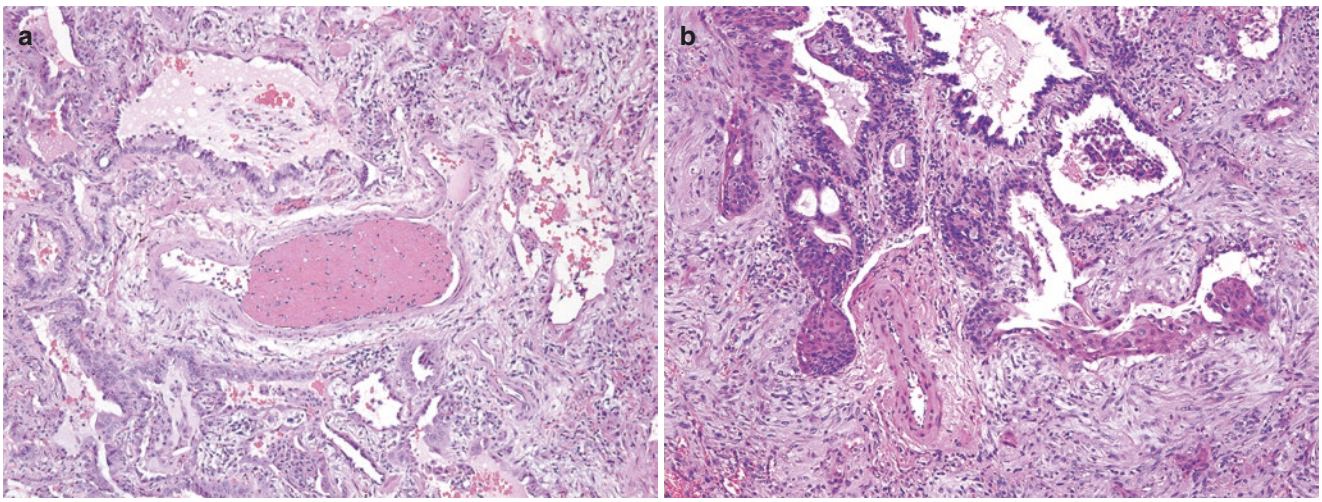

Fig. 6.12 DAD, proliferative phase. (**a**) Fibrin thrombi are a common although nonspecific finding in DAD, as illustrated in this photomicrograph of a surgical lung biopsy from a patient with ARDS (H&E). (**b**) High-magnification photomicrograph showing a distinctive pattern of squamous metaplasia involving bronchiolar epithelium in a patient with ARDS (H&E)

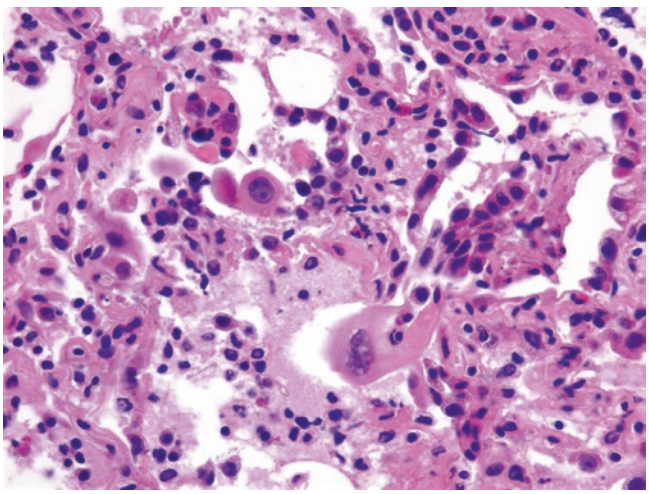

Fig. 6.13 Pneumocyte hyperplasia with reactive atypia in DAD. A high-magnification photomicrograph demonstrates hyperplastic pneumocytes in a patient with DAD (H&E). There is focal cytomegaly with nuclear enlargement and prominent nucleoli but without viral inclusions. This degree of reactive atypia is common in the organizing phase of DAD and should not be construed as either a malignancy or a marker for any specific etiology such as drug toxicity or viral infection

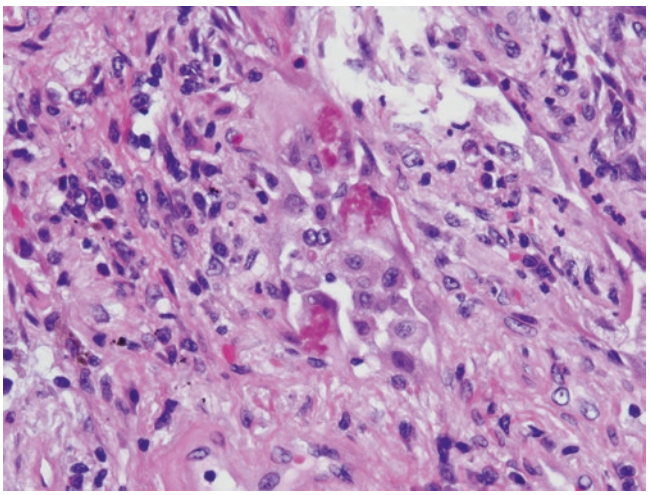

Fig. 6.14 Mallory hyaline in hyperplastic pneumocytes in DAD. This high-magnification photomicrograph illustrates densely eosinophilic cytoplasmic inclusions identical to the Mallory hyaline more commonly affiliated with hepatocytes in alcoholic hepatitis (H&E). This cytologic curiosity is not specific for DAD, occurring in other forms of diffuse lung disease including usual interstitial pneumonia

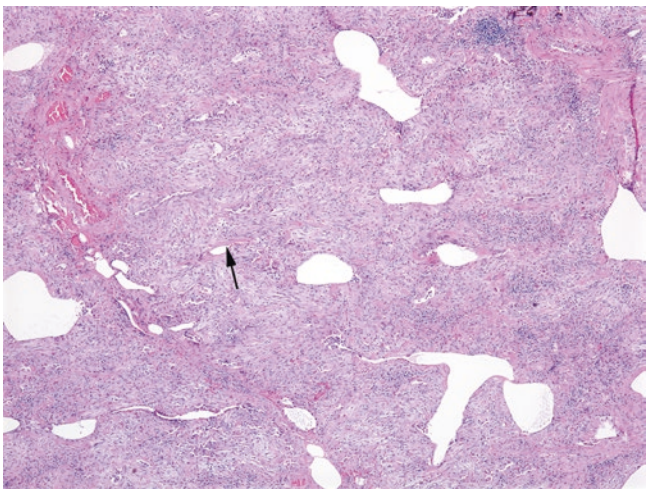

Fig. 6.15 DAD, proliferative phase. Low-magnification photomicrograph showing the proliferative phase of DAD in a patient with unexplained (idiopathic) ARDS (i.e., acute interstitial pneumonia, referred to historically as Hamman-Rich syndrome) (H&E). The lung architecture is distorted by proliferating fibroblasts and myofibroblasts and concomitant alveolar collapse. Rare hyaline membrane remnants mark some of the collapsed air spaces (arrow)

Fig. 6.16 End-stage fibrosis at autopsy in a patient with acute interstitial pneumonia. A gross photograph illustrates the cut surface of a lung from a young woman less than 35 years of age who died within 2 months of the acute onset of rapidly progressive respiratory failure. At autopsy her lung showed extensive fibrosis and honeycomb change. A surgical lung biopsy performed in the course of her hospitalization showed organizing DAD

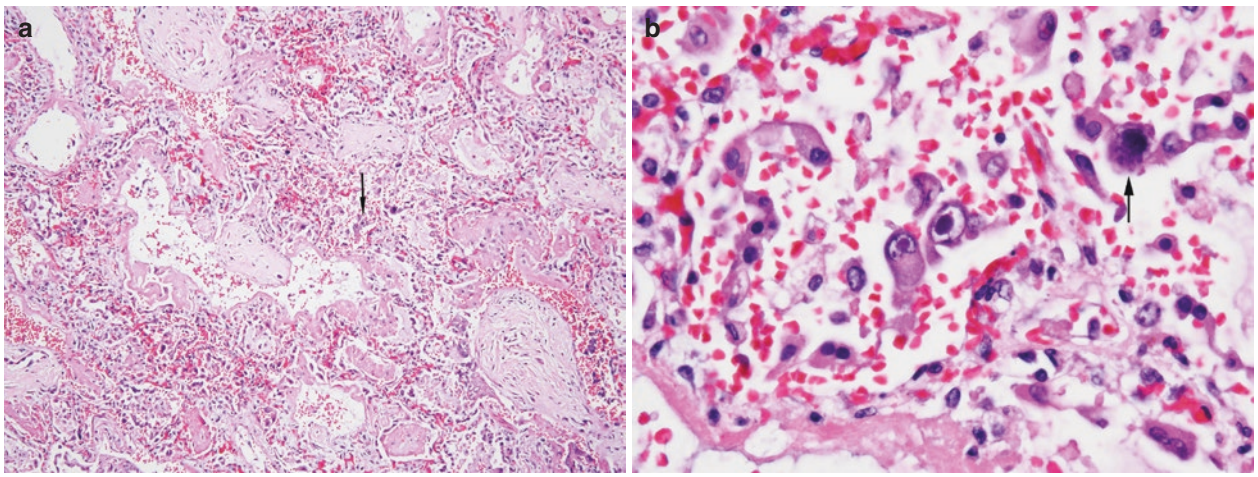

Fig. 6.17 DAD due to cytomegalovirus (CMV) infections. (**a**) Intermediate-magnification photomicrograph showing both acute and organizing DAD in which there are both well-formed hyaline membranes and organizing fibroblast/myofibroblasts; in this field, they form polypoid structures closely mimicking the appearance of organizing pneumonia (H&E). Two hyperplastic pneumocytes show nuclear inclusions typical of CMV (arrow). (**b**) High-magnification photomicrograph showing the CMV-infected cells with typical intranuclear inclusions (H&E). The cell in the upper right portion of the field shows basophilic cytoplasmic inclusions (arrow), another feature helpful in recognizing CMV (H&E)

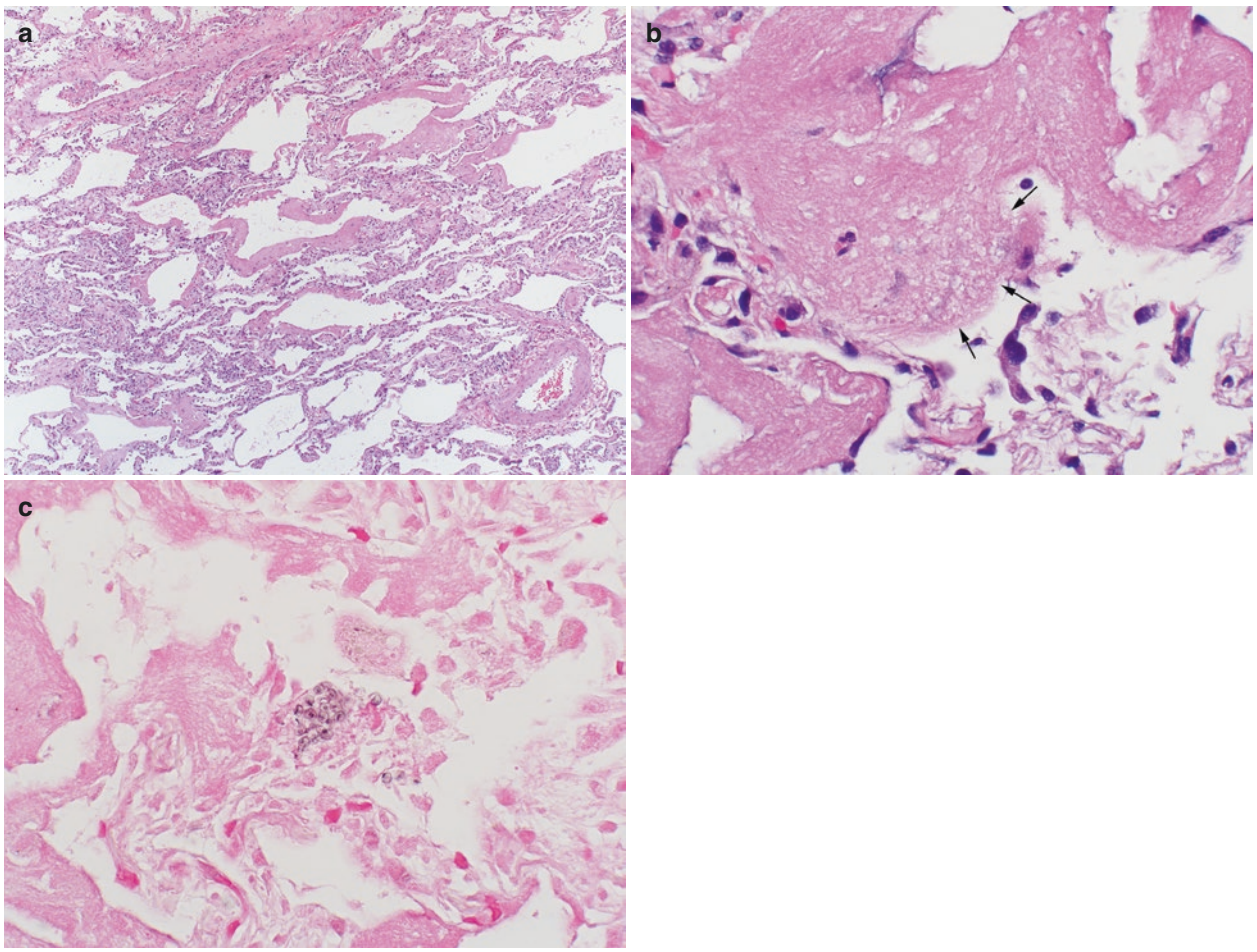

Fig. 6.18 DAD caused by infection with *Pneumocystis jiroveci* (*Pneumocystis* pneumonia). (**a**) Low-magnification photomicrograph of surgical lung biopsy from a patient with ARDS showing acute DAD with thick, lush hyaline membranes typical of those sometimes seen in patients with *Pneumocystis*-associated DAD (H&E). (**b**) High-magnification photomicrograph showing a small focus of frothy exudate (arrows) within one of the thick hyaline membranes in the same patient with *Pneumocystis*-associated DAD (H&E). (**c**) High-magnification photomicrograph illustrating organisms typical of *Pneumocystis jiroveci* in the same surgical lung biopsy showing DAD characterized by thick hyaline membranes (Gomori methenamine silver stain)

Noninfectious Air Space Diseases

A number of noninfectious, nongranulomatous lung diseases primarily affect the air spaces rather than the interstitial compartment. These conditions have overlapping clinical, radiologic, and histologic features and are therefore grouped together in this category. Symptoms in these noninfectious air space diseases tend to include some combination of cough, shortness of breath, and fever, and thus they mimic the clinical features of infection. At low magnification these lesions have in common a patchy and frequently bronchiolocentric distribution for which the differential diagnosis sometimes also includes infectious pneumonia (*see* Chap. 4). Differences are attributable primarily to differences in the histologic characteristics of the air space exudate itself.

Organizing Pneumonia

Organizing pneumonia (Figs. 6.19, 6.20, 6.21, 6.22, 6.23, 6.24, 6.25, 6.26 and 6.27) is predominantly an air space lesion that occurs in a variety of clinical and histopathologic contexts. Organizing pneumonia sometimes occurs as a secondary finding in patients with other primary pathologic processes. For example, organizing pneumonia is commonly seen distal to centrally obstructing tumors and is frequently combined with other histologic findings in patients with aspiration pneumonia, hypersensitivity pneumonia, and granulomatosis with polyangiitis (Wegener granulomatosis). Patients in whom organizing pneumonia represents the primary pathologic abnormality fall into several different clinical groups, including those with idiopathic disease (*cryptogenic* organizing pneumonia), those with underlying diseases or conditions known to cause or be associated with organizing pneumonia (*secondary* organizing pneumonia), and patients with localized PET-positive radiologic abnormalities that may mimic lung neoplasms (*focal* organizing pneumonia). Patients with cryptogenic organizing pneumonia (COP), referred to historically as bronchiolitis obliterans organizing pneumonia (BOOP), constitute the majority for whom organizing pneumonia is the primary finding in diagnostic lung biopsies. COP usually presents as a subacute respiratory illness characterized by several weeks of cough and shortness of breath, often following a viral-like prodrome. Fever is present in about half of affected patients. Pulmonary function studies show a mild to moderate ventilatory defect often accompanied by a diminished diffusion capacity for carbon monoxide (DLco). Typical radiologic findings include patchy, bilateral ground-glass attenuation with or without consolidation with preservation of lung volumes. COP usually responds favorably to oral corticosteroid therapy, although relapse occurs in as many as half of patients if steroids are tapered prematurely. The presence of collagen fibrosis has been associated with a worse prognosis and may indicate that the organizing pneumonia is a secondary rather than a primary finding in a patient with a clinically occult underlying fibrotic lung disease that is not well represented in the sampled tissue. Patients with COP, including those with localized radiologic abnormalities (*focal* organizing pneumonia), tend to have a better prognosis compared to patients with organizing pneumonia secondary to an underlying condition (e.g., connective tissue disease) or cause (e.g., drug-induced disease), although both groups of patients have high rates of treatment response and low disease-specific mortality.

Identifying organizing pneumonia in a lung biopsy is often an important preliminary step in recognizing patients with COP but requires correlation with other clinical and radiologic data to exclude other potential causes or associations (*secondary* organizing pneumonia). It is also important that biopsies be carefully evaluated for histologic clues helpful in establishing specific causes for organizing pneumonia. For example, aspiration of food and other particulates from the upper gastrointestinal tract has been highlighted as a circumstance in which organizing pneumonia may be a prominent histologic finding in surgical lung biopsies. Organizing pneumonia also may be a prominent finding in certain infections, and for that reason special stains should be performed whenever organizing pneumonia is accompanied by granulomatous and/or acute inflammation.

Organizing pneumonia that includes not only granulomatous inflammation but also necrotizing vasculitis may be a clue to the diagnosis of the BOOP-like variant of granulomatosis with polyangiitis (Wegener) and requires not only special stains to exclude infection but also correlation with clinical data to confidently establish a diagnosis of Wegener granulomatosis.

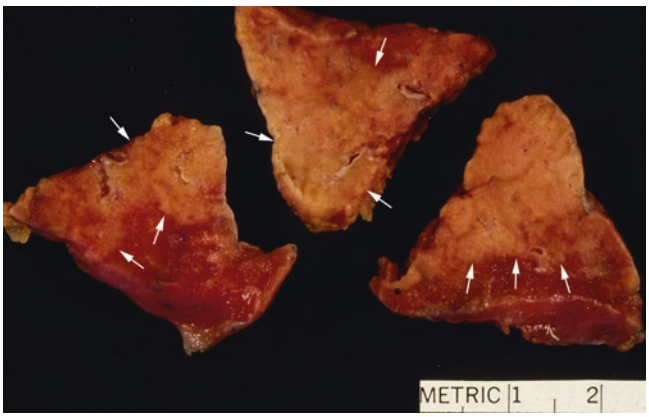

Fig. 6.19 Gross photograph of surgical lung biopsy from patient with COP. Areas of pallor were firm on palpation and corresponded to the areas of organizing pneumonia (arrows)

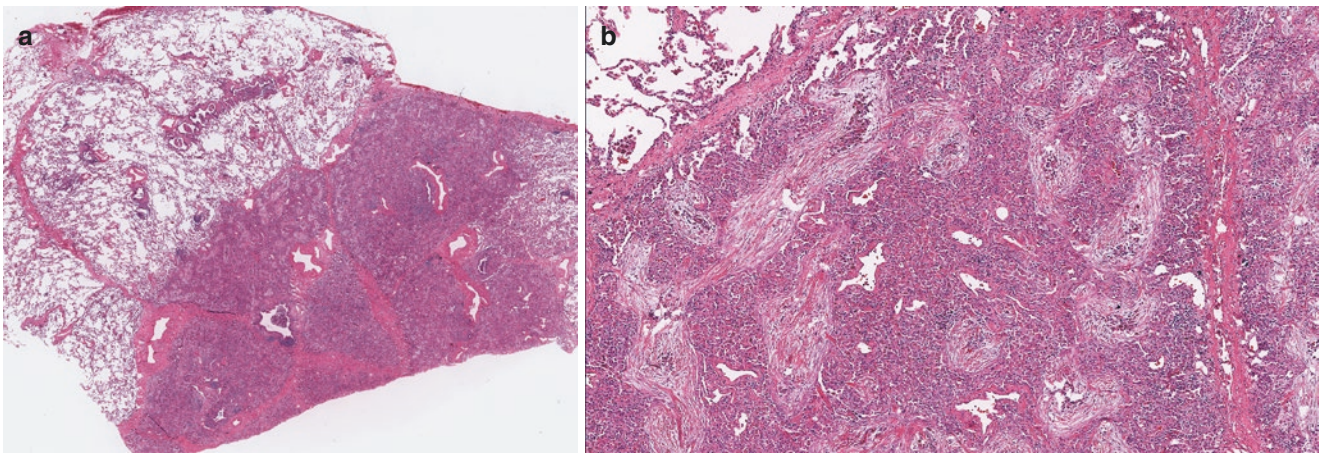

Fig. 6.20 Organizing pneumonia in a patient with COP. (**a**) This scanning magnification photomicrograph shows the sharp contrast between the area of organizing pneumonia at lower right and relatively normal lung in the upper left (H&E). Organizing pneumonia fills air spaces and therefore appears solid at lowest magnification. (**b**) Intermediate-magnification photomicrograph of organizing pneumonia illustrated in lower right portion of **a** showing to better advantage the characteristic polypoid plugs of organizing fibroblasts and myofibroblasts, in this case with an associated infiltrate of lymphocytes and plasma cells within the central areas of the plugs themselves (H&E). The configuration of the organizing fibrosis reflects the anatomy of the respiratory bronchioles and alveolar ducts in which it resides

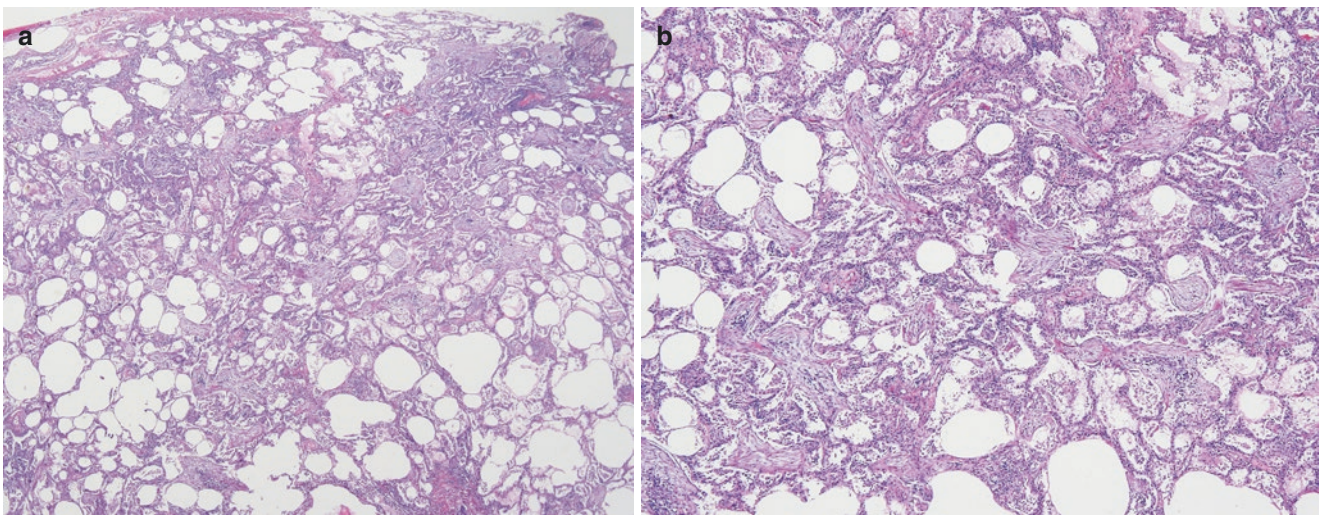

Fig. 6.21 Organizing pneumonia in a patient with COP. (**a**) Low-magnification photomicrograph showing organizing pneumonia in a well-inflated surgical lung biopsy (H&E). The patchy abnormality comprises very distinctive plugs of organizing fibroblasts and myofibroblasts situated mainly within the lumina of branching airways and alveolar ducts. (**b**) Intermediate-magnification photomicrograph from same surgical lung biopsy shows to better advantage the intraluminal plugs of organizing tissue affiliated with a scant infiltrate of mononuclear inflammatory cells (H&E). Alveolar septa show a similar infiltrate of mononuclear inflammatory cells, but the interstitial changes are limited to the areas with intraluminal fibrosis

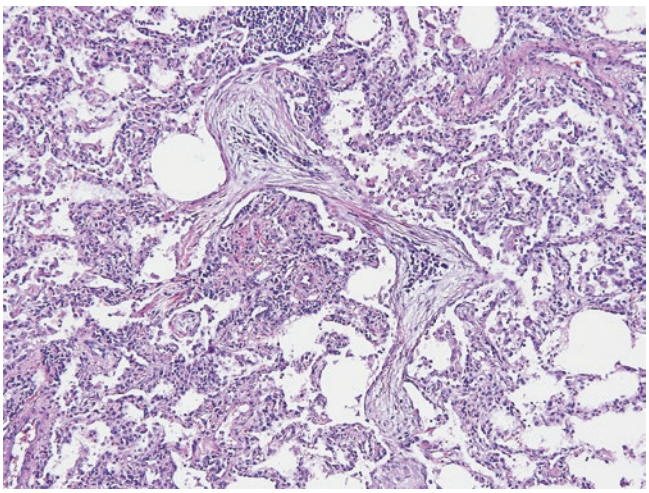

Fig. 6.22 Organizing pneumonia in a patient with COP. Higher-magnification view of the surgical lung biopsy illustrated in Fig. 6.21 showing the characteristic branching pattern of organizing pneumonia in a well-inflated lung biopsy. Note that while organizing pneumonia is centered on the airways, there are concomitant interstitial abnormalities that are limited to the areas of intraluminal fibrosis

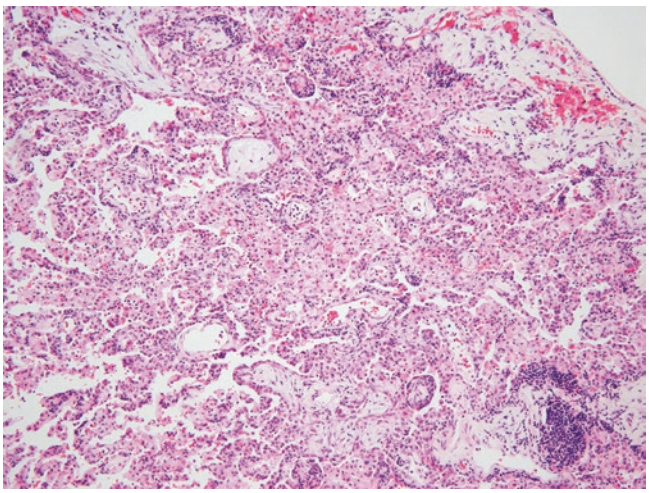

Fig. 6.24 Foamy alveolar macrophages in organizing pneumonia. Intermediate-magnification photomicrograph shows prominent foamy macrophages in the region of organizing pneumonia (H&E). This is a common although nonspecific finding in organizing pneumonia that represents microscopic obstructive pneumonia resulting from small airway dysfunction

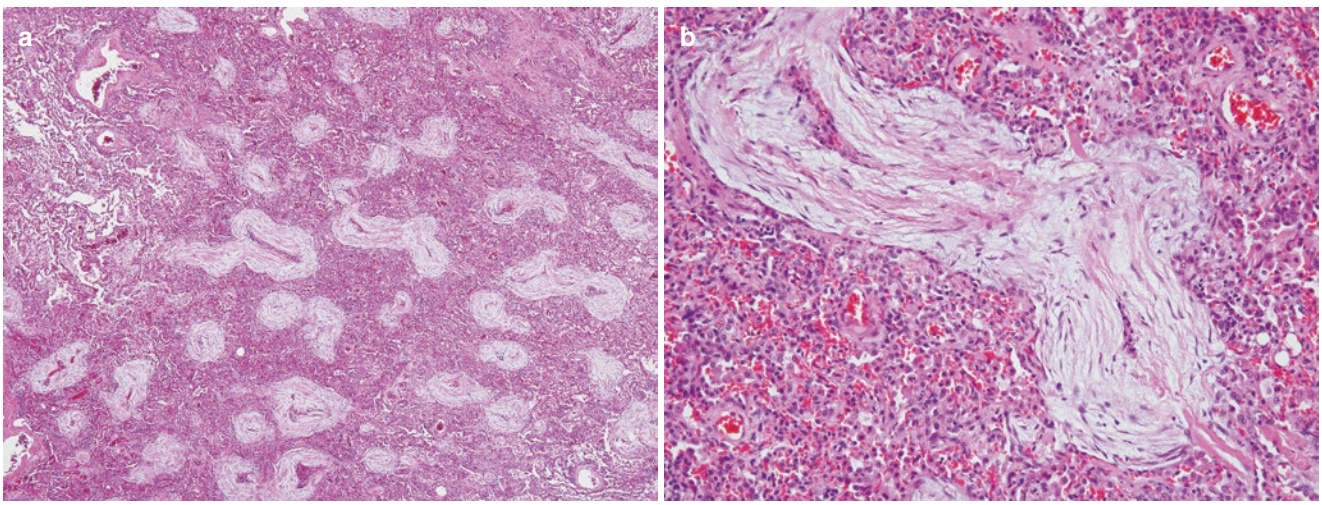

Fig. 6.23 Organizing pneumonia in a patient with COP. (**a**) Low-magnification photomicrograph showing the polypoid plugs of organizing fibroblasts and myofibroblasts outlined in sharp relief against a backdrop of collapsed intervening air spaces (H&E). The plugs of intraluminal fibroblastic tissue are centered on respiratory bronchioles and alveolar ducts, which accounts for this peculiar and distinctive low-magnification appearance. (**b**) Higher-magnification photomicrograph from low-magnification field illustrated in **a** showing bland fibroblasts and myofibroblasts arranged in a vaguely linear fashion within an edematous and focally collagenized matrix to form a cast of the affected distal airway surrounded by compressed alveolar spaces (H&E)

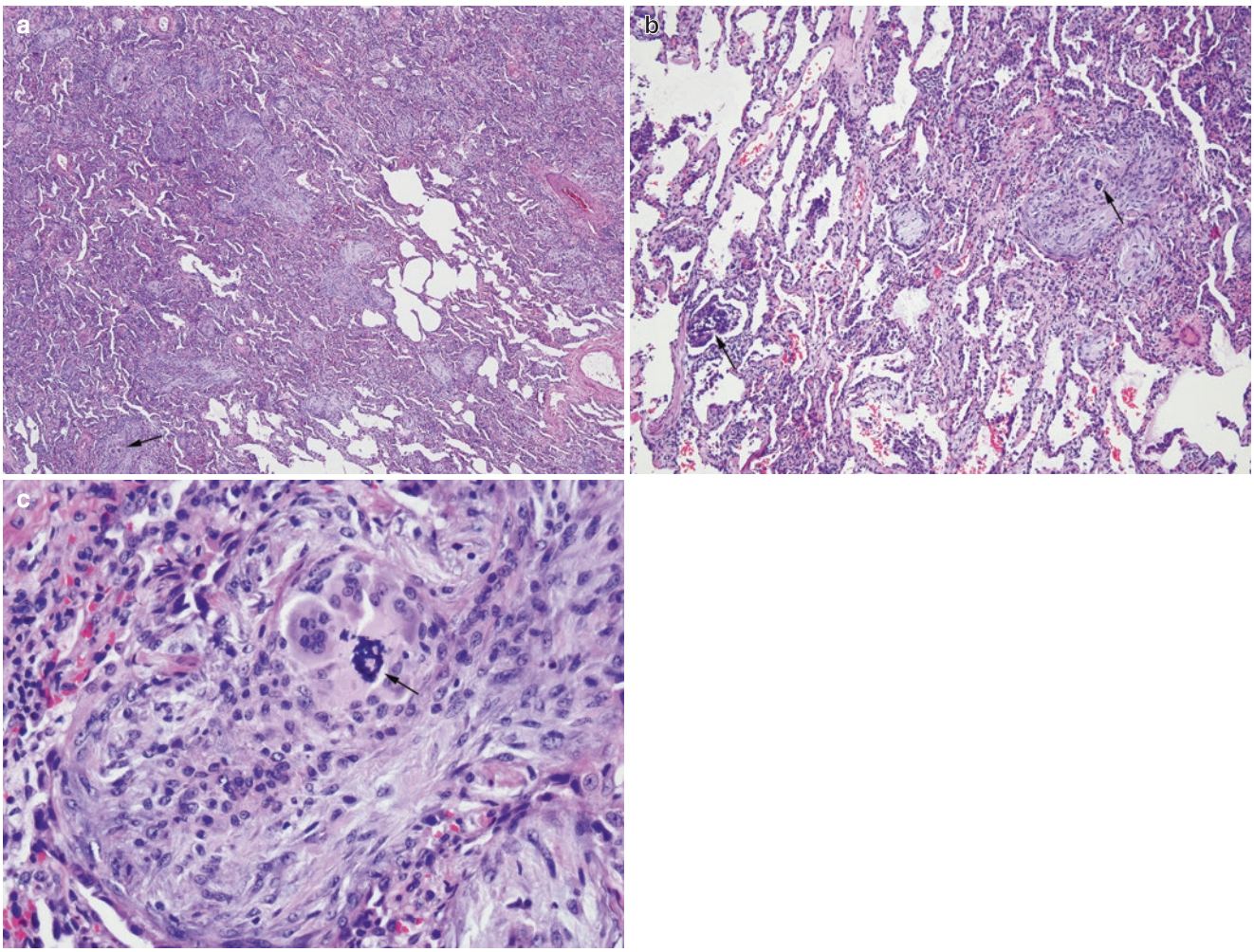

Fig. 6.25 Organizing pneumonia in a patient with aspiration of gastric particulates. (**a**) Low-magnification photomicrograph showing organizing pneumonia that might easily be construed as COP (H&E). In multiple areas throughout the biopsy, however, the organizing pneumonia is accompanied by foreign particulates with an associated giant cell reaction (arrow), as illustrated at higher magnification in **b**, **c**. (**b**) Intermediate-magnification photomicrograph from surgical lung biopsy showing extensive organizing pneumonia and associated multinucleated giant cells containing basophilic, coral-like cytoplasmic inclusions (arrows) typical of crospovidone, a chemically inactive filler (excipient) used in oral medications (H&E). (**c**) High-magnification photomicrograph showing crospovidone (arrow) affiliated with a foreign body giant cell reaction in the midst of what is otherwise typical organizing pneumonia (H&E)

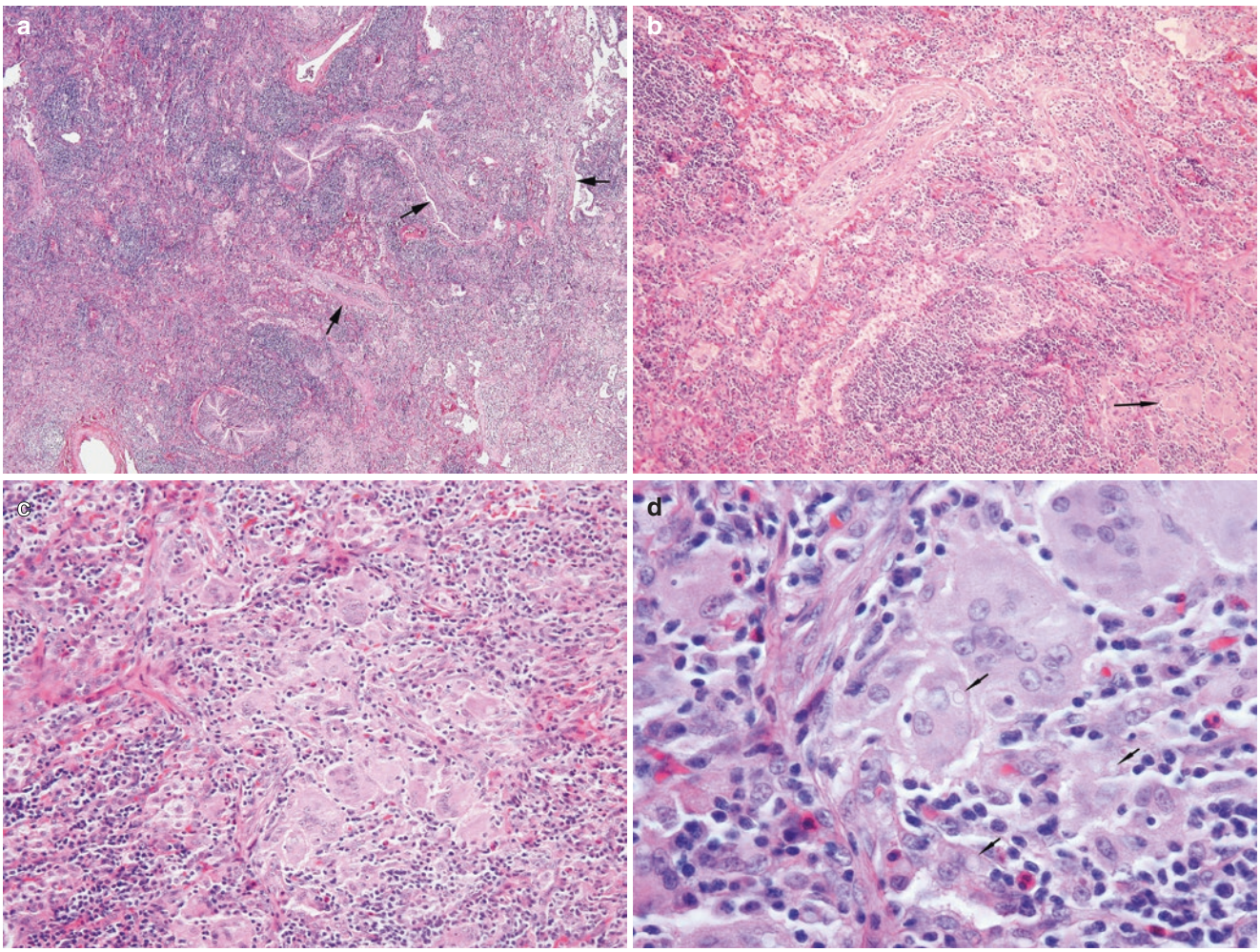

Fig. 6.26 Secondary organizing pneumonia in cryptococcosis. (**a**) Low-magnification photomicrograph showing organizing pneumonia (*arrows*) with prominent foamy macrophages and a dense inflammatory infiltrate (H&E). (**b**) Intermediate-magnification photomicrograph showing organizing pneumonia with foamy alveolar macrophages and an inflammatory background that includes loose clusters of epithelioid macrophages and giant cells (*arrow*), resulting in a vaguely granulomatous appearance (H&E). (**c**) High-magnification photomicrograph showing poorly formed granulomatous inflammation illustrated in **b** (H&E). (**d**) High-magnification photomicrograph of the granulomatous inflammation illustrated in **c** showing multiple fungal yeast forms (arrows) with clear halos, thin delicate pale-staining walls, and narrow-neck budding typical of *Cryptococcus neoformans* (H&E)

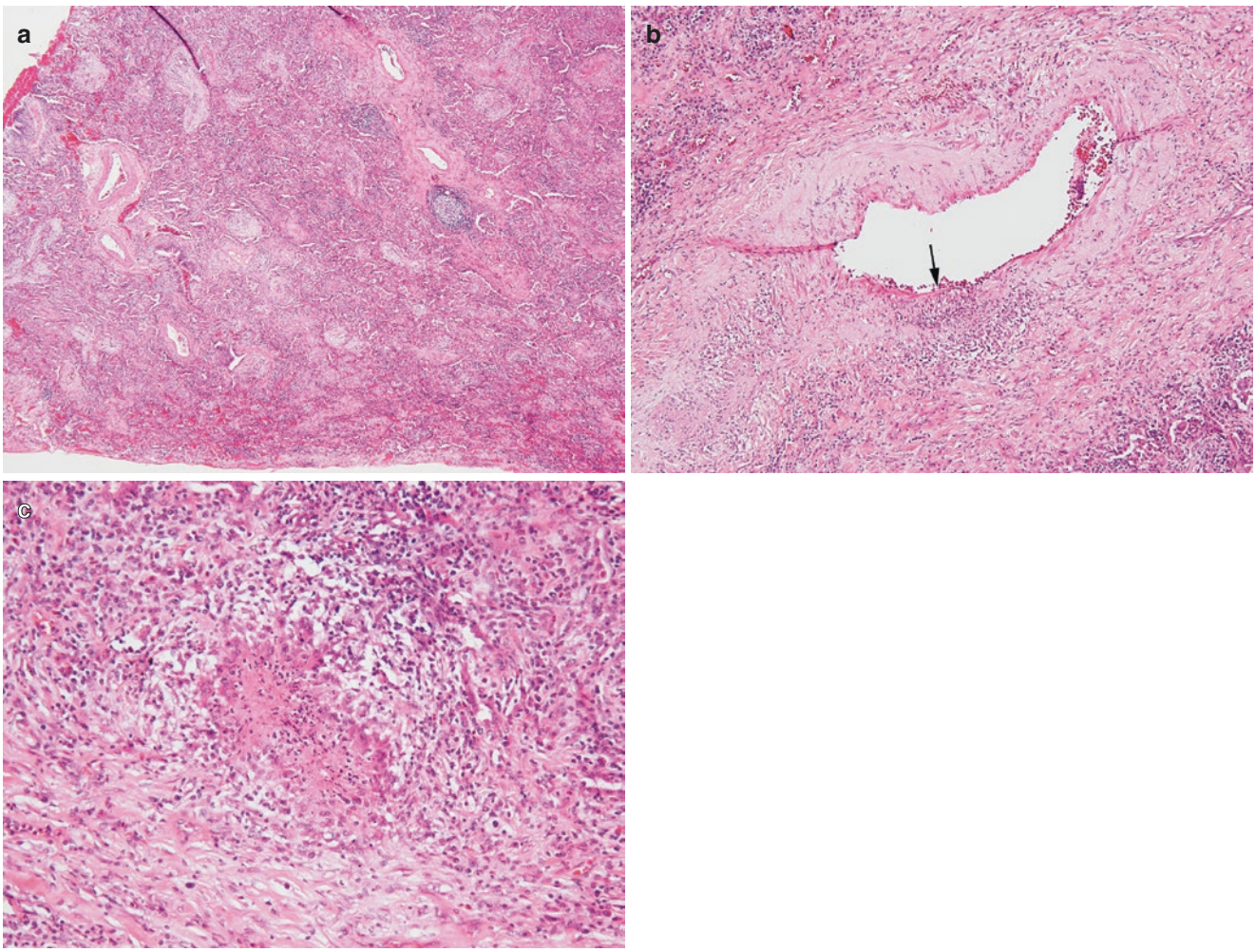

Fig. 6.27 BOOP-like variant of granulomatosis with polyangiitis (Wegener). (**a**) Low-magnification photomicrograph showing features typical of organizing pneumonia (H&E). (**b**) Intermediate-magnification photomicrograph from the same biopsy showing a necrotizing vasculitis characterized by a focal, transmural infiltrate of predominantly neutrophils with associated karyorrhexis (H&E). (**c**) Intermediate-magnification photomicrograph showing a palisaded granuloma typical of granulomatosis with polyangiitis (Wegener) in the same lung biopsy in which organizing pneumonia was the dominant feature (H&E). This combination of findings has been described in patients with the BOOP-like variant of Wegener granulomatosis

Eosinophilic Pneumonia

Eosinophilic pneumonia (Figs. 6.28, 6.29, 6.30, 6.31, 6.32, 6.33 and 6.34), like organizing pneumonia, refers to an air space-filling process that occurs as both a primary and a secondary finding in various clinical and histologic contexts. Löffler syndrome, also termed simple pulmonary eosinophilia, has distinctive clinical and radiologic findings and therefore rarely requires lung biopsy for diagnosis. The histologic findings are presumed to overlap with those seen in chronic eosinophilic pneumonia (CEP), a syndrome of unknown etiology characterized by a subacute or chronic course that likely accounts for most patients in whom surgical lung biopsy is required for diagnosis. Acute eosinophilic pneumonia differs in that patients present with rapidly progressive respiratory failure and experience equally rapid recovery either spontaneously or with corticosteroid therapy.

CEP accounts for the majority of patients with eosinophilic pneumonia diagnosed on the basis of surgical lung biopsies. Chronic eosinophilic pneumonia is characterized by a subacute or chronic course in which symptoms persist for weeks or months. Some patients experience a waxing and waning course that may persist for years. Women in their fourth or fifth decades of life account for the majority of patients, and nearly half have underlying asthma. Cough is the most common presenting complaint and may be accompanied by systemic symptoms, including fever, weight loss, and night sweats. Peripheral eosinophilia occurs in nearly 90% of patients. Like COP, most patients with CEP experience complete recovery with corticosteroid therapy. Relapses are common if treatment is withdrawn prematurely.

Acute eosinophilic pneumonia (AEP) is a febrile illness associated with rapidly progressive hypoxemic respiratory failure, diffuse radiologic abnormalities, bronchoalveolar lavage eosinophilia of greater than 25%, absence of an identifiable etiology (i.e., infection, parasitic infestation, drug exposure), and either spontaneous recovery or rapid response to corticosteroid therapy. A subset of patients with AEP develop ARDS and therefore resemble patients for whom DAD is a more common biopsy finding. Peripheral eosinophilia occurs in about half of patients with AEP. A syndrome identical to idiopathic AEP has been described in first-time cigarette smokers and less commonly in those who resume smoking after a period of smoking cessation. AEP is frequently diagnosed on the basis of clinical, radiographic, and bronchoalveolar lavage findings without resorting to lung biopsy. By definition, AEP is associated with an excellent prognosis, with all patients recovering either spontaneously or after corticosteroid therapy.

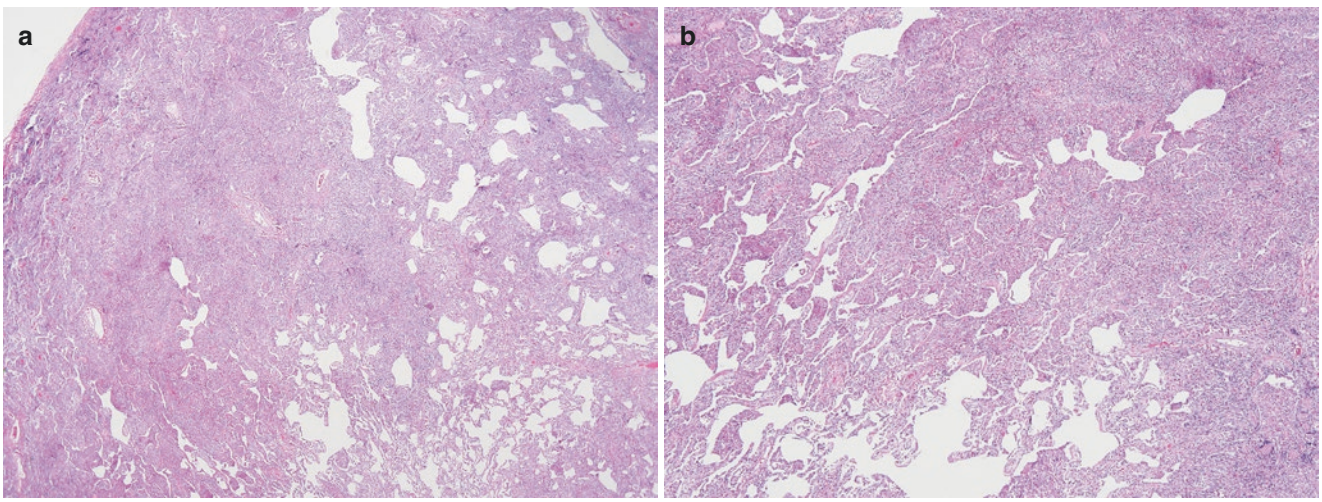

Fig. 6.28 Eosinophilic pneumonia in a patient with CEP. (**a**) Low-magnification photomicrograph of CEP showing patchy air space-filling process (H&E). (**b**) Intermediate-magnification photomicrograph showing a combination of inflammatory cells and fibrin in air spaces accompanied by expansion of the interstitium by a similar inflammatory infiltrate (H&E)

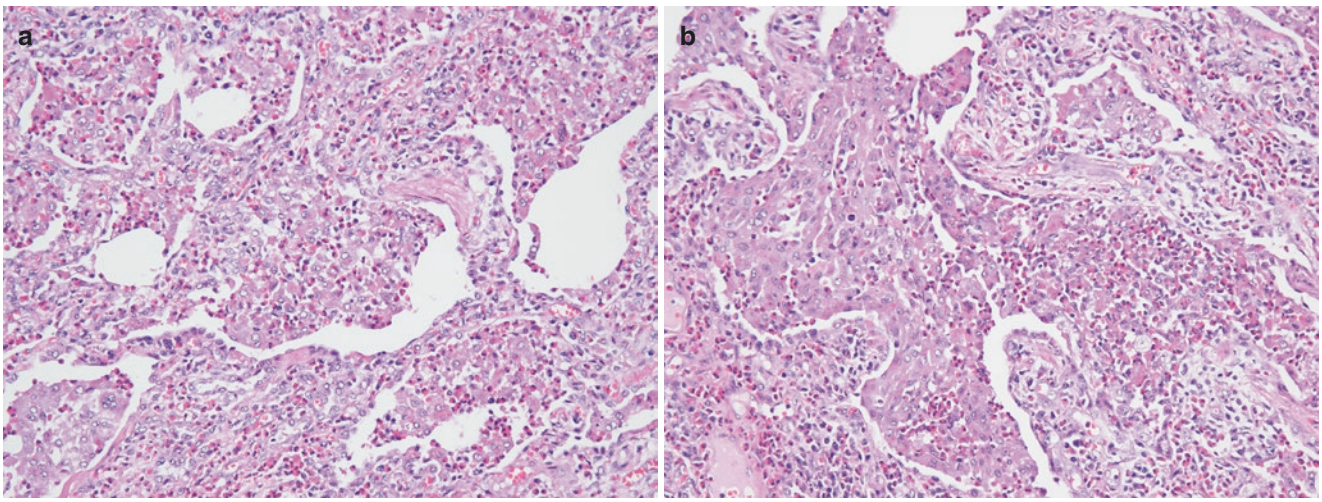

Fig. 6.29 Eosinophilic pneumonia in a patient with CEP. (**a**) High-magnification photomicrograph from patient with CEP whose biopsy is also illustrated in Fig. 6.28 showing air space and interstitial chronic inflammatory infiltrate in which eosinophils predominate (H&E). (**b**) High-magnification photomicrograph of a different field in the same biopsy showing both eosinophils and alveolar macrophages (H&E). Macrophages are often a prominent component of the air space exudate in eosinophilic pneumonia and sometimes overshadow the eosinophils

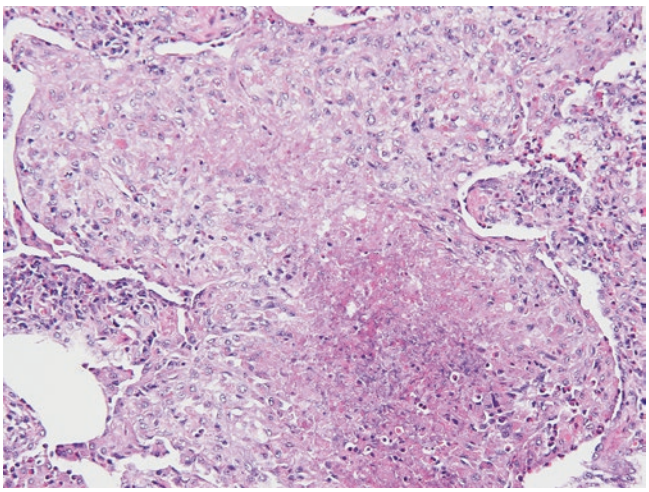

Fig. 6.30 Eosinophilic pneumonia in a patient with CEP. This high-magnification photomicrograph of a surgical lung biopsy from a patient with CEP shows focal necrosis in an air space exudate made up mainly of macrophages with eosinophils clustered at the periphery and within an expanded interstitial structure (H&E)

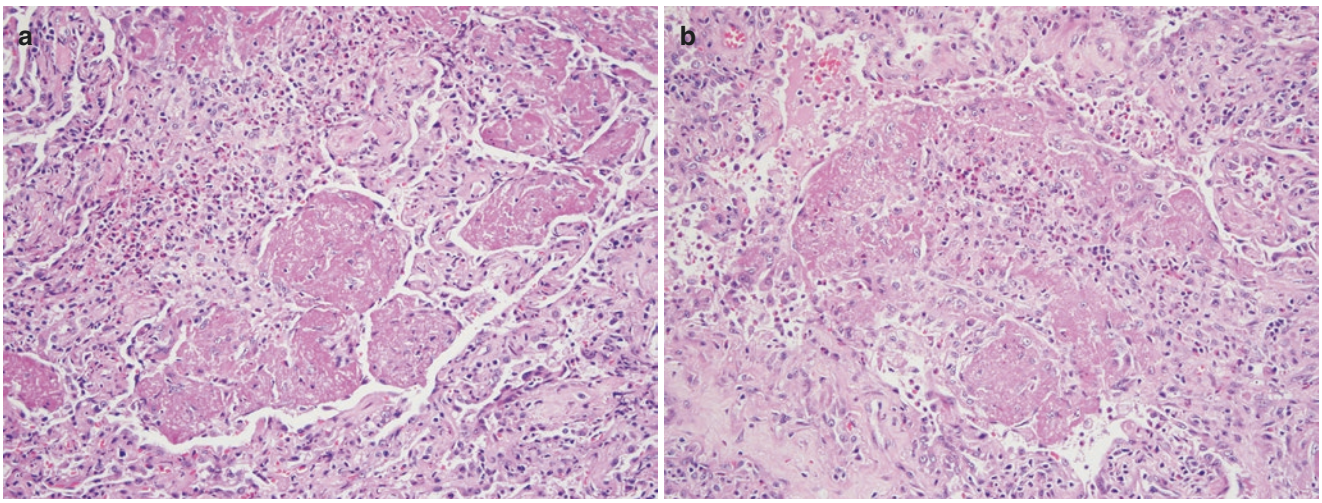

Fig. 6.31 Eosinophilic pneumonia in a patient with CEP. (**a**, **b**) Two high-magnification photomicrographs show a prominent fibrinous air space exudate that was a focal finding in a patient with biopsy findings that were otherwise typical of CEP (H&E). Fibrin predominates in the air spaces, but clusters of eosinophils are present within the air spaces as well as the interstitium and are key to distinguishing eosinophilic pneumonia from acute fibrinous and organizing pneumonia (AFOP)

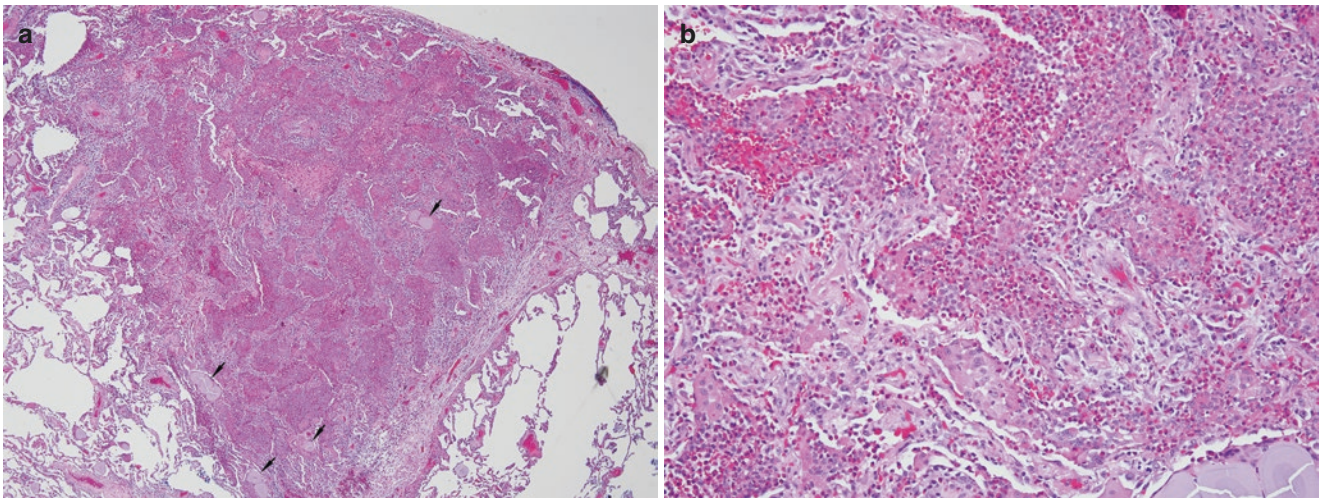

Fig. 6.32 Eosinophilic pneumonia in a patient with chronic eosinophilic pneumonia. (**a**) Low-magnification photomicrograph showing a very patchy air space-filling process in which fibrin is a prominent feature (H&E). Note multiple corpora amylacea (arrows) embedded in the fibrinous inflammatory infiltrate, an incidental finding of no special significance. (**b**) High-magnification photomicrograph of eosinophilic pneumonia showing a combination of fibrin, eosinophils, and macrophages in eosinophilic pneumonia (H&E). Note portion of corpora amylacea at lower right, an incidental finding

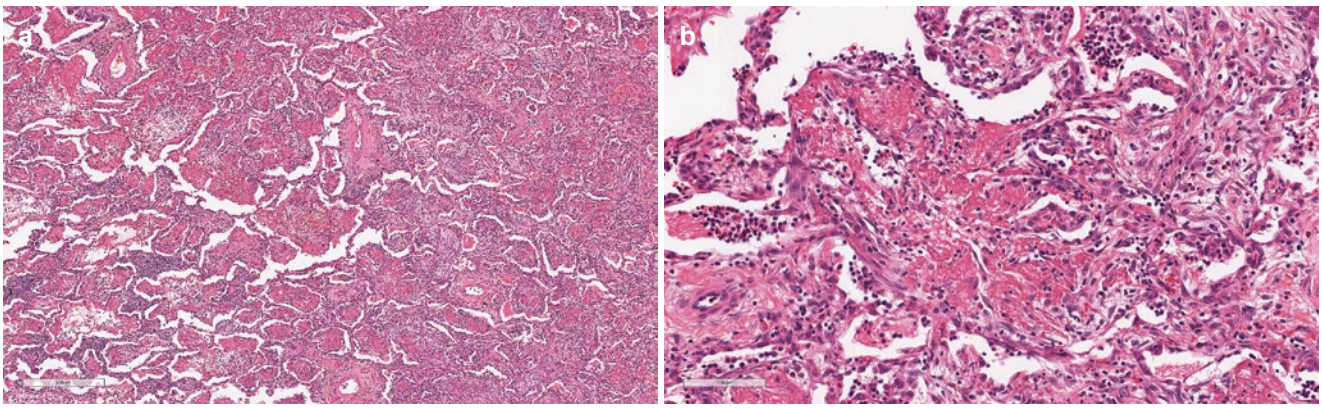

Fig. 6.33 Organizing eosinophilic pneumonia in a patient with chronic eosinophilic pneumonia. (**a**) Low-magnification photomicrograph showing a combination of air space fibrin, interstitial and air space inflammation, and organizing intraluminal fibrosis resembling organizing pneumonia (H&E). (**b**) High-magnification photomicrograph showing air space fibrin associated with a mixed inflammatory infiltrate that includes clusters of eosinophils, organizing fibroblasts, and myofibroblasts, resulting in a pattern of intraluminal fibrosis resembling organizing pneumonia (H&E)

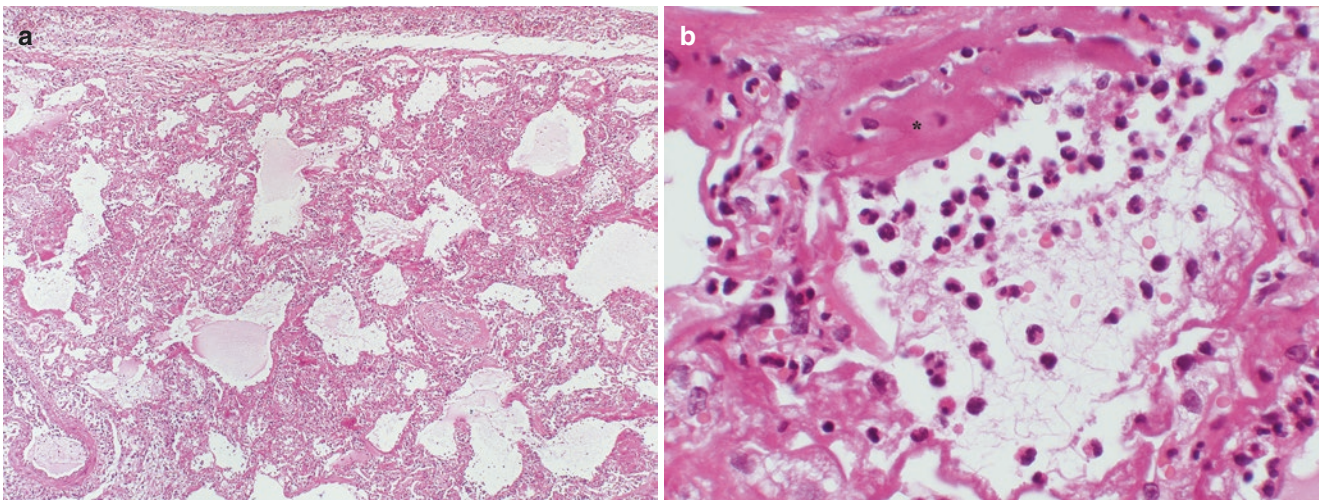

Fig. 6.34 AEP. (**a**) Low-magnification photomicrograph of a surgical lung biopsy from a patient with AEP showing a combination of interstitial thickening and a variably cellular fibrinous air space exudate with associated hyaline membranes (H&E). (**b**) High-magnification photomicrograph from same biopsy showing well-formed hyaline membrane (asterisk) and a cellular air space exudate that includes eosinophils and neutrophils (H&E). Some of the eosinophils are degranulated and recognizable only on the basis of a characteristic bilobed nucleus

Acute Fibrinous and Organizing Pneumonia (AFOP)

AFOP (Figs. 6.35 and 6.36) is a descriptive term intended from the outset to describe a fibrin-rich air space-filling lesion with features resembling those seen in DAD, organizing pneumonia, and eosinophilic pneumonia. Indeed, the original description suggested that in at least some patients, AFOP might be a histologic variant of DAD, given that just over half had a fulminant and fatal course that included mechanical ventilation. A fulminant clinical course linking AFOP with ARDS has now been documented in multiple reports. In other patients AFOP overlaps both clinical and histologic features of COP, a syndrome in which prominent fibrin may signify greater risk of relapse depending on the radiologic distribution of disease. In patients without more specific histologic findings such as hyaline membranes, classic organizing pneumonia, or eosinophilia, AFOP has been associated with various etiologies, including bacterial and viral infections, *Pneumocystis* pneumonia in HIV-infected patients, connective tissue diseases, and acute hypersensitivity pneumonia. AFOP, like the other lesions in the category of air space- filling diseases, should not be considered a specific diagnosis but rather a distinctive histology sometimes seen in other conditions (e.g., diffuse alveolar damage, organizing pneumonia, eosinophilic pneumonia). In patients without clinical or histologic features to suggest an alternative, AFOP occurs in a broad range of clinical contexts requiring not only special stains for organisms but also careful correlation with other data, including the results of microbiologic assays, to fully understand the significance of this finding.

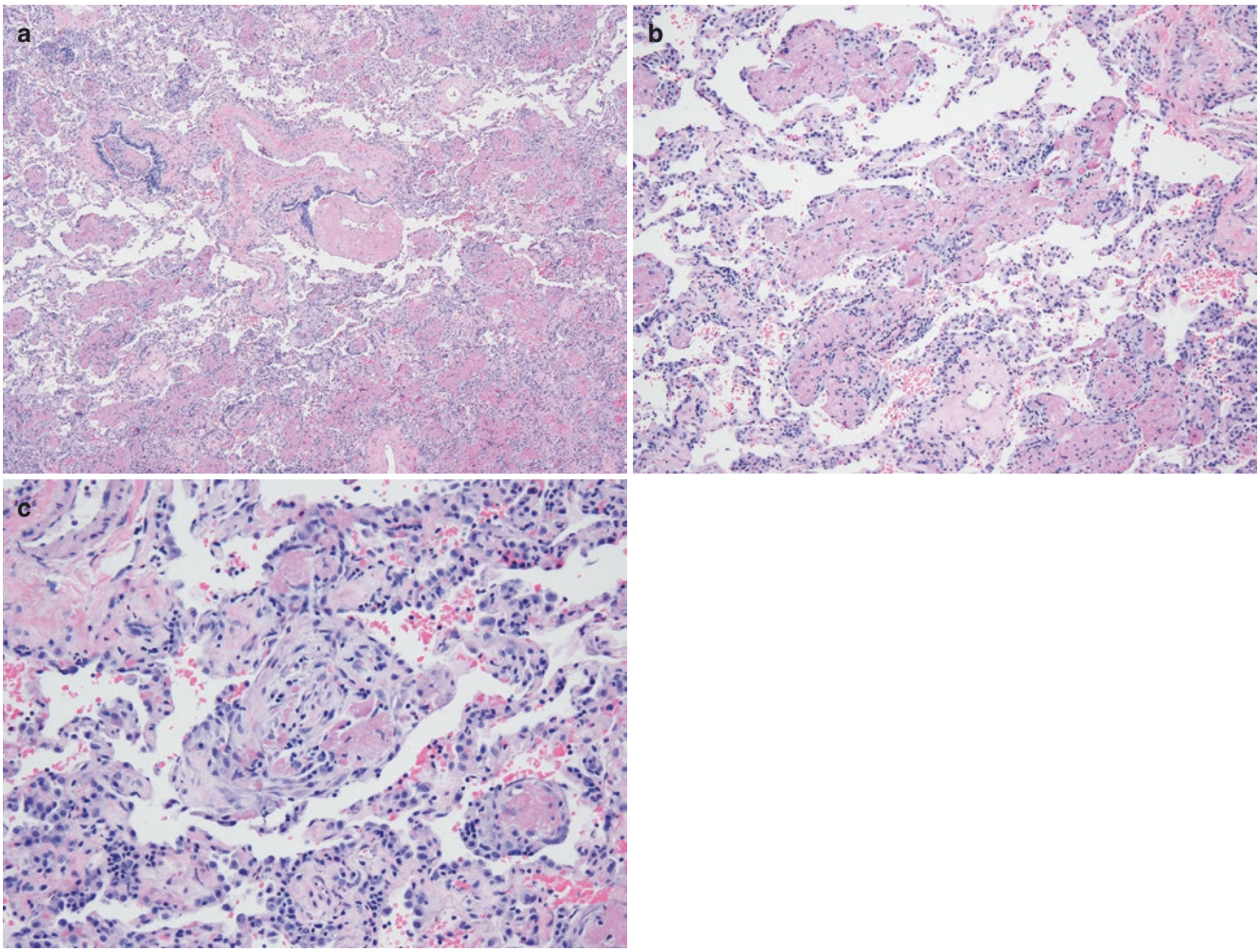

Fig. 6.35 Acute fibrinous and organizing pneumonia (AFOP). (**a**) Low-magnification photomicrograph of AFOP in a patient with unexplained bilateral opacities on CT scan (H&E). There is a patchy air space-filling process in which fibrin predominates and is accompanied by a very mild air space and interstitial infiltrate of mononuclear cells. In this field there is minimal organization of the fibrinous air space exudate. (**b**) Higher-magnification photomicrograph showing a fibrinous air space exudate with minimal association inflammation (H&E). Special stains and cultures were negative, and there was minimal eosinophilia to suggest eosinophilic pneumonia as an alternative to AFOP. (**c**) High-magnification photomicrograph from same surgical lung biopsy showing an area in which the fibrinous air space exudate illustrated in **a**, **b** is affiliated with ingrowth of organizing fibroblasts (H&E). This feature, common in AFOP, results in considerable histologic overlaps with organizing pneumonia. Indeed, some patients with lesions resembling AFOP almost certainly have a variant of organizing pneumonia (COP)

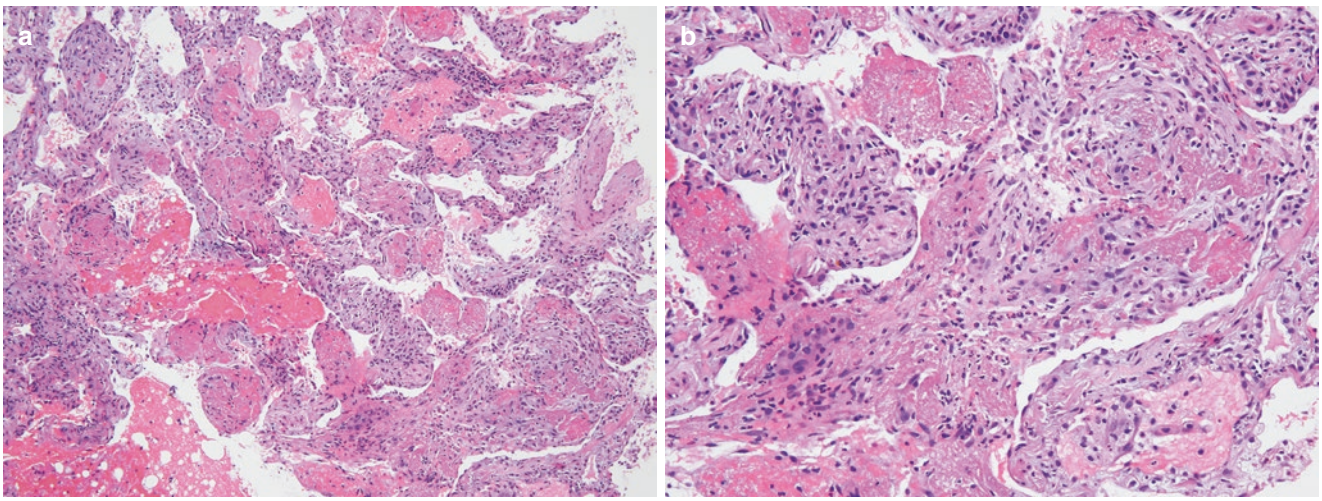

Fig. 6.36 AFOP. (**a**) Intermediate-magnification photomicrograph of core needle biopsy from patient with unexplained localized opacities on a chest CT scan (H&E). All special stains and cultures were negative for organisms, and there were no other histologic features (such as eosinophilia) to suggest a specific etiology. (**b**) Higher-magnification photomicrograph of area in lower right of field illustrated in **a** showing an organizing fibrinous air space exudate. This associated acute inflammation in this focus should at least raise the possibility of an infectious etiology (H&E)

Pulmonary Alveolar Proteinosis (PAP)

PAP (Figs. 6.37, 6.38, 6.39, 6.40 and 6.41), also called pulmonary alveolar lipoproteinosis or phospholipoproteinosis, is a distinctive lesion characterized by the presence of amorphous granular eosinophilic debris within alveolar spaces. Primary acquired PAP accounts for over 90% of patients and in most is a form of autoimmune disease driven by autoantibodies directed against granulocyte-macrophage colony-stimulating factor (GM-CSF). Secondary PAP refers to patients with certain underlying illnesses or associated conditions and has been reported most commonly in patients with hematologic malignancies and other forms of immunodeficiency. Associated opportunistic infections are common in immunocompromised patients. Less common causes of secondary PAP include occupational dust exposures and mutations in various genes that affect surfactant homeostasis in patients with congenital disease.

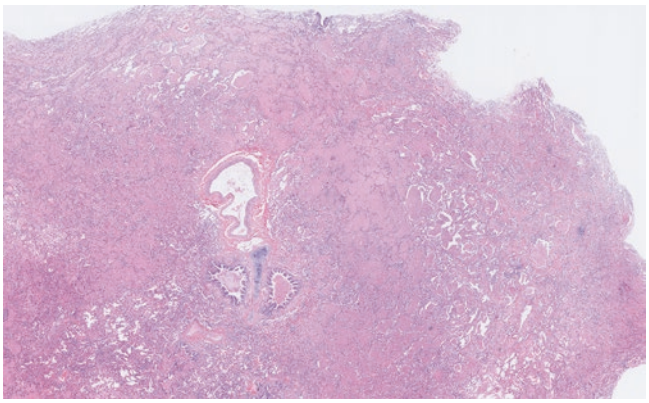

Fig. 6.37 PAP. Scanning magnification photomicrograph of surgical lung biopsy from a patient with primary acquired (autoimmune) PAP (H&E). Most of the air spaces in this sample are filled with eosinophilic debris that at first blush resembles pulmonary edema. Alveolar septa are nearly normal, showing only a mild, patchy infiltrate of chronic inflammatory cells without significant fibrosis

Primary acquired (autoimmune) PAP most commonly presents in the fourth decade of life. Nearly three fourths of patients are smokers at disease onset. Men are affected more commonly than women by a ratio of about 3:1, a disparity that may reflect historical smoking patterns. The most common symptoms at presentation are dyspnea and dry cough. Low-grade fever is seen in some, but the combination of an acute onset and fever should raise the possibility of superimposed infection. Pulmonary function studies usually show a mild restrictive ventilatory defect with a disproportionately severe reduction in the diffusing capacity for carbon monoxide (DLco). PAP is a disease with a generally good prognosis with 90% survival at 5 years. Whole lung lavage is the mainstay of therapy. PAP is an increasingly uncommon finding in surgical lung biopsies because many patients are now diagnosed on the basis of clinical and radiologic findings coupled with findings in bronchoalveolar lavage (BAL) fluid and/or transbronchial lung biopsy.

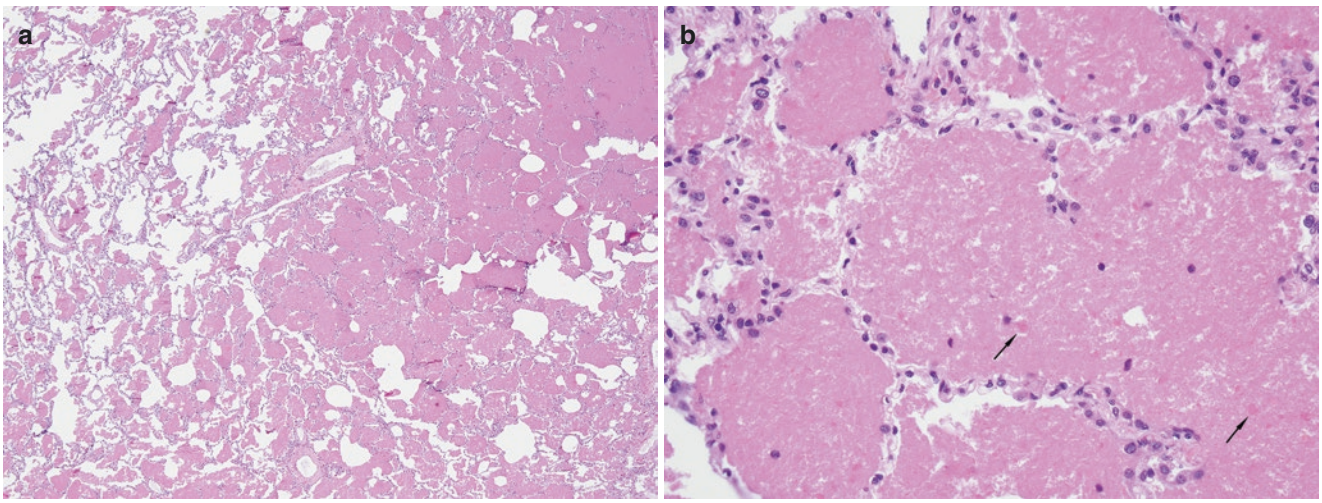

Fig. 6.38 PAP. (**a**) Low-magnification photomicrograph showing characteristic patchy distribution of a granular air space exudate in a patient with primary acquired (autoimmune) PAP (H&E). In many areas the air space exudate retracts from alveolar septa in a manner that is sometimes helpful in separating PAP from pulmonary edema. (**b**) High-magnification photomicrograph showing to better advantage the granular texture of the alveolar exudate with occasional coarse eosinophilic aggregates (*arrows*), rare mononuclear inflammatory cells, and degenerating erythrocytes (H&E). The granular nature of the exudate and associated cellular detritus is key to separating PAP from pulmonary edema

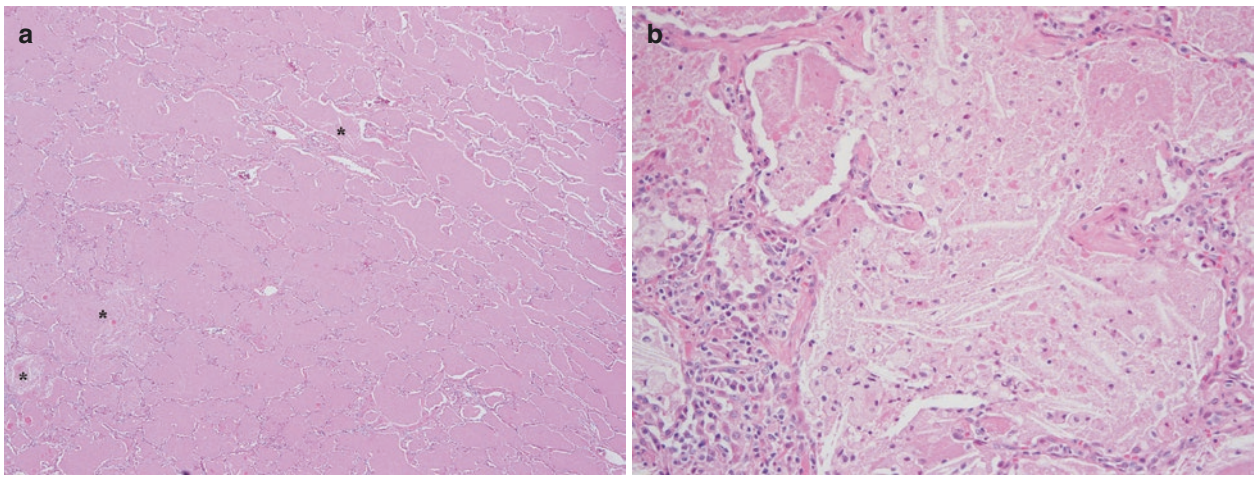

Fig. 6.39 PAP. (**a**) Low-magnification photomicrograph from another patient with primary acquired (autoimmune) PAP showing pulmonary edema-like eosinophilic air space exudate (H&E). Focal cholesterol-like clefts and granular debris with cell ghosts (asterisk) are important clues to the diagnosis of PAP. (**b**) High-magnification view of the same lung biopsy showing granular eosinophilic background, cholesterol-like clefts, macrophages, and cell ghost characteristic of PAP (H&E). Staining for periodic acid-Schiff stain, while characteristic, is relatively nonspecific. Diagnosis hinges instead on recognizing the distinctive histologic and cytologic characteristics that separate alveolar exudates of PAP from edema fluid

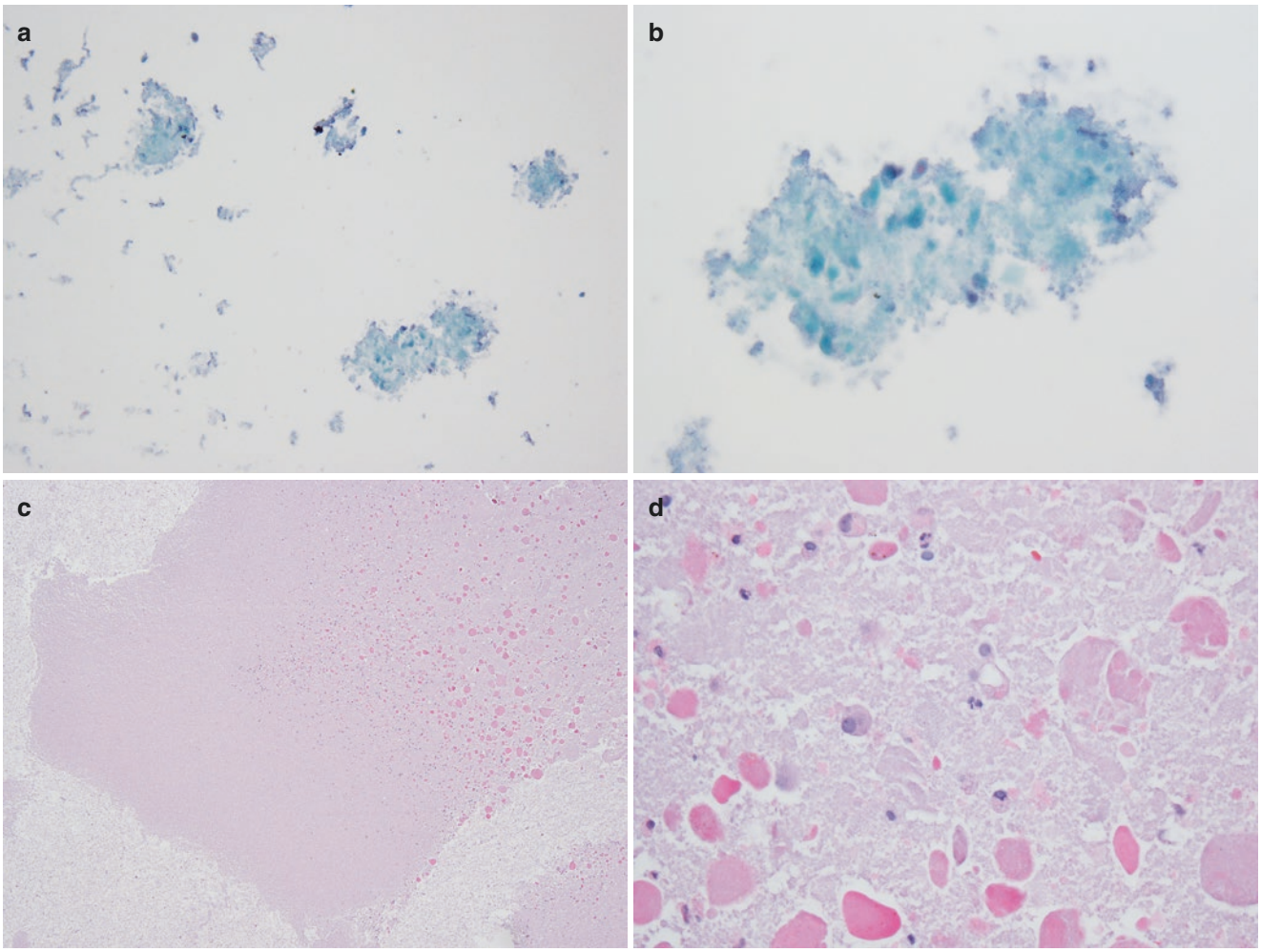

Fig. 6.40 PAP. (**a**) Intermediate magnification of ThinPrep preparation demonstrating bronchoalveolar lavage fluid from patient with PAP. Irregularly shaped fragments of a paucicellular granular exudate with coalescent globules and cell ghosts are characteristic of PAP. (**b**) High-magnification photomicrograph of one of the fragments illustrated in **a** showing PAP characterized by granular, paucicellular debris containing cell ghosts. (**c**) Low-magnification photomicrograph of cell block from a different patient using PAP (H&E). A paucicellular granular exudate shows larger aggregates or clumps of eosinophilic debris, a common finding in PAP. (**d**) High-magnification photomicrograph of cell block from same patient with PAP illustrated in **c**. A granular exudate is associated with rare macrophages, cell ghosts, and characteristic large eosinophilic aggregates (H&E)

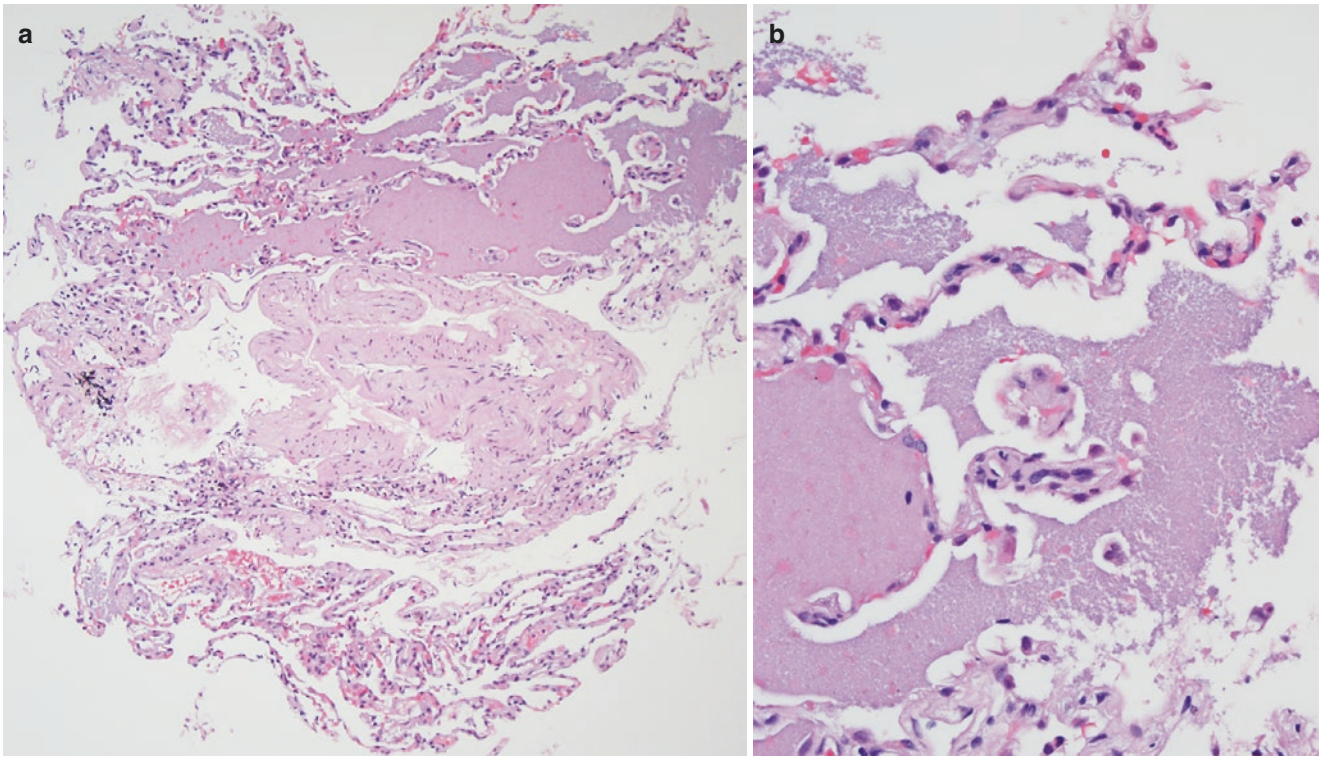

Fig. 6.41 PAP. (**a**) Low-magnification photomicrograph of transbronchial lung biopsy from a patient with primary acquired (autoimmune) PAP (H&E). The upper third of the photomicrograph shows alveolated lung parenchyma with a distinctive, paucicellular, granular air space exudate. Alveolated lung parenchyma at the bottom is unremarkable, attesting to the often patchy distribution of PAP. (**b**) High-magnification photomicrograph of the same transbronchial biopsy showing granular, eosinophilic, air space exudate typical of PAP (H&E)

Smoking–Related Lung Disorders

Cigarette smoking is associated with a range of overlapping histologic findings other than those traditionally attributed to chronic obstructive pulmonary disease (COPD). With the exception of Langerhans cell histiocytosis (LCH), the other smoking-related lesions (respiratory bronchiolitis, smoking-related interstitial fibrosis, and desquamative interstitial pneumonia) covered in this section are frequently seen in surgical specimens as incidental findings in patients who lack evidence of physiologically significant diffuse lung disease other than perhaps COPD. In asymptomatic patients without significant ventilatory defects other than those related to COPD, these frequently overlapping histologic findings serve only to corroborate a smoking history and should not by themselves be construed as evidence of diffuse restrictive lung disease. Similarly, any one or combination of these findings may be seen in smokers who have other forms of diffuse lung disease, most importantly UIP (*see* section "Usual Interstitial Pneumonia (UIP)"). On the other hand, these smoking-related lesions occasionally account for symptomatic diffuse lung disease in a highly select population of patients. In any individual patient, determining whether these lesions should be viewed as incidental, a cause of diffuse lung disease, or a confounding finding in a patient with something else altogether requires careful correlation with clinical and radiologic information.

Respiratory Bronchiolitis (RB)

Respiratory bronchiolitis (RB) is a common incidental finding in current or ex-smokers. While rare cases of RB are associated with clinical interstitial disease, the majority of the cases of RB are of no clinical significance. Histologically, RB is characterized by pigmented macrophages filling up respiratory bronchioles, alveolar ducts, and adjacent alveoli (Figs. 6.42 and 6.43).

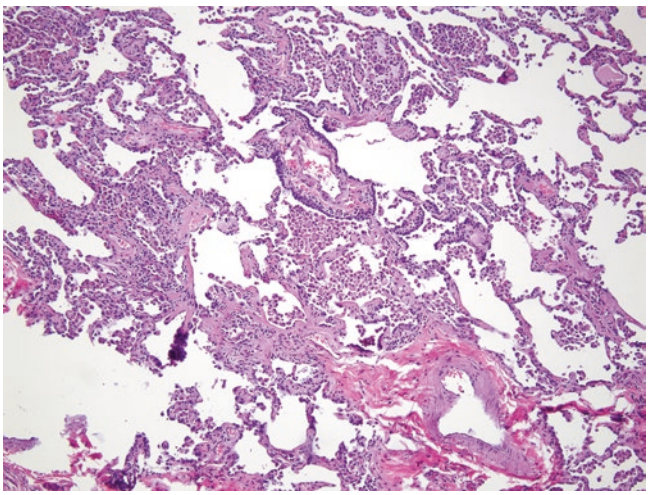

Fig. 6.42 RB. Intermediate-magnification photomicrograph showing a respiratory bronchiole and its adjacent alveoli filled with lightly pigmented macrophages typical of those seen in cigarette smokers. The air spaces away from the respiratory bronchiole are less involved

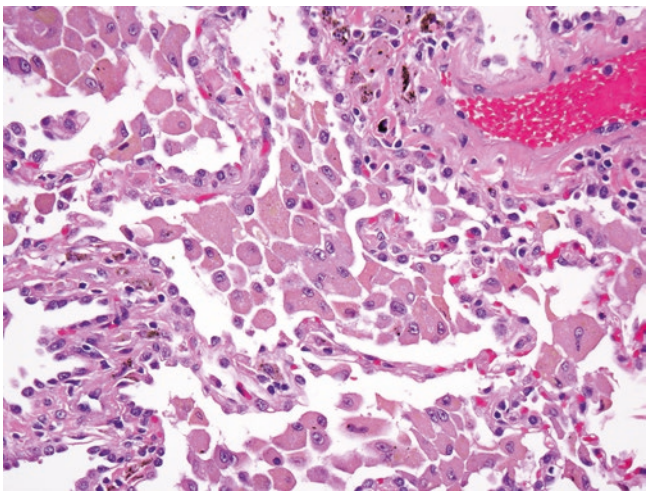

Fig. 6.43 RB. High-magnification photomicrograph showing smokers' macrophages within the air spaces that contained finely granular light brown pigment in the cytoplasm. The pigment is faintly positive on a Prussian-blue iron stain but lacks the coarse, refractile granules and bright blue staining characteristics of bleeding-related hemosiderin

Smoking-Related Interstitial Fibrosis (SRIF)

SRIF is a recently described entity that is characterized by marked alveolar septal fibrosis with distinct hyalinized collagen and minimal inflammation (Figs. 6.44 and 6.45). SRIF is most often encountered as an incidental finding in autopsy or lobectomy specimens from smokers. Rarely, SRIF causes symptoms and radiologic findings of interstitial lung disease, leading to lung biopsy.

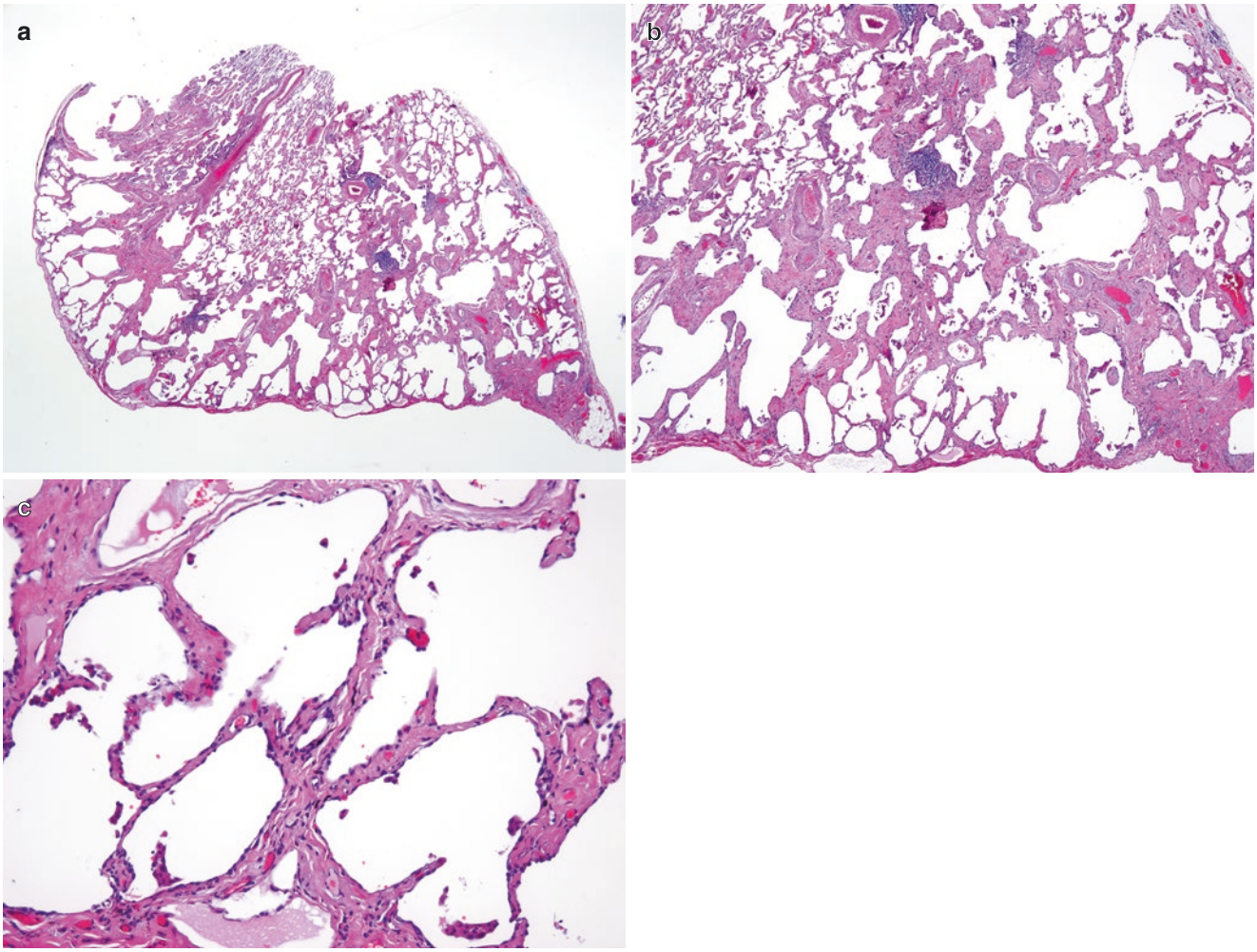

Fig. 6.44 Smoking-related interstitial fibrosis (SRIF). (**a**) Low-magnification photomicrograph showing patchy areas of lung parenchyma with thickened septa. The fibrosis involves the subpleural and centrilobular parenchyma with abrupt demarcation from uninvolved lung parenchyma. (**b**) At intermediate magnification, the involved areas show interstitial thickening by hyalinized collagen fibrosis with minimal inflammation. The alveolar spaces are enlarged and distorted. (**c**) High-magnification view of the thickened alveolar septa with hyalinized collagen bundles. No significant inflammation is present

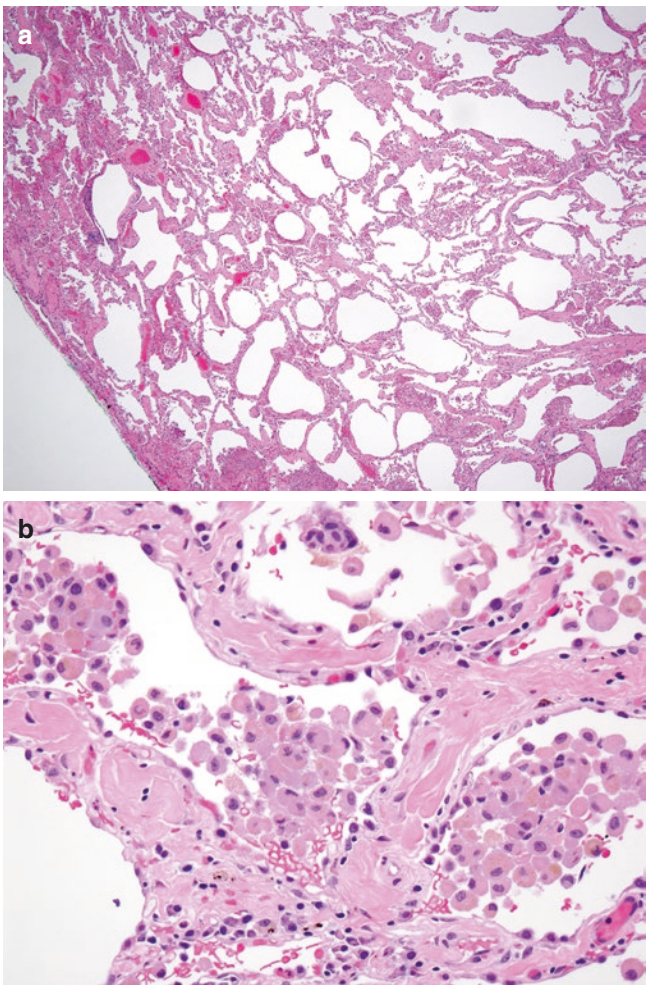

Fig. 6.45 SRIF with respiratory bronchiolitis. (**a**) At low magnification, alveolar septa are thickened, and some alveolar spaces are filled with pigmented macrophages. (**b**) High-magnification view showing alveolar septa thickened with hyalinized collagen bundles. Note the pigmented smokers' macrophages within the alveolar spaces

Desquamative Interstitial Pneumonia (DIP)

DIP, similar to RB, is also characterized by accumulation of pigmented smoker's macrophages within air spaces. Unlike RB, the changes are not limited to peribronchiolar parenchyma but instead diffusely affect air spaces with an associated interstitial pneumonia (Figs. 6.46, 6.47, 6.48 and 6.49). Ground-glass opacities and centrilobular nodules are common findings on chest CT scan. The prognosis is good in most cases.

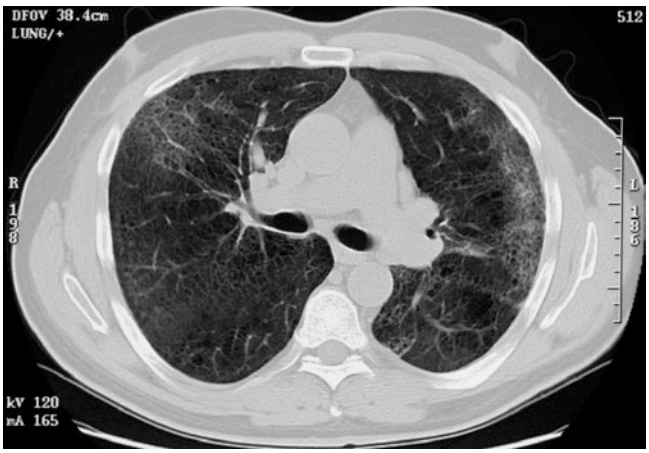

Fig. 6.46 Chest CT scan image of a patient with desquamative interstitial pneumonia (DIP). Patchy ground-glass opacities and emphysematous changes are commonly described. No significant fibrosis is noted, as evidenced by traction bronchiectasis and/or honeycomb change

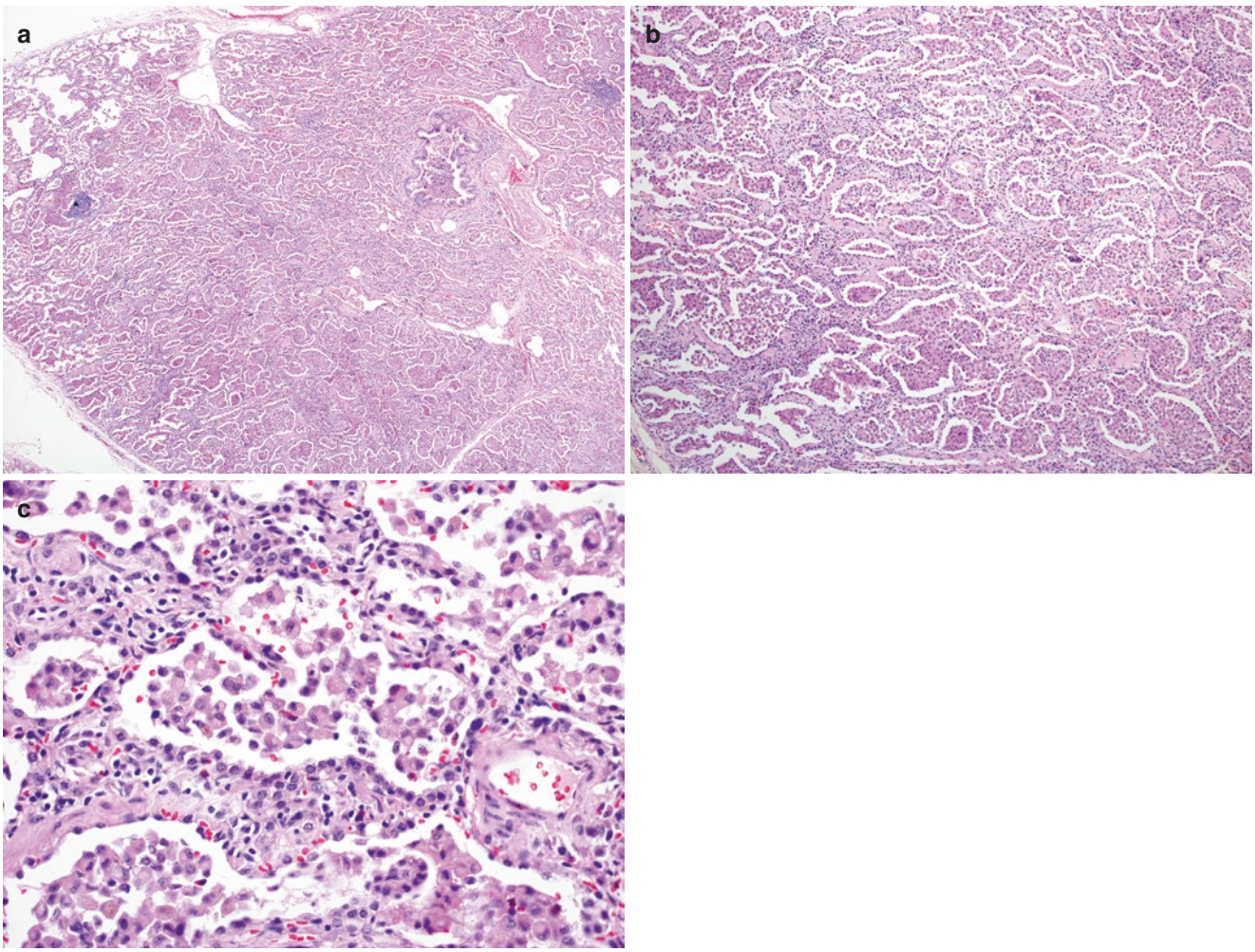

Fig. 6.47 DIP. (**a**) At low magnification, air spaces are diffusely filled by numerous pigmented macrophages. (**b**) Intermediate-magnification view showing intra-alveolar accumulation of pigmented macrophages with preserved alveolar structure and mildly thickened alveolar septa. (**c**) High-magnification photomicrograph demonstrating macrophages with light brown cytoplasmic pigment within the air spaces. The alveolar septa are expanded by chronic inflammation without the paucicellular hyalinized collagen typical of SRIF, and they are lined by reactive pneumocytes

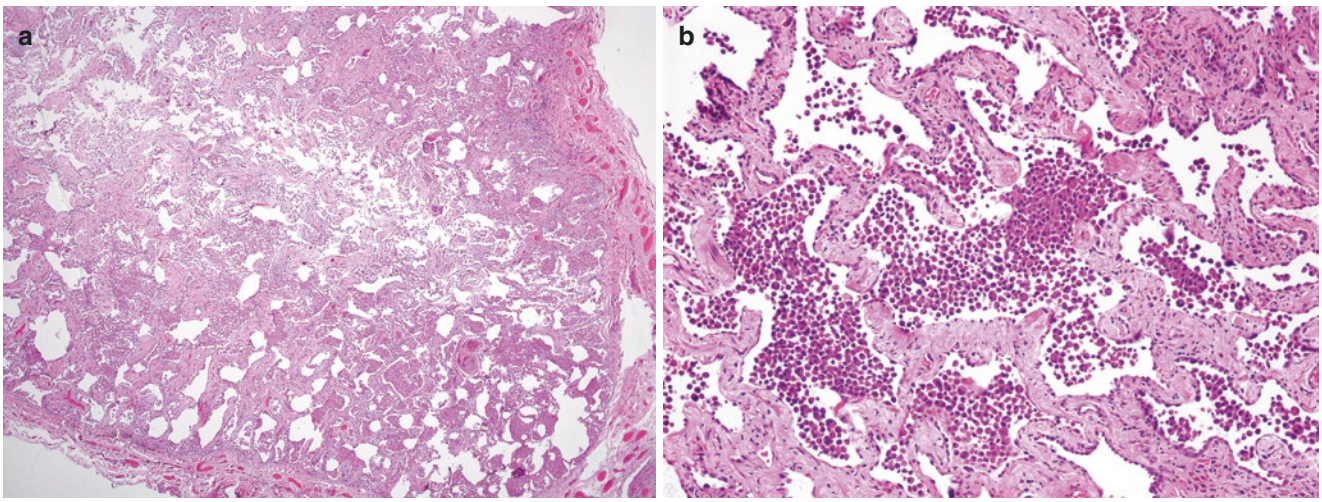

Fig. 6.48 Changes resembling DIP in smoking-related interstitial fibrosis (SRIF). (**a**) At low magnification, there is diffuse air space filling of pigmented macrophages. The alveolar architecture is preserved, but the alveolar septa are markedly thickened. (**b**) High-magnification view showing the typical pigmented macrophages filling up the air spaces and alveolar septa thickened with hyalinized collagen fibrosis

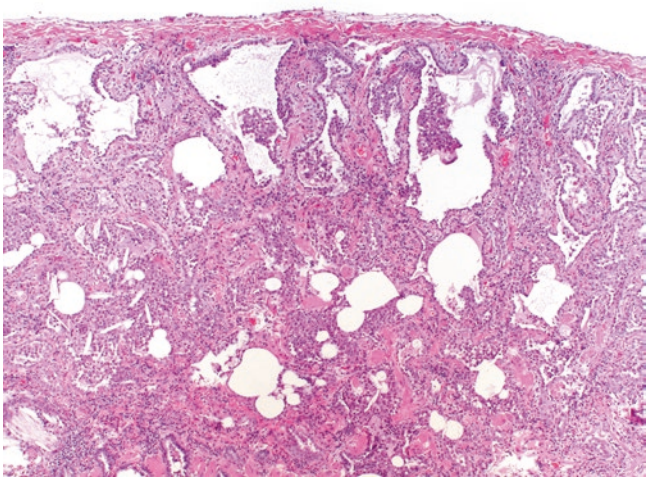

Fig. 6.49 DIP with emphysema. In addition to the typical pigmented macrophages filling up air spaces, there are also air space enlargement and concomitant interstitial pneumonia that include mild fibrosis

Langerhans Cell Histiocytosis (LCH)

LCH, formerly known as eosinophilic granuloma, is characterized by nodular bronchiolocentric infiltrates of Langerhans cells admixed with variable numbers of eosinophils and pigmented macrophages (Figs. 6.50, 6.51, 6.52, 6.53, 6.54, 6.55, 6.56 and 6.57). Some nodules may undergo central cystic changes. More commonly a distinctive pattern of paracicatricial air space enlargement (scar emphysema) accounts for the upper lobe predominant cysts and spiculated nodules that characterize radiologic findings on thoracic CT scans. In some patients fibrosis replaces the cellular infiltrate, forming a stellate-shaped scar as the only clue to the diagnosis of LCH. Definitive diagnosis of LCH requires identification of the Langerhans cell clusters and can often be made after careful examination of the rest of the specimen. LCH occurs exclusively in smokers. Coexisting smoking-related conditions such as RB, SRIF, and DIP-like changes are commonly present. Increased peribronchiolar Langerhans cells are commonly seen in smokers and are not indicative of LCH in the absence of expansile nodules. The prognosis of LCH is generally good. Many patients recover completely after quitting smoking. Identification of v-raf murine sarcoma viral oncogene homolog B1 (BRAF) mutations in a subset of patients has sparked interest in targeted therapies for those patients in whom smoking cessation alone may be insufficient. Pulmonary hypertension can occur in patients with fibrotic disease. Smoking-related comorbidities such as emphysema may also negatively impact overall prognosis.

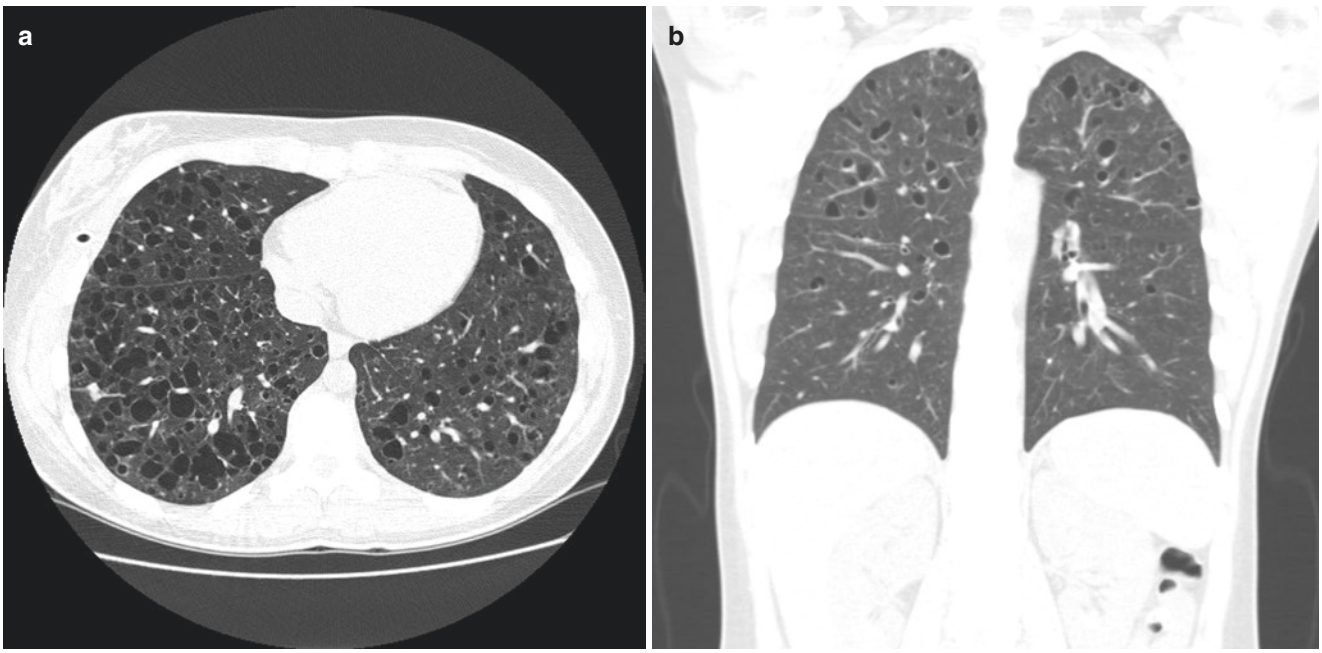

Fig. 6.50 Chest CT scan images of a patient with Langerhans cell histiocytosis (LCH). (**a**) A horizontal cross section of the chest showing numerous cysts and nodular densities. (**b**) A coronal cross section showing that the cystic and nodular lesions are predominantly within the upper lobes of the lung

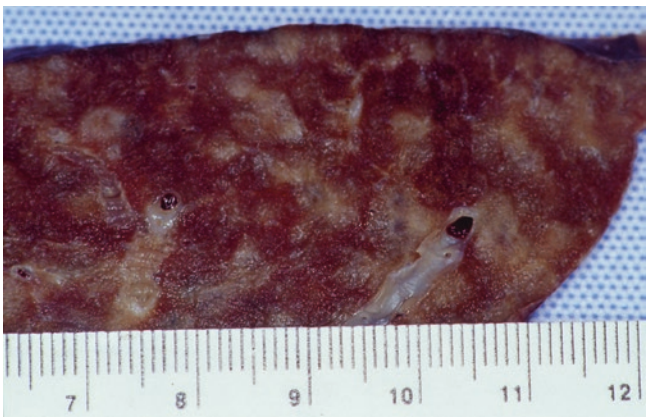

Fig. 6.51 LCH. Gross image of a lung wedge biopsy from a patient with early-stage LCH showing multiple tan-white centrilobular nodules on the cut surface

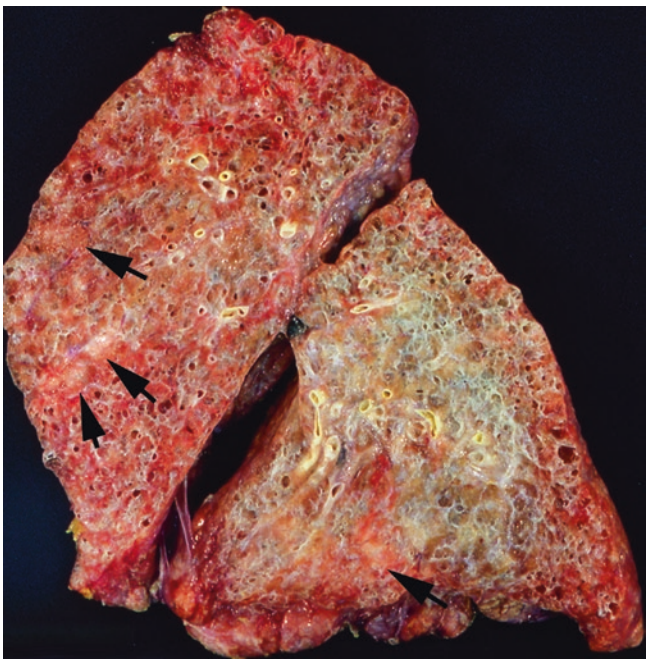

Fig. 6.52 LCH. Gross image of an explanted lung from a patient with late-stage LCH. Numerous cysts and tan-white nodules (arrows) are seen on the cut surface

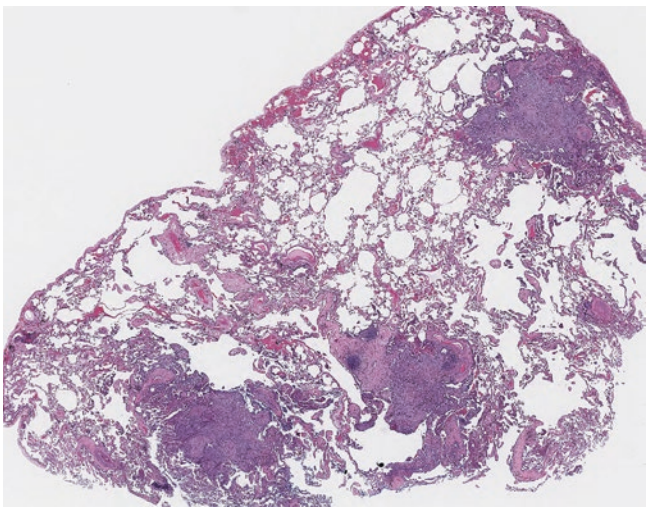

Fig. 6.53 LCH. Low-magnification photomicrograph showing multiple cellular, stellate nodules within the lung. Note the background lung parenchyma with emphysematous change and respiratory bronchiolitis

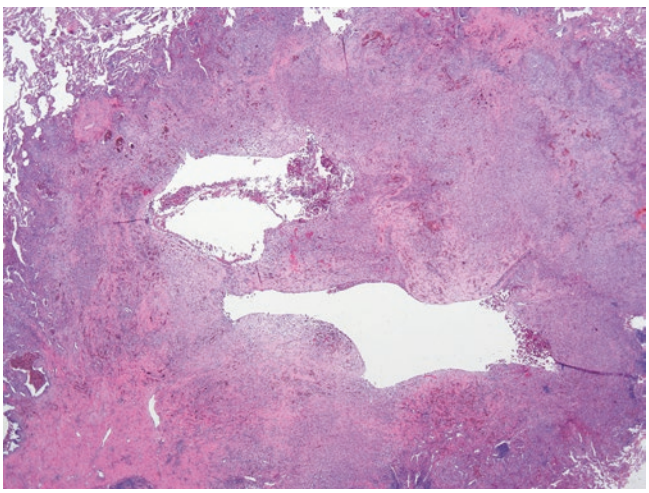

Fig. 6.54 LCH. Low-magnification view of a centrally cystic nodule from a patient with LCH. The central cyst represents the ectatic lumen of the affected airway, which is surrounded by a polymorphic infiltrate in which there are numerous Langerhans cells resulting in a vaguely granulomatous appearance

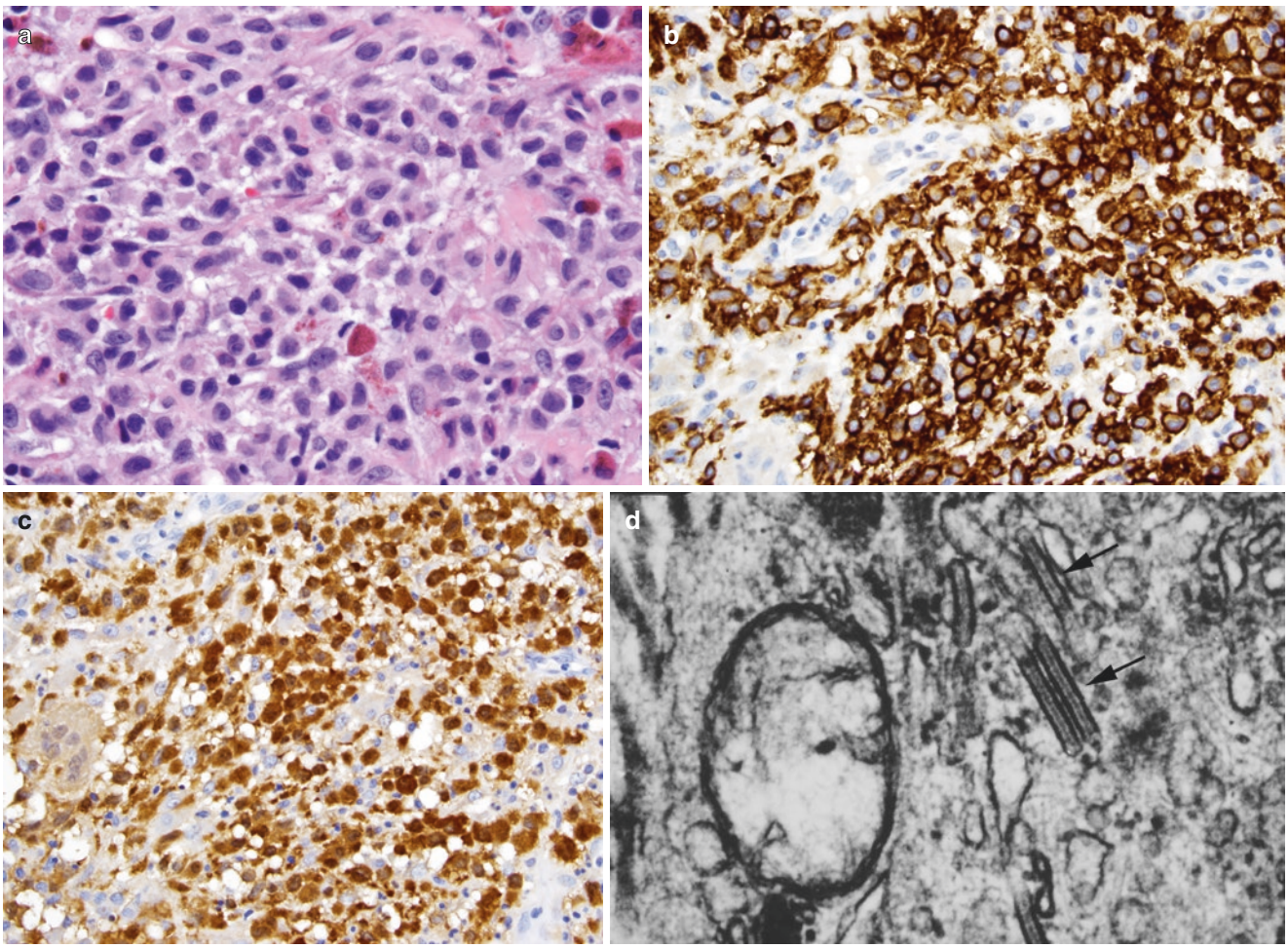

Fig. 6.55 LCH. (**a**) High-magnification view of Langerhans cells within the nodule illustrated in Fig. 6.54, mononuclear cells with folded or kidney bean-shaped nuclei, and abundant eosinophilic cytoplasm. (**b**) Immunohistochemical stain for CD1a shows positive membranous staining in Langerhans cells. (**c**) Immunohistochemical stain for S-100 shows positive nuclear and cytoplasmic staining in Langerhans cells. (**d**) Electron microscopy image of a Langerhans cell with intracytoplasmic rod-shaped Birbeck granules (*arrows*)

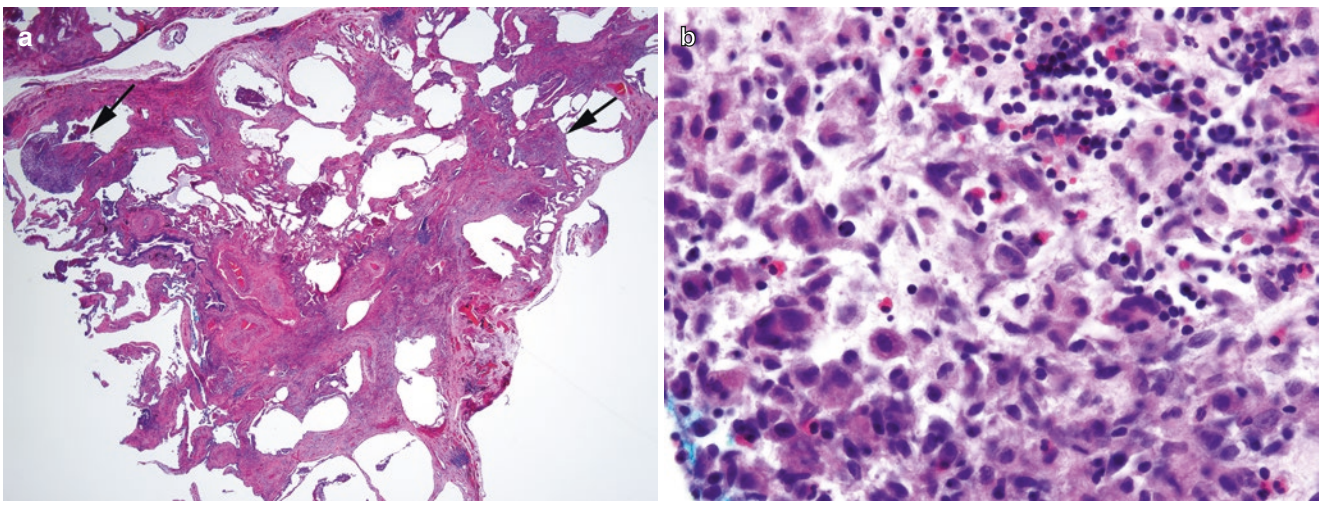

Fig. 6.56 LCH. (**a**) In this example, the lesion is almost completely replaced by fibrosis, forming a stellate-shaped scar with scar emphysema. At the periphery of the lesion, there are smaller clusters of cellular infiltrates (*arrows*). (**b**) High-magnification view of the cellular focus demonstrating typical Langerhans cells with folded or kidney bean-shaped nuclei and admixed eosinophils and lymphocytes

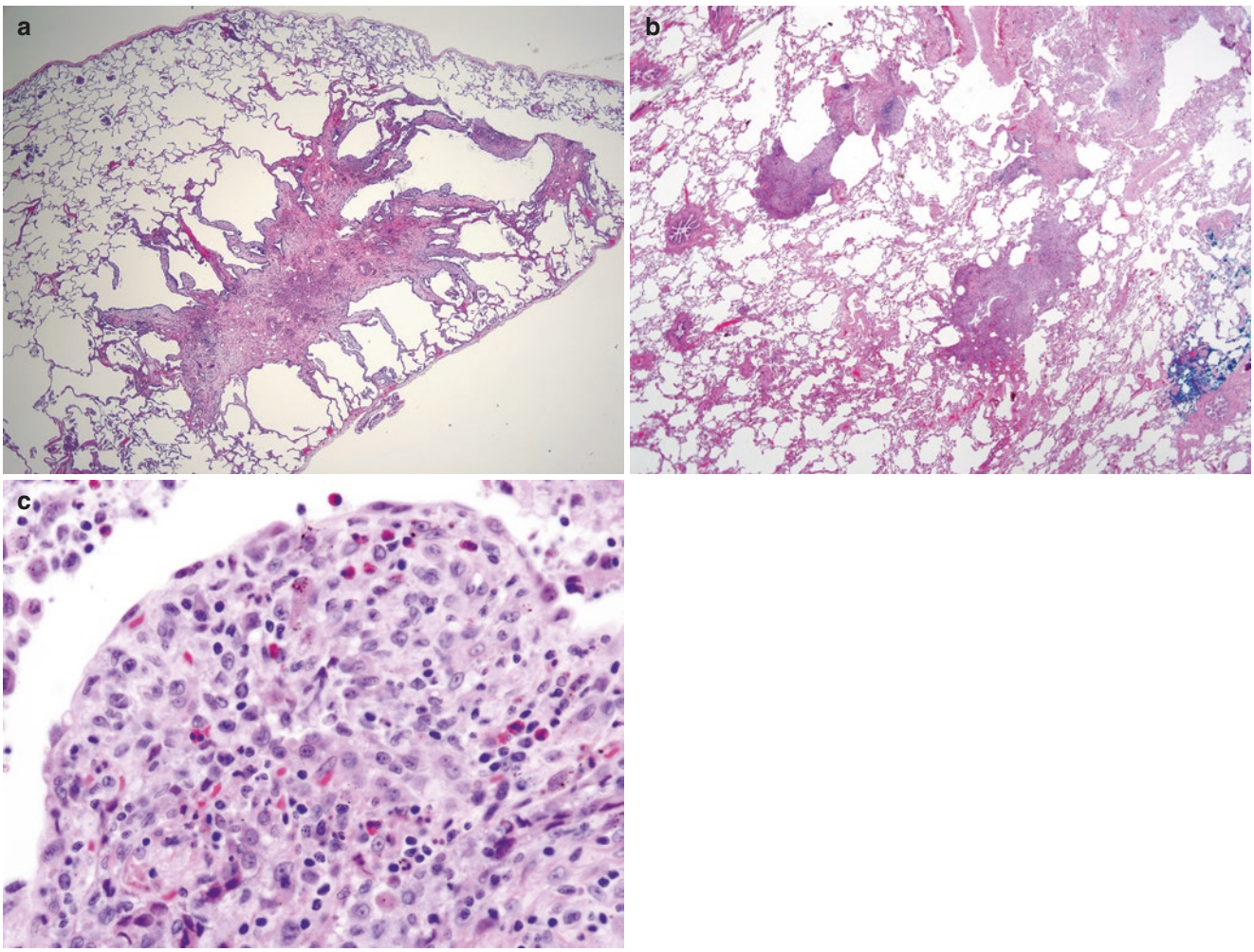

Fig. 6.57 LCH. (**a**) A stellate-shaped scar with the characteristic pattern of associated scar emphysema. Nonspecific chronic inflammatory cells and pigmented macrophages are present. This finding suggests LCH and should trigger careful examination for cellular lesion diagnostic of LCH. (**b**) Another low-magnification field from the same specimen shows two cellular nodules. (**c**) High-magnification view of one of the nodules illustrated in part **b** demonstrating numerous Langerhans cells admixed with scattered eosinophils and pigmented macrophages

Idiopathic Interstitial Pneumonias

Histopathologic classification of idiopathic interstitial pneumonias is useful in separating them into distinct clinical categories. In 2002 and again in 2013, an international committee, supported by the American Thoracic Society and the European Respiratory Society, proposed a classification scheme based primarily on expert opinion and influenced management strategies, study design for clinical trials, and research opportunities to challenge areas in which evidence was weak.

Usual Interstitial Pneumonia (UIP)

UIP (Figs. 6.58, 6.59, 6.60, 6.61, 6.62, 6.63, 6.64, 6.65, 6.66, 6.67, 6.68, 6.69, 6.70, 6.71, 6.72, 6.73, 6.74 and 6.75) is the most common of the idiopathic interstitial pneumonias, accounting for about two thirds of biopsied patients. An American Thoracic Society (ATS) consensus statement published in 2000 linked UIP to idiopathic pulmonary fibrosis (IPF) by defining the latter as a specific form of chronic fibrosing interstitial pneumonia limited to the lung and associated with the histologic appearance of UIP on surgical (thoracoscopic or open) lung biopsy. This definition was revised in 2011 to include HRCT as an important diagnostic tool capable of identifying UIP in a minority of patients, thus obviating the need for lung biopsy. As this definition implies, UIP and IPF are roughly interchangeable terms, the exceptions being those patients with underlying systemic illnesses or occupational exposures that may suggest an etiology for their lung disease (e.g., asbestosis). IPF is a disease of middle-aged to older adults and is more common in men than in women. It is a progressive disease, with an average survival of 2–6 years after diagnosis. Some antifibrotic agents have been shown to slow disease progression; lung transplantation is the only viable treatment for patients with late-stage disease. Clinical diagnosis of IPF is often made based on typical clinical and radiologic findings; however, in patients with atypical clinical and radiologic presentations, lung biopsy is the only way to establish the diagnosis and to qualify the patients for transplantation and/or clinical trials. Atypical clinical presentations of UIP/IPF are sometimes caused by coexisting air space or interstitial diseases such as emphysema, smoking-related diseases, eosinophilic pneumonia, and malignancies.

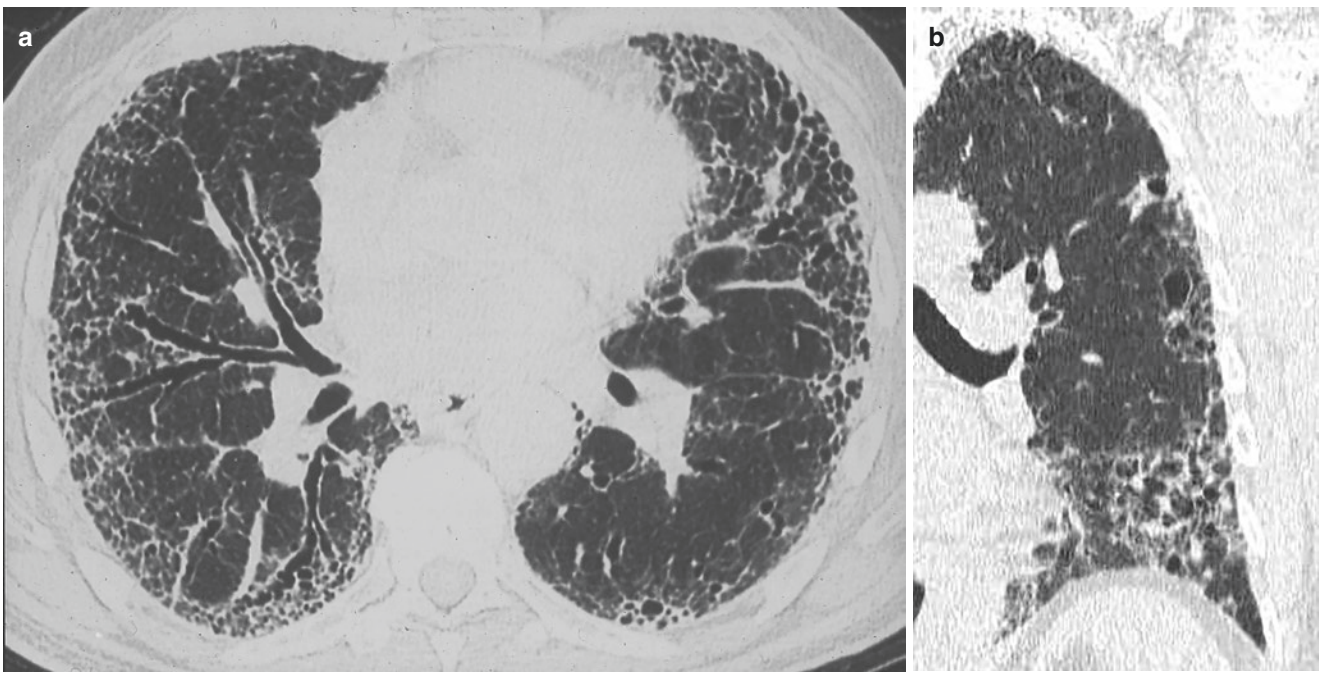

Fig. 6.58 UIP. High-resolution CT scan of the chest of a patient with UIP. (**a**) A horizontal cross-sectional image showing the typical findings of UIP: bilateral reticular marking with traction bronchiectasis and honeycomb change, more severe in the periphery. (**b**) A coronal cross-sectional image demonstrating the basilar predominant distribution of the lesions

Fig. 6.59 UIP. Gross photograph of an autopsy showing the right lung from a patient with end-stage UIP. The entire lung is smaller than normal, with diffuse scarring and subpleural honeycomb change that is more severe in the base

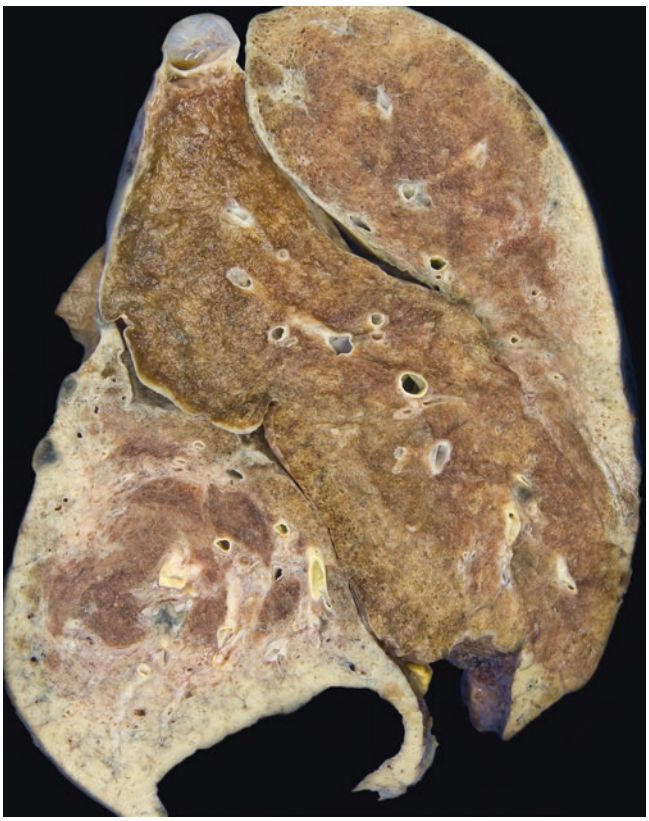

Fig. 6.60 UIP. In this explanted right lung, dense scarring and honeycomb changes are mainly seen in the shrunken lower lobe and the periphery of upper lobe

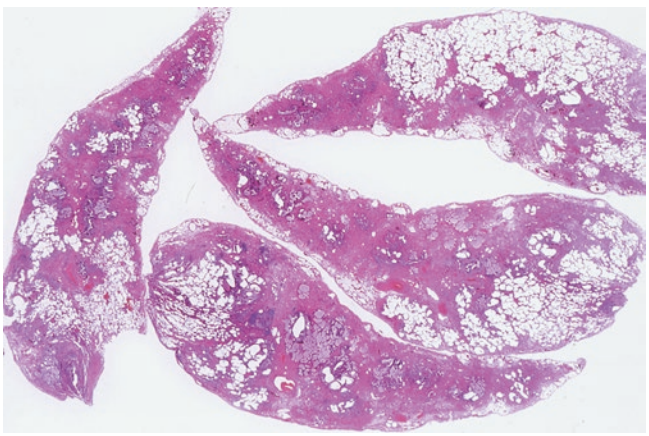

Fig. 6.61 UIP. Whole-mount sections of a lung wedge biopsy showing dense scarring and cystic changes are distributed in a patchwork pattern with peripheral accentuation (geographic or spatial heterogeneity). Areas of fibrosis completely efface the alveolar lung architecture and are juxtaposed with less affected or nearly normal lung parenchyma

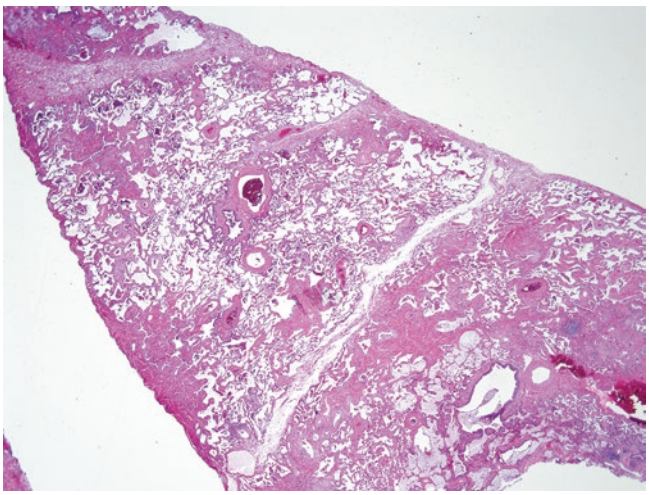

Fig. 6.62 UIP. Low-magnification photomicrograph of a surgical lung biopsy showing the typical patchwork and random distribution of collagen fibrosis that effaces the alveolar structure (architectural distortion). Less affected and nearly normal lung parenchyma is present between the areas of more severe fibrosis. Honeycomb change, architectural distortion in the form of cystic spaces containing mucus, is present at the upper left and lower right

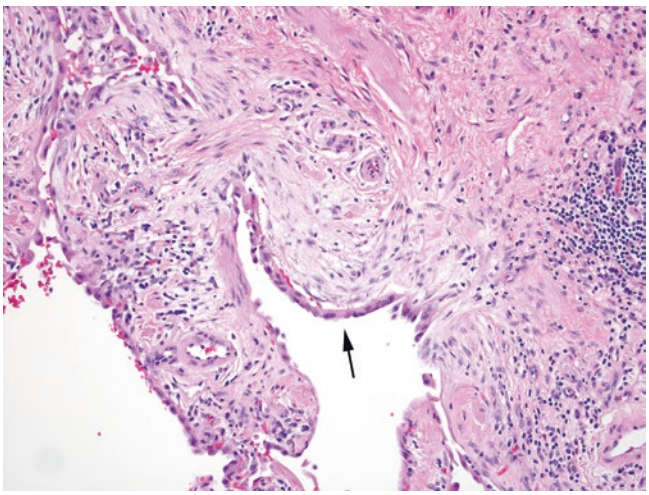

Fig. 6.64 UIP. Temporal heterogeneity, an important feature that is necessary for the diagnosis of UIP, is demonstrated in this intermediate-magnification photomicrograph. The fibrosis is composed of a mixture of newer active fibrosis in the form of a fibroblast focus (arrow) and older collagenous scar (right upper)

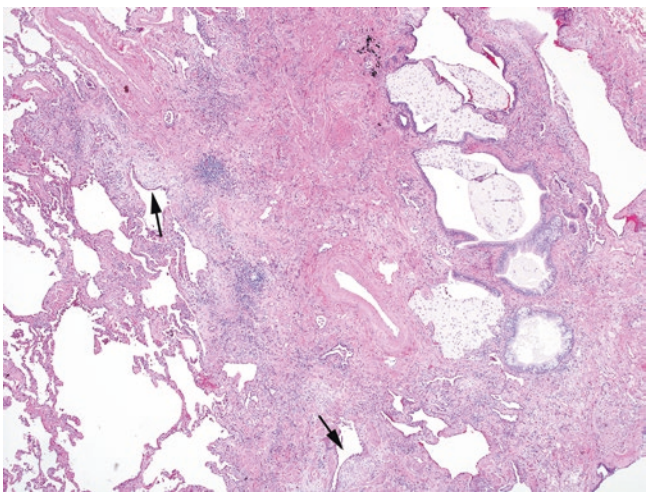

Fig. 6.63 UIP. Intermediate-magnification view of an area with significant architectural distortion caused by a dense collage scar (middle) and honeycomb change (right). A small amount of nearly normal lung parenchyma is seen in the lower left. Fibroblast foci (arrows) are visible at this magnification

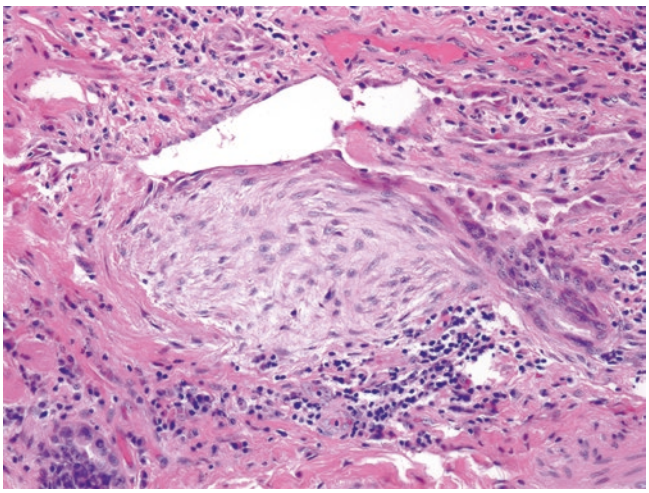

Fig. 6.65 UIP. High-magnification view of a fibroblast focus that is composed of plump spindle-shaped fibroblasts and myofibroblasts arranged in parallel within a lightly stained myxoid stroma. The luminal surface is covered with a layer of flattened pneumocytes and is sitting immediately on a bed of dense collagen fibrosis

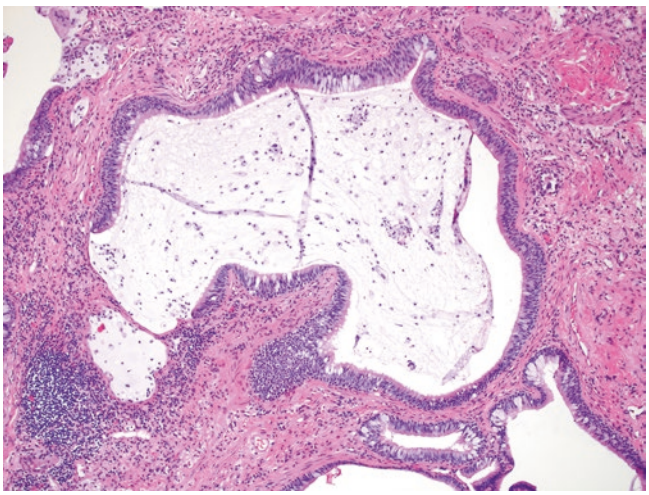

Fig. 6.66 UIP. High-magnification view of an area with honeycomb change. Multiple enlarged air spaces lined by ciliated respiratory epithelium are seen within a background of dense collagen fibrosis and chronic inflammation. There are mucin and mucin-containing macrophages within the enlarged air spaces

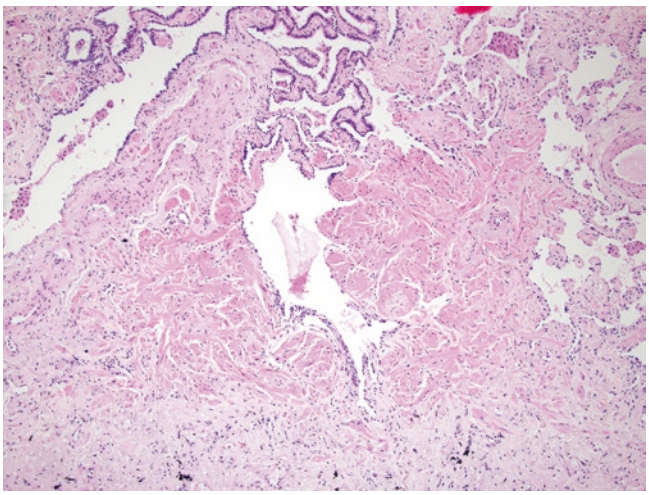

Fig. 6.68 UIP. Bundles of hyperplastic smooth muscles are admixed with collagen scars in an area of honeycomb change. The term muscular cirrhosis was used historically to convey prominent smooth muscle hyperplasia often affiliated with cobble stoning of the pleural surface

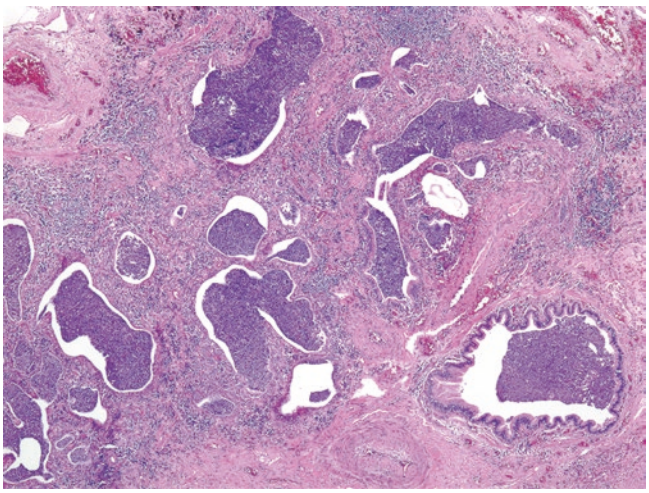

Fig. 6.67 UIP. Honeycomb areas are commonly associated with acute and chronic inflammation. Dense inflammatory infiltrates are present in the enlarged air spaces as well as the interstitium and an adjacent bronchiolar lumen (lower right)

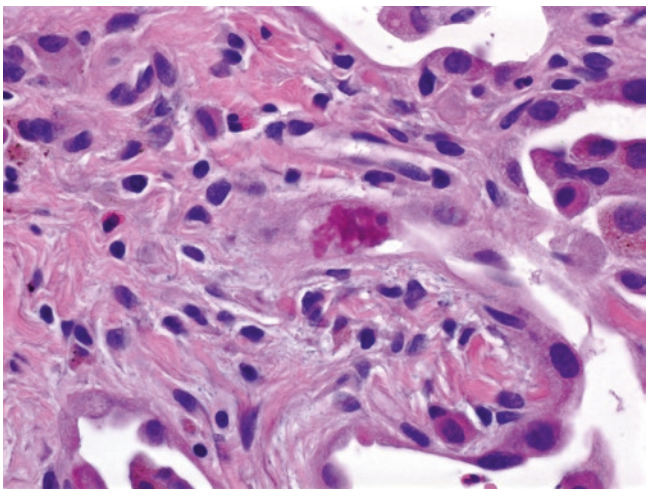

Fig. 6.69 UIP. High-magnification photomicrograph showing alveolar pneumocyte hyperplasia and amorphous eosinophilic material (Mallory hyaline) within the cytoplasm of a hyperplastic pneumocyte. Mallory hyaline is a common finding in UIP, but it is not specific and has no known clinical significance

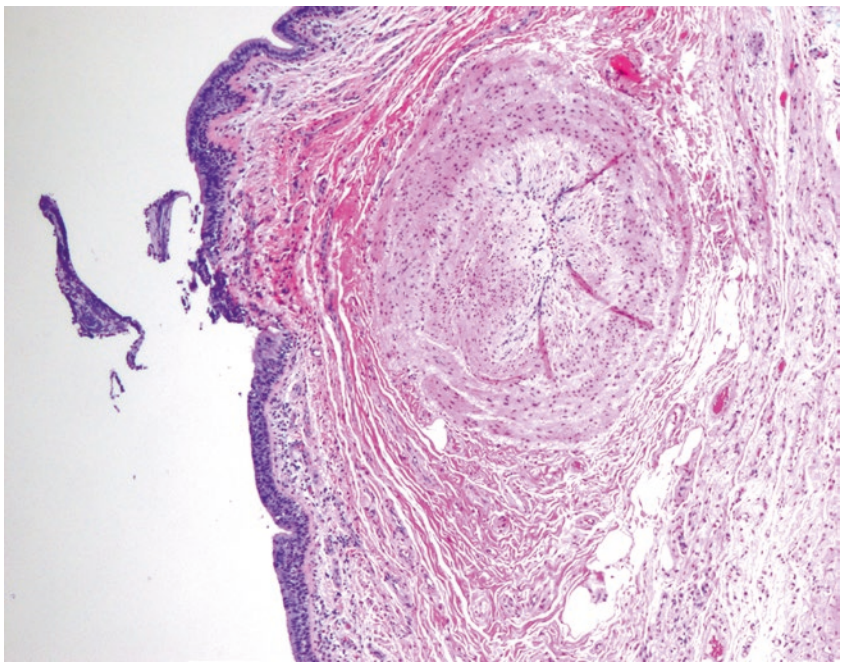

Fig. 6.70 Vascular changes in UIP. Hypertensive changes of small muscular pulmonary arteries characterized by intimal and medial hypertrophy are commonly seen associated with honeycomb changes. If the vascular hypertensive changes are prominent away from the honeycombing area, underlying collagen vascular disease such as scleroderma should be considered

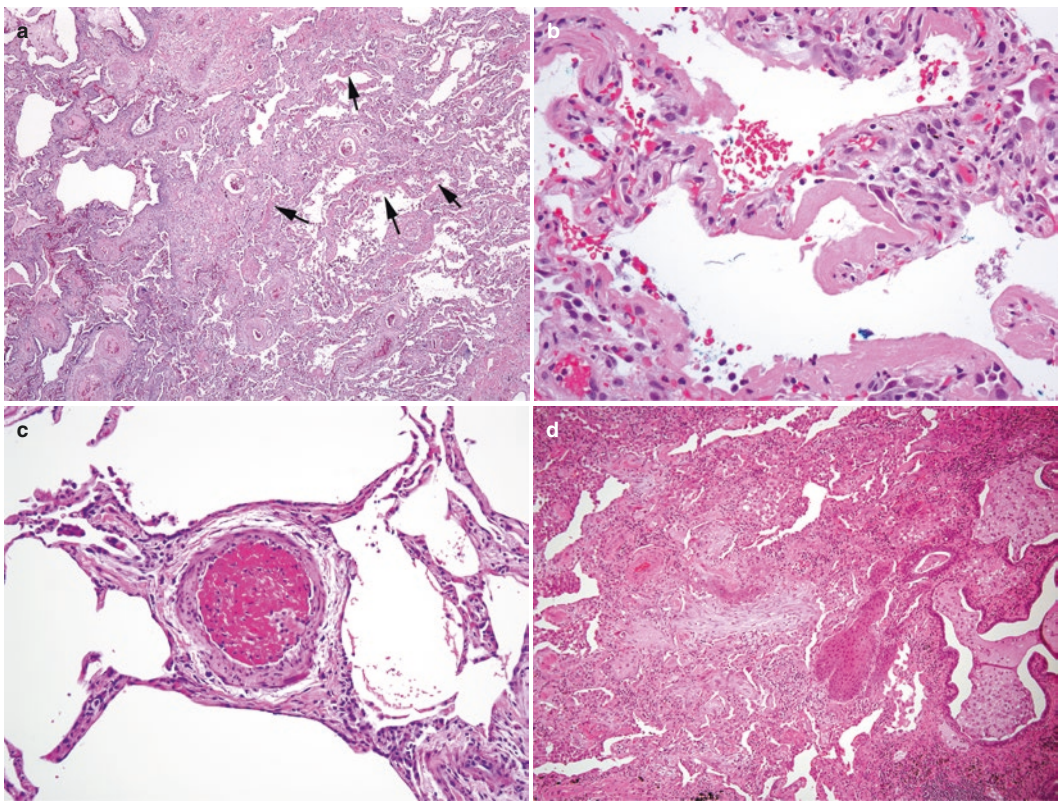

Fig. 6.71 UIP with diffuse alveolar damage (DAD) (acute exacerbation of idiopathic pulmonary fibrosis). (**a**) Low-magnification view showing patchy fibrosis and honeycomb change in the upper left. The nonfibrotic lung parenchyma on the right shows frequent hyaline membranes (arrows). (**b**) High-magnification view of the hyaline membranes, an eosinophilic membranous material lining alveolar septa. Pneumocyte hyperplasia with prominent reactive atypia is also present. (**c**) Fibrin thrombi within small arteries and arterioles are a common but nonspecific finding in DAD. (**d**) Bronchiolar squamous metaplasia is another common but nonspecific finding in DAD. Also present are changes of late organizing DAD, polypoid intraluminal proliferation of fibroblasts, and myofibroblasts mimicking organizing pneumonia

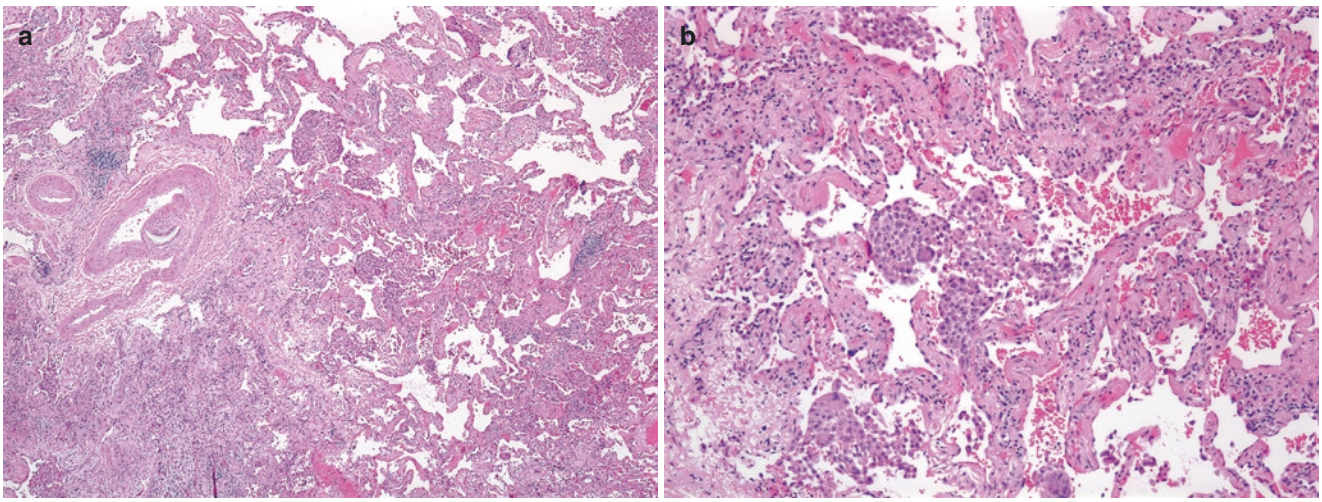

Fig. 6.72 UIP with DIP-like changes. (**a**) Low-magnification photomicrograph showing the patchwork fibrosis typical of UIP. Note the dense scarring on the lower left and relatively nonfibrotic lung parenchyma on the right. (**b**) High-magnification view of the relatively nonfibrotic lung parenchyma demonstrating the accumulation of pigmented macrophages (smoker's macrophages) within the alveolar spaces, closely mimicking the appearance of DIP

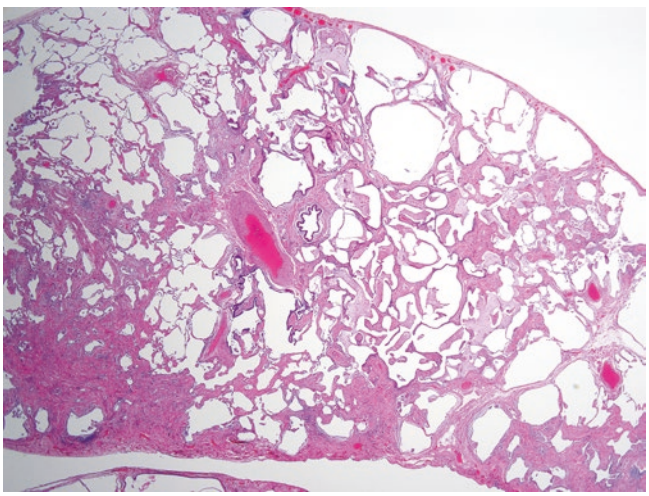

Fig. 6.73 UIP with coexisting emphysema. Low-magnification photomicrograph showing the patchwork fibrosis (lower left and lower right) and honeycomb change (upper middle and lower right) typical of UIP. The nonfibrotic lung parenchyma demonstrates emphysematous changes, including enlarged air spaces, and thinned, fragmented alveolar septa

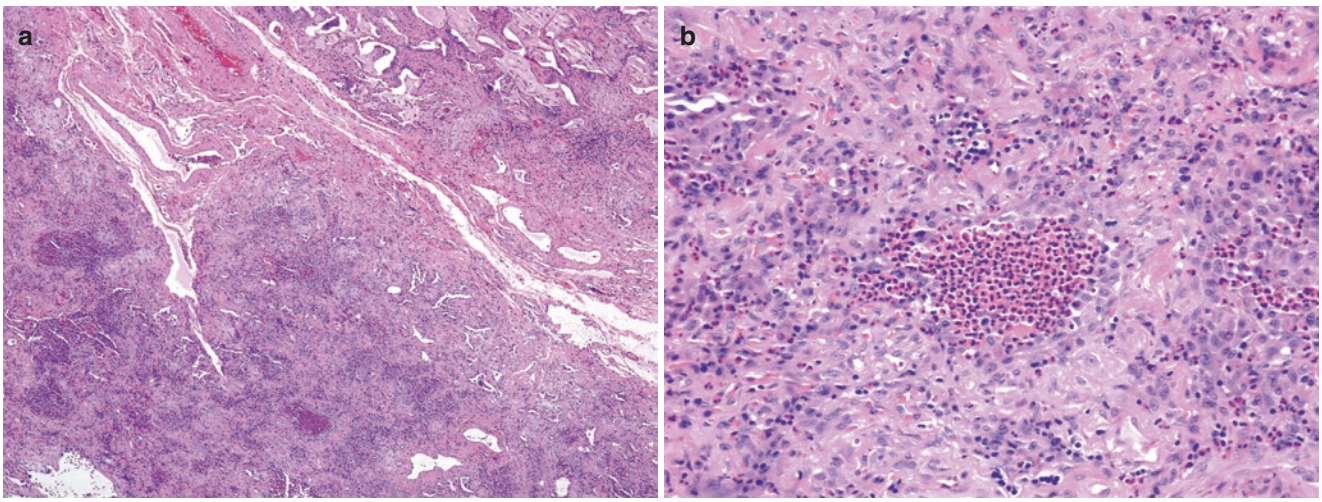

Fig. 6.74 UIP with coexisting eosinophilic pneumonia. (**a**) Low-magnification photomicrograph showing end-stage fibrosis and honeycomb change (upper right), typical of UIP. The residual air spaces are filled up with cellular infiltrates. (**b**) Higher-magnification view of the cellular air space infiltrates composed entirely of eosinophils

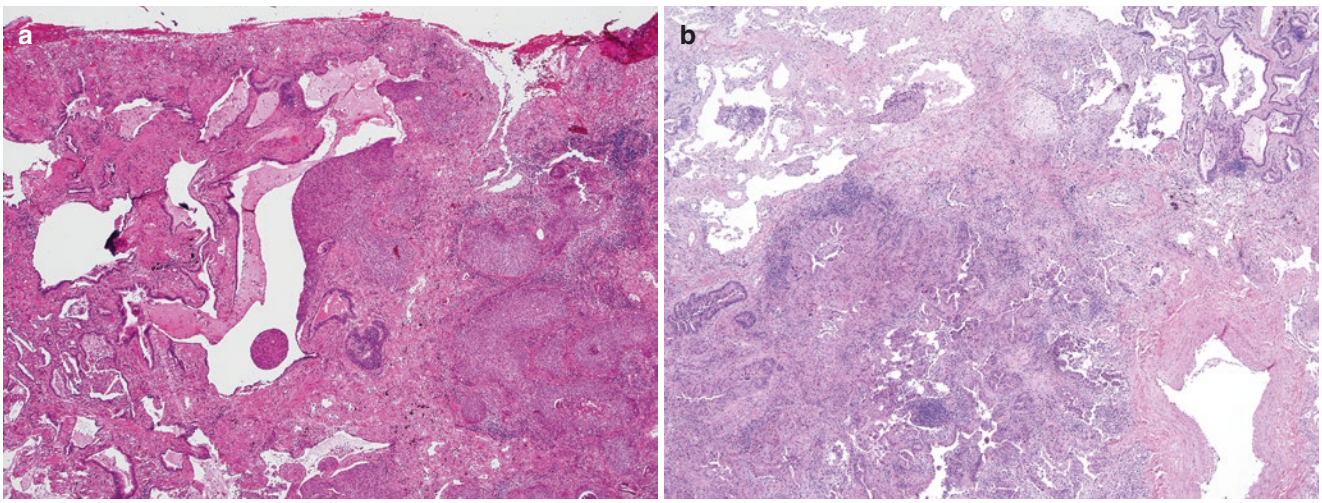

Fig. 6.75 UIP with coexisting carcinoma. (**a**) End-stage fibrotic lung with honeycomb change (left) and squamous cell carcinoma (right). (**b**) Honeycomb change and fibroblast foci typical of UIP (right upper) with coexisting adenocarcinoma in the lower left

Nonspecific Interstitial Pneumonia (NSIP)

NSIP (Figs. 6.76, 6.77, 6.78, 6.79, 6.79, 6.80 and 6.81) is the second most common form of idiopathic interstitial pneumonia. There are two histologic variants: cellular NSIP and fibrotic NSIP. The latter variant is more common and carries a worse prognosis. In addition to the clinical entity of idiopathic NSIP, the same histopathologic findings can occur focally (NSIP-like changes) in patients with other forms of diffuse lung disease, including most importantly patients with UIP. Furthermore, patients in whom NSIP represents the primary pathologic abnormality may have specific associated conditions or etiologies such as connective tissue disease, hypersensitivity pneumonia, or drug-induced lung disease. For these reasons a surgical lung biopsy diagnosis of NSIP is necessary but insufficient to establish a diagnosis of idiopathic NSIP, which is always a multidisciplinary process of exclusion requiring knowledge of clinical and radiologic findings. Patients with carefully defined idiopathic NSIP tend to be younger, more likely to be female, and less likely to have a smoking history compared to patients with UIP/IPF. They also have a more favorable prognosis and may respond favorably to immunosuppressive therapy.

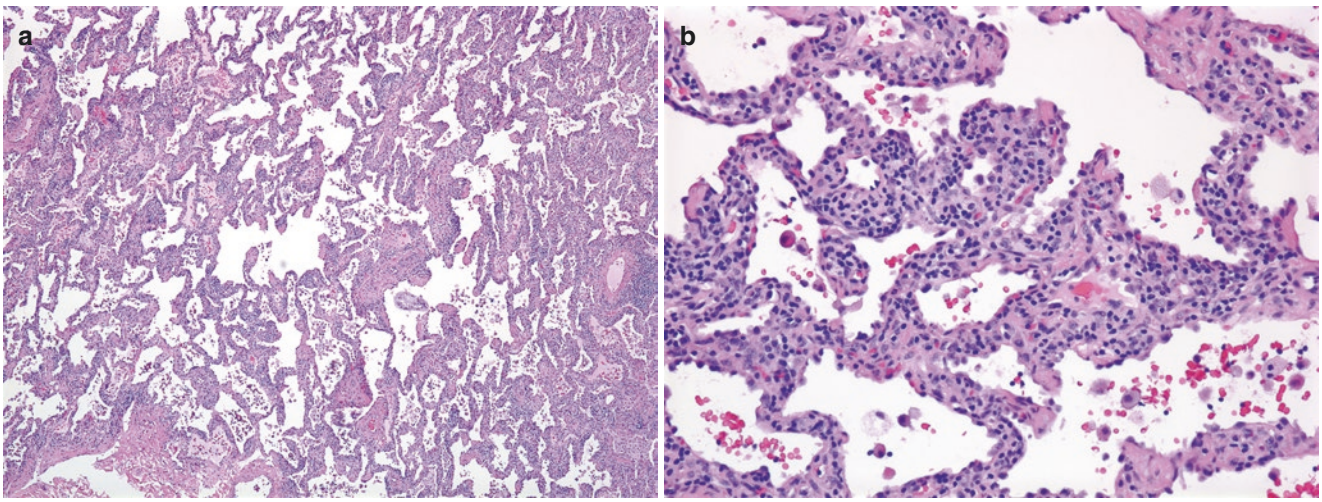

Fig. 6.76 NSIP. (**a**) Low-magnification photomicrograph showing uniform alveolar septal thickening by a cellular infiltrate. (**b**) At high magnification, the alveolar septa are thickened by a dense lymphoplasmacytic infiltrate. There is mild pneumocyte hyperplasia. No significant collagen deposition is present

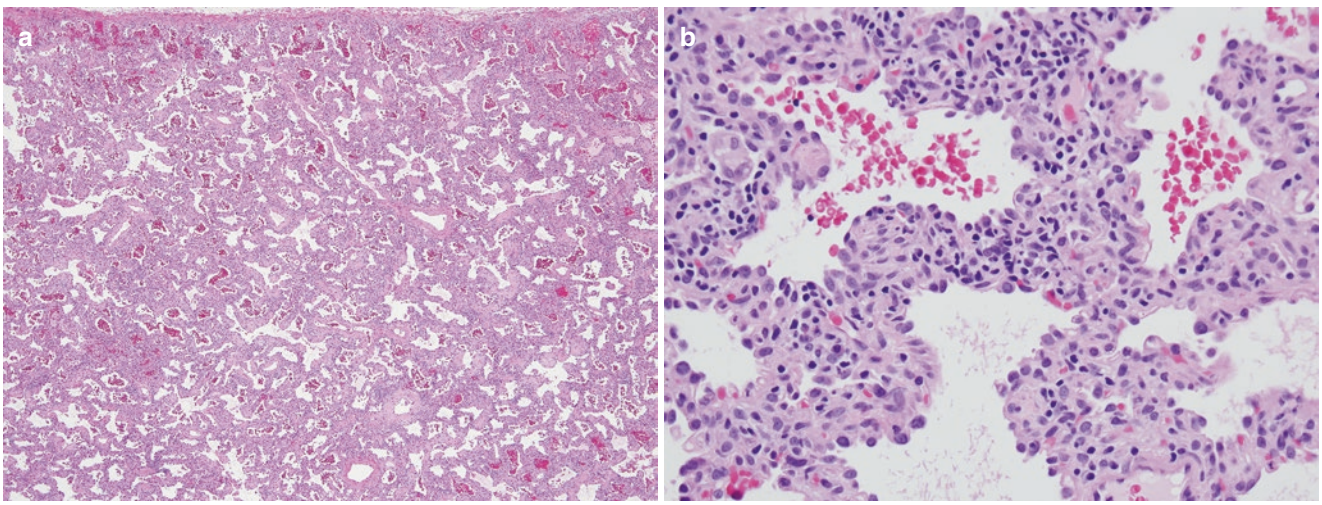

Fig. 6.77 Cellular NSIP. (**a**) At low magnification there is diffuse, uniform thickening of the alveolar septa. (**b**) In this example, the high-magnification view shows that the thickened alveolar septa contain lymphoplasmacytic infiltrates and minimal collagen deposition. Alveolar pneumocyte hyperplasia is also more prominent than the example in Fig. 6.76

Fig. 6.78 Fibrotic NSIP. Gross photograph of an explant lung with fibrotic NSIP. On a cut surface, the lung parenchyma is diffusely fibrotic, with no significant cystic or subpleural honeycomb change

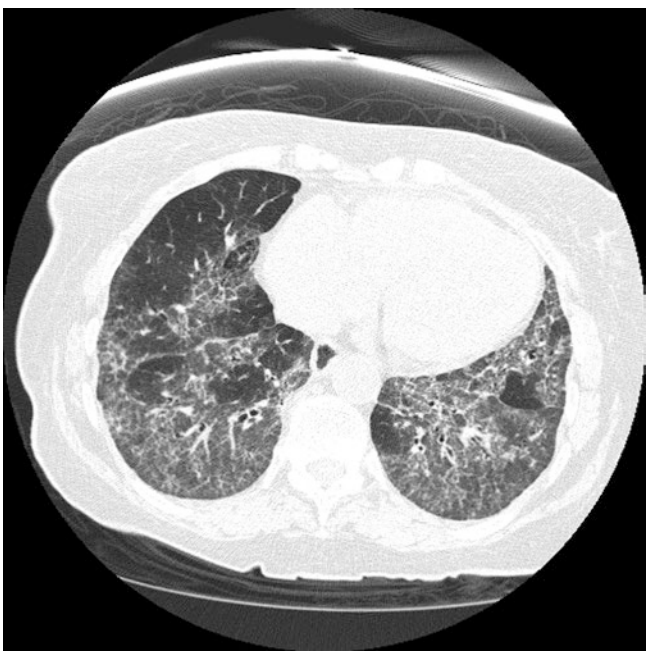

Fig. 6.79 Fibrotic NSIP. Chest CT scan of a patient with fibrotic NISP showing diffuse bilateral ground-glass opacities and interstitial reticular markings. No honeycomb change is present

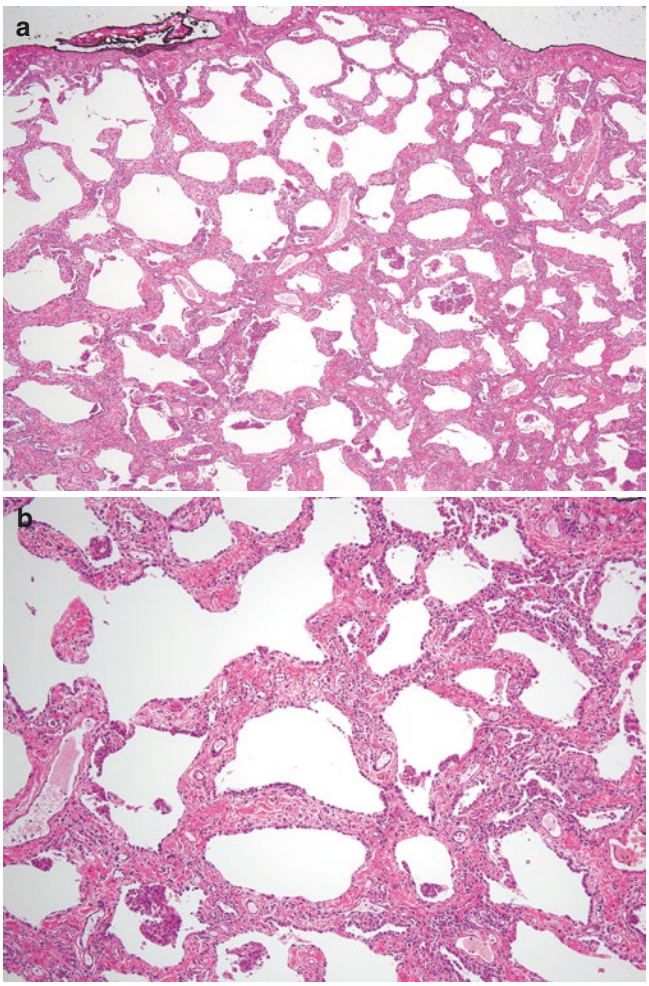

Fig. 6.80 Fibrotic NSIP. (**a**) At low magnification there is diffuse uniform thickening of alveolar septa by collagen fibrosis. The fibrosis does not cause significant architectural distortion in the form of honeycomb change or scars. (**b**) At high magnification the alveolar septa are thickened by collagen deposition and scant chronic inflammatory cells. There is also alveolar pneumocyte hyperplasia and focal intra-alveolar accumulation of macrophages. Fibroblast foci can be seen in NSIP (not shown in this image) but are generally scarce and are not a typical feature

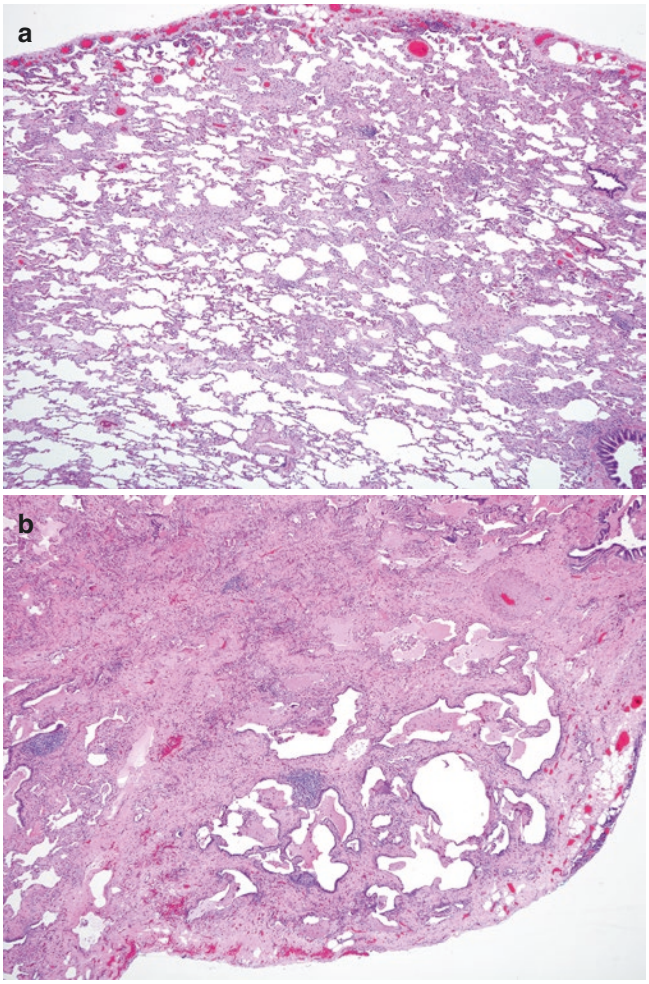

Fig. 6.81 NSIP-like area in UIP. (**a**) This area of uniform alveolar septal thickening by collagen fibrosis and mild chronic inflammation was taken from the upper lobe of an explanted lung with UIP. The features are consistent with fibrotic NSIP if the same changes were seen in the entire lung. (**b**) However, a section taken from the lower lobe lung demonstrated dense interstitial scars and honeycomb change typical of UIP. NSIP-like areas are actually common in otherwise typical UIP, which is why a pathologic diagnosis of NSIP requires correlation with the clinical and radiologic contexts to understand the significance of this finding

Connective Tissue Disease (CTD)-Associated Lung Diseases

Connective tissue disease (CTD)-associated lung diseases (Figs. 6.82, 6.83, 6.84 and 6.85). Pulmonary involvement is common in many systemic CTDs and is a major cause of morbidity and mortality in these patients. In addition to pleuritis and pleural effusions, the most common manifestations of thoracic involvement in almost all CTDs, interstitial lung diseases such as UIP or NSIP are also common findings in patients with CTD-associated lung disease. Some CTDs have uncommon but characteristic lesions that can be helpful in establishing the diagnosis (Table 6.1). In most the diagnosis hinges on the usual clinical and laboratory criteria, although certain histologic clues, such as prominent lymphoid hyperplasia, can be helpful in suggesting the possibility although with relatively low positive predictive values.

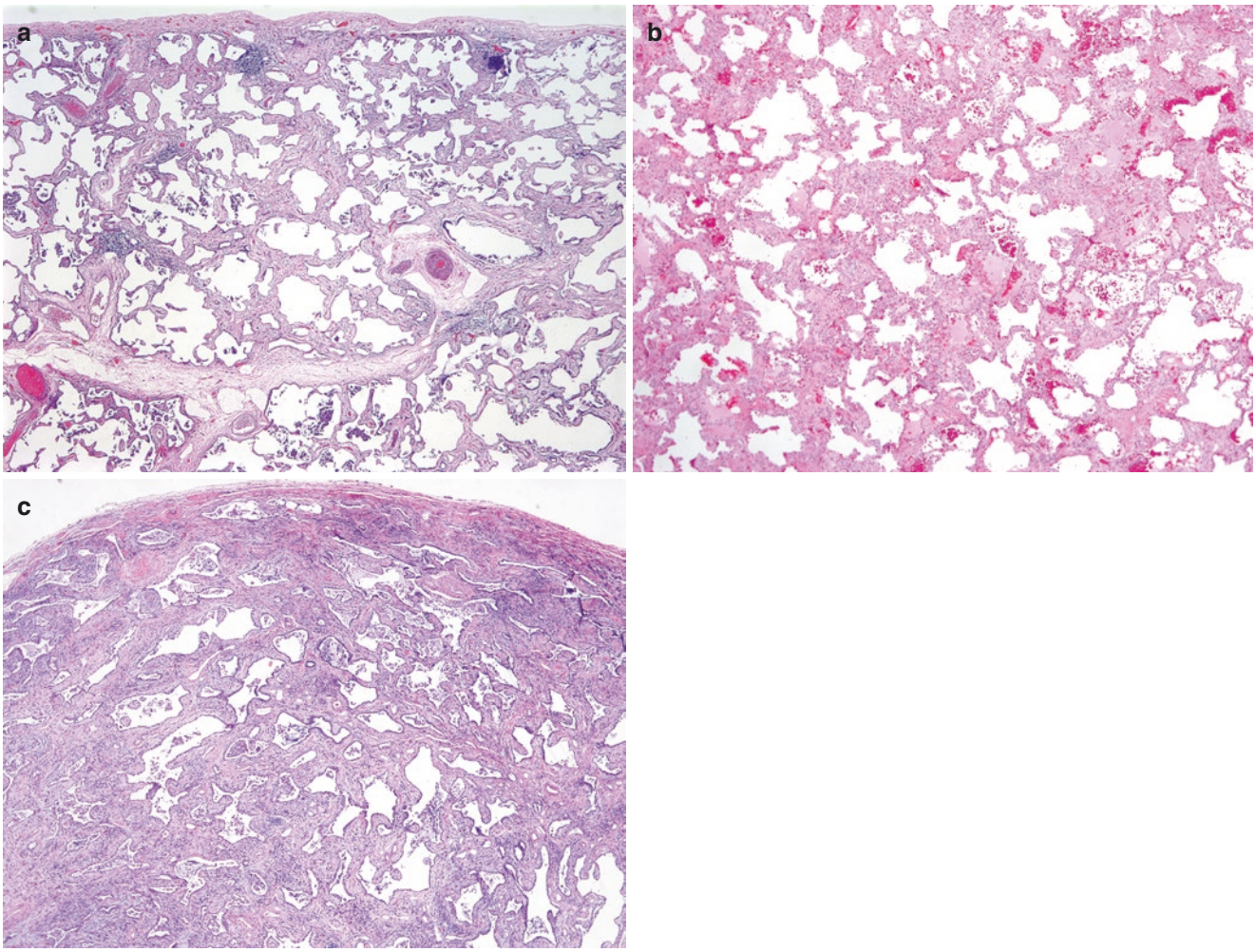

Fig. 6.82 CTD-associated fibrotic NSIP. The underlying CTDs are rheumatoid arthritis (**a**), scleroderma (**b**), and dermatomyositis (**c**). Both cellular and fibrotic variants of NSIP have been described in CTD-associated interstitial lung diseases. The histologic features are indistinguishable from those of idiopathic NSIP

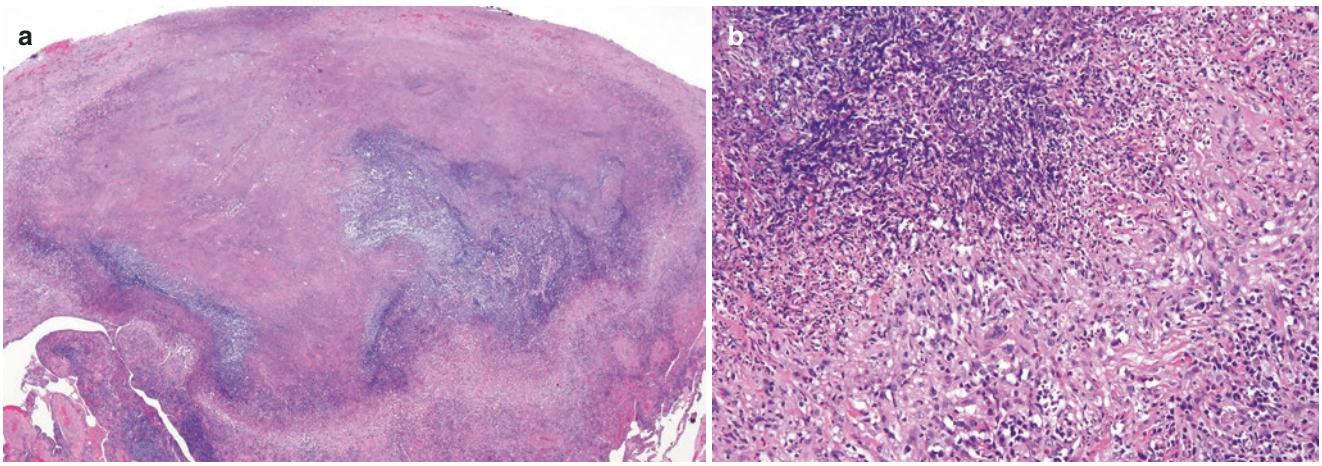

Fig. 6.83 Rheumatoid nodule. (**a**) Low-magnification photomicrograph showing a portion of lung parenchyma replaced by an irregularly shaped granuloma with a large geographic area of central necrosis. (**b**) At high magnification, the granuloma is characterized by central coagulative necrosis surrounded by peripheral palisading histiocytes admixed with acute and chronic inflammatory cells. No multinucleated giant cells are seen

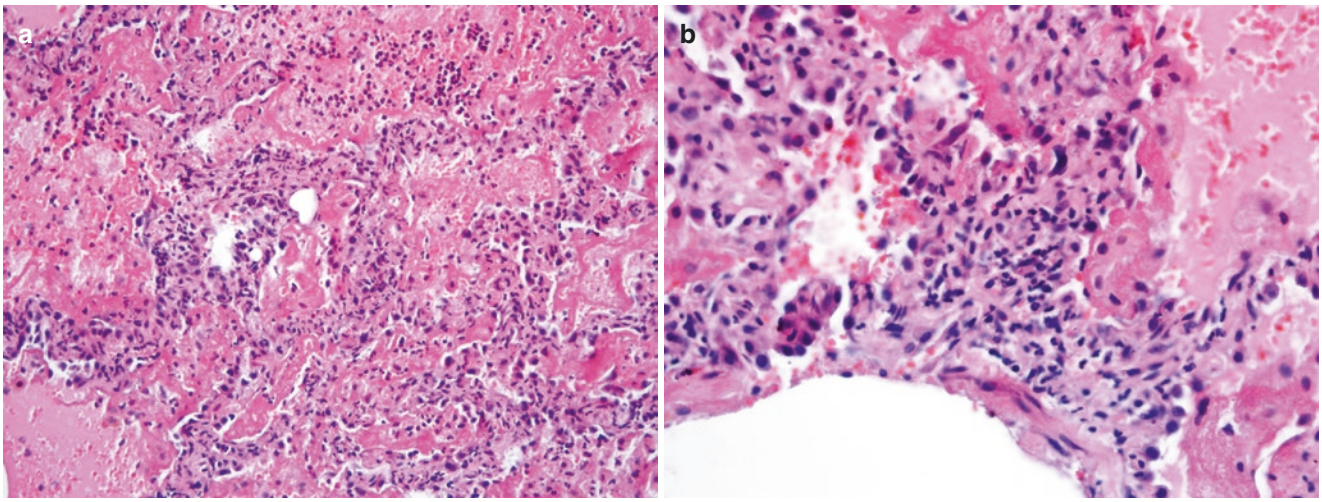

Fig. 6.84 Acute lupus pneumonitis. (**a**) Intermediate-magnification photomicrograph showing extensive intra-alveolar hemorrhage, reactive pneumocytes, and patchy acute inflammatory infiltrates centered on alveolar septa. (**b**) At high magnification, acute inflammatory cells with karyorrhexis are seen within alveolar septa, indicating necrotizing capillaritis

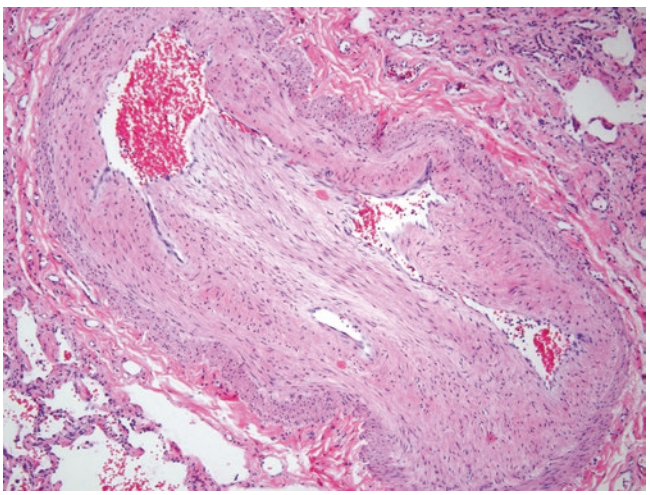

Fig. 6.85 Thromboembolic pulmonary hypertension in systemic lupus erythematosus. High-magnification view of an artery with eccentric intimal fibrosis and a recanalized lumen, indicating an organized thrombus

Table 6.1 The common manifestations of lung involvements associated with major connective tissue diseases

Diseases	Common interstitial disease patterns	Uncommon but characteristic lesions
Rheumatoid arthritis	UIP, NSIP	Rheumatoid nodule
Systemic lupus erythematosus	NSIP, UIP	Intralveolar hemorrhage and necrotizing capillaritis; pulmonary hypertension
Scleroderma	NSIP, UIP	Pulmonary hypertension
Polymyositis/ dermatomyositis	NSIP, occasionally UIP, DAD	Acute bronchopneumonia; occasionally hemorrhage and capillaritis

DAD diffuse alveolar damage, *NSIP* nonspecific interstitial pneumonia, *UIP* usual interstitial pneumonia

Lymphangioleiomyomatosis (LAM)

LAM (Figs. 6.86, 6.87, 6.88, 6.89, 6.90, 6.91, 6.92, 6.93 and 6.94) occurs almost exclusively in women of reproductive age; however, rare cases of LAM have been reported in men and postmenopausal women. Most cases are sporadic, while a small percentage are associated with tuberous sclerosis complex (TSC). Germline mutations in genes responsible for TSC, TSC1, and TSC2 are found in both sporadic and TSC-associated LAM. Patients with LAM usually present with breathlessness frequently attributable to recurrent spontaneous pneumothoraces. Some patients present with cough and hemoptysis. Serum VEGF-D is a useful diagnostic biomarker. Chest CT scans commonly show numerous thin-walled cysts and occasional nodules. The disease is usually slowly progressive and is variably responsive to hormonal therapy. More recently sirolimus has emerged as a potentially effective therapy that slows disease progression. End-stage disease may require lung transplantation.

Fig. 6.87 LAM. A high-resolution chest CT scan from the same patient whose surgical lung biopsy is illustrated in Fig. 6.86 shows a large right-sided pneumothorax with right upper lobe collapse. Numerous thin-walled cysts and some parenchymal nodules are seen in the non-collapsed lung

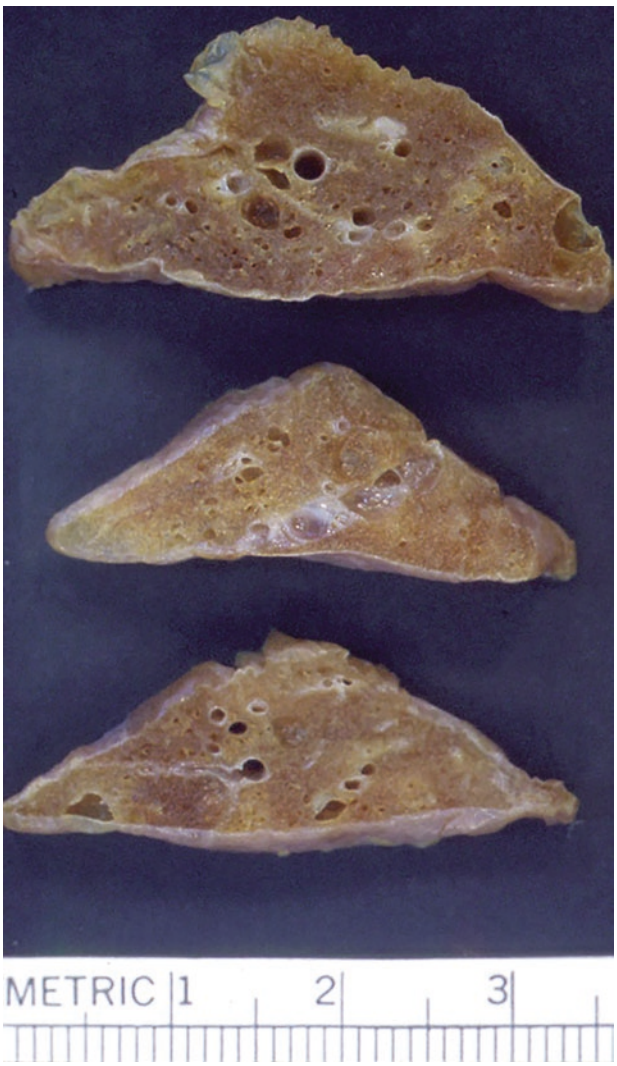

Fig. 6.86 LAM. Gross photograph of surgical lung biopsy from a 35-year-old woman with recurrent pneumothorax. The cut surface of the lung shows multiple variably sized thin-walled cysts. The intervening lung parenchyma is unremarkable, without significant fibrosis

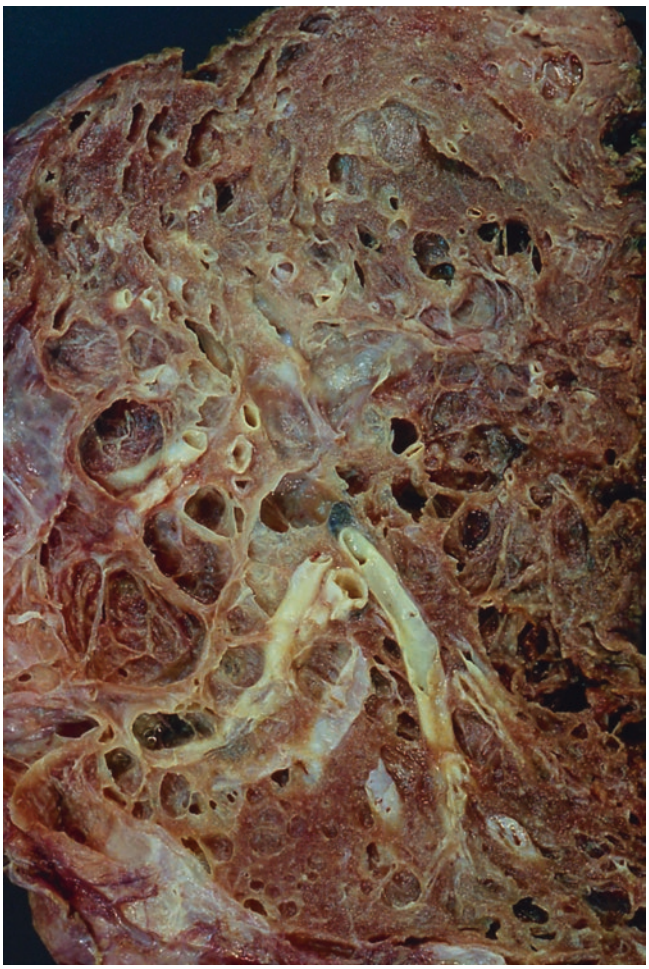

Fig. 6.88 LAM. Gross photograph of an explant lung from a patient with end-stage LAM. The lung is extensively involved with cystic lesions, with very few residual lung parenchyma

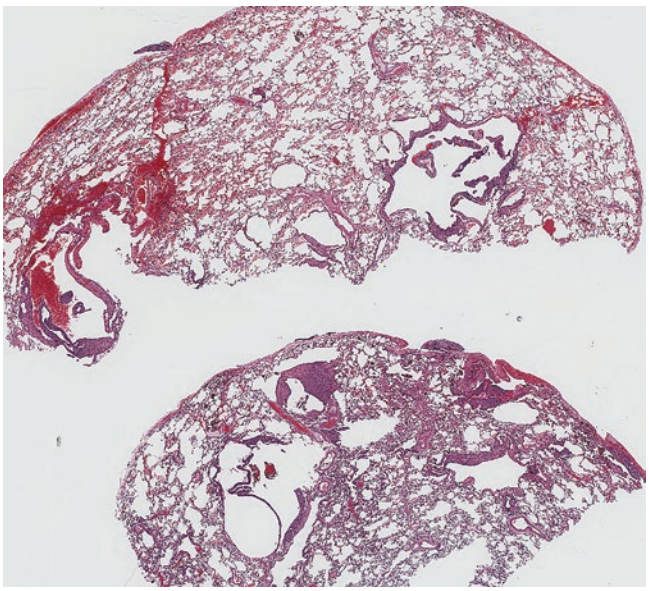

Fig. 6.89 LAM. Whole-mount section of a surgical lung biopsy showing multiple cystic lesions, some of which are surrounded by a variably thick and focally nodular wall. The two most nodular and cellular lesions are present in the lower piece of tissue

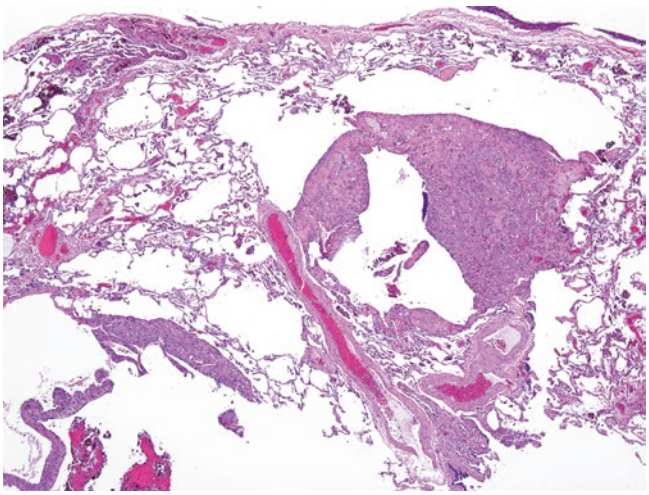

Fig. 6.90 LAM. Intermediate-magnification view of the lower piece of tissue illustrated in Fig. 6.89 showing nodular and cystic lesions. The thickened cyst walls comprise a proliferation of smooth muscle-like spindle cells. Some of the air spaces contain hemosiderin-laden macrophages, indicating old hemorrhage

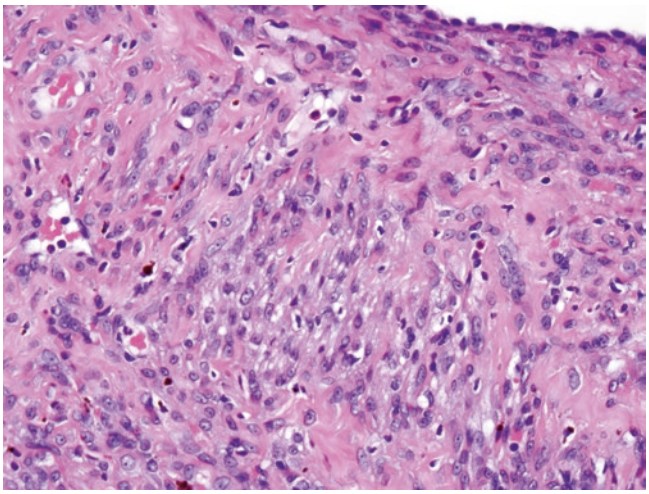

Fig. 6.91 LAM. High-magnification photomicrograph showing spindle and epithelioid LAM cells with bland, elongated nuclei and clear to eosinophilic cytoplasm. The cytoplasm is subtly vacuolated and slightly basophilic, resulting in tinctorial properties that differ from normal smooth muscle cells

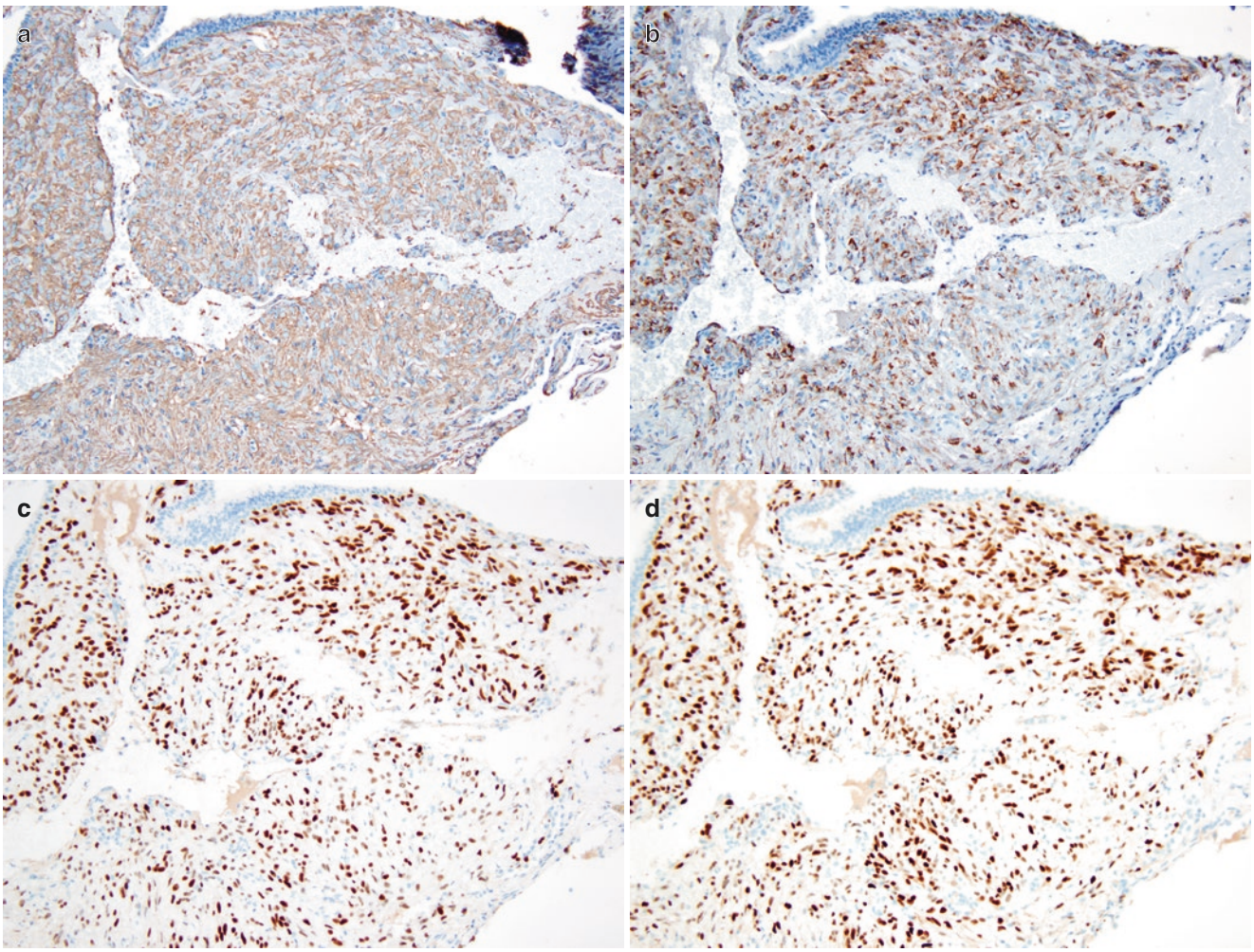

Fig. 6.92 LAM. The lesional cells are usually positive for smooth muscle actin (**a**), HMB-45 (**b**), estrogen receptor (**c**), and progesterone receptor (**d**). Staining for HMB-45 can be very patchy and therefore requires careful review of immunostained sections

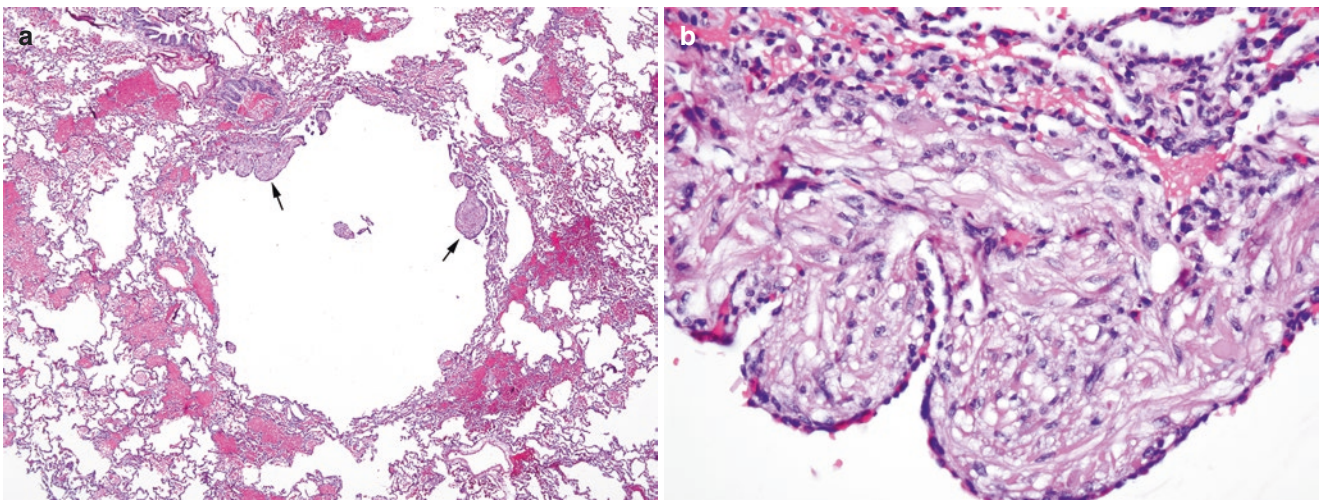

Fig. 6.93 LAM. (**a**) In this example, a thin-walled cyst is seen within the lung parenchyma, and the wall is focally thickened by bundles of smooth muscle-like LAM cells (arrows). (**b**) High-magnification view of the thickened area of the cyst wall showing bland-appearing spindle and epithelioid cells with overlying hyperplastic pneumocytes

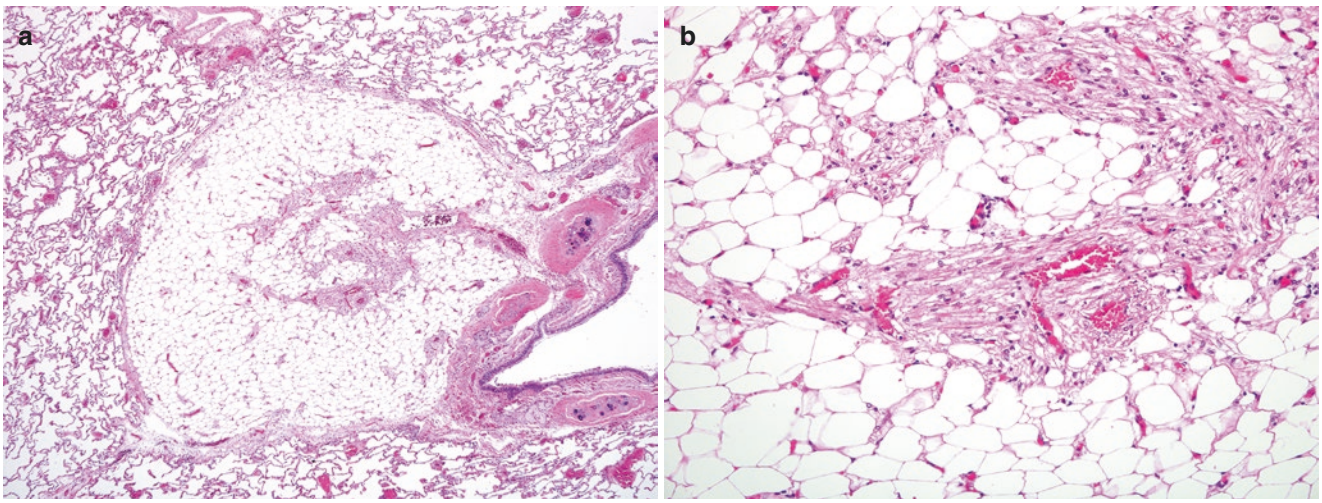

Fig. 6.94 Angiomyolipoma in the lung of a patient with tuberous sclerosis complex (TSC). (**a**) Low-magnification photomicrograph showing a well-demarcated lipomatous lesion next to a bronchus. (**b**) Higher-magnification photomicrograph from the center of the lesion shows features of angiomyolipoma: mature adipocytes, smooth muscle proliferation, and thick-walled blood vessels. Angiomyolipoma is more commonly seen in the kidneys of patients with TSC and has been reported in both sporadic and TSC-associated LAM

Suggested Reading

Beasley MB, Franks TJ, Galvin JR, Gochuico B, Travis WD. Acute fibrinous and organizing pneumonia: a histological pattern of lung injury and possible variant of diffuse alveolar damage. Arch Pathol Lab Med. 2002;126:1064–70.

Churg A, Muller NL, Silva CI, Wright JL. Acute exacerbation (acute lung injury of unknown cause) in UIP and other forms of fibrotic interstitial pneumonias. Am J Surg Pathol. 2007;31:277–84.

Force ADT, Ranieri VM, Rubenfeld GD, Thompson BT, Ferguson ND, Caldwell E, et al. Acute respiratory distress syndrome: the Berlin Definition. JAMA. 2012;307:2526–33.

Fraig M, Shreesha U, Savici D, Katzenstein AL. Respiratory bronchiolitis: a clinicopathologic study in current smokers, ex-smokers, and never-smokers. Am J Surg Pathol. 2002;26:647–53.

Heo JY, Song JY, Noh JY, Yong HS, Cheong HJ, Kim WJ. Acute fibrinous and organizing pneumonia in a patient with HIV infection and Pneumocystis jiroveci pneumonia. Respirology. 2010;15:1259–61.

Johnson SR, Cordier JF, Lazor R, Cottin V, Costabel U, Harari S, et al. Review panel of the European Respiratory Society guidelines for the diagnosis and management of lymphangioleiomyomatosis. Eur Respir J. 2010;35:14–26.

Katzenstein AL. Smoking-related interstitial fibrosis (SRIF): pathologic findings and distinction from other chronic fibrosing lung diseases. J Clin Pathol. 2013;66:882–7.

Katzenstein AL, Fiorelli RF. Nonspecific interstitial pneumonia/fibrosis. Histologic features and clinical significance. Am J Surg Pathol. 1994;18:136–47.

Katzenstein AL, Zisman DA, Litzky LA, Nguyen BT, Kotloff RM. Usual interstitial pneumonia: histologic study of biopsy and explant specimens. Am J Surg Pathol. 2002;26:1567–77.

Kitaichi M, Nishimura K, Itoh H, Izumi T. Pulmonary lymphangioleiomyomatosis: a report of 46 patients including a clinicopathologic study of prognostic factors. Am J Respir Crit Care Med. 1995;151(2 Pt 1):527–33.

Maldonado F, Daniels CE, Hoffman EA, Yi ES, Ryu JH. Focal organizing pneumonia on surgical lung biopsy: causes, clinicoradiologic features, and outcomes. Chest. 2007;132:1579–83.

Marchand E, Reynaud-Gaubert M, Lauque D, Durieu J, Tonnel AB, Cordier JF. Idiopathic chronic eosinophilic pneumonia. A clinical and follow-up study of 62 cases. The Groupe d'Etudes et de Recherche sur les maladies Orphelines Pulmonaires (GERMOP). Medicine (Baltimore). 1998;77:299–312.

Matsui K, Beasley MB, Nelson WK, Barnes PM, Bechtle J, Falk R, et al. Prognostic significance of pulmonary lymphangioleiomyomatosis histologic score. Am J Surg Pathol. 2001;25:479–84.

McCormack FX, Inoue Y, Moss J, Singer LG, Strange C, Nakata K, et al. National Institutes of Health Rare Lung Diseases and M. T. Group. Efficacy and safety of sirolimus in lymphangioleiomyomatosis. N Engl J Med. 2011;364:1595–606.

Mukhopadhyay S, Katzenstein AL. Pulmonary disease due to aspiration of food and other particulate matter: a clinicopathologic study of 59 cases diagnosed on biopsy or resection specimens. Am J Surg Pathol. 2007;31:752–9.

Myers JL, Katzenstein AL. Beyond a consensus classification for idiopathic interstitial pneumonias: progress and controversies. Histopathology. 2009;54:90–103.

Nishino M, Mathai SK, Schoenfeld D, Digumarthy SR, Kradin RL. Clinicopathologic features associated with relapse in cryptogenic organizing pneumonia. Hum Pathol. 2014;45:342–51.

Omote N, Taniguchi H, Kondoh Y, Watanabe N, Sakamoto K, Kimura T, et al. Lung-dominant connective tissue disease: clinical, radiologic, and histologic features. Chest. 2015;148:1438–46.

Parambil JG, Myers JL, Ryu JH. Histopathologic features and outcome of patients with acute exacerbation of idiopathic pulmonary fibrosis undergoing surgical lung biopsy. Chest. 2005;128:3310–5.

Patel SR, Karmpaliotis D, Ayas NT, Mark EJ, Wain J, Thompson BT, Malhotra A. The role of open-lung biopsy in ARDS. Chest. 2004;125:197–202.

Philit F, Etienne-Mastroianni B, Parrot A, Guerin C, Robert D, Cordier JF. Idiopathic acute eosinophilic pneumonia: a study of 22 patients. Am J Respir Crit Care Med. 2002;166:1235–9.

Raghu G, Rochwerg B, Zhang Y, Garcia CA, Azuma A, Behr J, et al., American Thoracic Society, European Respiratory, S. Japanese Respiratory and A. Latin American Thoracic. An Official ATS/ERS/JRS/ALAT Clinical Practice Guideline: Treatment of idiopathic pulmonary fibrosis. An Update of the 2011 Clinical Practice Guideline. Am J Respir Crit Care Med. 2015;192:e3–19.

Seymour JF, Presneill JJ. Pulmonary alveolar proteinosis: progress in the first 44 years. Am J Respir Crit Care Med. 2002;166: 215–35.

Song JW, Do KH, Kim MY, Jang SJ, Colby TV, Kim DS. Pathologic and radiologic differences between idiopathic and collagen vascular disease-related usual interstitial pneumonia. Chest. 2009;136:23–30.

Tansey D, Wells AU, Colby TV, Ip S, Nikolakoupolou A, du Bois RM, et al. Variations in histological patterns of interstitial pneumonia between connective tissue disorders and their relationship to prognosis. Histopathology. 2004;44:585–96.

Thille AW, Esteban A, Fernandez-Segoviano P, Rodriguez JM, Aramburu JA, Penuelas O, et al. Comparison of the Berlin definition for acute respiratory distress syndrome with autopsy. Am J Respir Crit Care Med. 2013;187:761–7.

Tomashefski JF. Pulmonary pathology of acute respiratory distress syndrome. Clin Chest Med. 2000;21:435–66.

Travis WD, Borok Z, Roum JH, Zhang J, Feuerstein I, Ferrans VJ, Crystal RG. Pulmonary Langerhans cell granulomatosis (histiocytosis X). A clinicopathologic study of 48 cases. Am J Surg Pathol. 1993;17:971–86.

Travis WD, Costabel U, Hansell DM, King TE, Lynch DA, Nicholson AG, et al. American Thoracic Society/European Respiratory Society statement: update of the international multidisciplinary classification of the idiopathic interstitial pneumonias. Am J Respir Crit Care Med. 2013;188:733–48.

Travis WD, Hunninghake G, King TE, Lynch DA, Colby TV, Galvin JR, et al. Idiopathic nonspecific interstitial pneumonia: report of an American Thoracic Society project. Am J Respir Crit Care Med. 2008;177:1338–47.

Uner AH, Rozum-Slota B, Katzenstein LA. Bronchiolitis obliterans-organizing pneumonia (BOOP)-like variant of Wegener's granulomatosis. A clinicopathologic study of 16 cases. Am J Surg Pathol. 1996;20:794–801.

Villar J, Sulemanji D, Kacmarek RM. The acute respiratory distress syndrome: incidence and mortality, has it changed? Curr Opin Crit Care. 2014;20:3–9.

Wang CW, Colby TV. Histiocytic lesions and proliferations in the lung. Semin Diagn Pathol. 2007;24:162–82.

Wang T, Lazar CA, Fishbein MC, Lynch JP. Pulmonary alveolar proteinosis. Semin Respir Crit Care Med. 2012;33:498–508.

Yousem SA, Lohr RY, Colby TV. Idiopathic bronchiolitis obliterans organizing pneumonia/cryptogenic organizing pneumonia with unfavorable outcome: pathologic predictors. Mod Pathol. 1997;10:864–71.

Noninfectious Diffuse Granulomatous Lung Diseases

7

Chen Zhang and Jeffrey L. Myers

This chapter illustrates the two main forms of noninfectious diffuse granulomatous lung disease likely to be encountered in lung biopsies: hypersensitivity pneumonia and sarcoidosis. Hypersensitivity pneumonia and sarcoidosis have in common an ability to cause respiratory symptoms in patients with diffuse radiologic abnormalities. Affected patients frequently undergo biopsies to rule out neoplasms and/or other forms of diffuse lung disease. Non-necrotizing granulomatous inflammation is an important diagnostic clue in both conditions, each distinguished by a very different combination of associated histologic findings. When encountered by surgical pathologists, the differential diagnosis for both often includes granulomatous infections, an especially important consideration in immunocompromised patients (*see* Chap. 4). Other conditions that may enter the differential diagnosis include aspiration pneumonia, which is illustrated in Chap. 5.

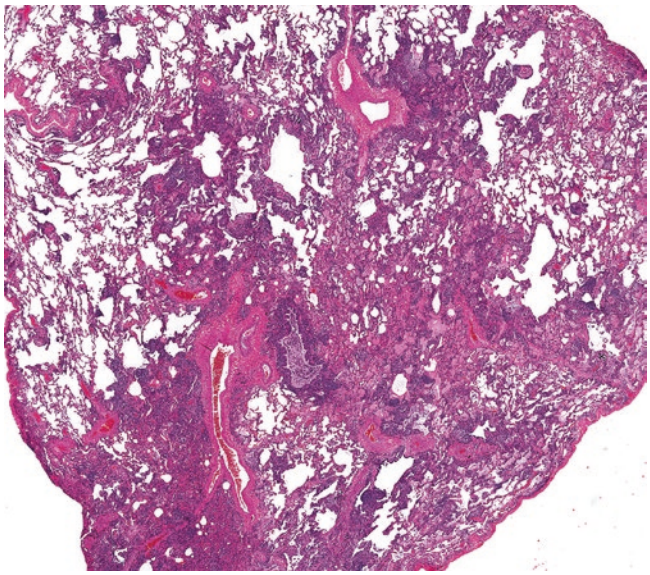

Fig. 7.1 Hypersensitivity pneumonia. A low-magnification whole-mount section showing a cellular interstitial pneumonia that is accentuated around the small airways. The more distal alveoli are less involved. The overall alveolar architecture is preserved with no significant fibrosis

Hypersensitivity Pneumonia

Hypersensitivity pneumonia (Figs. 7.1, 7.2, 7.3, 7.4, 7.5, 7.6, 7.7, 7.8 and 7.9) is an immunologic reaction of the lung to inhaled antigens, most frequently organic antigens from animal proteins, thermophilic bacteria, or molds. Animal proteins are mainly of avian origin; feather pillows and bedding are increasingly recognized as a potential antigenic source in patients with hypersensitivity pneumonia. An exposure source may not always be identifiable. The radiologic changes vary from ground-glass opacities with centrilobular nodules and mosaic attenuation in early disease to honeycomb changes resembling usual interstitial pneumonia (UIP) in patients with long-standing disease. Because the presenting symptoms and radiologic findings may be relatively nonspecific, especially in patients with no identifiable antigenic exposure, lung biopsy often plays a key role in diagnosis.

The combination of a bronchiolocentric chronic interstitial pneumonia and loosely formed epithelioid granulomas centered within peribronchiolar interstitium is the most important histologic clue to a diagnosis of hypersensitivity pneumonia. Although they are often included with the granulomatous lung diseases, granulomas may be absent altogether in lung biopsies from patients with well-established

C. Zhang (✉)
Department of Pathology and Laboratory Medicine, Indiana University School of Medicine, Indianapolis, IN, USA
e-mail: chenzhan@iupui.edu

J. L. Myers
Department of Pathology, Michigan Medicine, Ann Arbor, MI, USA
e-mail: myerjeff@med.umich.edu

© Springer Science+Business Media, LLC, part of Springer Nature 2018
C. Zhang, J. L. Myers (eds.), *Atlas of Lung Pathology*, Atlas of Anatomic Pathology,
https://doi.org/10.1007/978-1-4939-8689-7_7

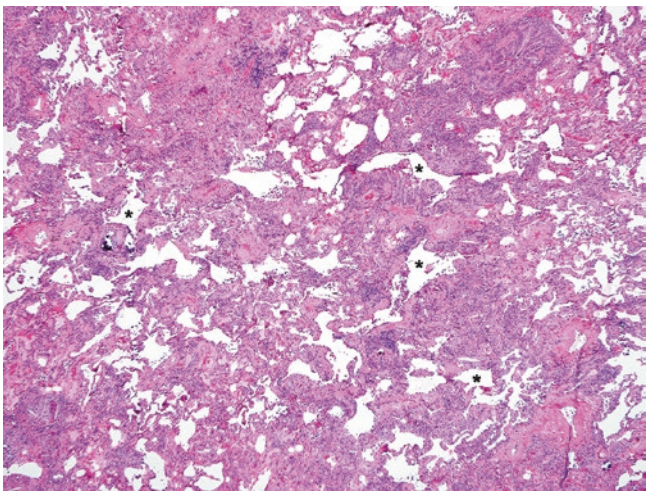

Fig. 7.2 Hypersensitivity pneumonia. Low-magnification photomicrograph showing a variably dense, lymphocyte-rich, cellular inflammatory infiltrate that expands the interstitium and is accentuated around distal bronchioles (asterisks)

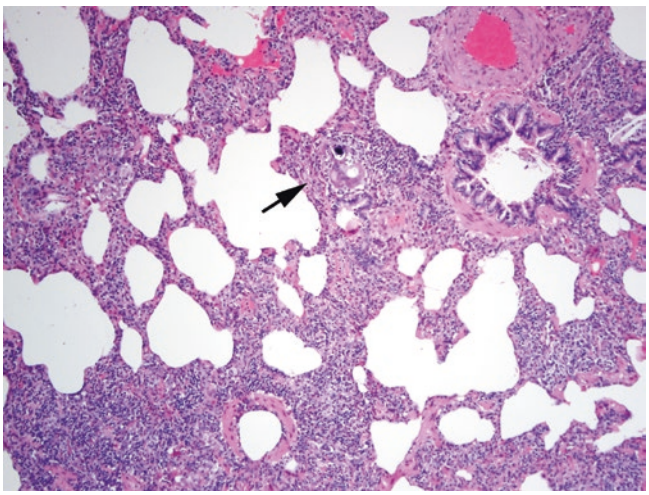

Fig. 7.3 Hypersensitivity pneumonia. Intermediate-magnification photomicrograph showing a small poorly formed granuloma composed of a loose cluster of multinucleated giant cells (arrow) situated within the peribronchiolar interstitium. Note the background cellular interstitial pneumonia with peribronchiolar accentuation. It is this combination of features that is most helpful in establishing a histologic diagnosis of hypersensitivity pneumonia

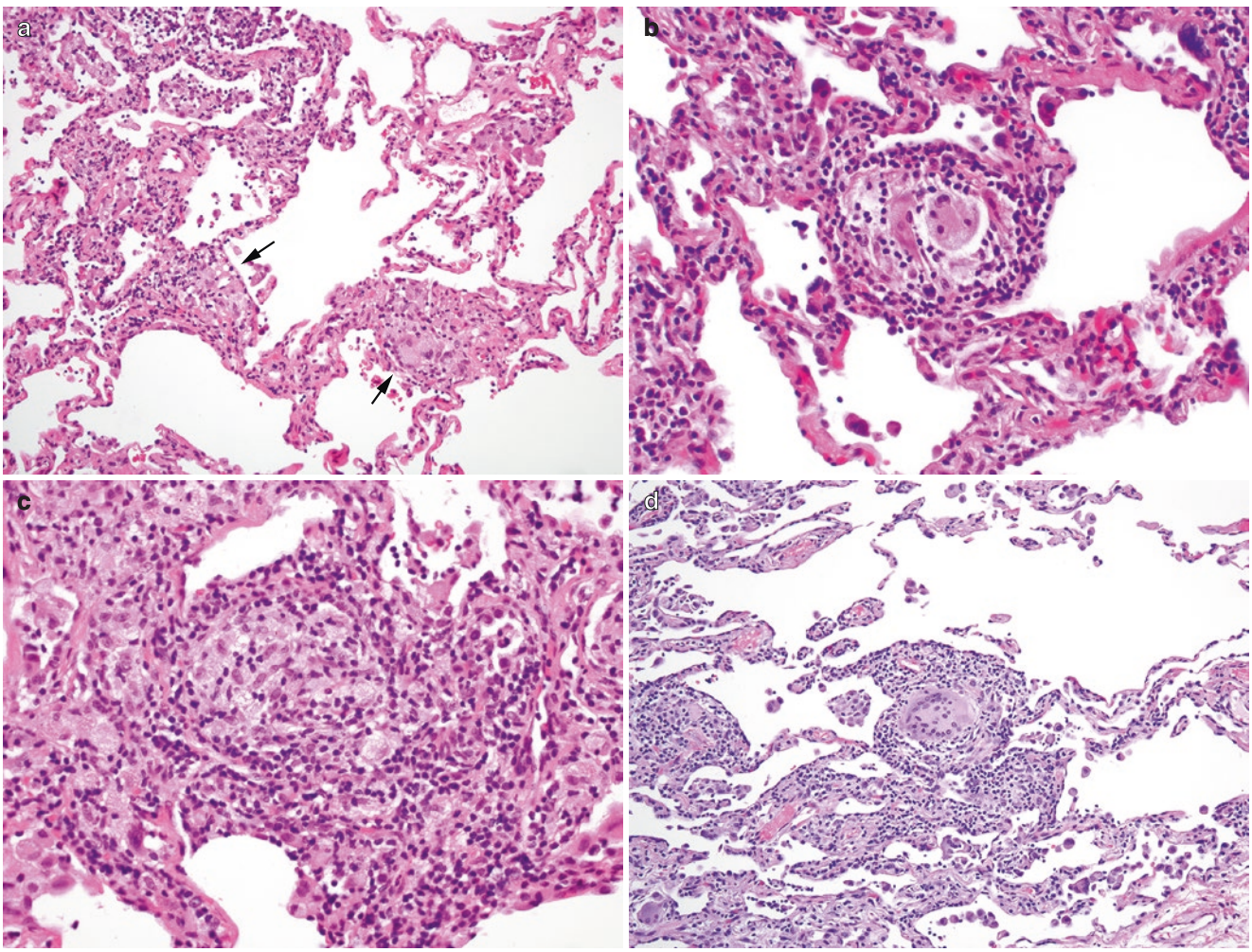

Fig. 7.4 Granulomatous inflammation in hypersensitivity pneumonia. (**a**) Photomicrograph showing a characteristic pattern of loosely formed granulomas (arrows) consisting of epithelioid histiocytes and giant cells centered on the peribronchiolar interstitium. (**b**) High-magnification view of a loosely formed granuloma consisting of a giant cell and a few histiocytes and surrounded by mononuclear inflammatory cells in which lymphocytes predominate. (**c**) Another example of a loosely formed granuloma consisting of epithelioid histiocytes within the peribronchiolar interstitium accompanied by a dense infiltrate of chronic inflammatory cells. (**d**) An isolated giant cell is seen within the interstitium in a background of chronic inflammatory cells

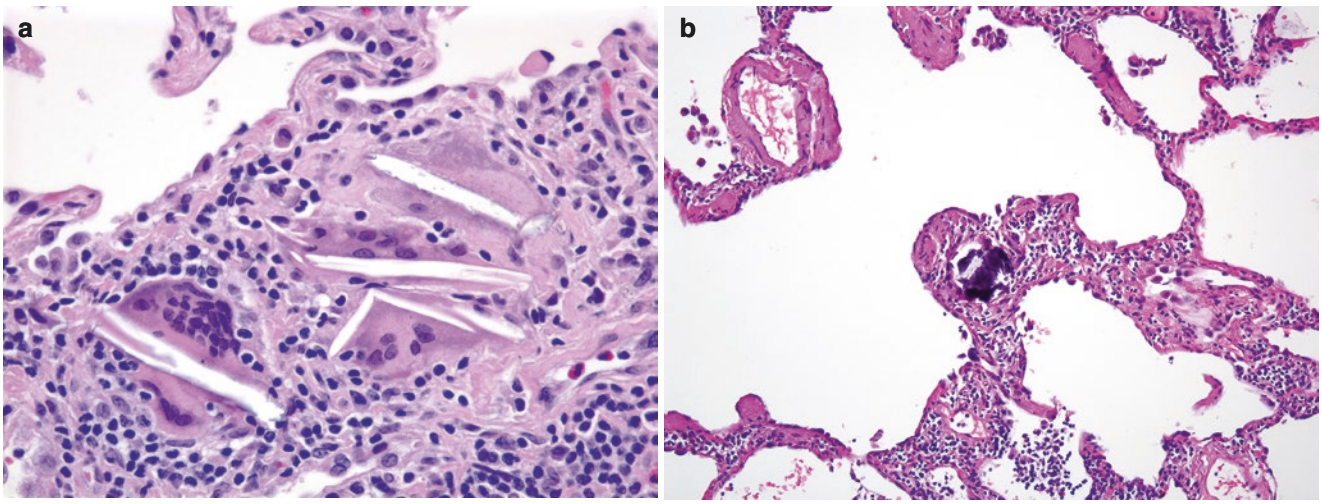

Fig. 7.5 Granulomatous inflammation in hypersensitivity pneumonia. The giant cells in hypersensitivity pneumonia often contain a variety of nonspecific endogenous cytoplasmic inclusions, including cholesterol-like clefts (**a**), calcified Schaumann bodies (**b**), and other nonspecific pale-staining birefringent crystalline salts (not illustrated). These inclusions are not linked to any specific antigenic exposures

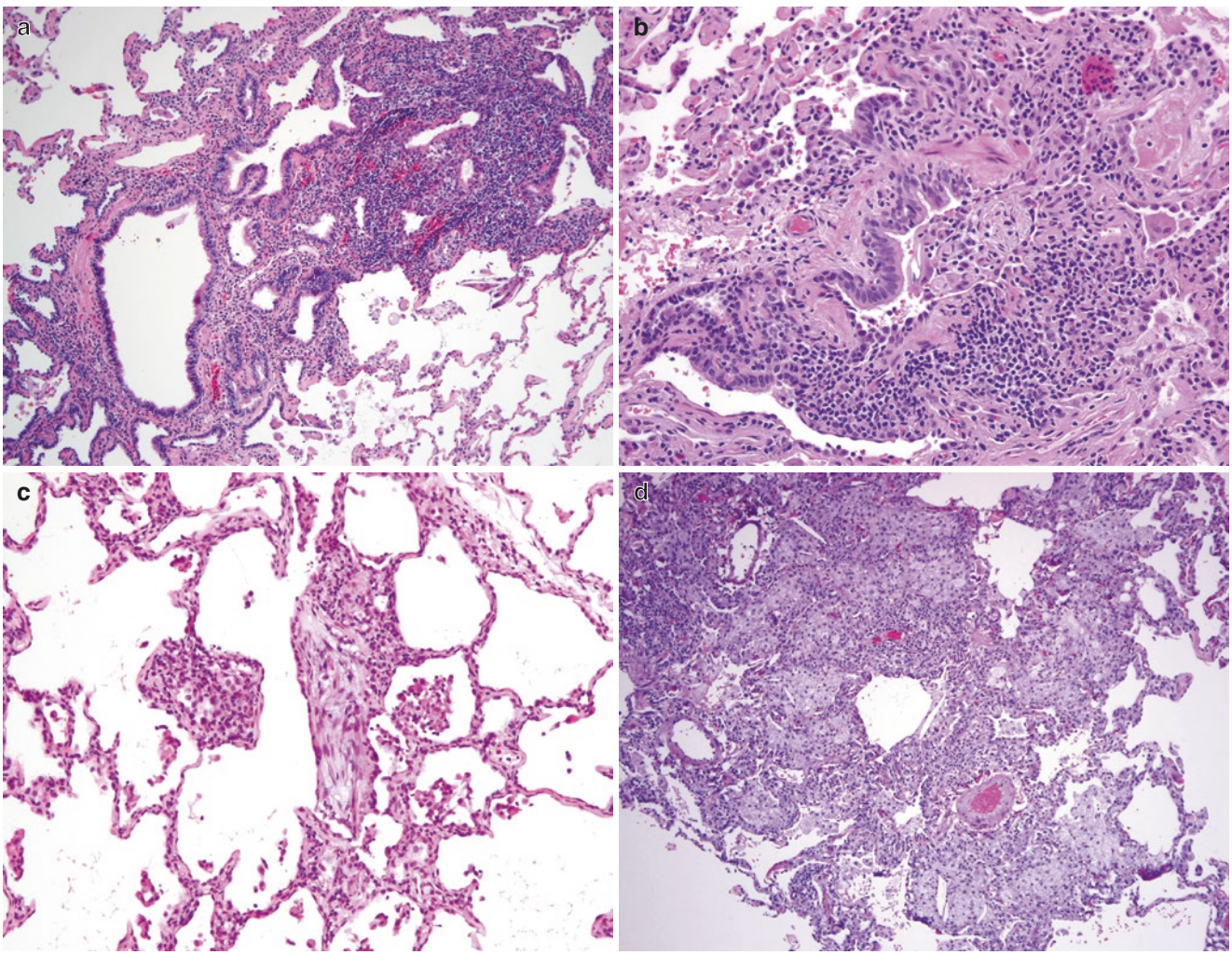

Fig. 7.6 Chronic bronchiolitis in hypersensitivity pneumonia. (**a**) High-magnification photomicrograph showing chronic bronchiolitis characterized by a chronic inflammatory infiltrate that expands the peribronchiolar interstitium. The hyperplastic columnar respiratory epithelium extends along peribronchiolar alveolar septa thickened by inflammation and fibrosis, a combination of findings referred to as peribronchiolar metaplasia (*see* Fig. 7.7). (**b**) Another high-magnification view showing chronic bronchiolitis with focal intraluminal fibroblast proliferation (bronchiolitis obliterans also referred to simply as organizing pneumonia). (**c**) Photomicrograph showing focal organizing pneumonia made up of a polypoid plug of organizing fibroblasts situated within the lumen of a respiratory bronchiole in a patient with hypersensitivity pneumonia. (**d**) Accumulation of foamy alveolar macrophages in peribronchiolar air spaces is a form of microscopic obstructive pneumonia and is another sign of small airway dysfunction that is common in lung biopsies from patients with hypersensitivity pneumonia

diagnoses of hypersensitivity pneumonia. The constant is a lymphocyte-rich interstitial infiltrate distributed in a distinctly bronchiolocentric fashion. Signs of small airway dysfunction such as organizing pneumonia and foamy alveolar histiocytes (microscopic obstructive pneumonia) are relatively nonspecific but are commonly seen.

Hot tub lung is a special variant in which a hypersensitivity pneumonia-like syndrome results from sensitization to hot tubs contaminated with atypical mycobacterial organisms, most commonly *Mycobacterium avium* complex (MAC). Unlike other forms of hypersensitivity pneumonia, the causative antigen/organism can be identified in and cultured from the tissue. The histology is also unique as illustrated in Chap. 4 (*see* Fig. 4.13) and consists of relatively well-formed and focally necrotizing granulomas situated within the lumens (rather than the interstitium) of distal bronchioles without the other features more typical of classic hypersensitivity pneumonia.

The presence of fibrosis in lung biopsies is associated with a greater likelihood of disease-related mortality in patients with hypersensitivity pneumonia. Fibrotic disease may include areas of honeycomb change that closely mimic UIP. Honeycomb change in patients with hypersensitivity pneumonia is accompanied by a distinctive pattern of airway-centered fibrosis referred to as peribronchiolar metaplasia, a finding that is not specific but is a clue to the possibility of hypersensitivity pneumonia. Establishing the diagnosis in patients with fibrotic disease hinges on identifying classic histologic features in less fibrotic lung tissue combined with supportive clinical and radiologic findings.

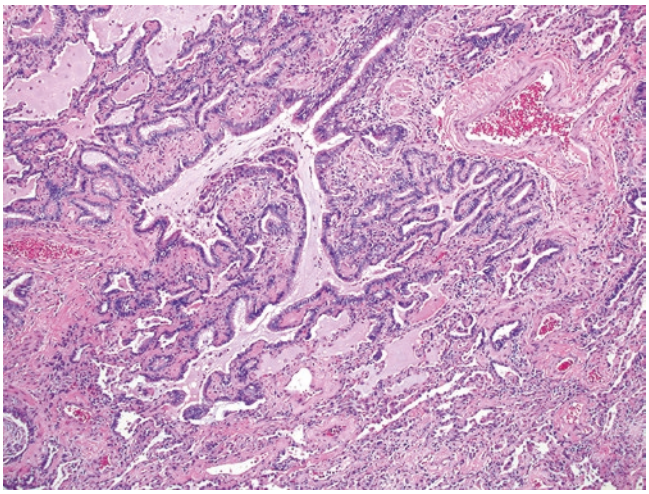

Fig. 7.7 Fibrotic hypersensitivity pneumonia. Photomicrograph showing prominent peribronchiolar metaplasia in a surgical lung biopsy from a patient with hypersensitivity pneumonia. Peribronchiolar metaplasia is not specific but is a very characteristic and universal finding in fibrotic hypersensitivity pneumonia. It is not sufficient to establish the diagnosis on its own but should spark a careful search for the other findings helpful in establishing a histologic diagnosis of hypersensitivity pneumonia

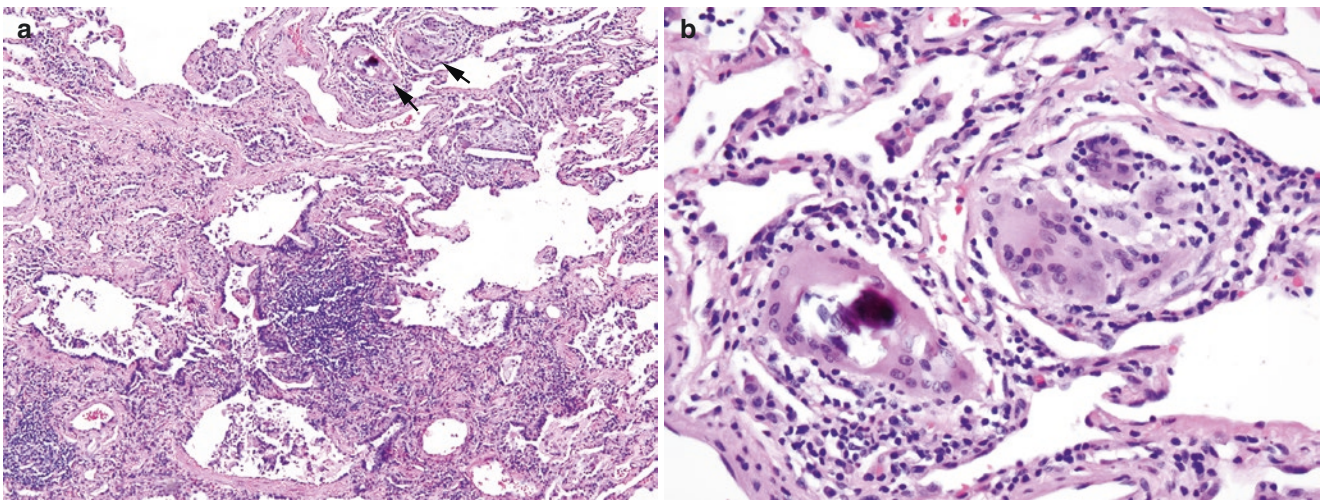

Fig. 7.8 Fibrotic hypersensitivity pneumonia. (**a**) Photomicrograph showing long-standing hypersensitivity pneumonia characterized by a considerable degree of fibrosis that includes architectural distortion in the form of scarring and early honeycomb change resembling usual interstitial pneumonia. However, the patchy peribronchiolar infiltrate of lymphocytes combined with the cluster of multinucleated giant cells (arrows) are clues to the diagnosis of hypersensitivity pneumonia. (**b**) High-magnification view of the small clusters of multinucleated giant cells, one of which contains calcified cytoplasmic inclusions

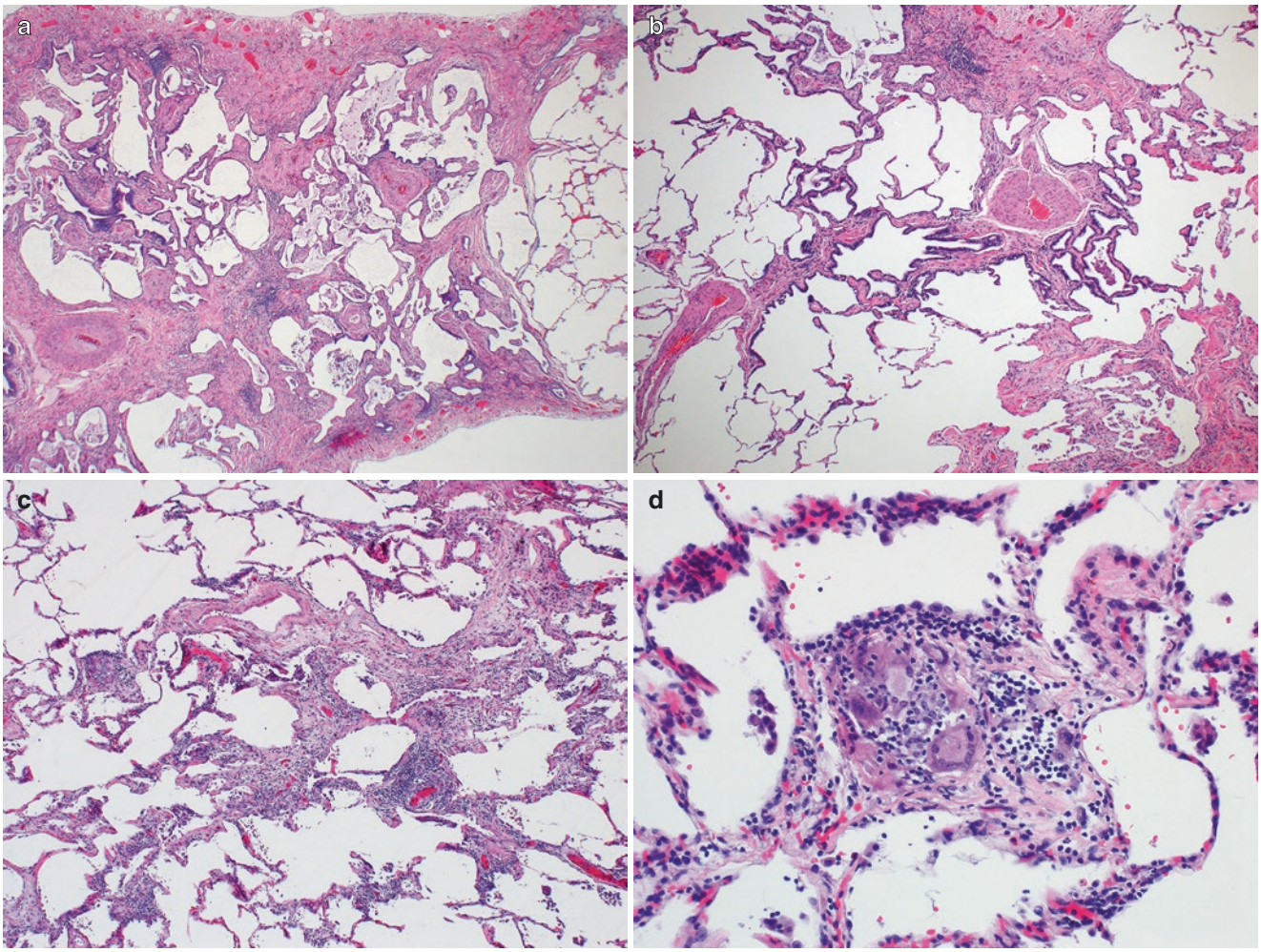

Fig. 7.9 Fibrotic hypersensitivity pneumonia. (**a**) Low-magnification photomicrograph of surgical lung biopsy showing patchwork fibrosis and microscopic honeycomb changes resembling UIP. (**b**) Photomicrograph from same biopsy showing prominent peribronchiolar metaplasia. (**c**) Low-magnification photomicrograph of a biopsy obtained from a different lobe from the same patient showing features typical of hypersensitivity pneumonia, including a bronchiolocentric lymphocytic infiltrate and a poorly formed granuloma in the peribronchiolar interstitium. (**d**) High-magnification photomicrograph showing a loose cluster of multinucleated giant cells in the peribronchiolar interstitium

Sarcoidosis

Sarcoidosis (Figs. 7.10, 7.11, 7.12, 7.13, 7.14, 7.15, 7.16, 7.17, 7.18, 7.19, 7.20 and 7.21) is a disease of unknown etiology characterized by granuloma formation involving multiple organ sites. The lung is the most commonly involved organ. Young and middle-aged adults are most often affected, although the age range is wide. The incidence rate is higher in women and in African-Americans. The diagnosis requires a combination of typical clinicoradiologic features, non-necrotizing epithelioid granulomas in a tissue biopsy, and exclusion of other possible etiologies, particularly granulomatous infection. Most cases of pulmonary sarcoidosis follow a benign course and tend to resolve spontaneously or with steroid treatment. However, 10–30% of patients develop progressive fibrosis resulting in respiratory failure and lung transplantation.

The classic histologic findings in sarcoidosis are well-formed, tightly clustered, non-necrotizing granulomas confined to the interstitial compartment and distributed in a characteristic lymphangitic pattern. The features illustrated here draw primarily on surgical lung biopsies, but most patients are diagnosed using smaller closed biopsies, including some combination of endobronchial ultrasound (EBUS)-guided transbronchial needle aspirations and transbronchial lung biopsies. The findings in these smaller biopsies may be subtle, but in experienced hands they have demonstrated high diagnostic sensitivity but lower specificity. Determining the significance of non-necrotizing granulomas in these smaller specimens hinges to a large degree on the clinical and radiologic context and the associated pretest probabilities.

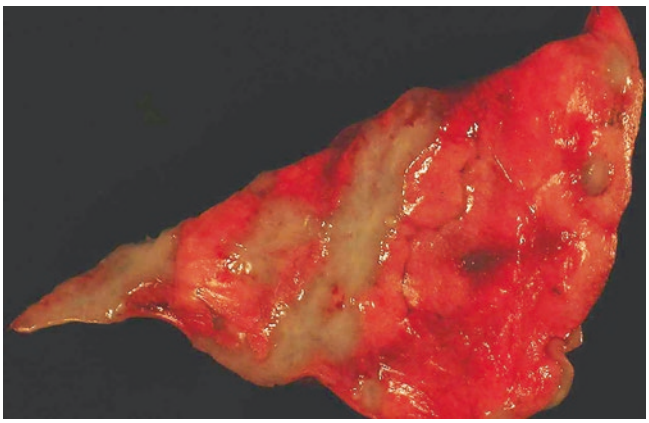

Fig. 7.10 Sarcoidosis. Gross photograph demonstrating the cut surface of a surgical lung biopsy involved by sarcoidosis. The abnormalities have an exquisitely lymphangitic distribution and include pale nodular and linear fibrous bands that expand interlobular septa, bronchovascular bundles, and visceral pleura

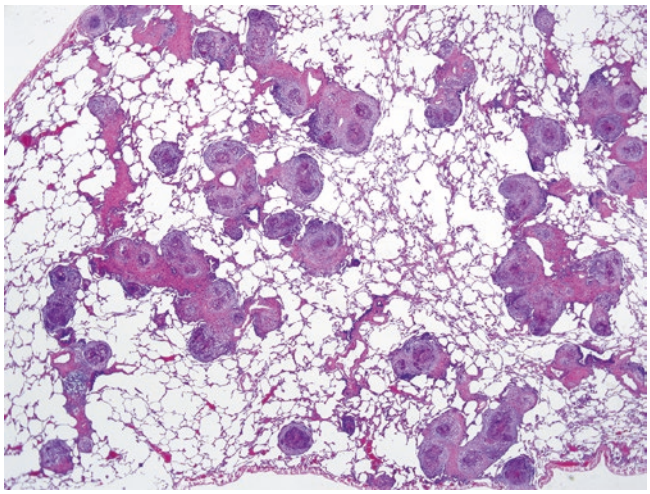

Fig. 7.11 Sarcoidosis. Low-magnification photomicrograph showing the lymphangitic distribution of non-necrotizing granulomas. The granulomas are confined to the interstitium and distributed within interlobular septa, bronchovascular bundles, and visceral pleura. As a consequence, vessel walls are frequently affected but without true necrotizing vasculitis

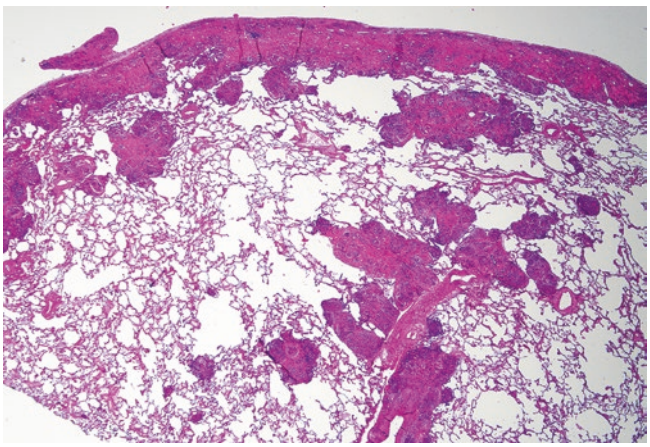

Fig. 7.12 Sarcoidosis. Low-magnification photomicrograph showing another example of sarcoidosis with classic lymphangitic distribution. Well-formed non-necrotizing granulomas are located along the visceral pleura, interlobular septa, and bronchovascular bundles

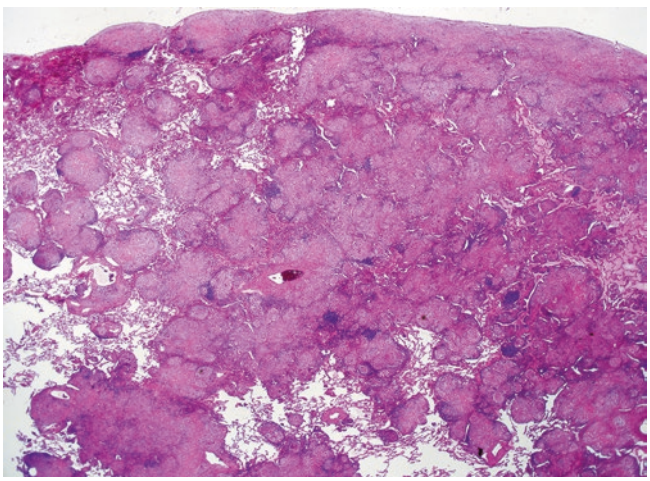

Fig. 7.13 Sarcoidosis. As illustrated in this low-magnification photomicrograph, sometimes the granulomas are confluent and form larger nodules that replace portions of lung parenchyma. The granulomas maintain their interstitial location and lymphangitic distribution

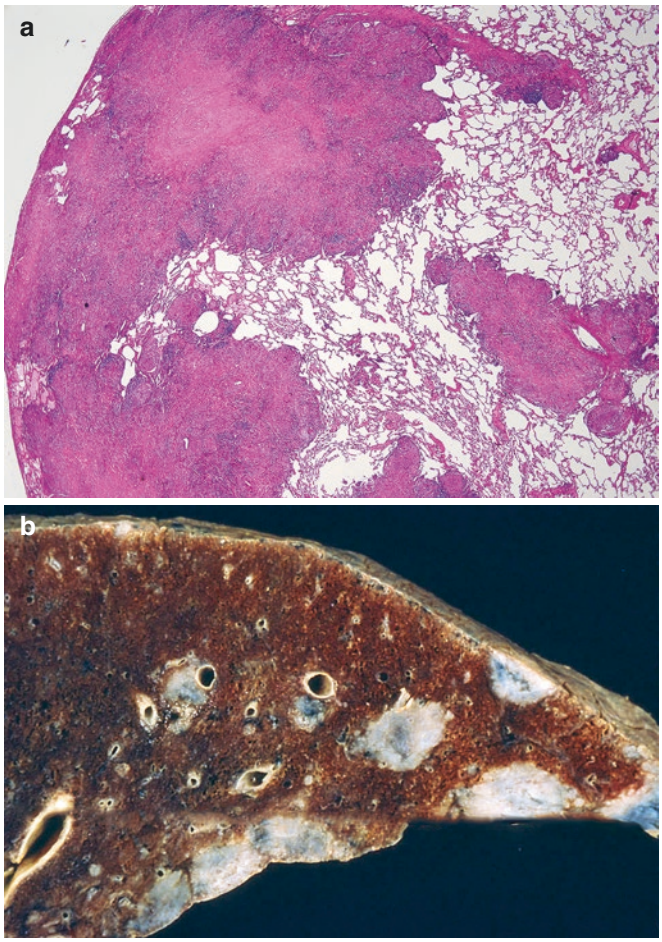

Fig. 7.14 Nodular sarcoidosis. (**a**) Low-magnification photomicrograph showing coalescence of well-formed granulomas in a collagenous stroma resulting in macroscopic nodules. (**b**) Cut surface of surgical lung specimen showing macroscopic nodules situated along visceral pleura and bronchovascular bundles in a patient with nodular sarcoidosis

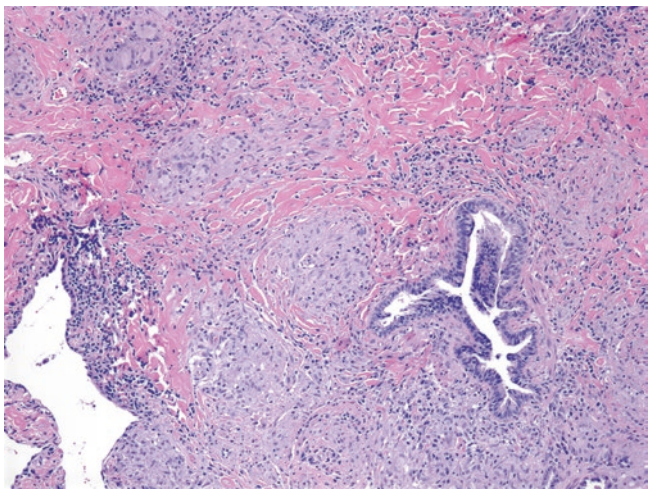

Fig. 7.15 Sarcoidosis. Photomicrograph showing multiple well-formed non-necrotizing granulomas next to a bronchiole, expanding the bronchovascular bundle. Dense collagen fibrosis characterized by concentric lamellar bands is characteristic of, but not specific for, sarcoidosis

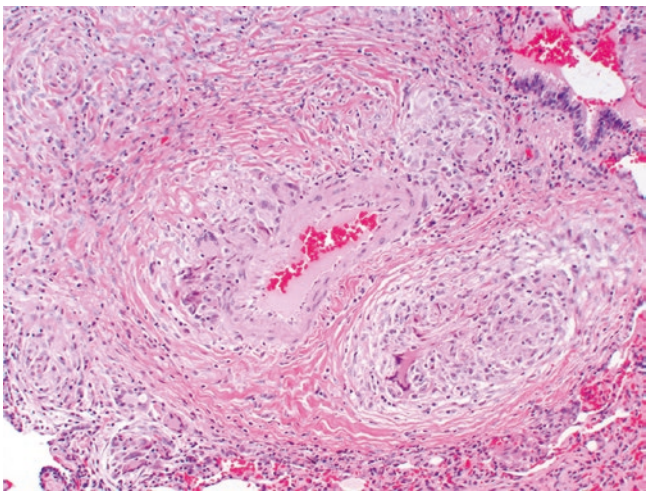

Fig. 7.16 Sarcoidosis. Photomicrograph showing non-necrotizing granulomas within a bronchovascular bundle (bronchiole in right upper corner), in this example involving the wall of a small muscular pulmonary artery. Non-necrotizing granulomatous vasculitis is a common finding in surgical lung biopsies from patients with sarcoidosis and is occasionally present in smaller transbronchial biopsies

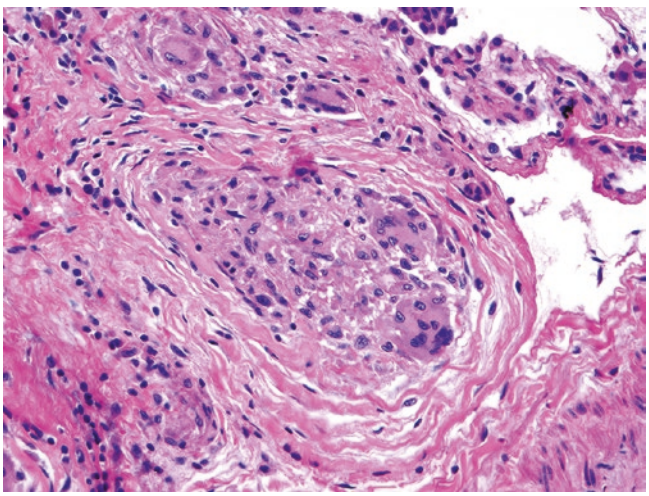

Fig. 7.17 Sarcoidosis. High-magnification photomicrograph showing a well-formed non-necrotizing granuloma consisting of tightly clustered multinucleated giant cells and epithelioid histiocytes, surrounded by a rim of fibroblasts and concentric bands of collagen fibrosis

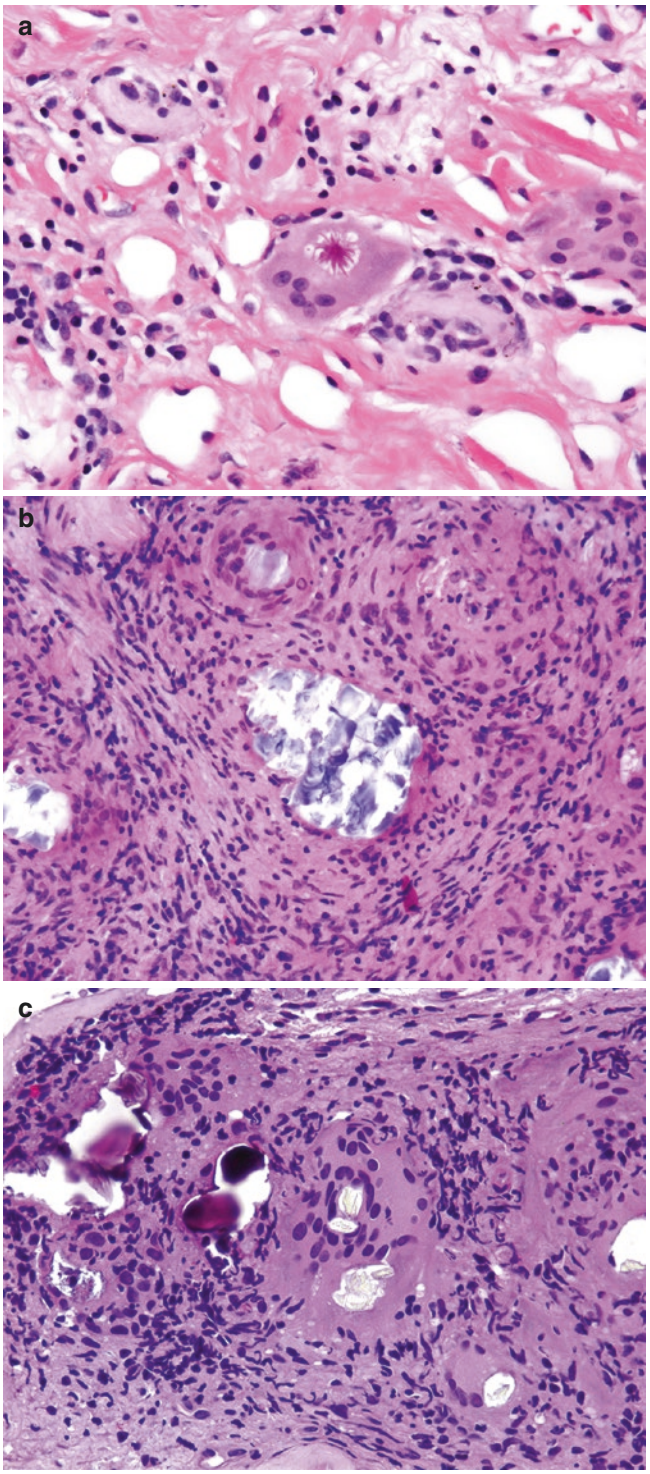

Fig. 7.18 Sarcoidosis. A number of cytoplasmic inclusions are commonly seen within the histiocytes and especially the giant cells of sarcoidosis, including asteroid bodies (**a**), Schaumann bodies (**b**), and calcium oxalate crystals (**c**), as illustrated in these high-magnification photomicrographs. The calcium oxalate crystals are relatively translucent in routinely stained sections but are brightly birefringent when viewed with polarized light. These inclusions are not specific for sarcoidosis and can be seen in any chronic granulomatous lesions, including infections and hypersensitivity pneumonia

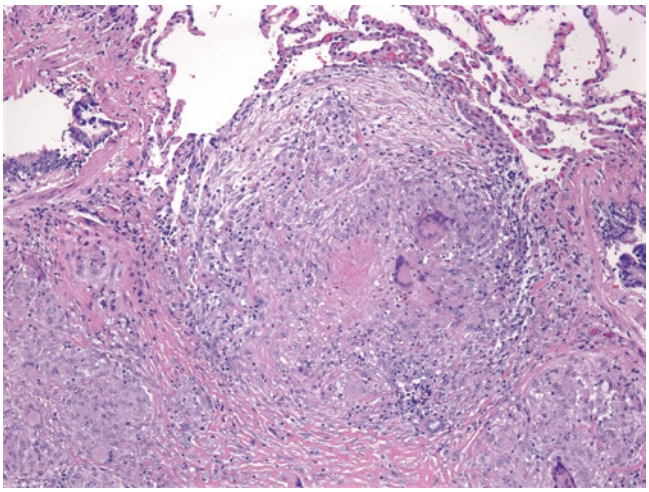

Fig. 7.19 Sarcoidosis. Photomicrograph showing a small focus of central necrosis in a granuloma in a patient with sarcoidosis. Although the predominant pattern of granulomatous inflammation in sarcoidosis is non-necrotizing, small foci of necrosis like this one in occasional granulomas are not uncommon in well-sampled cases

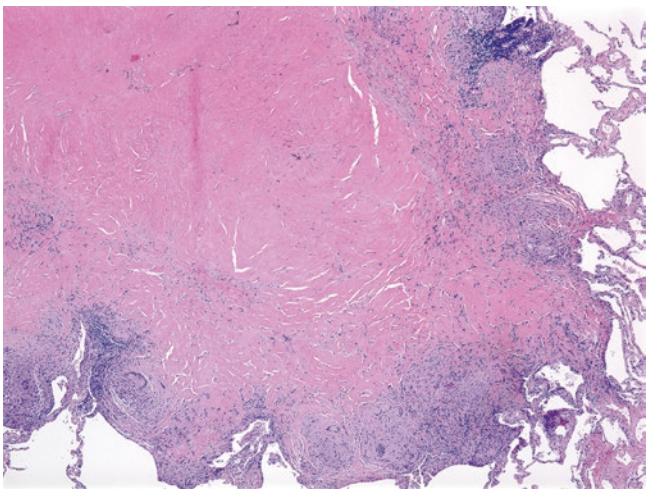

Fig. 7.20 Sarcoidosis. Low-magnification photomicrograph showing an example of late-stage disease characterized by a large area of dense hyalinized fibrosis. Tightly formed (sarcoidal) non-necrotizing granulomas are still appreciated at the edge of the fibrosis. This combination of features overlaps with the histology of hyalinizing infectious granulomas and is a finding that sometimes complicates diagnostic interpretation

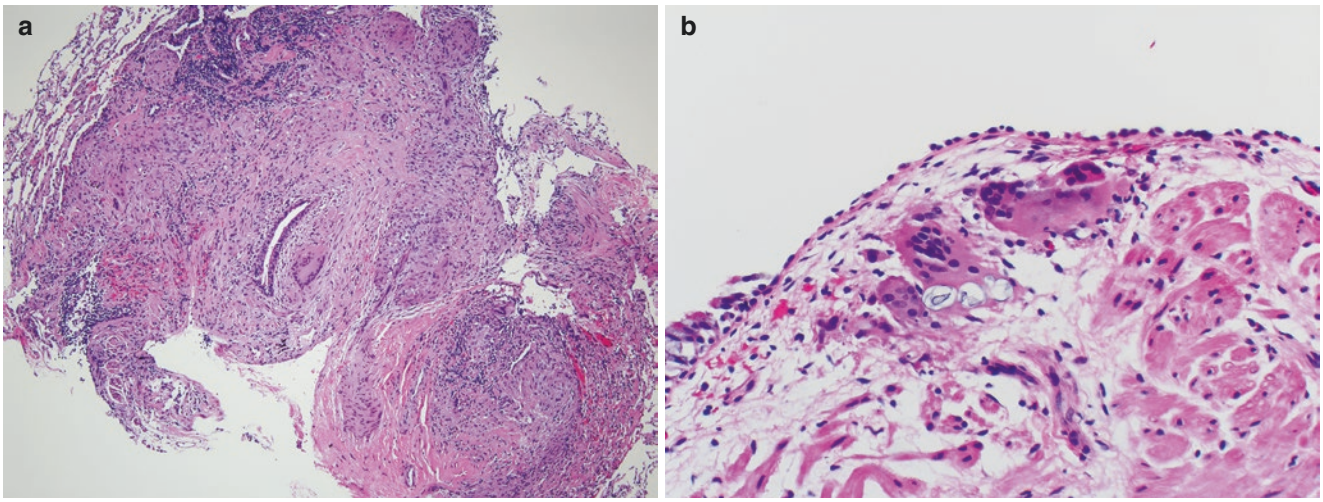

Fig. 7.21 Sarcoidosis in transbronchial and endobronchial biopsies. (**a**) Photomicrograph of transbronchial biopsy showing a classic combination of well-formed non-necrotizing granulomas with associated collagen fibrosis confined to the interstitium and involving a bronchovascular bundle. (**b**) High-magnification photomicrograph of endobronchial biopsy showing poorly formed granuloma containing a loose cluster of isolated multinucleated giant cells in a bronchial wall from a patient with sarcoidosis. In the appropriate clinical and radiologic setting, even poorly formed granulomas are supportive of sarcoidosis

Suggested Readings

Churg A, Muller NL, Flint J, Wright JL. Chronic hypersensitivity pneumonitis. Am J Surg Pathol. 2006;30:201–8.

Churg A, Sin DD, Everett D, Brown K, Cool C. Pathologic patterns and survival in chronic hypersensitivity pneumonitis. Am J Surg Pathol. 2009;33:1765–70.

Hsu RM, Connors AF, Tomashefski JF. Histologic, microbiologic, and clinical correlates of the diagnosis of sarcoidosis by transbronchial biopsy. Arch Pathol Lab Med. 1996;120:364–8.

Myers JL. Hypersensitivity pneumonia: the role of lung biopsy in diagnosis and management. Mod Pathol. 2012;25(Suppl 1):S58–67.

Ohtani Y, Saiki S, Kitaichi M, Usui Y, Inase N, Costabel U, Yoshizawa Y. Chronic bird fancier's lung: histopathological and clinical correlation. An application of the 2002 ATS/ERS consensus classification of the idiopathic interstitial pneumonias. Thorax. 2005;60:665–71.

Takemura T, Matsui Y, Saiki S, Mikami R. Pulmonary vascular involvement in sarcoidosis: a report of 40 autopsy cases. Hum Pathol. 1992;23:1216–23.

Takemura T, Akashi T, Kamiya H, Ikushima S, Ando T, Oritsu M, et al. Pathological differentiation of chronic hypersensitivity pneumonitis from idiopathic pulmonary fibrosis/usual interstitial pneumonia. Histopathology. 2012;61:1026–35.

Trahan S, Hanak V, Ryu JH, Myers JL. Role of surgical lung biopsy in separating chronic hypersensitivity pneumonia from usual interstitial pneumonia/idiopathic pulmonary fibrosis: analysis of 31 biopsies from 15 patients. Chest. 2008;134:126–32.

Visscher D, Churg A, Katzenstein AL. Significance of crystalline inclusions in lung granulomas. Mod Pathol. 1988;1:415–9.

Xu L, Kligerman S, Burke A. End-stage sarcoid lung disease is distinct from usual interstitial pneumonia. Am J Surg Pathol. 2013;37:593–600.

Zhang C, Chan KM, Schmidt LA, Myers JL. Histopathology of explanted lungs from patients with a diagnosis of pulmonary sarcoidosis. Chest. 2016;149:499–507.

Transplant-Related Disorders

8

Chen Zhang and Jeffrey L. Myers

With the advance of lung allogeneic transplantation, more and more transbronchial biopsies are encountered by surgical pathologists, mainly for the purpose of the monitoring and diagnosis of allograft rejection. Surgical lung biopsy and explanted allografts are also occasionally encountered. This chapter illustrates the classification and grading scheme of pulmonary allograft rejection defined by the 2007 International Society for Heart and Lung Transplantation (ISHLT) formula, which is a revision of the 1996 ISHLT working formulation. The grading and histologic criteria for acute cellular rejection, airway inflammation, and chronic airway and vascular rejection are listed in Table 8.1.

The diagnosis and recognition of antibody-mediated rejection (AMR; also known as acute humoral rejection) of the lung are more controversial and less well developed than for other solid-organ grafts such as heart and renal transplants. Although some histologic changes such as neutrophilic capillaritis and acute lung injury have been reported in association with AMR, these findings are nonspecific and can be seen in a variety of settings, including drug reactions, infection, and moderate or severe acute cellular rejection. The presence of these histopathologic changes should prompt further immunohistochemical stains complement 4 split product (C4d) and serologic testing. Definitive diagnosis of pulmonary AMR requires the combination of clinical dysfunction, circulating donor-specific antibodies, and C4d immunoreactivity.

In addition to the evaluation of rejection, the primary role of lung biopsies is to exclude alternate diagnoses, especially infections with opportunistic pathogens such as cytomegalovirus, pneumocystis, and other fungi (*see* Chap. 4). Special stains (e.g., Gomori methenamine silver) are performed routinely in some institutions for this purpose. Posttransplantation lymphoproliferative disorders (*see* Chap. 11) range from bronchiolitis-like lymphoproliferative lesions to tumorous masses with necrosis and are rare biopsy findings.

C. Zhang (✉)
Department of Pathology and Laboratory Medicine, Indiana University School of Medicine, Indianapolis, IN, USA
e-mail: chenzhan@iupui.edu

J. L. Myers
Department of Pathology, Michigan Medicine, Ann Arbor, MI, USA
e-mail: myerjeff@med.umich.edu

© Springer Science+Business Media, LLC, part of Springer Nature 2018
C. Zhang, J. L. Myers (eds.), *Atlas of Lung Pathology*, Atlas of Anatomic Pathology,
https://doi.org/10.1007/978-1-4939-8689-7_8

Table 8.1 Classification and grading of pulmonary allograft rejection (based on ISHLT 2007 formulation)

Classification	Grade	Histologic criteria
Acute cellular rejection	A0—No acute cellular rejection	Normal pulmonary parenchyma
	A1—Minimal acute cellular rejection	Scattered, infrequent perivascular mononuclear infiltrates; no significant expansion of the perivascular interstitium or extension of mononuclear cells into adjacent alveolar septa
	A2—Mild acute cellular rejection	Frequent perivascular mononuclear infiltrates with expansion of the perivascular interstitium, easily identifiable from scanning magnification; no extension of mononuclear cells into adjacent alveolar septa
	A3—Moderate acute cellular rejection	Extension of the inflammatory cell infiltrate into perivascular alveolar septa; commonly associated with endothelialitis
	A4—Severe acute cellular rejection	Diffuse perivascular and interstitial mononuclear infiltrates; prominent alveolar pneumocyte damage and endothelialitis
Airway inflammation	B0—No airway inflammation	No airway inflammation
	B1R—Low-grade airway inflammation	Sparse bronchiolar mononuclear inflammatory infiltrate that spares the respiratory epithelium
	B2R—High-grade airway inflammation	Dense mononuclear inflammatory infiltrate involving the epithelium with epithelial damage. Neutrophils and eosinophils are common
Chronic airway rejection	C1—Chronic airway rejection	Subepithelial scarring of the small airway, with or without bronchiolar inflammatory infiltrates
Chronic vascular rejection	D1—Chronic vascular rejection	Fibrointimal thickening of large or intermediate-sized blood vessels; not applicable in transbronchial biopsies

Acute Cellular Rejection

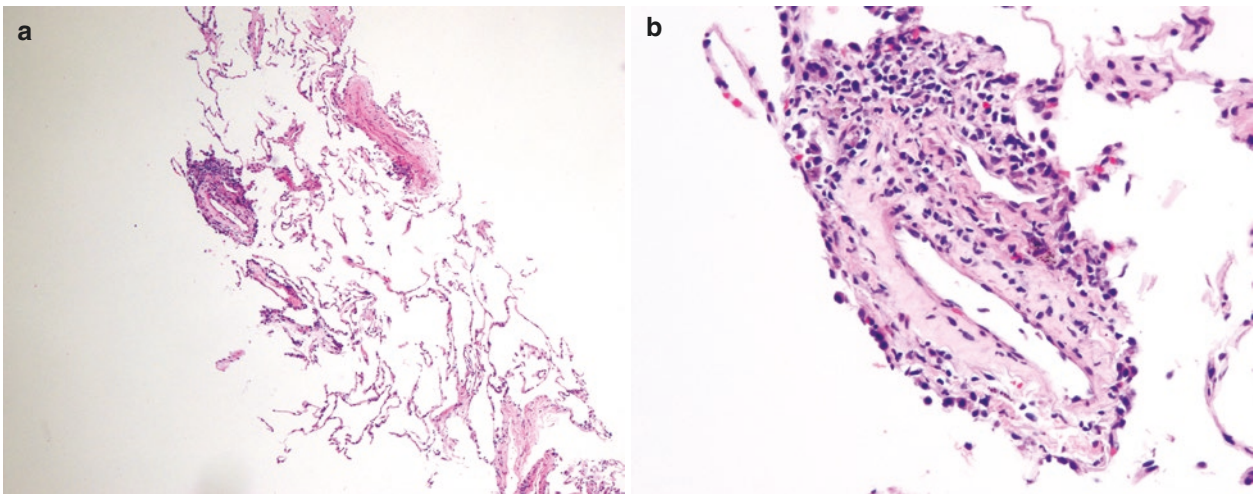

Fig. 8.1 Minimal acute cellular rejection (A1). (**a**) Low-magnification photomicrograph of a transbronchial biopsy showing a single small focus of perivascular inflammation in the background of unremarkable alveolar lung parenchyma. (**b**) At high magnification, there is a circumferential infiltrate of predominantly mononuclear inflammatory cells with occasional eosinophils within the loose perivascular interstitium, without extension into the adjacent alveolar septa. No significant expansion of the perivascular interstitium is present

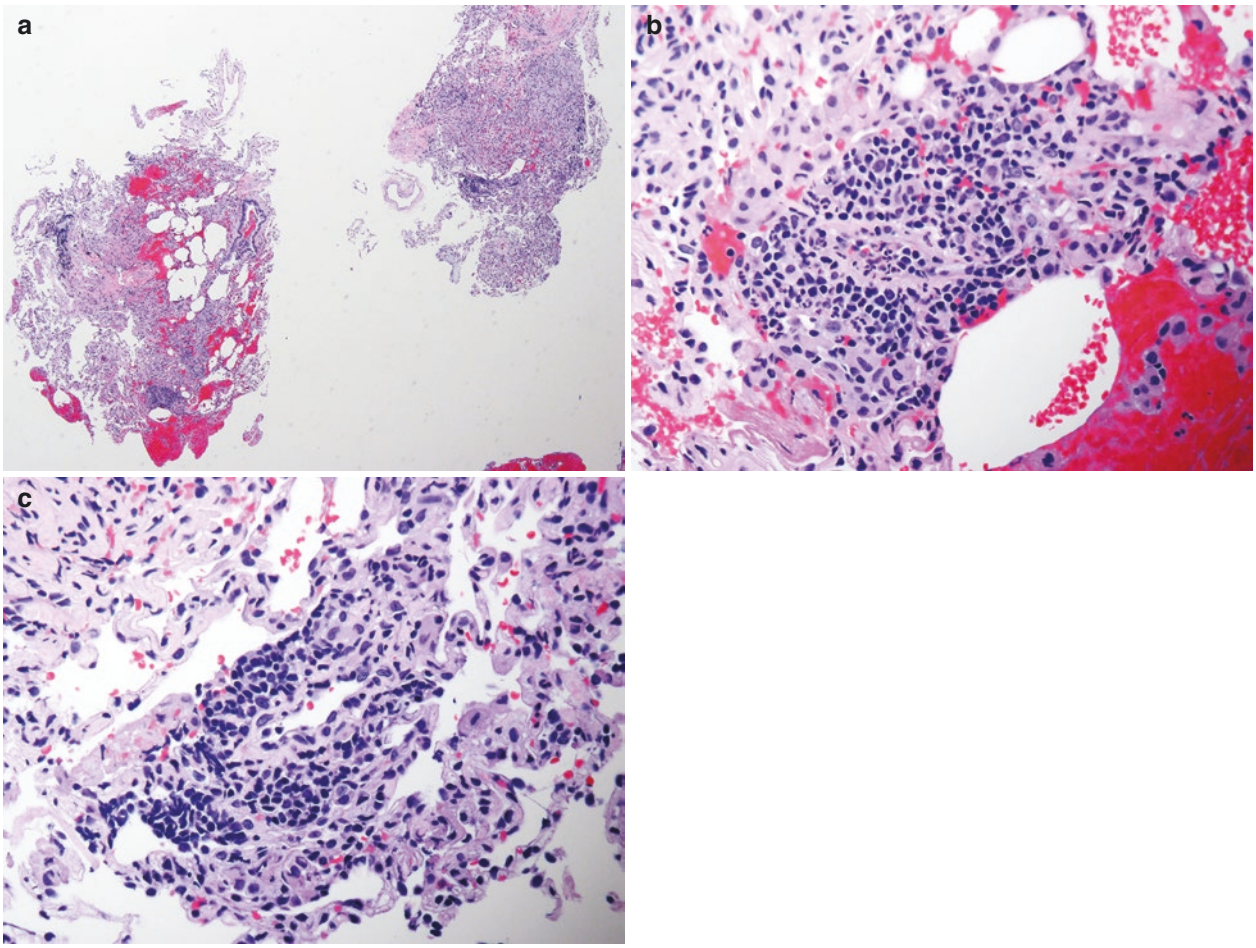

Fig. 8.2 Mild acute cellular rejection (A2). (**a**) Two small blood vessels show significant circumferential expansion of the perivascular interstitium by mononuclear inflammatory infiltrates, which are easily identifiable under low magnification. (**b**) and (**c**) At high magnification, the infiltrates consist largely of mononuclear cells with occasional activated lymphocytes and plasmacytoid lymphocytes. Accumulated alveolar macrophages are seen within the adjacent alveolar spaces. No inflammatory infiltrate is present within the adjacent alveolar septa

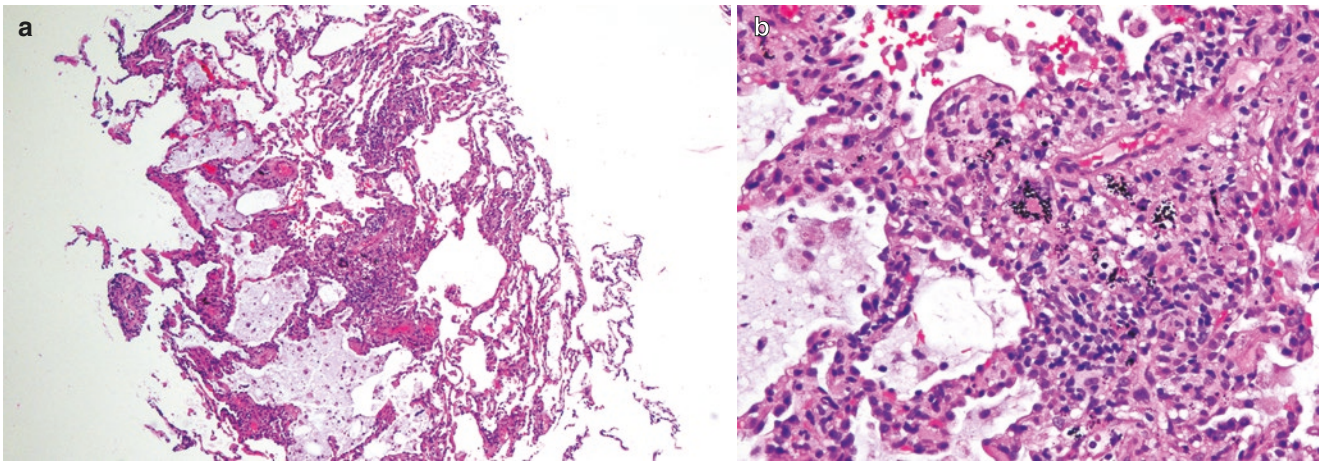

Fig. 8.3 Moderate acute cellular rejection (A3). (**a**) Low-magnification photomicrograph illustrates easily recognizable perivascular mononuclear inflammatory infiltrates that percolate into the adjacent alveolar septa. (**b**) High-magnification view showing expansion of perivascular interstitium by mononuclear cells with extension of the inflammatory infiltrate into adjacent perivascular alveolar septa. There is associated alveolar pneumocyte hyperplasia along thickened alveolar septa and alveolar macrophages clustered within alveolar spaces

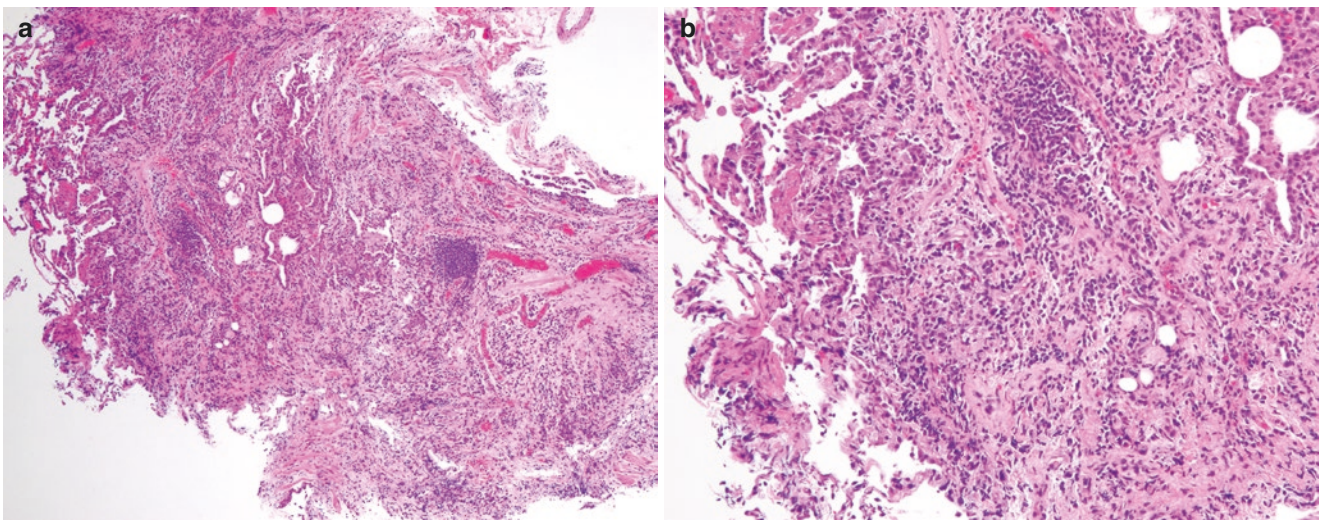

Fig. 8.4 Severe acute cellular rejection (A4). (**a**) Low-magnification photomicrograph showing perivascular spaces expanded by a mononuclear inflammatory infiltrate that percolates into alveolar septa. (**b**) High-magnification photomicrograph showing that the infiltrates are composed of lymphocytes, plasma cells, and occasional eosinophils and neutrophils. The characteristic feature of severe acute cellular rejection is pronounced acute lung injury, with alveolar collapse, reactive pneumocyte hyperplasia, and interstitial organization. Hyaline membranes are not evident in this example

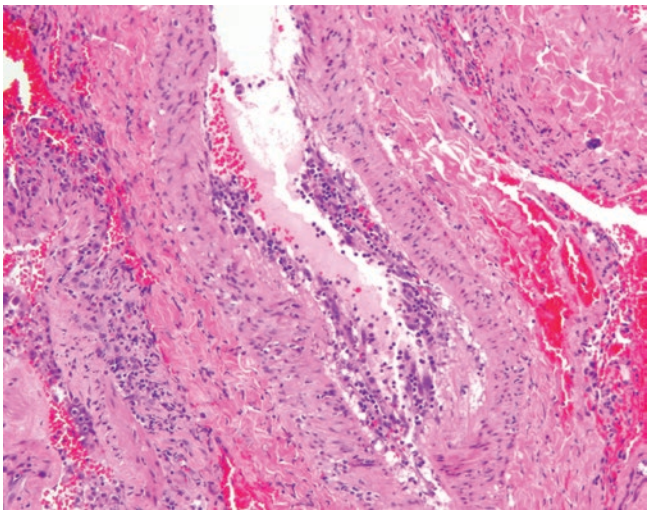

Fig. 8.5 Endothelialitis in acute rejection. High-magnification photomicrograph showing endothelialitis, which is present in most moderate and all severe acute cellular rejections. Subendothelial infiltrates of small round and plasmacytoid lymphocytes are characteristic and are often accompanied by eosinophils. The endothelial cells are swollen and often detached from the vascular wall

Airway Inflammation

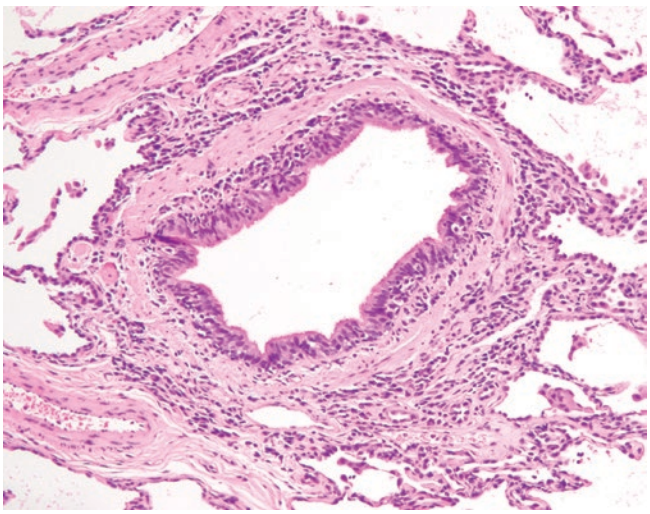

Fig. 8.6 Low-grade lymphocytic bronchiolitis (B1R). High-magnification photomicrograph demonstrating a bronchiole with a mild peribronchiolar and submucosal mononuclear cell infiltrate that spares the respiratory epithelium

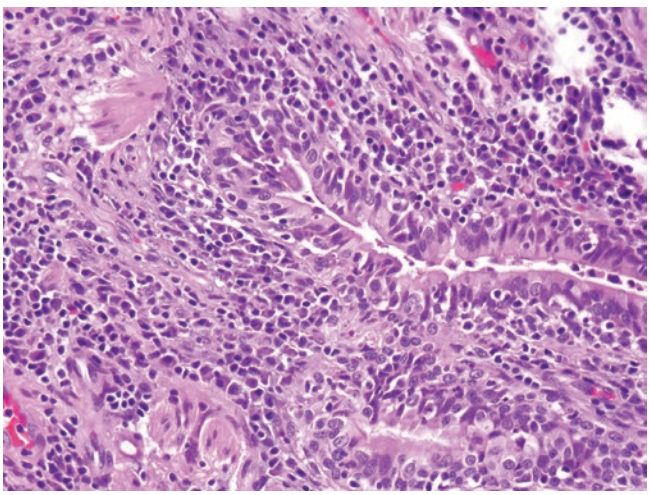

Fig. 8.7 High-grade lymphocytic bronchiolitis (B2R). High-magnification photomicrograph showing a bronchiole with a dense mononuclear cell infiltrate that expands the submucosa and involves the respiratory epithelium. Occasional neutrophils and eosinophils are also present

Chronic Airway Rejection (Obliterative Bronchiolitis)

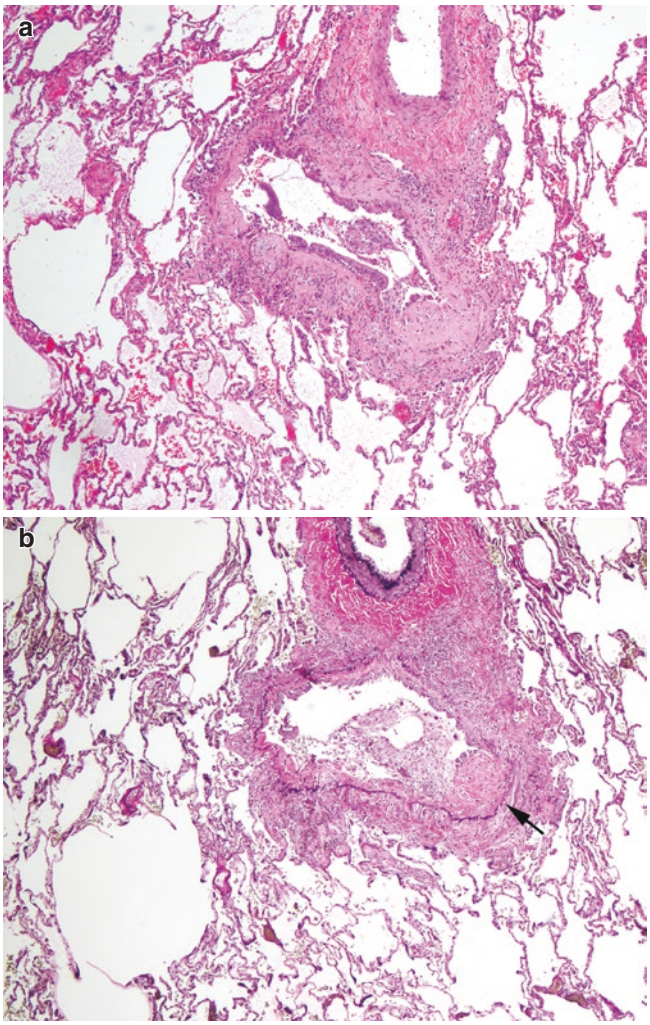

Fig. 8.8 Chronic rejection (obliterative bronchiolitis, C1). (**a**) Intermediate-magnification photomicrograph showing a bronchiole with patchy areas of scarring in the submucosa, associated with a peribronchiolar mononuclear infiltrate. The overlying epithelium appears injured, and the lumen of the airway is mildly narrowed. (**b**) An elastic stain shows that the scarring is located immediately beneath the epithelium and above the elastic layer. The scarring is most prominent in the lower right of the airway (arrow)

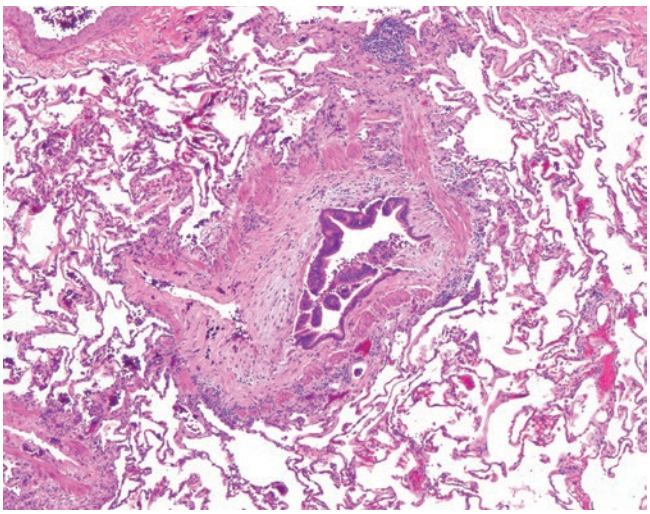

Fig. 8.9 Chronic rejection (obliterative bronchiolitis, C1). Photomicrograph showing an eccentric plaque of organizing fibroblasts and myofibroblasts within a myxoid stroma situated between the respiratory epithelium and the smooth muscle wall of the airway. The respiratory epithelium is focally attenuated, and the airway lumen is significantly narrowed

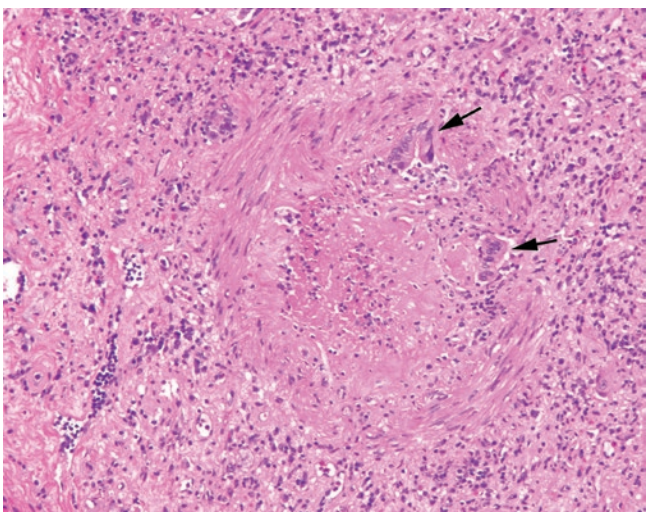

Fig. 8.10 Chronic rejection (obliterative bronchiolitis, C1). High-magnification photomicrograph showing an obliterated airway in which the entire airway lumen is occluded by scar tissue and mononuclear cells. There are rare fragments of residual respiratory epithelium (arrows) within the scarred lumen. The circumference of the small airway is defined by a relatively preserved layer of smooth muscle

Chronic Vascular Rejection

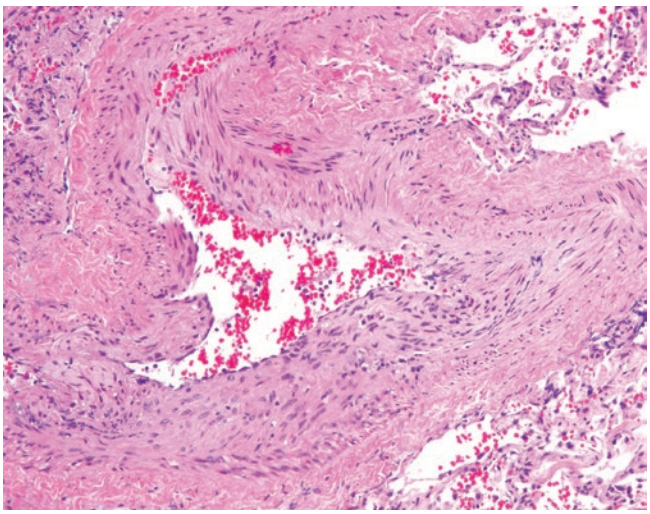

Fig. 8.11 Chronic vascular rejection/accelerated graft vascular sclerosis. High-magnification photomicrograph showing alloreactive injury resulting in fibrointimal thickening of a muscular pulmonary artery, which is similar to coronary artery disease in transplanted hearts. The changes are seen in large- and intermediate-sized arteries and are generally not seen in transbronchial biopsies

Suggested Reading

Badesch DB, Zamora M, Fullerton D, Weill D, Tuder R, Grover F, et al. Pulmonary capillaritis: a possible histologic form of acute pulmonary allograft rejection. J Heart Lung Transplant. 1998;17:415–22.

Berry G, Burke M, Andersen C, Angelini A, Bruneval P, Calabrese F, et al. Pathology of pulmonary antibody-mediated rejection: 2012 update from the pathology council of the ISHLT. J Heart Lung Transplant. 2013;32:14–21.

Magro CM, Deng A, Pope-Harman A, Waldman WJ, Bernard Collins A, Adams PW, et al. Humorally mediated posttransplantation septal capillary injury syndrome as a common form of pulmonary allograft rejection: a hypothesis. Transplantation. 2002;74:1273–80.

Magro CM, Abbas AE, Seilstad K, Pope-Harman AL, Nadasdy T, Ross P. C3d and the septal microvasculature as a predictor of chronic lung allograft dysfunction. Hum Immunol. 2006;67:274–83.

Stephenson A, Flint J, English J, Vedal D, Fradet G, Chittock D, et al. Interpretation of transbronchial lung biopsies from lung transplant recipients: inter- and intraobserver agreement. Can Respir J. 2005;12:75–7.

Stewart S, Fishbein MC, Snell GI, Berry GJ, Boehler A, Burke MM, et al. Revision of the 1996 working formulation for the standardization of nomenclature in the diagnosis of lung rejection. J Heart Lung Transplant. 2007;26:1229–42.

Tazelaar HD. Perivascular inflammation in pulmonary infections: implications for the diagnosis of lung rejection. J Heart Lung Transplant. 1991;10:437–41.

Yousem SA. Lymphocytic bronchitis/bronchiolitis in lung allograft recipients. Am J Surg Pathol. 1993;17:491–6.

Yousem SA, Berry GJ, Cagle PT, Chamberlain D, Husain AN, Hruban RH, et al. Revision of the 1990 working formulation for the classification of pulmonary allograft rejection: lung rejection study group. J Heart Lung Transplant. 2006;15(1 Pt 1):1–15.

Pneumoconiosis

9

Chen Zhang and Jeffrey L. Myers

Pneumoconiosis is a nonneoplastic reaction of the lung to inhaled inorganic particles. Most affected patients are diagnosed based on a combination of an occupational history, pulmonary function tests, and radiologic findings. Surgical specimens showing pneumoconiosis are uncommon. The histologic reactions of the lung to the inhaled particles vary, depending on the chemical properties and size of the particulates, the length and dose of exposure, and the individual susceptibility of the host. The characteristic pathologic features in the types of pneumoconiosis most commonly encountered in surgical lung specimens are summarized in Table 9.1 and are illustrated in this chapter.

Table 9.1 Major types of pneumoconiosis and their typical pathologic features

Diseases	Pathologic features
Silicosis	Concentric hyaline nodules; progressive massive fibrosis
Mixed dust fibrosis	Stellate interstitial fibrotic nodules
Asbestosis	Diffuse interstitial fibrosis
Coal workers' pneumoconiosis	Dust macules and collagen fibrosis
Berylliosis	Sarcoid-like granulomas
Hard metal pneumoconiosis	Giant cell interstitial pneumonia

Silicosis

Silicosis (Figs. 9.1, 9.2, 9.3 and 9.4) occurs in reaction to inhaled crystalline silica. Simple silicosis consists of silicotic nodules involving predominantly the upper lobes. Hilar or mediastinal lymph nodes may also be involved. Progressive massive fibrosis is defined by the presence of nodular fibrosis that is greater than 1 cm in size and is the form of disease most likely to be associated with physiologically significant lung disease and disability.

C. Zhang (✉)
Department of Pathology and Laboratory Medicine, Indiana University School of Medicine, Indianapolis, IN, USA
e-mail: chenzhan@iupui.edu

J. L. Myers
Department of Pathology, Michigan Medicine, Ann Arbor, MI, USA
e-mail: myerjeff@med.umich.edu

© Springer Science+Business Media, LLC, part of Springer Nature 2018
C. Zhang, J. L. Myers (eds.), *Atlas of Lung Pathology*, Atlas of Anatomic Pathology,
https://doi.org/10.1007/978-1-4939-8689-7_9

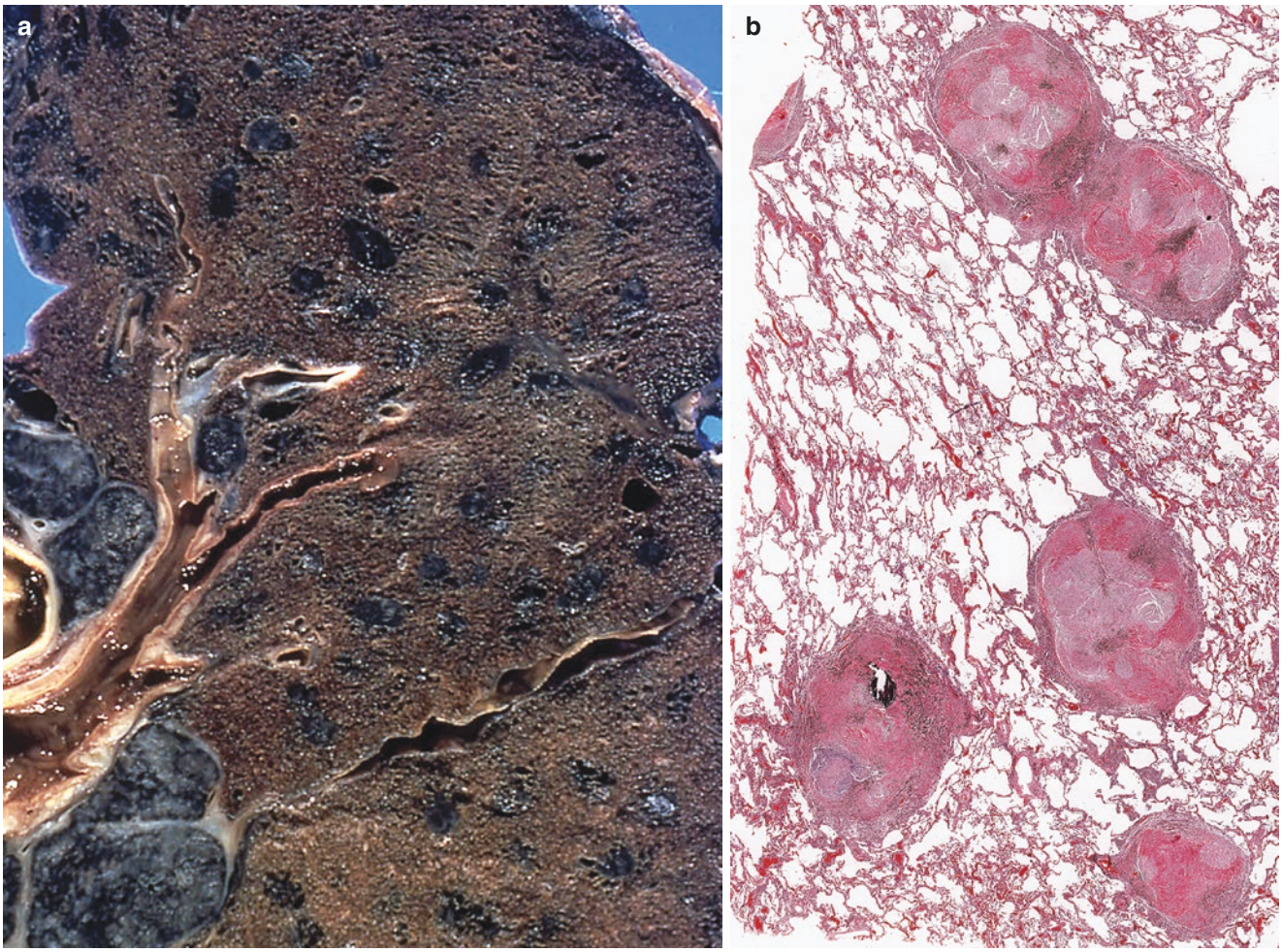

Fig. 9.1 Simple silicosis. (**a**) Cut surface of autopsy lung showing classic simple silicosis with multiple pigmented lung nodules measuring less than 1 cm in their greatest dimension. (**b**) Low-magnification photomicrograph of a section from the same autopsy lung showing multiple silicotic nodules consisting of concentric, hyalinized collagen bundles, and a peripheral rim of inflammatory cells in which dust-laden macrophages predominate

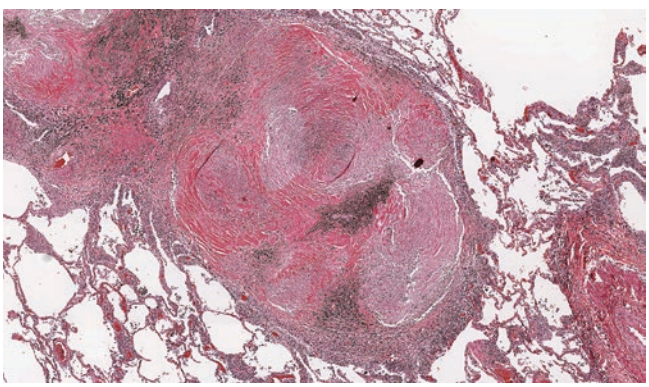

Fig. 9.2 Silicotic nodule. Higher-magnification view of nodule illustrated in Fig. 9.1b showing the coarse collagen bundles typical of silicotic nodules with the usual degree of associated dust-laden macrophages

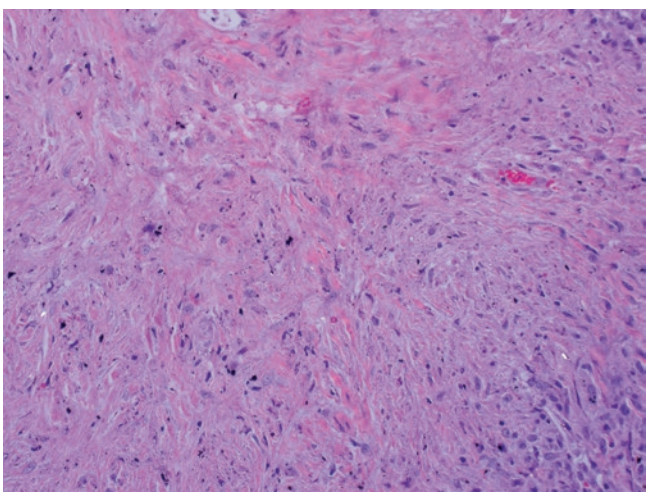

Fig. 9.3 Silicotic nodule. High-magnification photomicrograph taken using polarized light showing small, dimly birefringent crystalline particulates characteristic of free crystalline silica. Finding crystalline particles does not by itself establish the diagnosis of silicosis, which is predicated on the finding of particulates in the appropriate histologic context

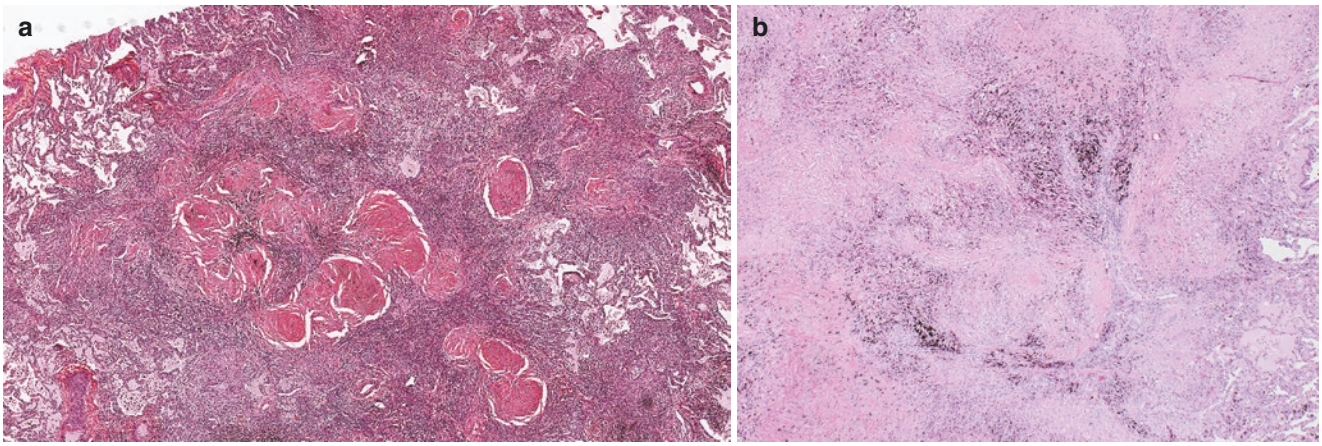

Fig. 9.4 Complicated silicosis (progressive massive fibrosis). (**a**) This low-magnification photomicrograph shows a conglomeration of silicotic nodules to form a larger complex lesion measuring more than 1 cm in greatest dimension. (**b**) Low-magnification photomicrograph showing another example of progressive massive fibrosis that involved nearly all of the right upper and middle lobes in an explanted lung from a patient with complicated silicosis

Mixed Dust Fibrosis

Mixed dust fibrosis (Figs. 9.5, 9.6 and 9.7) occurs when the inhaled particles consist of a mixture of silica and other less fibrogenic dusts such as anthracotic pigment and iron oxides. Compared to those of pure silicosis, the radiographic opacities of mixed dust fibrosis tend to be more irregular and stellate in shape. The main histologic finding is multiple bronchiolocentric stellate dust macules composed of dust-laden macrophages without well-formed silicotic nodules. Nonasbestos ferruginous bodies containing brown or black cores may also be present.

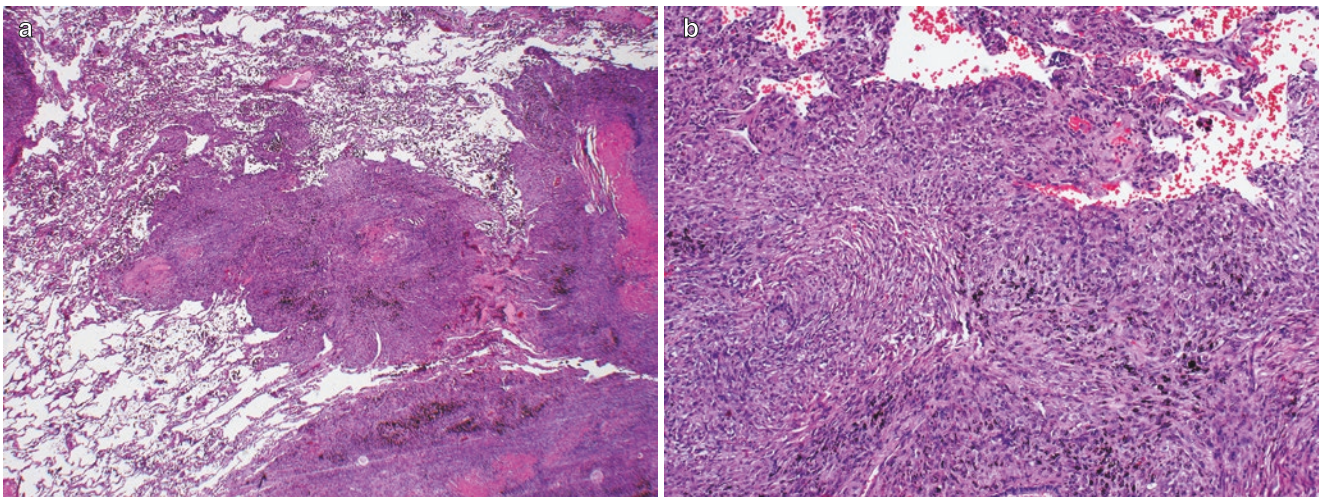

Fig. 9.5 Mixed dust fibrosis. (**a**) Low-magnification photomicrograph showing irregularly shaped dust macule without well-formed nodules. (**b**) Higher-magnification view showing epithelioid and spindled dust-laden macrophages making up the dust macule

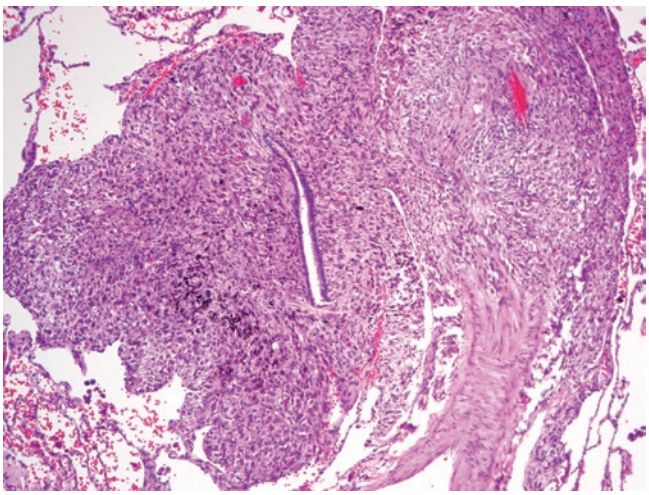

Fig. 9.6 Mixed dust fibrosis. High-magnification view of another dust macule surrounding a bronchiole in a patient with mixed dust fibrosis. The stellate macule consists of macrophages, fibroblasts, and various pigmented particulates without silicotic nodules

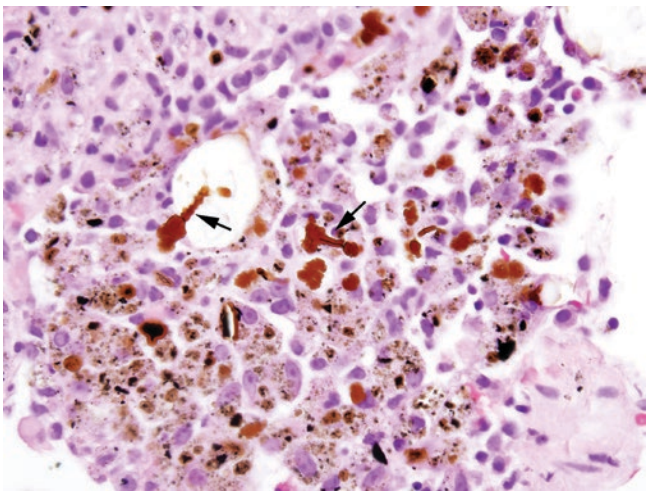

Fig. 9.7 Mixed dust fibrosis with nonasbestos ferruginous bodies. A high-magnification photomicrograph shows pigmented particulates and ferruginous bodies containing central black cores (arrows) that differ from the translucent cores typical of asbestos

Asbestosis

Asbestosis (Figs. 9.8, 9.9, 9.10 and 9.11) is interstitial fibrosis caused by inhaled asbestos fibers. The disease process preferentially involves the lower lobes of the lung and is commonly accompanied by pleural plaques/fibrosis. The interstitial fibrosis of asbestosis ranges from early peribronchiolar fibrosis to late stage disease that may be indistinguishable from usual interstitial pneumonia. Identifying asbestos bodies in a background of interstitial fibrosis in a patient with a supportive occupational history is key to the diagnosis of asbestosis.

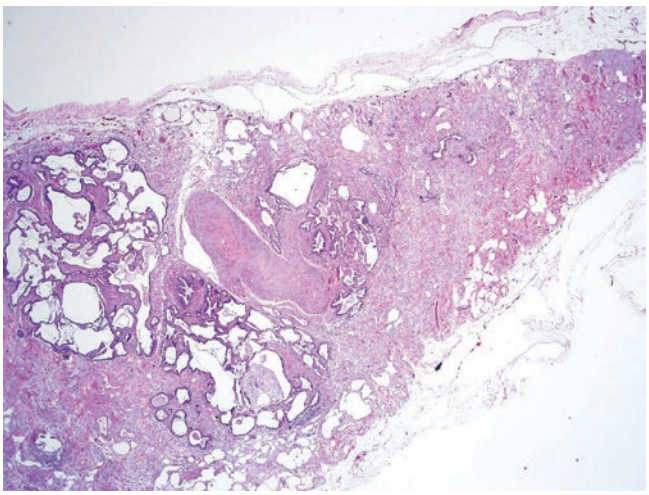

Fig. 9.8 Asbestosis. Low-magnification photomicrograph showing diffuse fibrosis with patchy scarring and honeycomb changes indistinguishable from usual interstitial pneumonia

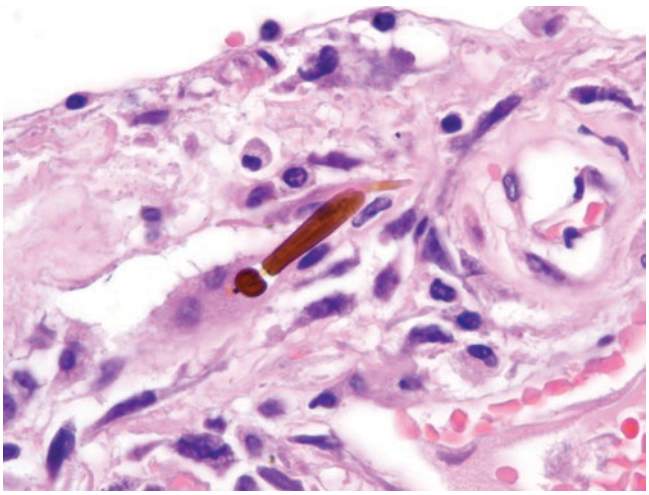

Fig. 9.10 Asbestosis. High-magnification photomicrograph showing a club-shaped asbestos body with a clear central core, a finding helpful in establishing the histologic diagnosis of asbestosis

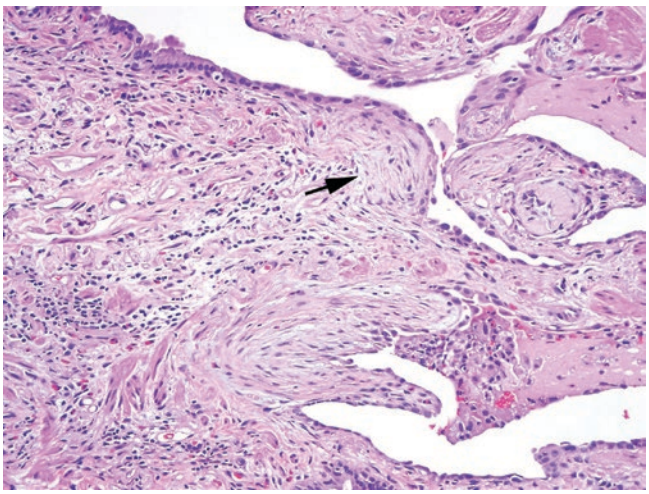

Fig. 9.9 Asbestosis. At high magnification, the interstitial fibrosis includes fibroblast foci (arrow) typical of those commonly seen in usual interstitial pneumonia of unknown cause (i.e., idiopathic pulmonary fibrosis)

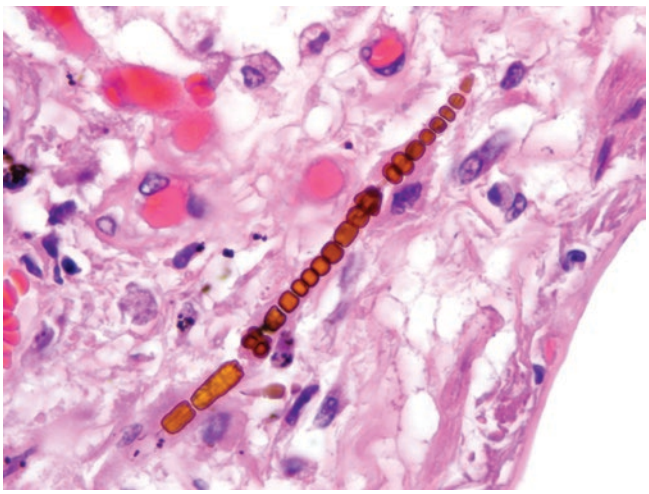

Fig. 9.11 Asbestosis. High-magnification photomicrograph showing another example of an asbestos body with a beaded appearance. Note the clear, refractile central core that distinguishes asbestos bodies from other forms of nonasbestos ferruginous bodies

Coal Workers' Pneumoconiosis

Coal workers' pneumoconiosis (CWP) (Figs. 9.12, 9.13, 9.14 and 9.15) occurs in reaction to inhaled coal dusts. Depending primarily on the silica content of the coal dust, CWP may be complicated by concomitant silicosis or mixed dust fibrosis. Simple CWP is characterized by a combination of dust macules and nodules with associated black coal dust. Complicated CWP is the term applied to those examples in which there is associated progressive massive fibrosis defined as conglomerate nodules measuring more than 1 cm in greatest dimension. As with complicated silicosis, progressive massive fibrosis in CWP can be very extensive and associated with severe respiratory impairment.

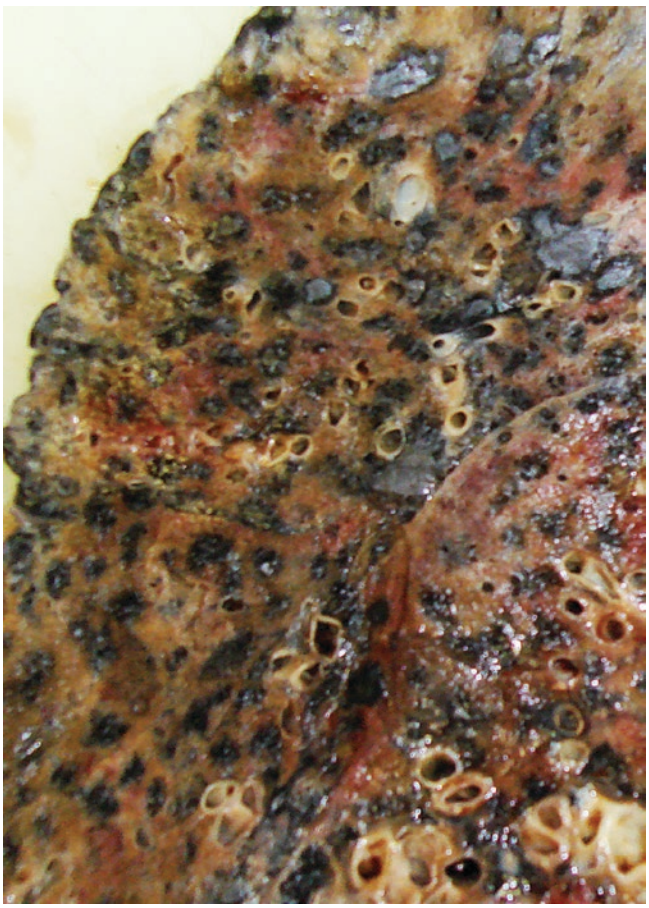

Fig. 9.12 Coal workers' pneumoconiosis (CWP). Cut surface of autopsy lung from a patient with CWP. There are numerous black pigmented macules and nodules with early complicated lesions measuring just over 1 cm in greatest dimension

Fig. 9.13 Simple CWP. Specially prepared Gough section of thinly sliced lung showing darkly pigmented dust macules characteristic of simple CWP

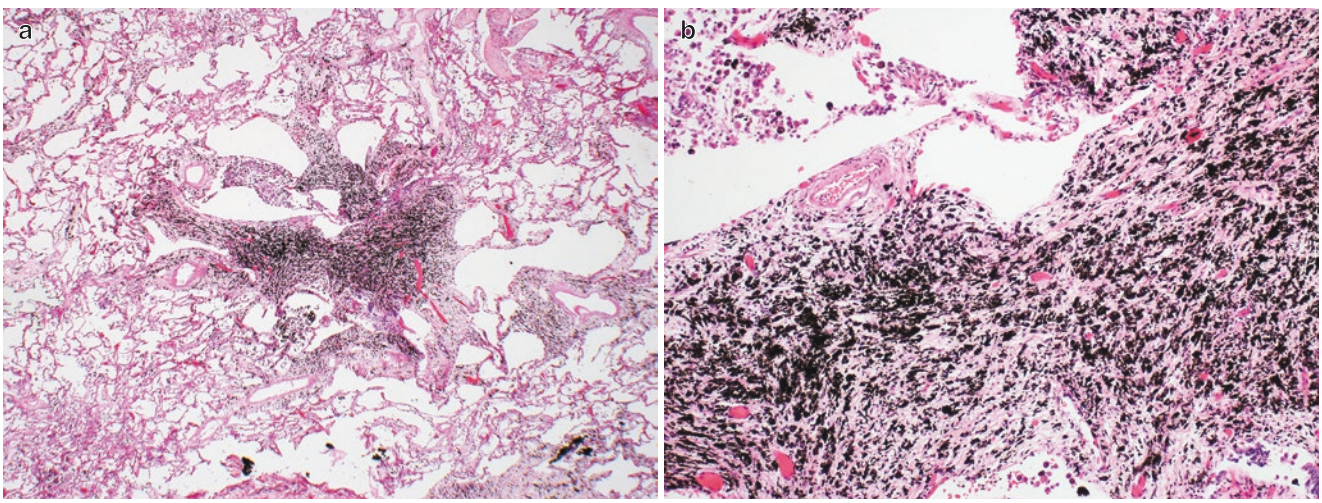

Fig. 9.14 Simple CWP. (**a**) Low-magnification photomicrograph showing a dust macule marked by deposits of black coal dust. (**b**) Higher-magnification view showing black coal dust in a dust macule characteristic of simple CWP

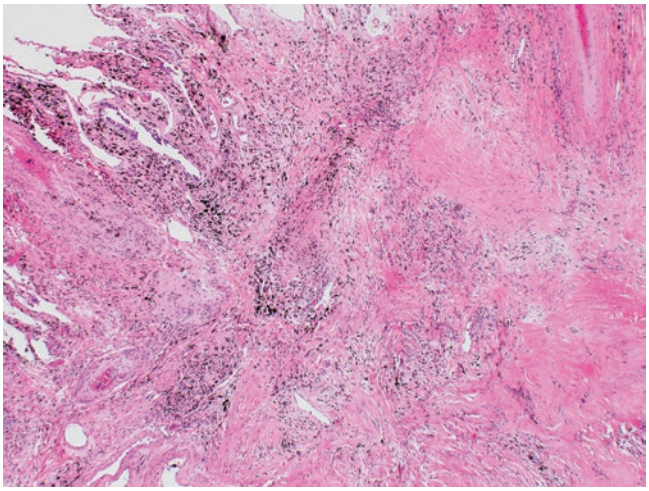

Fig. 9.15 Complicated CWP. Low-magnification photomicrograph of autopsy lung showing large area of progressive massive fibrosis in a patient with advanced CWP

Berylliosis

Berylliosis (Figs. 9.16 and 9.17) is a systemic disease caused by beryllium exposure. Chronic exposure may lead to pulmonary interstitial fibrosis accompanied by non-necrotizing granulomas, causing a pattern of granulomatous inflammation indistinguishable from pulmonary sarcoidosis in some patients. Beryllium is not visible on tissue sections. Differentiation from sarcoidosis requires correlation with exposure history, clinical course, and radiologic findings. The beryllium lymphocyte proliferation test is available only in specialized centers. If the test is positive, it confirms the diagnosis in an exposed worker with granulomatous disease in a lung biopsy.

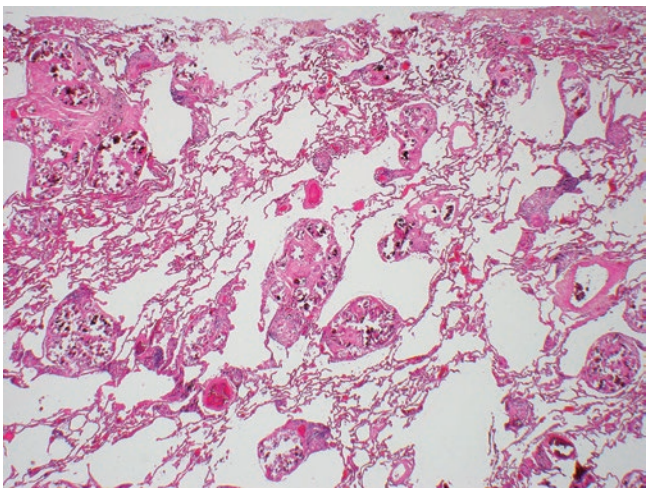

Fig. 9.16 Berylliosis. (**a**) low-magnification view showing interstitial fibrosis associated with multiple non-necrotizing granulomas. In this example, many of the granulomas show prominent cytoplasmic inclusions consisting of concentric calcifications (Schaumann bodies). Schaumann bodies are characteristic of the granulomas seen in berylliosis but are nonspecific and commonly seen in other granulomatous conditions such as sarcoidosis

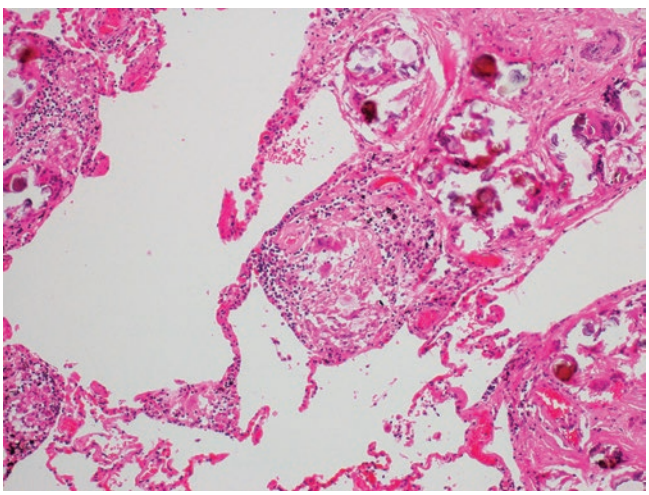

Fig. 9.17 Berylliosis. A high-magnification view of a non-necrotizing granuloma consisting of histiocytes, multinucleated giant cells, and a rim of lymphocytes

Hard Metal Pneumoconiosis

Hard metal pneumoconiosis is a diffuse interstitial lung disease caused by exposure to hard metals such as cobalt, tungsten carbide, titanium, chromium, and nickel. Cobalt is considered the etiologic driver in most patients. A common feature of hard metal pneumoconiosis is the intra-alveolar accumulation of multinucleated macrophages and epithelial giant cells, which is the reason why the disease is often referred to as giant cell interstitial pneumonia (Figs. 9.18, 9.19 and 9.20). Giant cell interstitial pneumonia is not pathognomonic, however, and also occurs in patients who lack evidence of cobalt exposure.

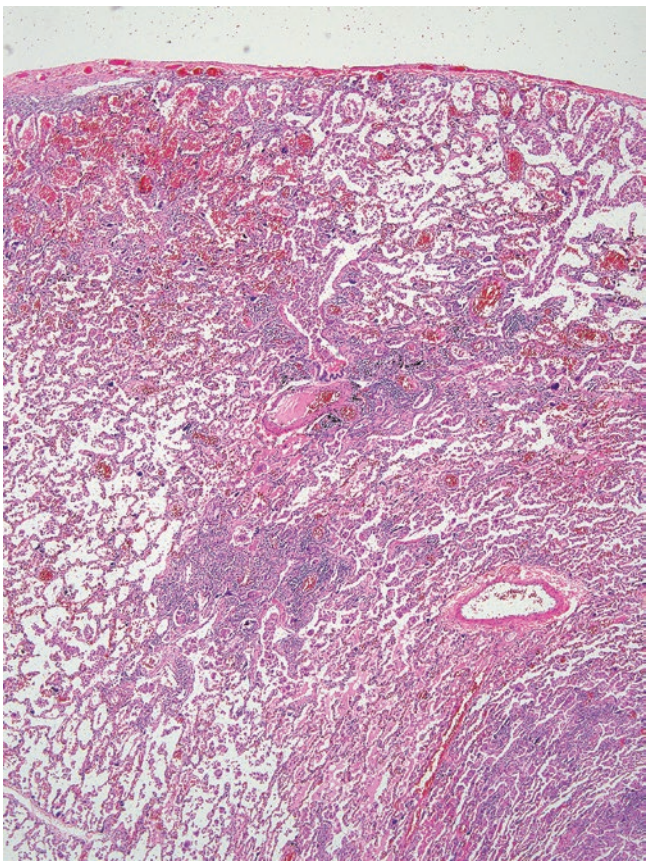

Fig. 9.18 Hard metal pneumoconiosis (giant cell interstitial pneumonia). A low-magnification view showing patchy interstitial thickening and cellular infiltrates distributed in a bronchiolocentric fashion. At this low magnification, you can see numerous multinucleated giant cells, many of them with hyperchromatic nuclei

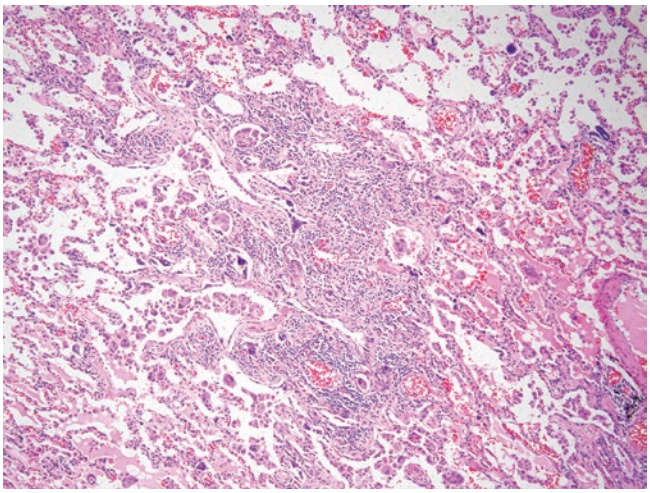

Fig. 9.19 Hard metal pneumoconiosis (giant cell interstitial pneumonia). A higher-magnification view showing expansion of peribronchiolar interstitium by inflammation with prominent multinucleated giant cells composed of both epithelium and alveolar macrophages. The multinucleated epithelial giant cells are TTF-1 positive (not shown) and represent pneumocytes

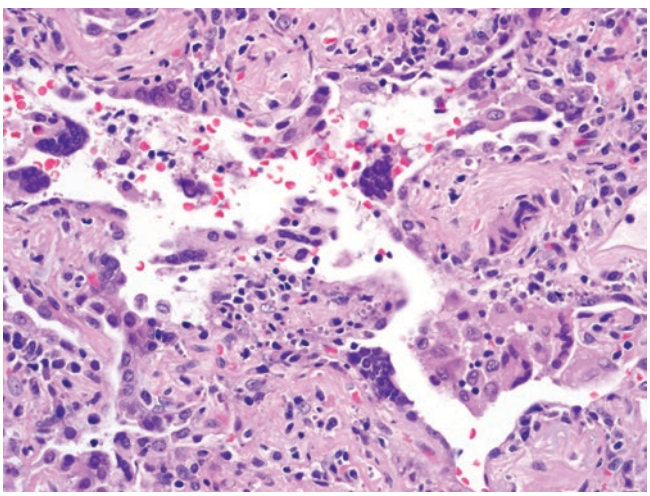

Fig. 9.20 Hard metal pneumoconiosis (giant cell interstitial pneumonia). High-magnification view showing intra-alveolar and surface epithelial giant cells

Other Rare Types of Pneumoconiosis

Other rare types of pneumoconiosis include a pattern of disease resembling simple coal workers' pneumoconiosis in workers exposed to aluminum dust (Figs. 9.21 and 9.22). Other inorganic particulates, including other metals, can occasionally cause occupational lung disease frequently characterized by the accumulation of a combination of dust macules and fibrosis.

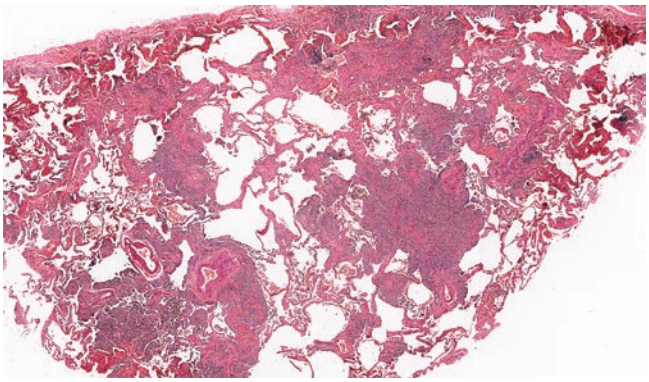

Fig. 9.21 Aluminum pneumoconiosis. Low-magnification photomicrograph showing multiple dust macules in which peribronchiolar interstitium is expanded by prominent collections of dust-laden macrophages

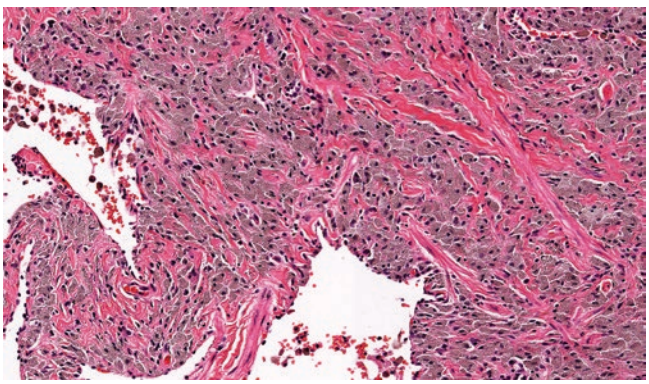

Fig. 9.22 Aluminum pneumoconiosis. High-magnification view of a dust macule showing macrophages containing finely granular, grayish-brown particles characteristic of aluminum

Suggested Reading

Anttila S, Sutinen S, Paananen M, Kreus KE, Sivonen SJ, Grekula A, Alapieti T. Hard metal lung disease: a clinical, histological, ultrastructural and x-ray microanalytical study. Eur J Respir Dis. 1986;69:83–94.

Aronchick JM, Rossman MD, Miller WT. Chronic beryllium disease: diagnosis, radiographic findings, and correlation with pulmonary function tests. Radiology. 1987;163:677–82.

Balmes JR, Abraham JL, Dweik RA, Fireman E, Fontenot AP, Maier LA, et al. Sensitivity and D. Chronic beryllium. An official American Thoracic Society statement: diagnosis and management of beryllium sensitivity and chronic beryllium disease. Am J Respir Crit Care Med. 2014;190:e34–59.

Churg A. The diagnosis of asbestosis. Hum Pathol. 1989;20:979.

Craighead JE, Abraham JL, Churg A, Gree FH, Kleinerman J, Pratt PC, et al. The pathology of asbestos-associated diseases of the lungs and pleural cavities: diagnostic criteria and proposed grading schema. Report of the pneumoconiosis Committee of the College of American pathologists and the National Institute for Occupational Safety and Health. Arch Pathol Lab Med. 1982;106:544–96.

Davis JM, Chapman J, Collings P, Douglas AN, Fernie J, Lamb D, Ruckley VA. Variations in the histological patterns of the lesions of coal workers' pneumoconiosis in Britain and their relationship to lung dust content. Am Rev Respir Dis. 1983;128:118–24.

De Vuyst P, Dumortier P, Rickaert F, Van de Weyer R, Lenclud C, Yernault JC. Occupational lung fibrosis in an aluminium polisher. Eur J Respir Dis. 1986;68:131–40.

Honma K, Abraham JL, Chiyotani K, De Vuyst P, Dumortier P, Gibbs AR, et al. Proposed criteria for mixed-dust pneumoconiosis: definition, descriptions, and guidelines for pathologic diagnosis and clinical correlation. Hum Pathol. 2004;35:1515–23.

Jederlinic PJ, Abraham JL, Churg A, Himmelstein JS, Epler GR, Gaensler EA. Pulmonary fibrosis in aluminum oxide workers. Investigation of nine workers, with pathologic examination and microanalysis in three of them. Am Rev Respir Dis. 1990;142:1179–84.

Jones RN. The diagnosis of asbestosis. Am Rev Respir Dis. 1991;144(3 Pt 1):477–8.

Khoor A, Roden AC, Colby TV, Roggli VL, Elrefaei M, Alvarez F, et al. Giant cell interstitial pneumonia in patients without hard metal exposure: analysis of 3 cases and review of the literature. Hum Pathol. 2016;50:176–82.

Pulmonary Vascular Diseases

10

Chen Zhang and Jeffrey L. Myers

Two major categories of pulmonary vascular diseases are discussed in this chapter: noninflammatory vascular disorders and inflammatory vascular diseases (vasculitis). Noninflammatory vascular disorders encompass pulmonary hypertension of diverse causes with corresponding heterogeneity in histopathologic features. Inflammatory vascular disease or vasculitides comprise mainly granulomatosis with polyangiitis (formerly Wegener granulomatosis), eosinophilic granulomatosis with polyangiitis (formerly Churg-Strauss syndrome), and microscopic polyangiitis. These three forms of vasculitis are often referred to as antineutrophil cytoplasmic antibody (ANCA)-associated small vessel vasculitides, and they are frequently characterized by some combination of parenchymal necrosis, hemorrhage, and necrotizing vasculitis.

C. Zhang (✉)
Department of Pathology and Laboratory Medicine, Indiana University School of Medicine, Indianapolis, IN, USA
e-mail: chenzhan@iupui.edu

J. L. Myers
Department of Pathology, Michigan Medicine, Ann Arbor, MI, USA
e-mail: myerjeff@med.umich.edu

© Springer Science+Business Media, LLC, part of Springer Nature 2018
C. Zhang, J. L. Myers (eds.), *Atlas of Lung Pathology*, Atlas of Anatomic Pathology,
https://doi.org/10.1007/978-1-4939-8689-7_10

Noninflammatory Vascular Disorders

Current classification schemes for pulmonary hypertension are based on a number of factors, including clinical presentation, hemodynamic studies, cytogenetic and molecular testing in selected patients, and occasionally histopathology. Pulmonary arterial hypertension in adults includes idiopathic (primary) pulmonary hypertension, pulmonary hypertension associated with various underlying conditions (e.g., systemic connective tissue disease, portal hypertension, HIV infection), and pulmonary veno-occlusive disease and/or capillary hemangiomatosis (Table 10.1). Evidence of pulmonary hypertension is more commonly seen in surgical specimens from patients with underlying lung disease and/or hypoxia.

Table 10.1 Adult pulmonary hypertension classification

Types	Etiologies
Pulmonary arterial hypertension	Primary/idiopathic
	Heritable Drug/toxin-induced Associated with other underlying diseases Pulmonary veno-occlusive disease and/or pulmonary capillary hemangiomatosis
Pulmonary hypertension caused by left-sided heart disease and/or venous outflow obstruction	
Pulmonary hypertension caused by lung disease and/or hypoxia	Chronic obstructive pulmonary disease Interstitial lung disease
Chronic thrombotic pulmonary hypertension	
Pulmonary hypertension with unclear multifactorial mechanisms	Sarcoidosis, pulmonary Langerhans cell histiocytosis, lymphangioleiomyomatosis

Chronic thrombotic pulmonary hypertension is less common but should be separated from the other categories of disease because of important differences in therapeutic strategies. Occasionally evidence of pulmonary hypertension can be more localized as a result of regional abnormalities, including obstructing neoplasms.

All forms of pulmonary hypertension may demonstrate some common pathologic changes, such as medial hypertrophy and intimal hyperplasia in small pulmonary arteries. However, occasionally there are distinct histologic findings that can be helpful in identifying a specific etiology or phenotype. Features suggestive of idiopathic (primary) arterial hypertension (Figs. 10.1, 10.2, 10.3 and 10.4) include severe concentric thickening of the vascular wall, concentric intimal fibrosis, plexiform lesions, and angiomatoid lesions; however, the diagnosis of idiopathic pulmonary arterial hypertension requires exclusion of other phenotypes and causes of pulmonary hypertension (Figs. 10.5, 10.6, 10.7, 10.8, 10.9 and 10.10). Pulmonary veno-occlusive disease (PVOD) (Figs. 10.11, 10.12, 10.13, 10.14, 10.15 and 10.16) and pulmonary capillary hemangiomatosis (Fig. 10.17) are two rare and overlapping conditions with clinical presentations that resemble other forms of pulmonary arterial hypertension. The histologic findings in these conditions show considerable overlap with chronic venous hypertension in patients with left-sided heart disease and venous outflow obstruction in conditions like fibrosing mediastinitis (Figs. 10.18 and 10.19). For that reason, correlation with clinical information is necessary before rendering either of these diagnoses. Chronic thrombotic pulmonary hypertension is another form of pulmonary hypertension with distinct histologic findings helpful in separating it from other types of pulmonary hypertension (Fig. 10.20).

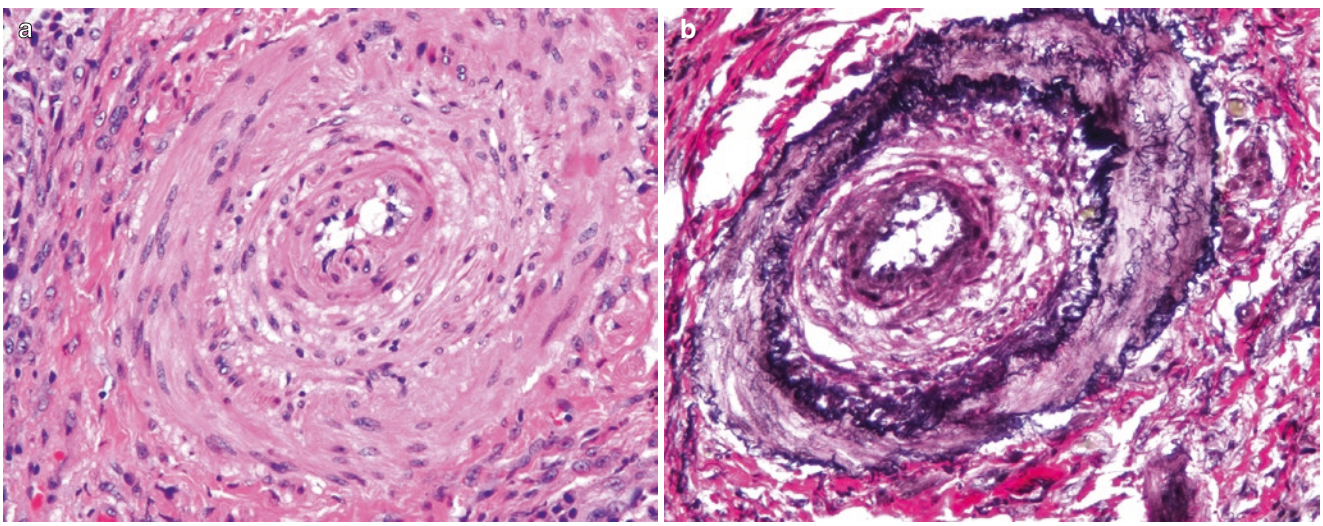

Fig. 10.1 Pulmonary arterial hypertension. (**a**) Photomicrograph of routinely stained section showing severe intimal hyperplasia and fibrosis with medial hypertrophy in a muscular pulmonary artery, leading to marked luminal narrowing. (**b**) An elastic tissue stain highlights the double elastic layers of the artery, with both intimal and medial thickening

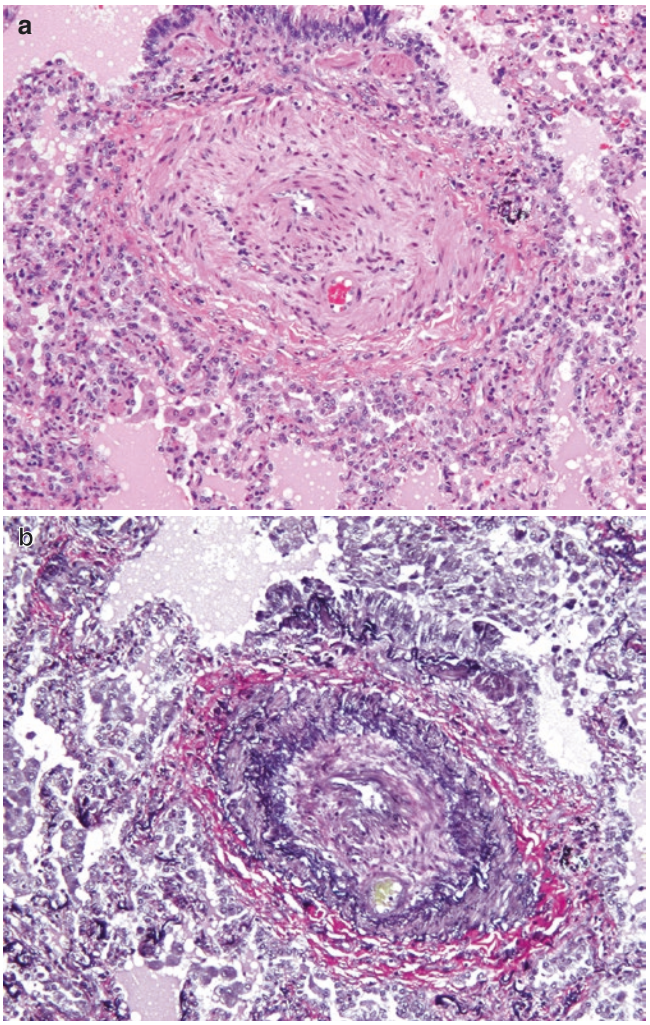

Fig. 10.2 Pulmonary arterial hypertension. (**a**) In this example, a photomicrograph of a routinely stained section demonstrates more prominent intimal fibrosis leading to near complete obliteration of the lumen. (**b**) An elastic tissue stain highlights the thickened intima

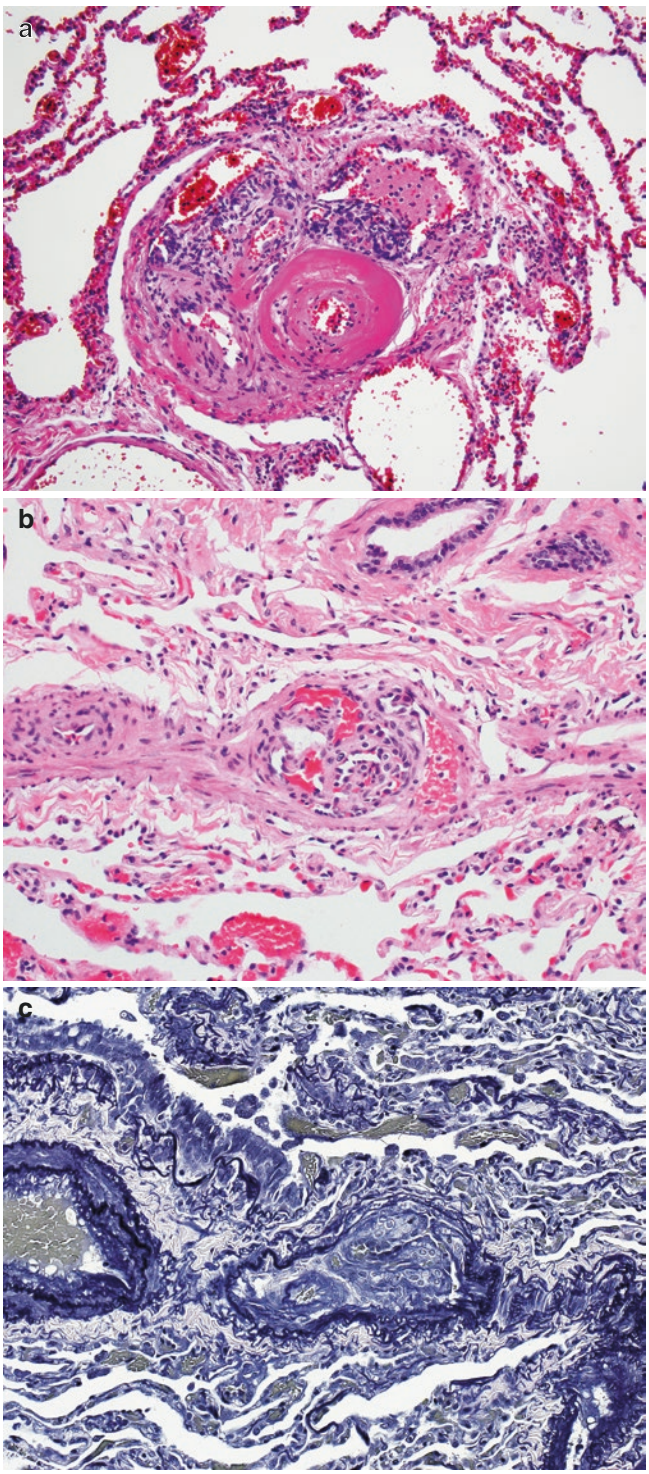

Fig. 10.3 Pulmonary arterial hypertension. (**a**) Photomicrograph showing a plexiform lesion, which in this example is a diverticular outpouching of the artery into perivascular connective tissue characterized by a proliferation of small vascular spaces and hyperplastic endothelial cells resulting in a glomeruloid appearance, often with associated fibrin thrombi resembling organized and recanalized thrombi. (**b**) Photomicrograph showing a plexiform lesion forming a glomeruloid proliferation of small vascular spaces with plump endothelial cells involving the wall of a small muscular artery. (**c**) Photomicrograph of an elastic tissue stained section from the same biopsy showing that the plexiform lesion penetrates from the intima through the vessel wall

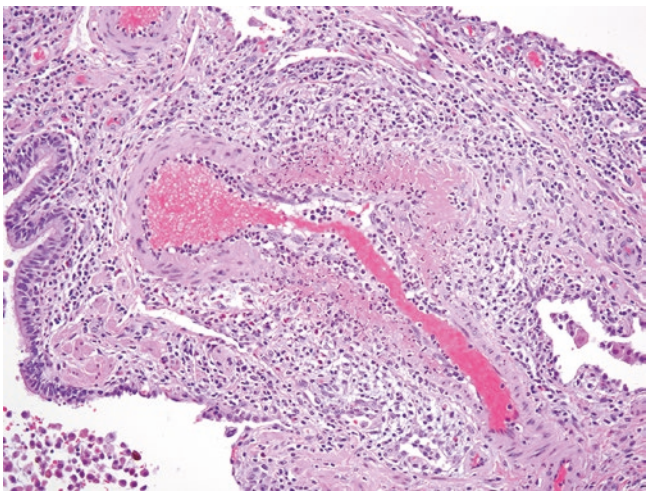

Fig. 10.4 Severe pulmonary arterial hypertension with necrotizing arteritis. Photomicrograph showing a small muscular pulmonary artery in which the arterial wall shows marked fibrinoid necrosis with an acute inflammatory infiltrate. This is an uncommon finding that only occurs in severe pulmonary hypertension

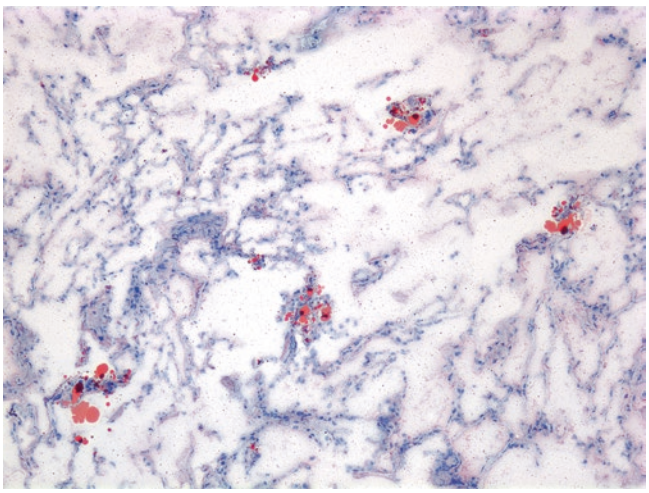

Fig. 10.6 Fat emboli. Photomicrograph showing an oil red O stain in which multiple fat droplets are situated within the lumina of small pulmonary arterioles. This 70-year-old man underwent a hip arthroplasty for a femoral head fracture. Fat droplets within the bone marrow space circulated to the pulmonary artery through the heart, embolizing to small arterioles resulting in acute pulmonary hypertension. Fat emboli are a rare cause of acute pulmonary hypertension and not usually accompanied by the morphologic features characteristic of chronic pulmonary hypertension

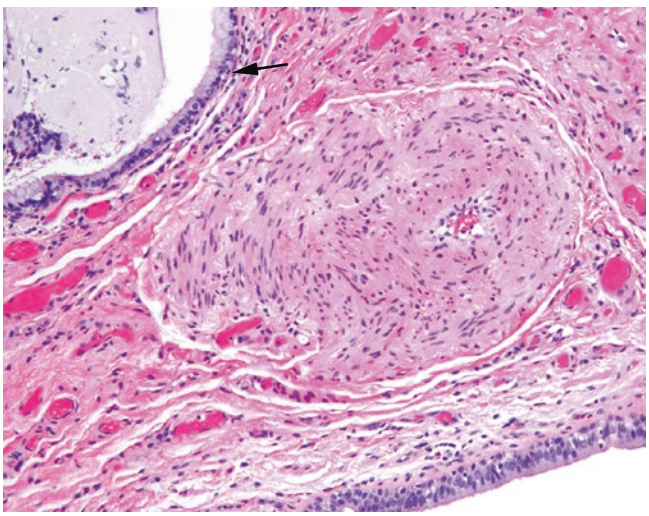

Fig. 10.5 Hypertensive changes in chronic fibrotic disease. High-magnification photomicrograph of a routinely stained section showing severe intimal and medial thickening in a small muscular pulmonary artery in a patient with usual interstitial pneumonia. Note the dense collagen fibrosis and honeycomb change (*arrow*) in the background

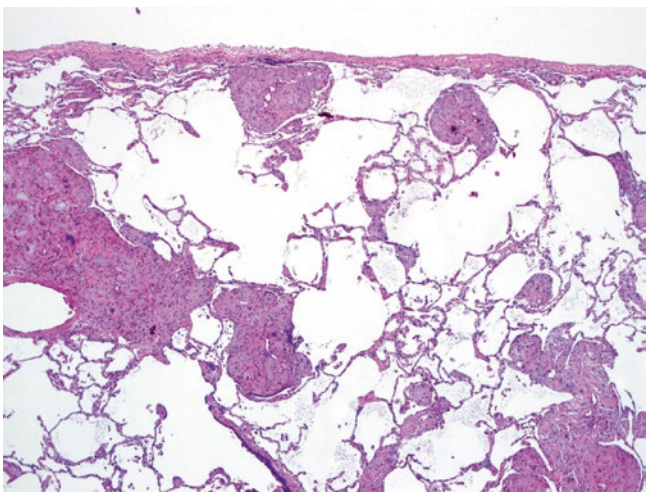

Fig. 10.7 Intravenous (IV) drug abusers' lung. IV injection of pulverized oral medications can result in embolization of inert fillers (excipients), commonly used as binding agents, in small pulmonary vessels, eliciting a foreign body giant cell reaction. In some patients, this may cause a syndrome of chronic pulmonary hypertension. In this example, a low-magnification photomicrograph shows patchy nodular lesions that seem to follow a lymphangitic distribution. Foreign body granulomatous reactions are visible at low magnification

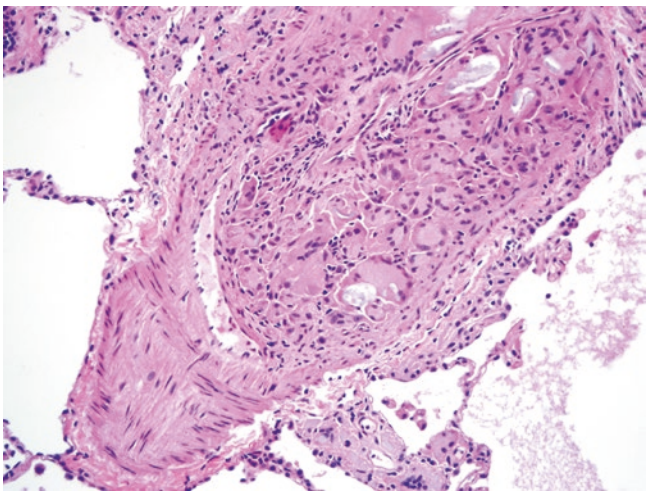

Fig. 10.8 IV drug abusers' lung. A higher-magnification photomicrograph shows foreign body granulomas affiliated with plate-like, pale-gray particulates of microcrystalline cellulose expanding the vessel wall

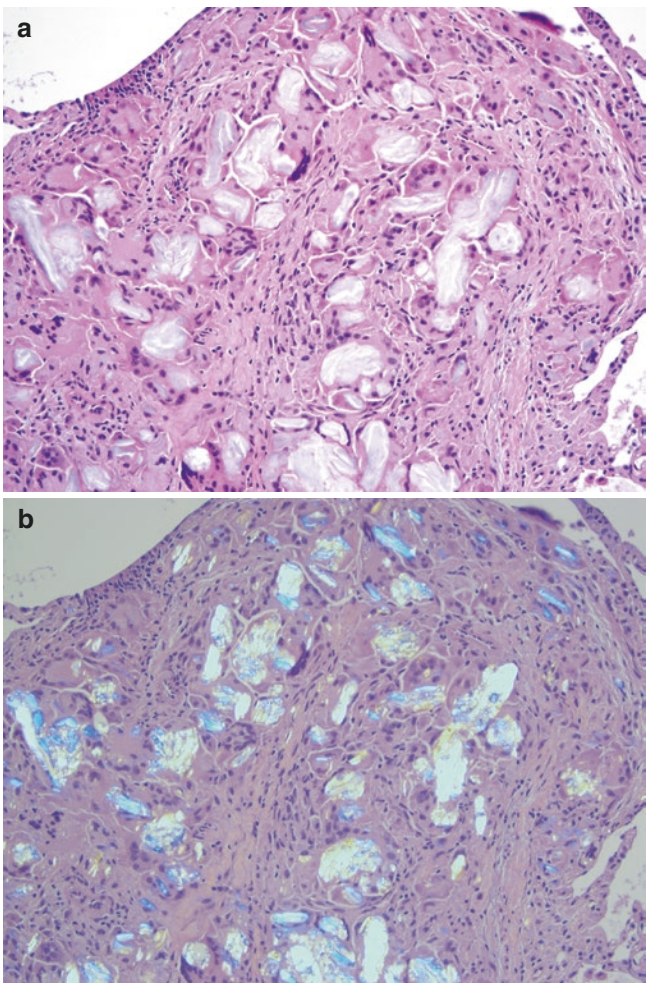

Fig. 10.9 IV drug abusers' lung. (**a**) High-magnification view showing mainly large, elongated, pale-gray microcrystalline cellulose, which is a common filler in drugs intended for oral use. (**b**) The same microscopic field viewed at the same magnification using polarized light. The microcrystalline cellulose particles show strong birefringence under polarized light

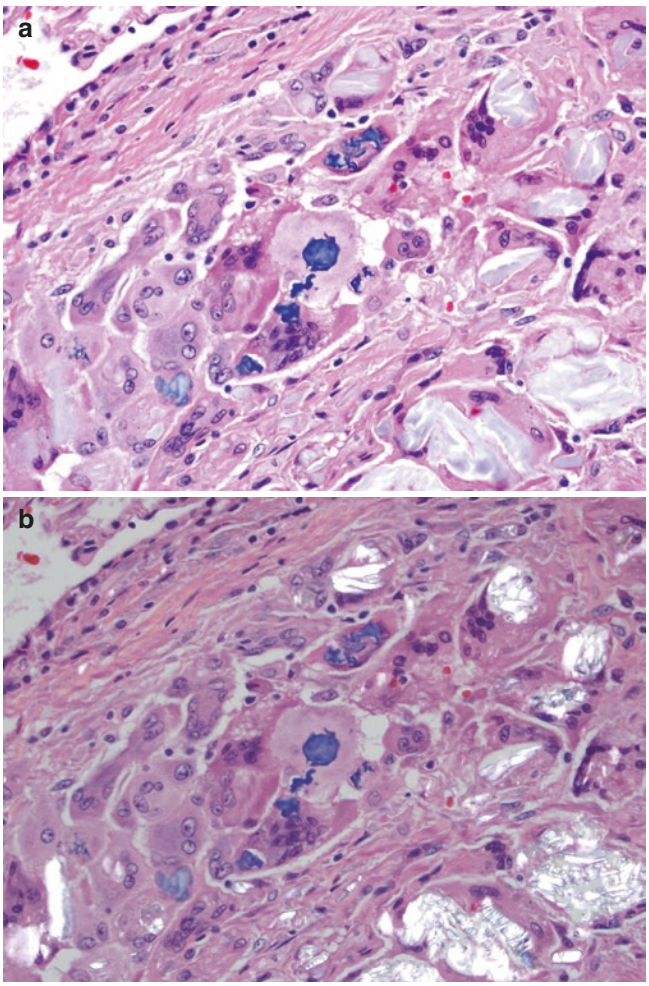

Fig. 10.10 IV drug abusers' lung. (**a**) A high-magnification view showing giant cells containing deeply basophilic crospovidone, another filler common in oral medications and dietary supplements. Microcrystalline cellulose particles and associated giant cells are also present. (**b**) Crospovidone is not birefringent when viewed with polarized light

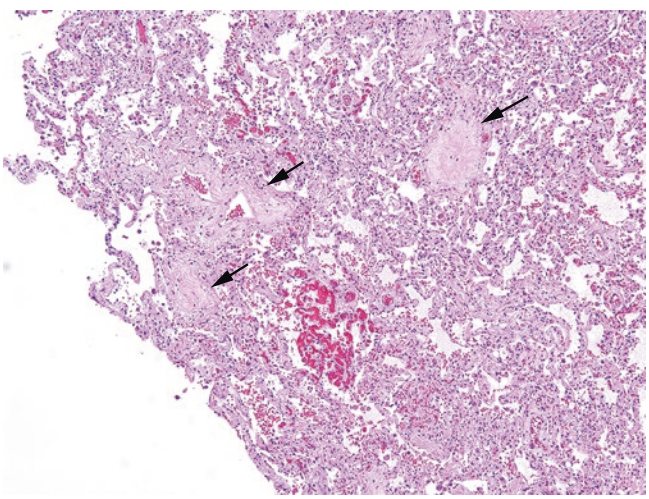

Fig. 10.11 Pulmonary veno-occlusive disease (PVOD). Low-magnification photomicrograph shows congested lung parenchyma and several pulmonary veins that are narrowed or occluded by fibrosis (*arrows*). These vessels do not have accompanying airways and are situated within interlobular septa, a finding helpful in identifying them as veins

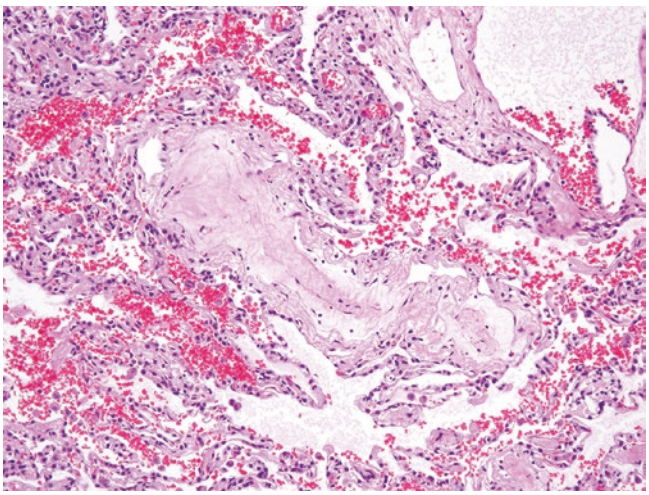

Fig. 10.12 PVOD. A high-magnification photomicrograph showing a vein completely occluded by fibrosis

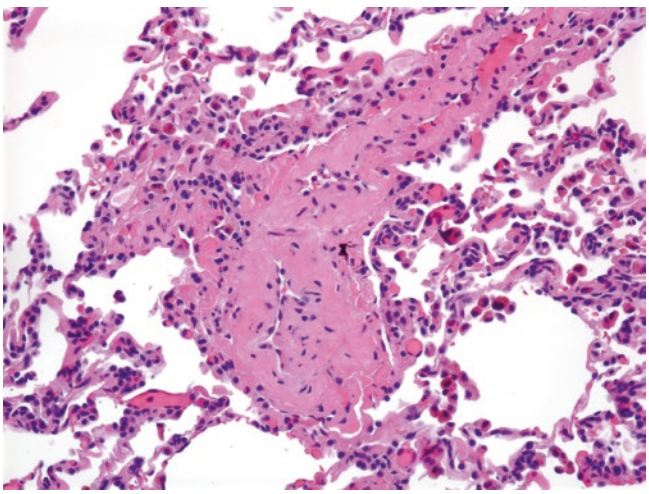

Fig. 10.13 PVOD. A high-magnification photomicrograph showing a small vein nearly occluded by fibrous thickening of its wall

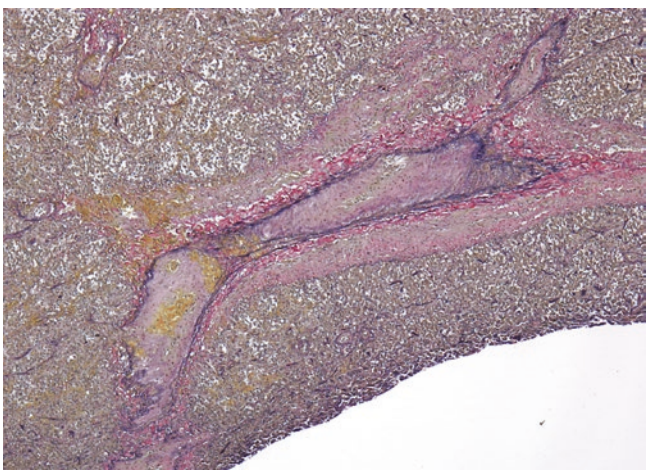

Fig. 10.14 PVOD. An elastic tissue stain reveals the single elastic layer of this nearly occluded vein

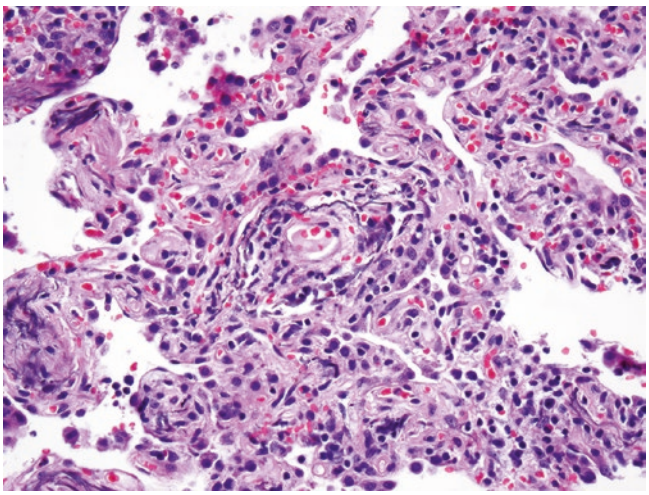

Fig. 10.15 PVOD. A high-magnification photomicrograph shows chronic congestive changes, including thickened alveolar septa with capillary hemangiomatosis-like changes (upper right) and a narrowed vein in the center. The wall of the narrowed vein demonstrates deeply basophilic elastic lamina resulting from encrustation by hemosiderin and calcium deposits, a finding referred to historically as endogenous pneumoconiosis. These are signs of severe chronic venous congestion, which can be caused by PVOD, left-sided heart disease, and extrapulmonary venous outflow obstruction

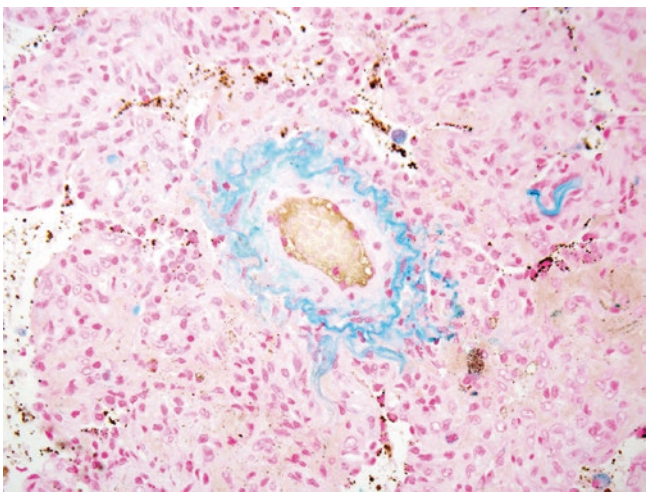

Fig. 10.16 PVOD. High-magnification photomicrograph of a Prussian blue iron-stained section showing iron deposition in the elastic lamina of a vein with fibrosis and a narrowed lumen

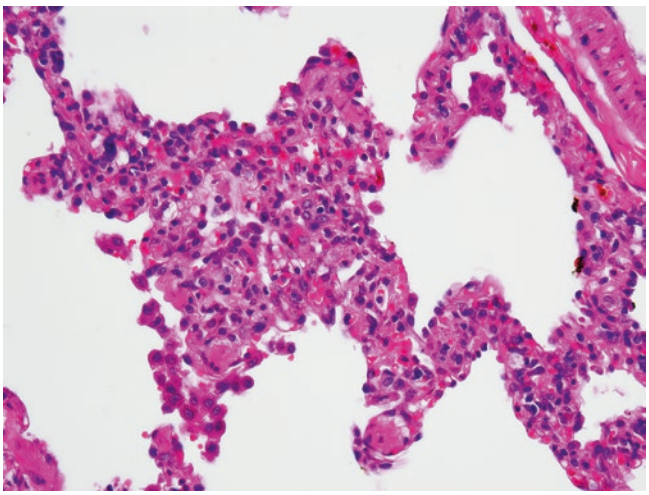

Fig. 10.17 Capillary hemangiomatosis. Intermediate-magnification photomicrograph showing expansion of alveolar septa by redundant blood-filled capillary loops. The changes can also be seen in PVOD and chronic venous hypertension caused by left-sided heart disease and venous outflow obstruction. The absence of fibrous obliterations of veins is the key to ruling out PVOD

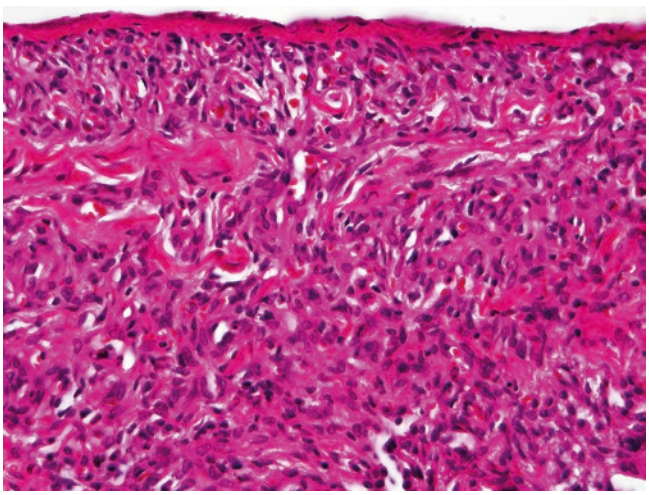

Fig. 10.18 Capillary hemangiomatosis-like change in venous outflow obstruction. High-magnification photomicrograph showing visceral pleura expanded by proliferating blood-filled capillary loops resembling capillary hemangiomatosis (capillary hemangiomatosis-like change) in a patient with fibrosing mediastinitis causing venous outflow obstruction

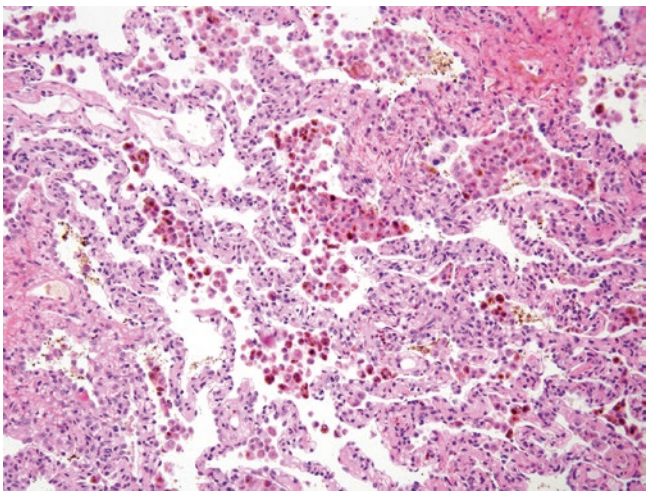

Fig. 10.19 Chronic congestive changes. Alveolar space containing numerous hemosiderin-laden macrophages and thickened alveolar septa with redundant capillaries that are features of chronic venous congestion; this can be seen in any condition causing venous hypertension, including PVOD, pulmonary capillary hemangiomatosis, left-sided heart disease, and venous outflow obstruction. In some patients, the thickened alveolar septa may mimic nonspecific interstitial pneumonia and can be affiliated with radiologic abnormalities resembling other forms of diffuse lung disease

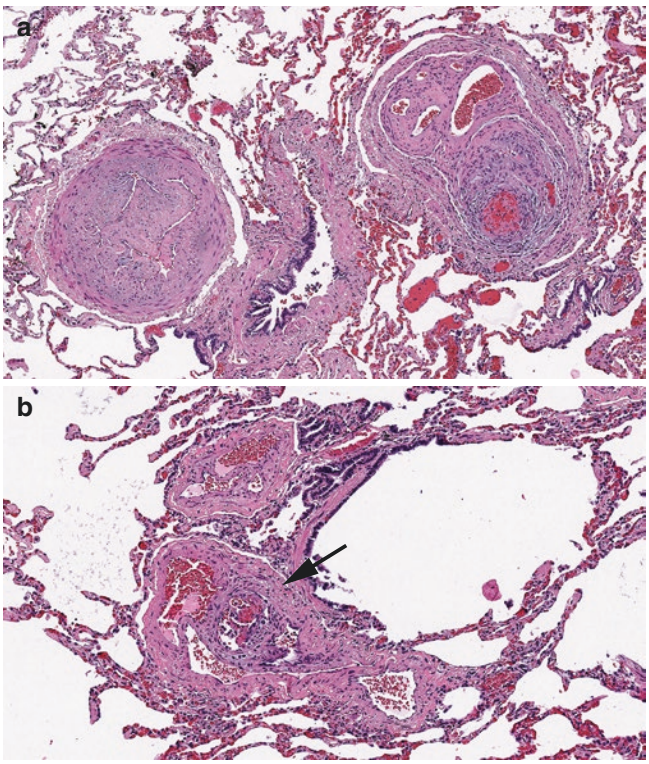

Fig. 10.20 Chronic thrombotic pulmonary hypertension. (**a**) Photomicrograph showing enlarged small muscular pulmonary arteries with multiple lumens (vascular webs) representing recanalized thrombi. The presence of these vascular webs combined with acute and organizing thrombi is an important clue to the diagnosis of chronic thrombotic pulmonary hypertension. An organizing thrombus occludes one of the lumens in the vessel on the right. (**b**) Photomicrograph from the same patient showing another recanalized thrombus involving a small muscular artery with an organizing thrombus and endothelial hyperplasia resembling a plexiform lesion (*arrow*)

Granulomatosis with Polyangiitis

Granulomatosis with polyangiitis (GPA, formerly Wegener granulomatosis) is a systemic vasculitis that commonly involves the upper respiratory tract, the lung, and the kidney. It is part of a family of ANCA-associated vasculitides, the others comprising eosinophilic granulomatosis with polyangiitis (EGPA, formerly Churg-Strauss syndrome) and microscopic polyangiitis; they have in common a propensity to involve smaller vessels. The lung is sometimes the only organ involved in GPA. ANCA testing is particularly important in the laboratory evaluation of patients suspected of having GPA; a positive cytoplasmic (C)-ANCA corresponding to an antileukocyte proteinase 3 (PR3) autoantibody is highly specific for GPA, although positive results can occur in other conditions, including most importantly inflammatory bowel disease and rheumatoid arthritis. For that reason, interpreting the significance of a positive C-ANCA/PR3 test remains heavily dependent on the clinical context. Most patients with systemic GPA are C-ANCA/PR3 positive, but patients with localized GPA are more commonly negative, which does not preclude the diagnosis in patients with characteristic histologic findings. Occasional cases are positive for perinuclear (P)-ANCA corresponding to an antimyeloperoxidase (MPO) autoantibody; this is less specific and more typical of patients with EGPA and microscopic polyangiitis.

In addition to classic GPA (Figs. 10.21, 10.22, 10.23, 10.24, 10.25, 10.26 and 10.27), other histologic subtypes include bronchiolitis obliterans organizing pneumonia (BOOP)-like, hemorrhage with capillaritis, and eosinophilic variants (Figs. 10.28, 10.29 and 10.30). Hemorrhage with capillaritis refers to necrotizing vasculitis centered on alveolar septal capillaries (capillaritis) with associated alveolar hemorrhage. It is a common focal finding in otherwise classical GPA. In some patients this histology may dominate or be the sole manifestation of disease. In the absence of any other features to establish a histologic diagnosis of GPA, hemorrhage with capillaritis is nonspecific in that it also occurs in other vasculitic syndromes such as microscopic polyangiitis and systemic lupus erythematosus. Rare patients with diffuse alveolar hemorrhage and capillaritis have no other clinical or laboratory evidence of systemic vasculitis.

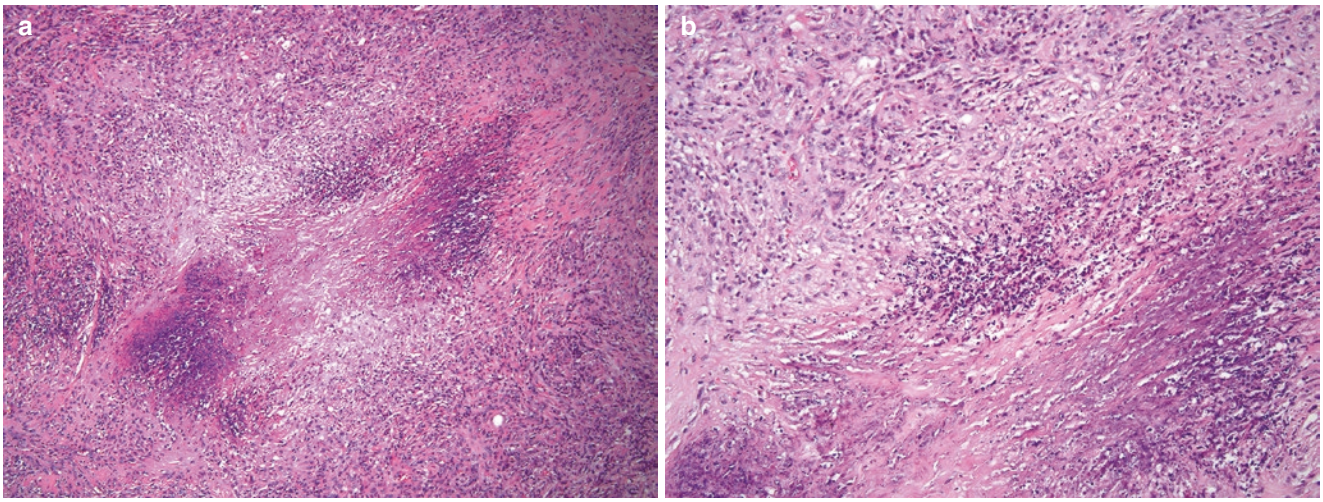

Fig. 10.21 Granulomatosis with polyangiitis (GPA; formerly Wegener granulomatosis), classic type. (**a**) Low-magnification photomicrograph showing the typical necrotizing granulomatous inflammation with irregular, geographic, basophilic dirty necrosis and background dense inflammatory infiltrates and fibrosis. (**b**) Higher-magnification view showing collagen necrosis as well as granular, basophilic nuclear debris. The necrotic area is surrounded by epithelioid histiocytes and rare multinucleated giant cells

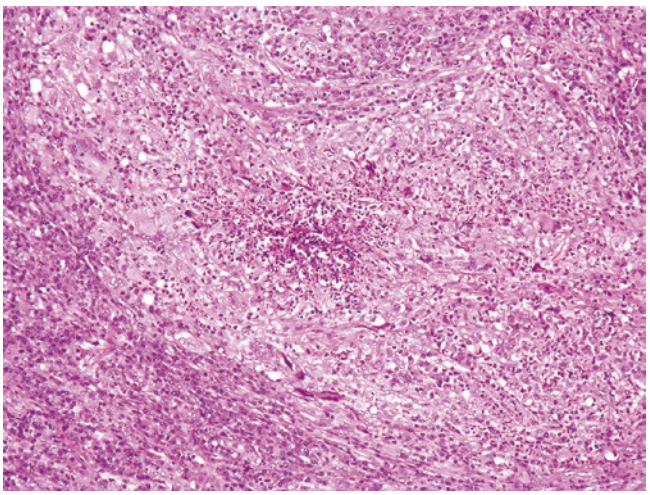

Fig. 10.22 Classic GPA. High-magnification photomicrograph showing a granulomatous microabscess characterized by a small focus of necrotic neutrophils surrounded by epithelioid histiocytes, multinucleated giant cells, and a mixed inflammatory infiltrate. Granulomatous microabscesses with these features are an extremely helpful finding in establishing a histologic diagnosis of GPA

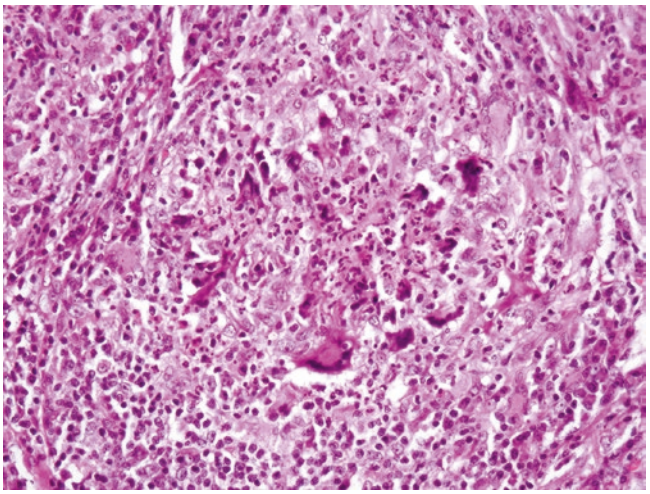

Fig. 10.23 Classic GPA. High-magnification photomicrograph showing another smaller and more subtle granulomatous microabscess with multinucleated giant cells demonstrating the hyperchromatic nuclei characteristic of GPA

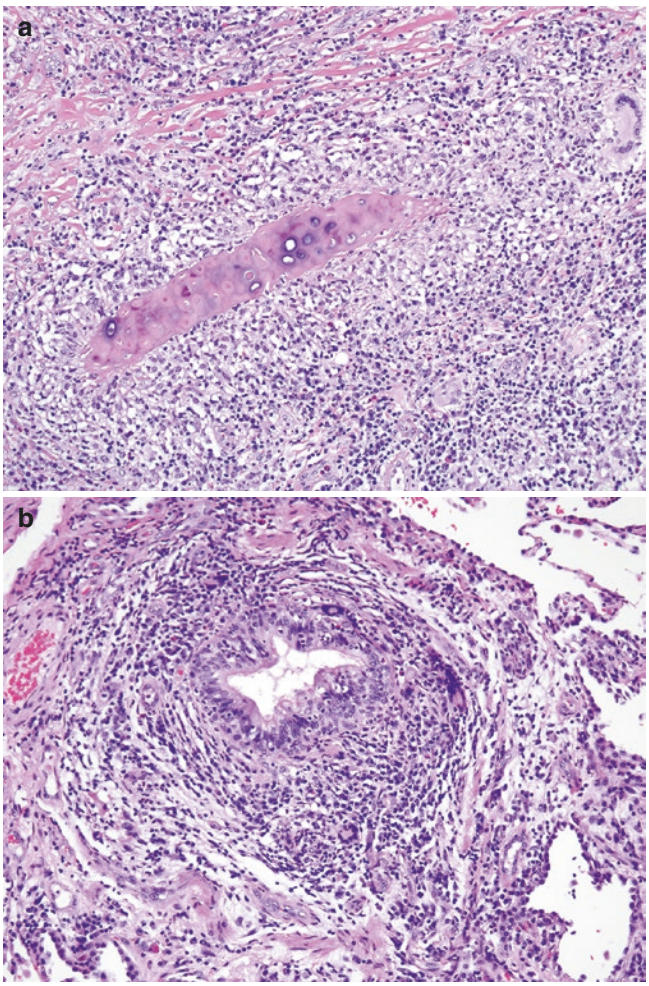

Fig. 10.24 Classic GPA. Large and/or small airways are commonly involved in GPA and when a dominant feature has been referred to by some as a bronchocentric variant. (**a**) High-magnification photomicrograph showing granulomatous inflammation with giant cells involving and partially destroying a cartilaginous airway. (**b**) Photomicrograph showing a small bronchiole circumferentially involved by a mixed inflammatory infiltrate that includes multinucleated giant cells resulting in a vaguely granulomatous appearance

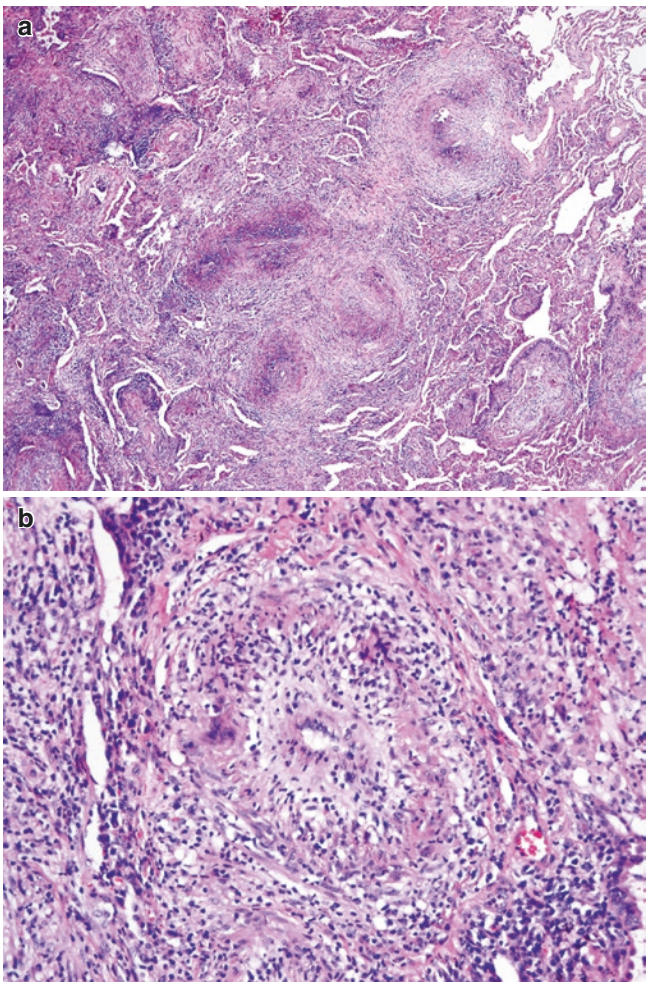

Fig. 10.25 Vasculitis in classic GPA. (**a**) Low-magnification photomicrograph showing necrotizing granulomatous inflammation involving several blood vessels. (**b**) High-magnification view of a small muscular artery involved by necrotizing granulomatous inflammation with fibrinoid necrosis, necrotic neutrophils, and a multinucleated giant cell

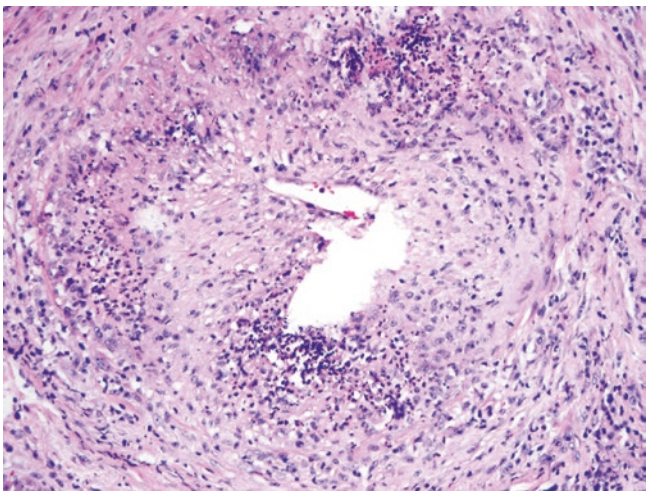

Fig. 10.26 Vasculitis in classic GPA. High-magnification photomicrograph showing another small muscular pulmonary artery involved by necrotizing inflammation with prominent karyorrhexis and granulomatous microabscesses

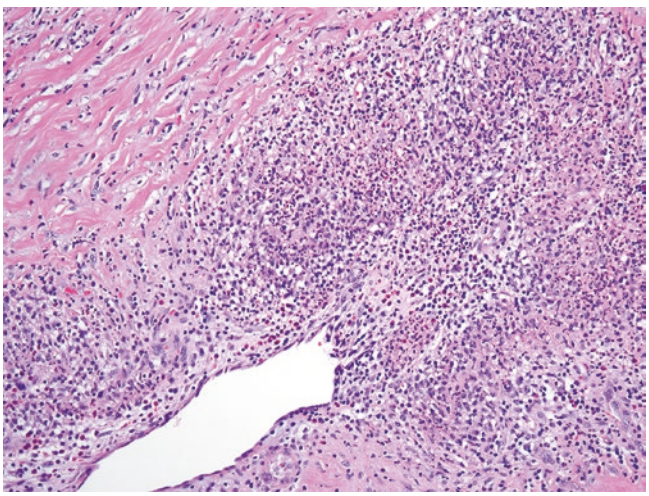

Fig. 10.27 Vasculitis in classic GPA. In this example, the blood vessel is involved by necrotizing inflammation with abundant neutrophils and eosinophils but without well-developed granulomatous features

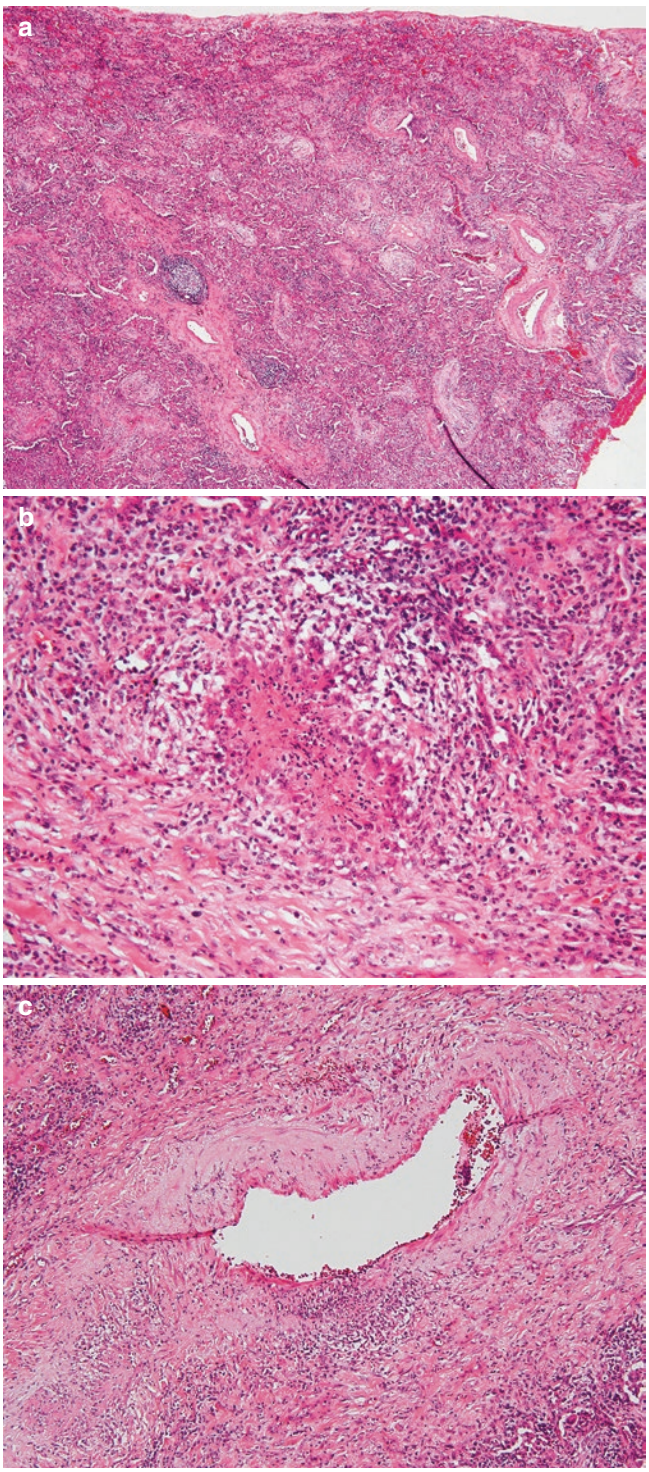

Fig. 10.28 BOOP-like GPA. (**a**) Low-magnification photomicrograph showing extensive organizing pneumonia, a lesion referred to historically as bronchiolitis obliterans organizing pneumonia (BOOP). (**b**) Higher-magnification photomicrograph showing a granulomatous microabscess typical of GPA in which there is central necrosis with prominent karyorrhexis of neutrophils surrounded by a mixed inflammatory infiltrate that includes palisaded and multinucleated macrophages. (**c**) Photomicrograph showing a pulmonary vein in the same biopsy in which there is necrotizing vasculitis characterized by a transmural infiltrate of inflammatory cells with fibrinoid necrosis and karyorrhexis

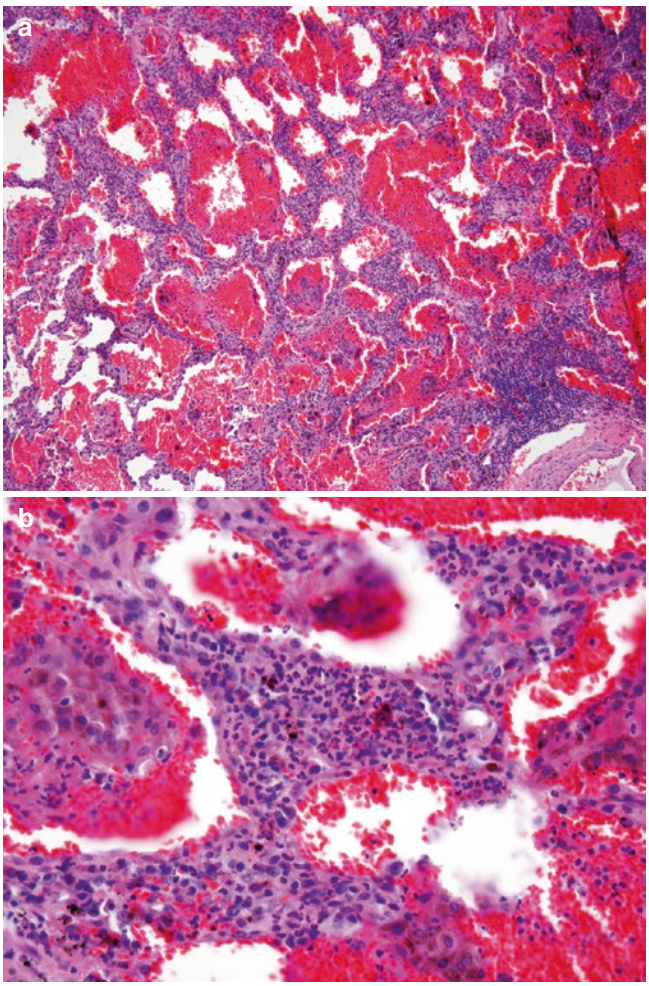

Fig. 10.29 Hemorrhage and necrotizing capillaritis in GPA. (**a**) Low-magnification photomicrograph showing prominent intra-alveolar hemorrhage and thickened alveolar septa with hemosiderin and inflammatory cells. (**b**) High-magnification view showing capillaritis characterized by expansion of alveolar septa predominantly by neutrophils, with karyorrhexis and occasional eosinophils. This variant may lack the necrotizing granulomas, granulomatous microabscesses, and giant cells typical of classic GPA. In the absence of classic features, the diagnosis of GPA cannot be made on the basis of histology alone because hemorrhage with capillaritis may occur in patients with other vasculitic syndromes, including microscopic polyangiitis and systemic lupus erythematosus

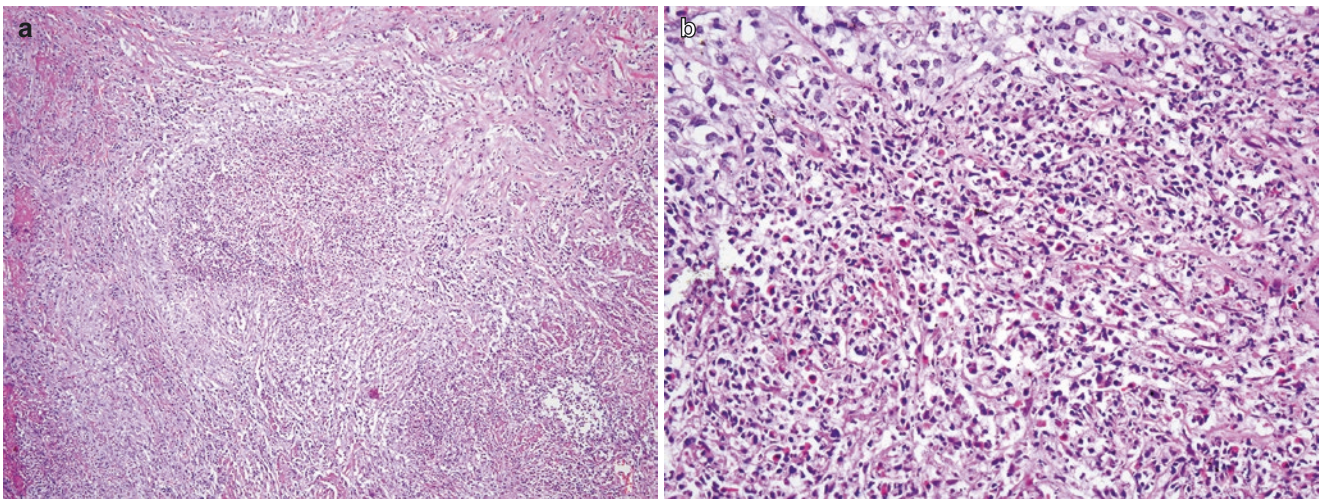

Fig. 10.30 Eosinophilic variant of GPA. (**a**) Low-magnification photomicrograph shows necrotizing granulomatous inflammation with dirty basophilic necrosis typical of GPA. (**b**) At higher magnification, there is prominent eosinophilia, a relatively common finding that does not by itself suggest eosinophilic granulomatosis with polyangiitis (formerly Churg-Strauss syndrome) as an alternative. Because eosinophils are nearly universal in GPA, prominent eosinophilia simply reflects an extreme in the histologic spectrum of classic GPA, although others separate these as eosinophilic variants

Eosinophilic Granulomatosis with Polyangiitis

Eosinophilic granulomatosis with polyangiitis (EGPA) is a systemic vasculitis that occurs in patients with asthma and blood eosinophilia. A minority of patients are P-ANCA/MPO positive. Common extrapulmonary sites involved by EGPA include the skin, nerve, muscle, and heart. The diagnosis of EGPA (Figs. 10.31, 10.32 and 10.33) on a lung biopsy relies on finding the combination of eosinophilic pneumonia, necrotizing granulomatous inflammation, and necrotizing vasculitis. Of these, the most common biopsy finding is eosinophilic pneumonia, which is not by itself diagnostic but is supportive in the appropriate clinical context.

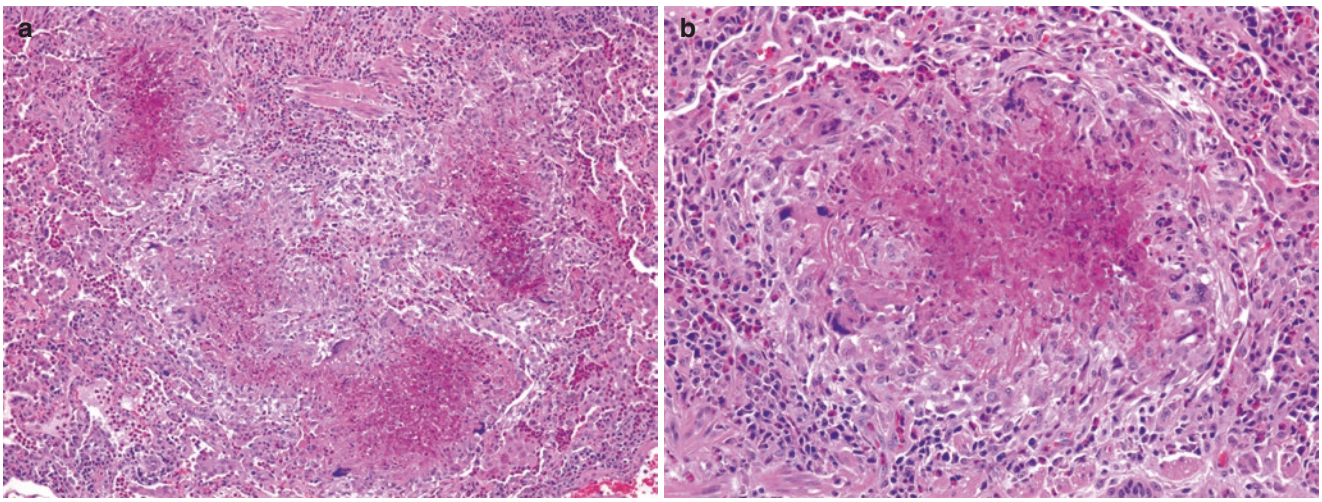

Fig. 10.31 Eosinophilic granulomatosis with polyangiitis (EGPA; formerly Churg-Strauss syndrome). (**a**) Low-magnification photomicrograph showing necrotizing granulomatous inflammation with prominent eosinophilic infiltrates. (**b**) High-magnification view of a granuloma composed of a necrotic center, palisading epithelioid histiocytes, and multinucleated giant cells. The surrounding inflammatory cells are rich in eosinophils

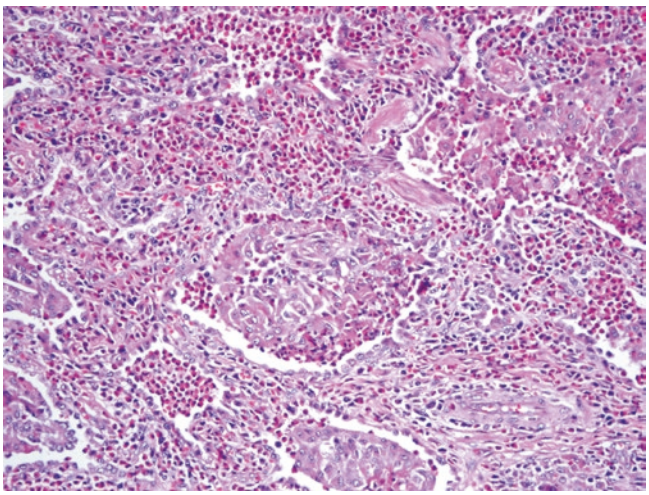

Fig. 10.32 EGPA. Photomicrograph showing eosinophilic pneumonia characterized by intra-alveolar accumulation of eosinophils and macrophages in a patient with EGPA

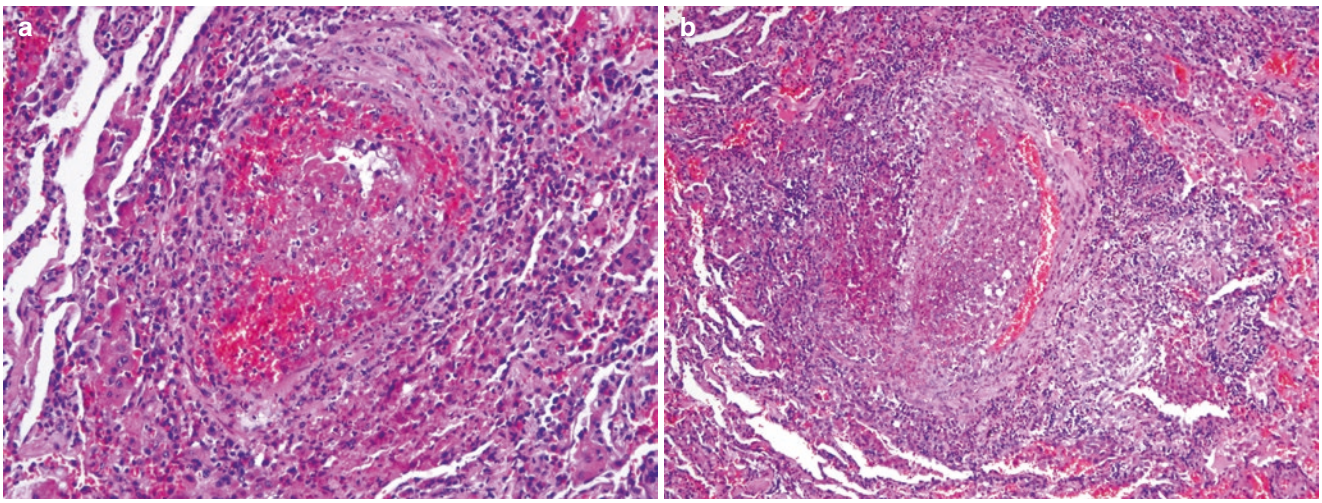

Fig. 10.33 Vasculitis in EGPA. (**a**) High-magnification photomicrograph showing necrotizing vasculitis in which the vascular wall is infiltrated by an eosinophil-rich mixed inflammatory infiltrate with associated vessel wall necrosis and fibrin thrombus. (**b**) Photomicrograph showing another example of vasculitis in EGPA in which the blood vessel is partially destroyed by necrosis with an eosinophil-rich inflammatory infiltrate. Note the background eosinophilic pneumonia characterized by intra-alveolar accumulation of eosinophils and macrophages

Suggested Readings

Bjornsson J, Edwards WD. Primary pulmonary hypertension: a histopathologic study of 80 cases. Mayo Clin Proc. 1985;60:16–25.

Faber CN, Yousem SA, Dauber JH, Griffith BP, Hardesty RL, Paradis IL. Pulmonary capillary hemangiomatosis. A report of three cases and a review of the literature. Am Rev Respir Dis. 1989;140:808–13.

Foshat M, Boroumand N. The evolving classification of pulmonary hypertension. Arch Pathol Lab Med. 2017;141:696–703.

Houben E, Bax WA, van Dam B, Slieker WA, Verhave G, Frerichs FC, et al. Diagnosing ANCA-associated vasculitis in ANCA positive patients: a retrospective analysis on the role of clinical symptoms and the ANCA titre. Medicine. 2016;95:e5096.

Jennette JC, Falk RJ, Bacon PA, Basu N, Cid MC, Ferrario F, et al. 2012 revised international Chapel Hill consensus conference nomenclature of Vasculitides. Arthritis Rheum. 2013;65:1–11.

Katzenstein AL. Diagnostic features and differential diagnosis of Churg-Strauss syndrome in the lung. A review. Am J Clin Pathol. 2000;114:767–72.

Katzenstein AL, Locke WK. Solitary lung lesions in Wegener's granulomatosis. Pathologic findings and clinical significance in 25 cases. Am J Surg Pathol. 1995;19:545–52.

Koss MN, Antonovych T, Hochholzer L. Allergic granulomatosis (Churg-Strauss syndrome): pulmonary and renal morphologic findings. Am J Surg Pathol. 1981;5:21–8.

Lantuejoul SM, Sheppard B, Corrin M, Burke M, Nicholson AG. Pulmonary veno-occlusive disease and pulmonary capillary hemangiomatosis: a clinicopathologic study of 35 cases. Am J Surg Pathol. 2006;30:850–7.

Miller P, Prahlow JA. Autopsy diagnosis of fat embolism syndrome. Am J Forensic Med Pathol. 2011;32:291–9.

Myers JL, Katzenstein AL. Wegener's granulomatosis presenting with massive pulmonary hemorrhage and capillaritis. Am J Surg Pathol. 1987;11:895–8.

Pai U, McMahon J, Tomashefski JF. Mineralizing pulmonary elastosis in chronic cardiac failure. Endogenous pneumoconiosis revisited. Am J Clin Pathol. 1994;101:22–8.

Pietra GG, Edwards WD, Kay JM, Rich S, Kernis J, Schloo B, et al. Histopathology of primary pulmonary hypertension. A qualitative and quantitative study of pulmonary blood vessels from 58 patients in the National Heart, Lung, and Blood Institute, primary pulmonary hypertension registry. Circulation. 1989;80:1198–206.

Tomashefski JF, Hirsch CS. The pulmonary vascular lesions of intravenous drug abuse. Hum Pathol. 1980;11:133–45.

Travis WD, Hoffman GS, Leavitt RY, Pass HI, Fauci AS. Surgical pathology of the lung in Wegener's granulomatosis. Review of 87 open lung biopsies from 67 patients. Am J Surg Pathol. 1991;15:315–33.

Uner AH, Rozum-Slota B, Katzenstein AL. Bronchiolitis obliterans-organizing pneumonia (BOOP)-like variant of Wegener's granulomatosis. A clinicopathologic study of 16 cases. Am J Surg Pathol. 1996;20:794–801.

Vaglio A, Buzio C, Zwerina J. Eosinophilic granulomatosis with polyangiitis (Churg-Strauss): state of the art. Allergy. 2013;68:261–73.

Wagenvoort CA, Mulder PG. Thrombotic lesions in primary plexogenic arteriopathy. Similar pathogenesis or complication? Chest. 1993;103:844–9.

Yousem SA. Bronchocentric injury in Wegener's granulomatosis: a report of five cases. Hum Pathol. 1991;22:535–40.

Yousem SA, Lombard CM. The eosinophilic variant of Wegener's granulomatosis. Hum Pathol. 1988;19:682–8.

Pulmonary Lymphoproliferative Diseases

11

Chen Zhang and Jeffrey L. Myers

Mucosa-associated lymphoid tissue (MALT) in the lungs, also known as bronchus-associated lymphoid tissue (BALT), is present along the respiratory mucosa and is normally inconspicuous in the adult lung. MALT participates in immunologic reactions to inhaled antigens and is the origin of various benign and malignant lymphoproliferative diseases (Table 11.1). Primary pulmonary malignant lymphoma is rare, although virtually all types of lymphoma have been reported in the lungs.

Table 11.1 Summary of primary pulmonary lymphoproliferative diseases

Benign
Nodular lymphoid hyperplasia
Follicular bronchiolitis
Lymphoid interstitial pneumonia
Non-Hodgkin lymphoma
Extranodal marginal zone B-cell lymphoma of mucosa-associated lymphoid tissue
Lymphomatoid granulomatosis
Follicular lymphoma
Mantle cell lymphoma
Intravascular large B-cell lymphoma
Posttransplant lymphoproliferative disorder
Anaplastic large cell lymphoma Extranodal natural killer/T-cell lymphoma, nasal type
Classic Hodgkin lymphoma

Nodular Lymphoid Hyperplasia

Nodular lymphoid hyperplasia (Fig. 11.1) is considered a healing inflammatory process with scarring, causing a localized mass-like lesion that at least partially obliterates the lung architecture. Patients are usually middle-aged asymptomatic adults. Association with autoimmune diseases such as Sjögren syndrome and systemic lupus erythematosus is not common but has been reported in some patients.

C. Zhang (✉)
Department of Pathology and Laboratory Medicine, Indiana University School of Medicine, Indianapolis, IN, USA
e-mail: chenzhan@iupui.edu

J. L. Myers
Department of Pathology, Michigan Medicine, Ann Arbor, MI, USA
e-mail: myerjeff@med.umich.edu

© Springer Science+Business Media, LLC, part of Springer Nature 2018
C. Zhang, J. L. Myers (eds.), *Atlas of Lung Pathology*, Atlas of Anatomic Pathology,
https://doi.org/10.1007/978-1-4939-8689-7_11

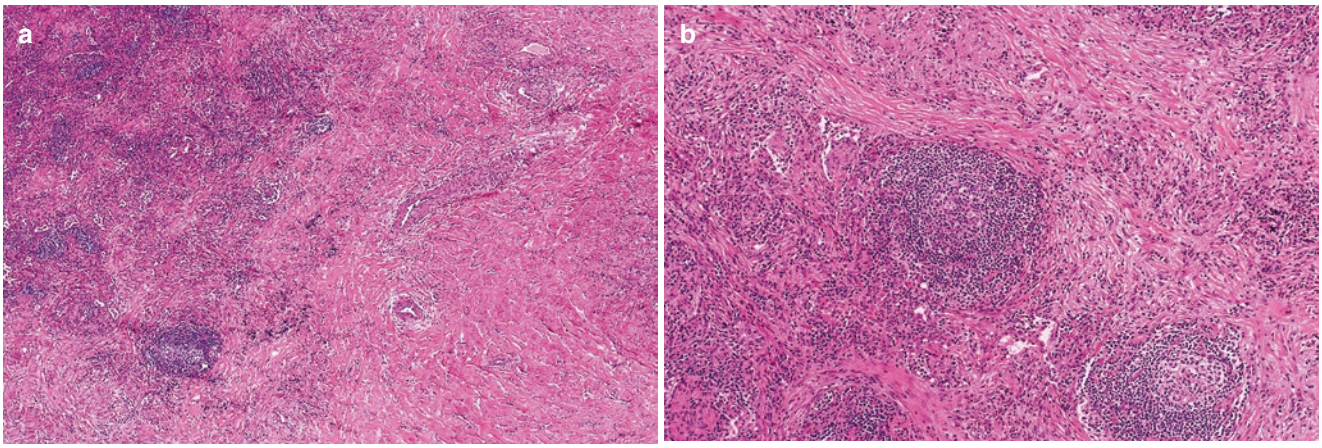

Fig. 11.1 Nodular lymphoid hyperplasia. (**a**) Low-magnification photomicrograph showing a combination of fibrotic scarring and a patchy infiltrate of mononuclear cells with lymphoid aggregates, one of which demonstrates a secondary germinal center. (**b**) Higher-magnification photomicrograph of the same lesion illustrated in **a** showing lymphoid aggregates with germinal centers in a background of dense collagen fibrosis and chronic inflammatory infiltrates. It lacks the tumefactive sheets of monocytoid B cell and plasma cells more characteristic of MALT lymphoma; however, distinguishing the two can be difficult and sometimes requires molecular testing for clonal light-chain expression or heavy-chain gene rearrangements

Follicular Bronchiolitis

Follicular bronchiolitis (Fig. 11.2), also known as follicular hyperplasia of bronchus-associated lymphoid tissue (BALT), is an uncommon condition that affects patients over a wide age range. It may occur in association with autoimmune disorders or immunodeficiency states such as acquired immunodeficiency syndrome (AIDS) or common variable immunodeficiency. Peribronchial nodules and ground-glass opacities are common radiologic findings.

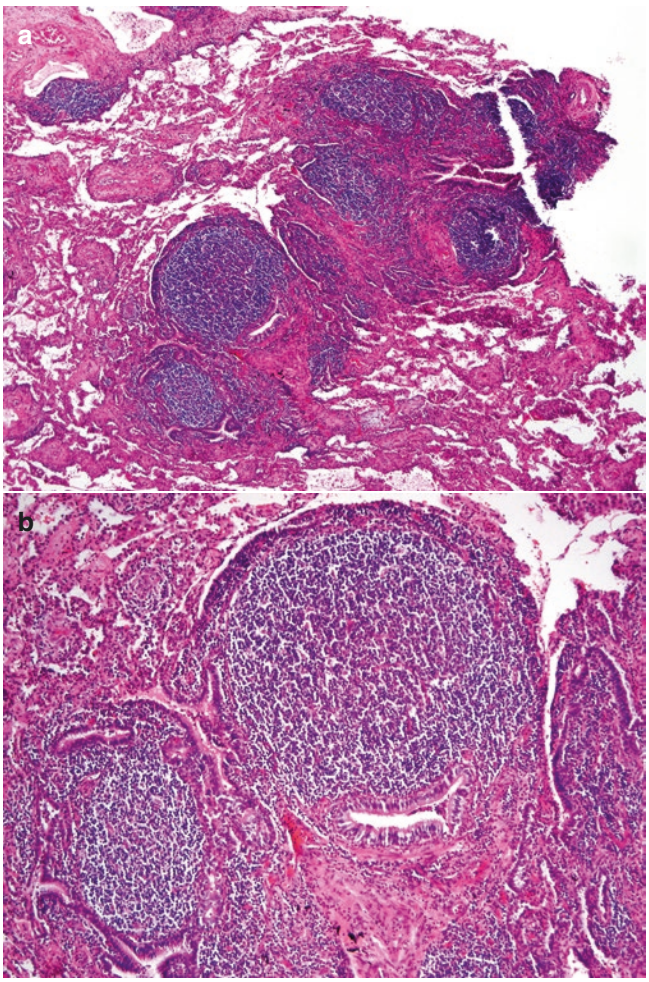

Fig. 11.2 Follicular bronchiolitis. (**a**) Low-magnification photomicrograph showing nodular lymphoid aggregates with germinal centers surrounding small bronchioles. The bronchiole lumens are narrowed. (**b**) Higher-magnification view showing the nodular lymphoid hyperplasia with germinal centers immediately beneath the respiratory epithelium. Follicular bronchiolitis is sometimes seen as a secondary feature in other conditions, including bronchiectasis; the term follicular bronchiolitis is generally reserved for those cases in which it represents the primary pathologic finding

Lymphoid Interstitial Pneumonia

Lymphoid interstitial pneumonia (Figs. 11.3, 11.4 and 11.5), a form of diffuse lymphoid hyperplasia, is commonly associated with systemic connective tissue diseases, especially Sjögren syndrome, other autoimmune conditions such as active chronic hepatitis, and certain forms of immunodeficiency including human immunodeficiency virus (HIV)/AIDS. Patients with lymphoid interstitial pneumonia usually present with dyspnea and cough. Computed tomography (CT) scans commonly show cystic lesions in addition to reticulations, but these findings are not specific and can be seen in clonal lymphoproliferative disorders in patients with Sjögren syndrome.

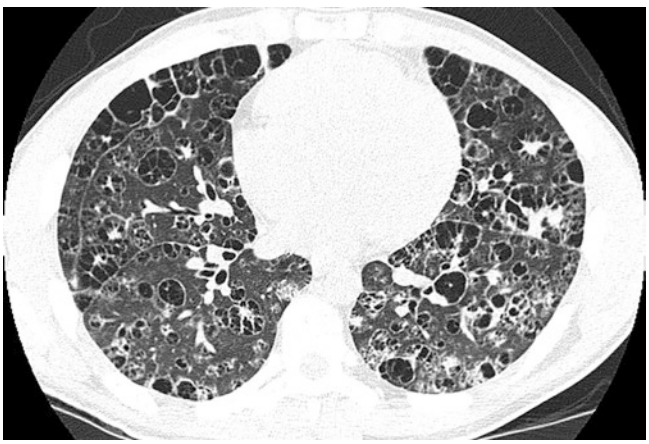

Fig. 11.3 Lymphoid interstitial pneumonia (LIP). Chest CT scan of a patient with Castleman disease and a surgical lung biopsy showing LIP. The CT scan shows a number of abnormalities, including numerous bilateral cysts that are a common finding in patients with LIP. This change is not specific for LIP and is also seen in patients with clonal B-cell lymphoproliferative disorders such as MALT lymphoma complicated by amyloid

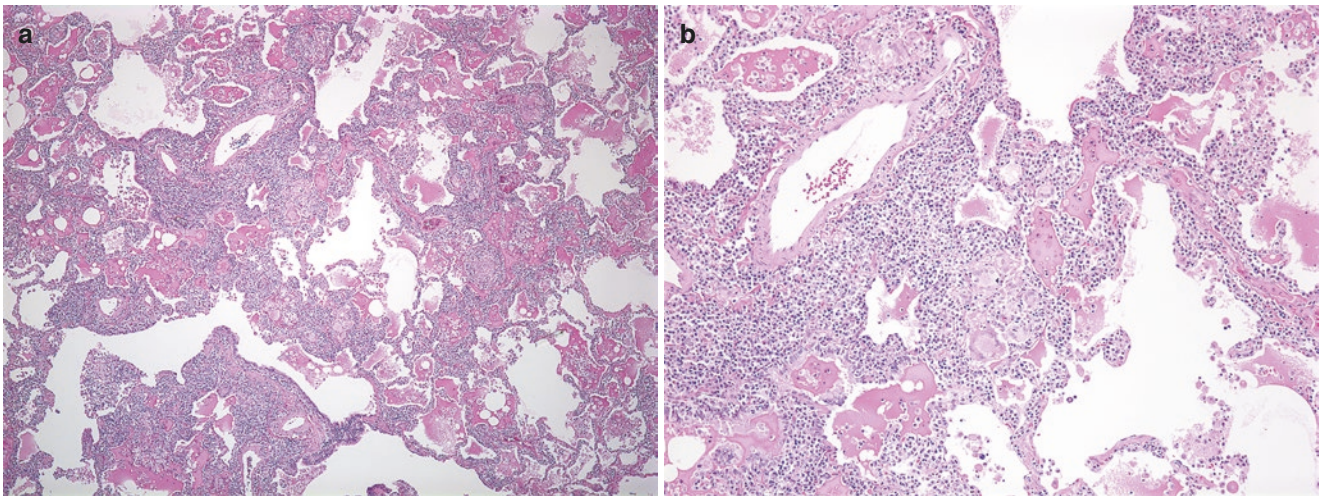

Fig. 11.4 Lymphoid interstitial pneumonia. (**a**) Low-magnification photomicrograph showing diffuse alveolar thickening by a dense inflammatory infiltrate without fibrosis. The predominantly lymphocytic infiltrate is accentuated around distal bronchioles, where it includes occasional lymphoid aggregates with germinal centers. (**b**) Higher-magnification view of lesion illustrated in **a** showing dense lymphoplasmacytic infiltrate with loose clusters of epithelioid and multinucleated histiocytes comprising poorly formed granulomas. This combination of findings resembles hypersensitivity pneumonia (*see* Chap. 7), although the clinical context combined with the presence of germinal centers and a conspicuous population of plasma cells is often helpful in making the distinction

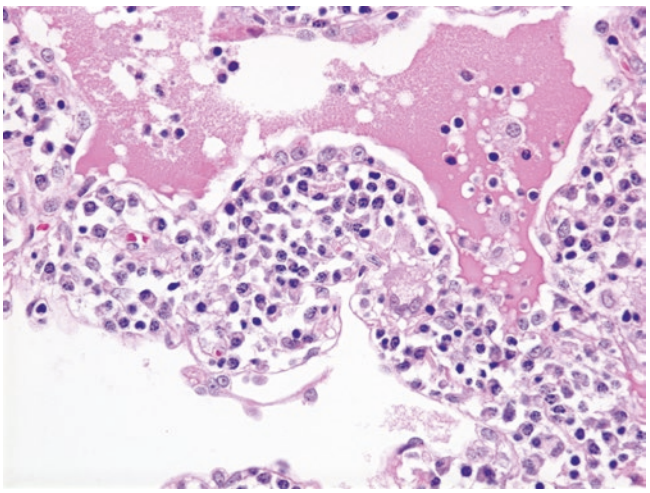

Fig. 11.5 Lymphoid interstitial pneumonia. High-magnification photomicrograph demonstrates alveolar septa expanded by predominantly plasma cells in this example

Extranodal Marginal Zone Lymphoma of MALT

Extranodal marginal zone lymphoma of MALT (Figs. 11.6, 11.7, 11.8, 11.9, 11.10, 11.11, 11.12, 11.13, 11.14, 11.15, 11.16 and 11.17) is the most common form of primary pulmonary lymphoma. It affects mainly older adults in their sixties or seventies. Patients are usually asymptomatic, with incidentally identified pulmonary opacities often characterized by a combination of consolidation and air bronchograms. Some patients have associated autoimmune diseases such as Sjögren syndrome. The prognosis is excellent; the disease often remains stable or progresses slowly over a period of years.

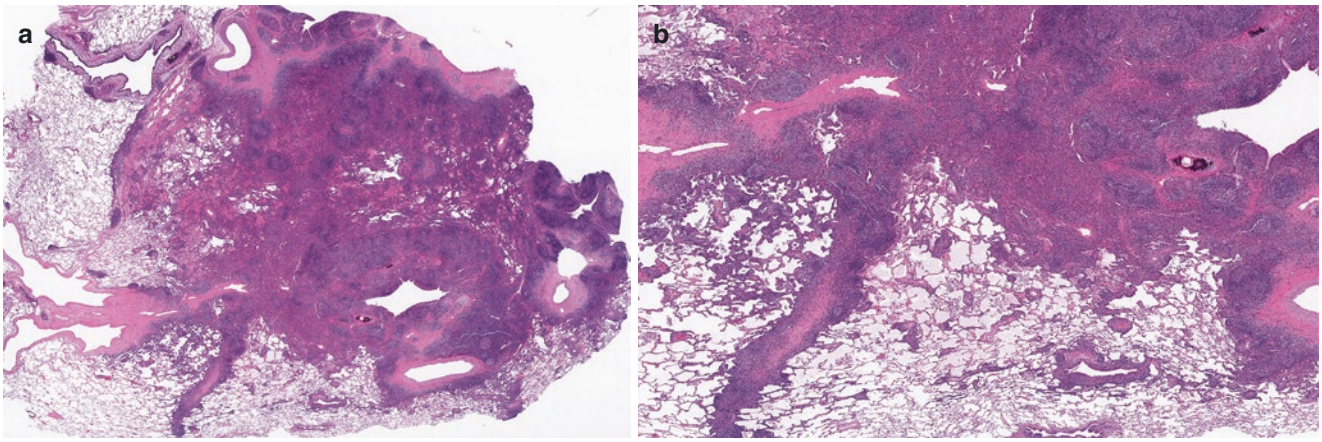

Fig. 11.6 Extranodal marginal zone lymphoma of MALT lymphoma. (**a**) Low-magnification photomicrograph showing dense lymphocytic infiltrates expanding the interstitium forming a tumefactive mass that extends along bronchovascular bundles and interlobular septa. The cellular infiltrate includes lymphoid aggregates with germinal centers and ill-defined islands of pallor that correspond to sheets of monocytoid B lymphocytes. (**b**) Higher-magnification view illustrating extension along lymphatic pathways at the periphery of the tumefactive mass

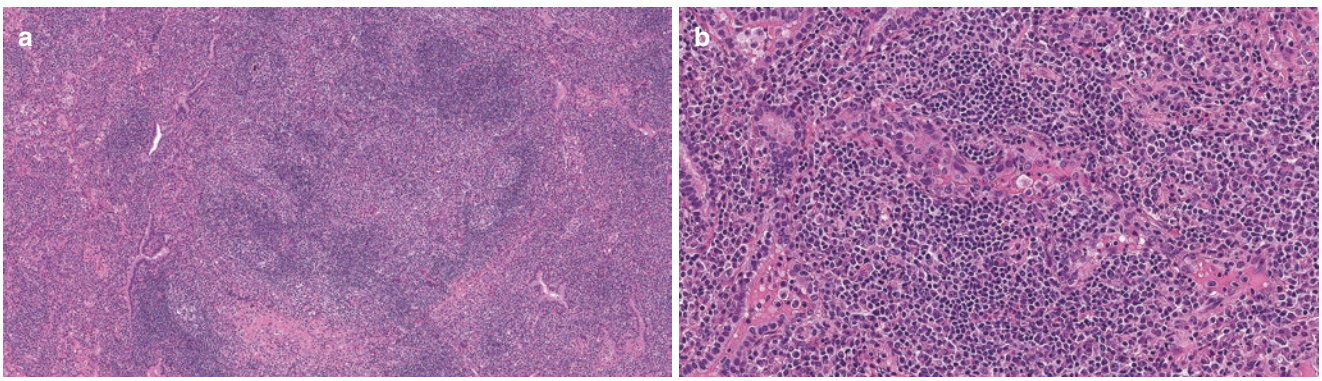

Fig. 11.7 Extranodal marginal zone lymphoma of MALT lymphoma. (**a**) Photomicrograph highlighting area in which tumefactive lymphocytic infiltrate overruns the normal lung architecture and includes ill-defined zones of pallor corresponding to monocytoid B cells. There are numerous lymphoepithelial lesions in which bronchiolar epithelium is partially or completely obscured by intraepithelial lymphocytes. (**b**) High-magnification photomicrograph showing lymphoepithelial lesion in which lymphocytes percolate into bronchiolar epithelium, partially or completely obscuring the airway lumen

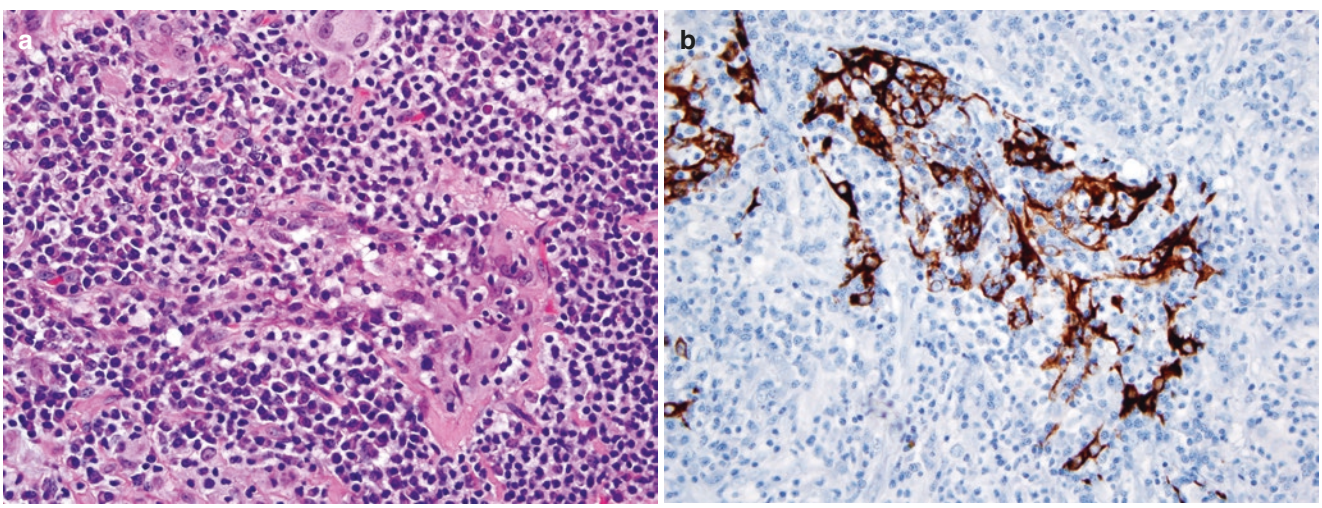

Fig. 11.8 Lymphoepithelial lesion in extranodal marginal zone lymphoma of MALT lymphoma. (**a**) High-magnification view showing the neoplastic lymphocytes and plasma cells, some of which are within the bronchiolar epithelium. (**b**) Immunohistochemical staining with a pan-cytokeratin cocktail highlights the bronchiolar epithelium infiltrated by lymphoid cells

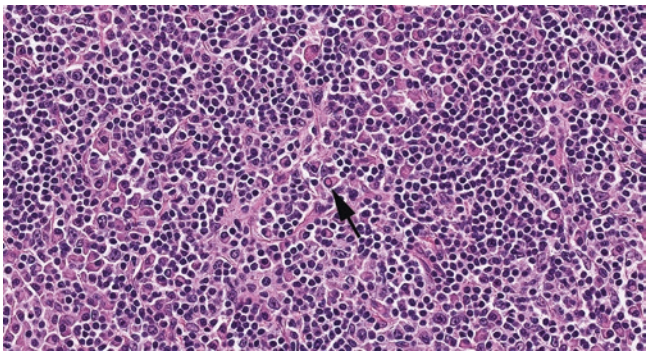

Fig. 11.9 Extranodal marginal zone lymphoma of MALT lymphoma. High-magnification view of the dense cellular infiltrate showing predominantly small lymphocytes, some with a narrow rim of cytoplasm resulting in a monocytoid appearance with associated plasma cells. Some of the plasma cells show brightly eosinophilic intranuclear immunoglobulin pseudoinclusions called Dutcher bodies (arrow), a helpful finding that is seen more commonly in lymphomas with plasmacytic differentiation than in benign lymphoplasmacytic infiltrates

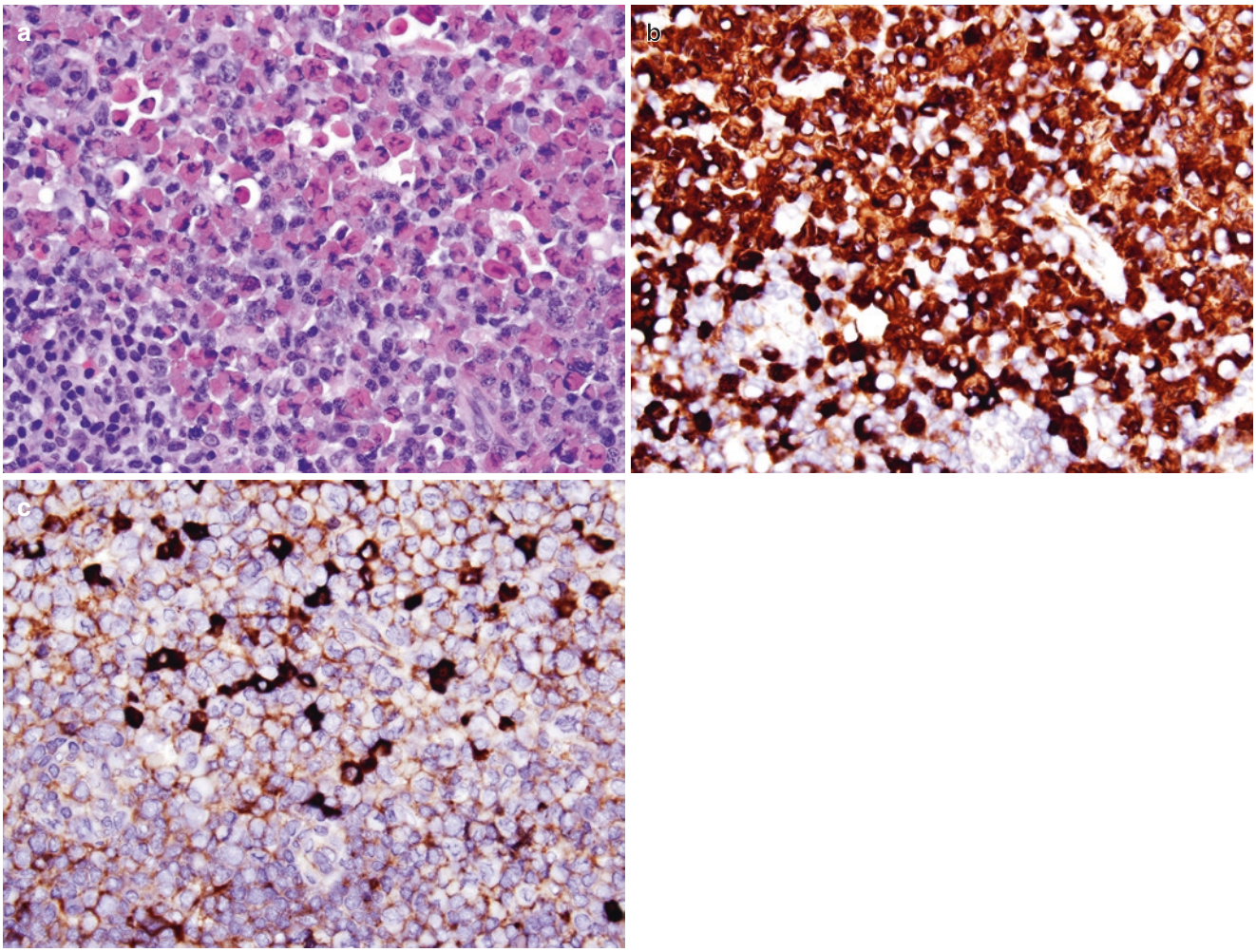

Fig. 11.10 Extranodal marginal zone lymphoma of MALT lymphoma. (**a**) Photomicrograph showing prominent Russell bodies, immunoglobulin-filled cytoplasmic inclusions, in a MALT lymphoma. The inclusions in this example compress and distort pyknotic nuclei. Unlike intranuclear Dutcher bodies, Russell bodies are not specific and frequently occur in benign lymphoplasmacytic infiltrates as well as immunoglobulin-synthesizing neoplasms. (**b**) and (**c**), Immunohistochemical stains show monotypical expression of lambda (**b**) compared to kappa (**c**) in the cytoplasmic Russell bodies illustrated in **a**

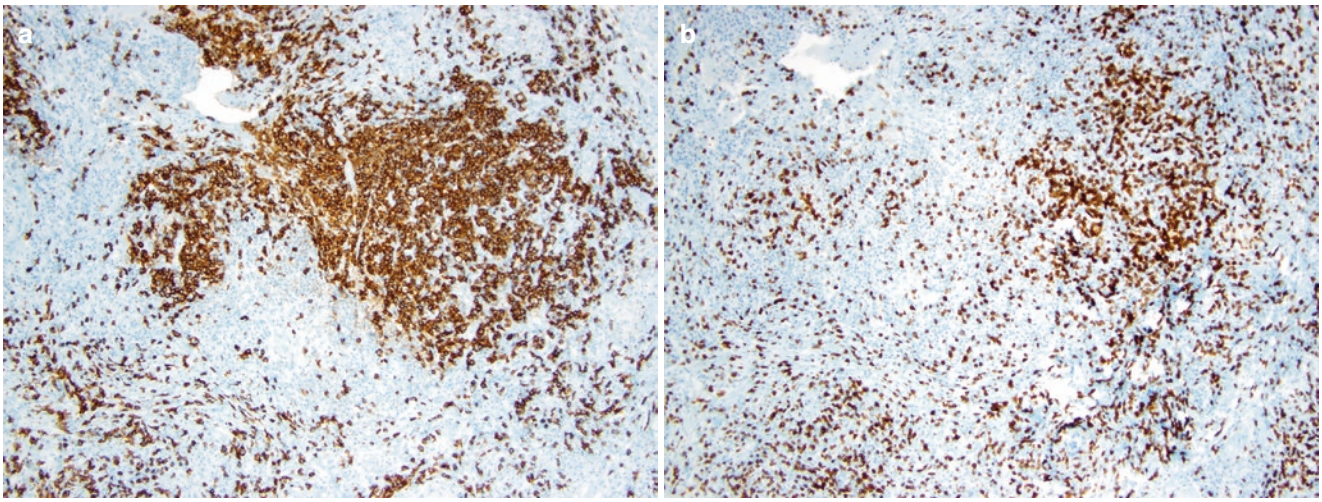

Fig. 11.11 Extranodal marginal zone lymphoma of MALT lymphoma. (**a**) The lymphoid cells are predominantly B cells as highlighted by CD20 immunostaining. (**b**) There are also variably abundant admixed T cells as highlighted by CD3 immunostaining. There remains a substantial subset of cells that stained with neither CD20 nor CD3, primarily plasma cells

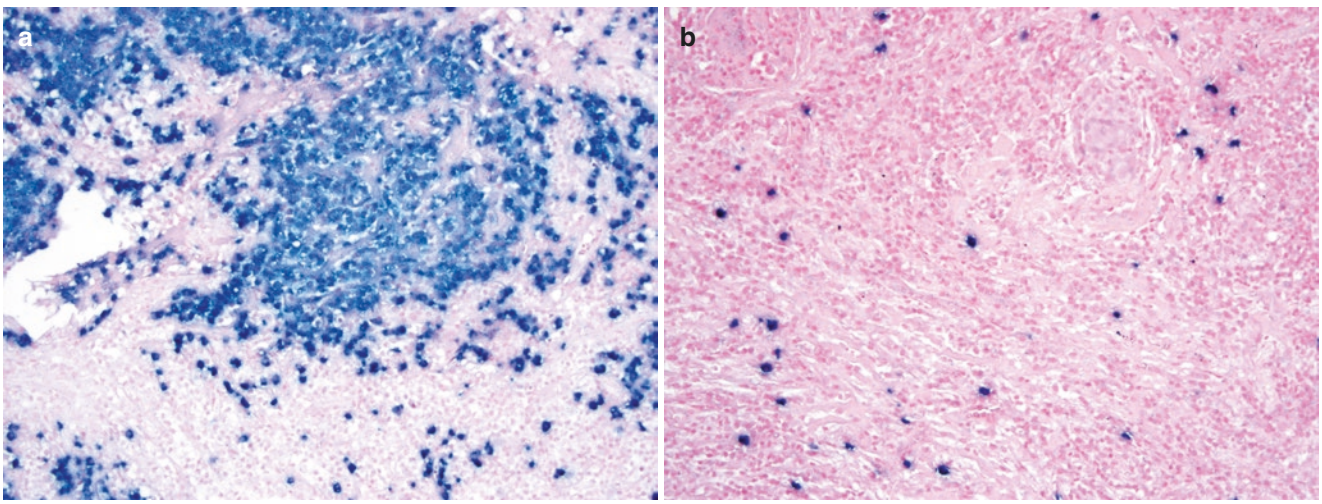

Fig. 11.12 Extranodal marginal zone lymphoma of MALT lymphoma. In situ hybridization studies using probes that recognize immunoglobulin light-chain RNA show monotypic expression of kappa (**a**) compared to lambda (**b**) in this example. Monotypic light-chain expression is not always demonstrable using immunohistochemistry and/or RNA in situ hybridization in otherwise typical examples of MALT lymphoma. Therefore failure to demonstrate light-chain restriction does not preclude the diagnosis in histologically classic cases

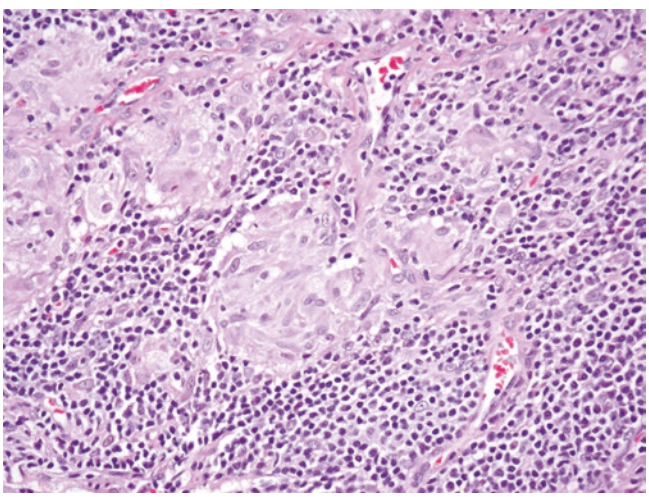

Fig. 11.13 Extranodal marginal zone lymphoma of MALT lymphoma. Photomicrograph showing non-necrotizing granulomas in MALT lymphoma, an uncommon finding that may confound the diagnosis in rare cases

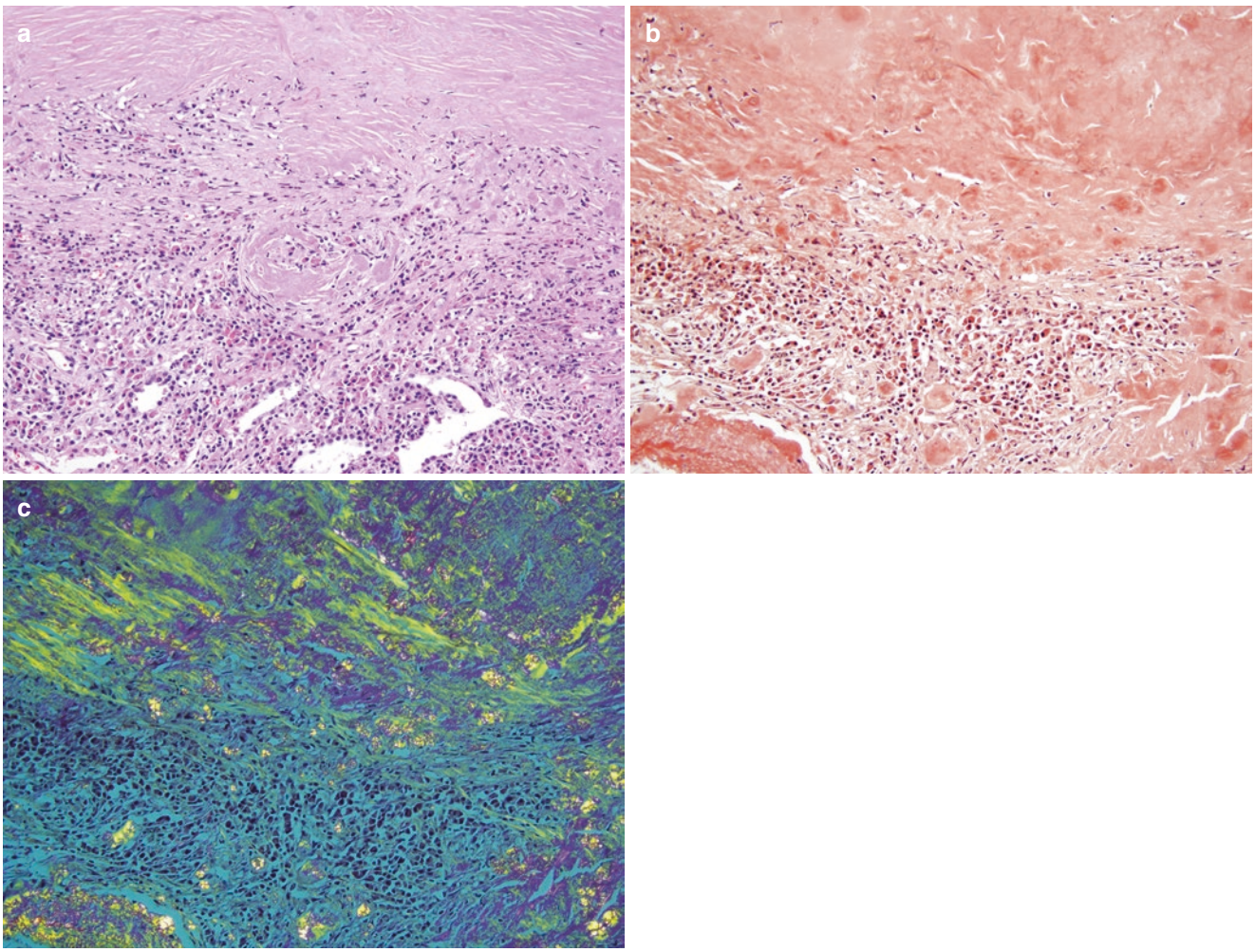

Fig. 11.14 Extranodal marginal zone lymphoma of MALT lymphoma. (**a**) Occasionally, as illustrated in this photomicrograph, amyloid deposits consisting of excessive immunoglobulin light chains are seen on H&E staining. Note also the plasma cell-rich lymphoid infiltrates in the background. Indeed, most cases of nodular amyloidosis are probably MALT lymphomas that have been overrun by amyloid deposits. (**b**) The amyloid deposits stain red on Congo red staining when viewed with normal illumination. (**c**) When viewed using polarized light, the Congo red-stained amyloid deposits show apple-green birefringence

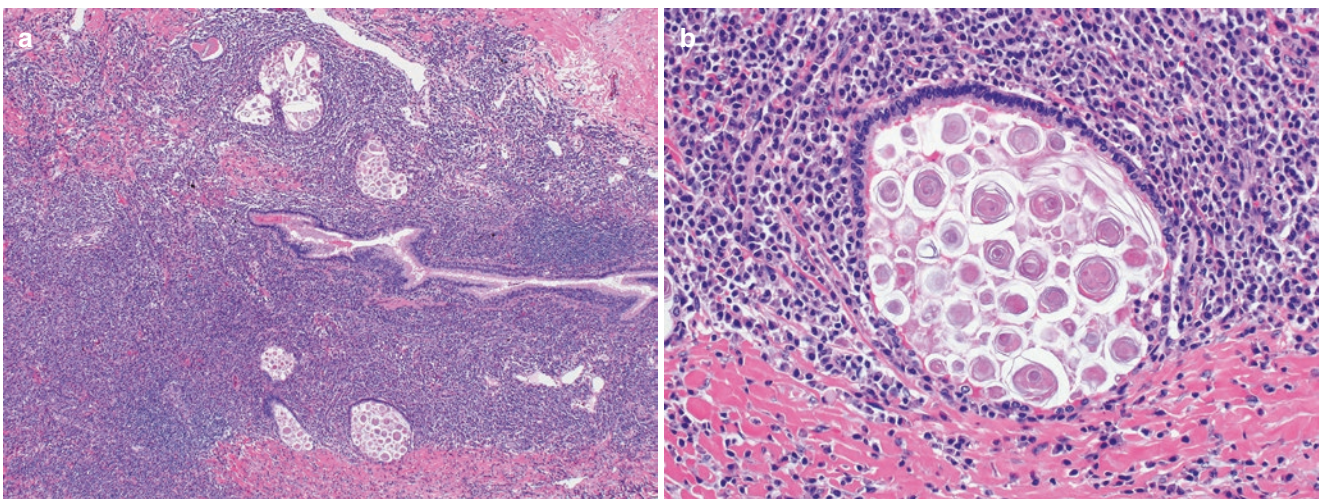

Fig. 11.15 Extranodal marginal zone lymphoma of MALT lymphoma. (**a**) Low-magnification photomicrograph of MALT lymphoma with associated giant lamellar bodies. Giant lamellar bodies are uncommon and not specific for MALT lymphoma, but when it comes to lymphoproliferative lesions, they occur almost exclusively in MALT lymphomas compared to benign, nonneoplastic lymphoplasmacytic proliferations. (**b**) Higher-magnification photomicrograph showing giant lamellar bodies in an air space entrapped within a MALT lymphoma. Giant lamellar bodies are extracellular inclusions consisting of concentric rings of surfactant degradation and cell breakdown products

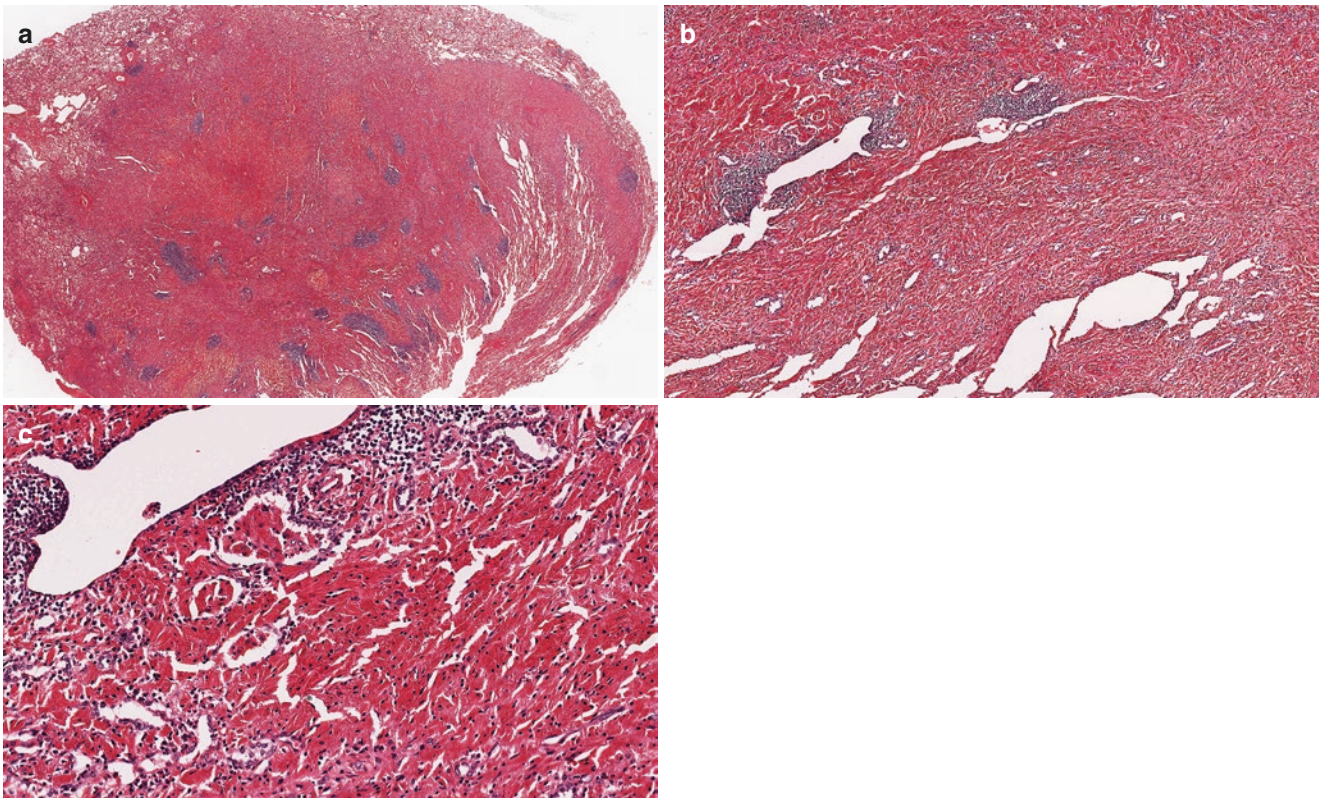

Fig. 11.16 Crystal-storing histiocytosis associated with extranodal marginal zone lymphoma of MALT lymphoma. (**a**) On rare occasions, tumor-related light chains may illicit a histiocytic response, arrayed as sheets of large polygonal cells as illustrated in this low-magnification photomicrograph of a lesion that presented as an asymptomatic solitary nodule. There are rare reports of crystal-storing histiocytosis unrelated to a clonal lymphoproliferative disorder, but most occur in the context of MALT lymphoma. (**b**) and (**c**) Higher-magnification photomicrographs show eosinophilic, linearly striated immunoglobulin inclusions characteristic of crystal-storing histiocytosis. The inclusions lack the globular configuration of Russell bodies (*see* Fig. 11.10) and are present in nonneoplastic histiocytes rather than plasma cells

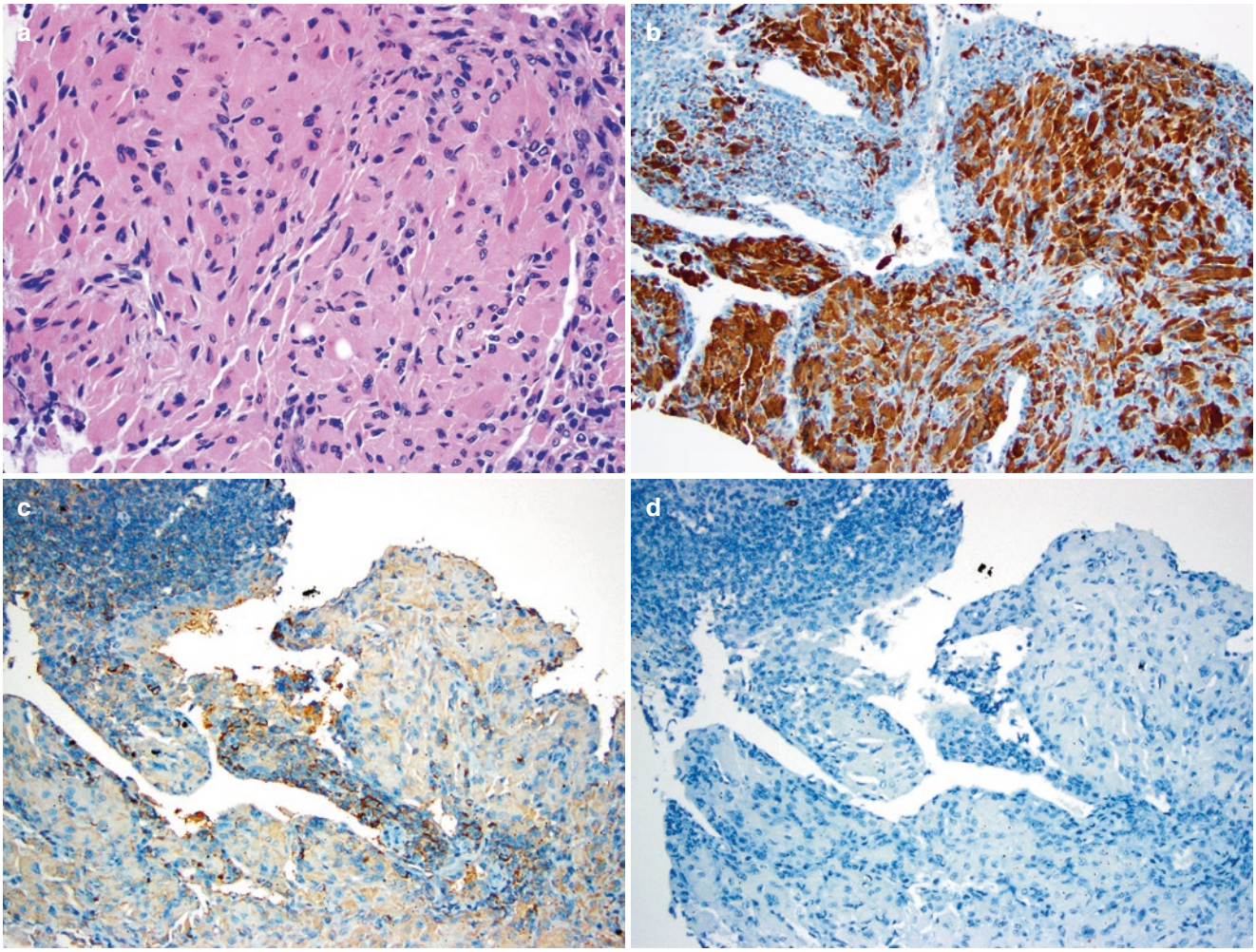

Fig. 11.17 Crystal-storing histiocytosis associated with extranodal marginal zone lymphoma of MALT lymphoma. (**a**) Another example of crystal-storing histiocytosis showing characteristic cytoplasmic inclusions in this high-magnification photomicrograph. (**b**) A CD68 immunostain confirms that the accumulated cells are histiocytes rather than plasma cells. (**c**) The cytoplasmic contents of the histiocytes show pale staining for kappa light chains with a monotypic pattern of dark cytoplasmic staining in a minor subpopulation of neoplastic plasma cells. (**d**) The cytoplasmic contents of histiocytes and neoplastic plasma cells are negative for lambda light-chain expression

Lymphomatoid Granulomatosis

Lymphomatoid granulomatosis (Figs. 11.18, 11.19, 11.20, 11.21, 11.22 and 11.23) is an Epstein-Barr virus (EBV)-driven B-cell lymphoproliferative disorder that targets extranodal sites, including the lung, central nervous system, skin, and kidney. Lymphomatoid granulomatosis occurs more commonly in patients with underlying immunodeficiency states such as HIV/AIDS. Patients usually present with respiratory symptoms and systemic complaints, including fever and weight loss. Radiologic abnormalities typically include bilateral opacities or nodules. Grading is based on the number of EBV-positive, CD20-positive large cells but shows an inconsistent relationship with outcome. If CD20-positive cells are sufficiently profuse to form sheets of large atypical cells without a background of small T lymphocytes, then the lesion is best diagnosed as an EBV-positive large B-cell lymphoma. The prognosis is poor. Occasionally infectious granulomatous diseases, especially acute histoplasmosis, may mimic some of the features of lymphomatoid granulomatosis and therefore should be included in the differential diagnosis.

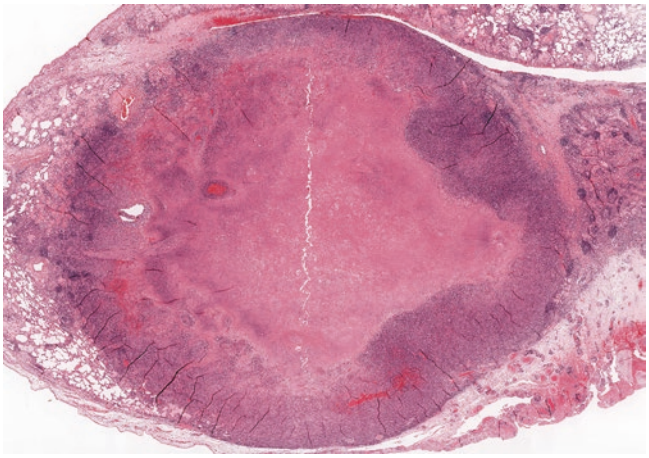

Fig. 11.18 Lymphomatoid granulomatosis. Low-magnification photomicrograph showing a central area of necrosis surrounded by a lymphocyte-rich cellular rim without the epithelioid, palisaded, and multinucleated histiocytes characteristic of granulomatous inflammation

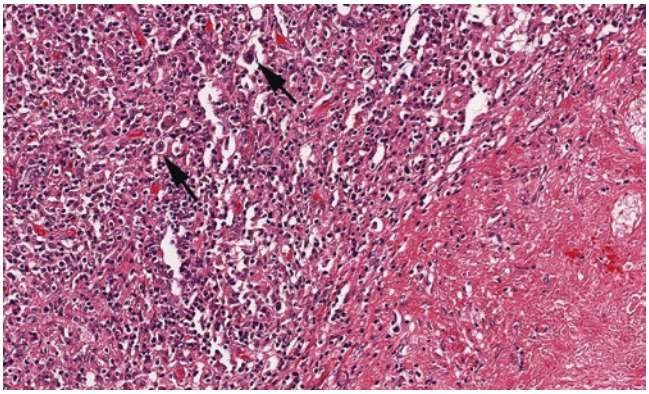

Fig. 11.19 Lymphomatoid granulomatosis. High-magnification photomicrograph demonstrates a polymorphic infiltrate comprising mainly small lymphocytes with widely scattered large atypical cells, including occasional variants with multilobated nuclei resembling Reed-Sternberg cells (arrows)

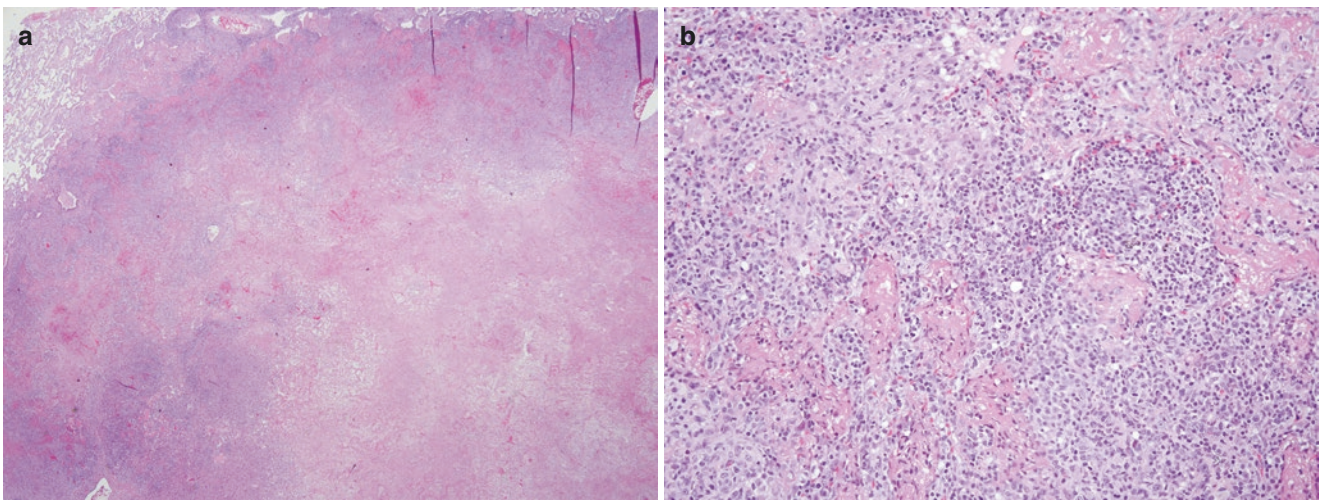

Fig. 11.20 Lymphomatoid granulomatosis. (**a**) Low-magnification photomicrograph showing large area of necrosis surrounded by a polymorphic infiltrate without frankly granulomatous features. (**b**) Higher-magnification view showing that the polymorphic infiltrate is composed of small lymphocytes, histiocytes, and scattered large atypical cells

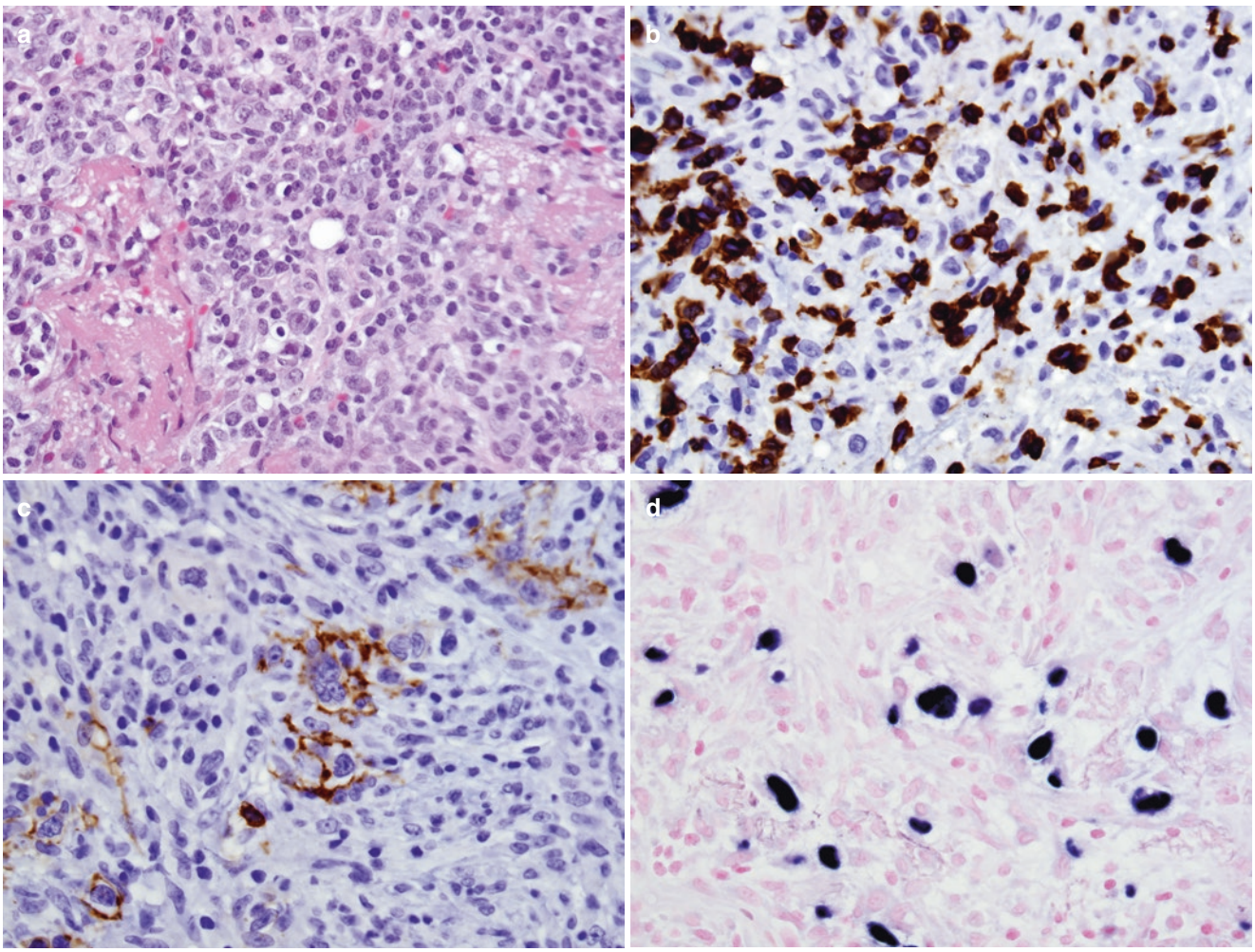

Fig. 11.21 Lymphomatoid granulomatosis. (**a**) High-magnification photomicrograph showing a portion of the polymorphic infiltrate illustrated in Fig. 11.20b. Large atypical cells with prominent eosinophilic nucleoli, vesicular chromatin, and irregularly shaped nuclei are scattered against a backdrop of small lymphocytes. (**b**–**d**), Immunostains shown in photomicrographs taken at the same magnification as **a** show that the predominant population of small cells is positive for CD3 (**b**), while the large atypical cells are positive for CD20 (**c**) and for EBV (**d**) in RNA in situ hybridization studies using probes that recognize EBV RNA (EBER). Almost all the large atypical cells are CD20-positive and EBV-positive

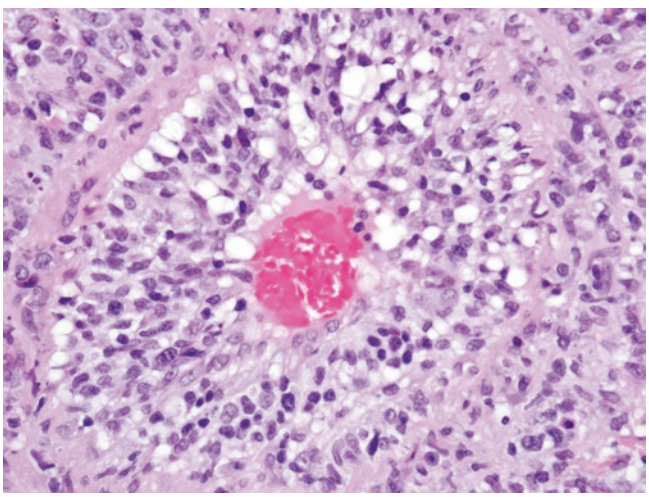

Fig. 11.22 Lymphomatoid granulomatosis. High-magnification photomicrograph of a blood vessel cut in cross section showing a dense mononuclear cell infiltrate that infiltrates and expands the vessel wall without vessel wall necrosis. The infiltrate consists of a combination of large and small lymphocytes. Vessel wall involvement is not unique to lymphomatoid granulomatosis and occurs in other benign and malignant lymphoproliferative disorders. But this pattern of vessel infiltration in the context of centrally necrotic nodules composed of predominantly small lymphocytes with variable numbers of large atypical cells is characteristic and should prompt appropriate phenotyping studies

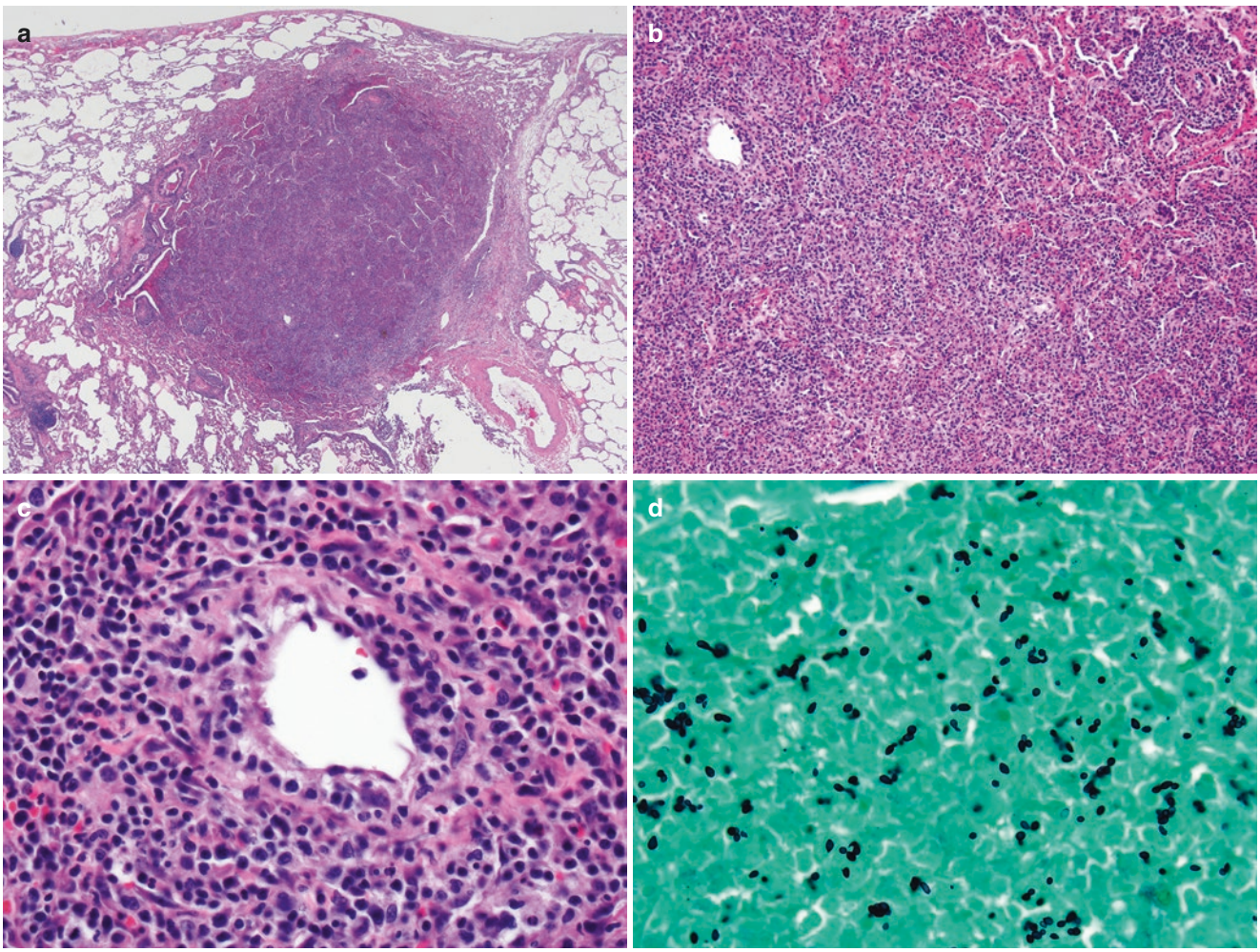

Fig. 11.23 Acute histoplasmosis mimicking lymphomatoid granulomatosis. (**a**) Low-magnification photomicrograph showing a lymphocyte-rich nodule in a patient with a 4-day history of chest pain and sweats affiliated with multiple bilateral small (< 1 cm) nodules on chest imaging studies. (**b**) Intermediate-magnification view shows a polymorphic infiltrate in which small lymphocytes predominate without granulomatous features. (**c**) High-magnification view shows vessel infiltration and scattered large cells that were positive for CD3 and CD30 on paraffin section immunostains (not shown) and negative for EBV on in situ hybridization studies (not shown). The atypical CD3-positive cells had an aberrant phenotype (partial loss of CD2, CD5, and CD7), and molecular studies showed clonal rearrangements of the T-cell receptor gamma gene locus. (**d**) Despite phenotypical evidence of a "lymphomatoid granulomatosis-like" peripheral T-cell lymphoma, a Gomori methenamine silver (GMS) stain showed numerous fungal yeast forms typical of *Histoplasma capsulatum* supporting the diagnosis of acute histoplasmosis

Other Non-Hodgkin Lymphomas

Other types of non-Hodgkin lymphoma rarely present with the lung as a dominant site of involvement and are nearly always affiliated with evidence of systemic disease. They include follicular lymphoma (Fig. 11.24) and mantle cell lymphoma (Figs. 11.25 and 11.26), two forms of low- to intermediate-grade B-cell lymphoma frequently in the differential diagnosis of nodular lymphoid hyperplasia and MALT lymphoma.

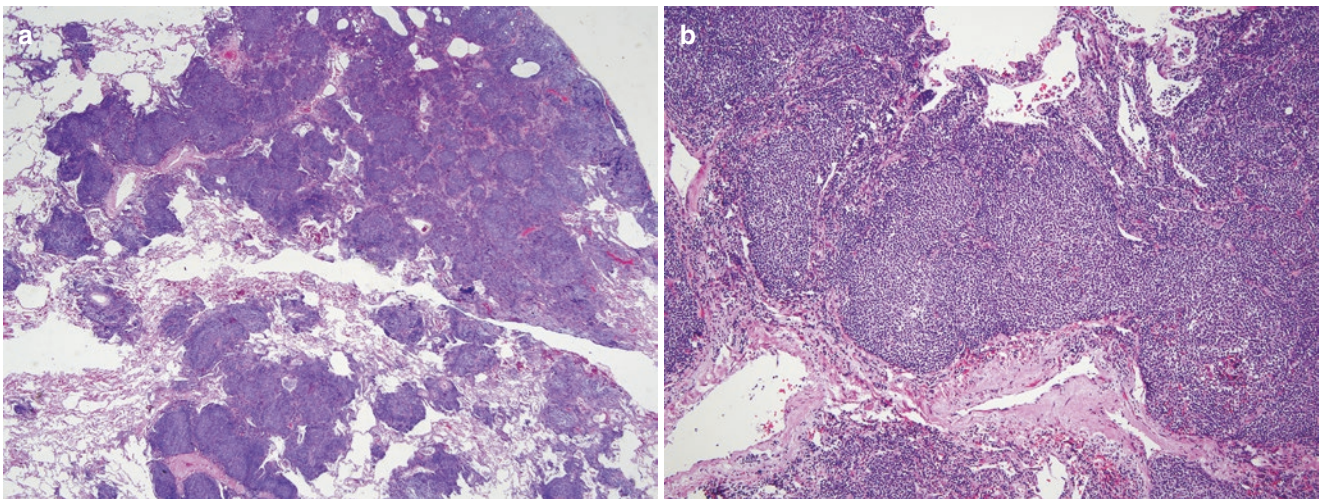

Fig. 11.24 Follicular lymphoma. (**a**) Low-magnification view showing a nodular lymphoid infiltrate with a predilection for visceral pleura, interlobular septa, and bronchovascular bundles. In addition to having a "lymphangitic" distribution typical of lymphomas and leukemic infiltrates in general, in some areas the confluent lymphoid nodules have a tumefactive growth pattern. (**b**) Higher-magnification photomicrograph showing ill-defined uniform follicles without well-demarcated germinal centers in which small and large lymphocytes were positive for CD20, CD10, BCL2, and BCL6 (not shown). This patient proved to have bone marrow and nodal disease

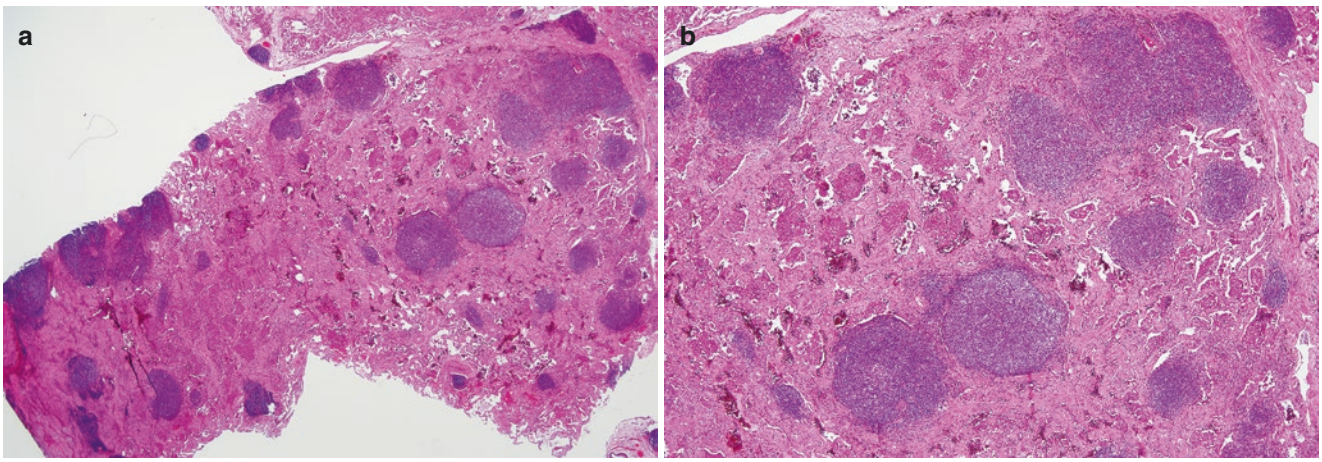

Fig. 11.25 Mantle cell lymphoma. (**a**) Low-magnification view showing multiple uniform lymphoid nodules randomly distributed in mildly fibrotic lung without the tumefactive growth and lymphangitic spread characteristic of other low-grade B-cell lymphomas involving the lung. (**b**) Intermediate-magnification view showing the uniform lymphoid follicles for which diagnostic concerns might reasonably include benign conditions and other low-grade B-cell lymphoproliferative disorders, especially follicular lymphoma

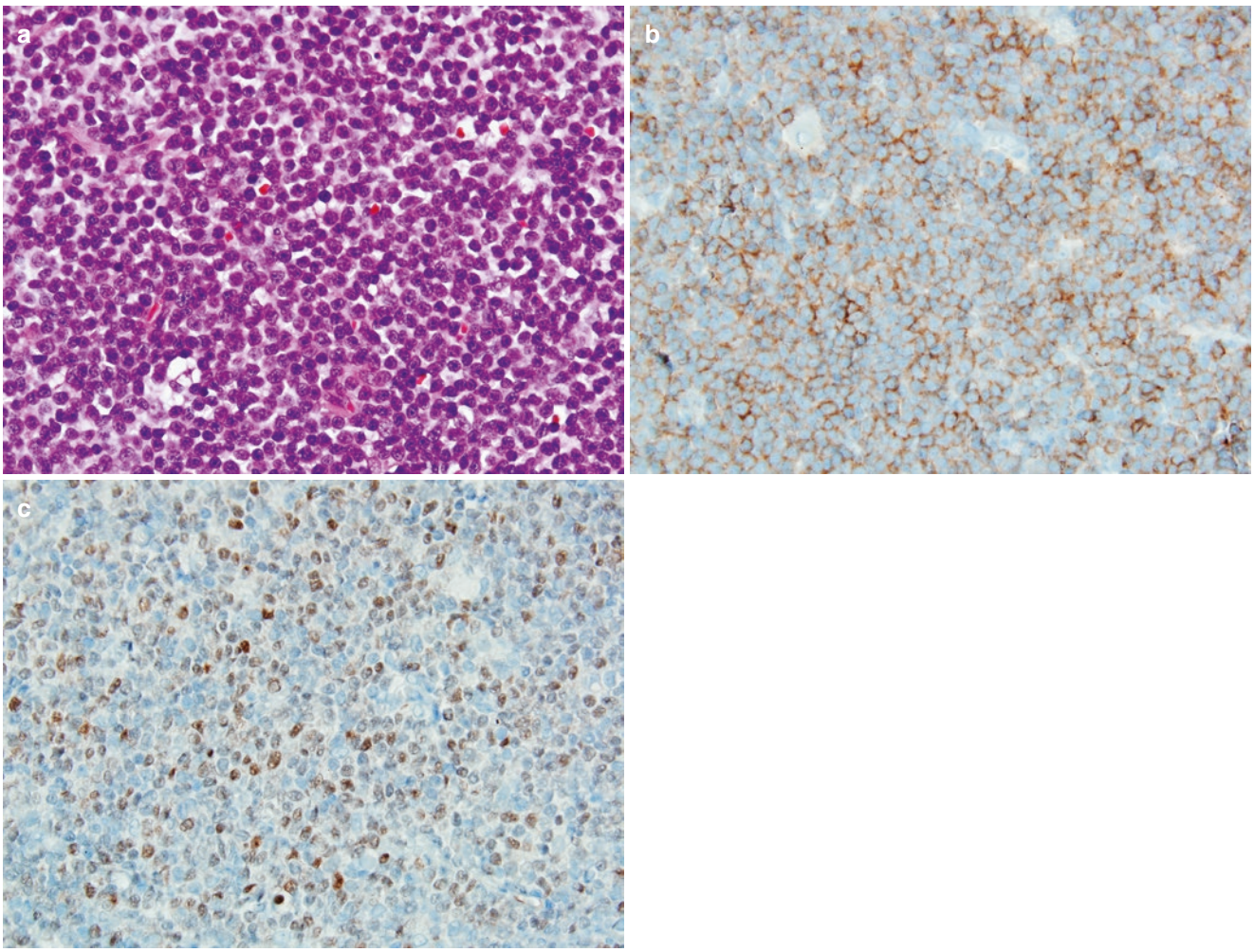

Fig. 11.26 Mantle cell lymphoma. (**a**) High-magnification view of one of the neoplastic nodules illustrated in Fig. 11.25 consisting of homogeneous tumor cells with coarse, evenly dispersed chromatin and inconspicuous nucleoli. (**b**) and (**c**), Paraffin section immunostains showed the neoplastic cells were positive not only for CD20 and BCL2 (not shown) but also for CD5 (**b**) and cyclin D1 (**c**). This patient proved to have bone marrow involvement

Intravascular large B-cell lymphoma usually presents in symptomatic patients with clinical and radiologic findings that may mimic nonneoplastic diffuse interstitial lung disease (Fig. 11.27). Affected patients may have concomitant cutaneous and/or central nervous system involvement. Posttransplant lymphoproliferative disorders occurring in the lung and/or intrathoracic lymph nodes show the same range of pathologic types described in other sites and may be seen in all solid organ and stem cell transplant populations (Fig. 11.28). Polymorphic variants are common and closely mimic lymphomatoid granulomatosis, the distinction hinging on a history of transplantation. Anaplastic large cell lymphomas (Figs. 11.29 and 11.30) and natural killer (NK)/T-cell lymphomas (Fig. 11.31) rarely present with primary lung involvement, but on those rare occasions when they do, they are easily mistaken for other neoplasms.

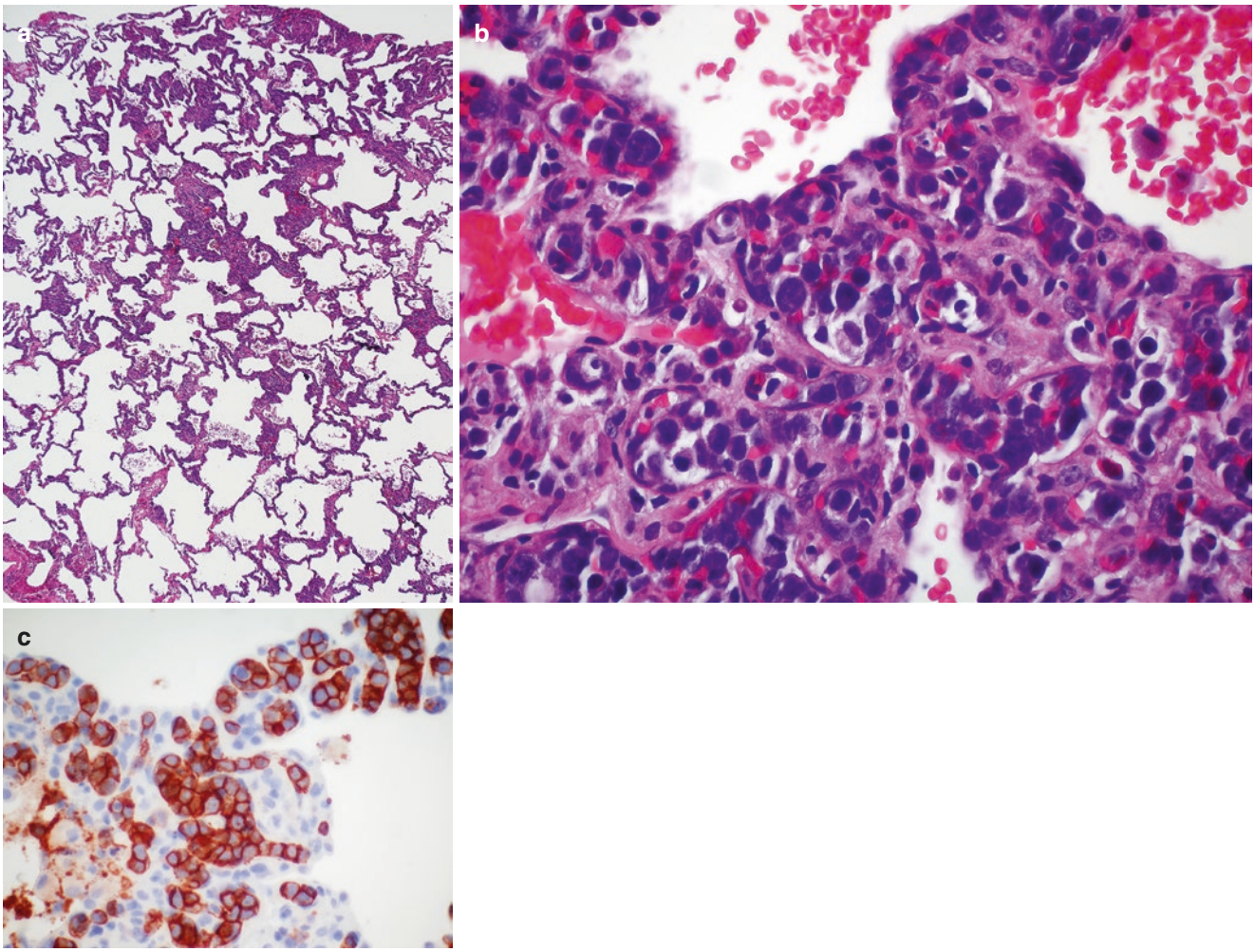

Fig. 11.27 Intravascular large B-cell lymphoma. (**a**) Low-magnification view showing preserved alveolar architecture with thickened alveolar septa in which alveolar septal capillaries are distended by a cellular infiltrate resembling an interstitial pneumonia. (**b**) High-magnification view showing large atypical neoplastic lymphocytes filling alveolar septal capillaries. (**c**) The neoplastic cells within the capillaries are positive for CD20 in paraffin section immunostains

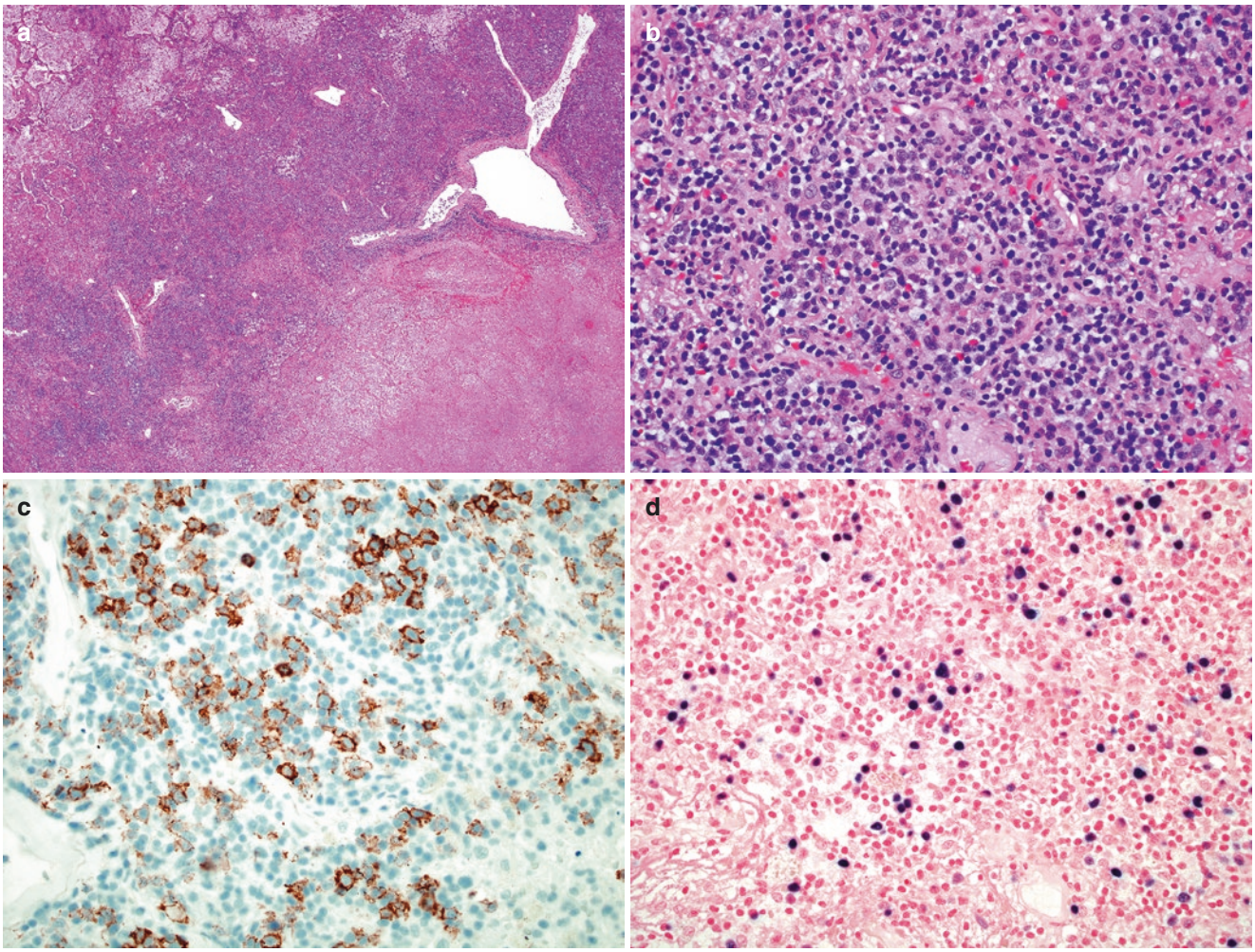

Fig. 11.28 Posttransplant lymphoproliferative disorder (PTLD), polymorphic type. (**a**) Low-magnification photomicrograph showing an area of necrosis bounded by a dense polymorphic lymphocytic infiltrate closely resembling lymphomatoid granulomatosis. (**b**) High-magnification photomicrograph showing a heterogeneous population of small to large lymphoid cells. (**c**) The large cells are positive for CD20 in paraffin section immunostain. (**d**) Some large cells are positive for EBV in in situ hybridization studies. The polymorphic type of PTLD may be indistinguishable from lymphomatoid granulomatosis based on morphology and immunostains alone; a history of organ transplant is key to the diagnosis in these patients

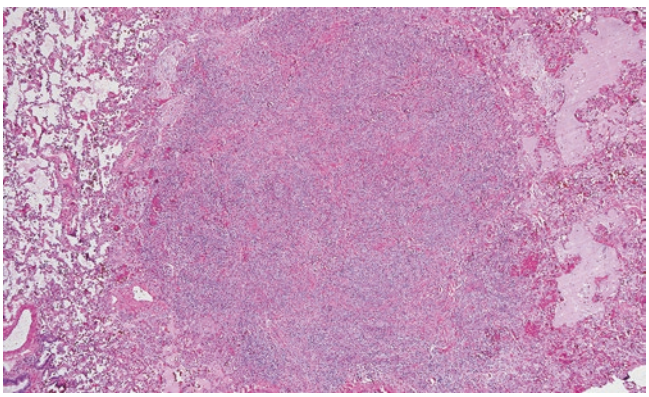

Fig. 11.29 Anaplastic large cell lymphoma. Low-magnification photomicrograph showing that the lung architecture is focally effaced by a well-demarcated nodular lesion

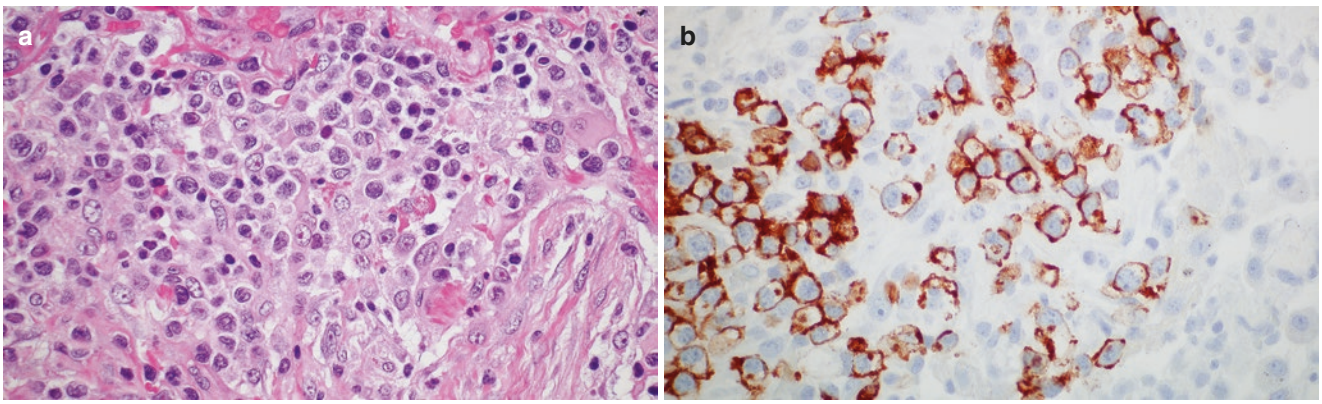

Fig. 11.30 Anaplastic large cell lymphoma (ALCL). (**a**) High-magnification view of the nodule illustrated in Fig. 11.29 showing that the lesion consists mainly of large cells with a rim of cytoplasm and large irregular nuclei. Prominent nucleoli are also seen. (**b**) High-magnification photomicrograph showing strong positivity for CD30 in the large atypical CD3-positive cells of ALCL. The cells may or may not be anaplastic lymphoma kinase (ALK)-positive

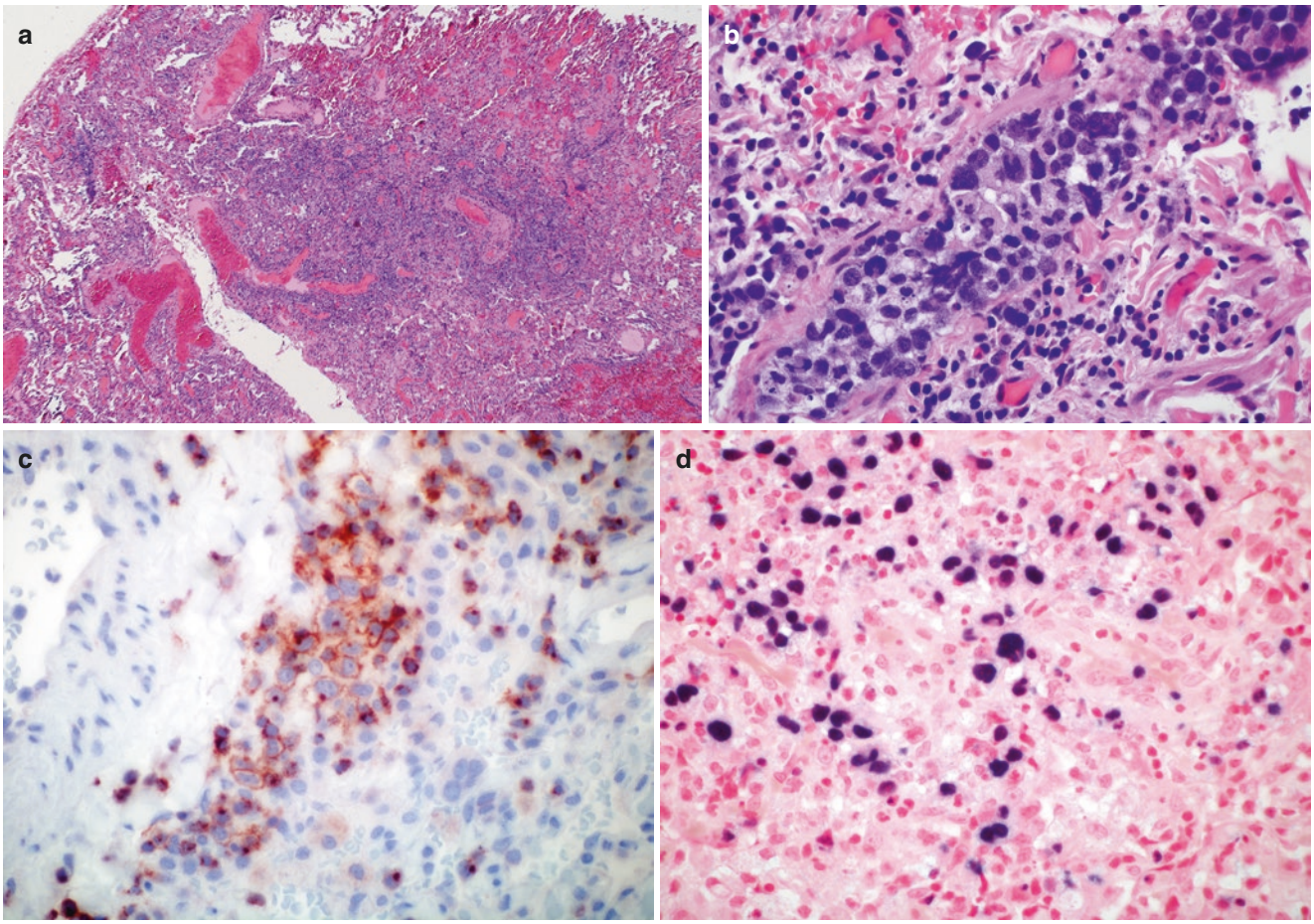

Fig. 11.31 Extranodal natural killer/T-cell lymphoma, nasal type. (**a**) Low-magnification photomicrograph showing an ill-defined localized area of increased cellularity. (**b**) High-magnification photomicrograph showing intravascular tumor cells that are markedly atypical with hyperchromatic chromatin, small nucleoli, and pale staining finely vacuolated cytoplasm. (**c**) and (**d**), The tumor cells are positive for CD2 on paraffin section immunostains (**c**) and for EBV on EBER in situ hybridization studies (**d**)

Classic Hodgkin Lymphoma

Classic Hodgkin lymphoma (Figs. 11.32, 11.33 and 11.34) commonly involves cervical and mediastinal lymph nodes. Secondary lung involvement is uncommon at initial staging but is present in about 60% of patients at autopsy. Predominant lung involvement at the time of diagnosis is rare and is seen most commonly as multiple unilateral nodular lesions in symptomatic patients, including B symptoms in about one third. Nodular sclerosis is the most common subtype seen in the lungs, although all histologic subtypes have been reported. Histologic and immunophenotypic features are identical to those seen in more traditional locations. Associated necrosis, granulomatous inflammation, and other secondary findings such as organizing pneumonia may confound the diagnosis in lung biopsies.

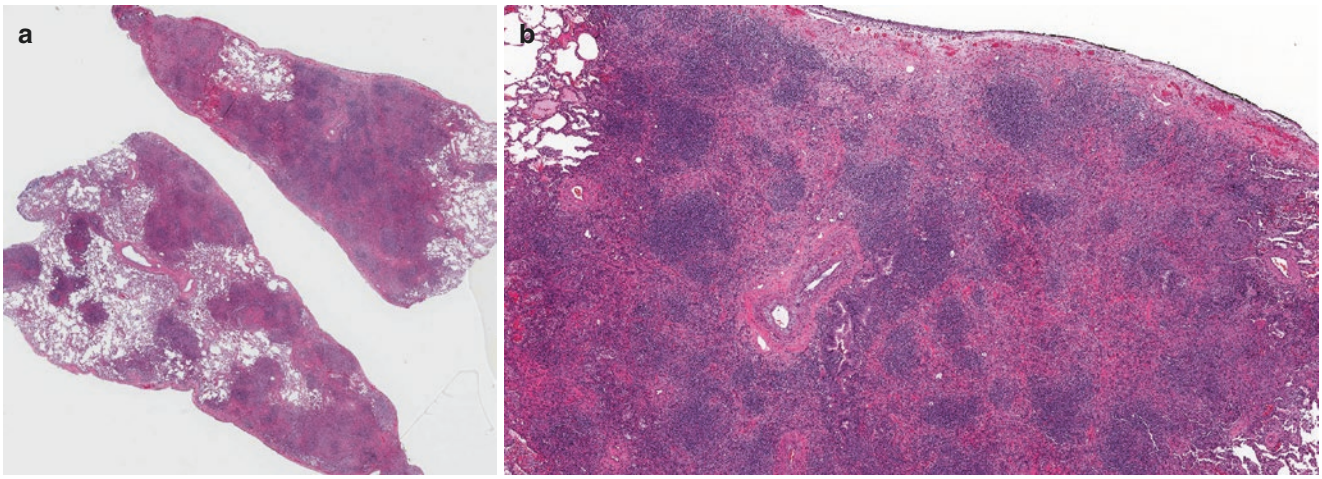

Fig. 11.32 Classic Hodgkin lymphoma. (**a**) Whole mount slide of a lung wedge biopsy showing multiple subpleural and intraparenchymal nodular lesions consisting of a polymorphic infiltrate with associated sclerosis. (**b**) Low-magnification view showing that the areas of abnormality are well-demarcated from the uninvolved lung parenchyma and are composed of cellular infiltrates separated by broad collagen bands

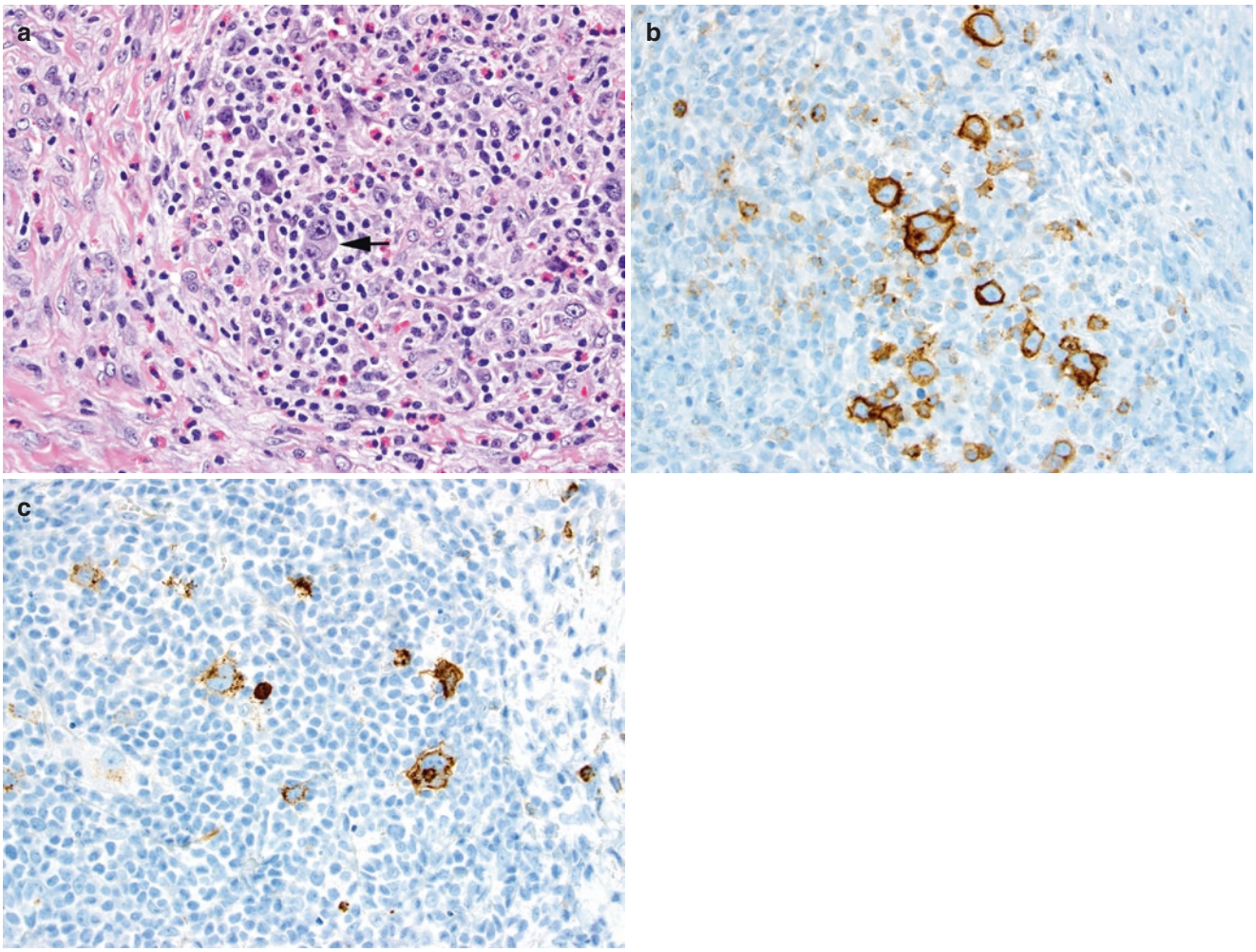

Fig. 11.33 Classic Hodgkin lymphoma. (**a**) High-magnification view of the cellular infiltrates demonstrates mixed small lymphocytes, plasma cells, histiocytes, abundant eosinophils, and multiple large atypical cells with prominent nucleoli. A binucleated Reed-Sternberg cell is seen (arrow). Note the dense collagen bands in the background. (**b**) The majority of the large atypical cells are positive for CD30 with a characteristic membranous and paranuclear dot-like distribution. (**c**) Some of the large atypical cells are also positive for CD15 with the same membrane and paranuclear dot-like staining pattern

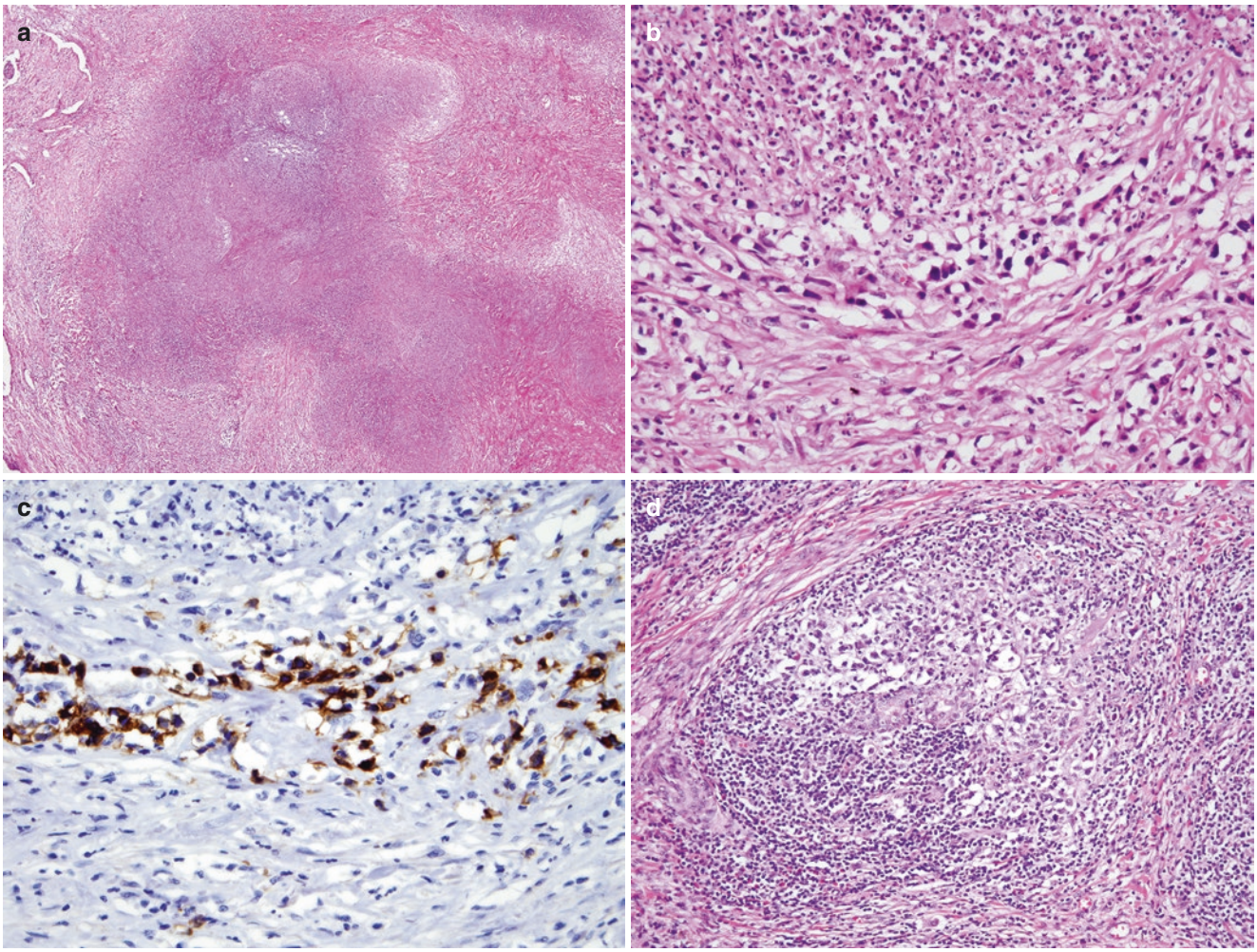

Fig. 11.34 Classic Hodgkin lymphoma. (**a**) Low-magnification photomicrograph showing a necrotizing nodule closely mimicking the appearance of a necrotizing granuloma. (**b**) At higher magnification the polymorphic infiltrate included prominent "smudge cells" aligned at the periphery of the necrosis. (**c**) The atypical cells illustrated in **b** were strongly positive for CD30 and focally positive for CD15. (**d**) Elsewhere, the biopsy showed classic mononuclear and binucleated Hodgkin cells

Suggested Reading

Abbondanzo SL, Rush W, Bijwaard KE, Koss MN. Nodular lymphoid hyperplasia of the lung: a clinicopathologic study of 14 cases. Am J Surg Pathol. 2000;24:587–97.

Begueret H, Vergier B, Parrens M, Lehours P, Laurent L, Vernejoux JM, et al. Primary lung small B-cell lymphoma versus lymphoid hyperplasia: evaluation of diagnostic criteria in 26 cases. Am J Surg Pathol. 2002;26:76–81.

Halkos ME, Miller JI, Mann KP, Miller DL, Gal AA. Thoracic presentations of posttransplant lymphoproliferative disorders. Chest. 2004;126:2013–20.

Katzenstein AL, Doxtader E, Narendra S. Lymphomatoid granulomatosis: insights gained over 4 decades. Am J Surg Pathol. 2010;34:e35–48.

Kurtin PJ, Myers JL, Adlakha H, Strickler JG, Lohse C, Pankratz VS, et al. Pathologic and clinical features of primary pulmonary extranodal marginal zone B-cell lymphoma of MALT type. Am J Surg Pathol. 2001;25:997–1008.

Mukhopadhyay S, Katzenstein AL. Biopsy findings in acute pulmonary histoplasmosis: unusual histologic features in 4 cases mimicking lymphomatoid granulomatosis. Am J Surg Pathol. 2010;34:541–6.

Perry L, Florio R, Dewar A, Nicholson A. Giant lamellar bodies as a feature of pulmonary low-grade MALT lymphomas. Histopathology. 2000;36:240–4.

Rush WL, Andriko JA, Taubenberger JK, Nelson AM, Abbondanzo SL, Travis WD, et al. Primary anaplastic large cell lymphoma of the lung: a clinicopathologic study of five patients. Mod Pathol. 2000;13:1285–92.

Song JY, Pittaluga S, Dunleavy K, Grant N, White T, Jiang L, et al. Lymphomatoid granulomatosis--a single institute experience: pathologic findings and clinical correlations. Am J Surg Pathol. 2015;39:141–56.

Swerdlow S, Campo E, Harris N, Jaffe E, Pileri S, Stein H, Thiele J. WHO Classification of Tumours of Haematopoietic and Lymphoid Tissues. 4th ed. Lyon: IARC; 2017.

Swigris JJ, Berry GJ, Raffin TA, Kuschner WG. Lymphoid interstitial pneumonia: a narrative review. Chest. 2002;122:2150–64.

Yousem SA, Weiss LM, Colby TV. Primary pulmonary Hodgkin's disease. A clinicopathologic study of 15 cases. Cancer. 1986;57:1217–24.

Yousem SA, Randhawa P, Locker J, Paradis IL, Dauber JA, Griffith BP, et al. Posttransplant lymphoproliferative disorders in heart-lung transplant recipients: primary presentation in the allograft. Hum Pathol. 1989;20:361–9.

Benign Lung Neoplasms

12

Chen Zhang and Jeffrey L. Myers

Although most lung neoplasms are malignant, a small subset of true lung neoplasms are benign (Table 12.1). Benign lung neoplasms include epithelial and mesenchymal tumors, with pulmonary hamartoma being the single most commonly encountered entity.

The etiology of most benign lung neoplasms is unknown except for some squamous papillomas. Human papillomavirus (HPV) plays a pathogenic role in less than half of solitary squamous cell papillomas and in virtually all multiple forms (papillomatosis). High-risk HPV infections (subtypes 16, 18, 31/33/35) may play a role in malignant transformation in squamous cell papilloma. Glandular papilloma and mixed squamous cell and glandular papilloma are not associated with HPV infection.

Most benign lung neoplasms are solitary, stable, or slow-growing nodules on chest radiographs. An exception are papillomas associated with respiratory papillomatosis, which may be multiple or even demonstrate diffuse, poorly defined noncalcified parenchymal nodules with occasional central cavitation. Positron emission tomography (PET) avidity is uncommon but has been reported.

Most patients with benign lung neoplasms are asymptomatic and are incidentally discovered to have intrapulmonary nodules in the course of radiologic studies performed for other reasons. Benign tumors involving the larger airways may cause obstructive or irritative symptoms, such as atelectasis, cough, and hemoptysis. Surgical resection is curative for most benign lung tumors. Malignant transformation is uncommon.

Table 12.1 Major benign lung neoplasms

Category	Tumor type
Epithelial tumors	Papilloma
	Squamous cell papilloma
	Glandular papilloma
	Mixed squamous cell and glandular papilloma
	Ciliated muconodular papillary tumor
	Adenoma
	Pleomorphic adenoma
	Mucous gland adenoma
	Alveolar adenoma
	Papillary adenoma
	Sclerosing pneumocytoma
Mesenchymal tumors	Hamartoma
	Chondroma
	PEComa (clear cell "sugar" tumor)
	Granular cell tumor
Miscellaneous tumors	Pneumocytic adenomyoepithelioma

C. Zhang (✉)
Department of Pathology and Laboratory Medicine, Indiana University School of Medicine, Indianapolis, IN, USA
e-mail: chenzhan@iupui.edu

J. L. Myers
Department of Pathology, Michigan Medicine, Ann Arbor, MI, USA
e-mail: myerjeff@med.umich.edu

© Springer Science+Business Media, LLC, part of Springer Nature 2018
C. Zhang, J. L. Myers (eds.), *Atlas of Lung Pathology*, Atlas of Anatomic Pathology,
https://doi.org/10.1007/978-1-4939-8689-7_12

Papilloma

Papillomas (Figs. 12.1, 12.2, 12.3, 12.4 and 12.5) are exophytic endobronchial lesions characterized by a papillary architecture. Most papillomas occur as solitary lesions in central large airways; rarely, they arise in smaller bronchioles to form peripheral nodules. Patients with HPV-driven recurrent respiratory papillomatosis who develop lower respiratory tract involvement may have multiple squamous papillomas, often with an inverted growth pattern. Squamous papillomas account for the majority of solitary papillomas; glandular and mixed types are less common. Papillomas of mixed epithelial type overlap with *ciliated muconodular papillary tumors*, a recently characterized peripheral lung neoplasm associated with a benign course. Associated somatic mutations in *BRAF V600E*, *AKT1*, *E7K*, and *KRAS* have been reported in some cases, raising concerns regarding their biologic potential. However, patients reported to date have not suffered recurrence after complete excision, hence their provisional inclusion here with benign papillomas.

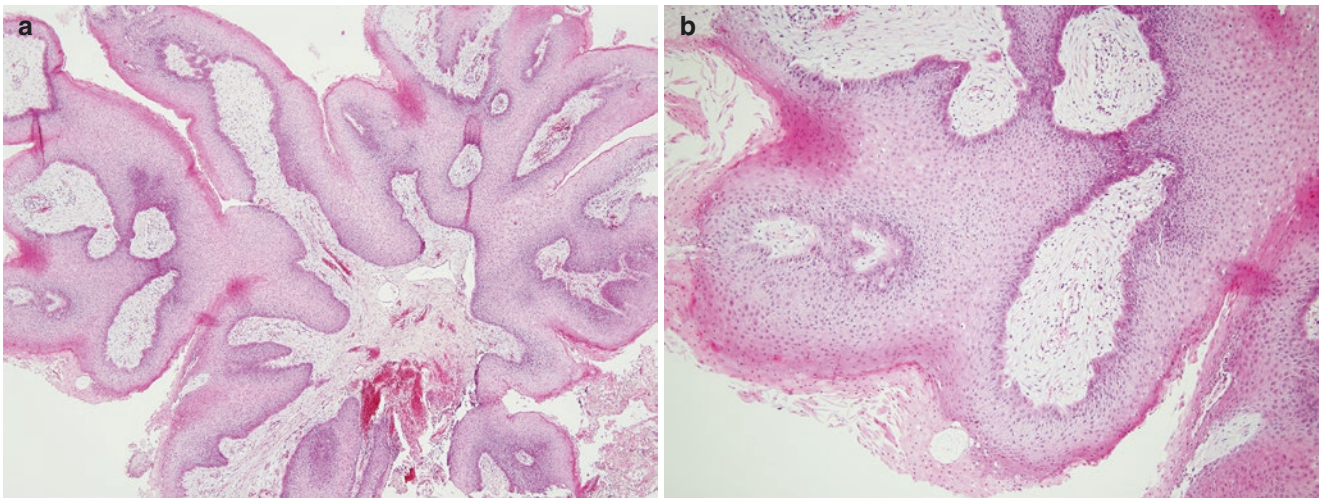

Fig. 12.1 Exophytic squamous cell papilloma. (**a**) Low-magnification photomicrograph shows an exophytic lesion featuring arborizing loose fibrovascular cores covered by stratified squamous epithelium. (**b**) Intermediate-magnification photomicrograph showing that the overlying squamous epithelium has an orderly epithelial maturation with surface keratinization

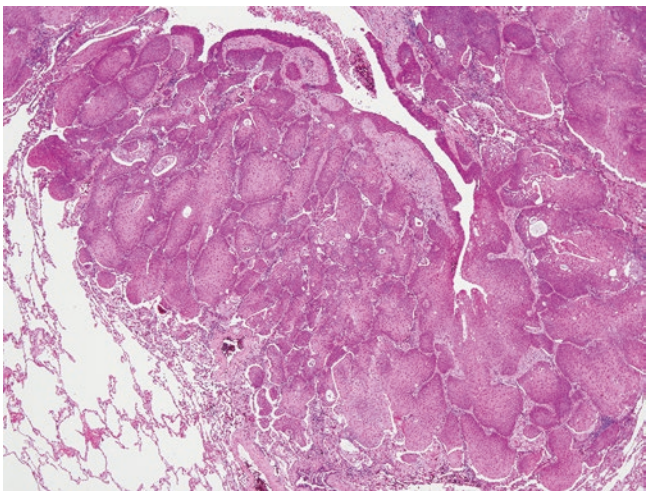

Fig. 12.2 Inverted growth pattern in recurrent respiratory papillomatosis. Low-magnification photomicrograph showing the inverted growth pattern typical of lower respiratory tract involvement in patients with recurrent respiratory papillomatosis

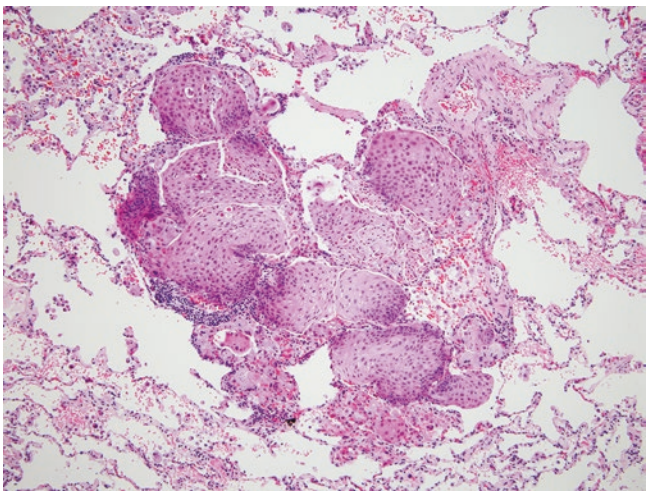

Fig. 12.3 Inverted growth pattern in recurrent respiratory papillomatosis. Photomicrograph of another lesion from same patient illustrated in Fig. 12.2 with parenchymal involvement featuring solid intra-alveolar nests of cytologically bland nonkeratinizing squamous cells

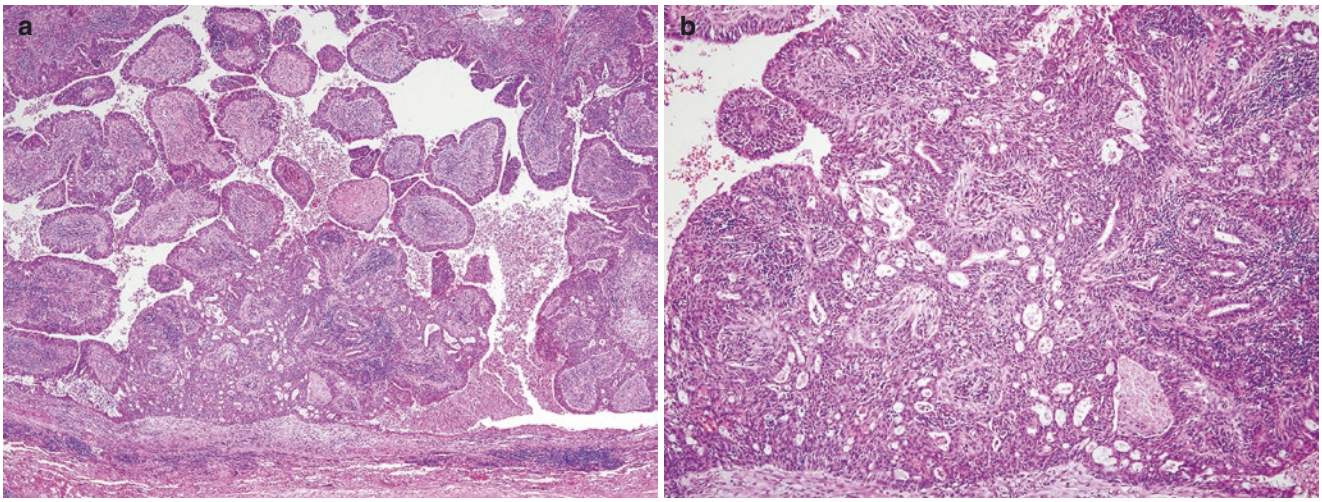

Fig. 12.4 Mixed squamous and glandular papilloma. (**a**) Low-magnification photomicrograph shows broad epithelial-lined fronds with connective tissue cores lined by both nonciliated columnar and squamous epithelia. (**b**) Higher-magnification view showing both squamous and glandular epithelia

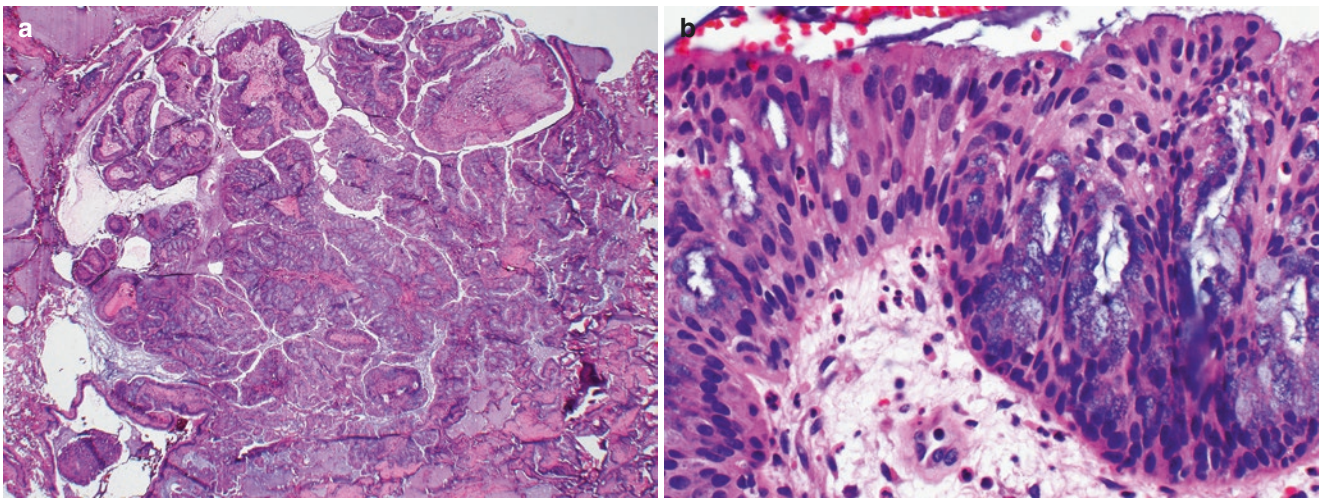

Fig. 12.5 Ciliated muconodular papillary tumor. (**a**) Low-magnification photomicrograph showing a peripheral papillary tumor unassociated with a bronchus and affiliated with acellular mucinous lakes in adjacent parenchyma. (**b**) High-magnification photomicrograph showing the combination of ciliated columnar cells, goblet mucinous cells, and basal cells that constitute this tumor. The findings overlap with those seen in mixed squamous and glandular papillomas, differing mainly in their peripheral location, associated mucinosis, and characteristic ciliated respiratory epithelium

Adenoma

Adenomas (Figs. 12.6, 12.7, 12.8, 12.9, 12.10 and 12.11) are benign epithelial proliferations with a circumscribed profile at low magnification that differs from the complex arborizing configuration of papillomas. Endobronchial variants comprise pleomorphic adenomas analogous to their major salivary gland counterparts and mucous gland adenomas, both of which may cause obstruction and symptomatic postobstructive changes. Alveolar and papillary adenomas, in contrast, present as small peripheral circumscribed lesions corresponding to asymptomatic solitary lung nodules usually discovered incidentally in patients who lack respiratory symptoms. Aside from rare reports of carcinomas arising in pleomorphic adenoma analogous to carcinoma ex pleomorphic adenoma in major salivary glands, these lesions are benign with no malignant potential.

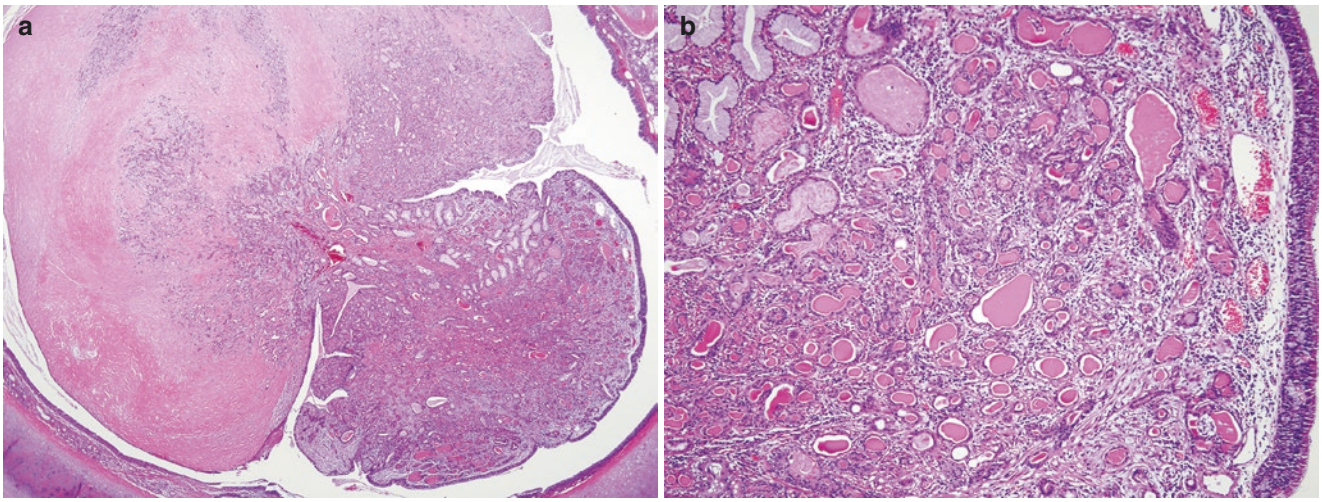

Fig. 12.6 Pleomorphic adenoma. (**a**) Low-magnification photomicrograph showing solid exophytic endobronchial mass covered by a surface layer of nonneoplastic respiratory epithelium. Pleomorphic adenomas of the lung show the same range of histologic heterogeneity typical of those seen more commonly in major salivary glands. (**b**) High-magnification photomicrograph showing the combination of epithelial cells, myoepithelial cells, and stroma that define pleomorphic adenomas at any site

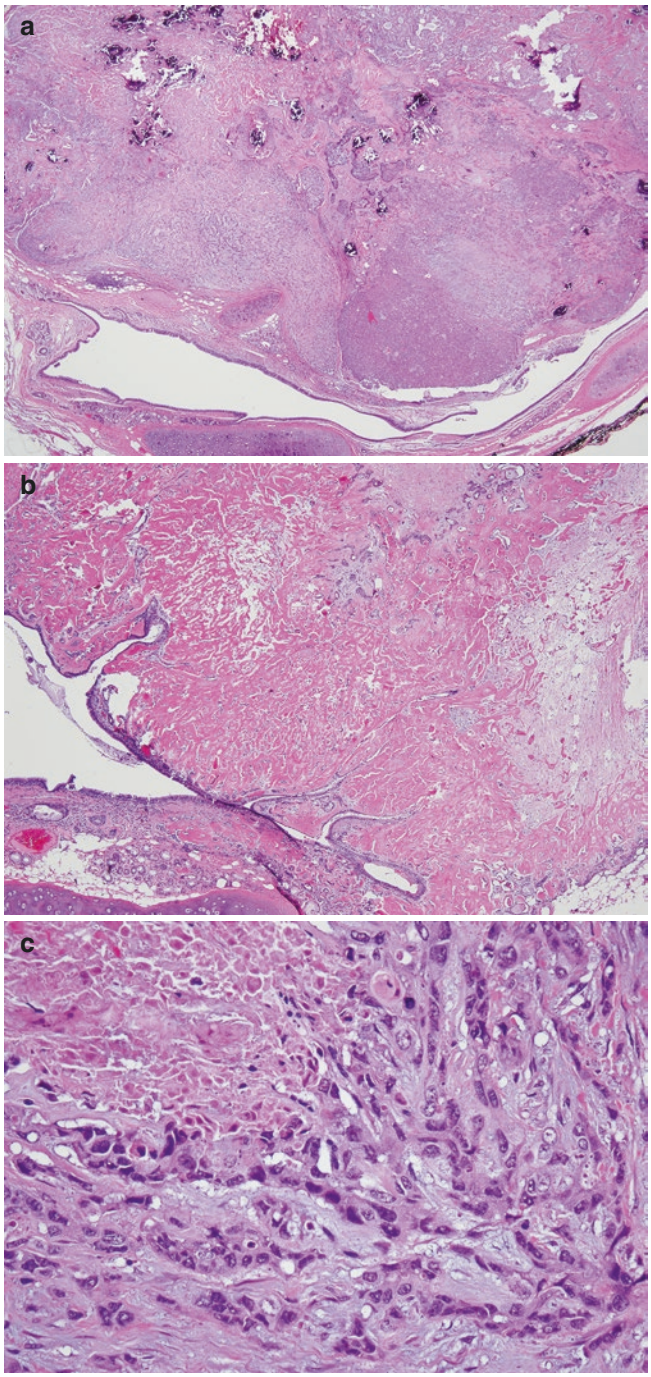

Fig. 12.7 Carcinoma arising in pleomorphic adenoma (carcinoma ex pleomorphic adenoma). (**a**) Low-magnification photomicrograph showing an exophytic endobronchial mass characterized by a combination of epithelium and stroma typical of pleomorphic adenoma. (**b**) Photomicrograph showing that a portion of the tumor comprises epithelial cells, myoepithelial cells, and both hyalinized and chondroid stromata characteristic of pleomorphic adenoma. (**c**) High-magnification photomicrograph showing that elsewhere this heterogeneous tumor demonstrates a population of highly atypical infiltrating carcinoma cells with associated coagulative tumor necrosis

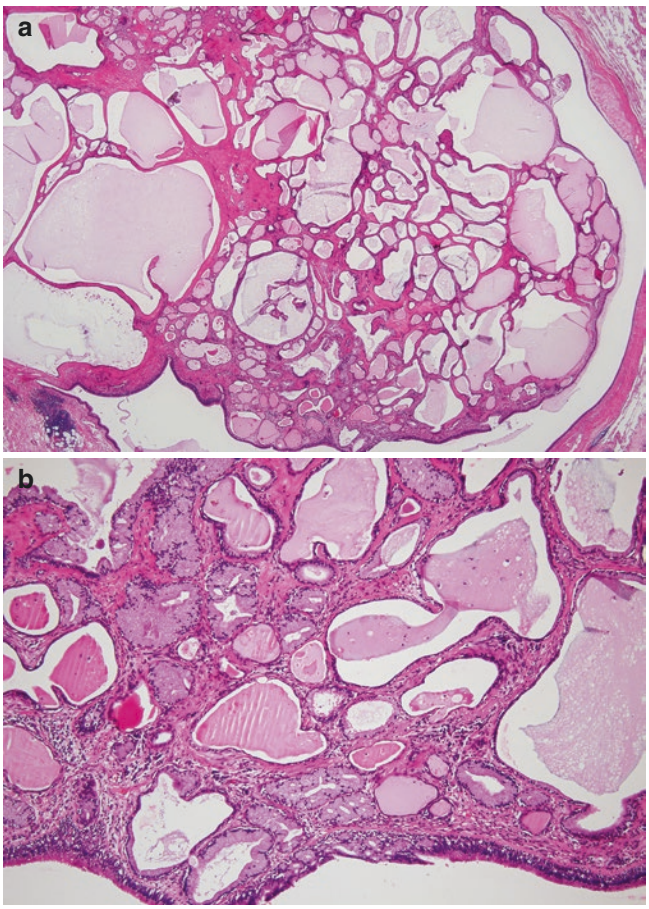

Fig. 12.8 Mucous gland adenoma. (**a**) Low-magnification photomicrograph showing an exophytic endobronchial mass covered by a smooth surface of benign respiratory epithelium without the arborizing papillary architecture of a papilloma. (**b**) Higher-magnification view showing cytologically bland columnar mucinous cells lining glandular and cystic spaces. The cystic spaces show mucinous lakes surrounded by attenuated mucinous epithelial cells

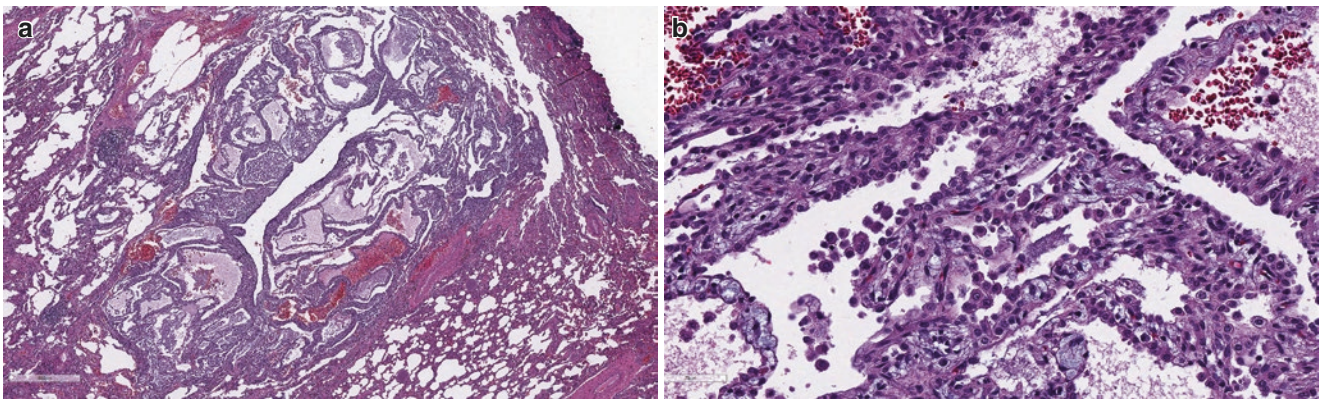

Fig. 12.9 Alveolar adenoma. (**a**) Low-magnification photomicrograph showing a solitary, well-circumscribed non-fluorodeoxyglucose (FDG) avid 1-cm lung tumor made up of a collection of cystic spaces separated by stroma of variable thickness. Some of the cystic spaces contain eosinophilic granular proteinaceous material. (**b**) High-magnification photomicrograph showing the septa separating the cystic spaces. The septa constitute bland mesenchymal spindle cells and occasional mononuclear inflammatory cells lined by surface cuboidal type 2 pneumocytes

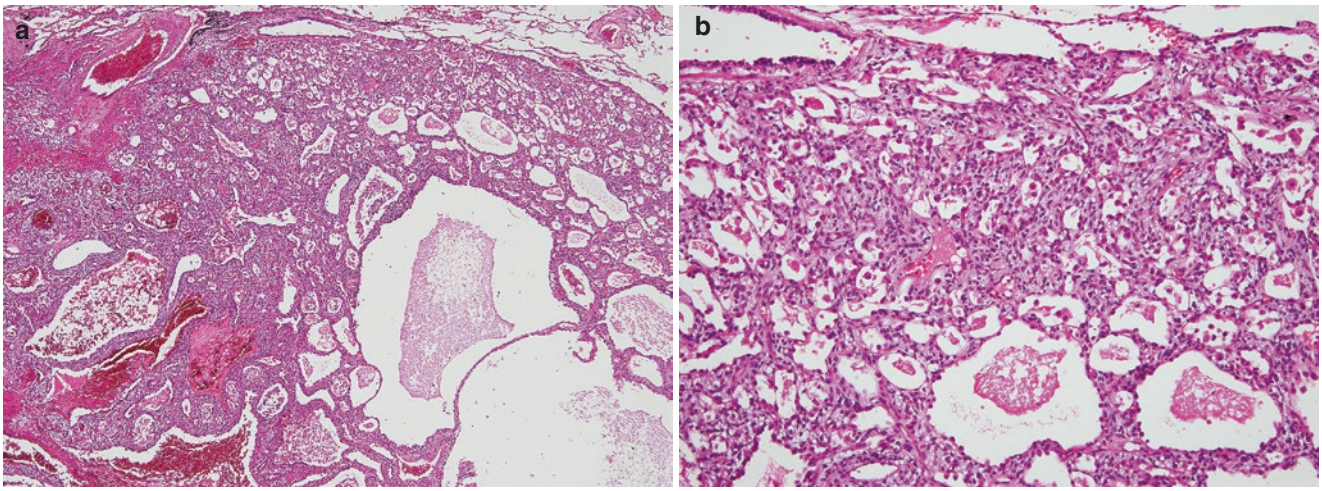

Fig. 12.10 Alveolar adenoma. (**a**) Low-magnification photomicrograph illustrating another example of alveolar adenoma with a sharply circumscribed interface with nonneoplastic lung tissue and cystic spaces partially filled with amorphous proteinaceous debris, macrophages, and procedure-related blood. (**b**) Higher-magnification photomicrograph shows that the cystic spaces are lined by cytologically bland, flattened to cuboidal cells resembling reactive type 2 pneumocytes. The intervening stroma contains cytologically bland oval to spindle cells as well as rare inflammatory cells

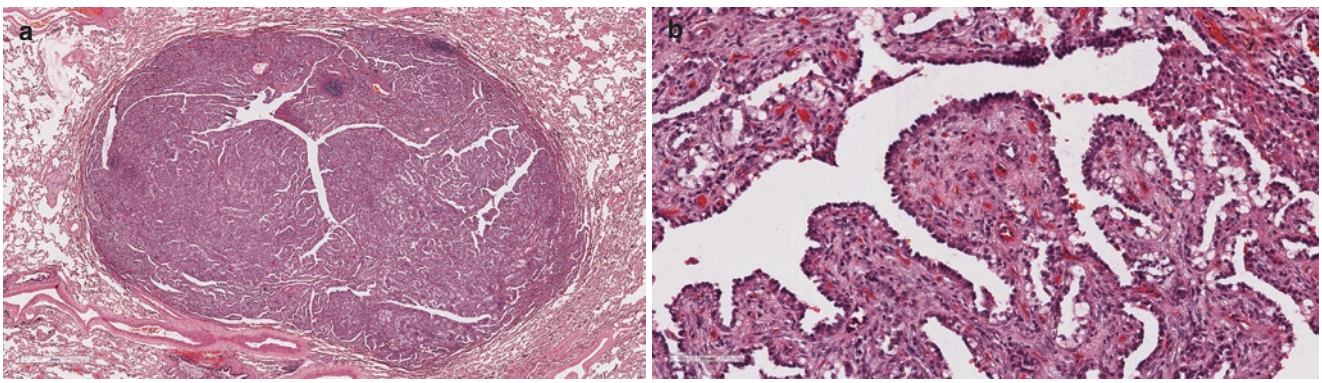

Fig. 12.11 Papillary adenoma. (**a**) Low-magnification photomicrograph shows a solid well-circumscribed peripheral lung tumor that consists of papillary structures containing fibrovascular cores lined by a single layer of epithelium. (**b**) High-magnification photomicrograph showing cuboidal epithelium lining the surface of the fibrovascular cores. The lining epithelial cells resemble reactive type 2 pneumocytes. Nuclear atypia, mitoses, and necrosis are absent

Sclerosing Pneumocytoma

Sclerosing pneumocytoma (Figs. 12.12, 12.13, 12.14, 12.15, 12.16, 12.17, 12.18, 12.19 and 12.20) is a unique form of benign lung neoplasm referred to historically as sclerosing hemangioma because of the blood-filled spaces characteristic of this lesion. Immunohistochemical stains demonstrate a primitive respiratory epithelial thyroid transcription factor 1 (TTF-1)-positive phenotype in the cytologically bland interstitial round cells that are the diagnostic hallmark of this histologically heterogeneous tumor. The key to diagnosis is recognizing a combination of growth patterns (hemorrhagic, solid, sclerotic, papillary) and a biphenotypical population of incorporated nonneoplastic type 2 pneumocytes and lesional round cells. There are anecdotal reports of N1 nodal deposits of sclerosing pneumocytoma but no reports of aggressive behavior or tumor-associated death.

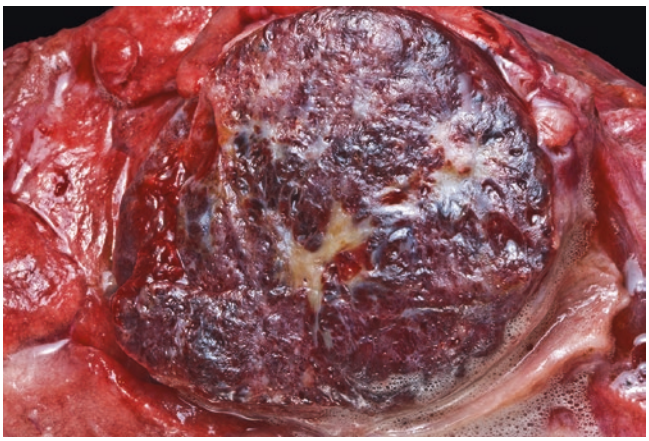

Fig. 12.12 Gross photograph of sclerosing pneumocytoma. Sclerosing pneumocytomas are traditionally solitary and peripherally located in the lung. The tumor is well circumscribed, with a solid and frequently hemorrhagic microcystic cut surface. Solid areas without hemorrhage vary from gray-white to tan in color

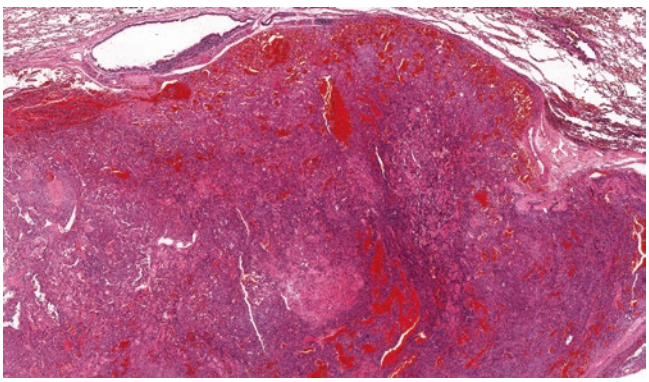

Fig. 12.13 Sclerosing pneumocytoma. Low-magnification photomicrograph shows a well-circumscribed tumor with a variegated pattern, ranging from cystic and hemorrhagic to solid

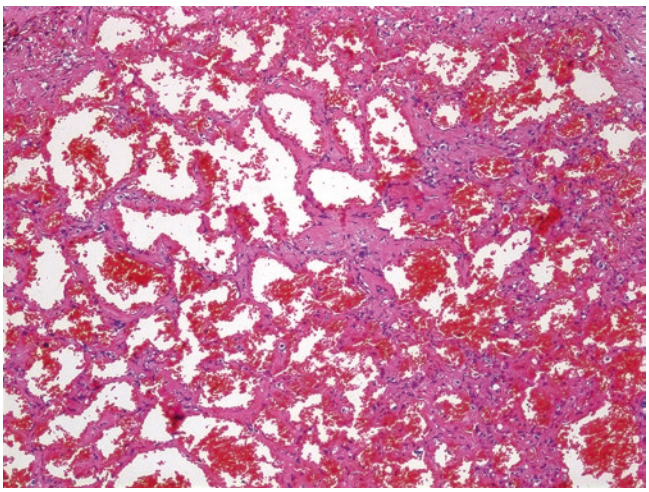

Fig. 12.14 Sclerosing pneumocytoma. Photomicrograph showing an area with prominent hemorrhagic "hemangioma-like" pattern. The tumor forms ectatic spaces filled with blood and separated by sclerotic stroma

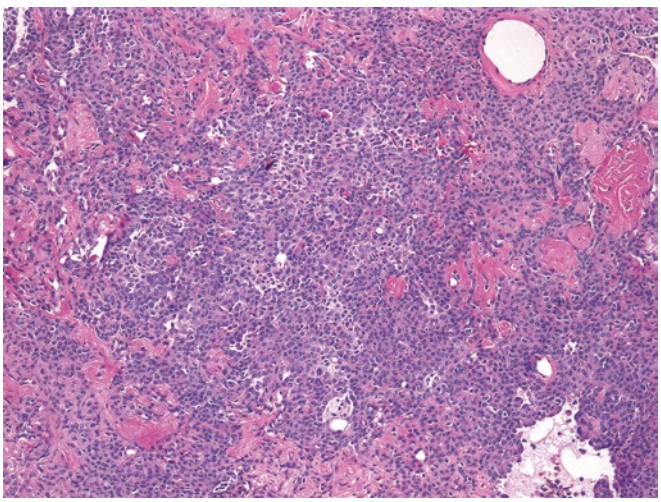

Fig. 12.15 Sclerosing pneumocytoma. Photomicrograph showing an area with solid growth pattern. Tumor cells form solid sheets with scant sclerotic stroma. The tumor cells are round and uniform, with a moderate amount of eosinophilic cytoplasm and small inconspicuous nucleoli. Cytologic atypia and mitoses are absent

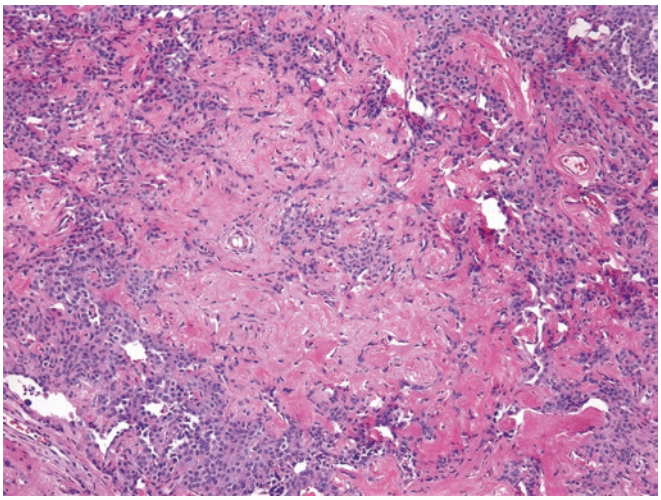

Fig. 12.16 Sclerosing pneumocytoma. Photomicrograph showing a sclerotic area. Dense collagen fibrosis and interstitial round tumor cells are seen

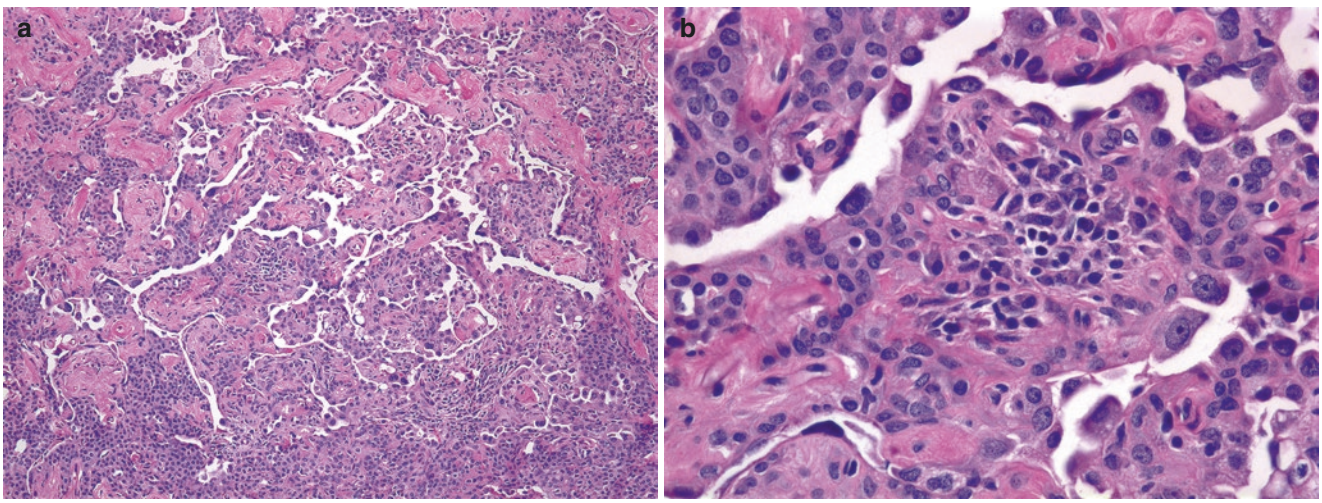

Fig. 12.17 Sclerosing pneumocytoma. (**a**) Photomicrograph showing an area with prominent papillary growth pattern. Type 2 pneumocytes with "reactive" atypia line the surface of sclerotic papillae that show, to varying degrees, associated interstitial round cells. (**b**) High-magnification view showing that papillary structures are covered with surface cuboidal to "hob-nailing" cells with mild cytologic atypia typical of type 2 pneumocytes. Underlying the surface cells are sclerotic connective tissue cores showing both inflammatory and interstitial round tumor cells

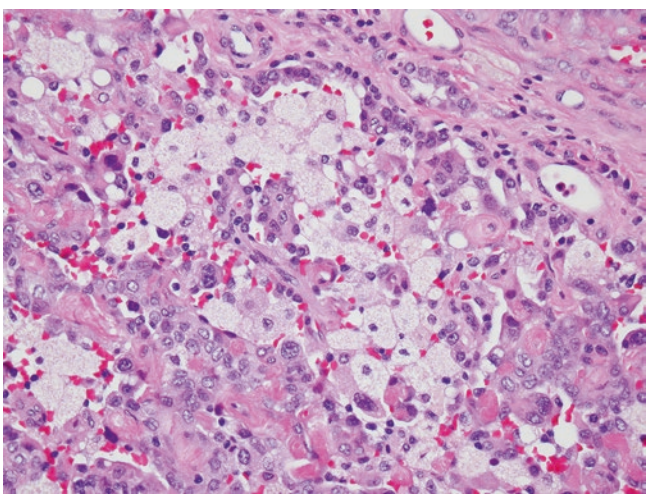

Fig. 12.18 Sclerosing pneumocytoma. High-magnification photomicrograph showing an area with abundant foamy macrophages. This is a common but nonspecific finding in sclerosing pneumocytoma

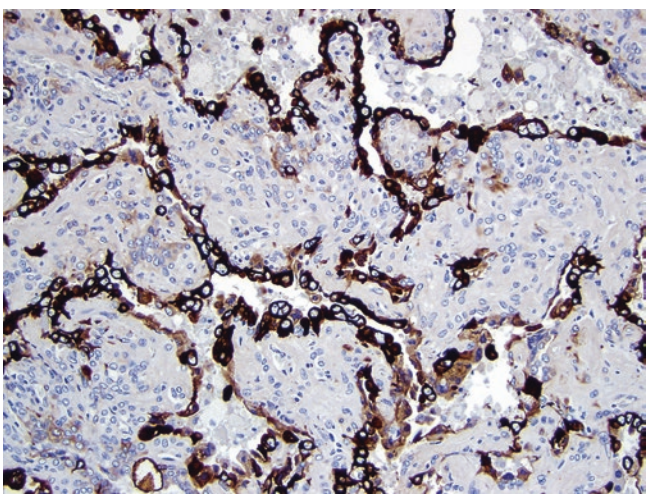

Fig. 12.19 Sclerosing pneumocytoma. Photomicrograph showing a pan-cytokeratin immunohistochemical stain in a papillary area. The surface cells are strongly positive for cytokeratin, whereas the interstitial round cells show only focal weak staining and are frequently negative altogether

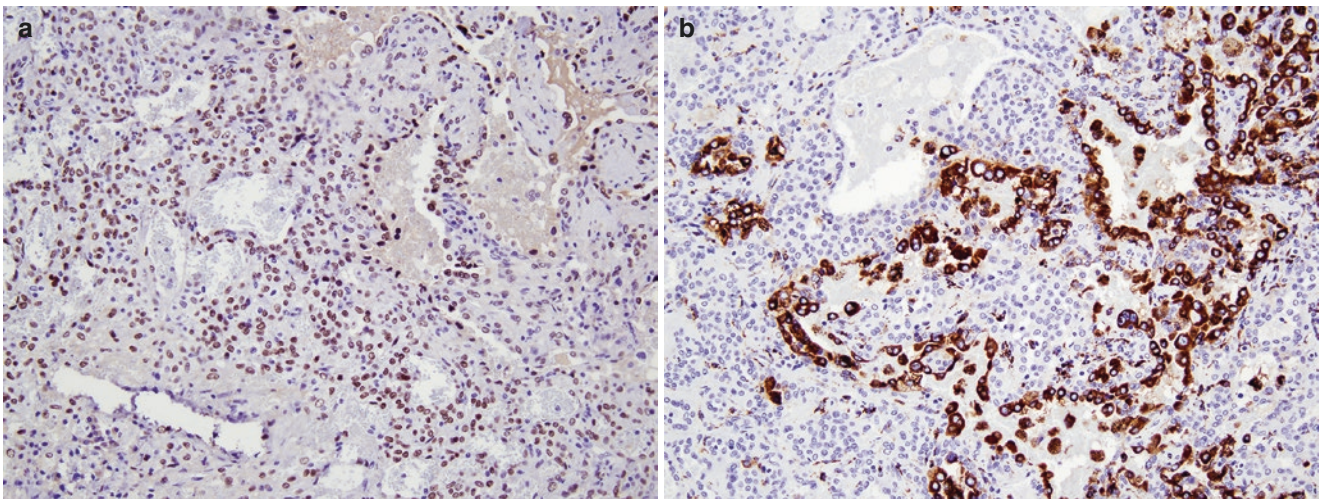

Fig. 12.20 Sclerosing pneumocytoma. (**a**) Photomicrograph showing a TTF-1 immunohistochemical stain in sclerosing pneumocytoma. Both surface cells and interstitial round cells are positive for TTF-1, with relatively stronger staining in the surface cells. (**b**) Photomicrograph showing napsin A immunohistochemical stain in which the surface cells are strongly positive and the interstitial round cells are negative

Hamartoma and Chondroma

Hamartomas (Figs. 12.21, 12.22, 12.23 and 12.24) are the most common benign lung neoplasms in adults. They are true neoplasms consisting of a combination of hyaline cartilage, adipose tissue, smooth muscle cells, and a distinctive fibromyxoid stroma that is often the histologic hallmark of this lesion. Incorporated nonneoplastic respiratory epithelial cells are common and result in a characteristic biphasic appearance. Chondromas (Figs. 12.25 and 12.26), often associated with other features of the Carney triad (i.e., paragangliomas and gastric stromal tumors), differ in being purely cartilaginous lesions with a well-circumscribed interface with nonneoplastic lung parenchyma.

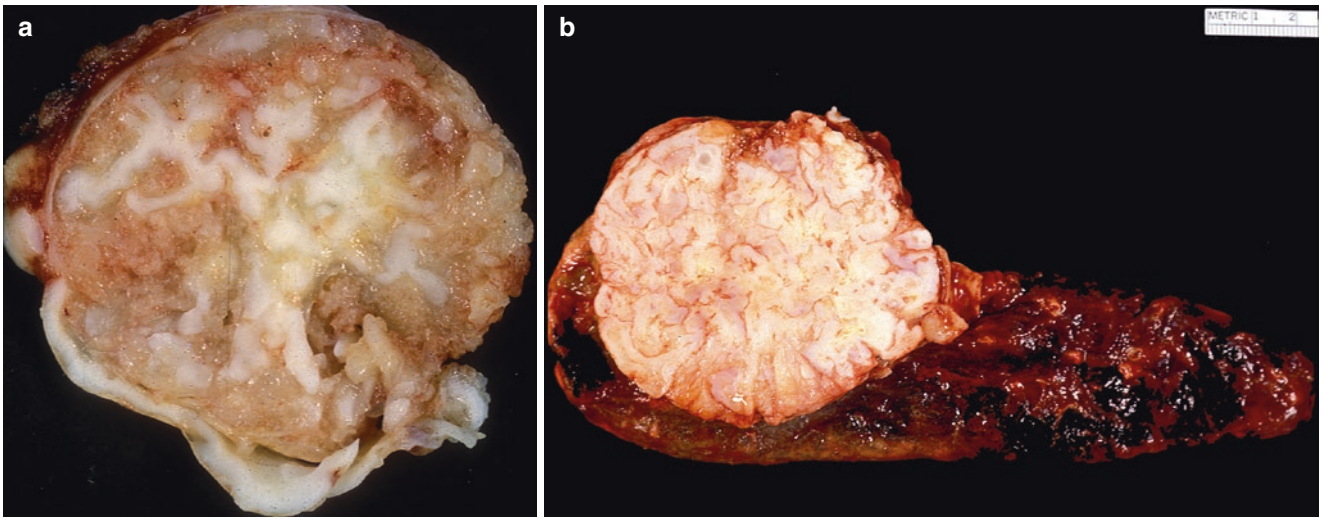

Fig. 12.21 Pulmonary hamartoma. (**a**) Gross photograph shows a well-circumscribed tumor adjacent to a major bronchus. The cut surface is gray-white to yellow-tan in color, with grossly discernable cartilaginous components. (**b**) Gross photograph of another large (7.7 cm) hamartoma showing irregular-shaped spicules of glistening hyaline cartilage separated by yellow soft tissue composed mainly of benign fat

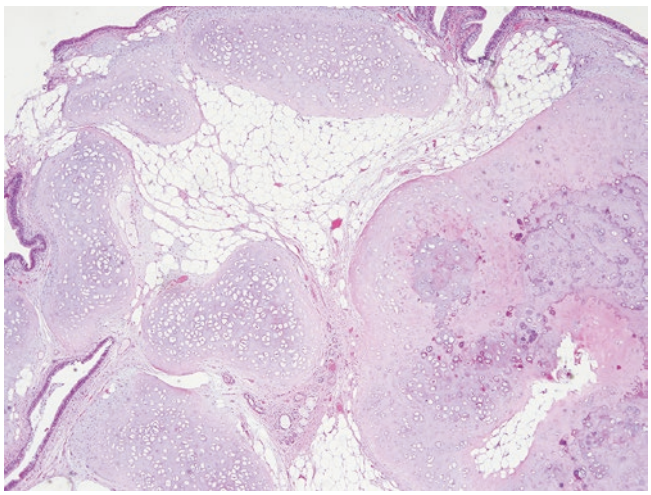

Fig. 12.22 Pulmonary hamartoma. Low-magnification photomicrograph shows a tumor composed predominantly of hyaline cartilage and mature adipose tissue, with a minor component of myxoid loose connective tissue. The clefted spaces lined by respiratory epithelium represent entrapment of normal nonneoplastic structures by the expanding tumor

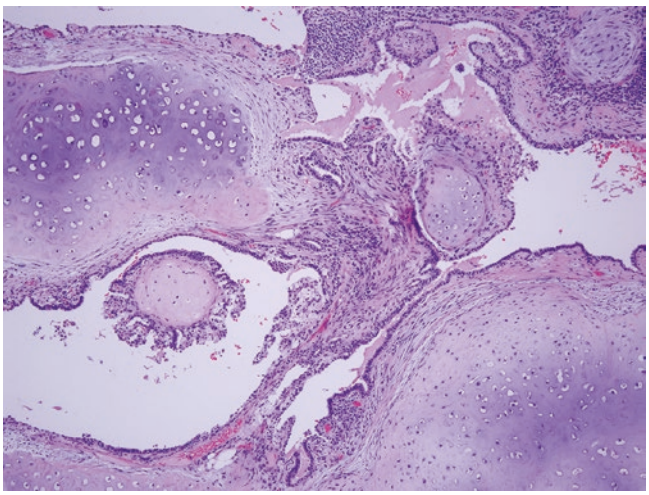

Fig. 12.23 Pulmonary hamartoma. Photomicrograph showing another example of a hamartoma made up of a combination of hyaline cartilage, the pale staining fibromyxoid tissue characteristic of hamartoma, and entrapped, nonneoplastic respiratory epithelial cells

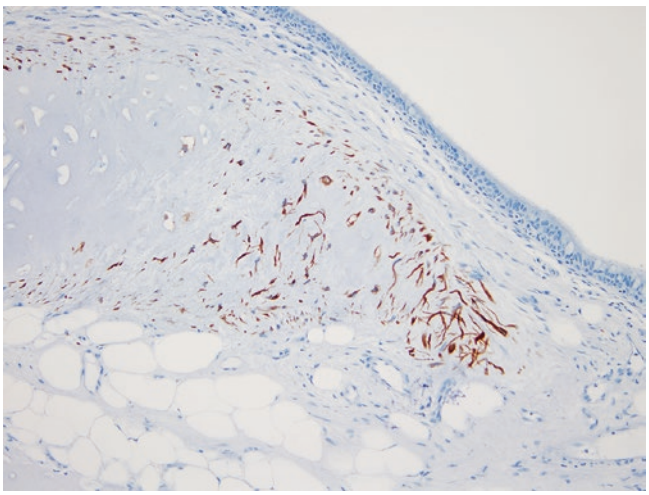

Fig. 12.24 Pulmonary hamartoma. Photomicrograph of an immunohistochemical stain for glial fibrillary acidic protein (GFAP) showing positive staining in hyaline cartilage and peri-cartilaginous fibromyxoid spindle cells. This pattern of GFAP staining is characteristic of hamartomas

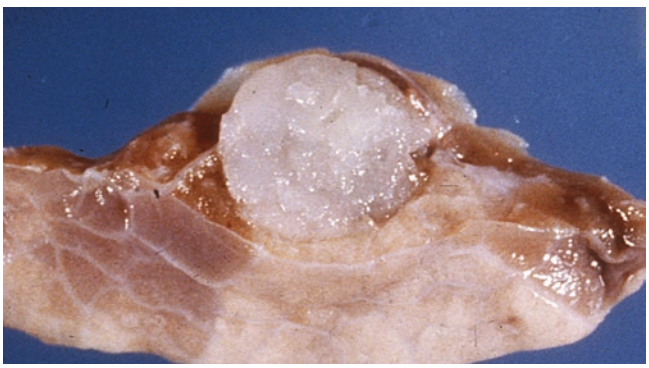

Fig. 12.25 Chondroma. Gross photograph showing a well-circumscribed, lobulated cartilaginous nodule. The cut surface is white and glistening

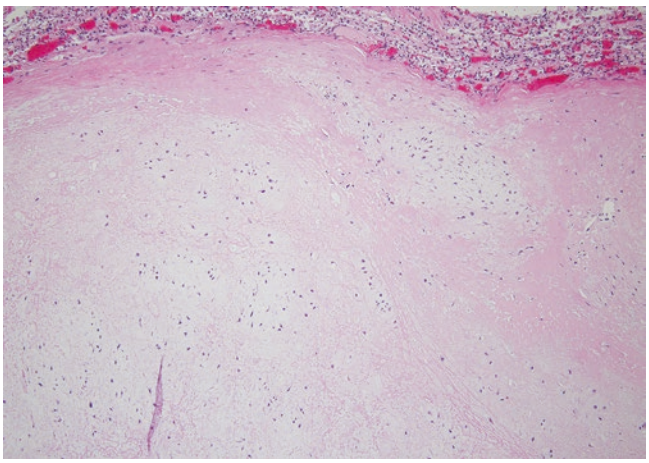

Fig. 12.26 Chondroma. Intermediate magnification photomicrograph shows a well-demarcated tumor composed entirely of hyaline and myxohyaline cartilage. Cytologic atypia is absent. The surrounding lung parenchyma is compressed to form a pseudocapsule

PEComa (Clear Cell "Sugar" Tumor)

PEComa (Figs. 12.27 and 12.28) is the currently preferred WHO terminology for a rare neoplasm referred to historically as clear cell or sugar tumor when it occurred in the lung. Localized PEComatous tumors of the lung are part of a larger family of widely distributed neoplasms thought to arise from perivascular epithelioid cells (PECs). The cytologic, immunophenotypic, and molecular features overlap with lymphangioleiomyomatosis, which is considered a diffuse form of PEComatous lung tumor (*see* Chap. 6). In addition to distinct histologic and cytologic features, PEComas have a unique immunophenotype in that they consistently stain for melanoma-associated proteins (i.e., HMB45, melan-A, and microphthalmia-associated transcription factor [MITF]).

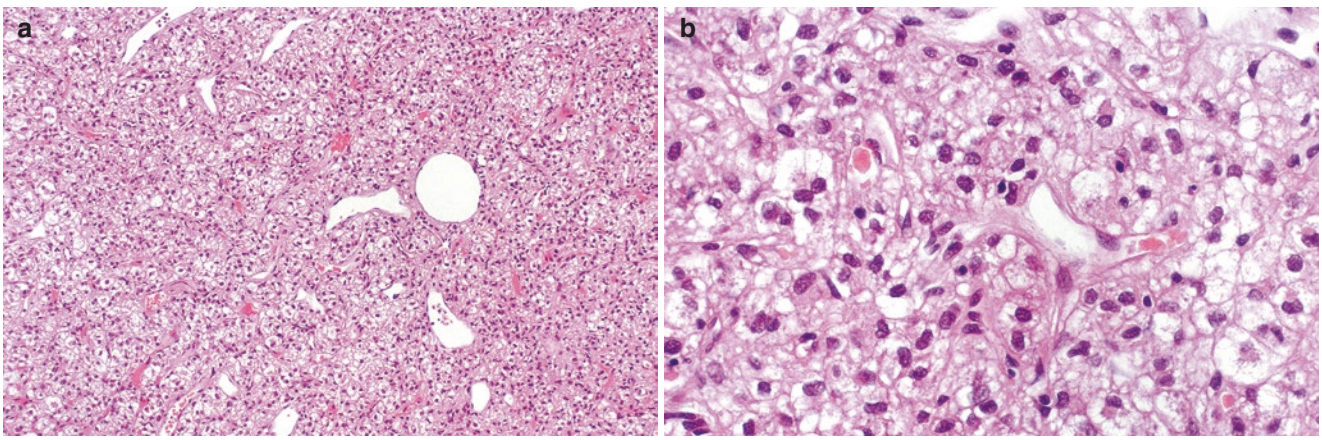

Fig. 12.27 PEComa (clear cell "sugar" tumor). (**a**) Photomicrograph showing tumor cells with clear to pale finely vacuolated cytoplasm forming solid nests separated by thin-walled sinusoidal vessels. (**b**) High-magnification photomicrograph shows rounded tumor cells with abundant clear or pale eosinophilic cytoplasm, mild variation of nuclear size, and occasional small nucleoli. Necrosis and mitoses are absent. Tumor cells were positive for HMB45 and S100 and negative for cytokeratins (not shown)

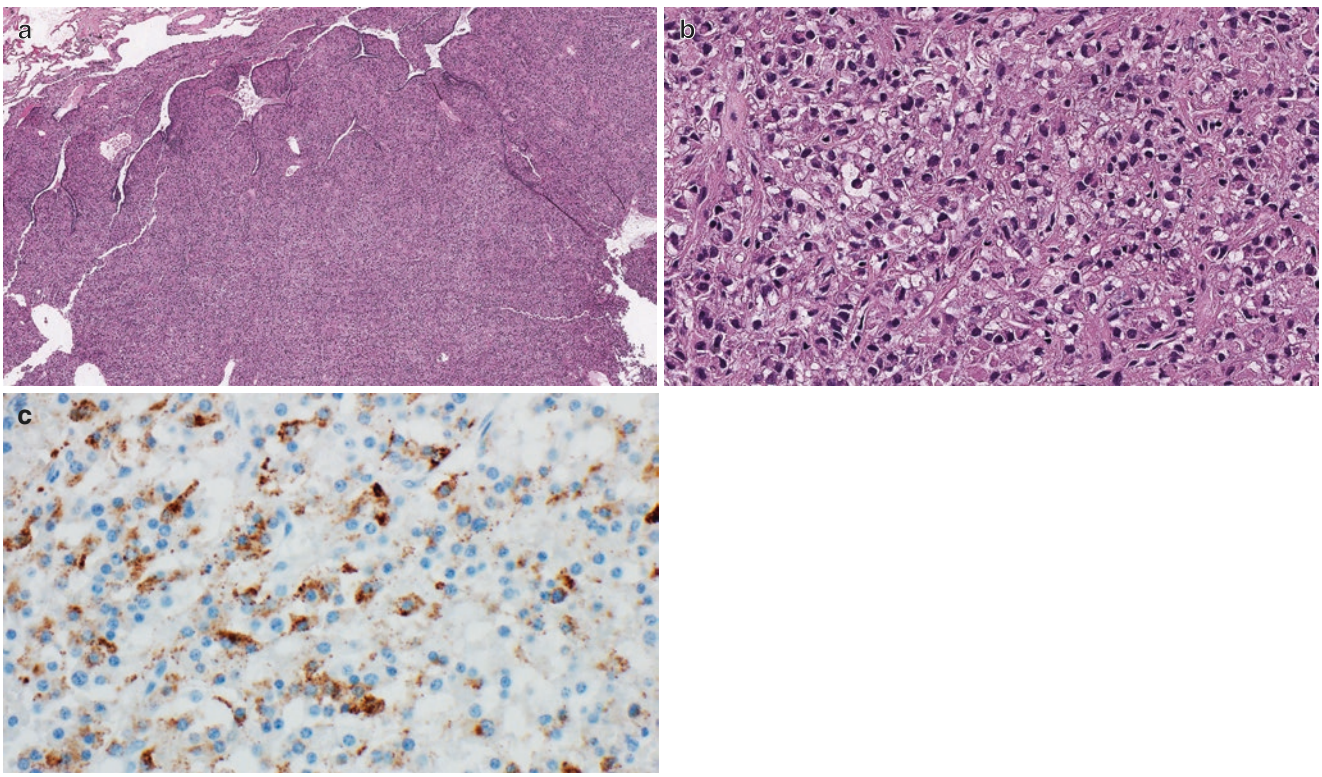

Fig. 12.28 PEComa (clear cell "sugar" tumor). (**a**) Low-magnification photomicrograph showing unencapsulated interface with nonneoplastic lung parenchyma and associated entrapment of nonneoplastic respiratory epithelium. (**b**) High-magnification photomicrograph showing cytologically bland cells with pale-staining eosinophilic to clear cytoplasm and mild anisonucleosis. The cells are arranged in a compact nested growth pattern. No mitotic figures or necrosis is seen. (**c**) Photomicrograph showing patchy staining for HMB45 in PEComa (clear cell "sugar" tumor)

Granular Cell Tumor

Granular cell tumors (Fig. 12.29) are extremely rare as primary lung neoplasms, typically presenting as small sessile or pedunculated endobronchial masses that may cause airway obstruction. All reported examples behaved in a benign fashion and were successfully managed with conservative complete excision. Like their soft tissue counterparts, granular cell tumors of the lung are positive for S100 protein.

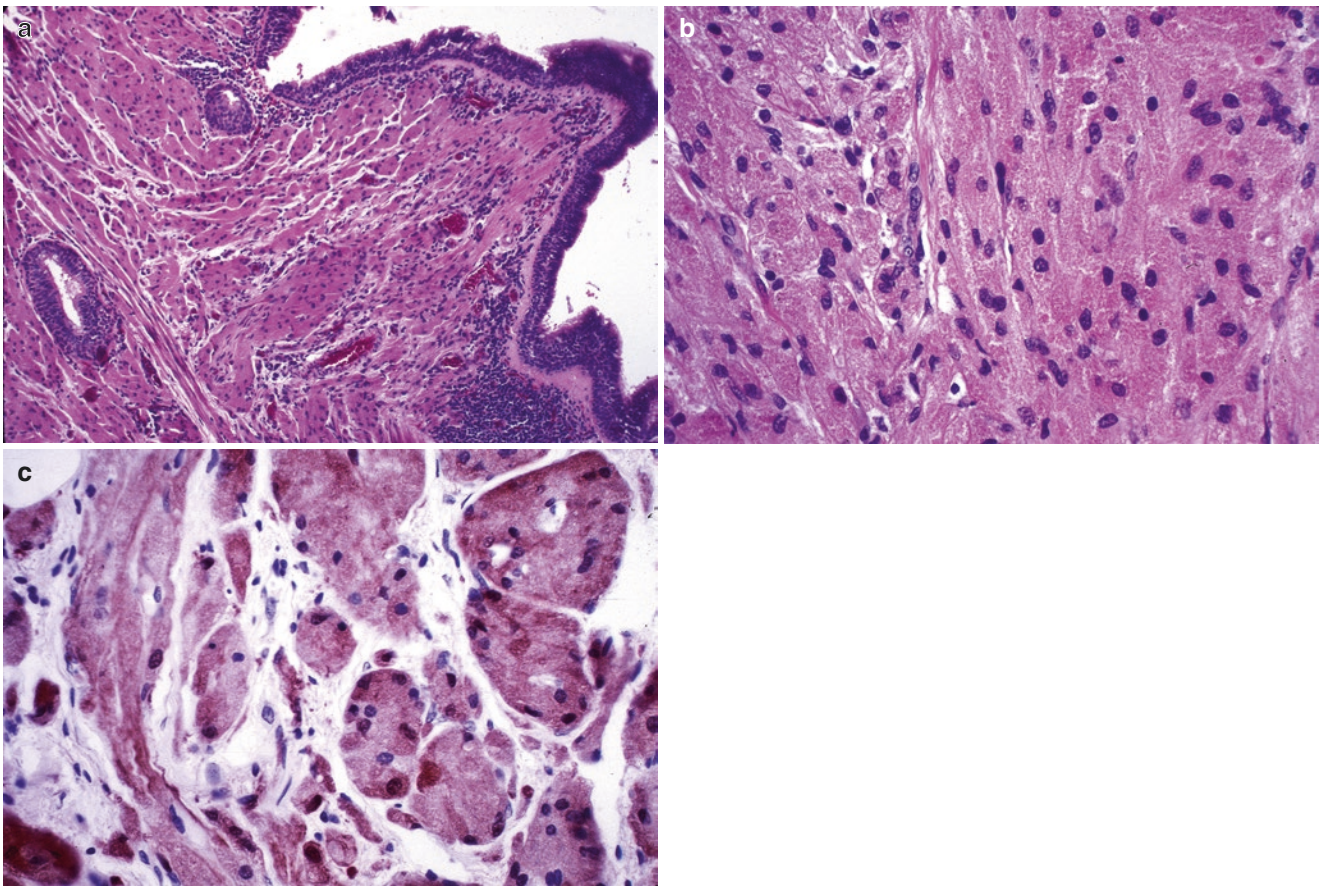

Fig. 12.29 Granular cell tumor. (**a**) Photomicrograph showing neoplastic granular cells infiltrating bronchial mucosa and submucosa without destruction of submucosal glands. Although lacking in this example, the overlying bronchial epithelium often shows a combination of squamous metaplasia and pseudo-epitheliomatous hyperplasia. (**b**) High-magnification photomicrograph showing large spindled and epithelioid cells with small, hyperchromatic, eccentrically located nuclei and abundant granular eosinophilic cytoplasm. (**c**) High-magnification photomicrograph showing strong cytoplasmic staining for S100 protein

Pneumocytic Adenomyoepithelioma

Pneumocytic adenomyoepithelioma (Figs. 12.30 and 12.31) is a rarely reported peripheral lung neoplasm that typically presents as an asymptomatic solitary lung nodule measuring less than 3 cm in greatest dimension. Of the few reported patients, none have suffered recurrence or metastases after complete surgical excision. Histologically these unique tumors resemble salivary gland neoplasms with mixed epithelial and myoepithelial differentiation; however, they differ in having a TTF-1-positive epithelial component.

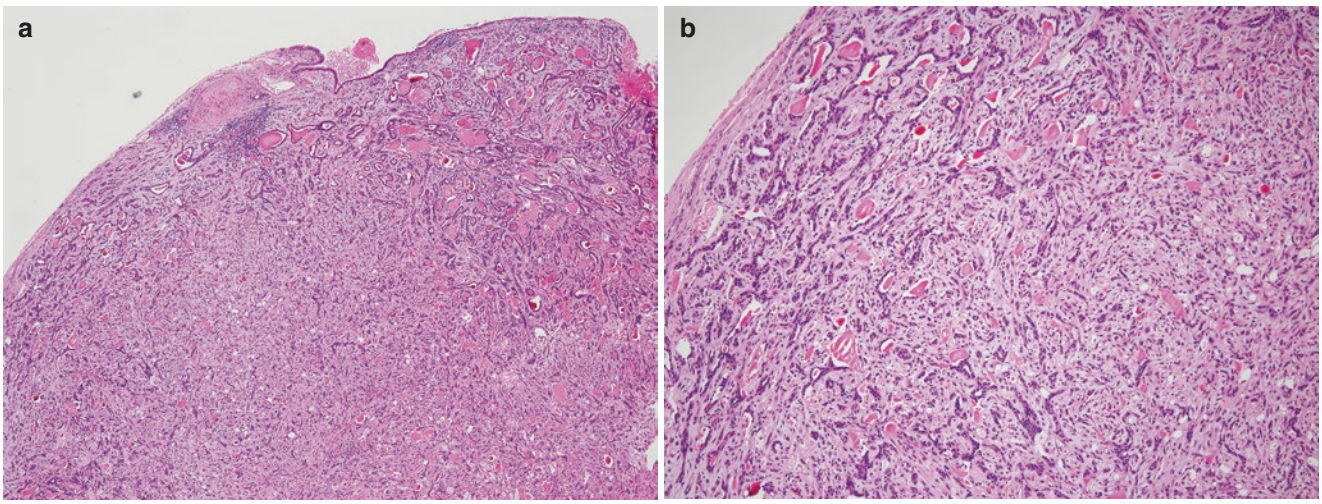

Fig. 12.30 Pneumocytic adenomyoepithelioma. (**a**) Low-magnification photomicrograph showing a circumscribed mixed epithelial and spindle cell tumor resembling pleomorphic adenoma. (**b**) Higher-magnification view shows a combination of epithelial cells, some of which form glandular spaces containing colloid-like secretions and blunt spindled cells

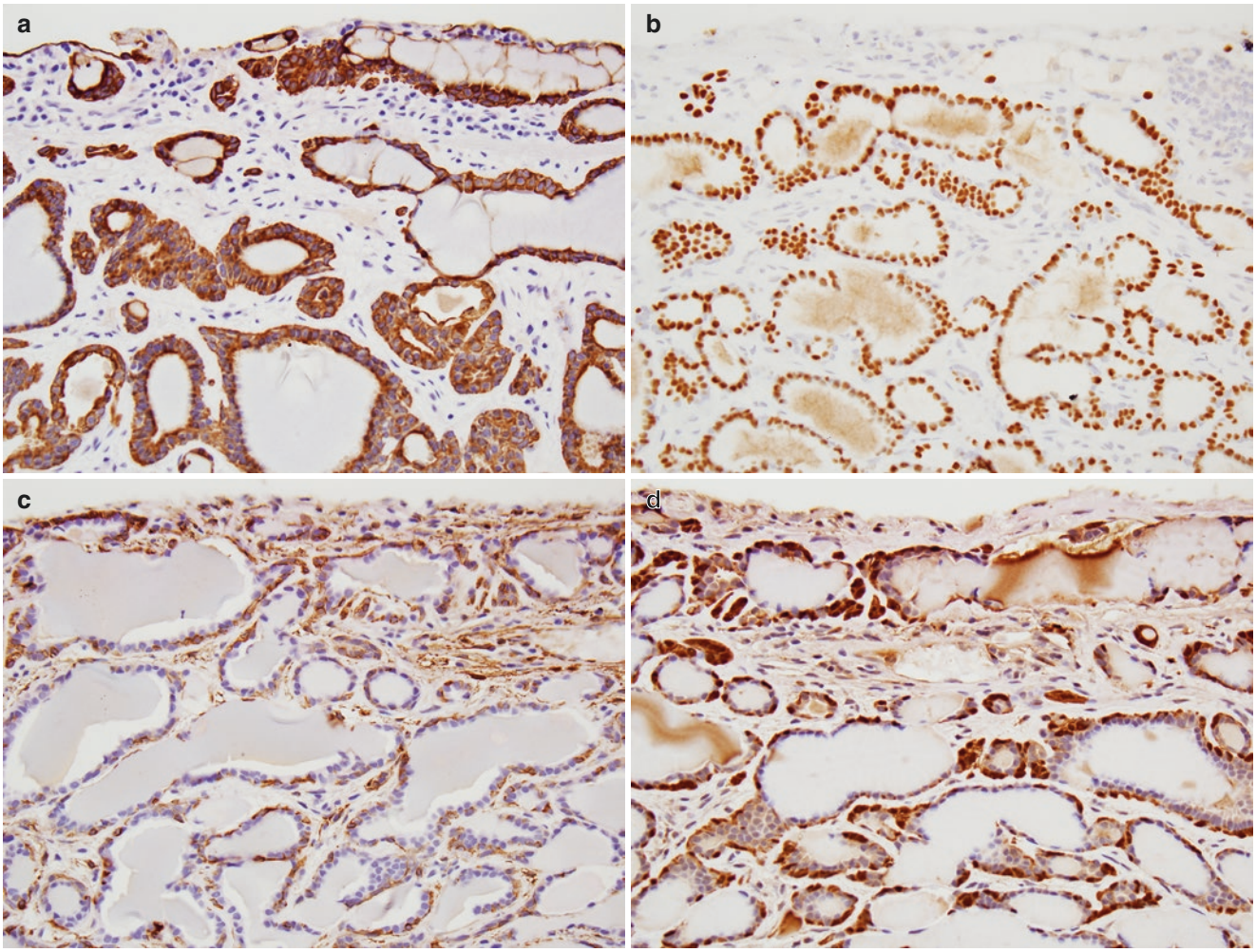

Fig. 12.31 Pneumocytic adenomyoepithelioma. High-magnification photomicrographs of the tumor illustrated in Fig. 12.30 showing a population of cytokeratin (**a**) and TTF-1 (**b**)-positive epithelial cells affiliated with a population of smooth muscle actin (**c**) and S100 (**d**)-positive myoepithelial cells

Suggested Reading

Abiko T, Koizumi S, Takanami I, Tanaka F. 18F-FDG-PET/CT findings in primary pulmonary mixed squamous cell and glandular papilloma. Ann Nucl Med. 2001;25:227–9.

Boukhris AA, Baccari S, Kamoun NS, Belhabib D, Horchani H, Kilani T. Pulmonary papillary adenoma: report of two cases. Ann Pathol. 2002;22:497–8.

Cavazz A, Paci M, De Marco L, Leporati G, Sartori G, Bigiani N, et al. Alveolar adenoma of the lung: a clinicopathologic, immunohistochemical, and molecular study of an unusual case. Int J Surg Pathol. 2004;12:155–9.

Chang T, Husain AN, Colby T, Taxy JB, Welch WR, Cheung OY, et al. Pneumocytic adenomyoepithelioma: a distinctive lung tumor with epithelial, myoepithelial, and pneumocytic differentiation. Am J Surg Pathol. 2007;31:562–8.

van den Bosch JM, Wagenaar SS, Corrin B, Elbers JR, Knaepen PJ, Westermann CJ. Mesenchymoma of the lung (so called hamartoma): a review of 154 parenchymal and endobronchial cases. Thorax. 1987;42:790–3.

England DM, Hochholzer L. Truly benign bronchial adenoma. Report of 10 cases of mucous gland adenoma with immunohistochemical and ultrastructural findings. Am J Surg Pathol. 1995;19:887–9.

Flieder DB, Koss MN, Nicholson A, Sesterhenn IA, Petras RE, Travis WD. Solitary pulmonary papillomas in adults: a clinicopathologic and in situ hybridization study of 14 cases combined with 27 cases in the literature. Am J Surg Pathol. 1998;22:1328–42.

Inamura K, Kumasaka T, Furuta R, Shimada K, Hiyama N, Furuhata Y, et al. Mixed squamous cell and glandular papilloma of the lung: a case study and literature review. Pathol Int. 2011;61:252–8.

Kozu Y, Maniwa T, Ohde Y, Nakajima T. A solitary mixed squamous cell and glandular papilloma of the lung. Ann Thorac Cardiovasc Surg. 2012;20(Suppl):625–8.

Larson DA, Derkay CS. Epidemiology of recurrent respiratory papillomatosis. APMIS. 2010;118:450–4.

Liu L, Aesif SW, Kipp BR, Voss JS, Daniel S, Aubry MC, Boland JM. Ciliated muconodular papillary tumors of the lung can occur in western patients and show mutations in BRAF and AKT1. Am J Surg Pathol. 2016;40:1631–6.

McNamee C, Lien D, Puttagunta L, Conlan AA. Solitary squamous papillomas of the bronchus: a case report and literature review. J Thorac Cardiovasc Surg. 2003;126:861–3.

Popper HH, Wirnsberger G, Juttner-Smolle FM, Pongratz MG, Sommersgutter M. The predictive value of human papilloma virus (HPV) typing in the prognosis of bronchial squamous cell papillomas. Histopathology. 1992;21:323–30.

Popper HH, el-Shabrawi Y, Wockel W, Hofler G, Kenner L, Juttner-Smolle FM, et al. Prognostic importance of human papilloma virus typing in squamous cell papilloma of the bronchus: comparison of in situ hybridization and the polymerase chain reaction. Hum Pathol. 1994;25:1191–7.

Rodriguez FJ, Aubry MC, Tazelaar HD, Slezak J, Carney JA. Pulmonary chondroma: a tumor associated with carney triad and different from pulmonary hamartoma. Am J Surg Pathol. 2007;31:1844–53.

Ruan SY, Chen KY, Yang PC. Recurrent respiratory papillomatosis with pulmonary involvement: a case report and review of the literature. Respirology. 2009;14:137–40.

Toomes H, Delphendahl A, Manke HG, Vogt-Moykopf I. The coin lesion of the lung. A review of 955 resected coin lesions. Cancer. 1983;51:534–7.

Lung Carcinoma

13

Chen Zhang and Jeffrey L. Myers

The classification and diagnostic criteria for lung carcinoma, the deadliest cancer in humans, undergo periodic updates. The 2015 World Health Organization (WHO) classification highlights changes in several categories of lung cancer, especially in the classification of adenocarcinomas and large cell carcinomas. For example, the clinically familiar term bronchioloalveolar carcinoma was discontinued and replaced with adenocarcinoma in situ and the related categories of minimally invasive and lepidic-predominant adenocarcinoma. Most of the tumors classified historically as mucinous bronchioloalveolar carcinomas are now considered invasive mucinous carcinomas. Basaloid carcinoma and large cell neuroendocrine carcinomas are separated as entities distinct from large cell carcinoma. In addition, immunophenotyping was introduced as an important criterion for phenotyping poorly differentiated non-small cell carcinomas, especially in small biopsies.

C. Zhang (✉)
Department of Pathology and Laboratory Medicine, Indiana University School of Medicine, Indianapolis, IN, USA
e-mail: chenzhan@iupui.edu

J. L. Myers
Department of Pathology, Michigan Medicine, Ann Arbor, MI, USA
e-mail: myerjeff@med.umich.edu

© Springer Science+Business Media, LLC, part of Springer Nature 2018
C. Zhang, J. L. Myers (eds.), *Atlas of Lung Pathology*, Atlas of Anatomic Pathology,
https://doi.org/10.1007/978-1-4939-8689-7_13

Adenocarcinoma

Preinvasive (Atypical Adenomatous Hyperplasia and Adenocarcinoma In Situ)

Atypical Adenomatous Hyperplasia

Atypical adenomatous hyperplasia (Fig. 13.1) is a small (no more than 5 mm in greatest dimension), localized proliferation of mildly atypical type 2 pneumocytes and/or Clara cells distributed along alveolar septa without invasion. It is usually an incidental microscopic finding.

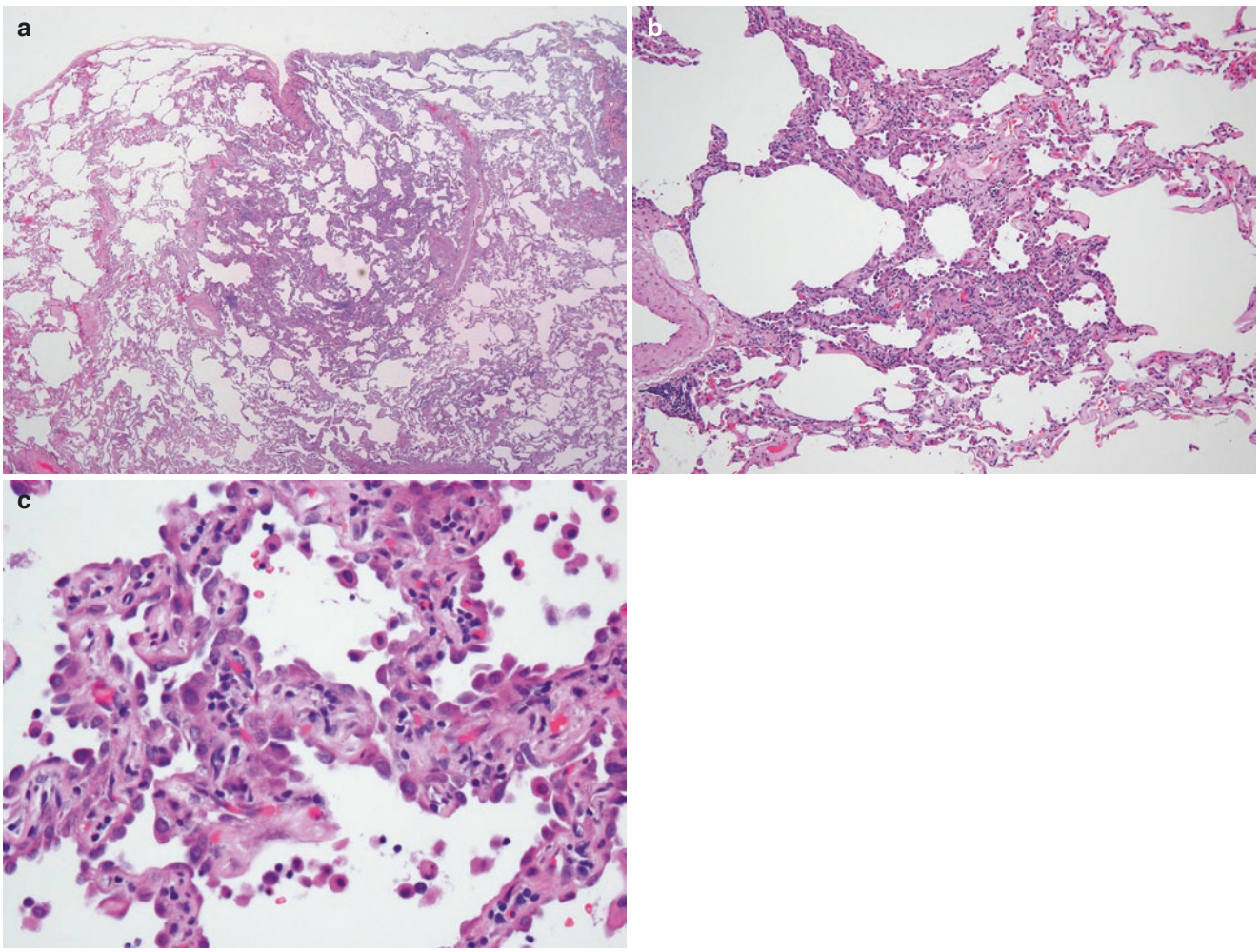

Fig. 13.1 Atypical adenomatous hyperplasia. (**a**) Low-magnification photomicrograph shows a small (2-mm) localized lesion. Compared to normal lung parenchyma, the lesion shows slightly thickened alveolar septa and atypical pneumocyte hyperplasia along the septa. The alveolar lung architecture is preserved, and there is no invasive component. (**b**) Higher magnification of area illustrated in **a** showing interface between atypical adenomatous hyperplasia (above) and normal lung (below). The former is characterized by thickening of alveolar septa and a proliferation of mildly atypical pneumocytes. (**c**) High-magnification view highlighting the atypical cells characterized by enlarged nuclei but with a very orderly single-cell layer without nuclear crowding or tufting. These atypical cells are positive for TTF-1 (not shown)

Adenocarcinoma In Situ

Adenocarcinoma in situ (Figs. 13.2, 13.3 and 13.4), formerly known as bronchioloalveolar carcinoma, is defined as a small (no more than 3 cm in greatest dimension) localized well-differentiated adenocarcinoma that grows along the pre-existing alveolar structure without invasion. There should also be no micropapillary component and/or detached tumor cells present away from the main tumor mass, a phenomenon referred to as spread through air spaces (STAS). Most adenocarcinomas in situ constitute nonmucinous columnar cells. Pure mucinous adenocarcinomas in situ without an invasive component are very rare.

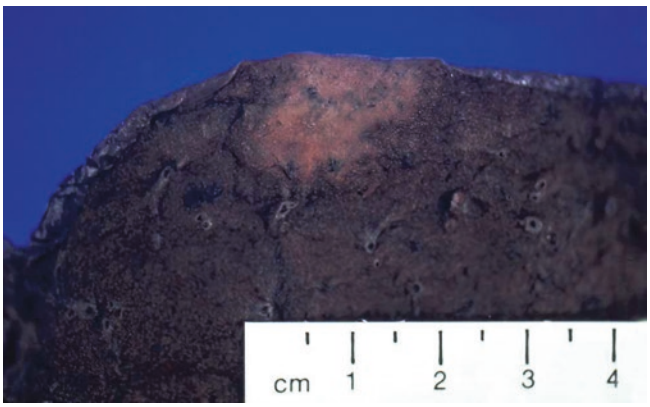

Fig. 13.2 Adenocarcinoma in situ. Gross photograph shows a 2-cm, poorly defined tan nodular lesion beneath the pleura. These lesions are commonly described as ground-glass opacities on chest CT scan

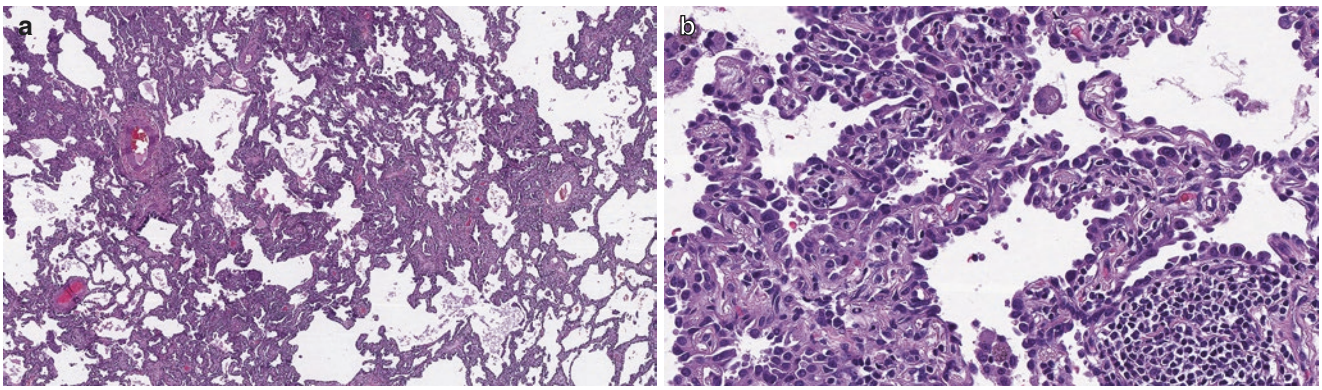

Fig. 13.3 Nonmucinous adenocarcinoma in situ. (**a**) Low-magnification photomicrograph shows a nonmucinous epithelial tumor growing along the preserved but thickened alveolar septa; no invasive foci are seen. (**b**) High-magnification view shows crowded tumor cells with hyperchromatic nuclei and occasional small nucleoli. Tumor cells grow along alveolar septa in a lepidic growth pattern without invasion

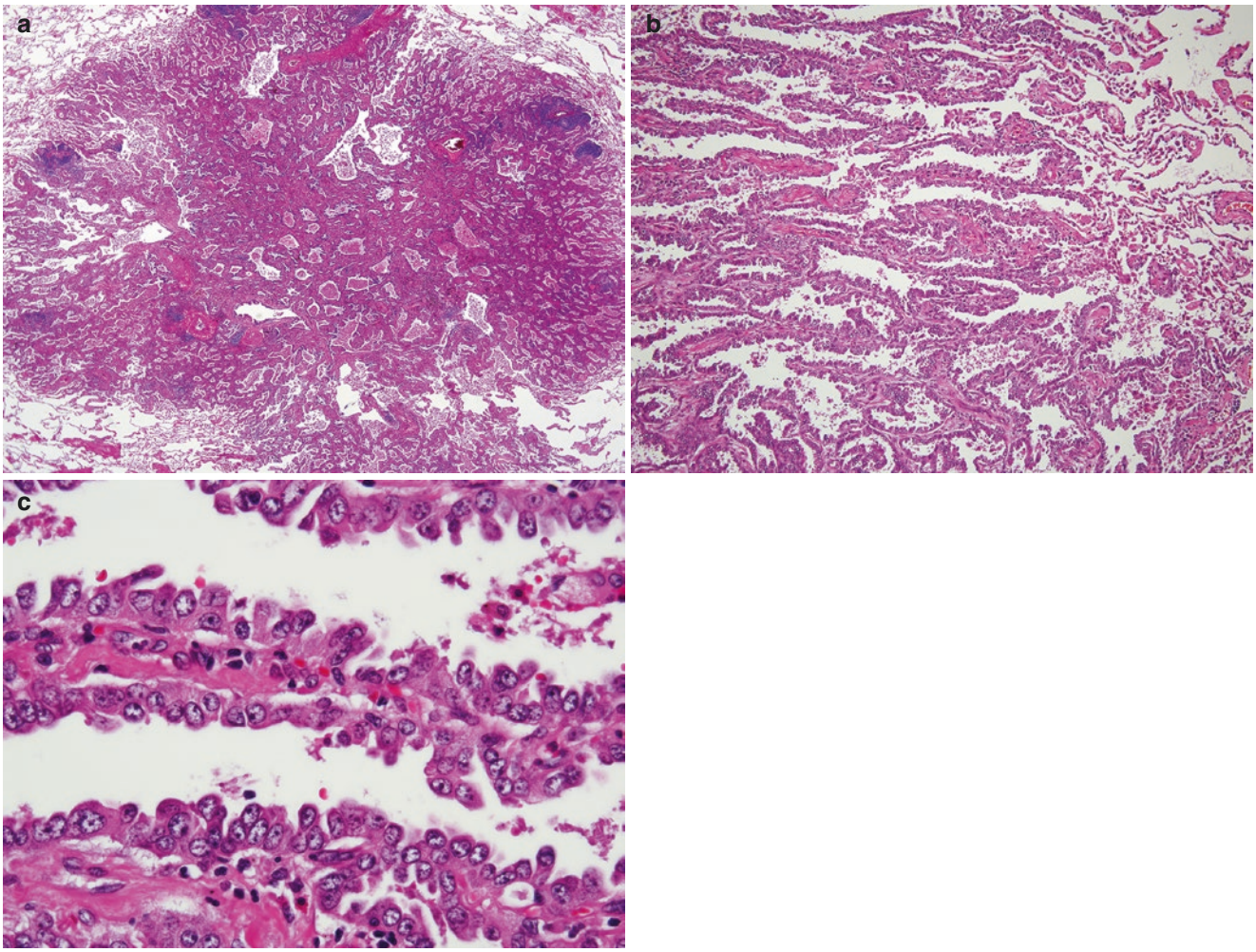

Fig. 13.4 Nonmucinous adenocarcinoma in situ. (**a**) Low-magnification view of another small (1.1 cm) adenocarcinoma in situ in which thickened but intact interstitial structures are lined by a population of atypical nonmucinous columnar cells. (**b**) Intermediate-magnification photomicrograph showing the interface between adenocarcinoma in situ and normal lung (right). (**c**) High-magnification view showing more rounded, cuboidal, and hobnail cells with a higher degree of cytologic atypia as evidenced by nuclear enlargement, anisonucleosis, and relatively scant cytoplasm

Minimally Invasive Adenocarcinoma

Minimally invasive adenocarcinoma (Figs. 13.5 and 13.6) is a small (no more than 3 cm in greatest dimension), solitary adenocarcinoma with a predominantly lepidic growth pattern and minimal invasion that measures no more than 5 mm in greatest dimension. The invasive component is most commonly an acinar subtype but can be any other subtype or variant. For all adenocarcinomas that have a prominent lepidic component comprising nonmucinous columnar cells, the current AJCC or *American Joint Committee on Cancer Staging Manual*, 8th edition, indicates that only the invasive component should be used for pT classification. Small (total gross tumors no more than 3 cm in greatest dimension) stage I adenocarcinomas in which a lepidic component consists of at least 50% of the cross-sectional area and in which there are no other histologic findings to suggest a more aggressive potential, such as angiolymphatic or visceral pleural invasion, a micropapillary component, spread through air spaces (STAS), and/or close parenchymal margins if less than lobectomy is performed, have the same excellent prognosis as adenocarcinoma in situ and minimally invasive adenocarcinomas.

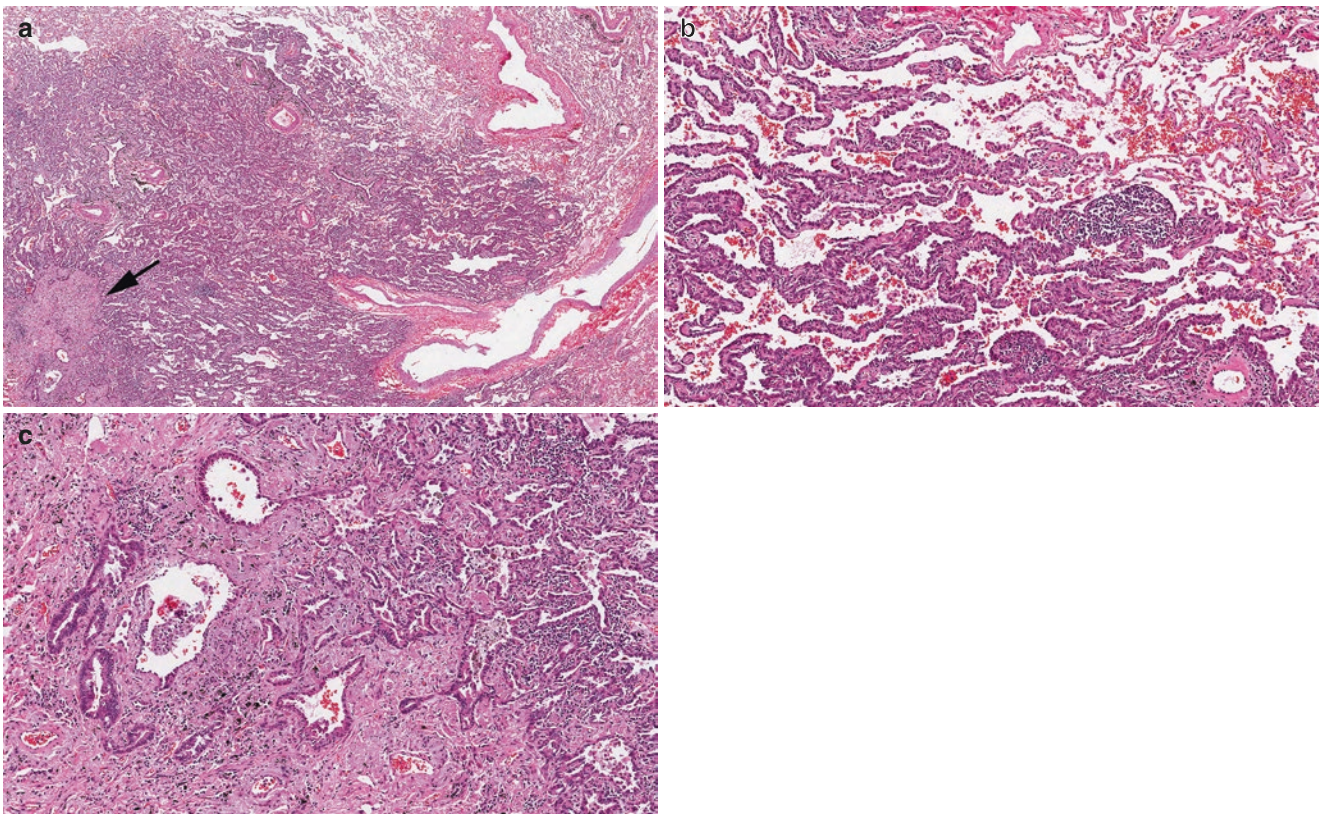

Fig. 13.5 Minimally invasive adenocarcinoma. (**a**) Low-magnification photomicrograph shows a small localized lesion (<3 cm) with a predominantly lepidic growth pattern and a small (<5 mm) focus of invasion (*arrow*). (**b**) Higher-magnification view of the noninvasive component in which tumor cells grow along intact alveolar septa in a lepidic pattern. (**c**) Photomicrograph showing the invasive component. The scarred area shows a small focus (<5 mm) of invasive adenocarcinoma, acinar type. The invasive component consists of small angulated glands inciting a myofibroblastic ("desmoplastic") stromal response. The tumor should be classified as a lepidic-predominant adenocarcinoma when the invasive component measures more than 5 mm

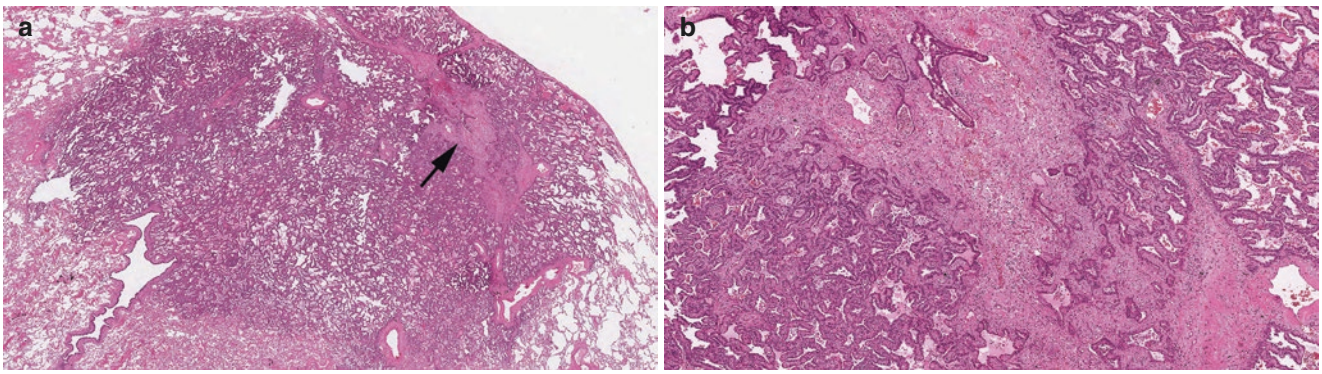

Fig. 13.6 Minimally invasive adenocarcinoma. (**a**) Low-magnification view of another example of a minimally invasive adenocarcinoma in which most of this small (just over 1 cm) peripheral, subpleural tumor has a lepidic growth pattern except for a small area of invasion in an area of scarring (*arrow*). (**b**) Photomicrograph showing the invasive component that measures only 4 mm and demonstrates features similar to those illustrated and described in Fig. 13.5c

Invasive Adenocarcinoma

Invasive adenocarcinoma (Figs. 13.7, 13.8, 13.9, 13.10, 13.11, 13.12, 13.13, 13.14, 13.15, 13.16 and 13.17) is a malignant epithelial tumor with glandular differentiation, mucin production, and/or immunohistochemical stains showing pneumocyte marker expression (i.e., TTF-1 and/or napsin A). In the 2015 WHO classification for resected tumors (*The 2015 World Health Organization Classification of Lung Tumors*), invasive adenocarcinomas are classified according to the predominant growth pattern or as a specific variant (Table 13.1). While the WHO recommends cataloguing all growth patterns identified in an adenocarcinoma in 5% increments, there is no proven clinical usefulness to this practice. Selecting the predominant pattern can be helpful in separating invasive adenocarcinomas into prognostically useful subsets as summarized in Table 13.2.

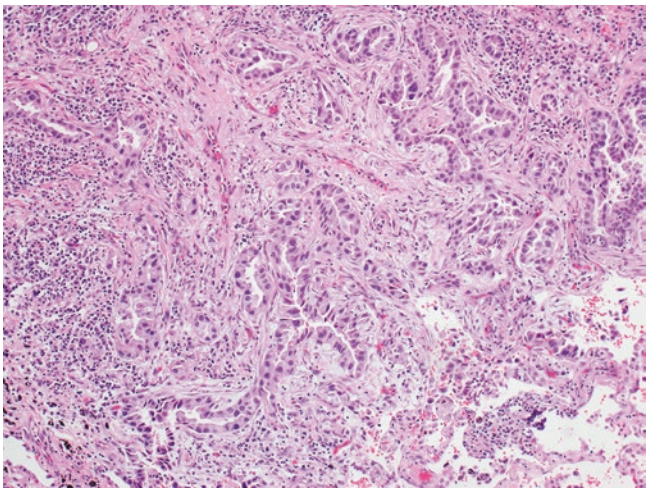

Fig. 13.7 Acinar adenocarcinoma. Photomicrograph showing a tumor composed of irregularly shaped glands with central luminal spaces invading a myofibroblastic stroma. Nuclei are enlarged and hyperchromatic, with anisonucleosis and occasionally prominent nucleoli

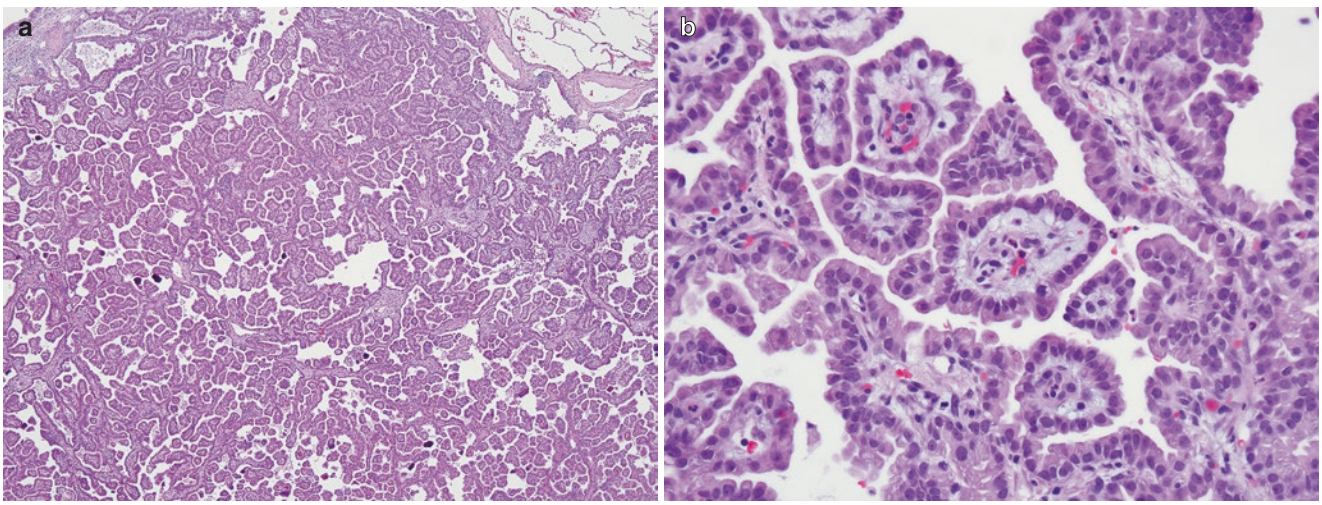

Fig. 13.8 Papillary adenocarcinoma. (**a**) Photomicrograph shows a tumor in which malignant columnar cells are growing on the surface of fibrovascular cores. (**b**) Higher-magnification view reveals cuboidal to columnar tumor cells growing on the surface of a true fibrovascular core

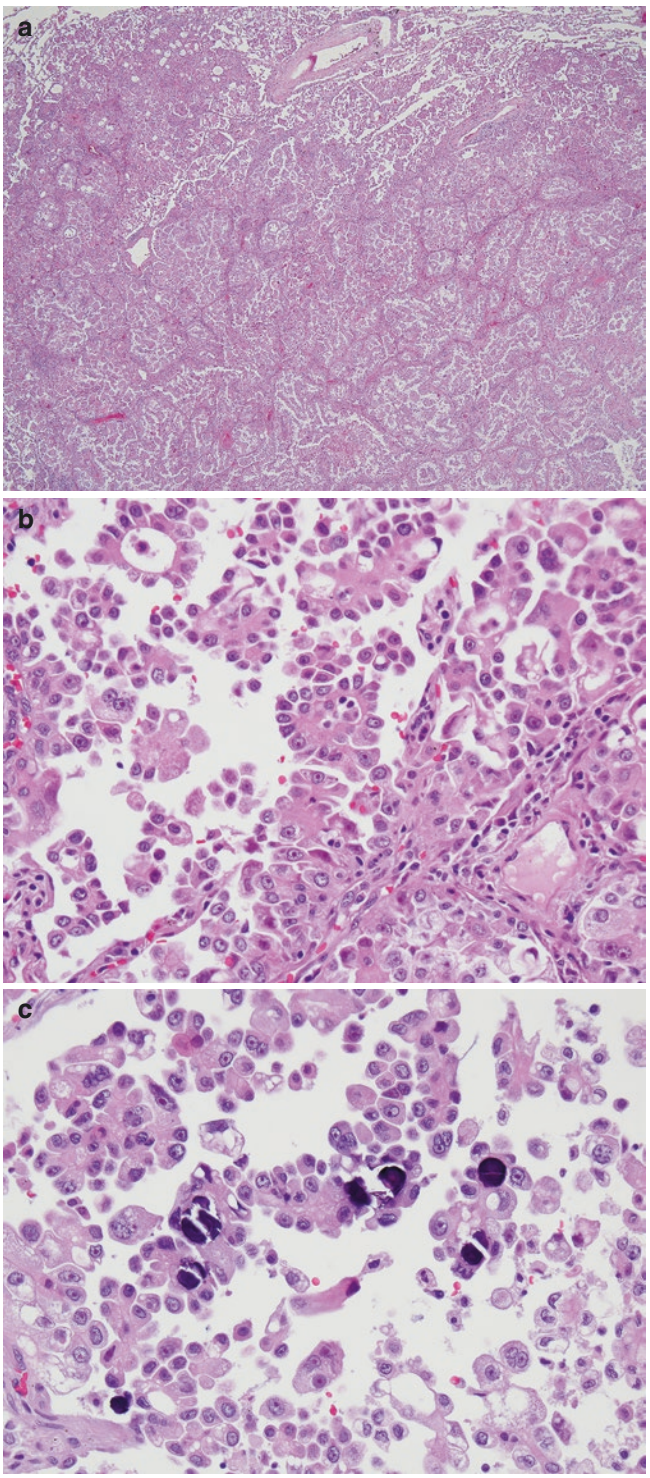

Fig. 13.9 Micropapillary adenocarcinoma. (**a**) Low-magnification photomicrograph shows tumor cells growing in numerous papillary tufts detached from or connected to alveolar walls. (**b**) High-magnification view shows tumor cells forming tufts and florets without a fibrovascular core. (**c**) Another high-magnification view shows detached small tumor aggregates with psammoma bodies floating in the alveolar air space. Tumor cells in this field show a higher degree of cytologic atypia

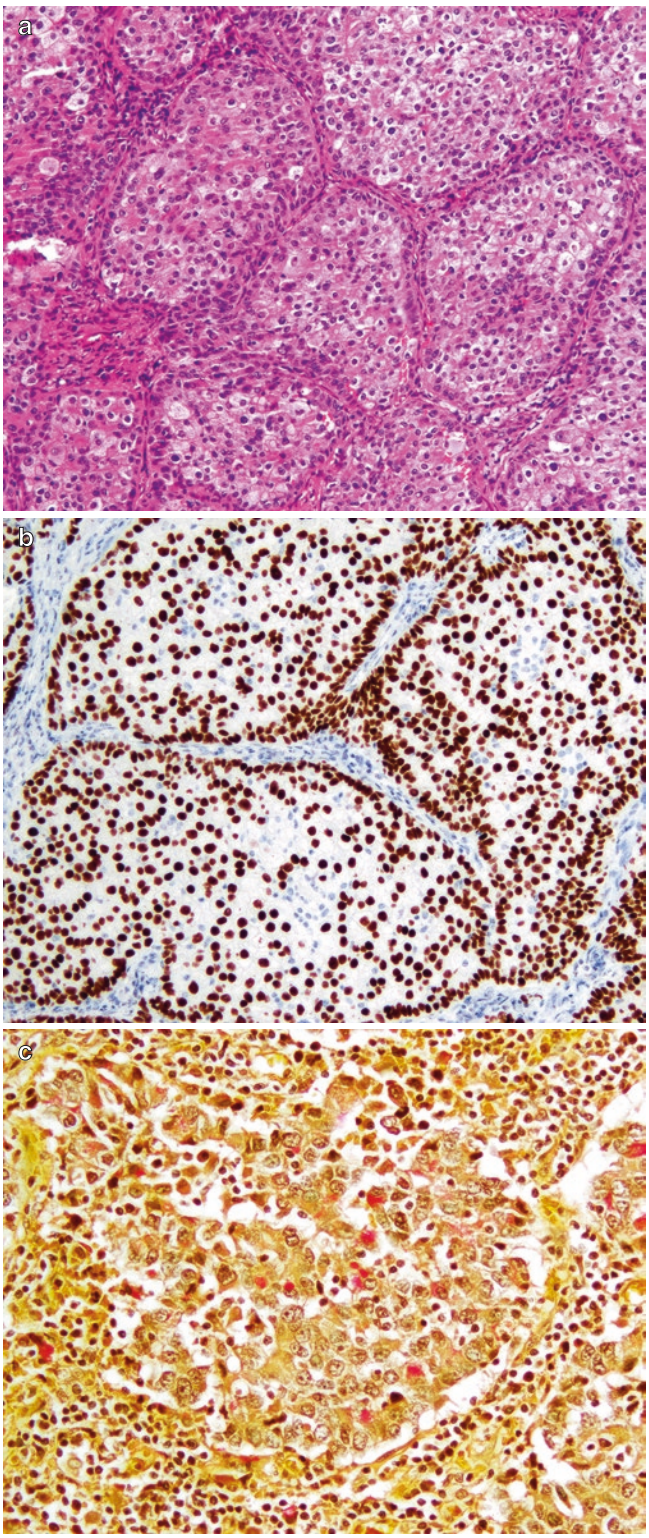

Fig. 13.10 Solid adenocarcinoma. (**a**) Photomicrograph showing tumor cells arranged as solid nests with abundant pale-staining eosinophilic to clear cytoplasm resembling squamous cell carcinoma. (**b**) Higher-magnification photomicrograph of an immunohistochemical-stained section shows strong positivity for TTF-1 in tumor cells. (**c**) Photomicrograph showing a mucicarmine stain that highlights intracellular mucin in occasional tumor cells

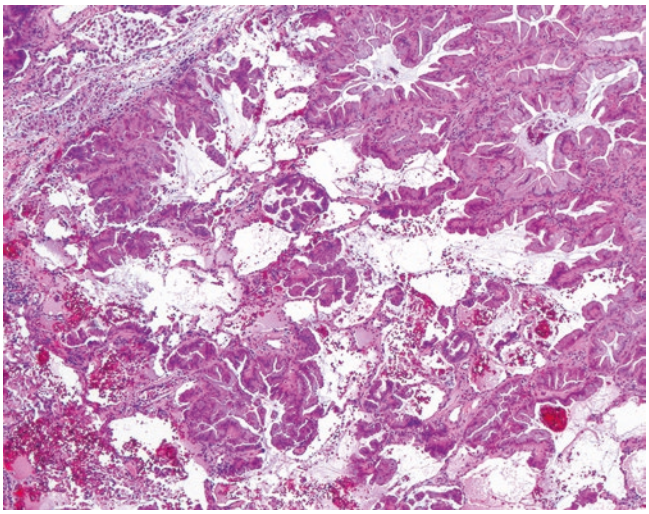

Fig. 13.11 Invasive mucinous adenocarcinoma. Low-magnification photomicrograph showing columnar neoplastic cells with abundant apical cytoplasmic mucin and basally oriented nuclei. This area shows both lepidic and papillary growth patterns, with variably conspicuous extracellular mucin

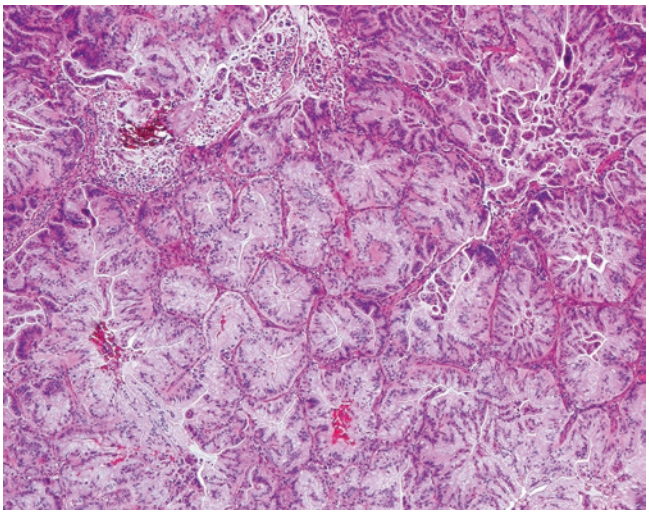

Fig. 13.12 Invasive mucinous adenocarcinoma. Photomicrograph showing a mucinous adenocarcinoma in which columnar mucinous cells are arranged in an acinar growth pattern characterized by closely packed, back-to-back glands separated by thin fibrotic septa. Foci of micropapillary growth are also present

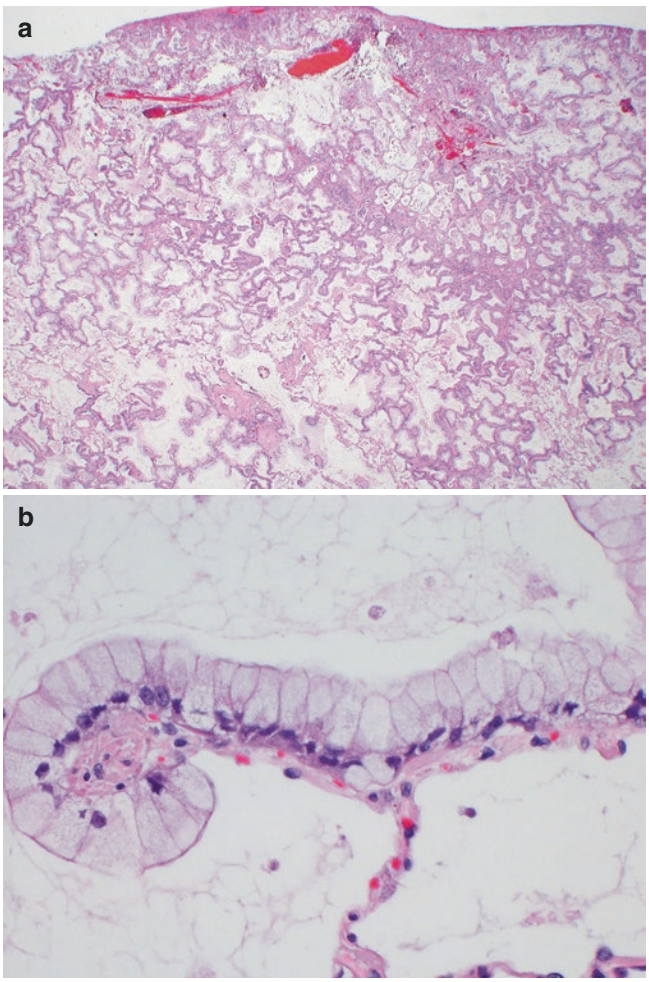

Fig. 13.13 Invasive mucinous adenocarcinoma. (**a**) Low-magnification photomicrograph of another example of invasive mucinous adenocarcinoma with a predominantly lepidic growth pattern. (**b**) High-magnification photomicrograph showing the remarkably bland cytologic features in neoplastic cells distributed along alveolar septa with small basally oriented nuclei and abundant apical mucin

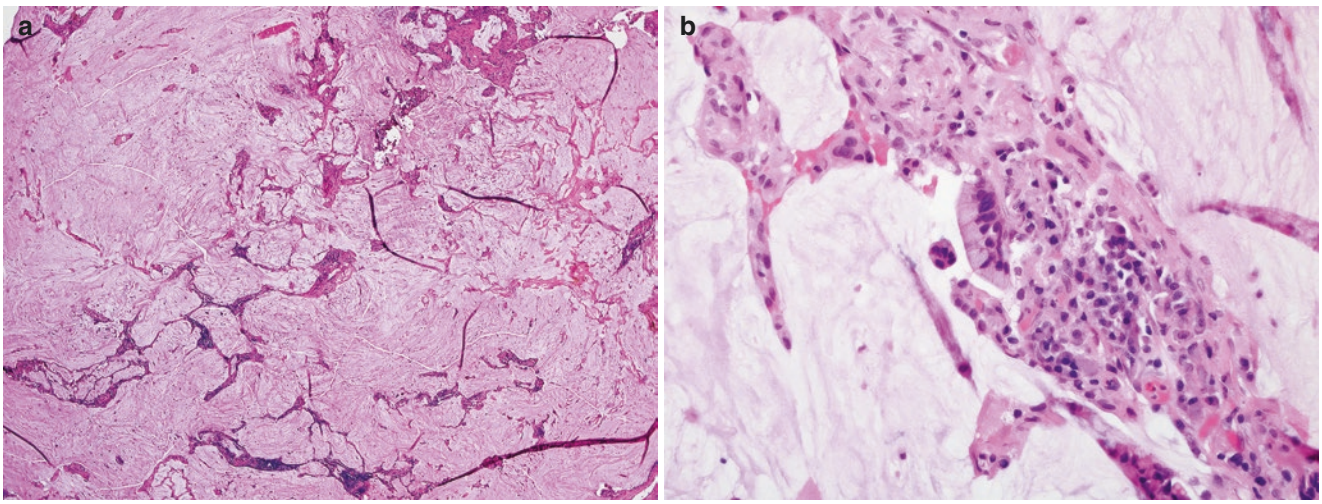

Fig. 13.14 Colloid adenocarcinoma. (**a**) Low-magnification photomicrograph showing a tumor characterized by pools of paucicellular pale-staining mucin, distending air spaces, and dissecting interstitial connective tissue. Tumor cells are rare and may be remarkably bland. (**b**) High-magnification view showing rare well-differentiated mucinous glandular epithelium growing along the fibrous septa and floating in pools of extracellular mucin

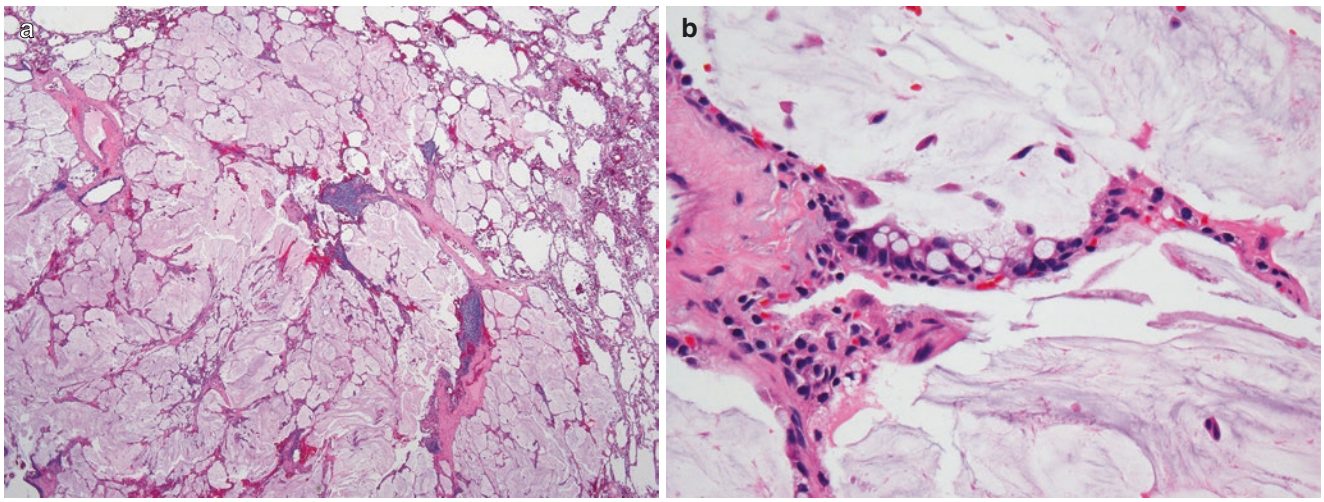

Fig. 13.15 Colloid adenocarcinoma. (**a**) Low-magnification photomicrograph showing another example of colloid adenocarcinoma in which large pools of paucicellular extracellular mucin distend air spaces. (**b**) High-magnification photomicrograph showing isolated clusters of neoplastic epithelium resembling intestinal epithelium with goblet cells

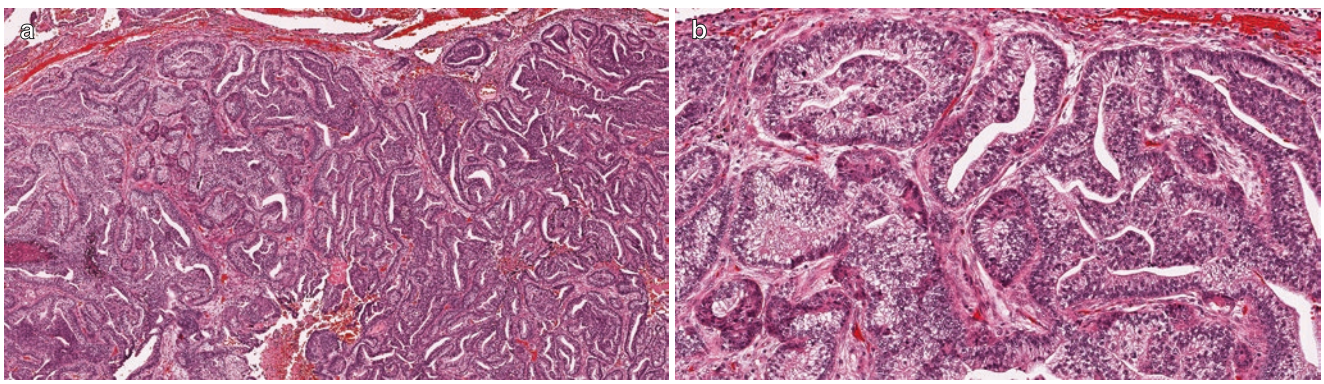

Fig. 13.16 Fetal adenocarcinoma. (**a**) Low-magnification photomicrograph showing an adenocarcinoma with a well-developed glandular growth pattern resembling fetal lungs with well-differentiated endometrioid adenocarcinomas. (**b**) High-magnification view showing columnar tumor cells with cytoplasmic glycogen vacuoles and nuclear stratification, furthering the resemblance to endometrioid adenocarcinoma

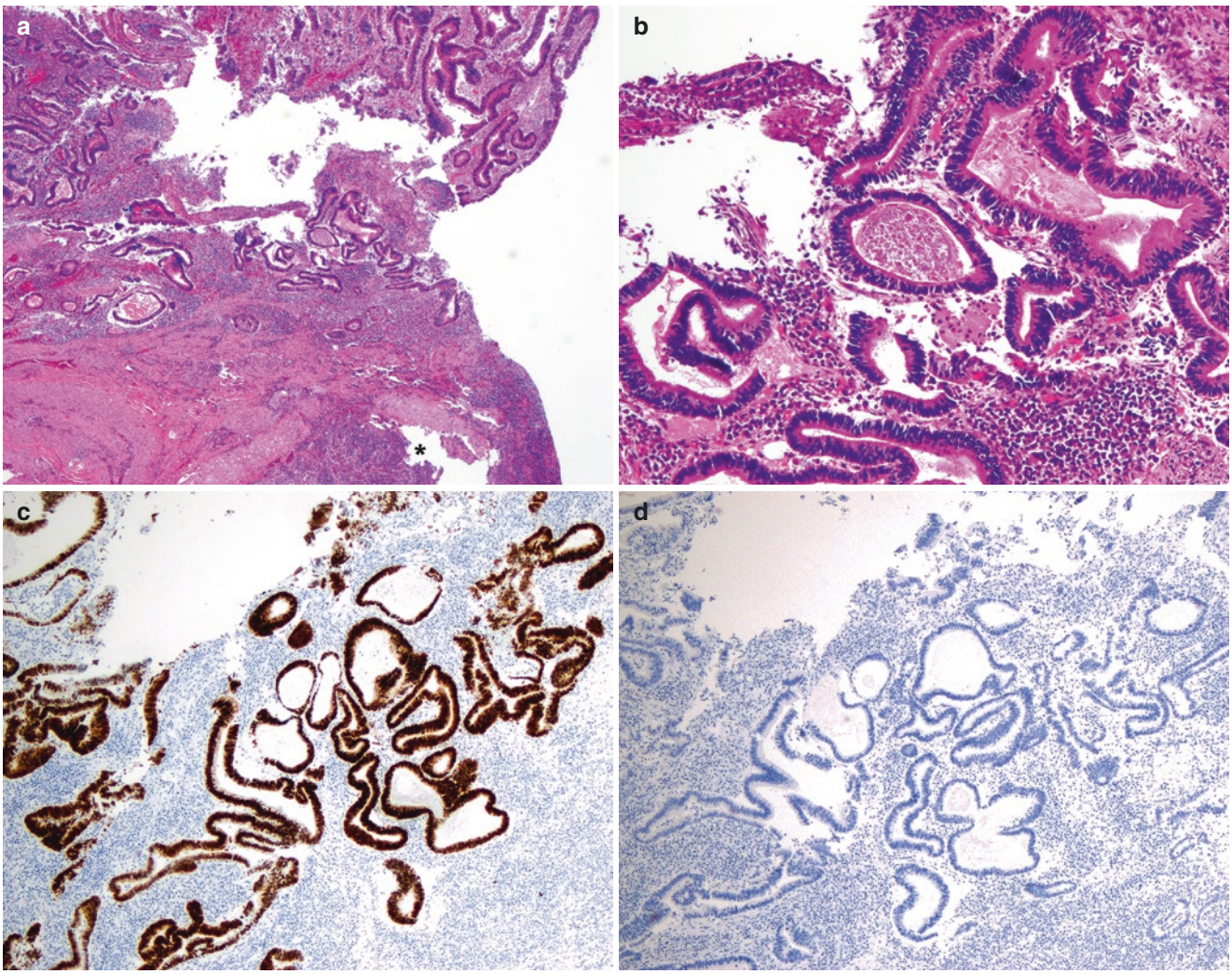

Fig. 13.17 Enteric adenocarcinoma. (**a**) Low-magnification photomicrograph shows an adenocarcinoma with well-formed glands and abundant inflammatory infiltrates next to a cartilaginous airway (*). (**b**) High-magnification view showing the tall, columnar stratified tumor cells forming glands with luminal necrosis. The morphologic features and immunoprofile are indistinguishable from those of colorectal adenocarcinoma. A clinical history and radiologic information are required to differentiate these two entities. (**c**) and (**d**), Immunohistochemical-stained sections showing strong, diffuse staining for CDX-2 (**c**) and negative staining for TTF-1 (**d**) in enteric adenocarcinoma

Table 13.1 Histologic subtypes and variants of adenocarcinoma

Subtypes (predominant growth pattern)	Lepidic
	Acinar
	Papillary
	Micropapillary
	Solid
Variants	Invasive mucinous adenocarcinoma
	Colloid adenocarcinoma
	Fetal adenocarcinoma
	Enteric adenocarcinoma

Table 13.2 Grading lung adenocarcinomas predominantly using histology

Grade	Predominant growth pattern/variant
Low grade/well differentiated	Adenocarcinoma in situ Minimally invasive adenocarcinoma Lepidic-predominant adenocarcinoma
Intermediate grade/moderately differentiated	Acinar Papillary Invasive mucinous
High grade/poorly differentiated	Solid Micropapillary

Squamous Cell Carcinoma

Squamous cell carcinoma in situ (Fig. 13.18) is a precursor lesion of invasive squamous cell carcinoma, arising in the bronchial epithelium of large airways

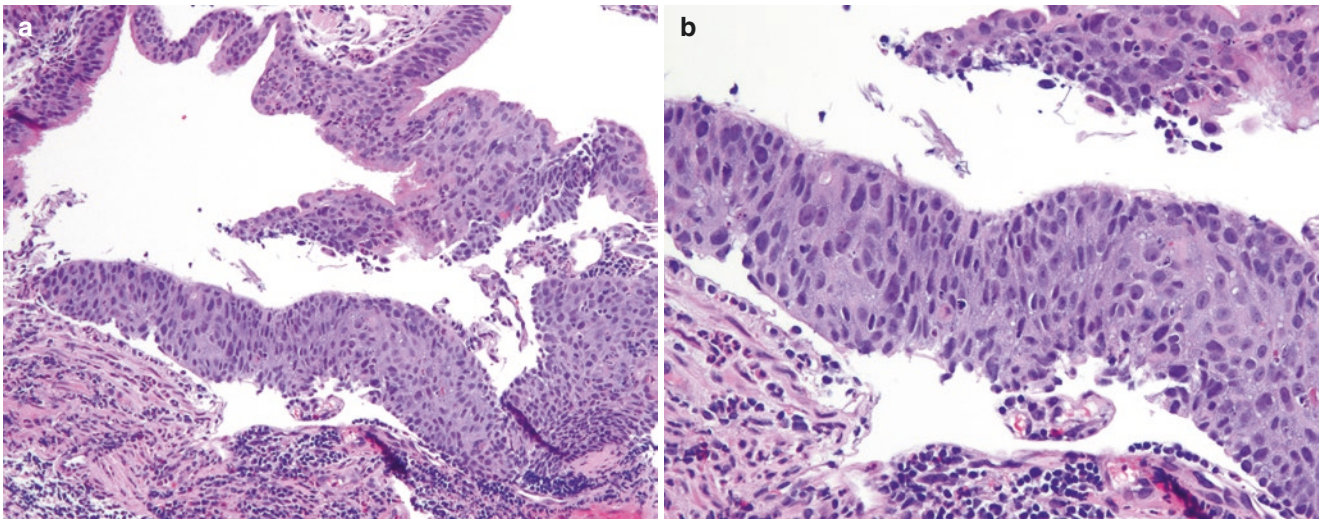

Fig. 13.18 Squamous cell carcinoma in situ. (**a**) Low-magnification photomicrograph showing squamous cell carcinoma in situ arising in a large respiratory airway with concomitant squamous metaplasia. (**b**) High-magnification photomicrograph showing dysplastic squamous cells with enlarged hyperchromatic nuclei, prominent nucleoli, mitotic figures above the basal cell layer, and anisonucleosis in the context of a disordered architecture extending from the base to the surface of the epithelium

Invasive Squamous Cell Carcinoma

Invasive squamous cell carcinoma (Figs. 13.19, 13.20 and 13.21) is defined as a malignant epithelial tumor that shows keratinization and/or intercellular bridges or a morphologically undifferentiated non-small cell carcinoma that expresses squamous cell markers (i.e., p63, p40, and/or high molecular weight cytokeratins for which CK5/6 has much higher specificity than 34βE12). It is negative for TTF-1.

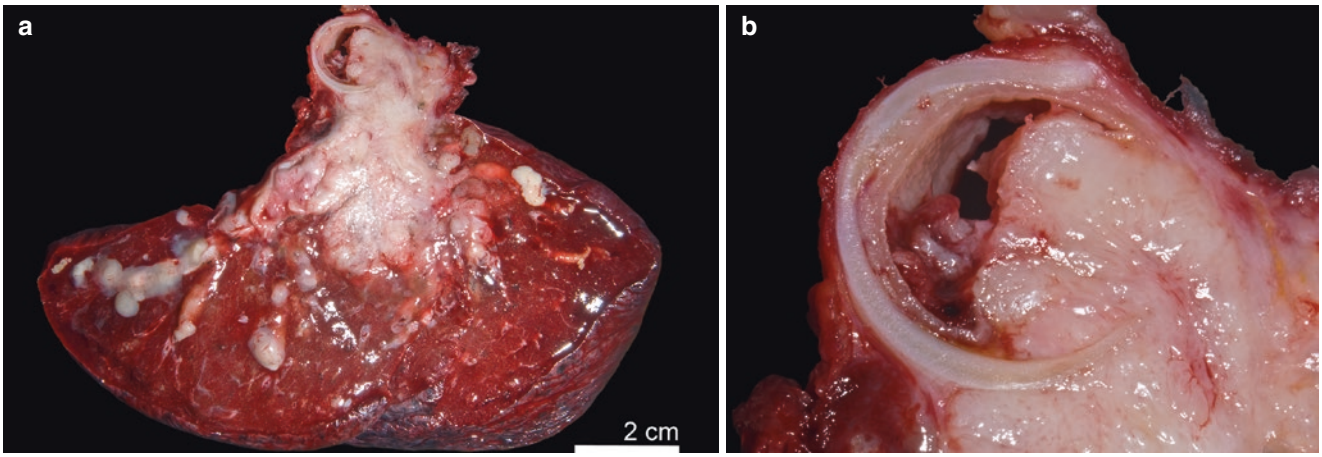

Fig. 13.19 Squamous cell carcinoma. (**a**) Gross photograph showing a centrally located obstructing mass extensively involving a large bronchus and surrounding lung parenchyma, with post-obstructive bronchiectasis in which dilated airways are filled with mucus. (Courtesy of J. Carvalho, Minneapolis, MN). (**b**) Closer view of the endobronchial mass. (Courtesy of J. Carvalho, Minneapolis, MN)

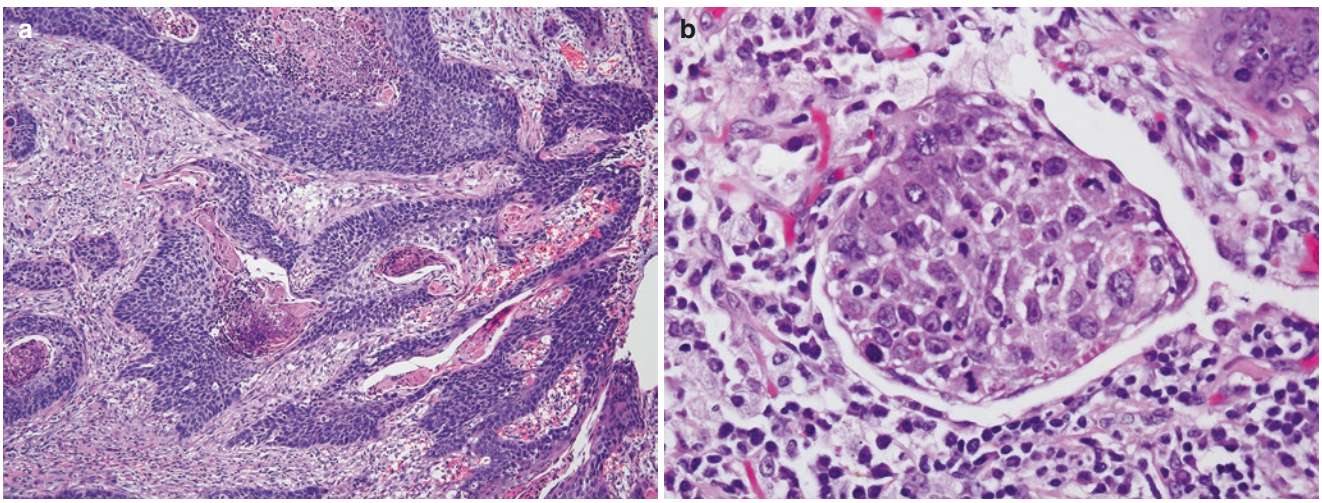

Fig. 13.20 Keratinizing squamous cell carcinoma. (**a**) Photomicrograph showing infiltrating nests with central keratinization in a desmoplastic stroma. (**b**) High-magnification photomicrograph showing another squamous cell carcinoma in which there are prominent intercellular bridges

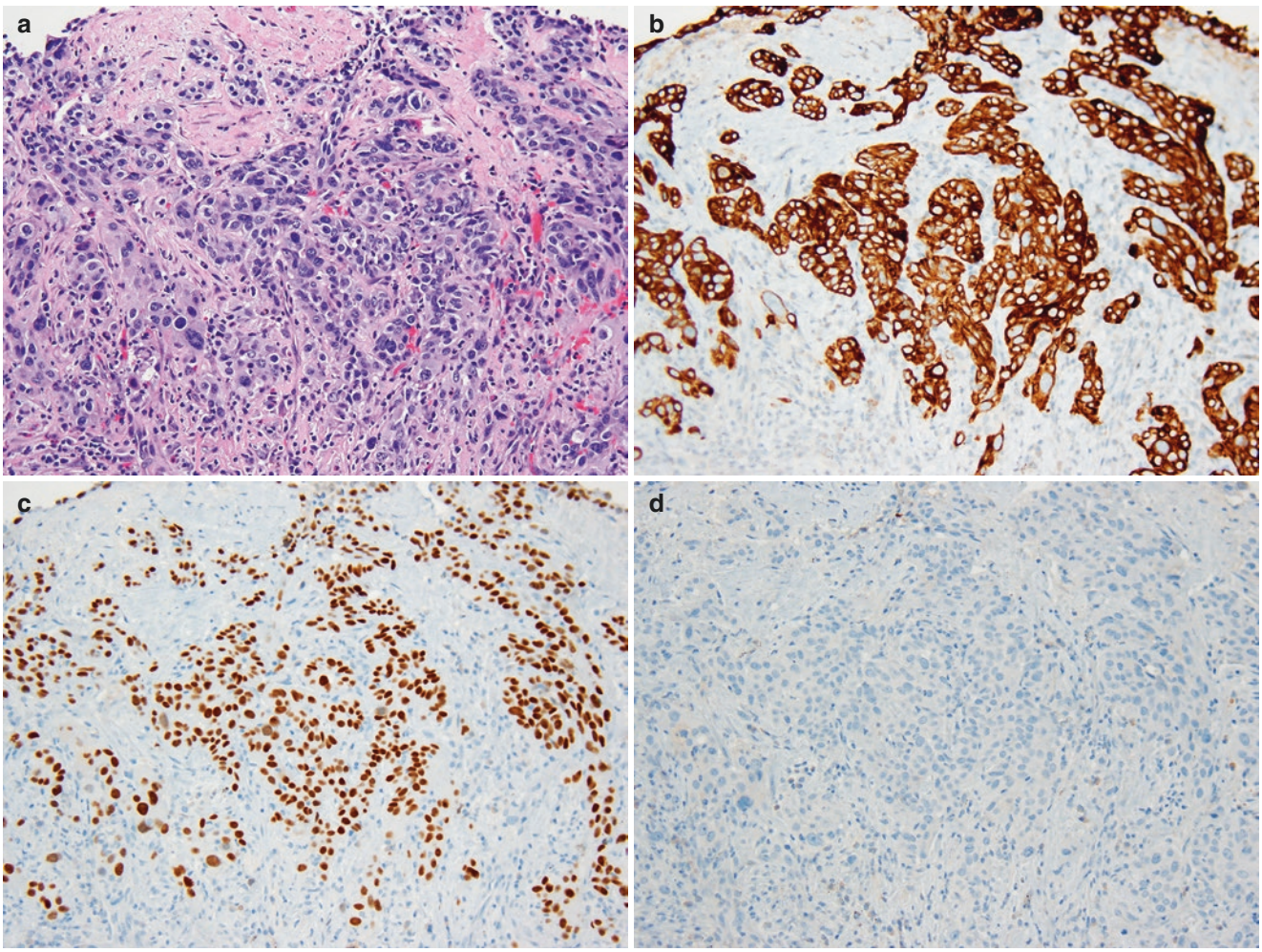

Fig. 13.21 Nonkeratinizing squamous cell carcinoma. (**a**) High-magnification photomicrograph showing poorly differentiated squamous cell carcinoma constituting infiltrating tumor cells with abundant cytoplasm but without easily identifiable intercellular bridging or keratinization. It is the sort of carcinoma that might be difficult to recognize as squamous based on routine histology alone. (**b–d**) Photomicrographs showing strong diffuse staining for high molecular weight cytokeratins (CK5/6) (**b**) and p63 (**c**) with negative staining for TTF-1 (**d**)

Basaloid Squamous Cell Carcinoma

Basaloid squamous cell carcinoma (Fig. 13.22) is a poorly differentiated malignant epithelial tumor composed of small cells arranged in large nests with a lobular architecture and peripheral palisading. The tumor cells lack squamous morphology but express squamous immunohistochemical markers such as p63 and p40. This tumor was previously considered a variant of large cell carcinoma but was recognized as a variant of squamous cell carcinoma in the 2015 WHO classification. Histologically, heterogeneous tumors with a component of conventional squamous cell carcinoma and a basaloid component that accounts for over 50% of the sample tumor are also classified as basaloid squamous cell carcinomas. These high-grade tumors tend to be associated with a prognosis that is poorer than that of other non-small cell carcinomas at the same stage.

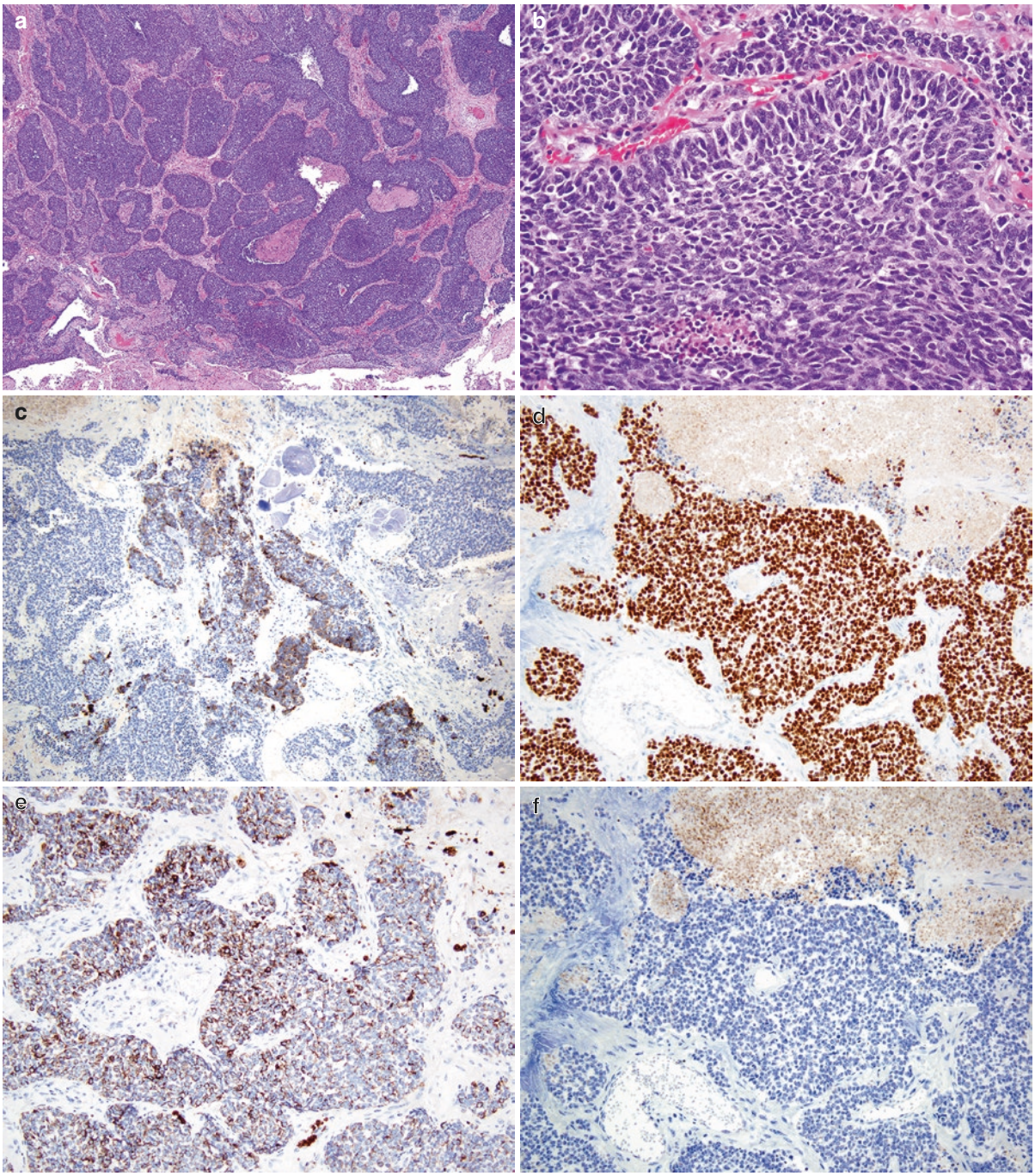

Fig. 13.22 Basaloid squamous cell carcinoma. (**a**) Low-magnification photomicrograph of basaloid squamous cell carcinoma shows solid, anastomosing nests with peripheral palisading and central comedo-type necrosis. (**b**) High-magnification view showing tumor cells that lack keratinization and intercellular bridges but demonstrate peripheral palisading and comedo-type necrosis. The tumor cells are relatively small and monomorphic, with hyperchromatic finely granular chromatin resembling small cell carcinoma. (**c**) As illustrated in this photomicrograph, the tumor may show focal and generally weak staining for synaptophysin, which may further confound the differential diagnosis with small cell carcinoma. However, positive staining for p63 (**d**) and CK5/6 (**e**) with negative staining for TTF-1 (**f**) can be extremely helpful, especially on small biopsies

Adenosquamous Carcinoma

Adenosquamous carcinoma (Fig. 13.23) is a carcinoma with components of both squamous cell carcinoma and adenocarcinoma, with each component constituting at least 10% of the tumor.

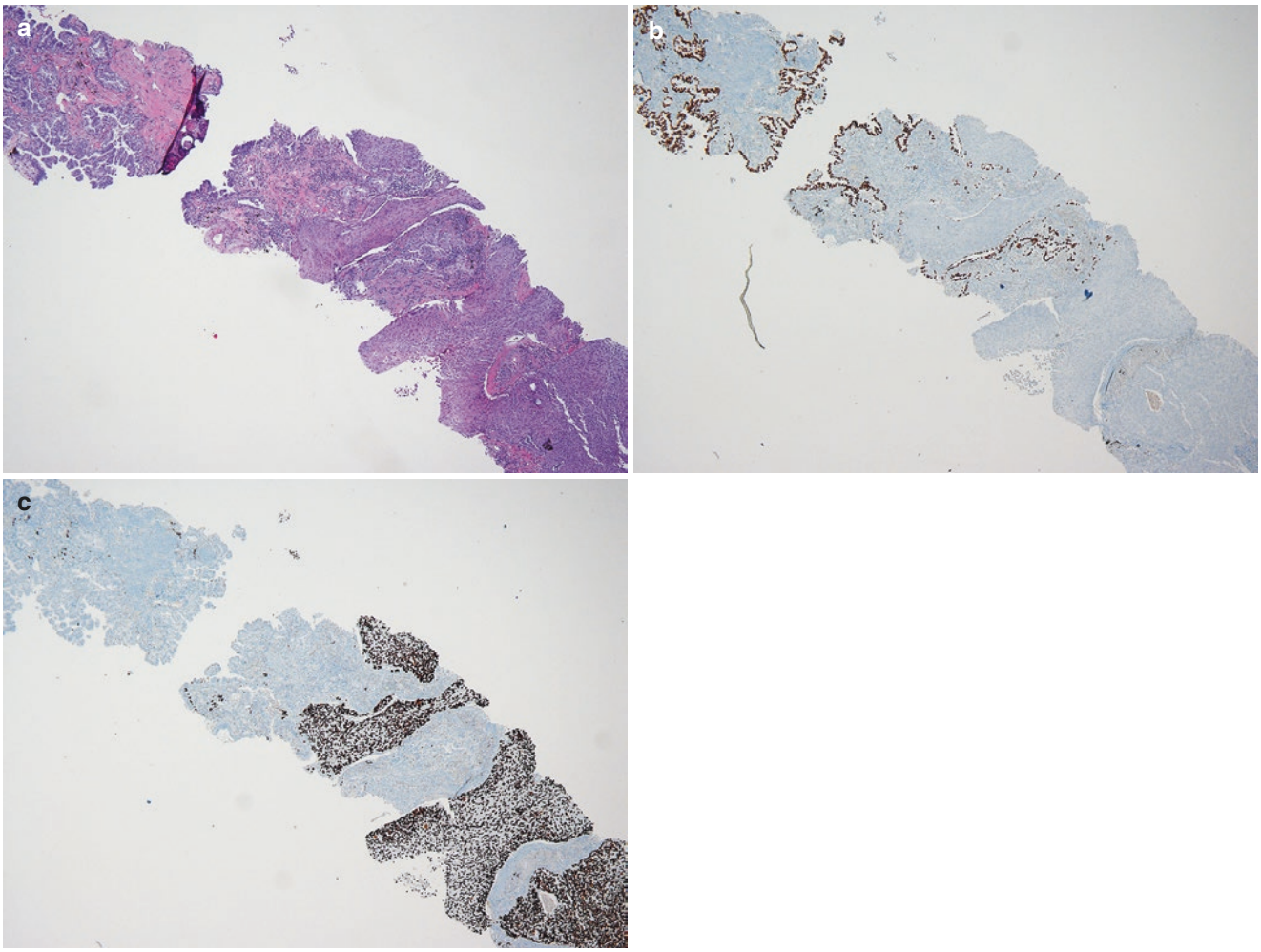

Fig. 13.23 Adenosquamous carcinoma. (**a**) Photomicrograph of core needle biopsy from a lung tumor showing both adenocarcinoma (upper left) and squamous cell carcinoma (lower right). (**b**) and (**c**), An immunohistochemical stain for TTF-1 highlights the adenocarcinoma component on the left (**b**), while p63 strongly and diffusely stains the squamous cell component on the right (**c**)

Neuroendocrine Tumors

Carcinoid Tumors

Carcinoid tumors (Figs. 13.24, 13.25, 13.26, 13.27, 13.28, 13.29, 13.30 and 13.31) are low- to intermediate-grade neuroendocrine malignancies that are divided into two subcategories: typical and atypical carcinoid tumors. Typical carcinoid tumors are the exemplars of neuroendocrine neoplasms in the lung and as such are distinguished by the same combination of growth patterns that characterize neuroendocrine neoplasms at other sites (Table 13.3). Typical carcinoid tumors consist of bland cuboidal and occasionally spindled cells with only modest degrees of anisonucleosis and with finely divided chromatin, small nucleoli, and variably abundant cytoplasm. Mitoses and tumor necrosis are not present, although endobronchial tumors may show surface ulceration with the anticipated degree of ulcer-related necrosis. Carcinoid tumors should measure at least 5 mm in greatest dimension to distinguish them from carcinoid tumorlets that are typically less than 5 mm in size and almost invariably are poorly circumscribed and intimately associated with bronchiolar epithelium.

Atypical carcinoid tumors are separated from typical carcinoid tumors based on a combination of necrosis and/or mitotic rate (Table 13.4). The Ki-67 labeling index correlates with histologic subclassification but does not improve on the prognostic value of the WHO classification criteria. Atypical carcinoid tumors overlap at the extreme with large cell neuroendocrine carcinoma but have lower mitotic rates ($\leq$ 10/2 mm^2).

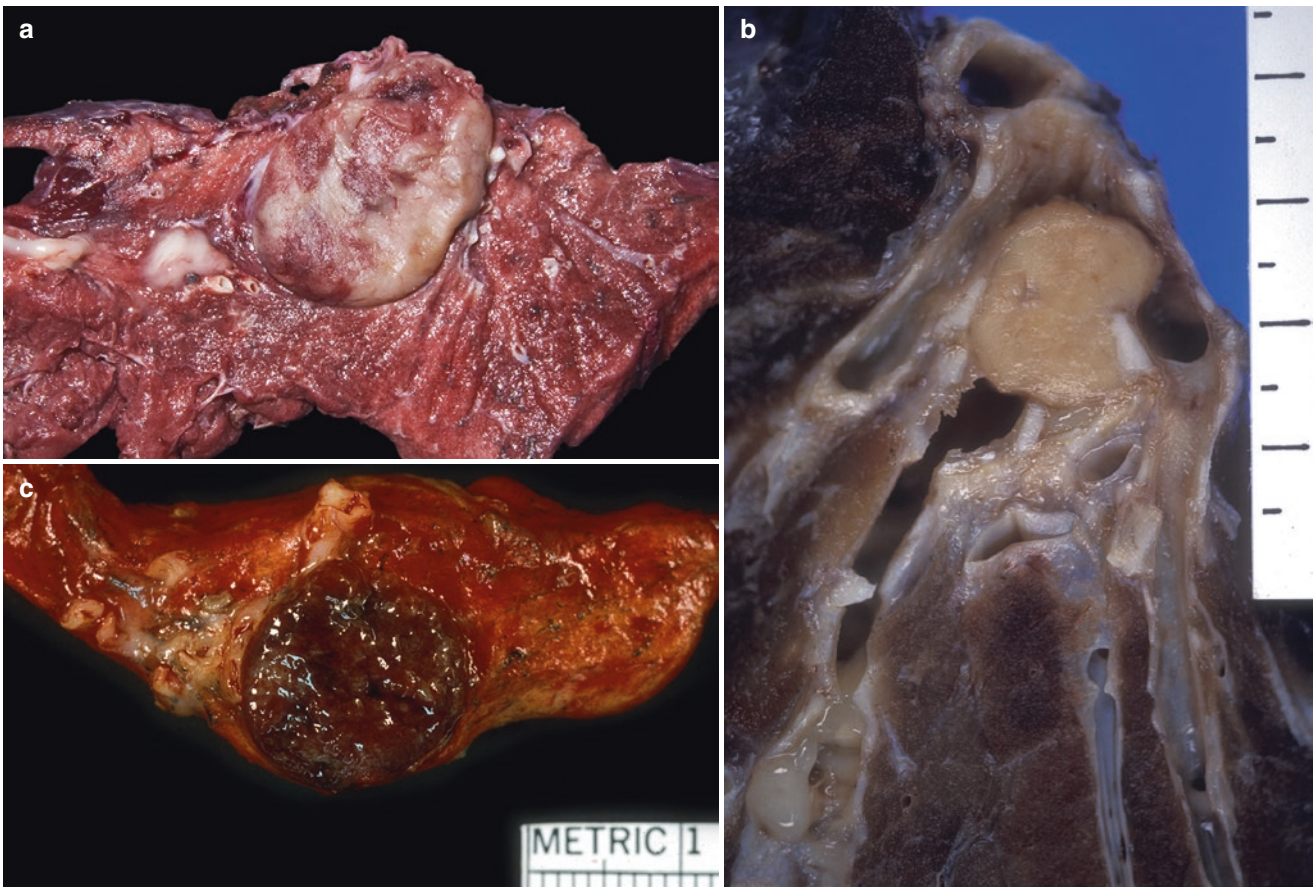

Fig. 13.24 Carcinoid tumor. (**a**) Gross photograph of a centrally located well-circumscribed tan-brown mass, partially obstructing the bronchus with post-obstructive mucus plugging on the left. (Courtesy of J. Carvalho, Minneapolis, MN). (**b**) Photograph showing cut surface of another centrally situated endobronchial carcinoid tumor. About three fourths of carcinoid tumors present as endobronchial masses. (**c**) Gross photograph of a peripheral carcinoid tumor with a deep mahogany color

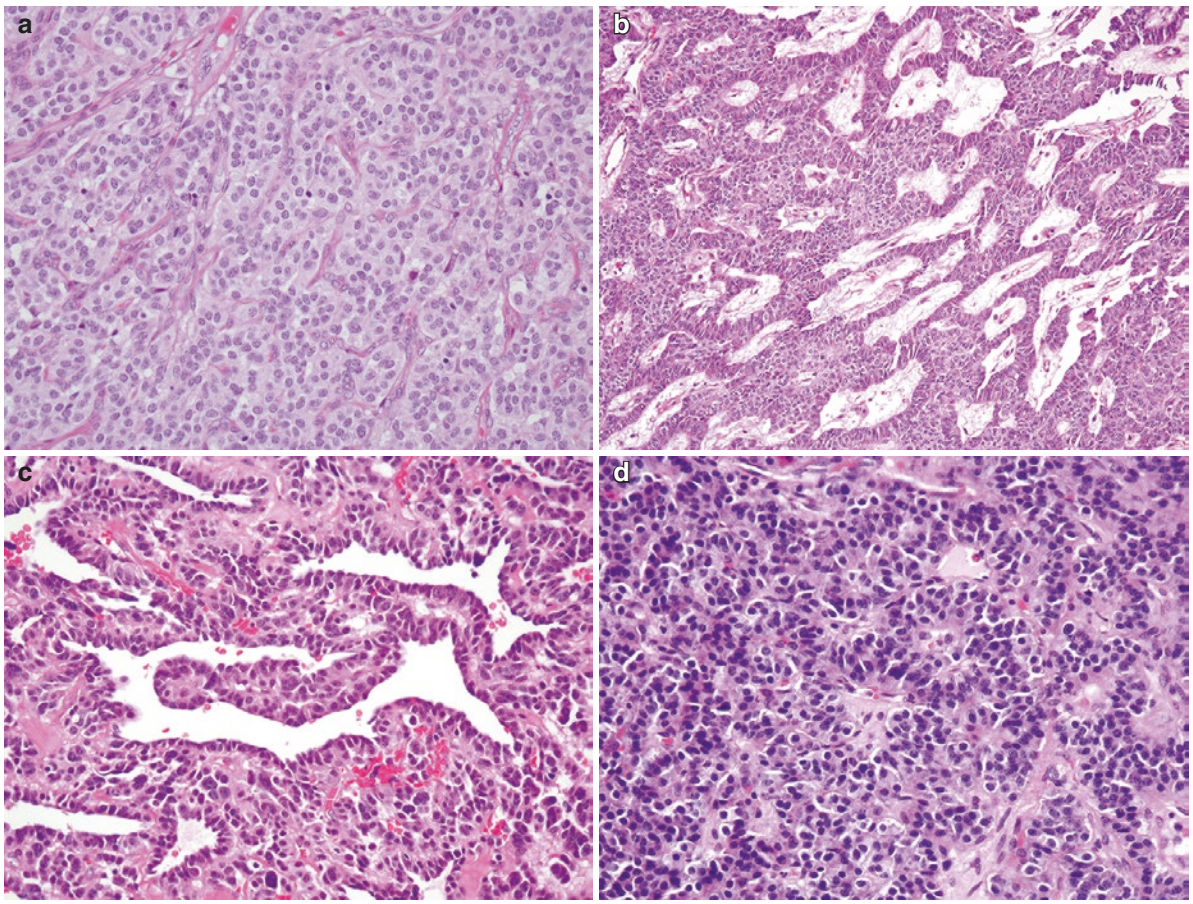

Fig. 13.25 Typical carcinoid tumor. (**a**) Photomicrograph showing tumor composed of bland cuboidal cells with a moderate amount of pale eosinophilic cytoplasm and finely granular chromatin. The cells are arranged in an organoid nesting pattern with delicate vascular stroma. No mitosis or necrosis is seen. (**b**) Photomicrograph showing trabecular pattern in a typical carcinoid tumor. Prominent edematous and pale-staining stroma are present between the trabecular bands of tumor cells. (**c**) Photomicrograph showing pseudoglandular and papillary patterns in a typical carcinoid tumor. Tumor cells demonstrate finely granular nuclear chromatin and inconspicuous nuclei, distinguishing them from adenocarcinoma. (**d**) Photomicrograph of a typical carcinoid tumor with rosette formation

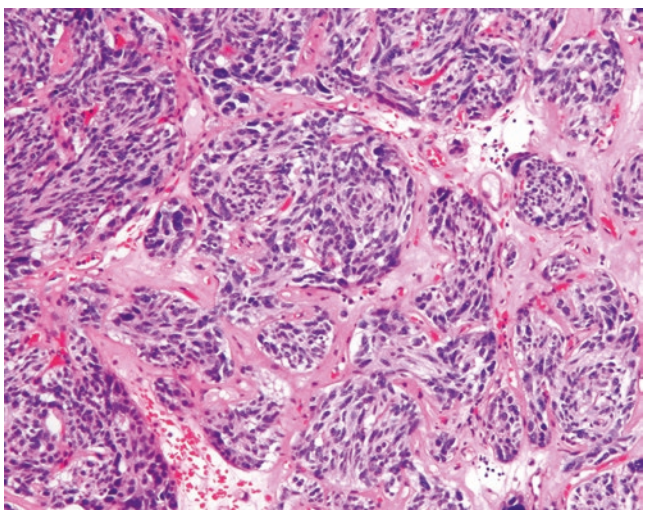

Fig. 13.26 Typical carcinoid tumor with prominent spindle cells. Photomicrograph showing a tumor composed of spindle cells with focally pronounced nuclear pleomorphism, which should not be taken as criteria for atypical carcinoid tumors. The tumor maintains a distinctly nested growth pattern without necrosis or mitotic figures

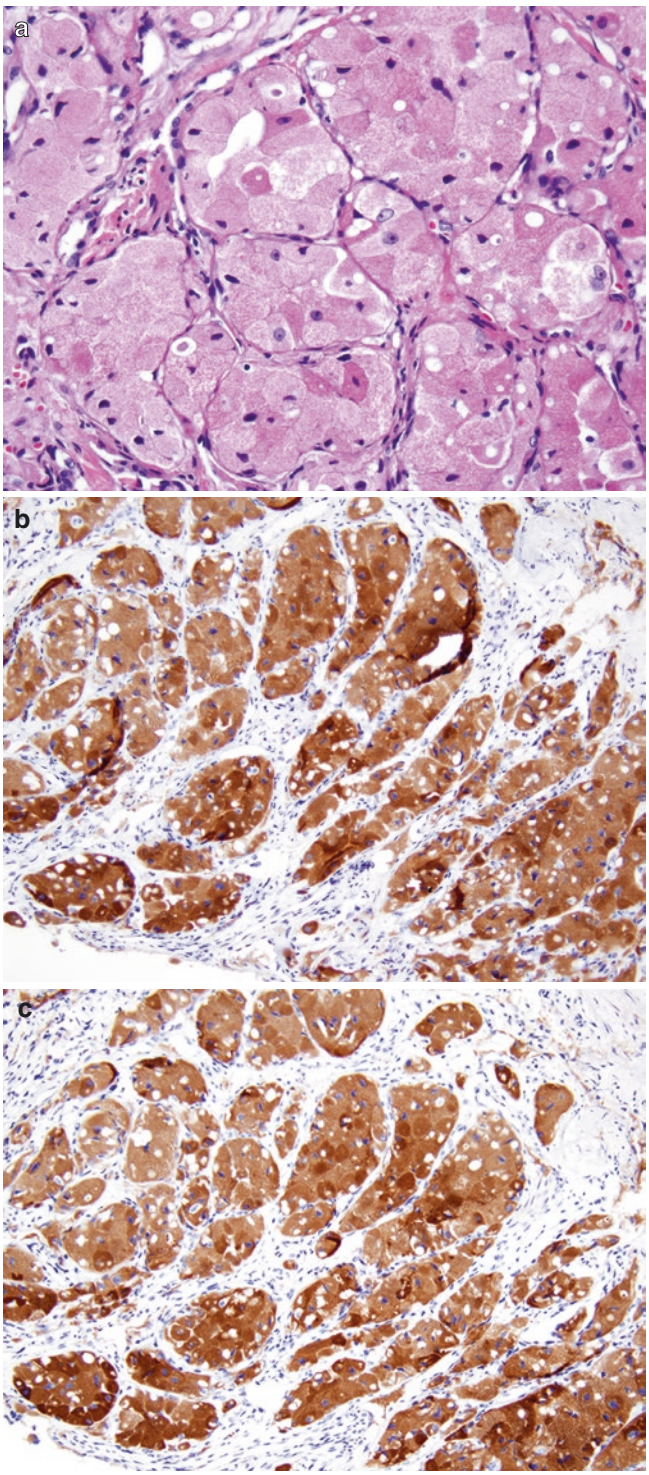

Fig. 13.27 Typical carcinoid tumor with oncocytic features. (**a**) Photomicrograph showing tumor cells with abundant eosinophilic granular cytoplasm and occasional prominent nucleoli on H&E stain. Immunohistochemical stains show strong cytoplasmic positivity for synaptophysin (**b**) and chromogranin (**c**)

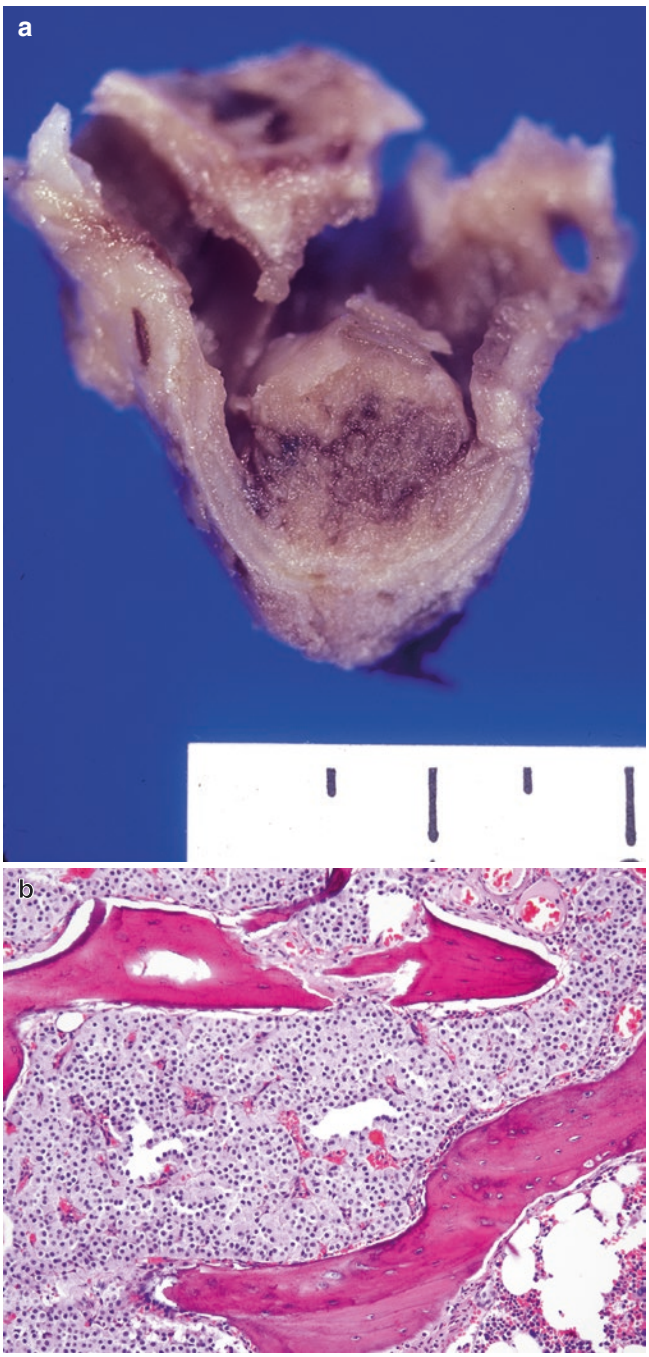

Fig. 13.28 Typical carcinoid tumor with ossification. (**a**) Gross photograph shows cut surface of heavily calcified endobronchial mass that required a saw to cut. (**b**) Photomicrograph shows osseous metaplasia of the stroma complete with bone marrow (lower right)

Fig. 13.29 Atypical carcinoid tumor. Gross photograph of a peripheral, well-circumscribed atypical carcinoid tumor measuring just over 3 cm in greatest dimension. There is no grossly detectable necrosis to distinguish this example from a low-grade typical carcinoid tumor. Microscopic necrosis and mitotic rate (≥2/2 mm^2) are the features that separate atypical from typical carcinoid tumor

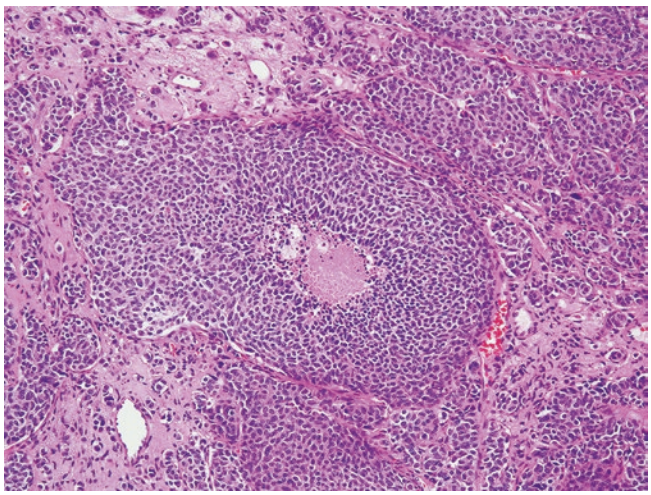

Fig. 13.30 Atypical carcinoid tumor. Photomicrograph shows a carcinoid tumor with small foci of comedo-type necrosis in tumor nests

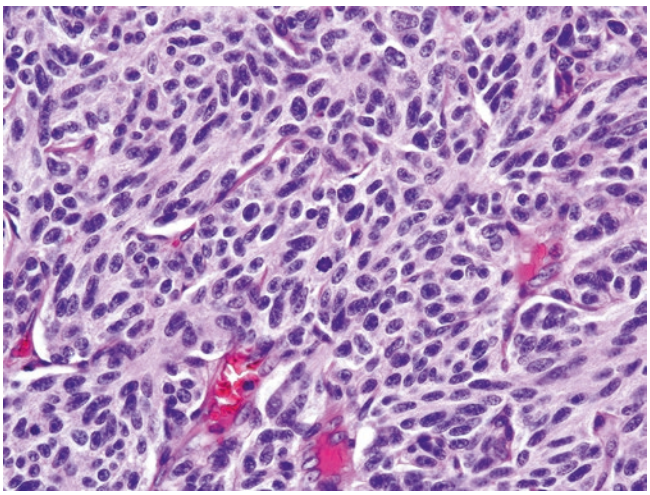

Fig. 13.31 Atypical carcinoid tumor. High-magnification photomicrograph shows a single mitotic figure in the center. Tumor cells show carcinoid morphology with a moderate amount of eosinophilic cytoplasm and finely granular nuclear chromatin

Table 13.3 Growth patterns seen in carcinoid tumors

Organoid nesting pattern
Trabecular pattern
Papillary pattern
Pseudoglandular or follicular pattern
Rosette formation

Table 13.4 Comparison between typical and atypical carcinoids

	Typical carcinoid	Atypical carcinoid
Histologic features	Neuroendocrine differentiation	
Mitosis	0–1 per 2 mm^2	2–10 per 2 mm^2
Necrosis	None	Focal, punctate necrosis
Prognosis	Excellent (90% 5-year survival)	Worse (60% 5-year survival)

Small Cell Carcinoma

Small cell carcinoma (Figs. 13.32, 13.33, 13.34, 13.35, 13.36 and 13.37) is defined morphologically as a malignant epithelial neoplasm consisting of relatively small cells (about three times the diameter of a small lymphocyte) with scant cytoplasm, finely dispersed granular chromatin, absent or inconspicuous nucleoli, and nuclear molding. The high nuclear-cytoplasmic ratio (N:C) and nuclear characteristics are more helpful than cell size in distinguishing small cell carcinoma from other tumor types. The cells are often arranged in sheets without the "neuroendocrine architecture" characteristic of carcinoid tumors. Necrosis is universal, although small biopsies may not always reflect this finding. Mitotic figures are abundant (>10/2 mm^2). Neuroendocrine markers are commonly expressed but are not necessary for the diagnosis. The majority of small cell carcinomas are positive for TTF-1 and are generally negative or show only focal staining for p63 or p40 and high molecular weight cytokeratins (i.e., CK5/6). This immunophenotype can be helpful in distinguishing small cell carcinoma from basaloid variants of squamous cell carcinoma, especially in small biopsies. Ki67 labeling indices are usually very high, which is useful in separating small cell carcinoma from typical and atypical carcinoid tumors in small biopsies, especially those with crush artifact.

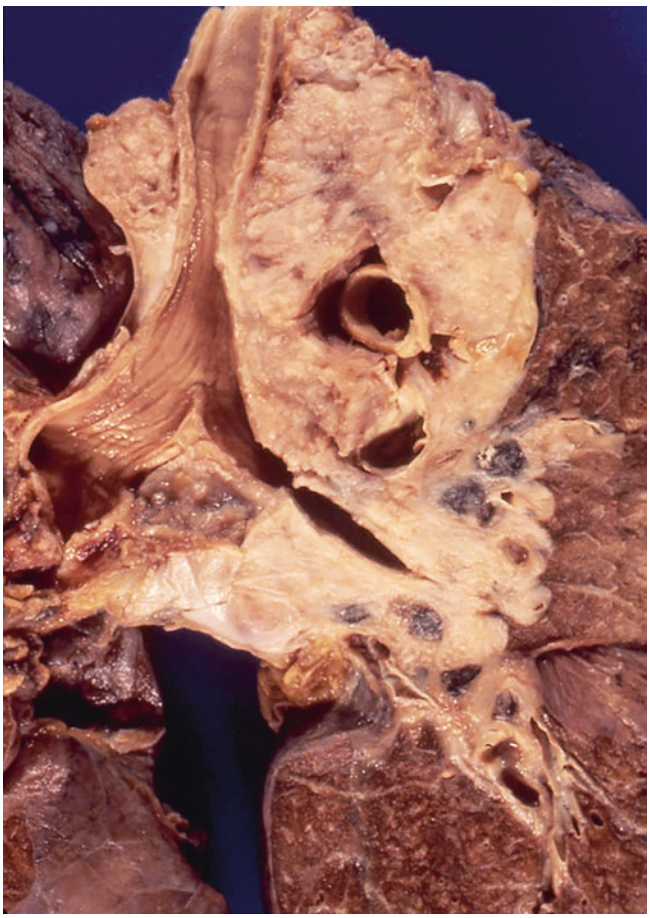

Fig. 13.32 Small cell carcinoma. Gross photograph of autopsy specimen showing small cell carcinoma distributed as a large centrally located mass involving the major bronchi, with bulky lymph node metastases

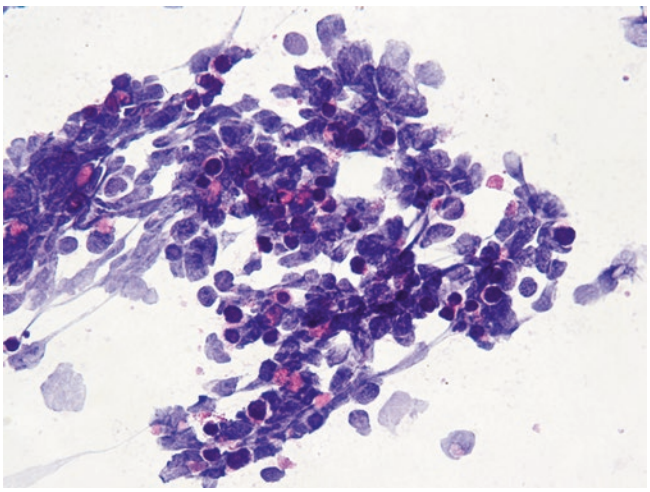

Fig. 13.33 Small cell carcinoma. High-magnification photomicrograph illustrating the distinctive cytologic features of small cell carcinoma in a smear prepared from a fine needle aspirate. Tumor cells show very scant cytoplasm, hyperchromatic nuclei, finely dispersed "salt and pepper" chromatin, absent nucleoli, nuclear molding, and prominent apoptosis. Cytology specimens can be extremely helpful in patients whose bronchial biopsies show extensive crush artifact

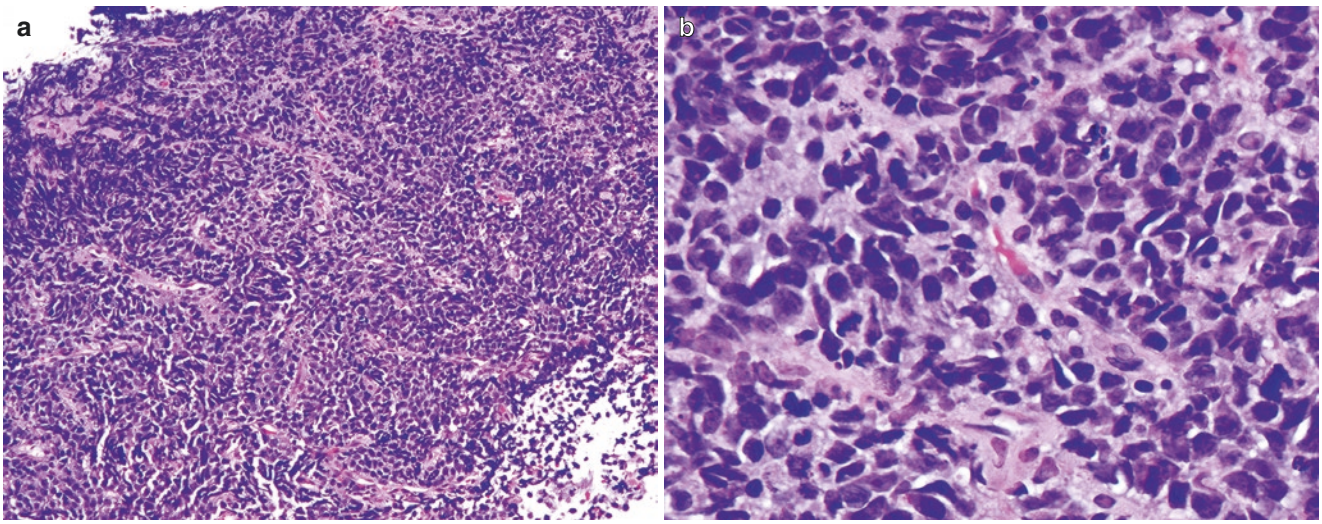

Fig. 13.34 Small cell carcinoma. (**a**) Low-magnification photomicrograph shows densely packed small- to intermediate-sized tumor cells. Crushing artifact is seen at the upper-left edge. (**b**) High-magnification view showing tumor cells with scant cytoplasm, dense chromatin, and occasional small nucleoli. Mitoses and apoptosis are frequently seen

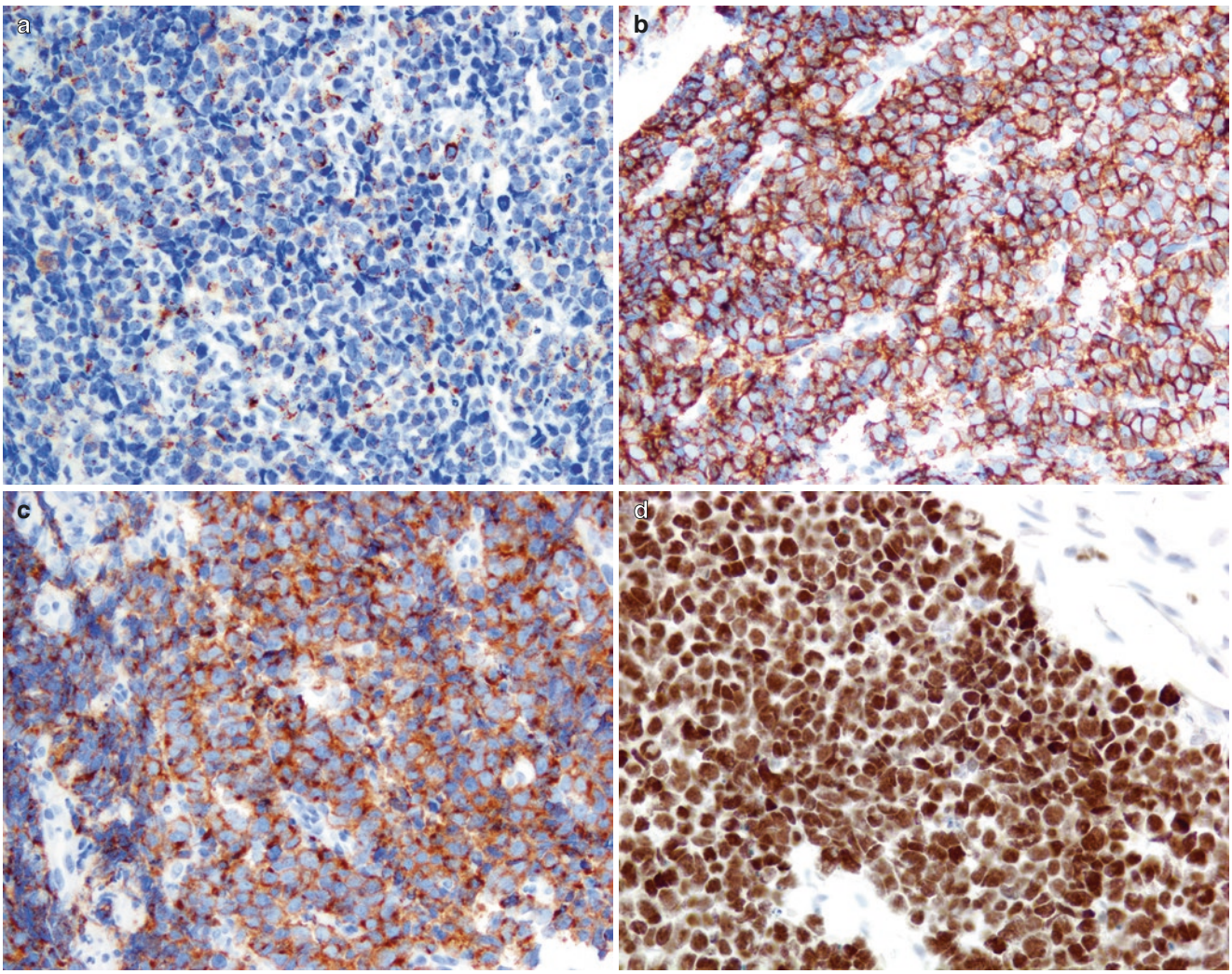

Fig. 13.35 Small cell carcinoma. (**a**–**d**), Photomicrographs of immunostained slides showing characteristic cytoplasmic perinuclear dot-like staining for cytokeratin (AE1/AE3) (**a**), diffuse membranous and cytoplasmic staining for CD56 (**b**), cytoplasmic staining for synaptophysin (**c**), and nuclear staining for TTF-1 (**d**). Not all small cell carcinomas show all of these features, including rare examples with a "null" phenotype. Absence of staining for CD20 and p63/p40 can be extremely helpful, especially in those with an otherwise "null" phenotype, in separating small cell carcinoma from lymphomas and basaloid squamous cell carcinomas on small biopsies

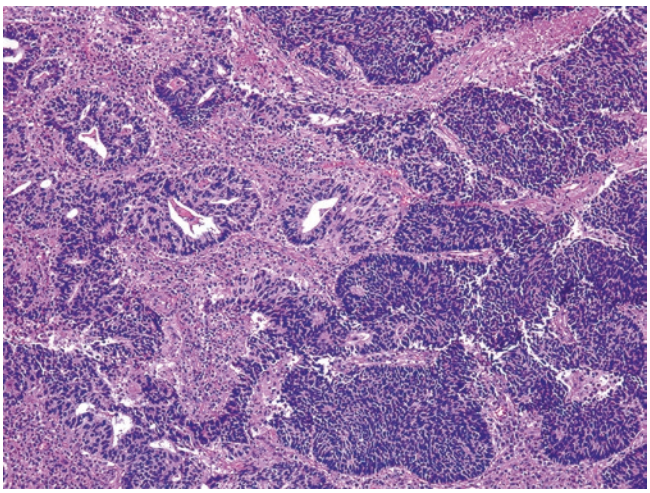

Fig. 13.36 Combined small cell carcinoma and adenocarcinoma. Photomicrograph showing malignant glands with cribriform architecture (*left*) immediately next to small cell carcinoma (*right*)

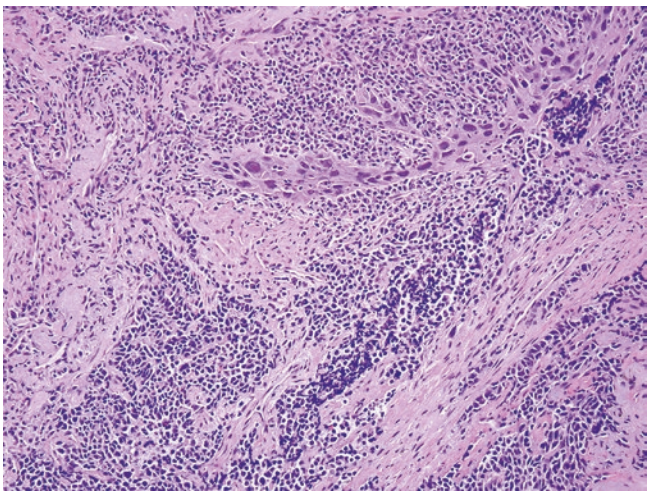

Fig. 13.37 Combined small cell carcinoma and squamous cell carcinoma. Photomicrograph showing a nest of squamous cell carcinoma consisting of polygonal cells with prominent intercellular bridging and occasional single dyskeratotic cells situated in the midst of an otherwise classic small cell carcinoma

Large Cell Neuroendocrine Carcinoma

Large cell neuroendocrine carcinoma (Figs. 13.38, 13.39 and 13.40) is defined as a high-grade malignant epithelial tumor with neuroendocrine growth patterns (i.e., the growth patterns characteristically seen in carcinoid tumors), cytologic features more closely resembling those seen in non-small cell carcinomas (i.e., large nucleoli and more abundant cytoplasm without nuclear molding), and immunohistochemical staining for neuroendocrine markers. Necrosis is universal and tends to be more extensive than the necrosis seen in atypical carcinoid tumors. Lung carcinomas with carcinoid morphology but more than ten mitoses per 2 mm^2 are better classified as large cell neuroendocrine carcinomas according to the 2015 WHO classification. There is significant histologic overlap with small cell carcinoma, which accounts for the relatively low rates of interobserver agreement even among experts in distinguishing these highly related variants of high-grade neuroendocrine carcinoma.

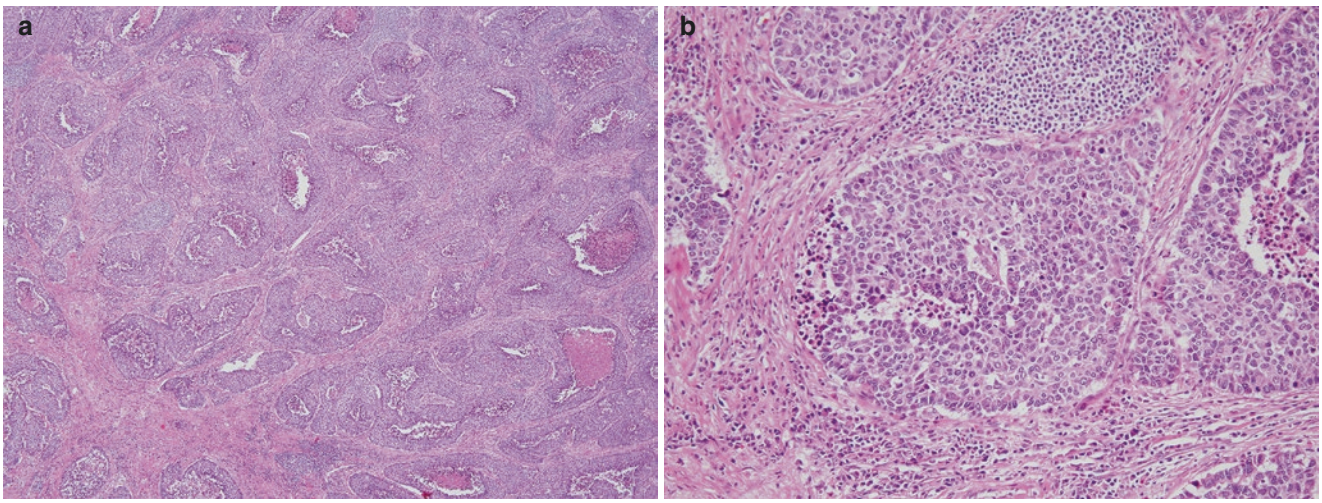

Fig. 13.38 Large cell neuroendocrine carcinoma. (**a**) Low-magnification photomicrograph shows a nested growth pattern with peripheral palisading and multifocal "comedo" necrosis situated centrally within the cell nests. The necrotic foci are much more extensive than that usually seen in atypical carcinoid tumors. (**b**) Higher-magnification view showing a tumor nest with peripheral palisading and foci of necrosis. The tumor cells show vesicular chromatin and abundant eosinophilic cytoplasm. Numerous mitoses are seen

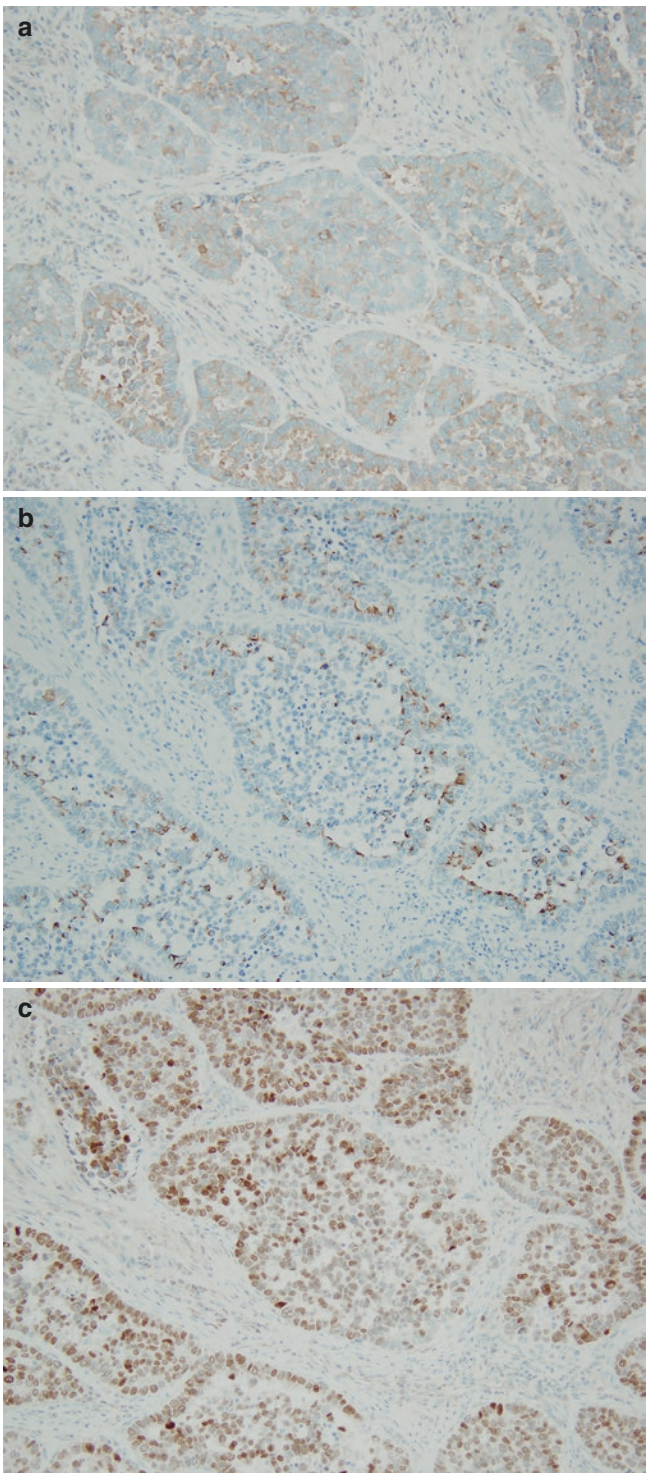

Fig. 13.39 Immunostaining of large cell neuroendocrine carcinoma. (**a**–**c**), A series of photomicrographs of immunostained sections from the tumor illustrated in Fig. 13.38 showing patchy cytoplasmic staining for synaptophysin (**a**) and chromogranin (**b**) and nuclear staining for TTF-1 in isolated tumor cells (**c**). TTF-1 immunoreactivity is not a consistent feature of large cell neuroendocrine carcinoma

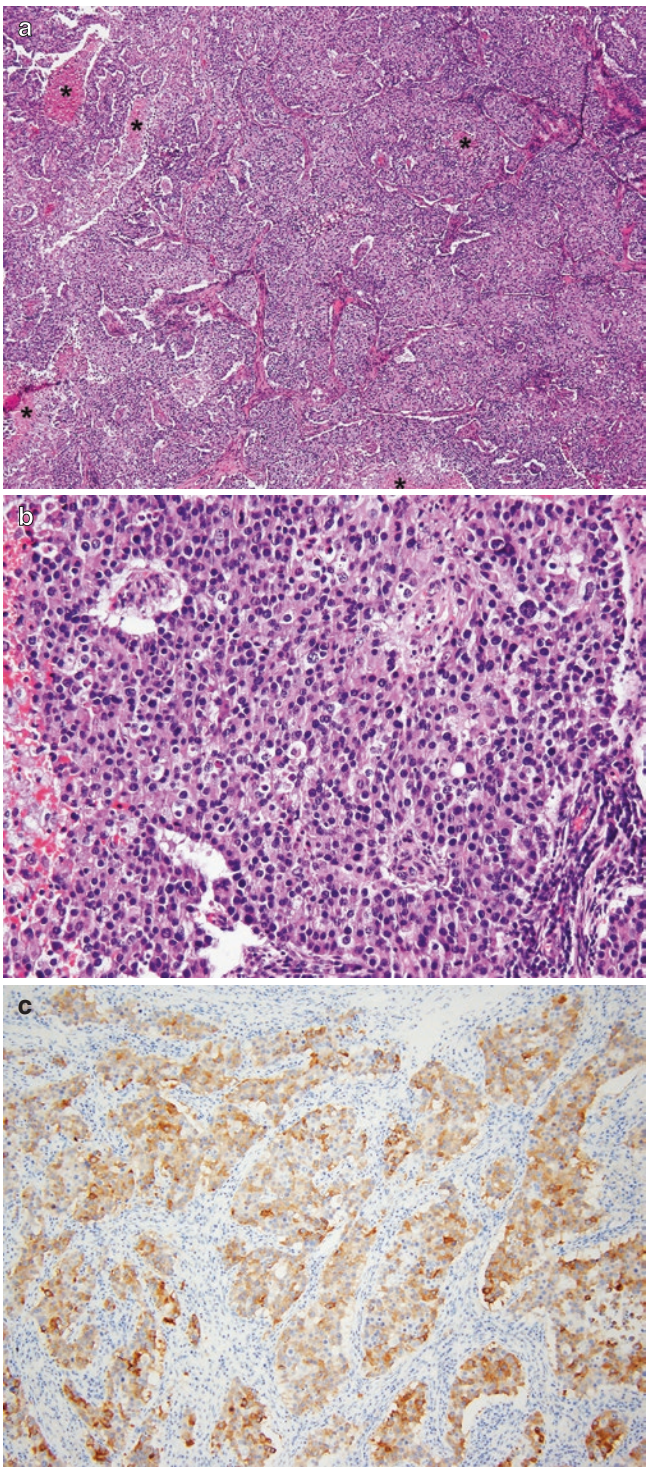

Fig. 13.40 Large cell neuroendocrine carcinoma. (**a**) Low-magnification photomicrograph showing another example of large cell neuroendocrine carcinoma with a nested growth pattern mimicking carcinoid tumor but with multifocal coagulative tumor necrosis (asterisk). (**b**) Higher-magnification photomicrograph showing coarse chromatin and easily identifiable nucleoli in tumor cells with abundant eosinophilic cytoplasm. Numerous mitotic figures are present. (**c**) Photomicrograph of an immunostained section shows diffuse immunoreactivity for synaptophysin. Tumor cells were also positive for CD56 but were negative for chromogranin (not shown)

Large Cell Carcinoma

Large cell carcinoma (Figs. 13.41 and 13.42) is undifferentiated non-small cell carcinoma lacking morphologic and immunohistochemical features of any other specific types and is therefore always a diagnosis of exclusion. For that reason, the diagnosis is made only after thorough examination of a resected tumor. Defined in this way, large cell carcinoma typically is composed of large polygonal cells with coarse or vesicular chromatin, prominent nucleoli, and abundant cytoplasm. The cells are arranged in sheets without distinct architectural features. Often the differential diagnosis on the basis of histology alone includes large cell or anaplastic lymphomas and melanoma. Immunostains are helpful in establishing an epithelial origin and are by definition negative for markers affiliated with adenocarcinoma (TTF-1, napsin A) and squamous cell carcinoma (CK5/6, p63, p40).

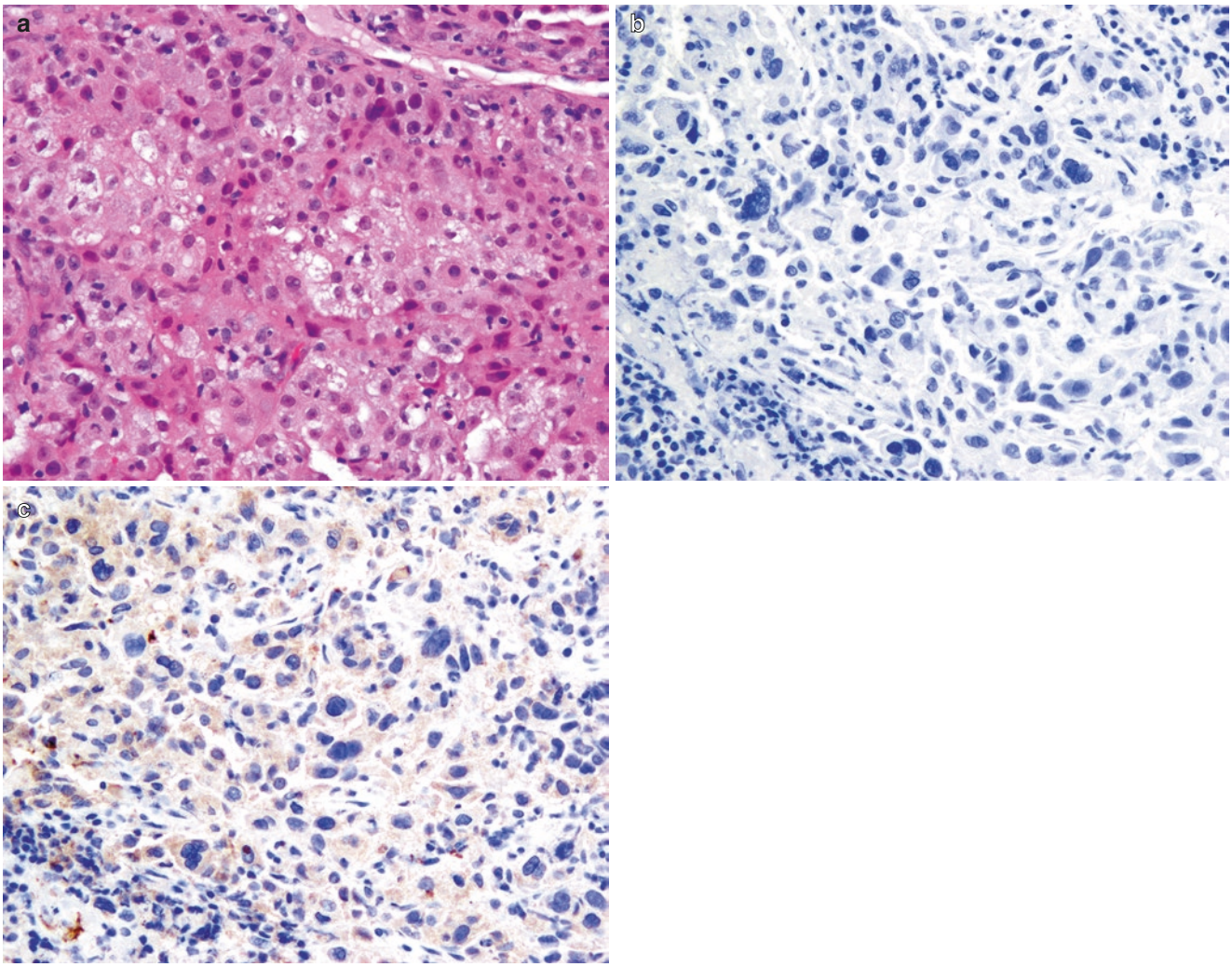

Fig. 13.41 Large cell carcinoma. (**a**) Photomicrograph showing sheets of large polygonal cells with prominent nucleoli and abundant finely vacuolated clear to eosinophilic cytoplasm on H&E stain. By definition, the tumor lacks staining for markers of squamous differentiation such as p40 (**b**) and markers affiliated with adenocarcinoma such as TTF-1 (**c**)

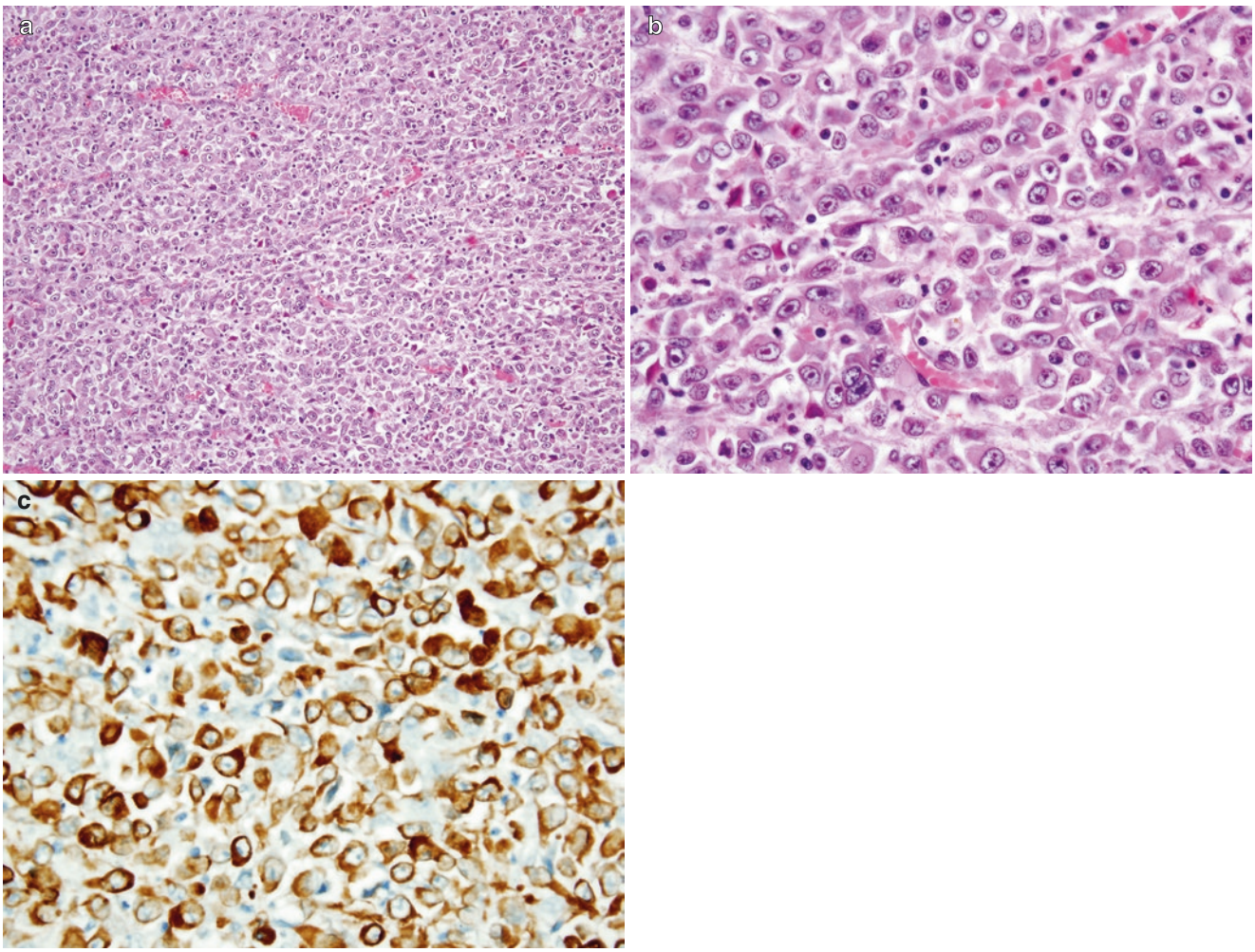

Fig. 13.42 Large cell carcinoma. (**a**) Photomicrograph showing high-grade carcinoma in which large polygonal cells are discohesive and arranged in sheets without evidence of glandular or squamous differentiation. (**b**) High-magnification view shows vesicular chromatin with giant solitary nucleoli and an eccentric rim of densely eosinophilic cytoplasm. Based on these findings alone, the differential diagnosis is likely to include not only large cell carcinoma but also other pleomorphic high-grade tumors such as anaplastic large cell lymphoma and melanoma. (**c**) High-magnification photomicrograph showing strong cytoplasmic staining using a pancytokeratin cocktail (AE1/AE3 and CAM5.2). Tumor cells were negative for all other markers tested including TTF-1, napsin A, CK5/CK6, and p63 (not shown)

Sarcomatoid Carcinoma

Sarcomatoid carcinoma (Figs. 13.43, 13.44, 13.45, 13.46, 13.47, 13.48, 13.49, 13.50 and 13.51) is a general term applied to high-grade variants of non-small cell carcinoma in which at least a portion of the tumor has histologic features resembling nonepithelial sarcomas.

Sarcomatoid carcinomas may or may not have a clearly identifiable epithelial component with histologic features indistinguishable from conventional carcinoma subtypes such as adenocarcinoma, squamous cell carcinoma, and/or large cell carcinoma. Rare examples of sarcomatoid carcinoma have a component of small cell carcinoma (e.g., "combined small cell and spindle-cell carcinoma"). Tumors that comprise both sarcomatoid and conventional carcinomatous components are often referred to as biphasic and are termed carcinosarcoma if the sarcomatous component duplicates the features of a classifiable sarcoma type such as osteosarcoma, chondrosarcoma, or rhabdomyosarcoma. Other variants of sarcomatoid carcinoma included under this generic heading may be specified as spindle-cell carcinomas, giant cell carcinomas, pleomorphic carcinomas (which are distinguished by a combination of spindle cells and giant cells with or without a conventional carcinomatous component), and pulmonary blastomas.

Subclassifying high-grade sarcomatoid carcinoma into these subtypes has little if any clinical significance but can be helpful in thinking about the differential diagnosis. Most nonscreening-detected sarcomatoid carcinomas present as large, centrally necrotic masses (high T stage) with paradoxically low rates of nodal or distant metastases (low N and M stage) at the time of diagnosis. The natural history tends to be an aggressive course with low survival rates.

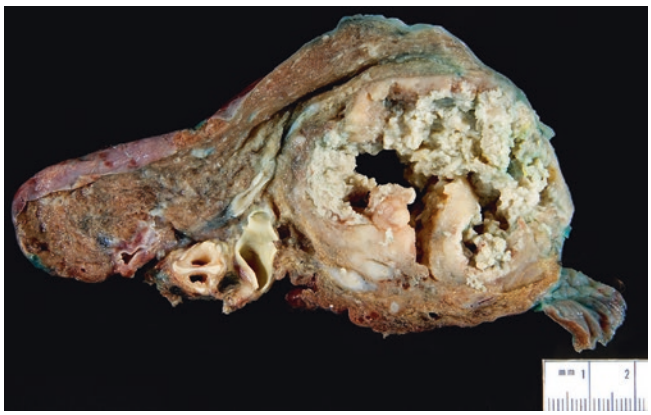

Fig. 13.43 Sarcomatoid carcinoma. Photograph illustrating cut surface of a large centrally necrotic sarcomatoid carcinoma. (Courtesy of Dr. J. Carvalho, Minneapolis, MN)

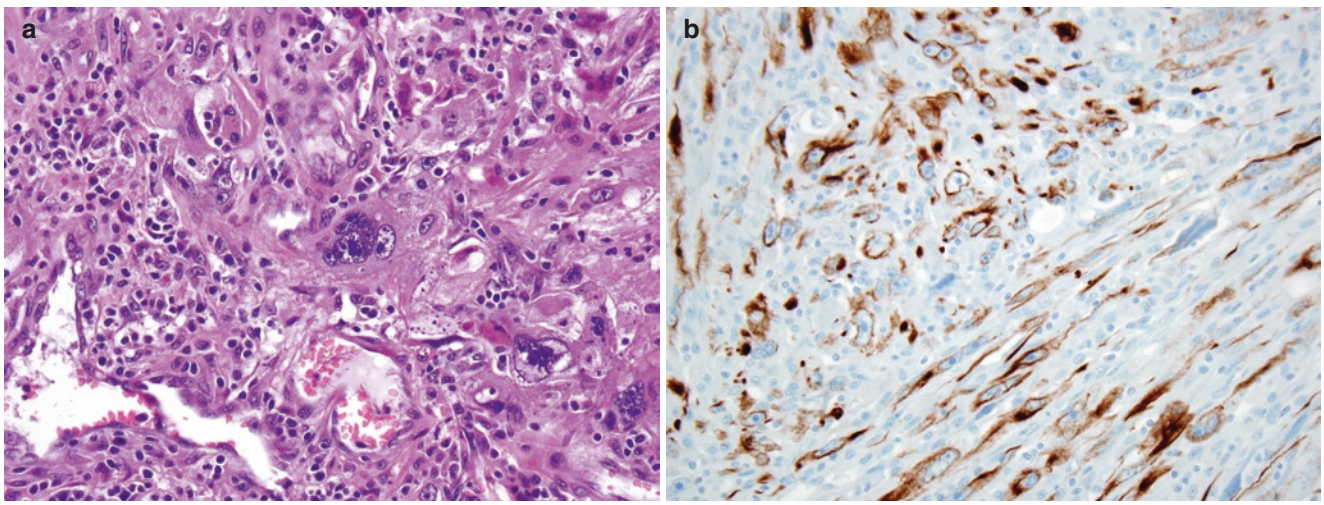

Fig. 13.44 Pleomorphic carcinoma. (**a**) High-magnification photomicrograph demonstrates an undifferentiated carcinoma with large bizarre nuclei, multinucleated giant cells, and spindle cells. (**b**) High-magnification photomicrograph showing that tumor cells are positive for pancytokeratins (AE1/AE3) but were negative for TTF-1 and p63 (not shown)

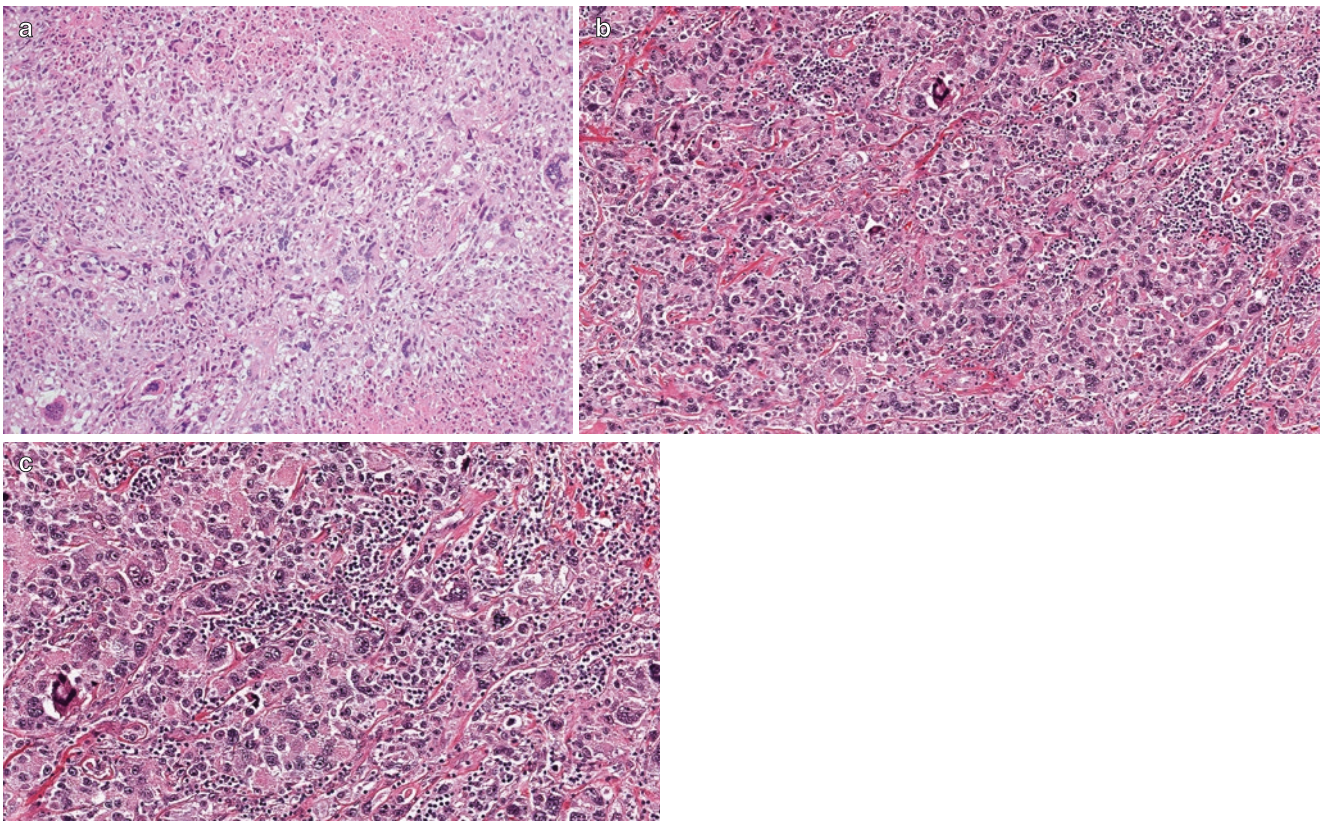

Fig. 13.45 Pleomorphic and giant cell carcinoma. (**a**) Photomicrograph showing a high-grade non-small cell carcinoma with prominent multinucleated giant cells. (**b**) and (**c**), Photomicrographs of a "pure" giant cell carcinoma, an extremely rare variant of sarcomatoid carcinoma that is associated with an extremely aggressive course

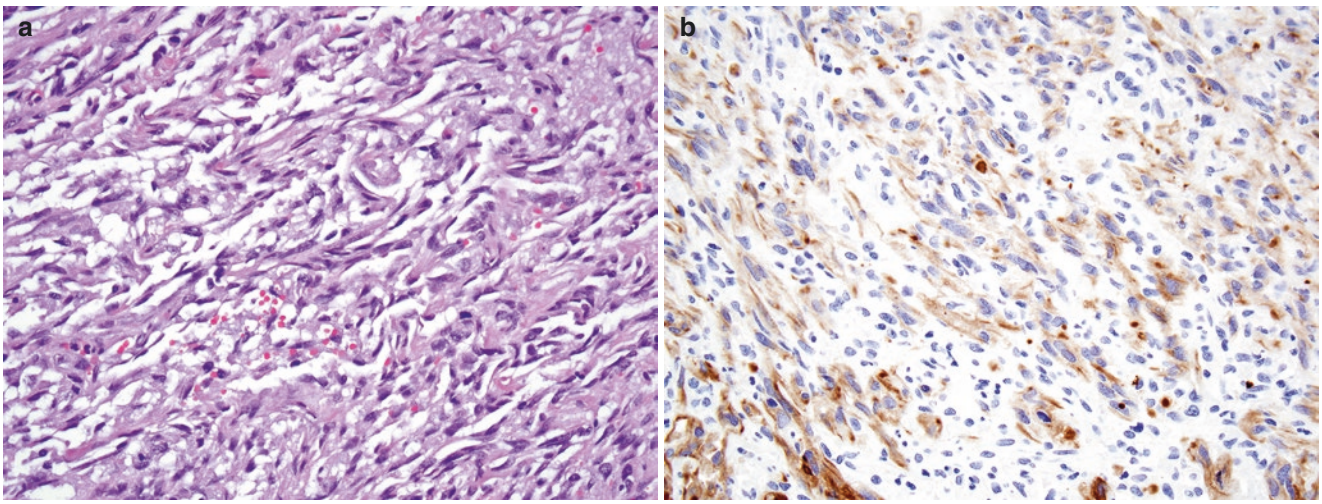

Fig. 13.46 Spindle-cell carcinoma. (**a**) High-magnification photomicrograph showing a tumor consisting entirely of spindle cells. The tumor cells are relatively uniform, growing in fascicles and whorls with surprisingly mild cytologic atypia. (**b**) High-magnification view of immunostained section showing that the spindle cells are positive for pancytokeratins (AE1/AE3)

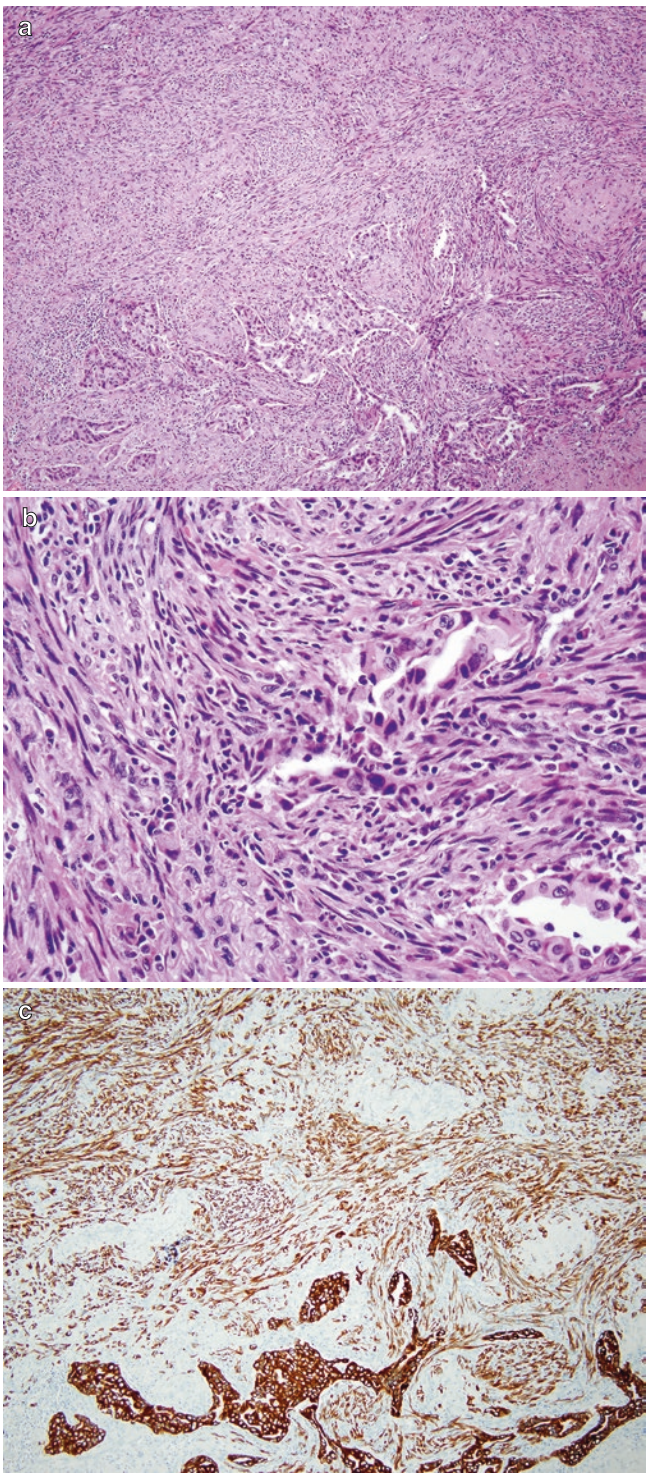

Fig. 13.47 Spindle-cell carcinoma with adenocarcinoma. (**a**) Low-magnification photomicrograph showing a tumor consisting of both spindle cells (at least 10% of the tumor) and adenocarcinoma with an acinar and cribriform growth pattern. (**b**) Higher-magnification photomicrograph showing an intimate admixture of neoplastic glands and spindle cells. (**c**) Photomicrograph of immunostained sections showing that both spindle-cell and glandular components are positive for pancytokeratins (AE1/AE3)

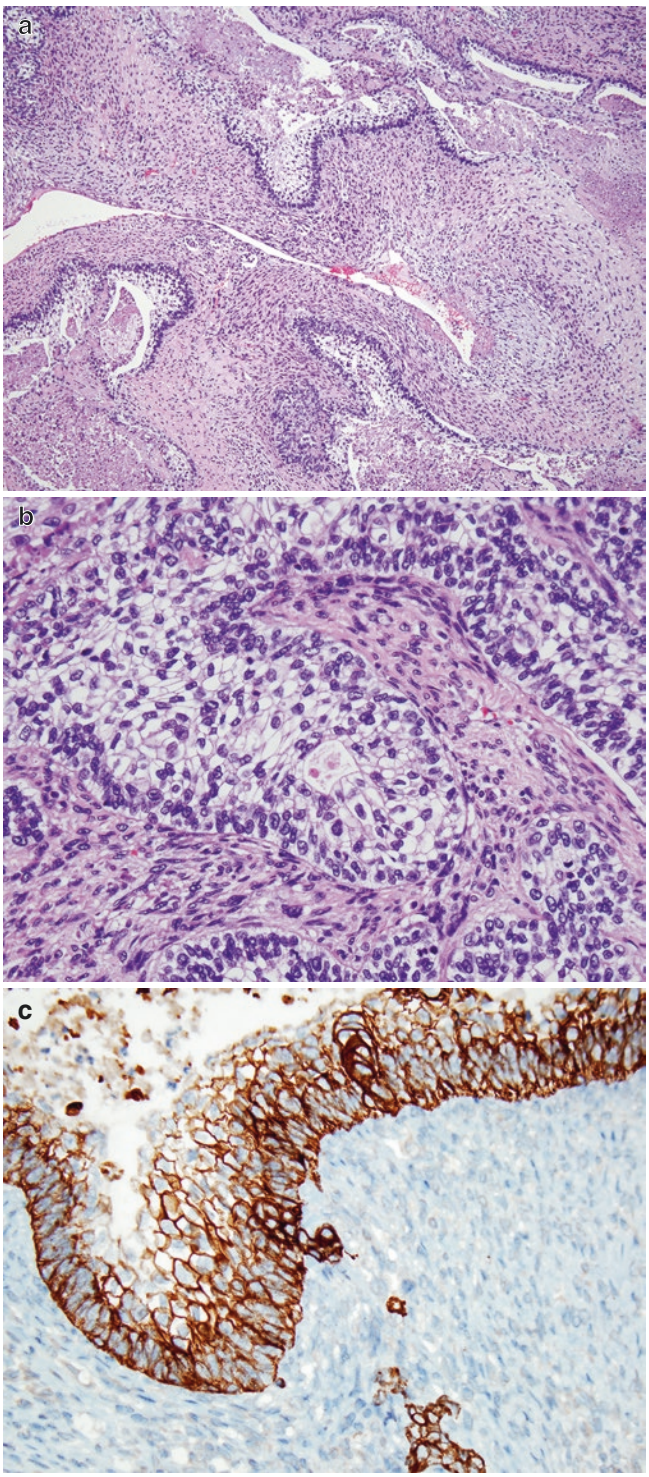

Fig. 13.48 Spindle-cell carcinoma with squamous cell carcinoma. (**a**) Low-magnification view of large, necrotizing, polypoid endobronchial tumor consisting of a combination of spindle cells (at least 10% of the tumor) and squamous cell carcinoma with clear cell change. (**b**) High-magnification photomicrograph showing squamous cell carcinoma in which polygonal cells have abundant clear cytoplasm and are arranged in a well-developed epidermoid growth pattern without keratinization. (**c**) High-magnification view of immunostained section shows staining for high molecular weight cytokeratins (CK5/6) limited to the squamous component. A stain for p63 showed the same distribution (not shown)

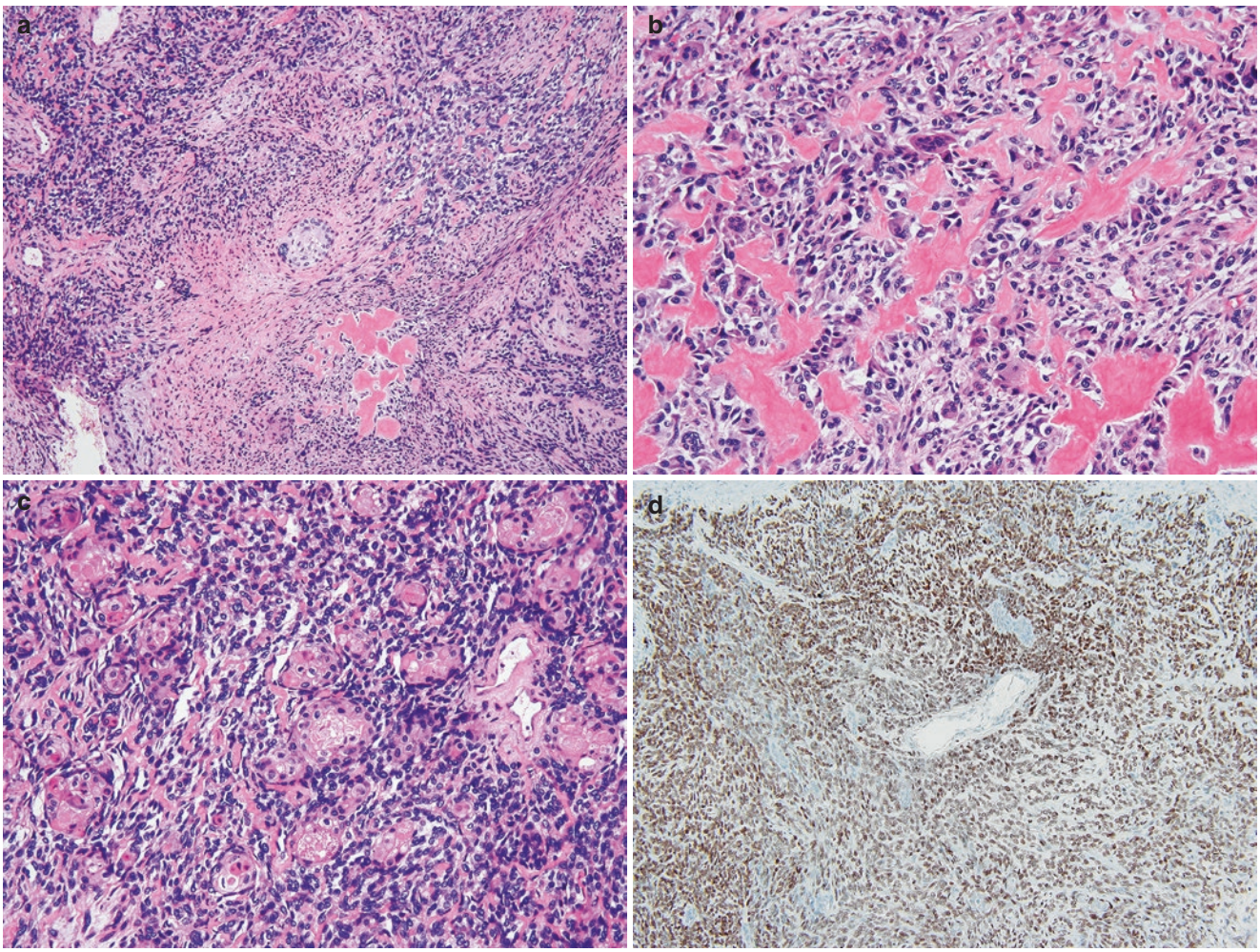

Fig. 13.49 Carcinosarcoma. (**a**) Photomicrograph of a tumor with admixed squamous cell carcinoma and both sarcomatoid (spindle-cell) and sarcomatous (osteosarcoma) components. (**b**) High-magnification view of differentiated sarcomatous component closely resembling osteosarcoma with spicules of neoplastic osteoid affiliated with undifferentiated neoplastic and osteoclast-like giant cells. (**c**) High-magnification view of the carcinomatous component in which there is abrupt squamous differentiation in the form of keratinizing squamous pearls. (**d**) Photomicrograph of immunostained sections showing that much of the tumor, including relatively undifferentiated spindle cells, was positive for p63

Fig. 13.50 Pulmonary blastoma. Gross photograph showing cut surface of a large, well-circumscribed pulmonary blastoma with patchy necrosis

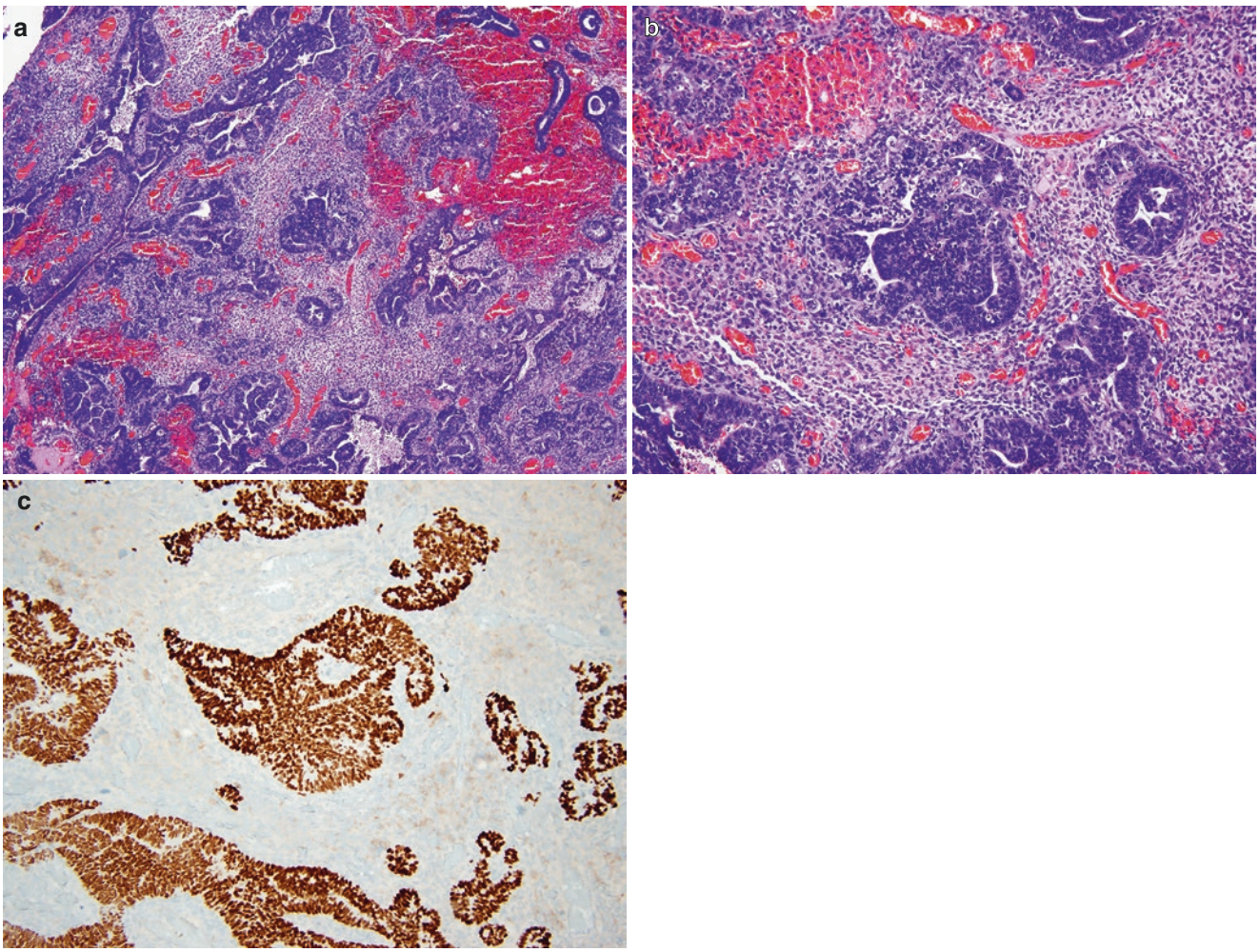

Fig. 13.51 Pulmonary blastoma. (**a**) Photomicrograph showing a biphasic tumor consisting of an adenocarcinoma resembling endometrioid carcinoma and a primitive ("blastematous") stromal component. (**b**) Higher-magnification photomicrograph showing pseudostratified nonmucinous columnar cells with a well-developed acinar and cribriform growth pattern. Associated morules may also be present, furthering the resemblance to endometrioid carcinomas. When present in pure form without the primitive stromal component, the "monophasic" epithelial component is termed fetal adenocarcinoma. (**c**) Photomicrograph of an immunostained section showing strong staining of the adenocarcinomatous component for TTF-1 with negative staining in the stromal component. The stromal cells are usually negative for TTF-1 and are also frequently negative for cytokeratins

Salivary Gland-Type Carcinomas

Salivary gland-type carcinomas (Figs. 13.52, 13.53, 13.54, 13.55, 13.56, 13.57 and 13.58) are generally rare and usually present as central tumors arising from cartilaginous airways. Common types include mucoepidermoid carcinoma and adenoid cystic carcinoma. Other rare variants, including primary mammary analogue secretory carcinoma, have also been reported.

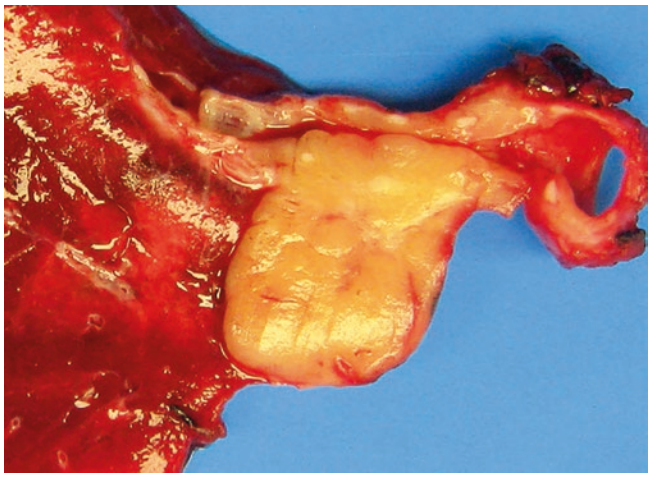

Fig. 13.52 Adenoid cystic carcinoma. Gross photograph of sleeve resection for adenoid cystic carcinoma. The tumor extensively infiltrates the submucosal tissues, extending beyond the airway cartilage to form a well-defined unencapsulated peribronchial mass

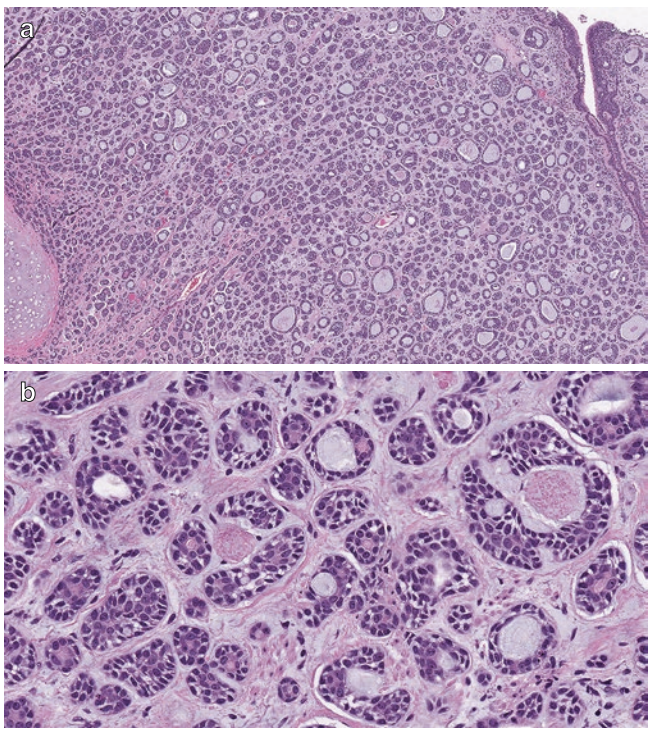

Fig. 13.53 Adenoid cystic carcinoma. (**a**) Low-magnification photomicrograph shows a tumor with a predominantly tubular growth pattern diffusely involving the bronchial wall and infiltrating into peribronchial soft tissue. (**b**) A higher-magnification view shows characteristic small myoepithelial cells with hyperchromatic angulated nuclei and occasional central clusters of cytologically distinct ductal epithelial cells. This tumor shows the characteristic pattern of associated extracellular pseudoglandular spaces containing granular and pale-staining basophilic myxoid secretions

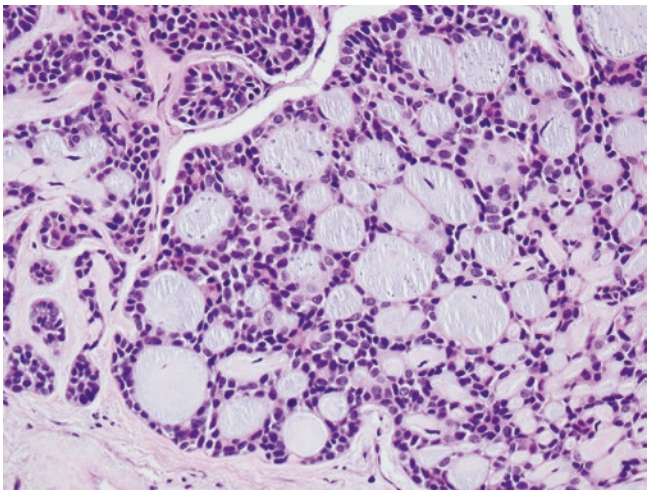

Fig. 13.54 Adenoid cystic carcinoma. High-magnification photomicrograph of another example showing classic cribriform architecture in which small tumor cells with scant cytoplasm and angulated hyperchromatic nuclei constitute the majority of the neoplasm with only scattered ductal epithelial cells with eosinophilic cytoplasm. No mitosis or necrosis is seen. The cribriform structure is created by pale-staining extracellular myxoid secretions accumulated within pseudoglandular spaces ("pseudocysts"). The stroma is fibrotic, with focal areas of eosinophilic basement membrane-like materials (upper left)

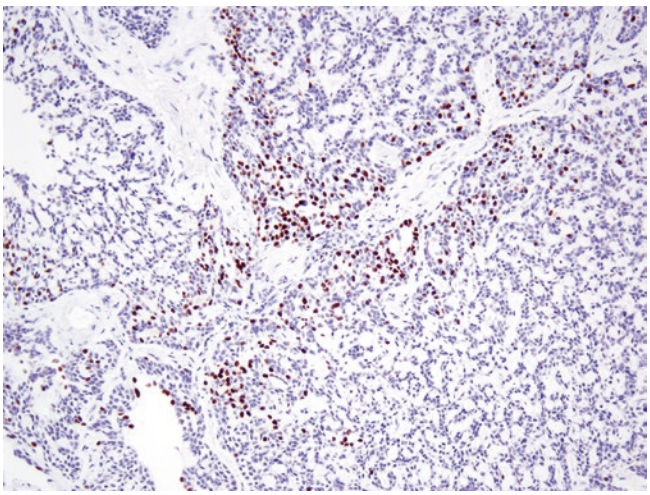

Fig. 13.55 Adenoid cystic carcinoma. Photomicrograph of an immunostained section shows that tumor cells may be focally positive for TTF-1

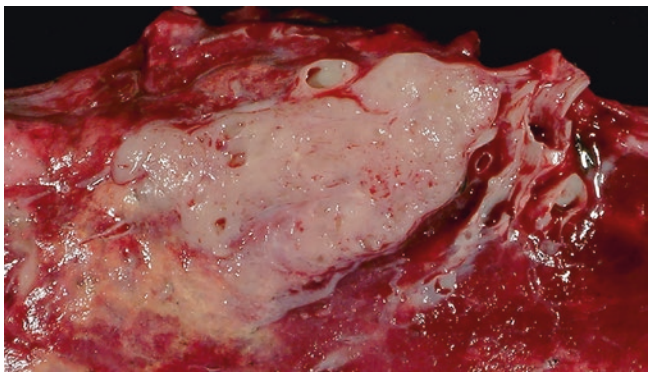

Fig. 13.56 Mucoepidermoid carcinoma. Gross photograph showing the cut surface of a well-demarcated polypoid endobronchial mass. Note that the tumor is focally cystic and affiliated with "golden [obstructive] pneumonia" at lower left. (Courtesy of J. Carvalho, Minneapolis, MN)

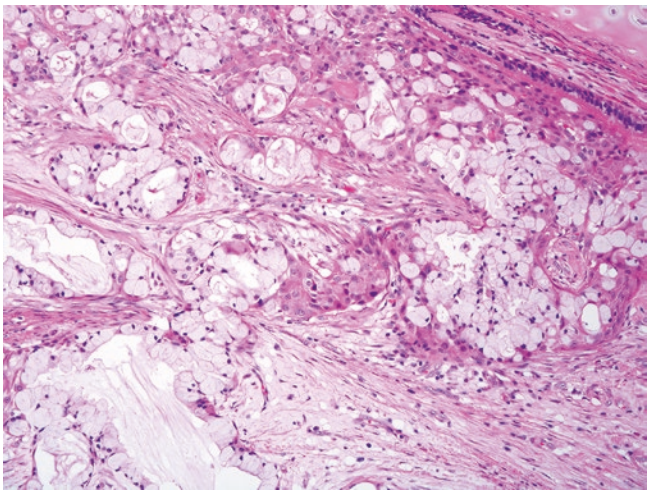

Fig. 13.58 Mucoepidermoid carcinoma. Photomicrograph of another mucoepidermoid carcinoma showing dramatic admixture of mucinous goblet cells and squamoid "intermediate" cells

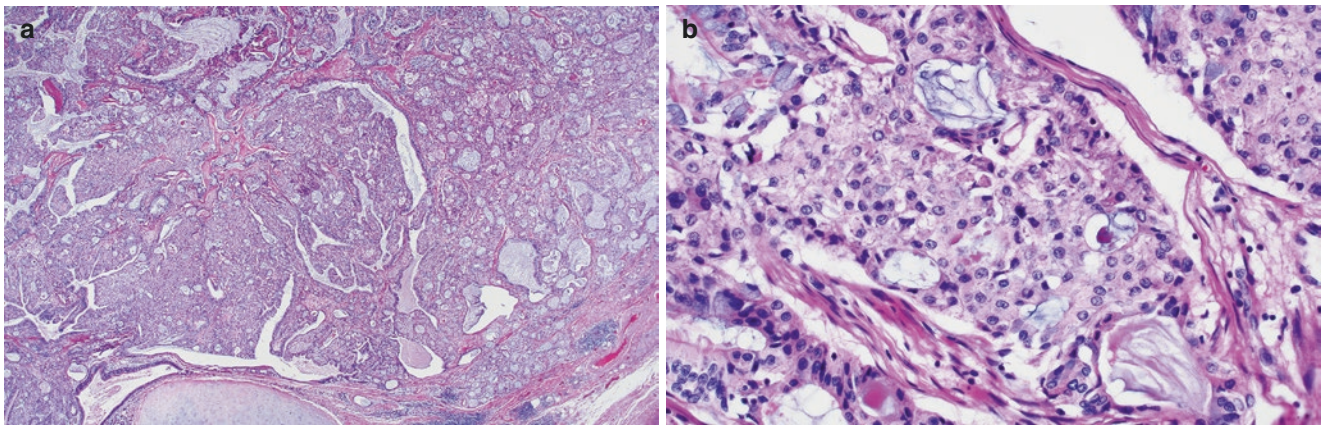

Fig. 13.57 Mucoepidermoid carcinoma. (**a**) Low-magnification photomicrograph shows an endobronchial tumor with mixed solid and cystic growth patterns. The cystic areas are affiliated with variably abundant extracellular mucin. (**b**) High-magnification view shows solid nests composed of a mixture of cuboidal "intermediate" cells and mucinous goblet cells

Suggested Reading

Brambilla E, Moro D, Veale D, Brichon PY, Stoebner P, Paramelle B, et al. Basal cell (basaloid) carcinoma of the lung: a new morphologic and phenotypic entity with separate prognostic significance. Hum Pathol. 1992;23:993–1003.

Kadota K, Villena-Vargas J, Yoshizawa A, Motoi N, Sima CS, Riely GJ, et al. Prognostic significance of adenocarcinoma in situ, minimally invasive adenocarcinoma, and nonmucinous lepidic predominant invasive adenocarcinoma of the lung in patients with stage I disease. Am J Surg Pathol. 2014;38:448–60.

Kitamura H, Kameda Y, Ito T, Hayashi H. Atypical adenomatous hyperplasia of the lung. Implications for the pathogenesis of peripheral lung adenocarcinoma. Am J Clin Pathol. 1999;111:610–22.

Koss MN, Hochholzer L, O'Leary T. Pulmonary blastomas. Cancer. 1991;67:2368–81.

Maziak DE, Todd TR, Keshavjee SH, Winton TL, Van Nostrand P, Pearson FG. Adenoid cystic carcinoma of the airway: thirty-two-year experience. J Thorac Cardiovasc Surg. 1996;112:1522–31. discussion 1531–22

Mori M, Rao SK, Popper HH, Cagle PT, Fraire AE. Atypical adenomatous hyperplasia of the lung: a probable forerunner in the development of adenocarcinoma of the lung. Mod Pathol. 2001;14:72–84.

Nakatani Y, Kitamura H, Inayama Y, Kamijo S, Nagashima Y, Shimoyama K, et al. Pulmonary adenocarcinomas of the fetal lung type: a clinicopathologic study indicating differences in histology, epidemiology, and natural history of low-grade and high-grade forms. Am J Surg Pathol. 1998;22:399–411.

Nicholson SA, Beasley MB, Brambilla E, Hasleton PS, Colby TV, Sheppard MN, et al. Small cell lung carcinoma (SCLC): a clinicopathologic study of 100 cases with surgical specimens. Am J Surg Pathol. 2002;26:1184–97.

Roden AC, Garcia JJ, Wehrs RN, Colby TV, Khoor A, Leslie KO, et al. Histopathologic, immunophenotypic and cytogenetic features of pulmonary mucoepidermoid carcinoma. Mod Pathol. 2014;27:1479–88.

Rossi G, Cavazza A, Sturm N, Migaldi M, Facciolongo N, Longo L, et al. Pulmonary carcinomas with pleomorphic, sarcomatoid, or sarcomatous elements: a clinicopathologic and immunohistochemical study of 75 cases. Am J Surg Pathol. 2003;27:311–24.

Rossi G, Mengoli MC, Cavazza A, Nicoli D, Barbareschi M, Cantaloni C, et al. Large cell carcinoma of the lung: clinically oriented classification integrating immunohistochemistry and molecular biology. Virchows Arch. 2014;464:61–8.

Terry J, Leung S, Laskin J, Leslie O, Gown AM, Ionescu DN. Optimal immunohistochemical markers for distinguishing lung adenocarcinomas from squamous cell carcinomas in small tumor samples. Am J Surg Pathol. 2010;34:1805–11.

Travis WD. Update on small cell carcinoma and its differentiation from squamous cell carcinoma and other non-small cell carcinomas. Mod Pathol. 2012;25(Suppl 1):S18–30.

Travis WD, Linnoila RI, Tsokos MG, Hitchcock CL, Cutler GB Jr, Nieman L, et al. Neuroendocrine tumors of the lung with proposed criteria for large-cell neuroendocrine carcinoma. An ultrastructural, immunohistochemical, and flow cytometric study of 35 cases. Am J Surg Pathol. 1991;15:529–53.

Travis WD, Rush W, Flieder DB, Falk R, Fleming MV, Gal AA, et al. Survival analysis of 200 pulmonary neuroendocrine tumors with clarification of criteria for atypical carcinoid and its separation from typical carcinoid. Am J Surg Pathol. 1998;22:934–44.

Travis WD, Brambilla E, Noguchi M, Nicholson AG, Geisinger KR, Yatabe Y, et al. International Association for the Study of Lung Cancer/American Thoracic Society/European Respiratory Society international multidisciplinary classification of lung adenocarcinoma. J Thorac Oncol. 2011;6:244–85.

Travis WD, Brambilla E, Noguchi M, Nicholson AG, Geisinger K, Yatabe Y, et al. Diagnosis of lung cancer in small biopsies and cytology: implications of the 2011 International Association for the Study of Lung Cancer/American Thoracic Society/European Respiratory Society classification. Arch Pathol Lab Med. 2013a;137:668–84.

Travis WD, Brambilla E, Noguchi M, Nicholson AG, Geisinger K, Yatabe Y, et al. Diagnosis of lung adenocarcinoma in resected specimens: implications of the 2011 International Association for the Study of Lung Cancer/American Thoracic Society/European Respiratory Society classification. Arch Pathol Lab Med. 2013b;137:685–705.

Yoshizawa A, Sumiyoshi S, Sonobe M, Kobayashi M, Fujimoto M, Kawakami F, et al. Validation of the IASLC/ATS/ERS lung adenocarcinoma classification for prognosis and association with EGFR and KRAS gene mutations: analysis of 440 Japanese patients. J Thorac Oncol. 2013;8:52–61.

Malignant Nonepithelial Lung and Pleural Neoplasms

14

Chen Zhang and Jeffrey L. Myers

Mesenchyme-derived malignant neoplasms of the lung are rare, although virtually any type of soft-tissue sarcoma can occur in the lungs, ranging from tumors of low malignant potential to high-grade sarcomas. Among them, the most common tumors include inflammatory myofibroblastic tumor, solitary fibrous tumor, epithelioid hemangioendothelioma, and synovial sarcoma. Other rare primary mesenchymal tumors are angiomatoid fibrous histiocytoma and primary pulmonary myxoid sarcoma. Some of these tumors tend to occur in young adults and children, and several have typical clinical presentations and specific cytogenetic and molecular alterations like their soft-tissue counterparts.

Inflammatory Myofibroblastic Tumor

Inflammatory myofibroblastic tumor (Figs. 14.1, 14.2, 14.3, 14.4, 14.5, 14.6, 14.7 and 14.8) is a histologically distinctive spindle-cell neoplasm that occurs most commonly in the deep soft tissues of children and young adults. Inflammatory myofibroblastic tumors present less

Fig. 14.1 Inflammatory myofibroblastic tumor. Gross image shows a large, firm, circumscribed tumor. The cut surface is fleshy white and tan with focal cystic degeneration and has gritty calcifications

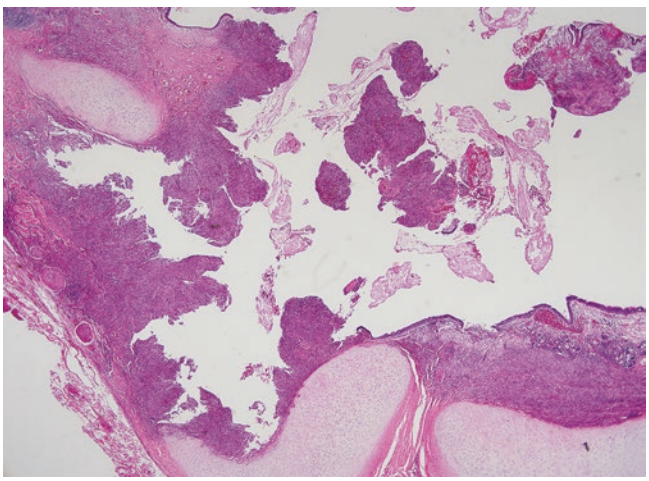

Fig. 14.2 Inflammatory myofibroblastic tumor (IMT). Low-magnification photomicrograph showing an endobronchial IMT that involves the mucosa and submucosa of a bronchus

C. Zhang (✉)
Department of Pathology and Laboratory Medicine, Indiana University School of Medicine, Indianapolis, IN, USA
e-mail: chenzhan@iupui.edu

J. L. Myers
Department of Pathology, Michigan Medicine, Ann Arbor, MI, USA
e-mail: myerjeff@med.umich.edu

© Springer Science+Business Media, LLC, part of Springer Nature 2018
C. Zhang, J. L. Myers (eds.), *Atlas of Lung Pathology*, Atlas of Anatomic Pathology,
https://doi.org/10.1007/978-1-4939-8689-7_14

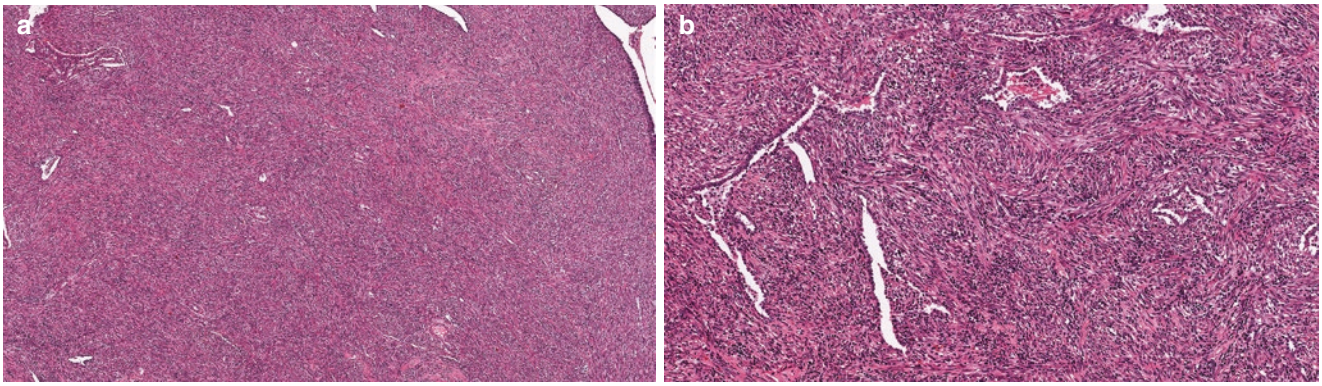

Fig. 14.3 Inflammatory myofibroblastic tumor. (**a**) Low-magnification photomicrograph shows a cellular tumor composed of spindle cells, arranged in an orderly fascicular pattern admixed with inflammatory cells. (**b**) High-magnification photomicrograph shows spindled tumor cells with pale eosinophilic cytoplasm and indistinct borders arranged in ill-defined short fascicles. Nuclear atypia is minimal, and mitotic figures are rare. The lesional cells are associated with a chronic inflammatory infiltrate in which plasma cells predominate. Entrapped alveolar space lined by reactive pneumocytes is present, resulting in a pseudobiphasic appearance

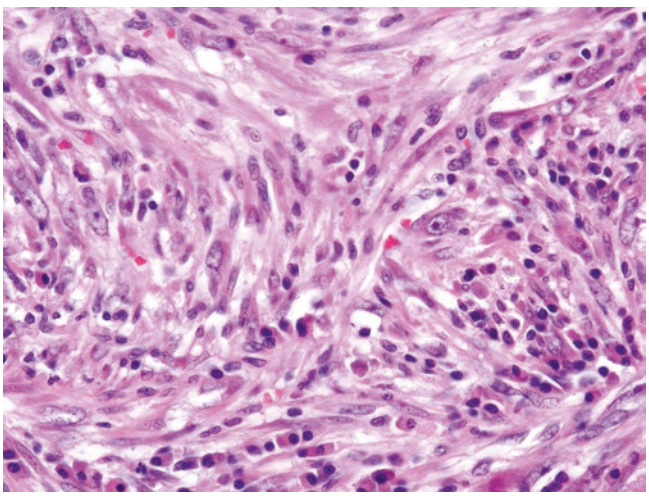

Fig. 14.4 Inflammatory myofibroblastic tumor. High-magnification photomicrograph from another inflammatory myofibroblastic tumor shows focal cytologic atypia, including occasionally prominent nucleoli

commonly as primary intrathoracic neoplasms involving the lung or mediastinum. Synonyms include inflammatory pseudotumor, a less specific term applied historically to a more heterogeneous group that includes nonneoplastic spindle-cell lesions and plasma cell granulomas. Inflammatory myofibroblastic tumors occur in a wide age range but most commonly affect pediatric patients and young adults. About 50% of inflammatory myofibroblastic tumors, particularly those arising in younger patients, are immunoreactive for ALK1 which corresponds to recurrent *ALK* gene rearrangements. Localized inflammatory myofibroblastic tumors have been described with increased numbers of IgG4-positive plasma cells, suggesting a relationship with IgG4-related disease in a subset of patients. Most inflammatory myofibroblastic tumors are indolent and cured with complete surgical excision, although recurrences after incomplete resection and even rare metastases have been reported.

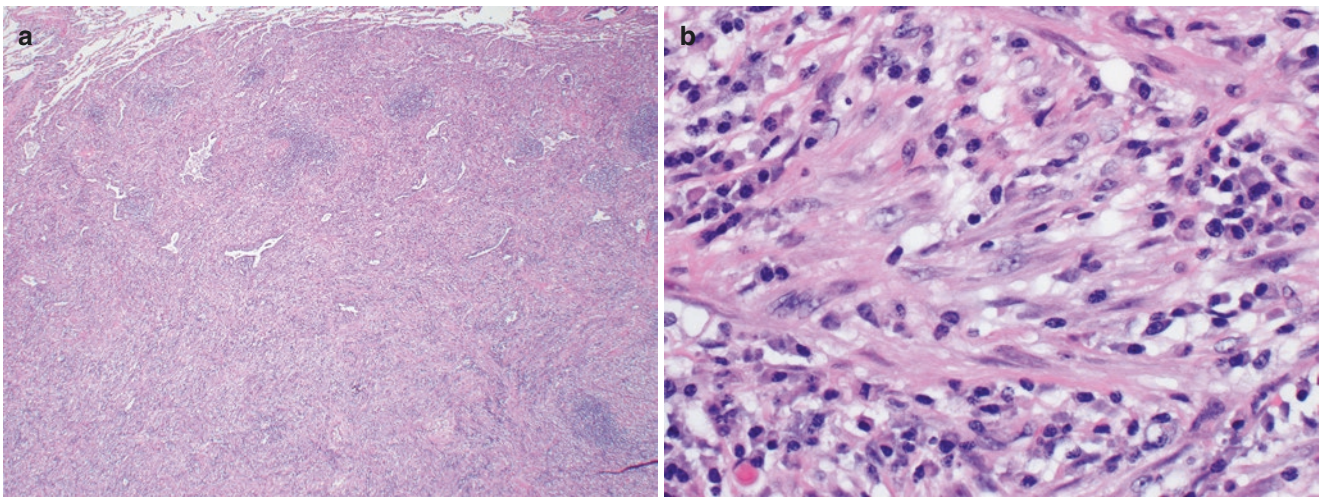

Fig. 14.5 Inflammatory myofibroblastic tumor. (**a**) Low-magnification photomicrograph showing a well-circumscribed spindle-cell neoplasm demonstrating an unencapsulated interface with nonneoplastic lung tissue. (**b**) High-magnification view shows neoplastic myofibroblasts partially obscured by a variably dense infiltrate of plasma cells

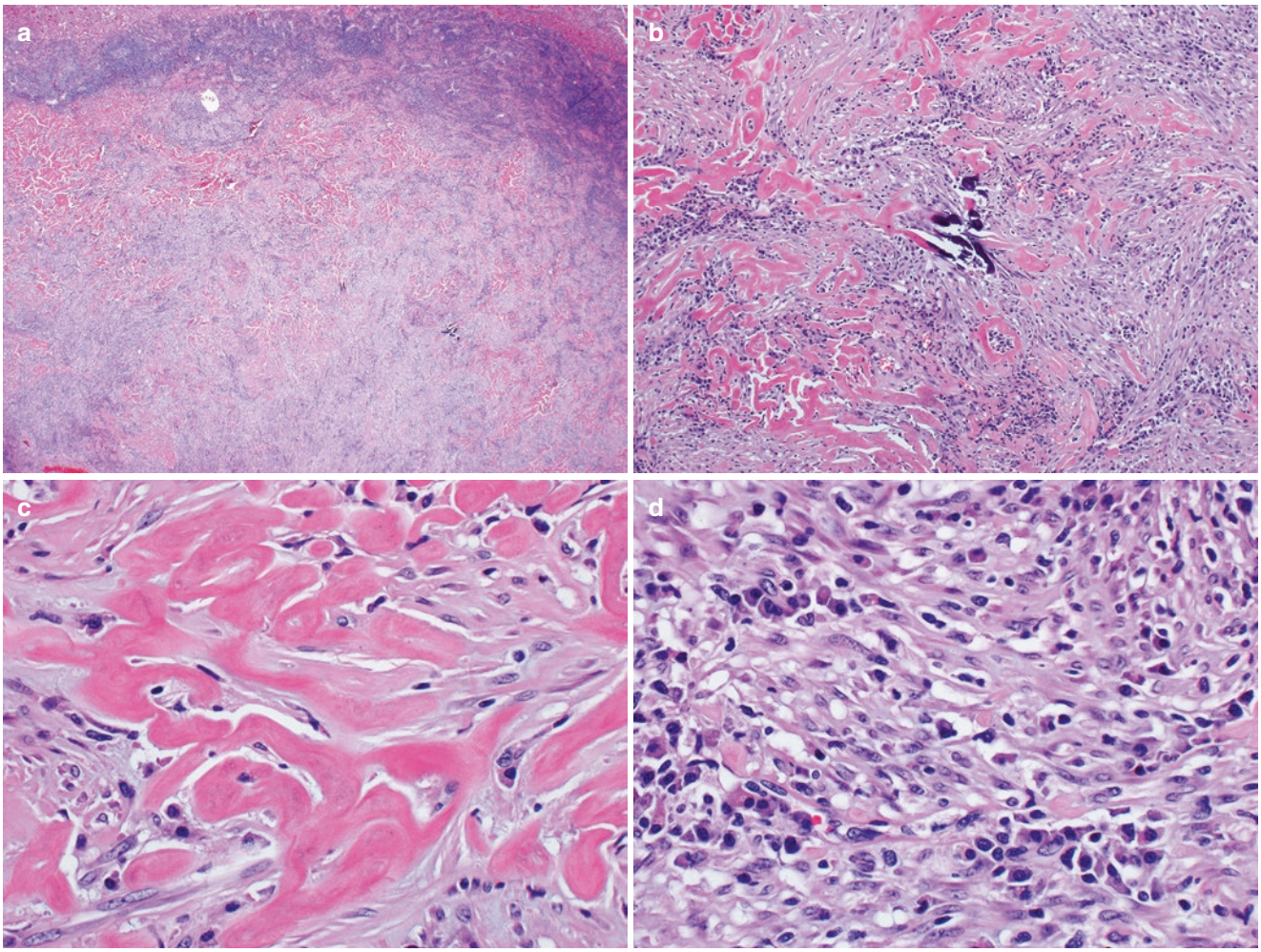

Fig. 14.6 Inflammatory myofibroblastic tumor. (**a**) Low-magnification photomicrograph showing an inflammatory myofibroblastic tumor with sclerosis. (**b**) Higher-magnification photomicrograph showing prominent stromal sclerosis with associated calcifications. (**c**) and (**d**), High-magnification photomicrographs showing coarse collagen bundles in the sclerotic zone (**c**) immediately adjacent to a histologically typical inflammatory myofibroblastic tumor (**d**)

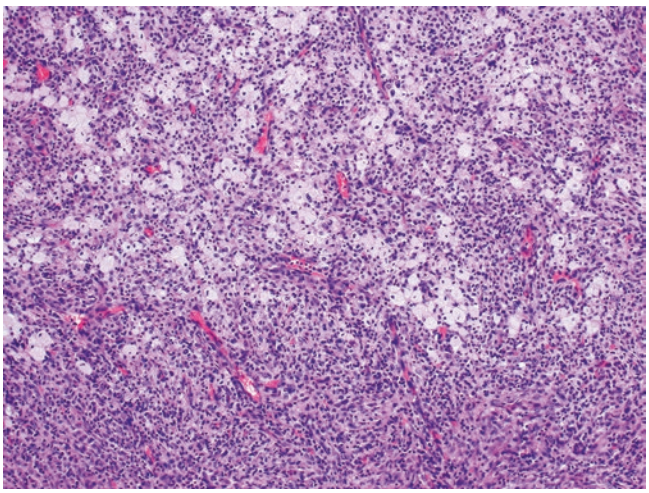

Fig. 14.7 Inflammatory myofibroblastic tumor. Photomicrograph showing prominent foamy histiocytes, a relatively common finding in inflammatory myofibroblastic tumors of the lung

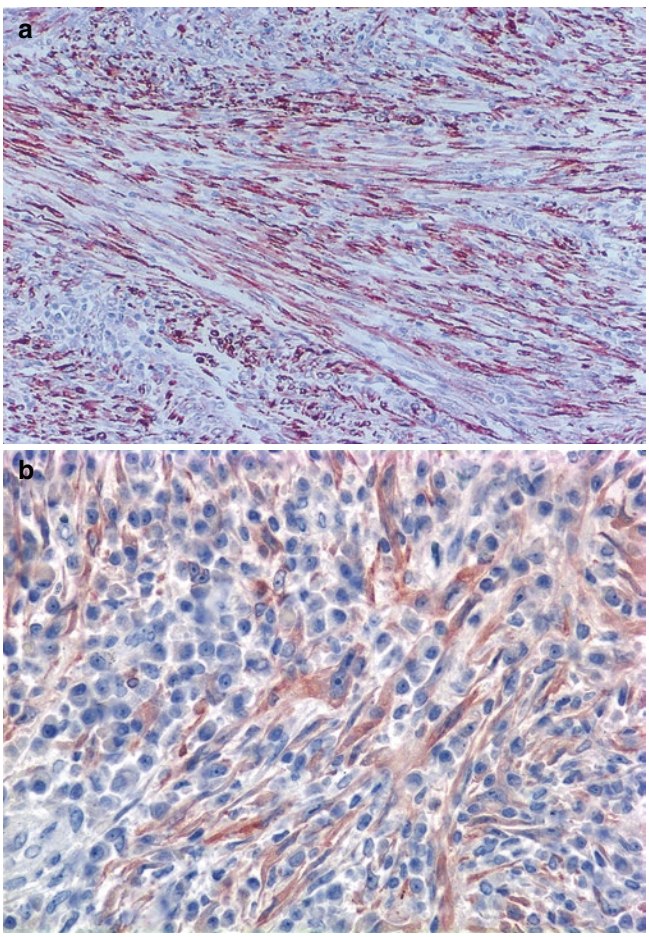

Fig. 14.8 Inflammatory myofibroblastic tumor. The tumor cells variably react to smooth muscle actin (**a**) and ALK1 (**b**) in paraffin section immunostains. Staining for ALK1 is usually cytoplasmic and is seen in about half of inflammatory myofibroblastic tumors. Staining for ALK1 correlates with clonal rearrangements of the *ALK* gene and is more common in pediatric patients

Solitary Fibrous Tumor

Solitary fibrous tumors (Figs. 14.9, 14.10, 14.11, 14.12, 14.13, 14.14 and 14.15) are mesenchymal neoplasms that often arise from visceral or parietal pleura but also occur as intraparenchymal lung tumors. Solitary fibrous tumors have been described in nearly all viscera and deep soft tissues, including the mediastinum. Intrathoracic tumors are often large at the time of diagnosis. Most behave as benign neoplasms, although a subset have malignant histologic features and are at higher risk of local recurrence and distant metastases. Recurrence risk for intrathoracic solitary fibrous tumors is dependent not only on histologic features of malignancy (hypercellularity, necrosis, high mitotic rate) but also on tumor size (≥10 cm), site of origin (parietal versus visceral pleura/intraparenchymal), and gross characteristics of pleural attachment site (sessile versus pedunculated). Immunohistochemical expression of CD34 and STAT6 is characteristic, the latter correlating with recurrent intrachromosomal rearrangements on chromosome 12, resulting in fusion of *NAB2* and *STAT6*.

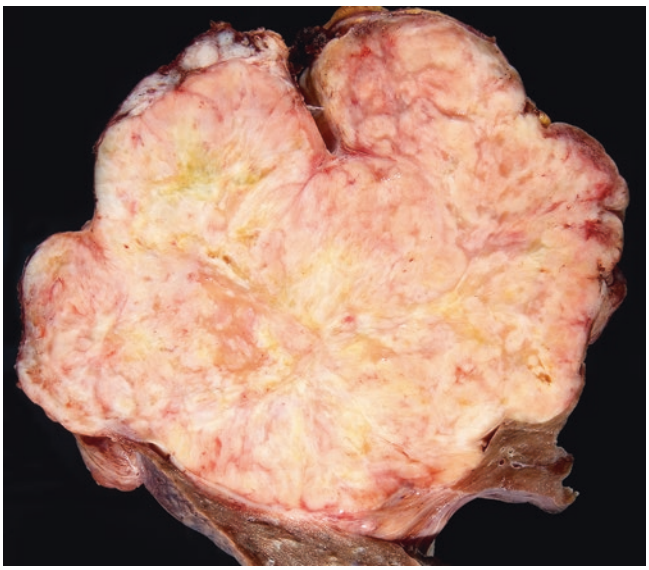

Fig. 14.9 Solitary fibrous tumor. Cut surface of resected solitary fibrous tumor arising from visceral pleura. Despite its large size, the tumor was histologically benign and completely resected, a combination of findings that favors a benign course

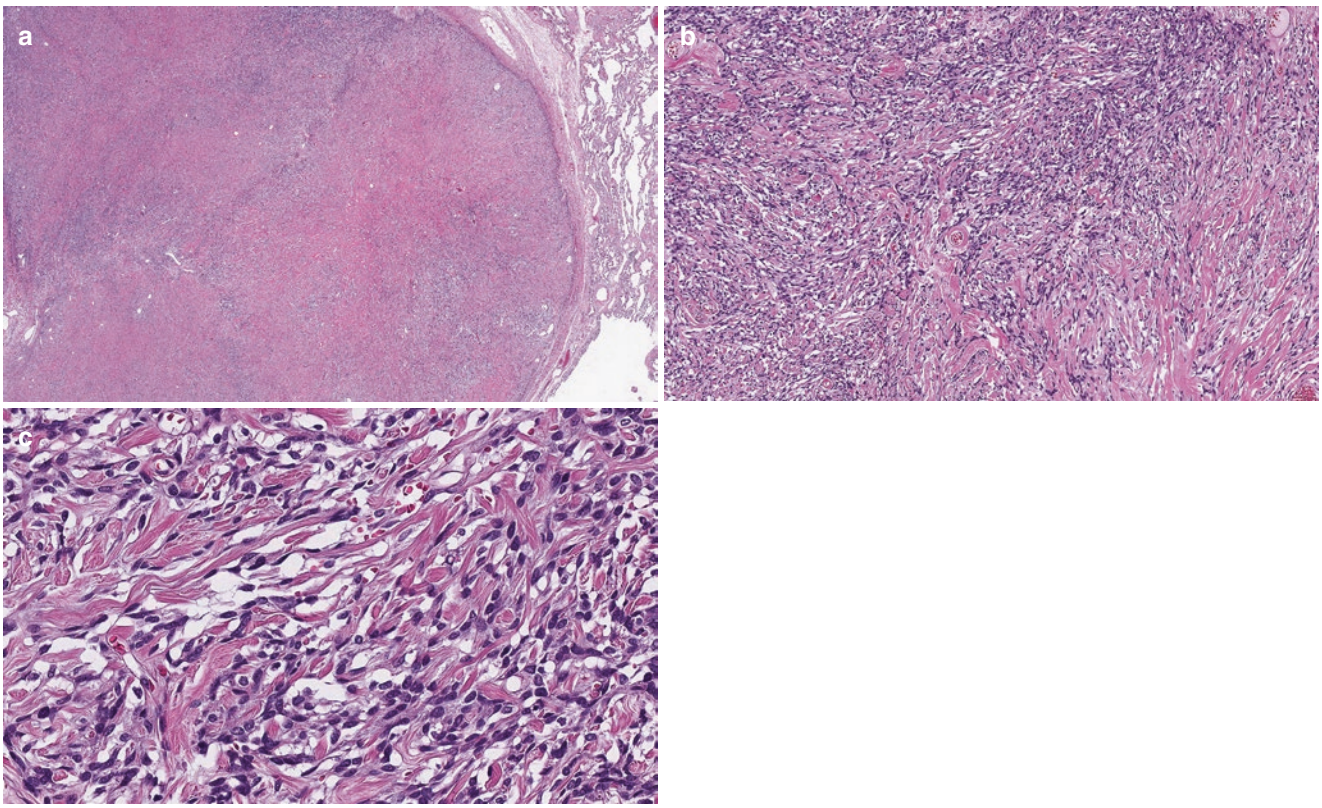

Fig. 14.10 Solitary fibrous tumor. (**a**) Low-magnification photomicrograph showing solitary fibrous tumor with visceral pleural attachment. (**b**) Higher-magnification photomicrograph showing characteristic bland spindle cells arranged haphazardly in a collagenous stroma characterized by thick, keloidal collagen bundles. (**c**) High-magnification view showing plump spindle cells haphazardly distributed within thick collagen bundles

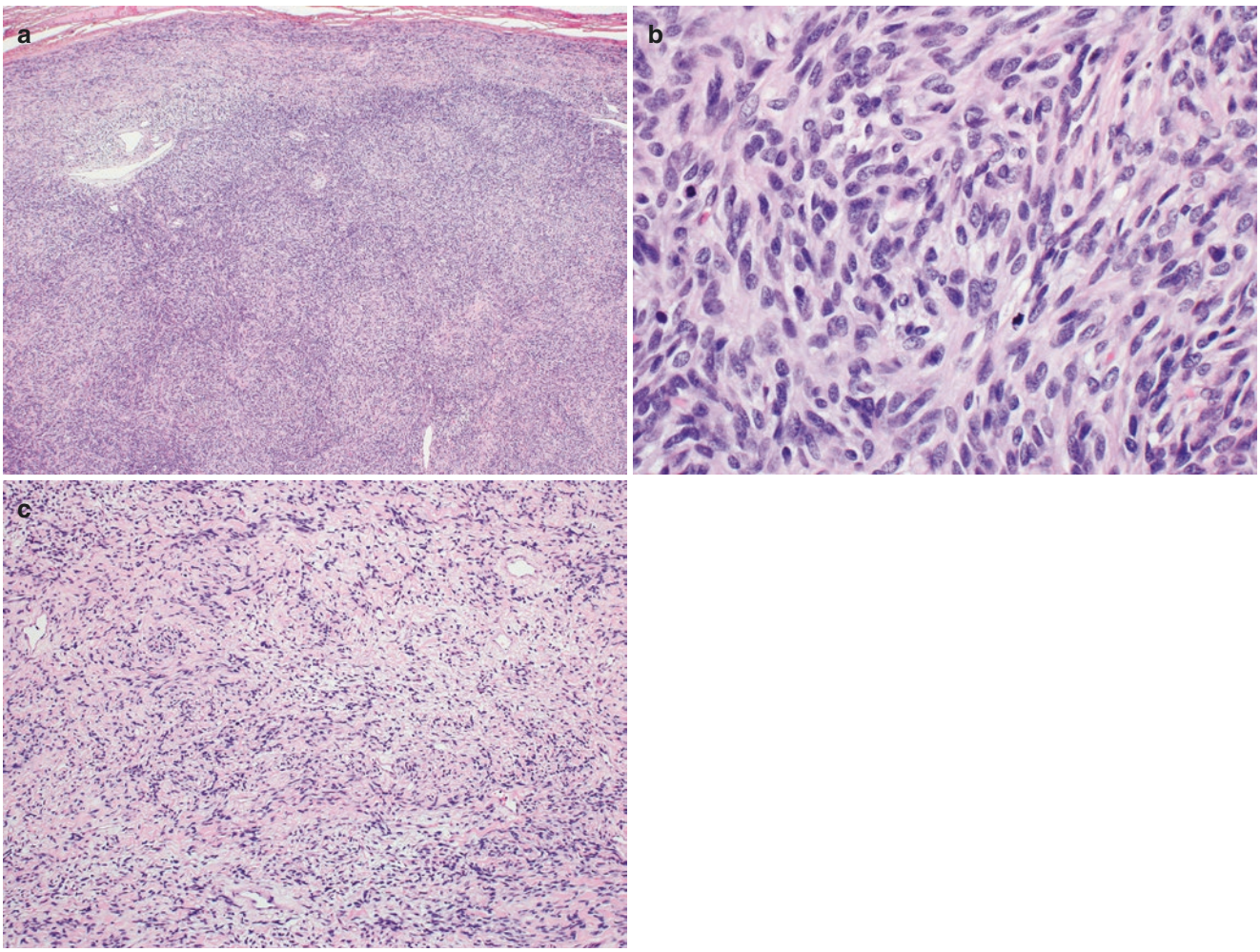

Fig. 14.11 Solitary fibrous tumor. (**a**) Low-magnification view of a more cellular example of a solitary fibrous tumor, a lesion synonymous with tumors referred to historically as hemangiopericytomas. (**b**) High-magnification photomicrograph showing a compact arrangement of neoplastic cells with minimal collagenous stroma and easily identifiable mitotic figures. (**c**) Elsewhere, as illustrated in this photomicrograph, this tumor showed histologic features typical of a solitary fibrous tumor; it lacked coagulative tumor necrosis and other features often affiliated with a recurrence risk

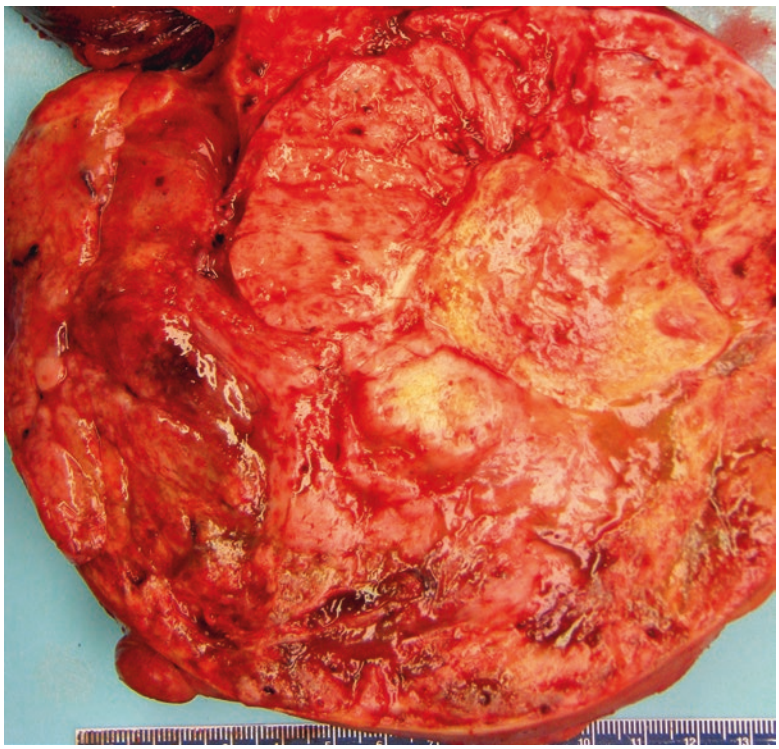

Fig. 14.12 Malignant solitary fibrous tumor. Cut surface of a large visceral pleural-based mass shows patchy necrosis and a fleshy surface different from the more typical firm, rubbery consistency of a conventional solitary fibrous tumor (*see* Fig. 14.9)

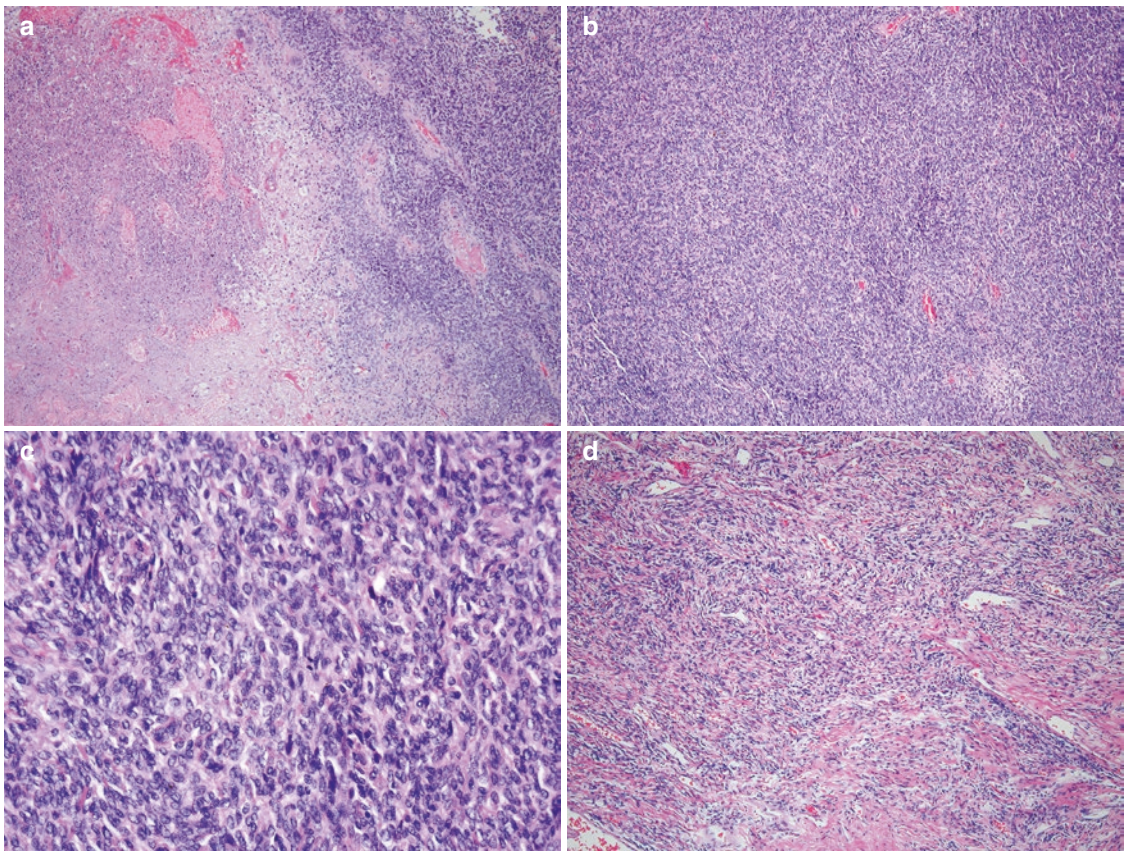

Fig. 14.13 Malignant solitary fibrous tumor. (**a**) Low-magnification photomicrograph showing tumor necrosis in a highly cellular neoplasm without the collagenous stroma and other architectural features more characteristic of a solitary fibrous tumor. (**b**) Low-magnification view of another field in the same tumor showing a highly cellular neoplasm resembling other high-grade sarcomas such as monophasic synovial sarcoma and malignant peripheral nerve sheath tumor. (**c**) High-magnification photomicrograph illustrating hyperchromatic nuclei and easily identifiable mitotic figures. (**d**) Very small foci representing a minor component of this well-sampled tumor showed histologic findings more closely resembling a classic solitary fibrous tumor

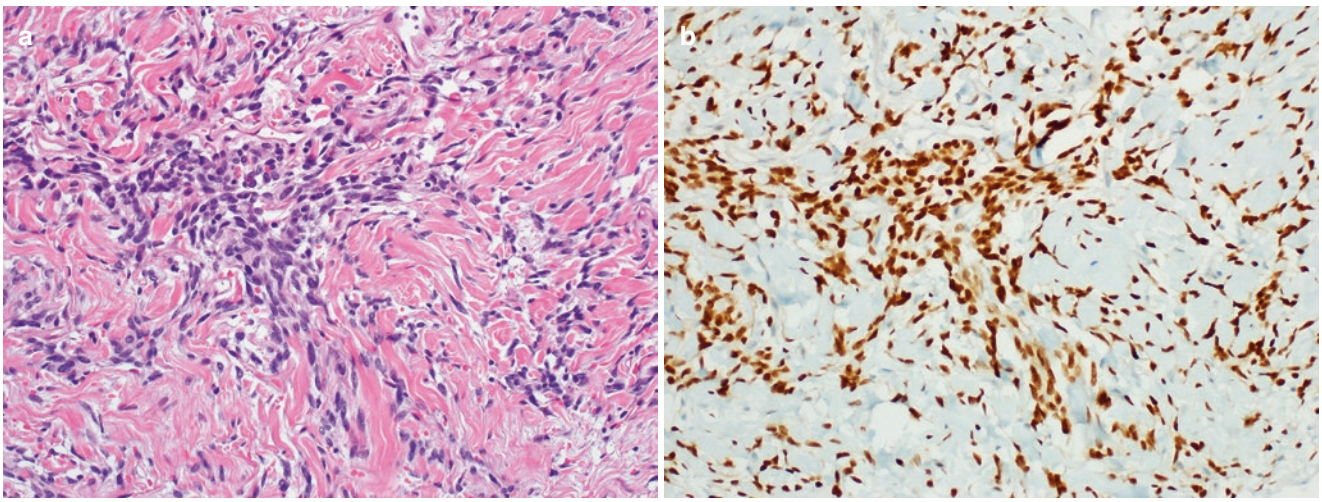

Fig. 14.14 Solitary fibrous tumor. (**a**) Photomicrograph showing bland spindle cells arranged in the patternless pattern of Stout typical of the solitary fibrous tumor. (**b**) Photomicrograph showing strong, diffuse, nuclear staining for STAT6, a very specific and helpful finding in establishing the diagnosis of the solitary fibrous tumor in diagnostically challenging cases

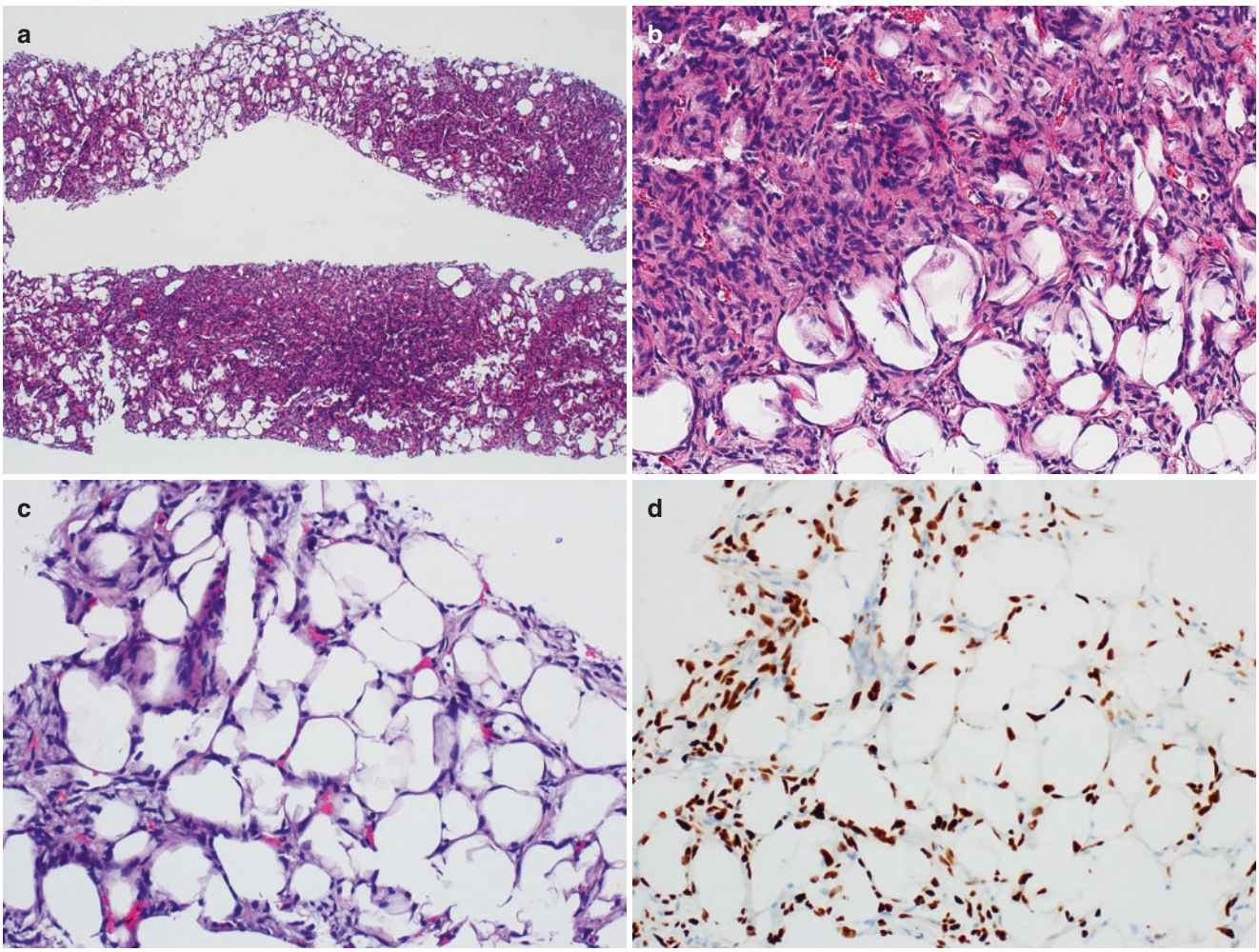

Fig. 14.15 Solitary fibrous tumor, fat-forming (lipomatous) variant. (**a**) Low-magnification photomicrograph of a needle biopsy from an intrathoracic mass discovered in a 36-year-old man. The tumor consists of bland adipose tissue and a spindle-cell neoplasm. (**b**) High-magnification photomicrograph showing the intersection between the more cellular spindle-cell component that dissects into adipose tissue. (**c**) Another high-magnification photomicrograph showing spindle cells sprinkled between the fat cells. (**d**) Photomicrograph of the same area showing strong diffuse staining for STAT6 in spindle cells

Epithelioid Hemangioendothelioma

Epithelioid hemangioendothelioma (Figs. 14.16, 14.17, 14.18, 14.19, 14.20 and 14.21) is a low- to intermediate-grade malignant vascular tumor that occurs in a variety of sites, including the bone, soft tissue, lung, mediastinum, and pleura. Intrapulmonary tumors are the most common among intrathoracic variants and preferentially affect younger women. The most common presentation is as multiple bilateral pulmonary nodules, mimicking the radiologic features of metastatic malignancy or granulomatous diseases. Less common presentations include solitary lung nodules, diffuse infiltrates mimicking interstitial lung disease, diffuse pleural disease mimicking mesothelioma, and primary mediastinal masses for which preoperative concerns often include other mediastinal neoplasms such as germ cell tumors and lymphoma. Nuclear pleomorphism, necrosis, and mitotic rate can separate them into low- and intermediate-grade tumors. Like their soft-tissue counterparts, intrathoracic epithelioid hemangioendotheliomas show recurrent *WWTR1-CAMTA1* and *YAP1-TFE3* translocations that correlate with nuclear staining for CAMTA1 and TFE3, respectively, in paraffin section immunostains.

Fig. 14.16 Epithelioid hemangioendothelioma. Gross photograph shows multiple circumscribed nodules with a gray-white chondroid cut surface

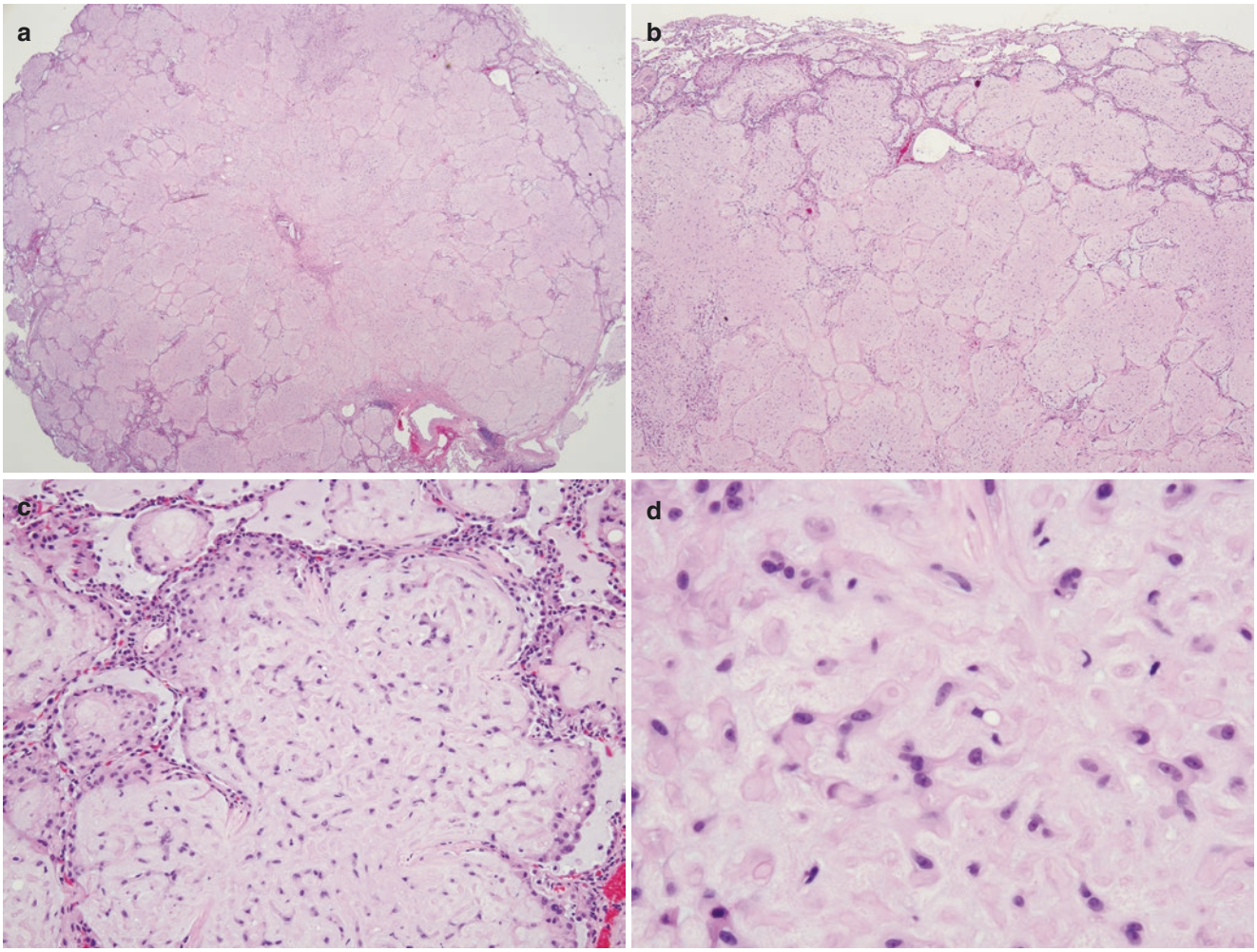

Fig. 14.17 Epithelioid hemangioendothelioma with a hypocellular hyalinized center and a polypoid intra-alveolar growth pattern at the periphery. (**b**) and (**c**), Higher-magnification views showing intra-alveolar extension of hypocellular polyps (**b**) with centrally hyalinized stroma and plump epithelioid histiocyte-like cells at the periphery (**c**). (**d**) High magnification of the intra-alveolar tumor nodule shows short cords of tumor cells with round-to-oval nuclei and intracytoplasmic vacuoles/lumina

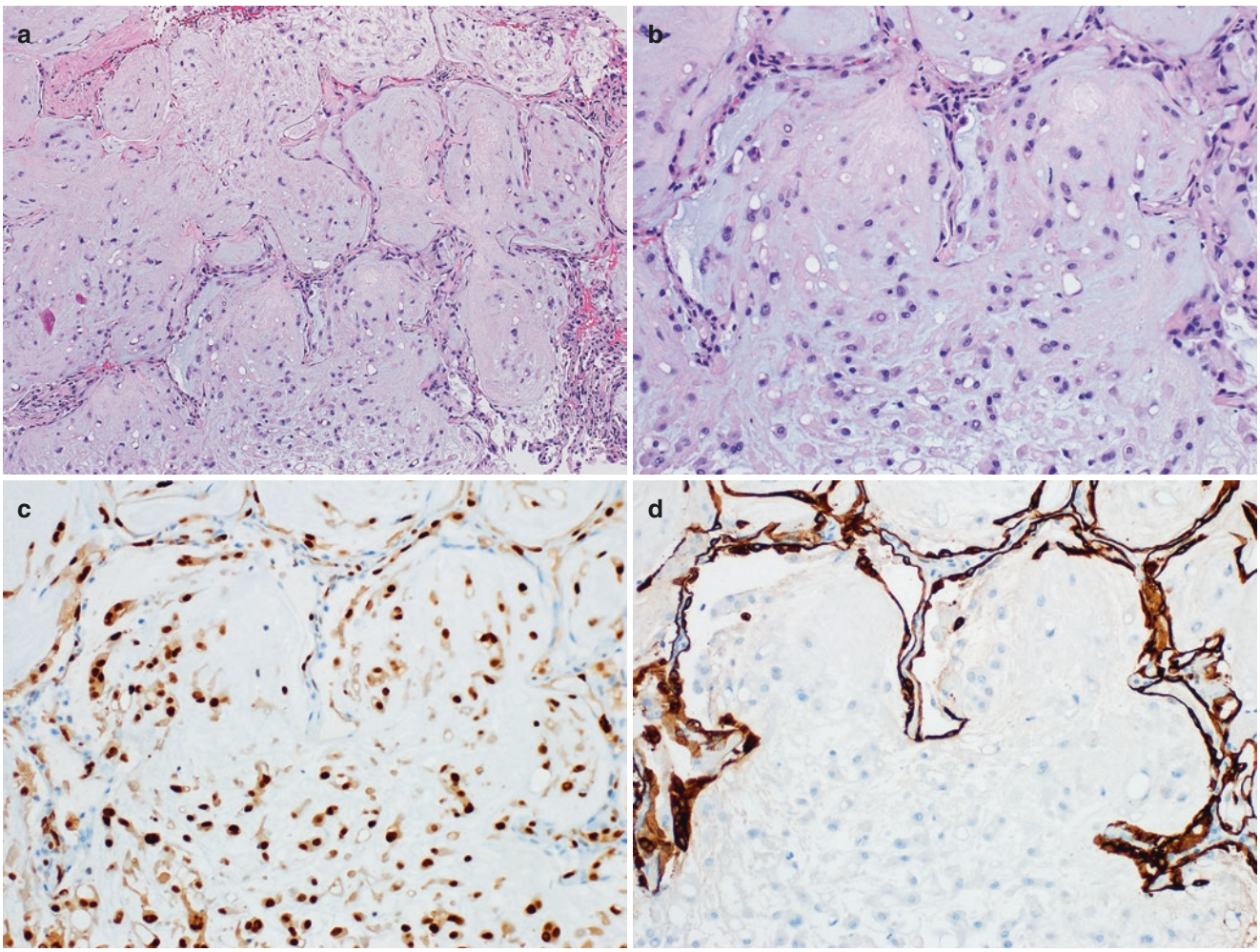

Fig. 14.18 Epithelioid hemangioendothelioma. (**a**) Photomicrograph showing polypoid intraluminal growth pattern typical of epithelioid hemangioendothelioma in the lung. (**b**) Higher-magnification view showing bland cytology in a low-grade variant in which neoplastic cells show a characteristic combination of cytoplasmic intranuclear pseudoinclusions, coarse cytoplasmic vacuoles, and a pale-staining chondroid matrix. (**c**) and (**d**) Immunostains show strong nuclear staining for ERG (**c**) and negative staining for cytokeratins (**d**). Tumor cells are positive for various endothelial-associated antigens, including not only ERG but also CD31, CD34, and factor VIII. Tumor cells may be focally positive for cytokeratins, depending on the antibody used, which can be a diagnostic trap

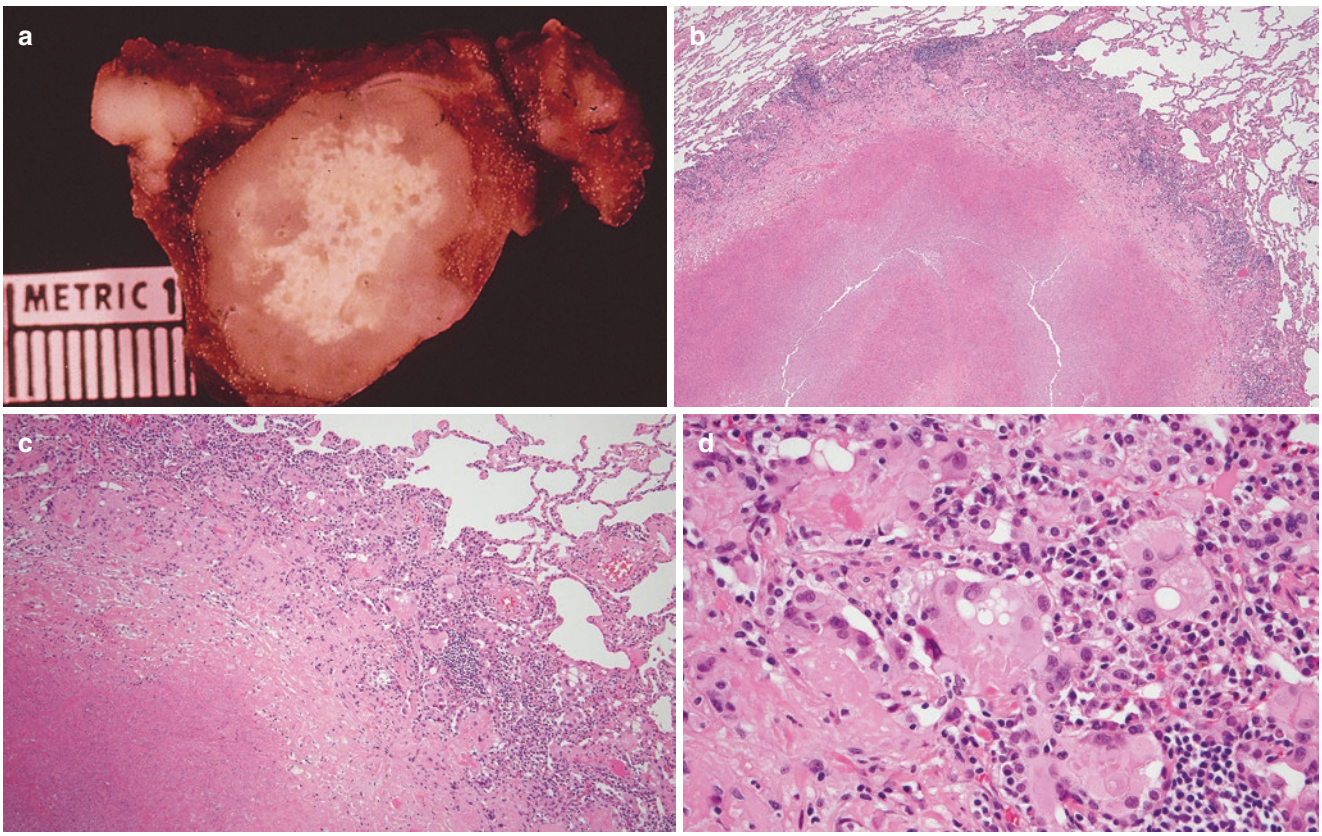

Fig. 14.19 Epithelioid hemangioendothelioma. (**a**) Gross photograph showing cut surface of epithelioid hemangioendothelioma that presented as a solitary lung nodule with gross features resembling a necrotizing granuloma. (**b**) Low-magnification photomicrograph showing a centrally necrotic nodule. (**c**) Higher-magnification view showing a population of epithelioid cells at the periphery, furthering resemblance to a granuloma. (**d**) High-magnification photomicrograph showing epithelioid cells with abundant cytoplasm, cytoplasmic intranuclear pseudoinclusions, coarse cytoplasmic vacuoles, and polypoid growth characteristic of epithelioid hemangioendotheliomas

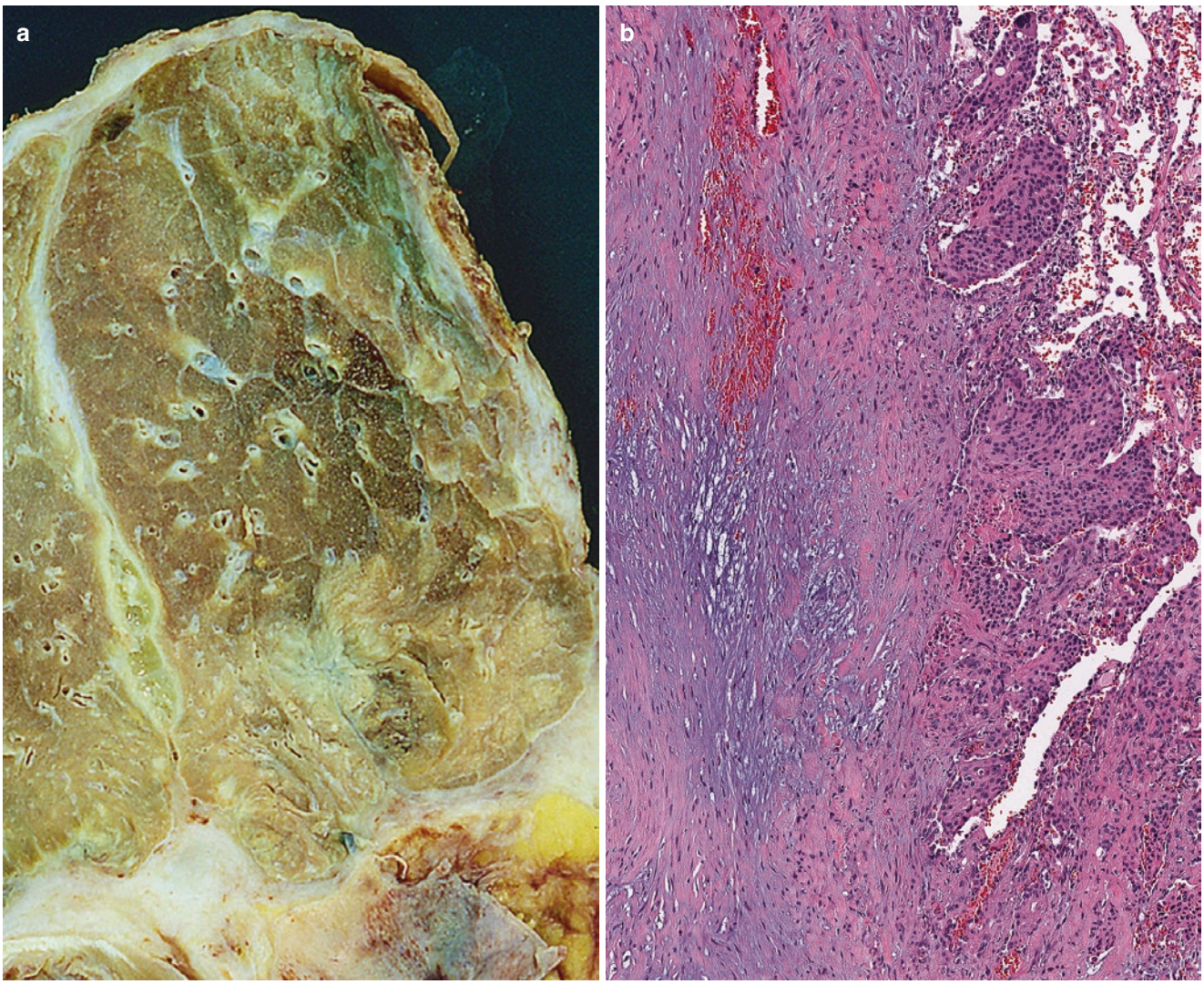

Fig. 14.20 Epithelioid hemangioendothelioma involving the pleura. (**a**) Gross photograph shows that the tumor diffusely thickens the pleura, mimicking malignant mesothelioma. (**b**) Low-magnification photomicrograph shows that the pleura is thickened by a paucicellular tumor with myxohyaline stroma associated with intraluminal polypoid growth at the interface with lung parenchyma in a pattern more typical of epithelioid hemangioendothelioma

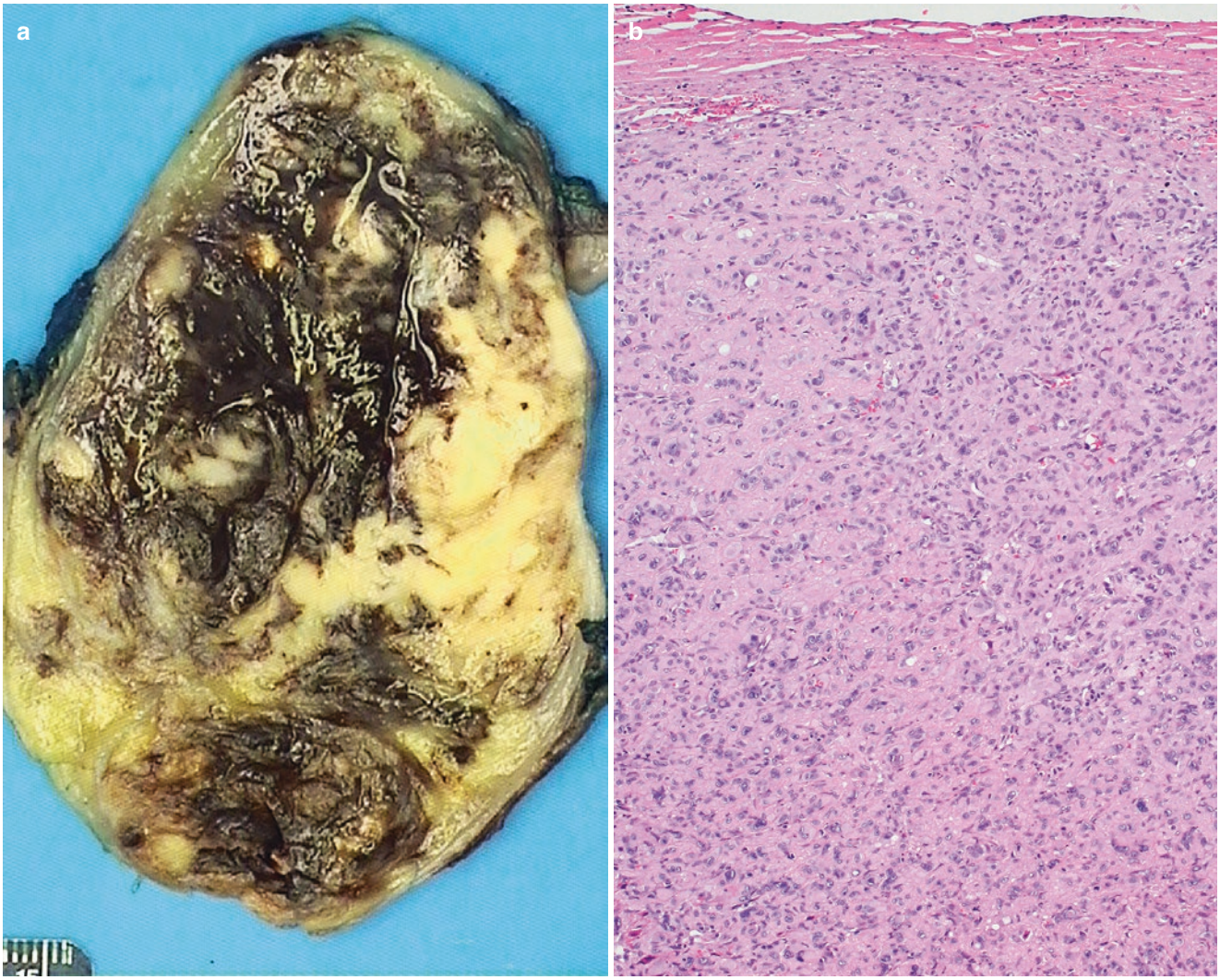

Fig. 14.21 Epithelioid hemangioendothelioma arising in mediastinum. (**a**) Photograph showing cut surface of a large 11-cm mediastinal mass with areas of hemorrhagic necrosis. (**b**) Photomicrograph showing epithelioid neoplastic cells with numerous intranuclear pseudoinclusions and coarse cytoplasmic vacuoles

Synovial Sarcoma

Synovial sarcoma (Figs. 14.22, 14.23 and 14.24), which is histologically, immunophenotypically, and genetically identical to its soft-tissue counterparts, is the most common form of high-grade soft-tissue sarcoma arising as a primary lung and/or pleural neoplasm. The lung is also a favored site for metastatic synovial sarcoma in patients with soft-tissue primary tumors. Distinguishing between the two often hinges on knowing the history and the radiologic distribution of disease. Intrathoracic synovial sarcomas have the same t(X;18)(p11.2;q11.2) chromosomal translocation characteristic of all synovial sarcomas. Variable mesenchymal and epithelial differentiation is the key to diagnosis.

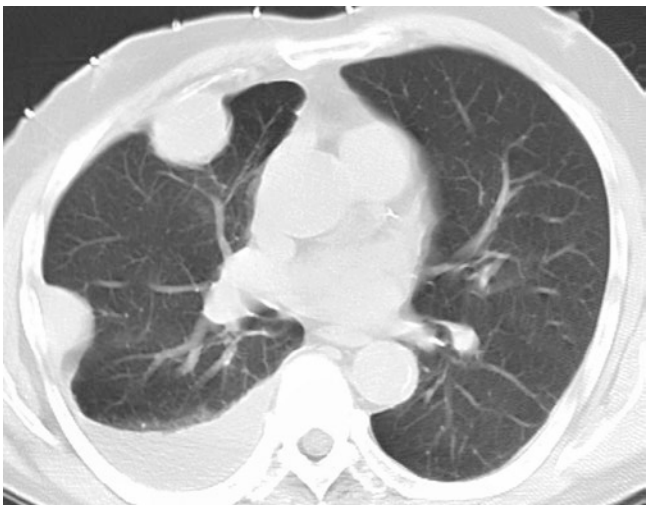

Fig. 14.22 Synovial sarcoma. A chest CT image showing two peripheral pleural-based masses that infiltrate chest wall soft tissue

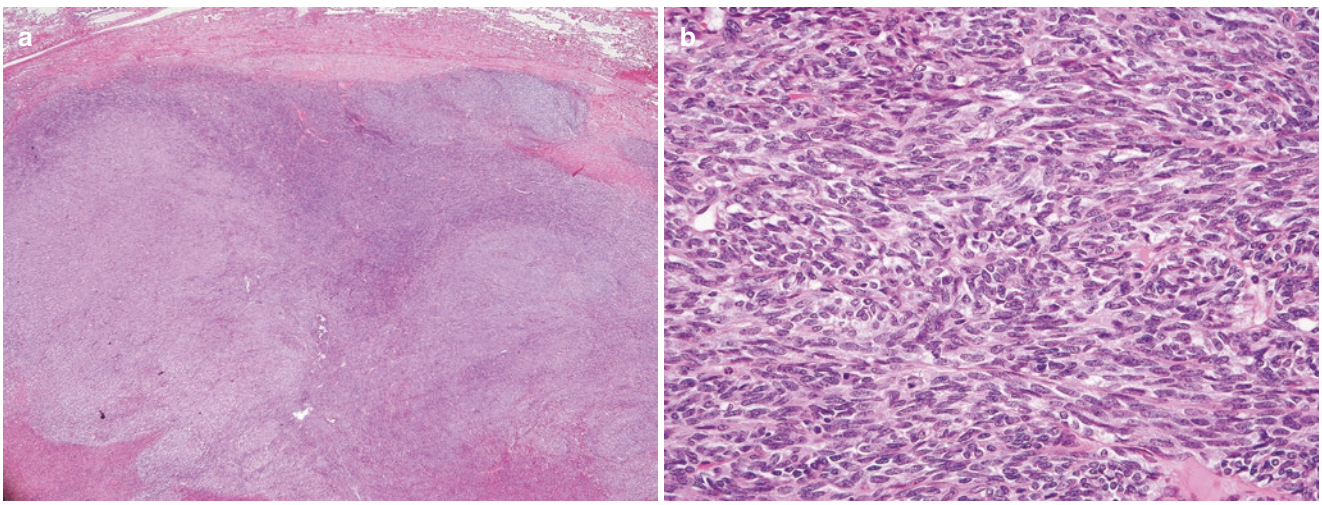

Fig. 14.23 Monophasic synovial sarcoma. (**a**) Low-magnification photomicrograph showing cellular intrapulmonary neoplasm. (**b**) At high magnification, the tumor consists of sheets and fascicles of uniform spindle cells with scant cytoplasm and indistinct cell borders

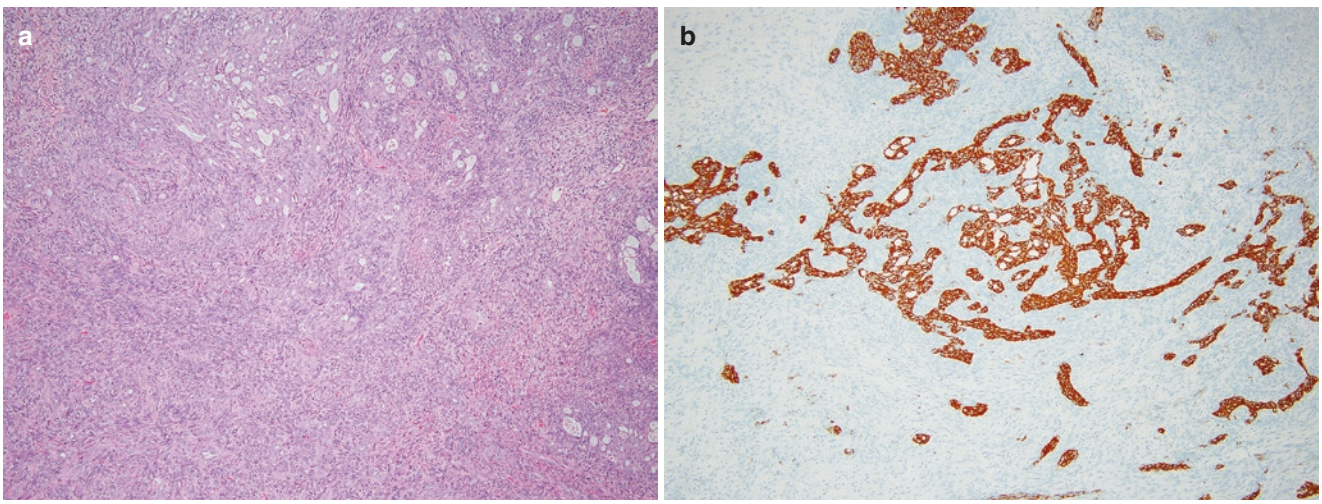

Fig. 14.24 Biphasic synovial sarcoma. (**a**) Low-magnification photomicrograph showing mixed spindle-cell and epithelioid cell components. The epithelioid cells form solid nests, cords, and acini. (**b**) Photomicrograph showing patchy immunoreactivity for cytokeratins in the clearly identifiable epithelial component

Angiomatoid Fibrous Histiocytoma and Primary Pulmonary Myxoid Sarcoma

Angiomatoid fibrous histiocytoma (Fig. 14.25) is a low-grade soft-tissue neoplasm that rarely presents as a primary lung tumor. Angiomatoid fibrous histiocytomas arising in soft tissues are capable of recurrence but rarely metastasize, but the few reported examples of primary lung tumors have behaved in a benign fashion. These tumors demonstrate a number of characteristic and nonspecific translocations, including most commonly t(2;22)(q33;q12) *EWSR1-CREB1* and t(12;22)(q13;q12) *EWSR1-ATF1*.

Primary pulmonary myxoid sarcoma (Fig. 14.26) is a rare form of intermediate-grade soft-tissue tumor arising in the lung and shows both histologic and genetic overlap with angiomatoid fibrosis histiocytoma.

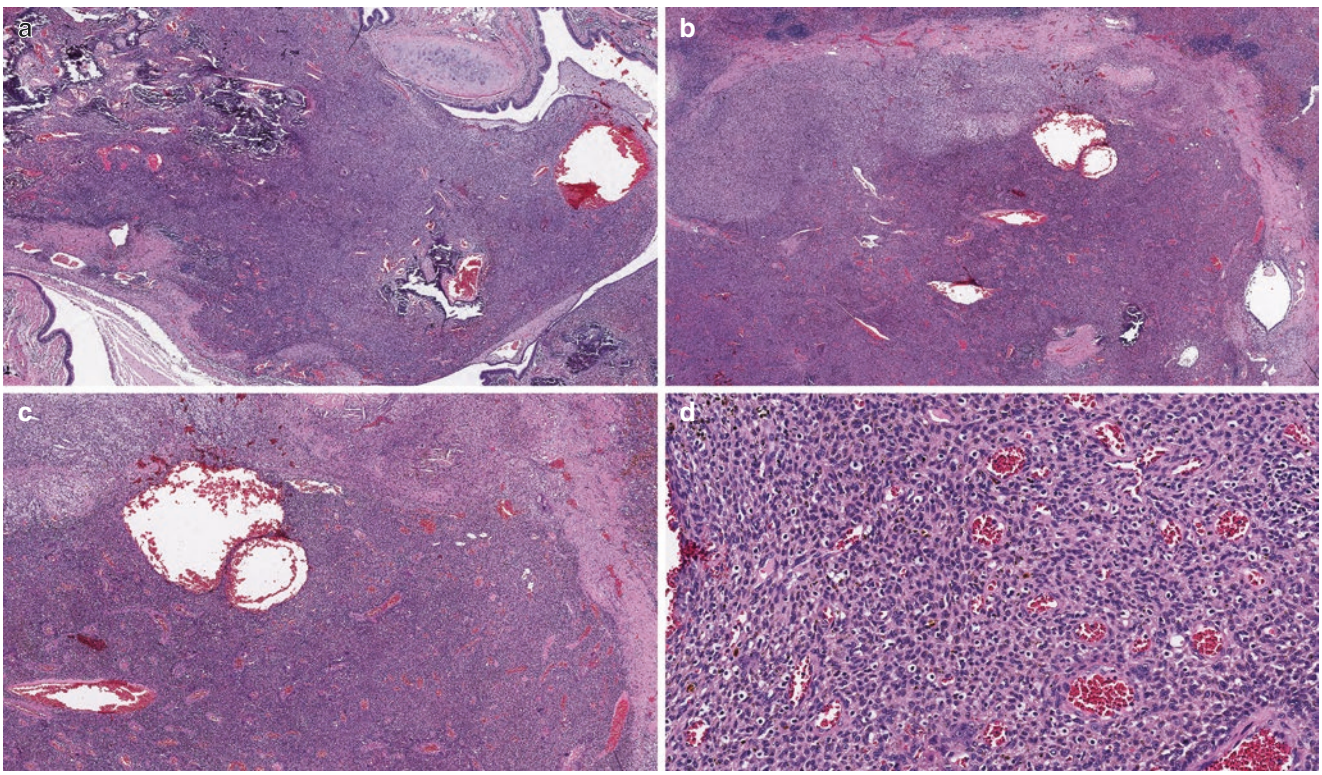

Fig. 14.25 Angiomatoid fibrous histiocytoma. (**a**) Low-magnification photomicrograph showing a polypoid endobronchial tumor with a peripheral fibrous pseudocapsule, ectatic blood-filled spaces, and calcifications. (**b**) and (**c**) Photomicrographs at higher magnification demonstrating the vascular pattern typical of angiomatoid fibrous histiocytoma, including areas in which sinusoidal blood vessels have a hemangiopericytoma-like pattern. (**d**) High-magnification photomicrograph showing bland plump spindle cells arranged in ill-defined, short fascicles resulting in a vaguely storiform architecture. Associated histiocytes and scattered hemosiderin deposits are characteristic

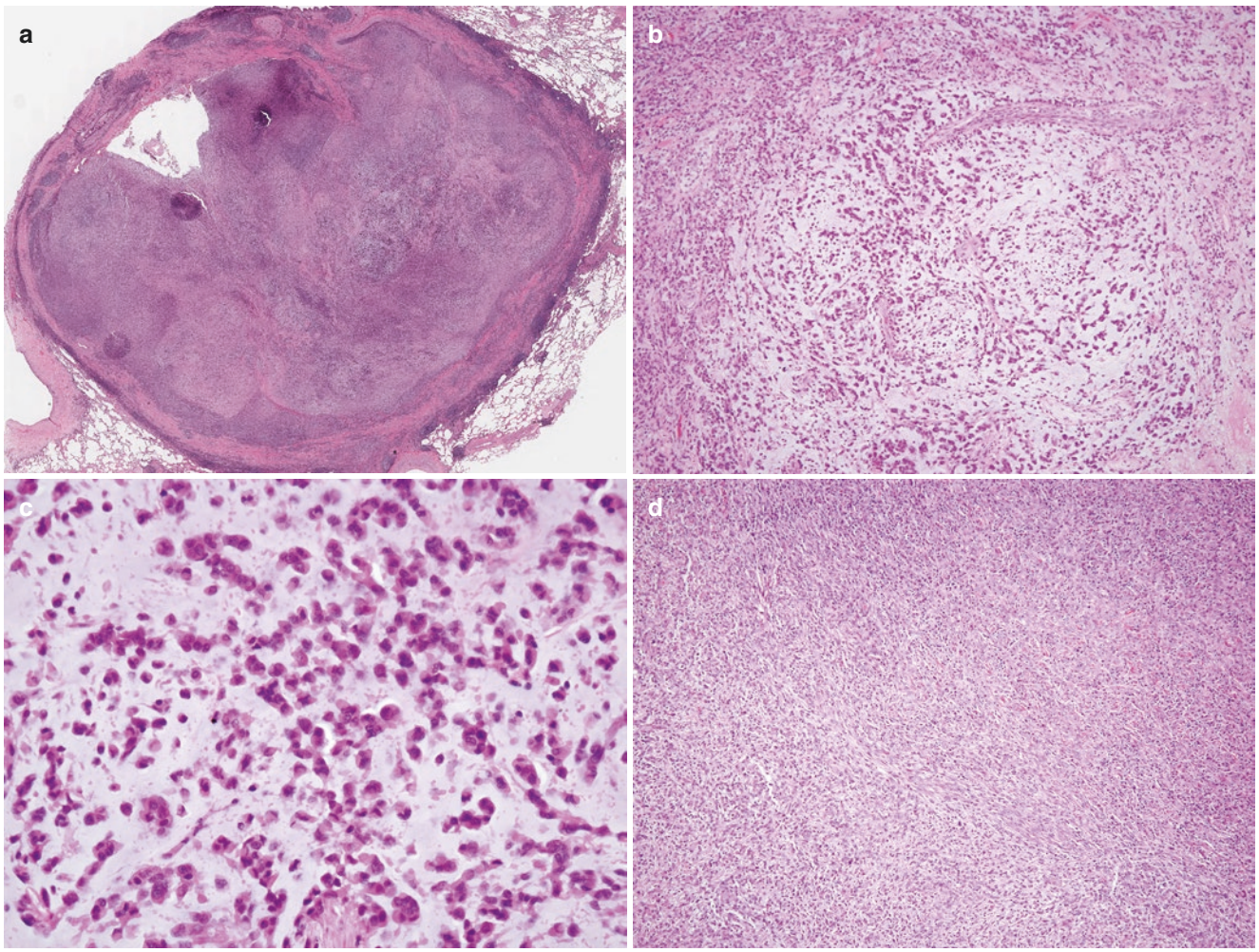

Fig. 14.26 Primary pulmonary myxoid sarcoma. (**a**) Scanning magnification photomicrograph showing a variably cellular well-circumscribed bronchus-associated neoplasm with a lobulated appearance and a fibrous pseudocapsule accompanied by a peripheral lymphocytic infiltrate. (**b**) Higher-magnification view showing that in much of the tumor neoplastic cells are arranged in a reticular growth pattern with a pale-staining myxoid matrix. (**c**) Neoplastic cells in the reticular areas have eccentric nuclei and a relatively nondescript appearance. (**d**) Solid areas are common but rarely the dominant finding and comprise variably atypical spindle cells

Diffuse Malignant Mesothelioma

Nearly all intrathoracic malignant mesotheliomas (Figs. 14.27, 14.28, 14.29, 14.30, 14.31, 14.32, 14.33, 14.34, 14.35, 14.36, 14.37, 14.38 and 14.39) present as diffuse neoplasms involving parietal and visceral pleura. Localized mesotheliomas presenting as solitary masses are rare and show the same range of histologic and immunophenotypic findings described in the much more common diffuse variants. Asbestos exposure is related to the pathogenesis of some malignant mesotheliomas. Common histologic types of diffuse malignant mesothelioma are listed in Table 14.1. The majority are of the epithelioid type. The sarcomatoid type, including the desmoplastic variant, accounts for less than 10% of cases. Biphasic or mixed types, defined as tumors showing at least 10% each of epithelioid and sarcomatoid patterns, account for 10–15% of cases. The primary differential diagnosis of epithelioid mesothelioma is metastatic adenocarcinoma, most commonly of primary pulmonary origin and presenting with a diffuse pseudomesotheliomatous distribution of disease. Immunohistochemistry is often helpful in resolving this differential diagnosis (Table 14.2). Sarcomatoid mesothelioma may lack the immunohistochemical phenotype traditionally associated with epithelioid mesothelioma but is nearly always positive for pancytokeratins. The differential diagnosis between sarcomatoid mesothelioma and sarcomatoid carcinoma relies mainly on clinical information, including especially the radiologic distribution of disease.

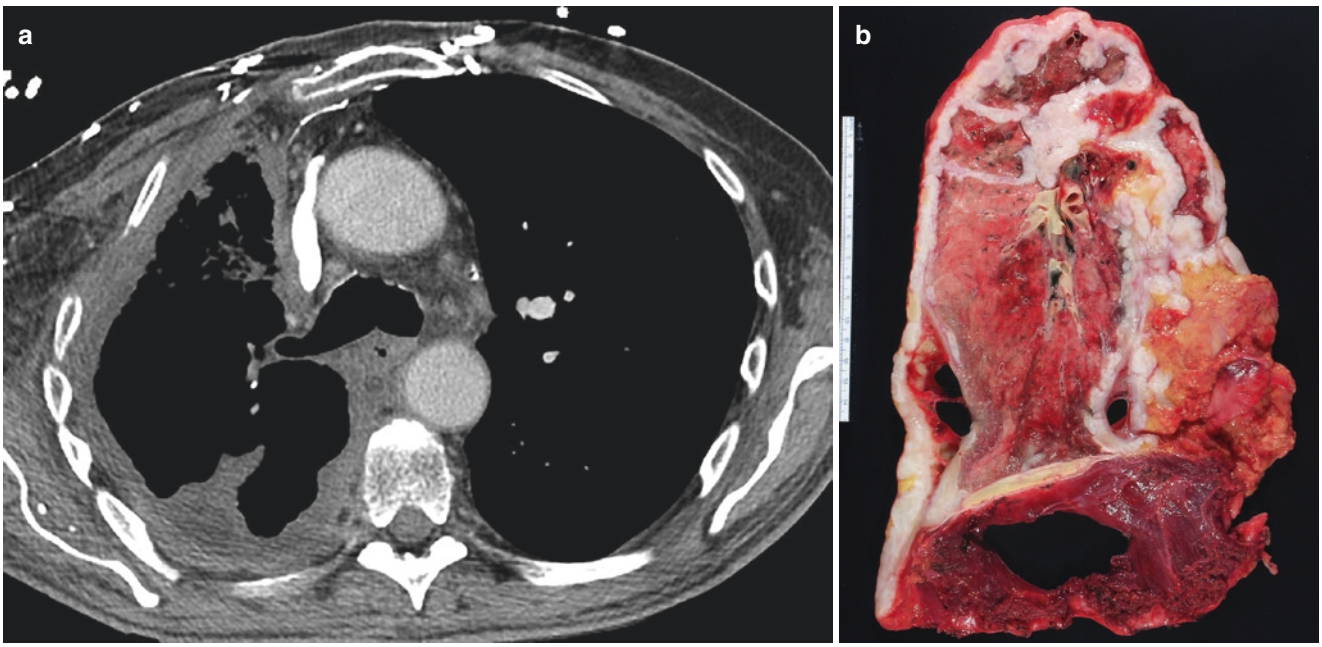

Fig. 14.27 Diffuse malignant mesothelioma. (**a**) CT scan showing right-sided diffuse pleural thickening and nodularity extending along the interlobular septum and involving the mediastinal pleura, a useful finding in separating benign from malignant diffuse pleural lesions. (**b**) Cut surface of an extrapleural pneumonectomy specimen showing a diffuse mesothelioma that encases the lung as a rind. The tumor also grows along the interlobar septa and compresses the lung parenchyma

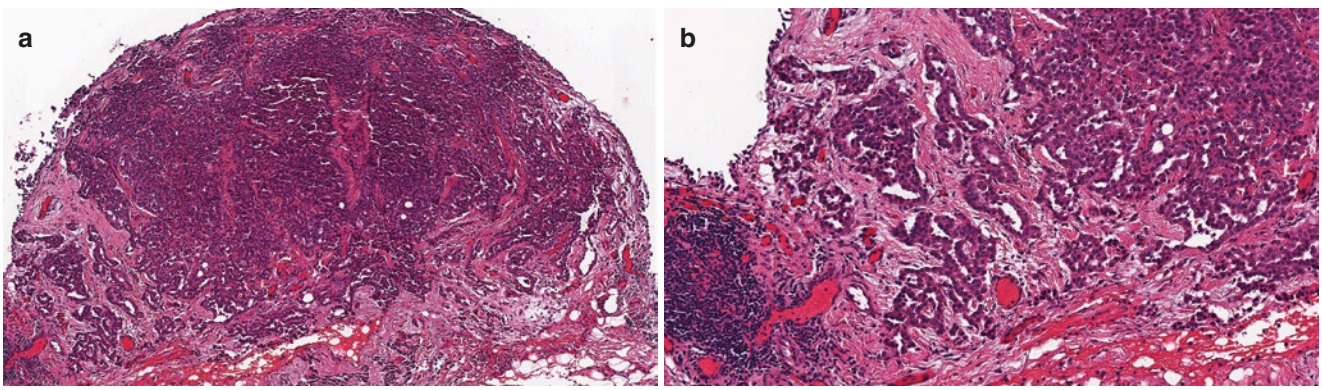

Fig. 14.28 Epithelioid malignant mesothelioma. (**a**) Low-magnification view showing a classic tubular (sometimes called tubulopapillary) mesothelioma forming a parietal pleural nodule. (**b**) High-magnification view showing remarkably bland cuboidal cells arranged in a well-developed tubular growth pattern

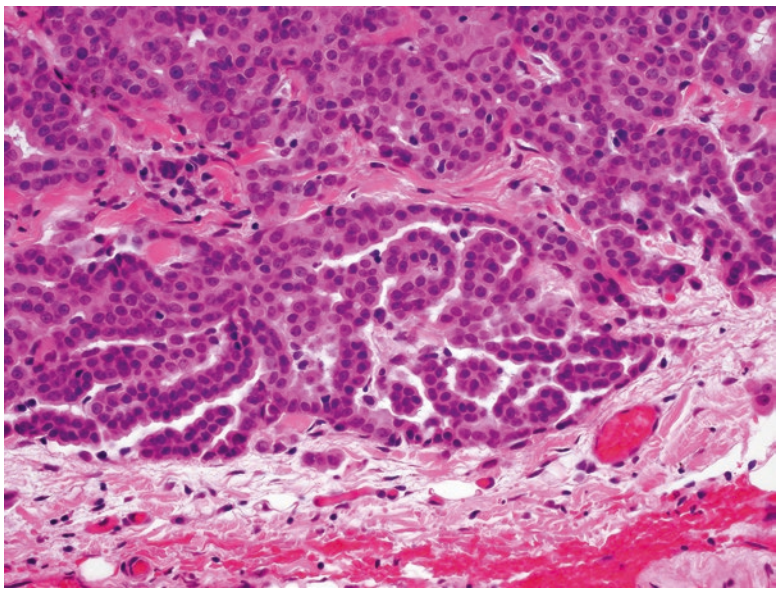

Fig. 14.29 Epithelioid malignant mesothelioma. Photomicrograph showing another example of a classic tubular epithelioid mesothelioma

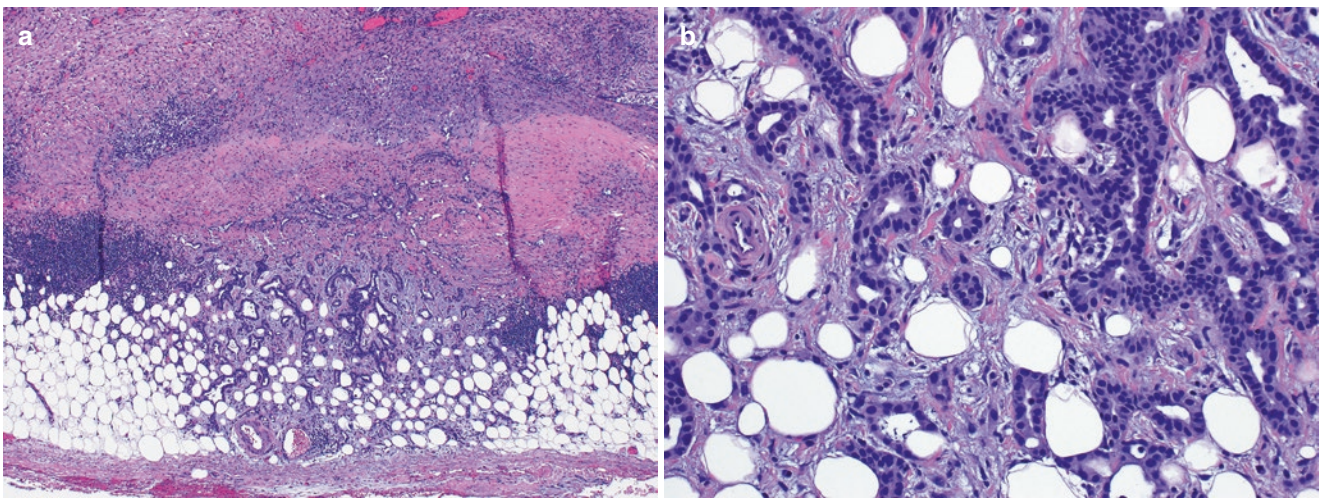

Fig. 14.30 Epithelioid malignant mesothelioma. (**a**) Photomicrograph showing an epithelioid mesothelioma with a class tubular growth pattern invading into chest wall fat, an extremely helpful finding in distinguishing malignant from benign atypical mesothelial proliferations. (**b**) High-magnification view showing bland, low columnar cells invading chest wall fat with an associated stromal reaction

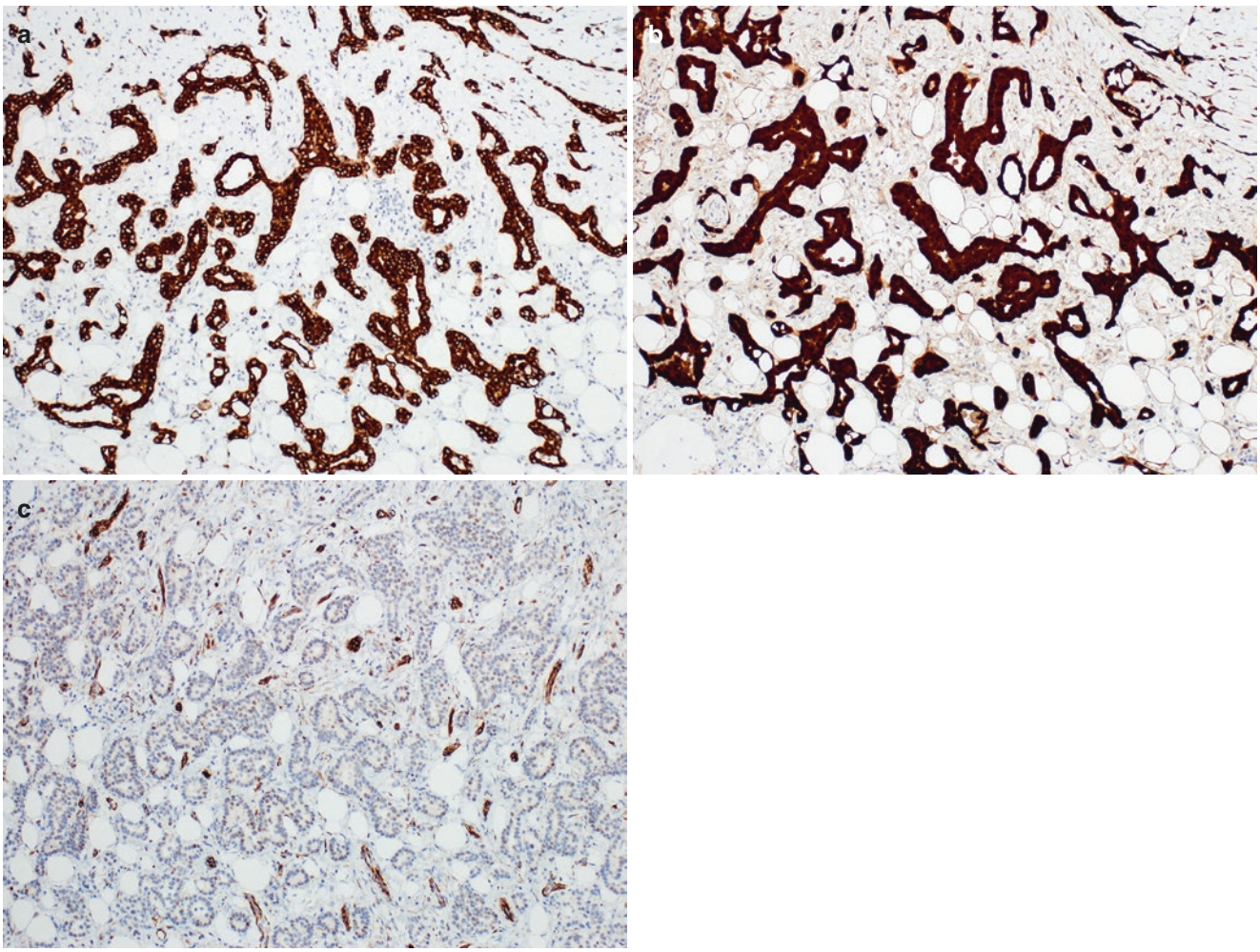

Fig. 14.31 Epithelioid malignant mesothelioma, immunophenotype. (**a**–**c**) Photomicrographs demonstrating immunostains performed on sections of the tumor illustrated in Fig. 14.30. Tumor cells were strongly positive for high molecular weight cytokeratins (CK5/6) (**a**) and calretinin (**b**), the latter with strong cytoplasmic and nuclear staining. There was patchy, weak, nuclear staining for WT-1 (**c**). Cytoplasmic staining for WT-1 is of no diagnostic value in distinguishing metastatic adenocarcinoma from mesothelioma

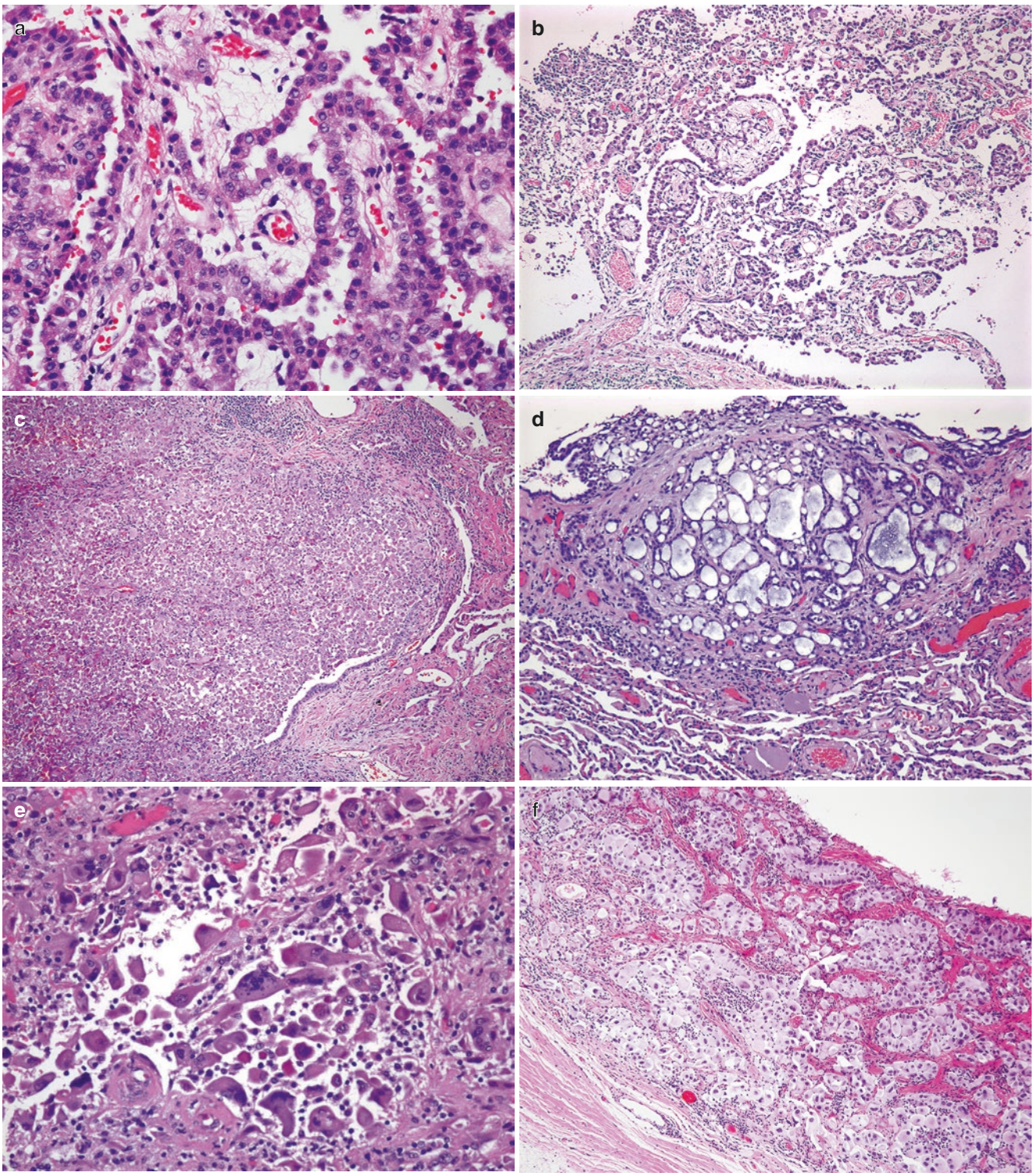

Fig. 14.32 Epithelioid malignant mesothelioma, histologic variants. (**a**) *Papillary* growth pattern in mesothelioma in which tumor cells lining fibrovascular cores are cuboidal and relatively bland, with occasional small nucleoli and a moderate amount of cytoplasm. (**b**) Combined papillary and *micropapillary* growth pattern, the latter characterized by detached papillary fragments of tumor cells without associated connective tissue cores. (**c**) *Solid* growth pattern in mesothelioma invading the lung as solid sheets of relatively noncohesive epithelioid tumor cells with uniform nuclei, small nucleoli, and abundant eosinophilic cytoplasm. (**d**) *Microcystic (adenomatoid)* growth pattern in which attenuated tumor cells line cystic spaces of variable sizes and shapes resembling adenomatoid tumors. (**e**) *Pleomorphic* cytology in mesothelioma composed of a population of highly anaplastic cells, including multinucleated giant cells. (**f**) Deciduoid features in a mesothelioma composed of large polygonal cells with abundant eosinophilic cytoplasm and distinct cell borders resembling decidual cells of the pregnant endometrium

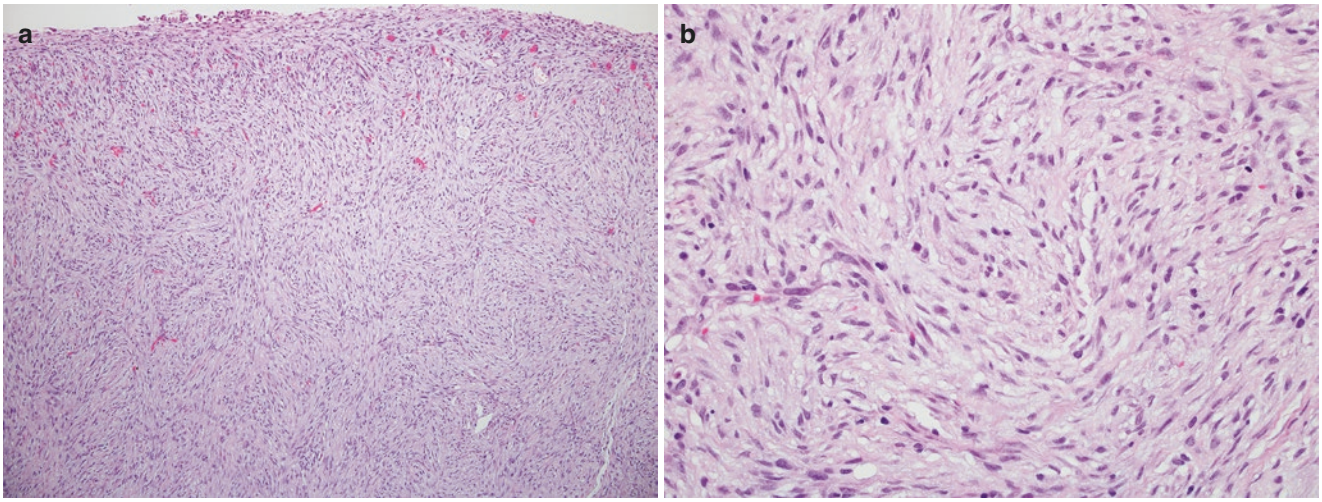

Fig. 14.33 Sarcomatoid mesothelioma. (**a**) Low-magnification photomicrograph showing a mesothelioma consisting of a pure population of keratin-positive (immunostain not shown) neoplastic spindle cells. (**b**) Higher-magnification view shows plump spindle cells with mild nuclear atypia and a vaguely fascicular growth pattern

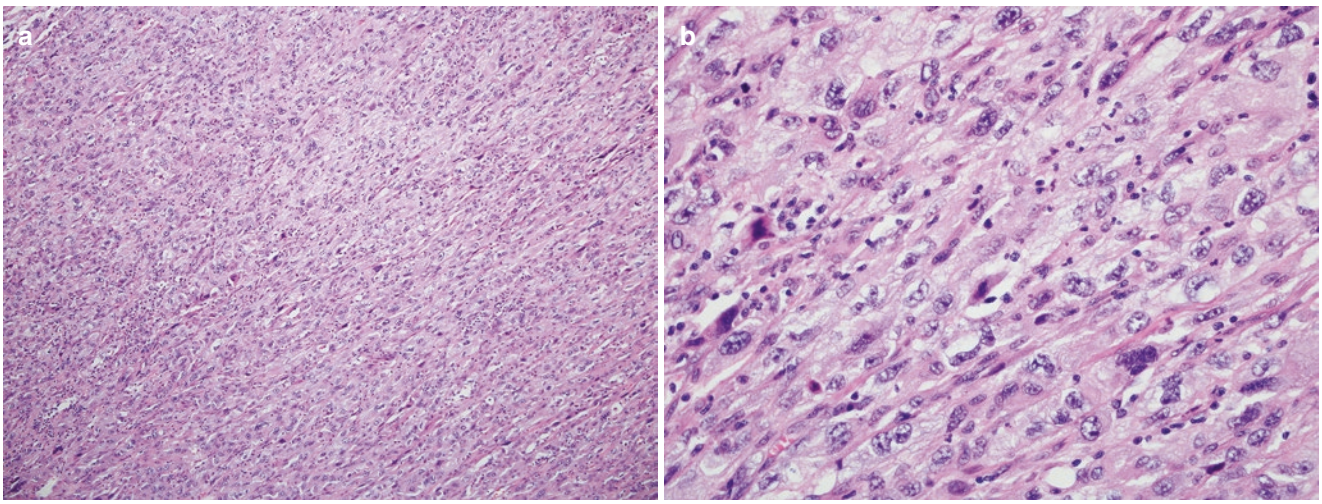

Fig. 14.34 Sarcomatoid mesothelioma. (**a**) Low-magnification photomicrograph showing highly atypical spindle cells arranged in sheets without distinct architectural features in sarcomatoid mesothelioma. (**b**) High-magnification photomicrograph shows marked atypia characterized by pleomorphic nuclei with vesicular chromatin and prominent nucleoli

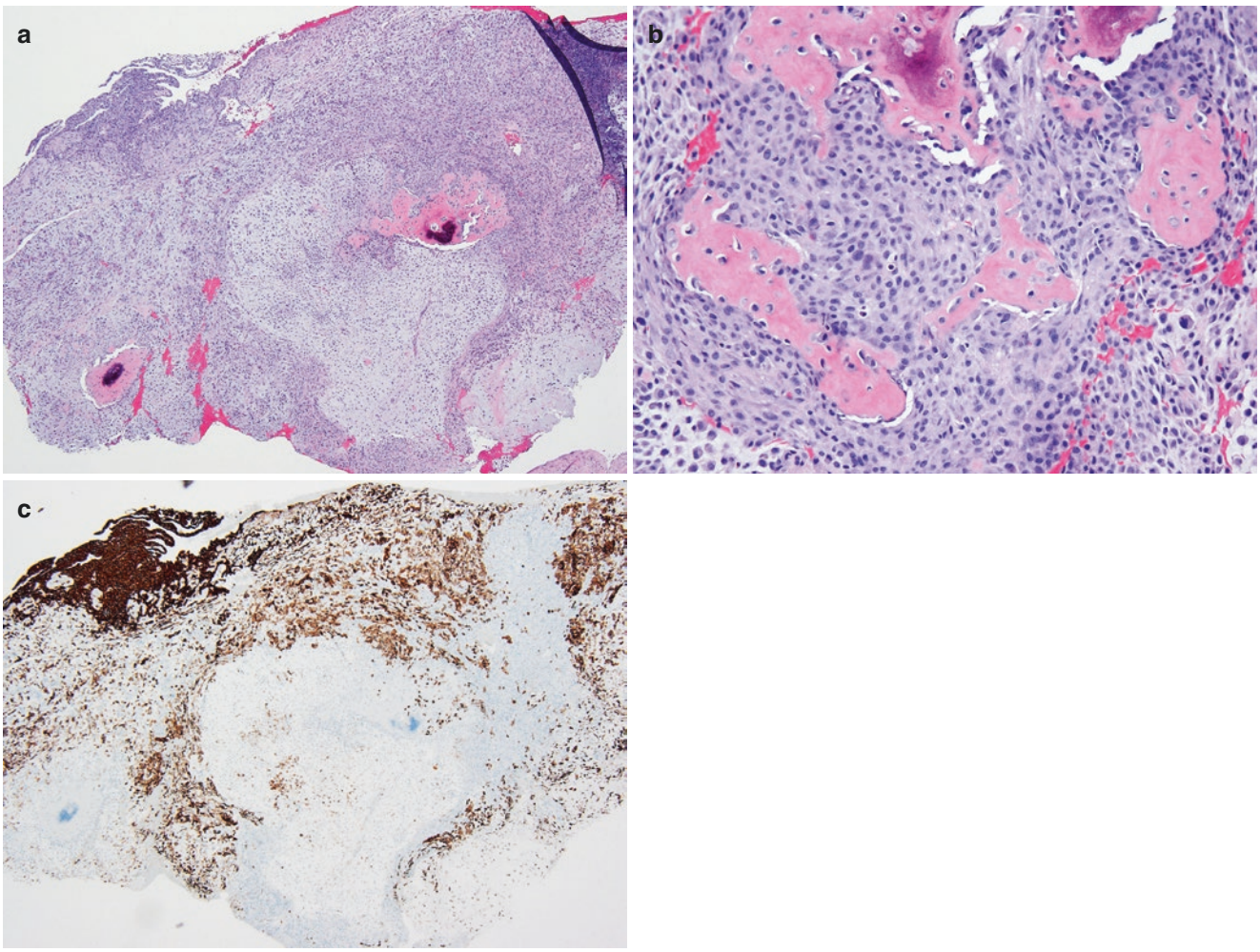

Fig. 14.35 Mesothelioma with heterologous differentiation. (**a**) Low-magnification photomicrograph showing a biopsy from a diffuse pleural lesion with only a very minor epithelial component (top left) and a predominantly sarcomatoid component in which there are heterologous elements, including neoplastic bone and cartilage. (**b**) Higher-magnification view showing osseous differentiation resembling osteosarcoma. (**c**) Low-magnification view of the same field depicted in part (**a**) showing strong staining for pancytokeratins in the surface epithelial component (top left) as well as much of the sarcomatoid component. Cytoplasmic and nuclear staining for calretinin showed a similar distribution (not shown)

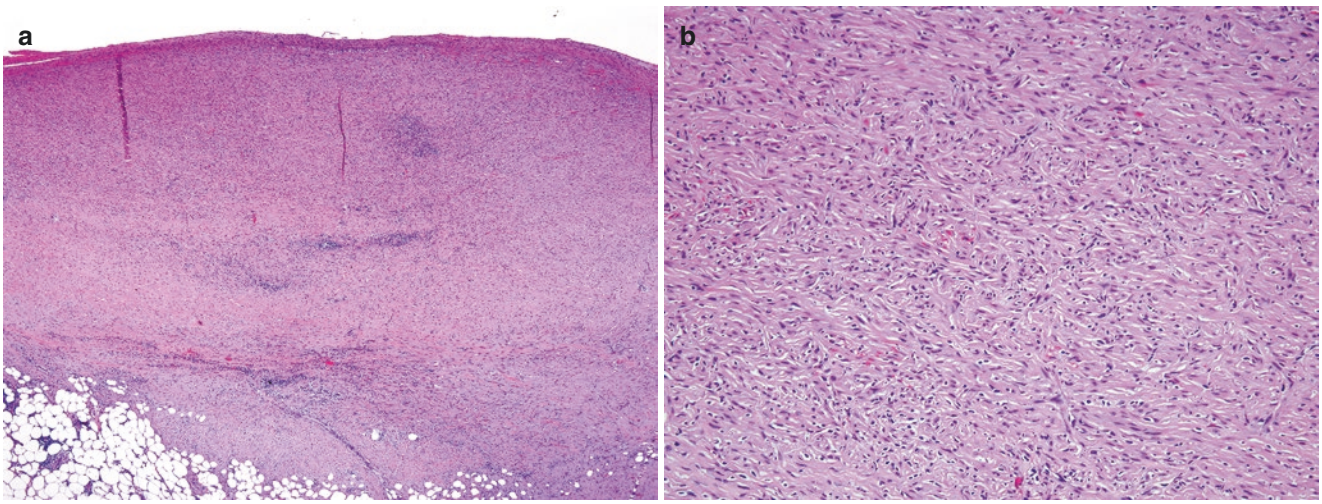

Fig. 14.36 Desmoplastic mesothelioma. (**a**) Low-magnification photomicrograph shows diffuse pleural thickening characterized by random variation in cellularity in a densely collagenous stroma. At the interface with the chest wall the soft-tissue tumor extends into adipose tissue. (**b**) High-magnification photomicrograph shows that the more cellular areas include a population of mildly atypical spindle-cell proliferation with a vaguely storiform architecture in hyalinized fibrous stroma. This storiform growth pattern in areas of increased cellularity is nearly universal in desmoplastic mesothelioma and is a helpful diagnostic feature

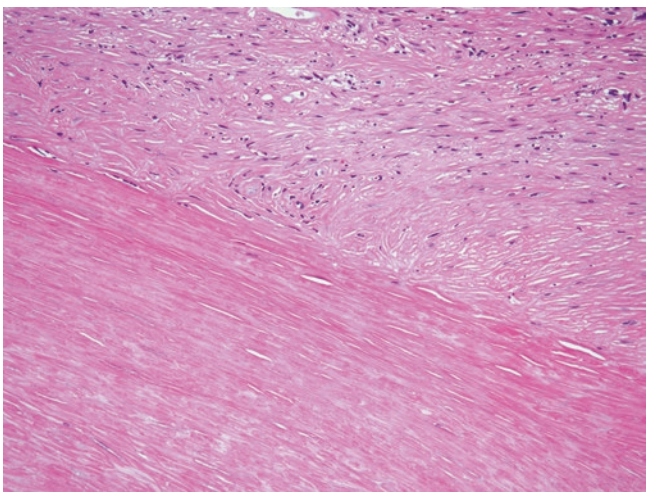

Fig. 14.37 Desmoplastic mesothelioma. Photomicrograph showing abrupt transition from atypical spindle cells in a densely hyalinized stroma (top right) to bland acellular necrosis (lower left). Bland necrosis is another feature helpful in distinguishing desmoplastic mesothelioma from benign fibrous lesions of the pleura

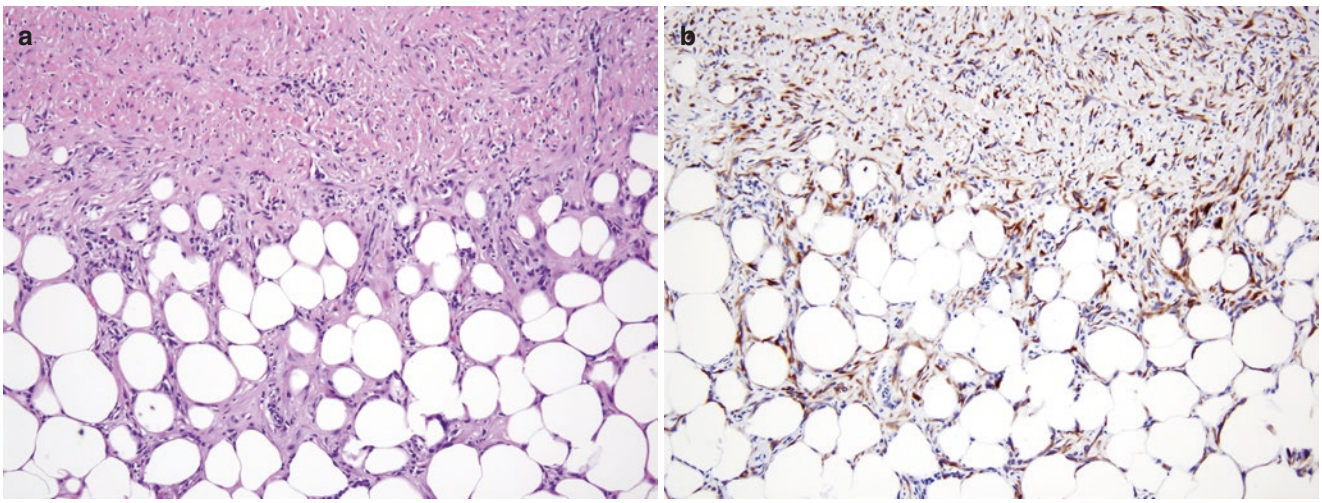

Fig. 14.38 Desmoplastic mesothelioma. (**a**) High-magnification photomicrograph showing tumor invading the chest wall adipose tissue, perhaps the single most helpful histologic feature in distinguishing desmoplastic mesothelioma from nonneoplastic diffuse fibrotic lesions of the pleura. (**b**) Positive staining for cytokeratins does not by itself distinguish benign from malignant mesothelial proliferations but can be helpful in identifying the invasion of adipose tissue with greater confidence

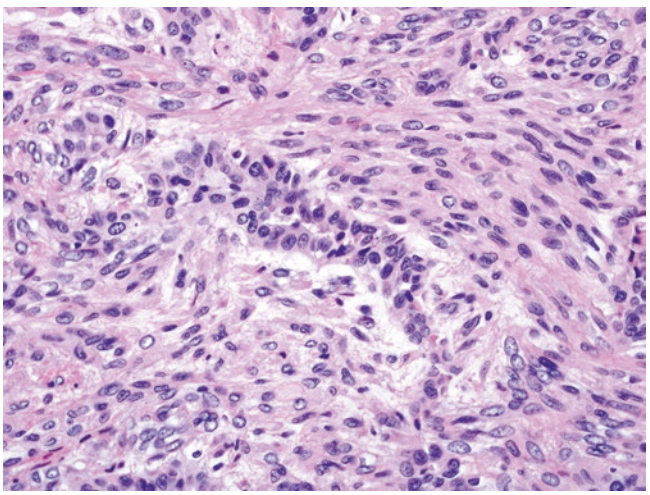

Fig. 14.39 Biphasic malignant mesothelioma. The tumor consists of a tubular epithelioid component and a sarcomatoid spindle-cell component

Table 14.1 Common histologic types of diffuse malignant mesothelioma

Epithelioid
Tubular
Papillary
Solid
Micropapillary
Microcystic (adenomatoid)
Clear cell
Pleomorphic
Deciduoid
Small cell
Sarcomatoid
Desmoplastic
Biphasic (mixed)

Table 14.2 Immunohistochemical markers useful in the differential diagnosis of epithelioid mesothelioma and metastatic adenocarcinoma

Mesothelial markers	Lung adenocarcinoma markers
Calretinin	MOC31
CK5/6	BerEP4
WT-1	Monoclonal CEA
D2–40	TTF-1 or Napsin A

Suggested Reading

Anderson T, Zhang L, Hameed M, Rusch V, Travis WD, Antonescu CR. Thoracic epithelioid malignant vascular tumors: a clinicopathologic study of 52 cases with emphasis on pathologic grading and molecular studies of WWTR1-CAMTA1 fusions. Am J Surg Pathol. 2015;39:132–9.

Bahrami A, Allen TC, Cagle PT. Pulmonary epithelioid hemangioendothelioma mimicking mesothelioma. Pathol Int. 2008;58:730–4.

Begueret H, Galateau-Salle F, Guillou L, Chetaille B, Brambilla E, Vignaud JM, et al. Primary intrathoracic synovial sarcoma: a clinicopathologic study of 40 t(X;18)-positive cases from the French sarcoma group and the Mesopath group. Am J Surg Pathol. 2005;29:339–46.

Cessna MH, Zhou H, Sanger WG, Perkins SL, Tripp S, Pickering D, et al. Expression of ALK1 and p80 in inflammatory myofibroblastic tumor and its mesenchymal mimics: a study of 135 cases. Mod Pathol. 2002;15:931–8.

Chirieac LR, Pinkus GS, Pinkus JL, Godleski J, Sugarbaker DJ, Corson JM. The immunohistochemical characterization of sarcomatoid malignant mesothelioma of the pleura. Am J Cancer Res. 2011;1:14–24.

Churg A, Galateau-Salle F. The separation of benign and malignant mesothelial proliferations. Arch Pathol Lab Med. 2012;136:1217–26.

Churg A, Colby TV, Cagle P, Corson J, Gibbs AR, Gilks B, et al. The separation of benign and malignant mesothelial proliferations. Am J Surg Pathol. 2000;24:1183–200.

Churg A, Cagle P, Colby TV, Corson JM, Gibbs AR, Hammar S, et al. The fake fat phenomenon in organizing pleuritis: a source of confusion with desmoplastic malignant mesotheliomas. Am J Surg Pathol. 2011;35:1823–9.

Coffin CM, Patel A, Perkins S, Elenitoba-Johnson KS, Perlman E, Griffin CA. ALK1 and p80 expression and chromosomal rearrangements involving 2p23 in inflammatory myofibroblastic tumor. Mod Pathol. 2001;14:569–76.

Coffin CM, Hornick JL, Fletcher CD. Inflammatory myofibroblastic tumor: comparison of clinicopathologic, histologic, and immunohistochemical features including ALK expression in atypical and aggressive cases. Am J Surg Pathol. 2007;31:509–20.

Essary LR, Vargas SO, Fletcher CD. Primary pleuropulmonary synovial sarcoma: reappraisal of a recently described anatomic subset. Cancer. 2002;94:459–69.

Gleason BC, Hornick JL. Inflammatory myofibroblastic tumours: where are we now? J Clin Pathol. 2008;61:428–37.

Hartel PH, Fanburg-Smith JC, Frazier AA, Galvin JR, Lichy JH, Shilo K, Franks TJ. Primary pulmonary and mediastinal synovial sarcoma: a clinicopathologic study of 60 cases and comparison with five prior series. Mod Pathol. 2007;20:760–9.

Husain AN, Colby T, Ordonez N, Krausz T, Attanoos R, Beasley MB, et al. International mesothelioma interest. Guidelines for pathologic diagnosis of malignant mesothelioma: 2012 update of the consensus statement from the international mesothelioma interest group. Arch Pathol Lab Med. 2013;137:647–67.

Kadota K, Suzuki K, Sima CS, Rusch VW, Adusumilli PS, Travis WD. Pleomorphic epithelioid diffuse malignant pleural mesothelioma: a clinicopathological review and conceptual proposal to reclassify as biphasic or sarcomatoid mesothelioma. J Thorac Oncol. 2011;6:896–904.

Okamoto S, Hisaoka M, Daa T, Hatakeyama K, Iwamasa T, Hashimoto H. Primary pulmonary synovial sarcoma: a clinicopathologic, immunohistochemical, and molecular study of 11 cases. Hum Pathol. 2004;35:850–6.

Ordonez NG. Deciduoid mesothelioma: report of 21 cases with review of the literature. Mod Pathol. 2012a;25:1481–95.

Ordonez NG. Mesotheliomas with small cell features: report of eight cases. Mod Pathol. 2012b;25:689–98.

Ordonez NG. Pleomorphic mesothelioma: report of 10 cases. Mod Pathol. 2012c;25:1011–22.

Ordonez NG. Application of immunohistochemistry in the diagnosis of epithelioid mesothelioma: a review and update. Hum Pathol. 2013;44:1–19.

Thway K, Nicholson AG, Lawson K, Gonzalez D, Rice A, Balzer B, et al. Primary pulmonary myxoid sarcoma with EWSR1-CREB1 fusion: a new tumor entity. Am J Surg Pathol. 2011;35:1722–32.

Thway K, Nicholson AG, Wallace WA, Al-Nafussi A, Pilling J, Fisher C. Endobronchial pulmonary angiomatoid fibrous histiocytoma: two cases with EWSR1-CREB1 and EWSR1-ATF1 fusions. Am J Surg Pathol. 2012;36:883–8.

Weissferdt A, Moran CA. Primary vascular tumors of the lungs: a review. Ann Diagn Pathol. 2010;14:296–308.

Zhang PJ, Livolsi VA, Brooks JJ. Malignant epithelioid vascular tumors of the pleura: report of a series and literature review. Hum Pathol. 2000;31:29–34.

Index

A
Actinomycosis, 32, 36
Acute bronchiolitis, 78
Acute bronchopneumonia, 32, 33
Acute eosinophilic pneumonia (AEP), 102
Acute fibrinous and organizing pneumonia (AFOP), 106–108
Acute humoral rejection, *see* Antibody-mediated rejection (AMR)
Acute rejection, endothelialitis in, 151
Acute respiratory distress syndrome (ARDS), 45, 88
Adenocarcinoma in situ, 221–222
Adenomas, 206–208
Adenosquamous carcinoma, 234
Adenovirus pneumonia, 40
Adipose tissue, 4
Air spaces, 18, 20
Airway diseases, 65
Airway inflammation, 151
Allergic bronchopulmonary aspergillosis (ABPA), 52, 66, 67, 69
Aluminum pneumoconiosis, 163
Alveolar duct (AD), 1, 3
Alveolar septa, 28
Alveolar spaces, 28
Alveoli, 1
  high-magnification photomicrograph, 3
Amoebiasis, 61
Anaplastic large cell lymphoma, 197–198
Anaplastic lymphoma kinase (*ALK*) gene, 26
Angiomatoid fibrous histiocytoma, 270
Antibody-mediated rejection (AMR), 147
Apical cap, 11
Asbestosis, 159
Aspergilloma, 51
Aspergillus
  hyphae, 51
  infections, 51–55
  mycetoma, 51
Aspiration pneumonia, 82–86
Asthma, 66–70
Atretic bronchus, 13
Atypical adenomatous hyperplasia, 220

B
Bacterial pneumonia, 32–37
Basaloid squamous cell carcinoma, 233
Benign lung neoplasm
  adenomas, 206–208
  chondroma, 212–213
  etiology, 203
  granular cell tumors, 215
  hamartomas, 212–213
  papillomas, 204–205
  PEComa, 214
  pneumocytic adenomyoepithelioma, 216–217
  sclerosing pneumocytoma, 209–211
Berylliosis, 161
Biphasic malignant mesothelioma, 279
Biphasic synovial sarcoma, 269
Bland necrosis, 278
Blastomycosis, 44–46
Blue bodies, 10
Bronchiectasis, 70–73
Bronchiole(s), 1, 3, 9
Bronchiolitis, 78–80
  chronic, 79
  constrictive, 75, 76, 78
Bronchiolitis obliterans organizing pneumonia (BOOP), 96
Bronchioloalveolar carcinoma, *see* Adenocarcinoma in situ
Bronchoalveolar lavage fluid, 62
Bronchocentric granulomatosis, 84
Bronchovascular bundle, 1, 3
Bronchus, 2
Bubble artifact, *see* Pseudolipids

C
Candidiasis, 56–57
Carbon monoxide, 96
Carcinoid tumorlet, 9
Carcinoid tumors, 235–238
Cavitary coccidioidomycosis, 50
Centrilobular emphysema, 80
Chest wall soft tissues, 4
Chondroma, 212–213
Chronic airway rejection, 152
Chronic bronchiolitis, 78
Chronic eosinophilic pneumonia (CEP), 102
Chronic granulomatous disease, 56
Chronic obstructive pulmonary disease (COPD), 111
Chronic pneumonitis, of infancy, 28
Chronic thrombotic pulmonary hypertension, 166
Chronic vascular rejection, 153
Cigarette smoking, 111
Classic Hodgkin lymphoma, 199–201
Coal workers' pneumoconiosis (CWP), 160–161
Coccidioidomycosis, 49–51
Collagen fibrosis, 96
Congenital cystic adenomatoid malformation (CCAM), 16
Congenital pulmonary airway malformation (CPAM), 13, 16–18
Congenital pulmonary lymphangiectasia, 21
Congenital pulmonary overinflation, 18
Connective tissue disease (CTD)-associated lung diseases, 129–131

© Springer Science+Business Media, LLC, part of Springer Nature 2018

C. Zhang, J. L. Myers (eds.), *Atlas of Lung Pathology*, Atlas of Anatomic Pathology,
https://doi.org/10.1007/978-1-4939-8689-7

Constrictive (obliterative) bronchiolitis, 75–77
Corpora amylacea, 7
CPAM, *see* Congenital pulmonary airway malformation (CPAM)
Cryptococcosis, 46–49
Cryptococcus neoformans, 46
Cytomegalovirus (CMV) pneumonia, 39

D
DAD, *see* Diffuse alveolar damage (DAD)
Dendriform, 10
Dendriform ossification, 10
Desmoplastic mesothelioma, 278, 279
Desquamative interstitial pneumonia (DIP)
  CT, 113
  air spaces, 114
  with emphysema, 115
  in smoking-related interstitial fibrosis, 115
Diffuse alveolar damage (DAD), 58
  acute fibrinous and organizing pneumonia, 106–108
  to cytomegalovirus infection, 95
  early exudative phase, 90–91
  end-stage fibrosis, 94
  eosinophilic pneumonia, 102
  etiology, 88
  hyperplastic pneumocytes, 93
  organizing pneumonia, 96
  with patchy distribution, 89
  pneumocyte hyperplasia, 93
  with *Pneumocystis jiroveci*, 95
  proliferative phase, 91–94
  pulmonary alveolar proteinosis, 108
Diffuse bilateral bronchiectasis, 70
Diffuse bronchiectasis, 71
Diffuse idiopathic pulmonary neuroendocrine cell hyperplasia (DIPNECH), 9, 75
Diffuse interstitial lung diseases, 28
Diffuse lymphangiomatosis, 21
Diffuse malignant mesotheliomas, 272–280
Diffuse meningotheliomatosis, 8
Diffuse neuroendocrine cell hyperplasia, 76
Diffuse, nonneoplastic lung diseases
  acute and chronic disorders, 87
  acute fibrinous and organizing pneumonia, 106–107
  cigarette smoking, 111
  connective tissue disease, 129–131
  desquamative interstitial pneumonia, 113–115
  eosinophilic pneumonia, 102–105
  idiopathic interstitial pneumonias, 120
  Langerhans cell histiocytosis, 116–119
  lymphangioleiomyomatosis, 132–135
  noninfectious air space diseases, 96
  nonspecific interstitial pneumonia, 127–128
  organizing pneumonia, 96–101
  pulmonary alveolar proteinosis, 108–110
  respiratory bronchiolitis, 111
  smoking-related interstitial fibrosis, 112–113
  usual interstitial pneumonia, 120–126
Diffuse panbronchiolitis, 77–78
Diffuse pulmonary lymphangiomatosis, 22
Dirofilarial nodule, 61, 62
Distal acinar emphysema, 80
Dystrophic calcification, 10

E
Emphysema, 18, 80
Endothelial lining cells, 21
Eosinophilic granuloma, *see* Langerhans Cell Histiocytosis (LCH)
Eosinophilic granulomatosis with polyangiitis (EGPA), 177–178
Eosinophilic pneumonia, 102–105
Epithelial membrane antigen (EMA), 8
Epithelioid hemangioendothelioma, 263–269
Epithelioid malignant mesothelioma, 272–275, 279
Epithelium, 15
Extranodal marginal zone lymphoma of MALT, 184–190

F
Fetal lung interstitial tumor (FLIT), 26–27
Fibroelastosis, 11
Fibrosis, 10
Fibrotic hypersensitivity pneumonia, 140, 141
FLIT, *see* Fetal lung interstitial tumor (FLIT)
Follicular bronchiolitis, 183
Follicular lymphoma, 194
Fungal infections
  blastomycosis, 44–46
  candidiasis, 56–57
  coccidioidomycosis, 49–51
  cryptococcosis, 46–49
  histoplasmosis, 42–44
  invasive mucormycosis, 55–56
  Pneumocystis pneumonia, 57–60
  types, 42

G
Glucose transporter-1 (GLUT-1), 27
Gomori methenamine silver (GMS), 69
Granular cell tumors, 215
Granulomatosis with polyangiitis (GPA)
  ANCA test, 172
  BOOP-like, 175
  classic, 172, 173
  collagen necrosis, 172
  eosinophilic variant, 176
  hemorrhage and necrotizing capillaritis, 175
  vasculitis in, 174
Granulomatous microabscess, 35

H
Hamartomas, 212–213
Hard metal pneumoconiosis, 162
Herpes simplex virus (HSV) pneumonia, 39
High-grade lymphocytic bronchiolitis (B2R), 151
High-resolution computed tomography (HRCT) scans, 87
Histoplasmosis, 42–44
Human papillomavirus (HPV), 203
Hyperplasia, 9
Hyperplastic alveolar pneumocytes, lack of, 4
Hypersensitivity pneumonia, 137–140
  cellular interstitial pneumonia, 137
  chronic bronchiolitis, 139
  granulomatous inflammation, 139
  low-magnification photomicrograph, 138

I
Idiopathic interstitial pneumonias, 120
Infantile hemangioma, 27
Infantile hemangiomas, 27
Inflammatory myofibroblastic tumor (IMT), 255–258
Influenza virus H1N1 pneumonia, 41

Interlobular septum, 21
Intra-alveolar hemorrhage, 4
Intralobar pulmonary sequestration, 14
Intravascular large B-cell lymphoma, 196
Invasive adenocarcinoma, 225–229
Invasive aspergillosis, 52, 53
Invasive mucormycosis, 55–56
Invasive squamous cell carcinoma, 231–232

L
Lamellar bone spicules, 10
Langerhans cell histiocytosis (LCH)
  centrally cystic nodule, 117
  characteristics, 116
  CT, 116
  diagnosis, 116
  late-stage, 117
  lung wedge biopsy, 117
  multiple cellular, stellate nodules, 117
  stellate-shaped scar, 118, 119
Large cell carcinoma, 244–245
Large cell neuroendocrine carcinoma, 242–243
Legionnaires' disease, 32, 34
Lobectomy, 27
Low-grade lymphocytic bronchiolitis (B1R), 151
Lung
  fluke, 62
  infections, 31
  low-magnification photomicrograph, 4
  outer surface, 1
  parenchyma, 11
  structure, 1
Lymphangioleiomyomatosis (LAM), 132–135
Lymphangitic distribution, 1
Lymphatic channels, 22
Lymphatic spaces, 22
Lymphatics, 1
Lymphoid interstitial pneumonia, 183–184
Lymphomatoid granulomatosis, 191–194

M
Malakoplakia, 32, 36
Maldeveloped air spaces, 26
Maldeveloped parenchymal cysts, 14
Mantle cell lymphoma, 194–195
Measles pneumonia, 40
Mediastinum/chest wall adipose tissue, 4
Megakaryocytes, 10
Meningothelial-like nodule (MLN), 8
Meningothelium, 8
Mesothelioma
  deciduoid features, 275
  with heterologous differentiation, 277
  pleomorphic cytology, 275
  solid growth pattern, 275
Metastatic adenocarcinoma, 279
Metastatic calcification, 10
Michaelis-Gutmann body, 36
Mild acute cellular rejection (A2), 149
Mild chronic inflammation, 11
Minimal acute cellular rejection (A1), 149
Minimally invasive adenocarcinoma, 223–224
Mixed dust fibrosis, 158
Moderate acute cellular rejection (A3), 150
Monophasic synovial sarcoma, 269
Mucinous epithelium, 17
Mucoid impaction of bronchi (MIB), 52, 68
Mucosa-associated lymphoid tissue (MALT), 181
  extranodal marginal zone lymphoma, 184–190
Multiloculated cystic lesion, 22
Multiple air-filled cysts, 19
Multiple small cysts, 17
Mycobacterial disease, 37
Mycobacterium avium complex (MAC), 37, 140
Mycobacterium tuberculosis infection, 37

N
Necrotizing granulomatous inflammation, 49
Necrotizing tracheobronchitis, 54
Neuroendocrine cell hyperplasia, 9
Neuroendocrine markers, 9
Neuroendocrine tumors
  carcinoid, 135–238
  large cell carcinoma, 244–245
  large cell neuroendocrine carcinoma, 242–243
  salivary gland-type carcinomas, 251–252
  sarcomatoid carcinoma, 246–250
  small cell carcinoma, 239–241
Nocardia pneumonia, 32, 35
Nocardiosis, 32
Nodular lymphoid hyperplasia, 181–182
Nodular metaplastic ossification, 9
Nodular sarcoidosis, 143
Nonspecific interstitial pneumonia (NSIP), 127–128
Nontuberculous mycobacteria infection, 38
Nontuberculous mycobacterial infection, 38
North American blastomycosis, 44
NSIP, *see* Nonspecific interstitial pneumonia (NSIP)
Nuclear chromatin, 9

O
Obliterative bronchiolitis, 152
Osseous metaplasia, 9
Overinflation, 18

P
Panacinar emphysema, 80
Papillomas, 204–205
Paragonimiasis, 62
Paraseptal emphysema, 80, 81
PEComa, 214
Pediatric disorders, 13
Peribronchiolar metaplasia, 78, 79
Periodic acid–Schiff (PAS), 29
Phospholipoproteinosis, 108
Placental transmogrification, 80, 81
Plastic bronchitis, 73–74
Pleural tissue, 4
Pleuropulmonary blastoma, 22–24
  with chondrosarcomatous differentiation, 25
Pneumoconiosis
  aluminum pneumoconiosis, 163
  asbestosis, 159
  berylliosis, 161
  coal workers' pneumoconiosis, 160–161
  hard metal pneumoconiosis, 162
  mixed dust fibrosis, 158
  silicosis, 155–157
Pneumocystis pneumonia, 57–60, 106
Pneumocytic adenomyoepithelioma, 216–217
Posttransplant lymphoproliferative disorder (PTLD), 197

Primary pulmonary myxoid sarcoma, 270, 271
Proteinaceous lymphatic fluid, 21
Protozoal and parasitic infestations, 60
Proximal acinar structures, 1
Pseudolipids, 4
Pseudoneoplasm, 11
Pulmonary acinus, 1
Pulmonary allograft rejection, 148
Pulmonary alveolar lipoproteinosis, 108
Pulmonary alveolar proteinosis (PAP), 108–110
Pulmonary arterial hypertension, 166–167
  capillary hemangiomatosis, 171
  chronic congestive changes, 171
  in chronic fibrotic disease, 168
  fat emboli, 168
  intravenous drug abusers, 168–169
  with necrotizing arteritis, 168
  pulmonary veno-occlusive disease, 169–170
Pulmonary hypertension, 166
Pulmonary infections, 31
Pulmonary interstitial emphysema, 19, 20
Pulmonary interstitial glycogenosis, 28, 29
Pulmonary lymphangiectasia, 21
Pulmonary lymphoproliferative diseases
  anaplastic large cell lymphoma, 197–198
  classic Hodgkin lymphoma, 199–201
  extranodal marginal zone lymphoma of MALT, 184–190
  extranodal natural killer/T-cell lymphoma, 198
  follicular bronchiolitis, 183
  follicular lymphoma, 194
  intravascular large B-cell lymphoma, 195–196
  lymphoid interstitial pneumonia, 183–184
  lymphomatoid granulomatosis, 191–193
  MALT, 181
  Mantle cell lymphoma, 194–195
  nodular lymphoid hyperplasia, 181–182
  posttransplant lymphoproliferative disorder, 197
Pulmonary sequestration, 13–16
Pulmonary vascular diseases
  eosinophilic granulomatosis with polyangiitis, 177–178
  granulomatosis with polyangiitis, 172–176
  noninflammatory vascular disorders, 165–171
Pulmonary veno-occlusive disease (PVOD), 166

R
Respiratory bronchiole (RB), 3
Respiratory bronchiolitis (RB), 74–75, 111
Respiratory syncytial virus (RSV) pneumonia, 41
Rhabdomyoblastic differentiation, 23
Rhabdomyosarcoma-like area, 24
Rhodococcus equi pneumonia, 32, 36
Round atelectasis, 11

S
Salivary gland-type carcinomas, 251–252
Sarcoidosis, 142
  cytoplasmic inclusions, 144
  high-magnification photomicrograph, 143
  in transbronchial and endobronchial biopsies, 145
  low-magnification photomicrograph, 142, 144
  non-necrotizing granulomas, 143
Sarcomatoid carcinoma, 246, 250
Sarcomatoid mesothelioma, 272, 276
Sclerosing pneumocytoma, 209–211
Severe acute cellular rejection (A4), 150
Silicosis, 155–157
Small cell carcinoma, 239–241
Smoking-related interstitial fibrosis (SRIF), 112–113
Solid cystic lesion, 14
Solitary capillary hemangiomas, 27
Solitary fibrous tumor, 258–262
Solitary fibrous tumors, 258–263
Squamous cell carcinoma in situ, 230
SRIF, *see* Smoking-related interstitial fibrosis (SRIF)
Strongyloidiasis, 62
Synovial sarcoma, 269–270
Systemic feeding artery, 13

T
Toxoplasmosis, 60
Tuberculosis, 37
Type 1 CPAM, 17
Type I pleuropulmonary blastoma, 22
Type II pneumocytes, 1
Types II and III pleuropulmonary blastoma, 22

U
Usual interstitial pneumonia (UIP)
  alveolar pneumocyte hyperplasia, 123
  architectural distortion, 122
  with coexisting carcinoma, 126
  with coexisting emphysema, 125
  with coexisting eosinophilic pneumonia, 126
  CT scan, 120
  cystic changes, 121
  with diffuse alveolar damage, 124
  end-stage, 121
  honeycomb changes, 121, 123
  patchwork and random distribution, 122
  plump spindle-shaped fibroblasts and myofibroblasts, 122
  temporal heterogeneity, 122
  vascular changes in, 124

V
Viral pneumonia, 39–42

W
Wegener granulomatosis, *see* Granulomatosis with polyangiitis (GPA)
Woven bone, 9